CONFERENCE PROCEEDINGS

Low-dimensional thermoelectric materials

M. S. Dresselhaus

Department of Electrical Engineering and Computer Science and Department of Physics, Massachusetts Institute of Technology, Cambridge MA 02139-4307

G. Dresselhaus

Francis Bitter Magnet Laboratory, Massachusetts Institute of Technology, Cambridge, MA 02139-4307

X. Sun, Z. Zhang, and S. B. Cronin

Department of Physics, Massachusetts Institute of Technology, Cambridge MA 02139-4307

T. Koga

Division of Engineering and Applied Sciences, Harvard University, Cambridge, MA 02138
Fiz. Tverd. Tela (St. Petersburg) **41**, 755–758 (May 1999)

The promise of low dimensional thermoelectric materials for enhanced performance is reviewed, with particular attention given to quantum wells and quantum wires. The high potential of bismuth as a low-dimensional thermoelectric material is discussed. © *1999 American Institute of Physics.* [S1063-7834(99)00105-7]

Professor Abram Ioffe and his collaborators at the Ioffe Institute in St. Petersburg, Russia did pioneering work[1] in introducing semiconductors as promising thermoelectric materials and in showing how semiconductors could be used in practical devices for cooling and for electrical power generation.[1] This early work led to a very active period in thermoelectrics research in the 1950s and early 1960s, when many new thermoelectric materials were discovered and investigated. At this early time, the high potential of Bi_2Te_3 as a thermoelectric material was discovered by H. J. Goldsmid and coworkers in the U.K.,[2] and this material system remains the basis for the thermoelectric industry up to the present time.[3] Ioffe's proposal to employ semiconductor alloys rather than simple binary compounds in order to lower the thermal conductivity of semiconductors[4] proved very useful for thermoelectric applications, thereby leading to the industrial use of alloys in the Bi_2Te_3, Bi_2Se_3, and Sb_2Te_3 family.

For a 30 year period since the early 1960s, research activity in the field of thermoelectricity has been greatly reduced, and only modest progress was made in improving the performance of thermoelectric materials.[3] Recently, the study of thermoelectric materials has once again become an active research field, in part due to the recent demonstration of enhancement in the thermoelectric figure of merit of a two-dimensional PbTe quantum-well system, relative to its three-dimensional (3D) bulk counterpart.[5] Calculations suggest that the thermoelectric performance of any 3D material should show an enhanced thermoelectric figure of merit, when prepared as a 2D multi-quantum-well superlattice, by utilizing the enhanced density of states at the onset of each electronic subband and the increased scattering of vibrational waves at the boundary between the quantum well and the adjacent barrier of the superlattice. In addition, low dimensionality allows certain materials such as bismuth, which are poor thermoelectrics in 3D, to become good thermoelectrics, in principle, in 2D quantum-well or 1D quantum-wire structures.

It is customary to express the usefulness of a thermoelectric material for use in refrigeration or power generation applications in terms of the dimensionless quantity ZT where T is the temperature (in degrees Kelvin) and Z is the thermoelectric figure of merit

$$Z=\frac{S^2\sigma}{\kappa}. \tag{1}$$

Here S is the thermoelectric power or Seebeck coefficient, σ is the electrical conductivity and κ is the thermal conductivity. Large values of ZT require high S, high σ, and low κ. Since an increase in S normally implies a decrease in σ because of carrier density considerations, and since an increase in σ implies an increase in the electronic contribution to κ as given by the Wiedemann–Franz law, it is very difficult to increase Z in typical thermoelectric materials. The best commercial 3D thermoelectric material is in the $Bi_{2(1-x)}Sb_{2x}Te_{3(1-y)}Se_{3y}$ family with room temperature $ZT\approx 1$ for $Bi_{0.5}Sb_{1.5}Te_3$.[3]

Reduced dimensionality offers one strategy for increasing ZT relative to bulk values.[6,7] The use of low-dimensional systems for thermoelectric applications is of interest because low dimensionality provides: (1) a method for enhancing the density of states near E_F, leading to an enhancement of the Seebeck coefficient, (2) opportunities to take advantage of the anisotropic Fermi surfaces in multi-valley cubic semiconductors, (3) opportunities to increase the boundary scattering

of phonons at the barrier-well interfaces, without as large an increase in electron scattering at the interface, (4) opportunities for increased carrier mobilities at a given carrier concentration when quantum confinement conditions are satisfied, so that modulation doping and δ-doping can be utilized.

1. THEORETICAL MODELING

In early models for thermoelectricity in 2D quantum-well structures[6–9] it was assumed that the electrons in the valence and conduction bands are in simple parabolic energy bands and that the electrons occupy only the lowest subband of the quantum well. The electronic dispersion relations for a 2D system are then given by

$$\mathcal{E}_{2D}(k_x,k_y)=\frac{\hbar^2k_x^2}{2m_x}+\frac{\hbar^2k_y^2}{2m_y}+\frac{\hbar^2\pi^2}{2m_zd_W^2}, \tag{2}$$

where d_W is the width of the quantum well, and m_x, m_y, and m_z are the effective mass tensor components of the constant energy surfaces. It is further assumed that the current flows in the x direction and that quantum confinement is in the z direction. The corresponding relation used for a square 1D quantum wire is

$$\mathcal{E}_{1D}(k_x)=\frac{\hbar^2k_x^2}{2m_x}+\frac{\hbar^2\pi^2}{2m_yd_W^2}+\frac{\hbar^2\pi^2}{2m_zd_W^2}, \tag{3}$$

where the current flow is also along the x direction, and quantum confinement occurs in the y and z directions. Solutions of Boltzmann's equation were then obtained for S, σ, and κ_e (the electronic contribution to the thermal conductivity) for both the 2D and 1D systems.[6,9–11]

2. EXPERIMENTAL PROOF-OF-PRINCIPLE

An early phase of the experimental work was devoted to showing proof-of-principle,[5] in order to confirm the validity of the basic theoretical model for low dimensional thermoelectric materials.[6,9] PbTe was chosen as the quantum-well material for demonstrating proof-of-principle of an enhanced ZT in a 2D system because of its desirable thermoelectric and materials properties.[12,13] Regarding its thermoelectric properties, PbTe has a reasonably high ZT at 300 K in bulk form ($ZT\simeq 0.4$), reflecting its high carrier mobility, multiple anisotropic carrier pockets, and low thermal conductivity that can be achieved by isoelectronic alloying. Measurements of $S^2\sigma$ by Hicks *et al.*[5] corroborated that quantum confinement could be achieved in a $PbTe/Pb_{1-x}Eu_xTe$ superlattice, for $x=0.073$, by using large barrier widths $d_b \gg d_W$. Good agreement between experiment and theory was demonstrated in plots of $S^2\sigma$ as a function of carrier concentration and quantum-well width, thereby corroborating the model, using no adjustable parameters (only literature values measured by other techniques).[5] High carrier mobilities were found for these superlattice samples.[5]

3. RECENT 2D SUPERLATTICE STUDIES

Having demonstrated experimental evidence in support of the basic theoretical model, the focus of research on low-dimensional thermoelectricity has shifted to two new directions. One research direction focused on observations of the enhancement of ZT in other 2D superlattice systems, so that the basic phenomenon could then be studied in more detail, and the barrier widths could be reduced, noting that the barrier regions contribute only to κ in Eq. (1) and not to the power factor $S^2\sigma$. Some of the systems that were studied include *p*-type PbTe, where power factors higher than for *n*-type PbTe were reported, while at the same time using d_b/d_W ratios reduced by a factor of more than two, relative to *n*-type PbTe.[14] Another superlattice system that was studied was the Si/SiGe system, where an increase in the room-temperature power factor of the superlattice relative to the bulk silicon value was predicted, and where even better performance could be expected at elevated ($\gg 300$ K) temperatures.[15]

As a second approach, achieving higher $Z_{3D}T$ for the whole superlattice sample (both for the quantum well and barrier regions) and to studying superlattices which do not show quantum confinement effects[16] was emphasized. By using the same basic model, as was developed for the $PbTe/Pb_{1-x}Eu_xTe$ superlattice, study the GaAs/AlAs superlattice, it was shown that, when the d_W and d_b values are sufficiently small, the electronic density of states is basically two-dimensional in both the quantum well and barrier regions,[17] and an increase in power factor relative to bulk values could be achieved. One great advantage of allowing conduction in both the barrier and the quantum-well region is that much smaller barrier widths can be used and a significant contribution to $S^2\sigma$ from the barrier region can be obtained. The gains in $S^2\sigma$ from the quantum-well region relative to bulk values more than compensate for the somewhat lower contribution to $S^2\sigma$ from the barrier region, so that $S^2\sigma$ for the whole superlattice (denoted by $Z_{3D}T$) exceeds that of the bulk. In addition, a large reduction in thermal conductivity is expected, due to the strong interface phonon scattering, so that significant increases in $Z_{3D}T$ are expected from this approach.

Calculations suggest that another effect that may come into play relates to carrier pocket engineering, where by proper selection of d_W, d_b and their ratio (d_b/d_W), it is possible to raise the energy of the lowest Γ-point subband so that it lies higher than the *L*- and *X*-point subbands, thereby leading to an enhancement of $Z_{3D}T$ because of the high density of states for the *L*- and *X*-point subbands.[17] Simple calculations suggest that such carrier pocket engineering can be carried out in the case of GaAs/AlAs superlattices with d_W and d_b in the 20–30 Å range.[17]

Experimentally, enhancement in the power factor and $Z_{3D}T$ have been reported for several superlattice systems not exhibiting quantum carrier confinement effects, including the Bi_2Te_3/Bi_2Se_3,[16] $PbTe/PbSe_{1-x}Te_x/Te$ ($x=0.02$),[18] and Si/Ge systems.[19] In fact, the highest ZT value ever reported for any thermoelectric material is $Z_{3D}T=1.9$ for the $PbTe/PbSe_{1-x}Te_x/Te$ system ($x=0.02$) at 570 K.[18] It is expected that we will see considerably more activity in the near future, both experimentally and theoretically, on the study of such composite superlattice systems, which may exhibit some type of lower dimensional electronic properties, but do not

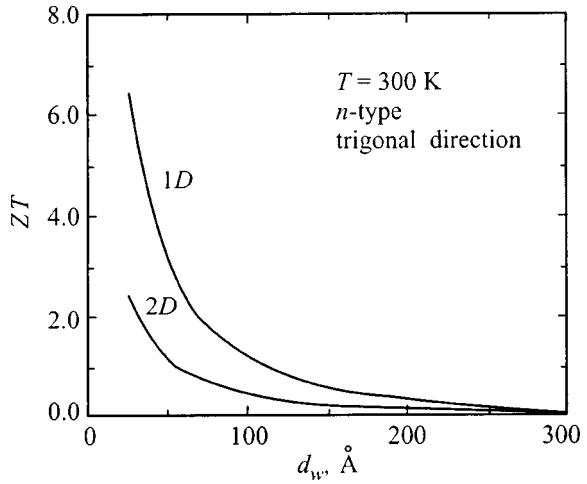

FIG. 1. Dependence of $Z_{2D}T$ and $Z_{1D}T$ on quantum-well and quantum-wire widths d_W for the layers of the Bi quantum wells normal to the trigonal direction and the Bi wire axis along the trigonal direction.

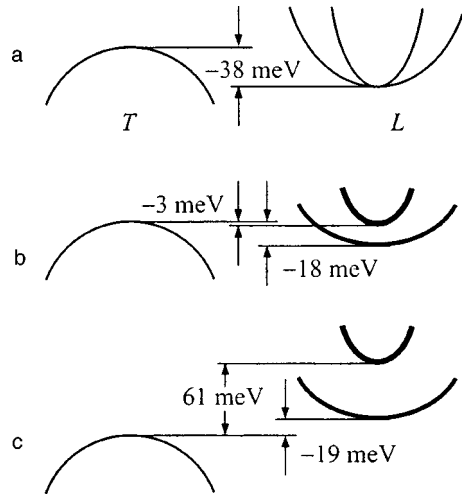

FIG. 2. Schematic energy band diagram showing the energies of the subband edges for the heavy and light electrons and for the holes for: (a) bulk Bi, (b) 100 nm diameter Bi nanowires along the bisectrix direction, and (c) 50 nm diameter Bi nanowires along the bisectrix direction.

exhibit significant carrier quantum confinement.

4. BISMUTH AS A LOW DIMENSIONAL THERMOELECTRIC

Bismuth is a very attractive material for low-dimensional thermoelectricity because of the large anisotropy of the three ellipsoidal constant energy surfaces for electrons at the L point in the rhombohedral Brillouin zone ($m_x^* = 0.00651m_0$, $m_y^* = 1.362m_0$, $m_z^* = 0.00993m_0$), the very long mean free path of the L-point electrons, and the high mobility of the carriers ($\mu = 3.5\times10^4$ cm^2/Vs in the binary direction).[20] Furthermore, the heavy mass of the Bi ions results in efficient phonon scattering and low phonon mean free paths. Since bulk bismuth is a semimetal, the contribution from the holes to the Seebeck coefficient approximately cancels that for the electrons, so that S is quite small, and high magnetic fields are needed to make bulk Bi interesting for thermoelectric applications.[21]

The situation for 2D Bi in a quantum well is, however, quite different. As the quantum well width decreases, the lowest bound state in the conduction band rises above the highest bound state in the valence band, thereby leading to a semimetal–semiconductor transition at some critical value of d_W.[11] If the 2D bismuth system is then doped to the optimum doping level, a large enhancement in $Z_{2D}T$ within the quantum well is predicted with decreasing d_W, as shown in the plot of $Z_{2D}T$ vs d_W in Fig. 1 for a Bi superlattice normal to the trigonal direction, for which all the electron carrier pockets are equivalent. Considerable progress has been made recently by use of CdTe as a barrier material for synthesizing Bi quantum wells.[22] While study of 2D Bi superlattices continues, recent effort has also been expended to study 1D bismuth nanowires.[23,24] Calculations for transport in the trigonal direction indicate that 1D bismuth nanowires with very small wire diameter could be even better than 2D bismuth for thermoelectric applications (see Fig. 2).

Although no enhancement in ZT has yet been demonstrated experimentally with Bi nanowires, progress has been made toward making proof-of-principle studies of this system. Small diameter Bi wires have been successfully fabricated by pressure-injecting liquid Bi into the cylindrical nano-channels of a porous anodic alumina template.[23] Such anodic alumina templates with pore diameters ranging from 13–110 nm have been filled with liquid Bi to reach a density as high as 7×10^{10} parallel wires/cm^2, with template thicknesses and wire lengths up to 100 μm. As shown by high resolution electron microscopy and selected area electron diffraction experiments, the individual Bi nanowires are essentially single crystals, with nearly the same crystal structure and lattice parameters as bulk Bi. The individual wires are of uniform diameter along their entire length, and the nanowires in a given template have a similar crystal orientation along their common wire axes.[23] The large bandgap of the anodic alumina host material ensures good carrier quantum confinement. Optical transmission[23] and magnetoresistance studies[24–26] provide evidence for a semimetal to semiconducting transition as the wire diameter decreases and reaches the critical diameter d_c, below which a semiconducting gap is found. Our theoretical calculations, based on values of the effective masses for bulk bismuth, indicate on the basis of a simple parabolic band model for the electron states, that for the binary, trigonal and bisectrix directions, $d_c \approx 30$ nm, 45 nm and 81 nm, respectively.[24]

Figure 2 shows a schematic diagram of the electronic energy-band structure for bismuth nanowires in comparison to bulk bismuth, which is a semimetal with electrons in 3 carrier pockets at the L points in the rhombohedral Brillouin zone and holes in a single carrier pocket at the T point, and the band overlap of bulk Bi is 38 meV.[20] For Bi nanowires oriented along the bisectrix direction, there are two electron pockets in which the electrons have a heavy cyclotron effective mass (m_c^h) and one electron pocket with a light cyclotron effective mass (m_c^l), where the cyclotron mass is an average for the in-plane motion. Figures 2b and 2c show schematically the calculated ground state energies of the heavy electron and light electron subbands and also the hole subband for a Bi wire oriented along the bisectrix direction

with a diameter of 100 nm and 50 nm, respectively, in comparison to the bulk Bi band structure shown in Fig. 2a.[24] Here we see that the lowest heavy electron subband lies lower than the corresponding light electron subband. Figure 2 further shows that the 100 nm wire is a semimetal with a small band overlap of 3 meV, and thermal energy (25 meV) is sufficient to cause significant occupation of the light electron subband. However, the 50 nm diameter wire along the bisectrix direction is a semiconductor and thermal excitation excites only heavy electrons. Thus, we can expect rather different transport properties for a 100 nm and a 50 nm diameter wire.

Experimental transport studies are in progress to verify the predictions of the model for semiconducting bismuth for small wire diameters. In the semiconducting regime, work is in progress to estimate the thermoelectric properties of the bismuth nanowires theoretically and to measure them experimentally, focusing on the conditions needed for realizing an enhancement in ZT.

5. CONCLUSIONS

Some of the recent achievements that have been made in the use of low-dimensional materials for thermoelectric applications include a $ZT \sim 1.2$ within *n*-type PbTe quantum wells at room temperature.[5] Higher values are expected for this system at higher temperatures. The highest value of ZT for any thermoelectric material under any conditions ($ZT > 1.9$) was achieved for a $PbTe/PbSe_{0.98}Te_{0.02}/Te$ superlattice at 570 K (Ref. 18) where the system showed no quantum confinement effects. Since research in this field is still at an early stage of development, significantly more progress in enhancing ZT further is expected for the future. It is thus appropriate to review recent progress on thermoelectric materials in celebration of the 80th birthday of the Ioffe Institute, which has made so many important historical contributions to the field of thermoelectricity.

The authors would like to thank T. C. Harman, J. P. Heremans, G. Chen, J. Ying, and K. L. Wang for valuable discussions.

The authors gratefully acknowledge support by the US Navy under Contract N N00167-98-K-0024 (MIT), and ONR under MURI (UCLA). Support from the Honda Corporation for temperature dependent studies is gratefully acknowledged.

[1] A. F. Ioffe, in *Semiconductor Thermoelements and Thermoelectric Cooling* (Infosearch, London, 1956).
[2] H. J. Goldsmid and R. W. Douglas, Br. J. Appl. Phys. **5**, 386, 458 (1954).
[3] H. J. Goldsmid, in *Electronic Refrigeration* (Pion, London, 1986).
[4] A. F. Ioffe, S. V. Airapetyants, A. V. Ioffe, N. V. Kolomoets, and L. S. Stil'bans, Dokl. Akad. Nauk SSSR **102**, 981 (1956).
[5] L. D. Hicks, T. C. Harman, X. Sun, and M. S. Dresselhaus, Phys. Rev. B **53**, 10493 (1996).
[6] L. D. Hicks and M. S. Dresselhaus, Phys. Rev. B **47**, 12727 (1993).
[7] M. S. Dresselhaus, T. Koga, X. Sun, S. B. Cronin, K. L. Wang, and G. Chen, in *16th International Conference on Thermoelectrics: Proceedings, ICT'97; Dresden, Germany*, edited by A. Heinrich and J. Schumann, p. 12–20.
[8] M. S. Dresselhaus, X. Sun, S. B. Cronin, T. Koga, G. Dresselhaus, K. L. Wang, in *Thermoelectric Materials – New Directions and Approaches: MRS Symposia Proceedings, San Francisco*, Vol. 478, edited by T. M. Tritt, M. G. Kanatzidis, H. B. Lyon, Jr., and G. D. Mahan (Materials Research Society Press, Pittsburgh, PA, 1997), p. 55.
[9] L. D. Hicks and M. S. Dresselhaus, Phys. Rev. B **47**, 16631 (1993).
[10] Lyndon D. Hicks, ''The effect of quantum-well superlattices on the thermo-electric figure of merit,'' PhD thesis, Department of Physics, Massachusetts Institute of Technology (1996).
[11] L. D. Hicks, T. C. Harman, and M. S. Dresselhaus, Appl. Phys. Lett. **63**, 3230 (1993).
[12] Shu Yuan, H. Krenn, G. Springholz, and G. Bauer, Phys. Rev. B **47**, 7213 (1993).
[13] G. Springholz, G. Ihninger, G. Bauer, M. M. Oliver, J. Z. Pastalan, S. Romaine, and B. B. Goldberg, Appl. Phys. Lett. **63**, 2908 (1993).
[14] T. C. Harman, D. L. Spears, D. R. Calawa, S. H. Groves, and M. P. Walsh, in *16th International Conference on Thermoelectrics: Proceedings, ICT'97; Dresden, Germany*, edited by A. Heinrich and J. Schumann p. 416.
[15] X. Sun, G. Chen, K. Wang, and M. S. Dresselhaus, in *17th International Conference on Thermoelectrics: Proceedings, ICT'98; Nagoya, Japan*, edited by Kunihito Koumoto, (Institute of Electrical and Electronics Engineers, Inc., Piscataway, 1998).
[16] R. Venkatasubramanian, in *17th International Conference on Thermoelectrics: Proceedings, ICT'98; Nagoya, Japan*, edited by Kunihito Koumoto (Institute of Electrical and Electronics Engineers, Inc., Piscataway, 1998).
[17] T. Koga, X. Sun, S. B. Cronin, and M. S. Dresselhaus, Appl. Phys. Lett., in press.
[18] T. Harman *et al.*, in *The 40th Electronic Materials Conference. Charlottesville, VA, USA*, (1998), abstract.
[19] H. Kato, A. Yamamoto, M. Takimoto, T. Ohta, K. Sakamoto, K. Miki, L. Whitlow, K. Kamisako, and T. Matsui, in *17th International Conference on Thermoelectrics: Proceedings, ICT'98; Nagoya, Japan*, edited by Kunihito Koumoto (Institute of Electrical and Electronics Engineers, Inc., Piscataway, 1998).
[20] V. S. Edel'man, Adv. Phys. **25**, 555 (1976).
[21] K. F. Cuff, R. B. Horst, J. L. Weaver, S. R. Hawkins, C. F. Kooi, and G. M. Enslow, Appl. Phys. Lett. **2**, 145 (1963).
[22] S. Cho, A. DiVenere, G. K. Wong, and J. B. Ketterson, in *16th International Conference on Thermoelectrics: Proceedings, ICT'97; Dresden, Germany*, edited by Armin Heinrich and Joachim Schumann (Institute of Electrical and Electronics Engineers, Inc., Piscataway, 1997), p. 188.
[23] Z. Zhang, J. Y. Ying, and M. S. Dresselhaus, J. Mater. Res. **13**, 1745 (1998).
[24] Z. Zhang, X. Sun, M. S. Dresselhaus, J. Y. Ying, and J. Heremans, Appl. Phys. Lett. **73**, 1589 (1998).
[25] J. P. Heremans, C. M. Thrush, Z. Zhang, X. Sun, M. S. Dresselhaus, J. Y. Ying, and D. T. Morelli, Phys. Rev. B **58**, R10091 (1998).
[26] M. Gurvitch, J. Low Temp. Phys. **38**, 777 (1980).

Published in English in the original Russian journal. Reproduced here with stylistic changes by the Translation Editor.

Electronic properties of quasi-one-dimensional compounds with a charge/spin-density wave ground state

P. Monceau

Centre de Recherches sur les Trés Basses Températures, associé á l'Université Joseph–Fourier, CNRS, BP 166, 38042 Grenoble cedex 9, France

Fiz. Tverd. Tela (St. Petersburg) **41**, 759–763 (May 1999)

First, a review of the general properties of the collective transport induced by the charge (CDW)/spin (SDW) density wave motion in quasi-one-dimensional conductors is presented. Then the three recent developments in this field are emphasized, namely: high spatial resolution x-ray study of the field-induced CDW deformations; quantum interference effects in magnetotransport of a sliding CDW through columnar defects; manifestation of disorder in the CDW/SDW ground state in thermodynamic properties at very low temperatures. © *1999 American Institute of Physics.* [S1063-7834(99)00205-1]

1. COLLECTIVE TRANSPORT IN QUASI-ONE-DIMENSIONAL SYSTEMS

Collective transport phenomena are among the most fascinating properties in solid state phisics. The best known example is superconductivity where the energy gap in the excitations at the Fermi level, as found by BCS, does not prevent conductivity. This is so because the interaction involved does not require a specified reference frame and because Coopers pairs can be built either in states ''k and $-k$'' or ''$k+\kappa$ or $-k+\kappa$.'' The latter state leads to a uniform velocity such as $mv_s=\hbar\kappa$.

However in 1954, before BCS, Frölich[1] proposed a model in a jellium approximation in which a sliding charge-density wave (CDW) could lead to a superconducting state. It is now well recognized that in systems of restricted dimensionality the interaction between ions and electrons, the so-called electron–phonon interaction, leads to structural (Peierls) instabilities at low temperature. According to the relative strength of several electron–electron coupling, the modulated ground state can be a CDW or, if the spin orientation is concerned, a spin–density wave (SDW).

Below the Peierls transition temperature T_p, the system is driven in a modulated state of the conduction electron density: $\rho(x)=\rho_0[1+\cos(Q_0x+\phi)]$, accompanied by a periodic lattice distortion of the same wavelengh, $2\pi/Q_0$, where $Q_0=2k_F$ is the modulation wave vector (generally incommensurate; k_F is the electronic Fermi momentum). The new periodicity opens a Fermi surface gap in the electron density of states and leads to the appearance of new satellite Bragg reflections.

The opening of a gap below the Peierls transition temperature is reminiscent of semiconductors, but the essential feature of a CDW is that its wavelength, $\lambda_{CDW}=2\pi/2k_F$, is controlled by the Fermi surface dimensions and is generally unrelated to the undistorted lattice periodicities, i.e., the CDW is incommensurate with the lattice. Consequently the crystal no longer has a translation group and in contrast to semiconductors, the phase ϕ of the lattice distortion is not fixed relative to the lattice but is able to slide along q. This phenomenon is easy to understand if we recognize that if the lattice is regular, no position is energetically favored and no locking results. In more theoretical terms: if we think of the CDW as resulting from an electronic interaction via the lattice phonons, this interaction is the same in every galilean frame, provided that the frame velocity is small compared to the sound velocity. CDW condensation may thus arise in any set of galilean frames with uniform velocity, v, giving in the laboratory frame an electronic current density,

$$J=-n_0ev, \tag{1}$$

where n_0 is of the order of the electron number density condensed in the band below the CDW gap. This Frölich mode is a direct consequence of translation invariance. In practice, as shown by Lee, Rice and Anderson[2] this translation invariance is broken because the phase, ϕ, can in fact be pinned to the lattice, for example, by impurities or by a long–period commensurability between the CDW wave–length and the lattice or by Coulomb interaction between adjacent chains. An applied dc electric field, however, can supply the CDW with an energy sufficient to overcome the pinning, so that above a threshold field, the CDW can slide and carry a current. Unfortunately, damping prevents superconductivity. This extra conductivity associated with the collective CDW motion, called Frölich conductivity, has been observed[3] for the first time in 1976 and since that time, an intense experimental and theoretical activity has been devoted to the understanding of the properties of this collective transport model.[4,5]

Non-linear transport properties have been observed in transition metal trichalcogenides as $NbSe_3$, TaS_3, halogened transition metal tetrachalcogenides as $(TaSe_4)_2I$, $(NbSe_4)_{10}I_3$, in molybdenum oxide $K_{0.3}MoO_3$, etc. A similar behavior has also been found in SDW organic Bechgaard salts $(TMTST)_2X$.

The properties of the new current-carrying state can be summarized as follows.

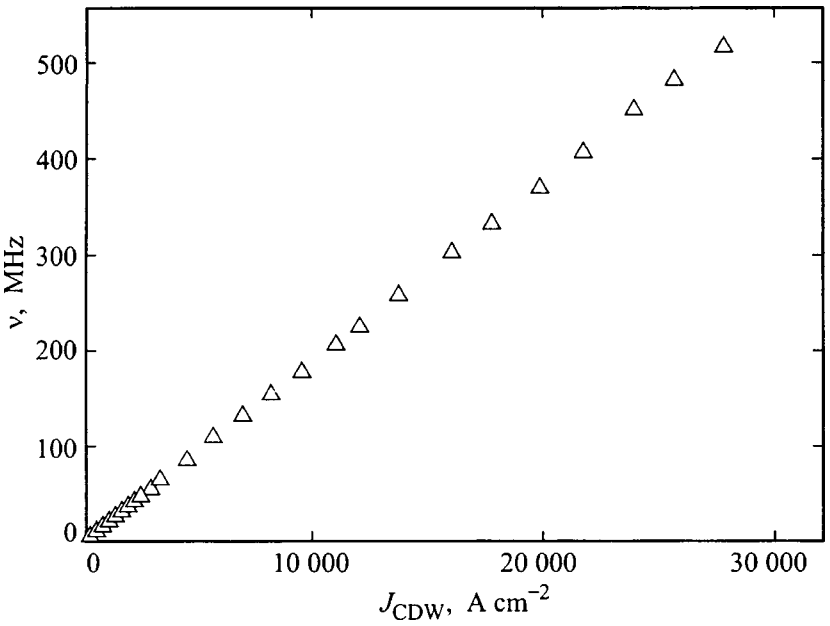

FIG. 1. Variation of the current J_{CDW} carried by the CDW as a function of the fundamental frequency measured in the Fourier-transformed voltage for an orthorhombic TaS_3 sample at $T=127$ K. The slope $J_{CDW}/\nu = ne\lambda_{CDW}$ leads to the number of electrons condensed below the CDW gap.

The dc electrical conductivity increases above a threshold field E_T.

The conductivity is strongly frequency-dependent in the range of 100 MHz to a few GHz.

Above the threshold field, noise is generated in the crystal which can be analyzed as the combination of a periodic time dependent voltage and a broad noise following a $1/f$ variation.

Interference effects occur between the ac voltage generated in the crystal in the non-linear state and an external rf field (Shapiro steps).

Hysteresis and memory effects are observed, principally at low temperature.

Inside a domain, where the phase ϕ is only time dependent, a simple equation of motion has been derived[4]:

$$\phi'' + \Gamma\phi'' + \omega_p^2 \sin\phi = Q_0 \frac{eE}{M^*}, \tag{2}$$

where E is the applied field, $Q_0 = 2\pi/\lambda_{CDW}$, ω_p the pinning frequency and M^* the Frölich mass.

For a dc field E higher than E_T, the ''sin ϕ'' force term gives rise to a velocity modulation at a fundamental frequency, ν, and its harmonics which can be considered as the origin of the ac voltage generated in these systems. It has to be noted that the λ_{CDW} assumed periodicity for the force means that the fundamental frequency is linked to the mean CDW velocity by $v_{CDW} = \lambda_{CDW}\nu$. Therefore, according to Eq. 1, the extra-current carried by the CDW is given by

$$J_{CDW} = n_0 e v_{CDW} = n_0 e \lambda_{CDW} \nu. \tag{3}$$

According to Eq. 3, the slope of J_{CDW}/ν is a measurement of the number of electrons condensed below the CDW gap. The extra-current J_{CDW} is measured from the non-linear $V(I)$ characteristics. Figure 1 shows the linear relationship between J_{CDW} and ν for an orthorhombic TaS_3 sample. The number of electrons deduced from the ν/J_{CDW} slope is of the order of the electron concentration in the bands affected by the CDW condensation, as it can be calculated from band structures or from chemical bonds. This result can be considered as proof of the Frölich conductivity.[4] When the field overcomes the threshold one, the electrons, which were trapped below the CDW gap, coherently participate in the electrical conductivity.

The general properties of the sliding CDW state are now relatively well established. New lines of research are being developed at the present time. Some of them are described in the following.

2. CURRENT CONVERSION IN THE SLIDING CDW STATE OF $NbSe_3$

Phase slippage is a general phenomenon in condensed matter systems having complex order parameters. When external forces impose different order parameter phase velocities ϕ_1 and ϕ_2 in two regions 1 and 2 of the same system, the phase conflict at the boundary between the two regions is released by the formation of vortices at a rate given by $\dot{\phi} = \dot{\phi}_1 + \dot{\phi}_2$. Phase slippage has been intensively studied in narrow superconducting channels, in superfluids and, more recently, in quasi-one-dimensional conductors having a CDW ground state.

Phase slippage is required at the current electrodes for the conversion from free to condensed carriers.[6] CDW wave fronts must be created near one electrode and destroyed near the other. This process is mediated by CDW-phase dislocation loops which climb to the sample surface, each dislocation loop allowing the CDW to progress by one wavelength.

We have performed[7] at the ESRF high-resolution x-ray scattering measurements of the variation $q(x)$ of the CDW wave vector $Q(x) = Q_0 + q(x)$ along a thin $NbSe_3$ whisker of cross section $10\mu\text{m} \times 2\mu\text{m}$ and length 4.1 mm (between electrodes).

For a fixed *direct current* of $I/I_T = 2.1$ (I_T: threshold current), the shift $q_{\pm} = Q(+I) - Q(-I)$ between satellite

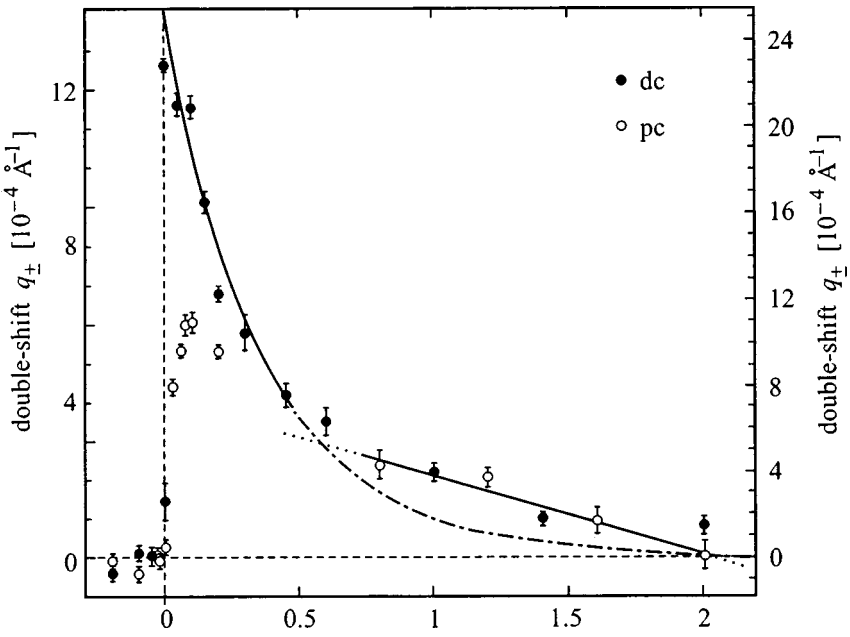

FIG. 2. (Double-)Shift $q_{\pm}=Q(+I)-Q(-I)$ of the satellite position Q as a function of the position x between the injection electrode $x=0$ and the midpoint between electrodes ($x=2$ mm) in $NbSe_3$ at $T=90$ K ($I/I_T=2.13$). The vertical and horizontal dashed lines indicate the contact boundary and the line of zero shift, respectively (from Ref. 7).

positions Q measured with positive and negative current polarities vanishes below the electrodes and rises abruptly to a maximum value at the electrode boundary (Fig. 2). With increasing distance x from the contact, $q_{\pm}(x)$ decays exponentially. For $x>0.5$ mm, a cross-over to a linear decrease of the satellite shift is observed with $q_{\pm}(x)$ crossing the line of zero shift at the midpoint between the electrodes ($x=2$ mm; beyond ($x>2$ mm) the sign of $q_{\pm}(x)$ is inverted).

The corresponding data for the applied *pulsed current* (100 Hz, 100 μs pulses) of the same amplitude I reveal a different spatial profile: vanishing below the electrode, $q_{\pm}$ rises smoothly with increasing x to reach its maximum at a distance of about 100 μm from the contact boundary, the maximum shift taking half the maximum value observed for the direct current. After a smooth decrease with increasing distance x, $q_{\pm}\{\text{pc}\}$ joins the linear dependence of $q_{\pm}\{\text{dc}\}$ with the same slope ($x>0.5$ mm). This important difference between the satellite shift profiles $q_{\pm}(x)$ for applied direct and pulsed current indicates a strongly spatially dependent relaxational behavior of the CDW deformations.

A semi-microscopic model[8] relates the CDW deformation q to the mismatch η between the longitudinal CDW stress U and the electrochemical potential μ_n of the charge carriers remaining metallic or being excited above the Peierls-gap at the given temperature:

$$q \propto \eta \equiv \mu_n - U. \tag{4}$$

Using this model, one can interpret the exponential regime as phase-slip dominated and the linear regime as a consequence of transverse pinning of the CDW dislocation loops blocking the normal-to-condensed carreir conversion.

3. MAGNETO-OSCILLATIONS OF THE CDW CONDUCTION IN PRESENCE OF COLUMNAR DEFECTS

Akin to superconductivity, the aim of the experiment was the search for a flux quantification effect produced by the collective response of the CDW condensate. Quantum interference phenomena occur around ''holes'' of a diameter $D=100$ Å produced by heavy-ion irradiation of thin $NbSe_3$ samples. One expects the CDW in motion to pass over a hole without conversion if the diameter of the hole is smaller than the transverse amplitude coherence length $\xi_{\perp}$. In a magnetic field, each defect hole serves as a ''solenoid'' which contributes to the flux dependent scattering of the depinned CDW. It was shown in Ref. 9 that the presence of columnar defects induces oscillations in the non-linear CDW conductivity as a function of H, when H is oriented parallel to the axes of the defects.

Irradiation was carried out with Xe, Pb, or U ions with energy ranging from 0.25 to 6 GeV. Structural analysis performed by transmission electron microscopy on thin (thickness: 0.1 μm) $NbSe_3$ samples irradiated simultaneously with the samples used for electrical measurements reveal latent traces with amorphous cores (columnar defects) in the crystal matrix with diameter 15 ± 2 nm.

Figure 3 shows the variation of the oscillatory part of the magnetoresistance as a function of H.[9] If the columnar defect size is taken for the scattering of the sliding CDW, the expected period of the magnetoresistance oscillation can be evaluated as $\Delta H=\alpha\phi_0(\pi D^2/4)$, with $D=15$ nm and $\alpha=1/2$, $\Delta H=11.3$ T consistent with the experimental value of 9.8 T (as shown in Fig. 3). The $\phi_0/2$ periodicity is in agreement with the instanton model.[10] An alternative model has been developed,[11] in which the Aharonov–Bohm flux is shown to modulate the CDW threshold; then the periodicity $\phi_0/2$ results from ensemble averaging over random scattering phases, similarly to the case of a collection of mesoscopic metallic rings.

The magnetoresistance of the irradiated part of a $NbSe_3$ sample has been measured with H parallel and perpendicular to the axes of columnar defects. Clearly, oscillations in the magnetoresistance are only observed when H is parallel to the defects and disappear for the perpendicular orientation.

An important feature for the observation of the oscilla-

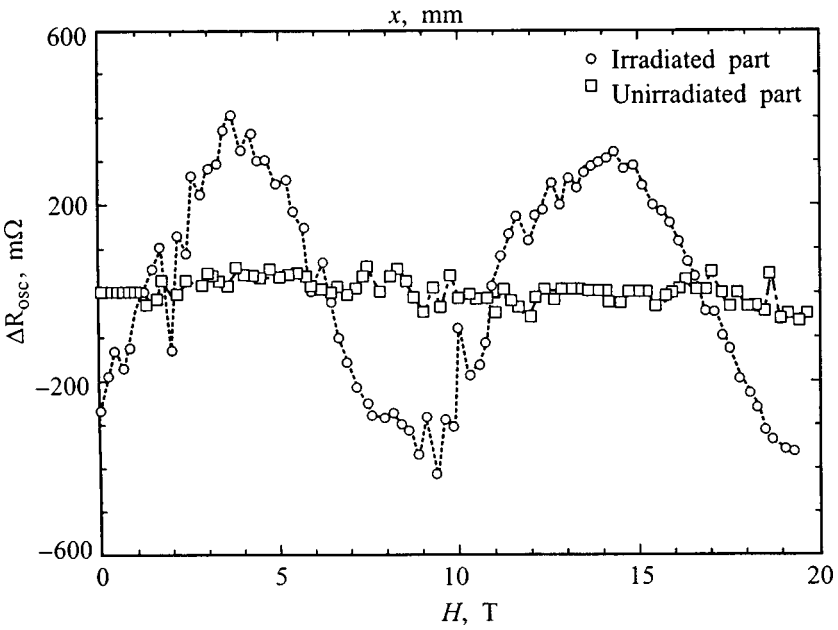

FIG. 3. Variation of the oscillatory part of the magnetoresistance of irradiated $NbSe_3$, ΔR_{OSC}, as a function of the magnetic field at $T=52$ K for an applied current 2.5 times the threshold value (from Ref. 9).

tory behavior of $R(H)$ is the phase coherence of the sliding CDW between potential probes: this phase coherence is lost for samples thicker than the phase correlation length perpendicular to the chains (typically less than $1\,\mu$m) and also for dc current above $2\sim3I_T$ (as seen from the lost of complete mode locking above these currents on irradiated samples).

4. SLOW DYNAMICS OF ENERGY RELAXATION AT VERY-LOW TEMPERATURE IN CDW/SDW COMPOUNDS

DW systems in their grond state exhibit typical ''glassy behavior'' for numerous electrical properties, the deep origin of the disorder being the pining of the DW phase by randomly distributed impurities, lattice defects, or approach of the commensurability. This random ground state is characterized by many metastable states with very broad relaxation times spectrum.

These metastable states are best revealed by low-temperature thermodynamical measurements. In a systematic study of numerous CDW compounds [$(TaSe_4)_2I$, TaS_3, $NbSe_3$ (Ref. 12)] and SDW [in organic $(TMTSF)_2PF_6$ (Ref. 13), $(TMTTF_2)Br$ (Ref. 14)] by means of specific heat (Fig. 4) and energy relaxation techniques in the T range between ~70 mK an ~10 K, we have established several characteristic ''glassy'' properties:

i) Additional excitations to regular phonons contribute to the specific heat for $T\leqslant1$ K according to a T^{ν} law, with $\nu<1$.[12]

ii) In the same T range, the specific heat becomes strongly time-dependent: the heat relaxation after a short heat perturbation of order of 1s, becomes nonexponential. We have also shown that the relaxation kinetics depend strongly on the duration of the heat perturbation (''aging effect'' similar to the case of spin glasses). The time necessary to achieve thermodynamic equilibrium at $T<1$ K exceeds hours. The heat relaxation is thermally activated with an activation energy depending on the duration of the perturbation. It is of the order of $\sim1-2$ K if the system has reached its thermodynamic equilibrium.[15,16] Properties i) and ii) are common to structural glasses or orientationally disordered crystals. However, energy relaxation effects are here of much larger intensity than in usual glasses. A theoretical

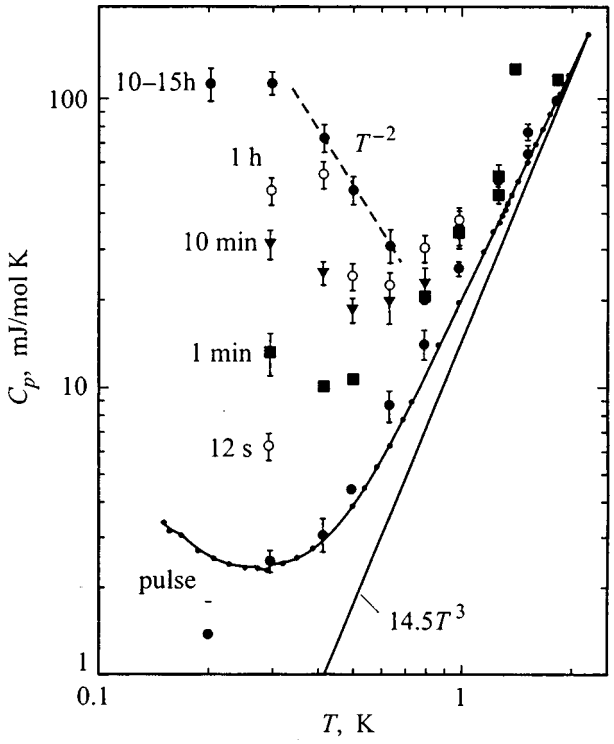

FIG. 4. Dependence of the specific heat of $(TMTSF)_2PF_6$ on the duration of energy delivery: from a pulse of less than 1 s up to 10–15 h. The continuous curve represents data calculated from the initial T increment in response to heat pulses. Other data are obtained by total integration of the energy release. The straight line (T^3) is the estimated lattice contribution. The contribution of metastable states below 0.5 K evolves from a T^{-2} tail for short time relaxation to a well-defined Schottky anomaly at the thermal equilibrium [splitting energy $\epsilon_s=0.9$ K and ratio of degeneracy $g_1/g_0\simeq12$ (from Ref. 14)].

model[17] which ascribes the origin of the long-lived metastable states to strong pinning centers located close to commensurability regions could interpret the experimental features.

iii) Finally, in the case of the SDW system $(TMTSF)_2PF_6$, an anomaly in the specific heat at $T \approx 3$ K has been identified as a glassy transition, since it exhibits all properties such as hysteretic behavior, sensitivity to the previous thermal history, characteristic of the usual freezing of supercooled liquids.[18] This interpretation is supported by low-frequency dielectric measurements.[19]

5. CONCLUSIONS

Our recent experiments in CDW/SDW systems have allowed the study of CDW phase dislocation loops for the current conversion at electrodes, of the role of long-lived metastable states in the thermodynamic properties at very low temperature, of quantum interference phenomena in presence of columnar defects. Thanks to a recent development in lithography techniques on single crystals,[19] multiply connected submicron structures were patterned on CDW samples, opening the possibility of studies at the mesoscopic scale.

I am deeply indebted to my colleagues H. Berger, K. Biljakavić, S. Brazovskii, R. Currat, Th. Fournier, G. Grübel, N. Kirova, O. Laborde, J. C. Lasjaunias, Yu. I. Latyshev, L. Levy, J. E. Lorenzo, F. Nad', P. Pannetier, Ch. Vettier for their active and stimulating collaboration.

[1] H. Frölich, Proc. R. Soc. London, Ser. A **223**, 296 (1954).
[2] P. A. Lee, T. M. Rice, and P. W. Anderson, Solid State Commun. **14**, 703 (1974).
[3] P. Monceau *et al.*, Phys. Rev. Lett. **37**, 602 (1976).
[4] For reviews: *Electronic Properties in Inorganic Quasi-One-Dimensional Compounds. Parts I and II*, edited by P. Monceau D. Reidel (Dordretch, 1985).
[5] *Density Wave in Solids*, edited by G. Grüner (Addison–Wesley, Reading, MA, 1994).
[6] N. P. Ong and K. Maki, Phys. Rev. **32**, 6582 (1985).
[7] H. Requardt *et al.*, Phys. Rev. Lett. **80**, 5631 (1998).
[8] S. Brazovskii and N. Kirova, to be published.
[9] Yu. I. Latyshev *et al.*, Phys. Rev. Lett. **78**, 919 (1997).
[10] E. N. Bogachek *et al.*, Phys. Rev. B **42**, 7614 (1990).
[11] M. I. Visscher and B. Rejaei, Europhys. Lett. (1998), in press.
[12] J. C. Lasjaunias *et al.*, Physica **165–166**, 893 (1990).
[13] K. Biljaković, J. C. Lasjaunias, P. Monceau, and F. Lévy, Phys. Rev. Lett. **62**, 1512 (1989); **67**, 1902 (1991).
[14] J. C. Lasjaunias, K. Biljaković, and P. Monceau, Phys. Rev. B **53**, 7699 (1996).
[15] Yu. Ovchinnikov *et al.*, Europhys. Lett. **34**, 645 (1996).
[16] J. C. Lasjaunias, P. Monceau, D. Staresinić, K. Biljakovi, and J. M. Fabre, J. Physique I (France) **7**, 1417 (1997).
[17] J. C. Lasjaunias, K. Biljakovi, Ya. F. Nad', P. Monceau, and K. Bechgaard, Phys. Rev. Lett. **72**, 1283 (1994).
[18] Ya. F. Nad', P. Monceau, and K. Bechgaard, Solid State Commun. **95**, 655 (1995).
[19] Yu. I. Latyshev, B. Pannetier, and P. Monceau, Eur. Phys. J. B **3**, 421 (1998).

Published in English in the original Russian journal. Reproduced here with stylistic changes by the Translation Editor.

Multi-purpose nonlinear optical microscope. Its principle and applications to polar thin-film observation

Y. Uesu* and N. Kato

Department of Physics, Waseda University, 3–4–1 Okubo, Shinjuku-ku, Tokyo 169-8555, Japan
Fiz. Tverd. Tela (St. Petersburg) **41**, 764–769 (May 1999)

Multi-purpose nonlinear optical microscope is an optical microscope which images $2D$ distribution of the optical second harmonic (SH) waves from a specimen. Image contrast can be obtained either by inhomogeneous distribution of nonlinear optical tensor components or by the interference between SH waves from a specimen and a standard plate. This microscope also functions as a fluorescence (FL) microscope, and SH and FL images can be obtained from the same part of a specimen. Absorption and FL spectra from a specific part of a specimen are measured through an optical fiber which connects an ocular with a polychromator. These functions are especially useful for investigation of the *J*-aggregate state of polar dye molecules. Several photographs taken by the microscope revealed the structure of merocyanine dye/arachidic acid mixed monolayer and the role of bridge ions in the subphase. © *1999 American Institute of Physics.* [S1063-7834(99)00305-6]

Experiments started in the 1970s to visualize inhomogeneous distributions in a specimen use the second harmonic (SH) waves which the specimen produces.[1,2] Recent improvements of the spatial resolution and sensitivity of a Charge Coupled Device (CCD) camera and image processing techniques enable us to obtain more easily high quality images of various kinds of bulk materials and surfaces. We made good use of this development of technology and constructed a multi-purpose nonlinear optical microscope called SHCM and successfully applied it to observations of ferroelectric domain structures[3–5] and periodically inverted domain structures in quasi-phase-match devices for frequency-conversion.[6] Recently we have installed a Langmuir trough in the SHGM and performed *in situ* observations of monolayer molecules at air–water interface, in particular, those of the *J*-aggregate state of polar dye molecules. In this paper, we discuss the principle of the SHGM, describe its structure and show several photographs taken by the SHGM, emphasizing useful application to polar thin film studies.

1. PRINCIPLE OF MEASUREMENT

The SHGM has some distinctive features: First, it can distinguish areas not only with different magnitude but also different sign of the second-order nonlinear optical tensor component (d-tensor). This is especially important to observe anti-parallel ferroelectric domain structures, which have not been observed by conventional optical microscopes. Second, SH images of monolayer molecules at an air–water interface or on a substrate can be obtained with relatively short exposure time. Third, $2D$ fluorescence images can be obtained from the same part of the specimen as the SH image. As the forth feature, quantitative measurements of absorption and fluorescence spectra can be performed in a specific part of a specimen. These are quite useful to study the *J*-aggregate state of polar dye molecules.

When a specimen contains domains with different crystallographic orientations, the anisotropy of the d-tensor can image the domain structure. The d-tensor d_{ijk}, the third-rank polar tensor, connects the nonlinear dielectric polarization component $P_i^{(2\omega)}$ with the product of electric fields $E_j^{\omega}E_k^{(\omega)}$ of the incident light wave as follows:

$$P_i^{2\omega}=\varepsilon_0 d_{ijk}E_j^{(\omega)}E_k^{(\omega)}. \tag{1}$$

Therefore, if the crystallographic orientation differs, the intensity contrast Γ is produced by the effective magnitude of d-tensor and coherence length l_c of the specimen. An example is the case where d_{311} and d_{333} are concerned as is shown in the case of ferroelectric 90° domain structures in $BaTiO_3$

$$\Gamma=(d_{311}l_c(d_{311})/d_{333}l_c(d_{333}))^2, \tag{2}$$

where l_c is defined as $l_c=\lambda/4(n^{(2\omega)}-n^{(\omega)})$ using refractive indeces $n^{(2\omega)}$ and $n^{(\omega)}$ of fundamental and SH waves, respectively.

In the case of ferroelectric anti-parallel domain structures, the magnitude of the d-tensor is the same but the sign

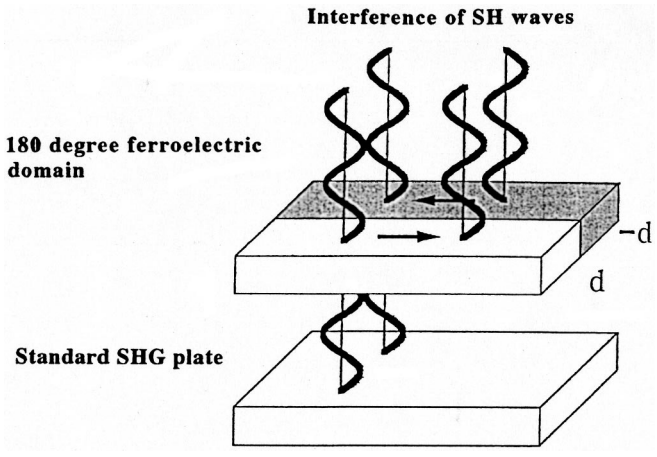

FIG. 1. Principle of the SHG microscope for observing anti-parallel ferroelectric domain structures.

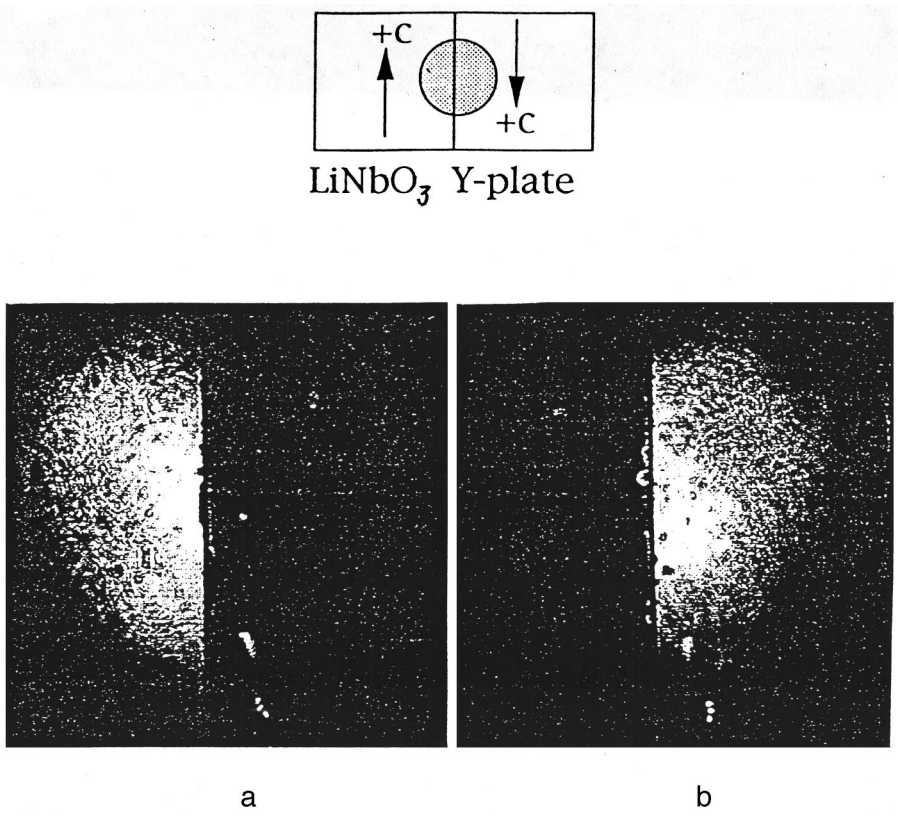

FIG. 2. SH images of two *Y*-cut plates of MgO; $LiNbO_3$ with opposite *z* axes. The intensity contrast is reversed by rotating a glass phase plate.

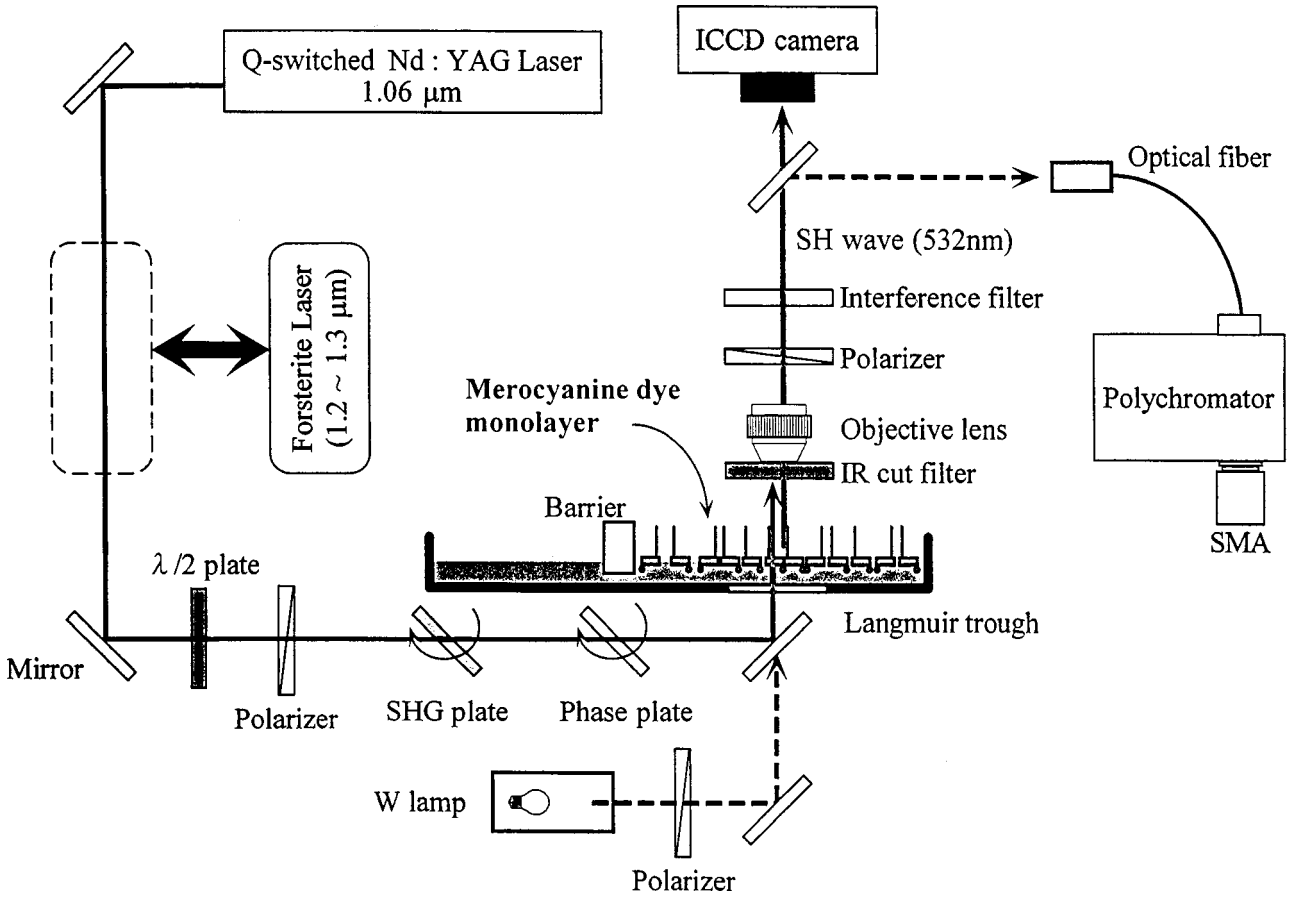

FIG. 3. Schematic illustration of the SHGM.

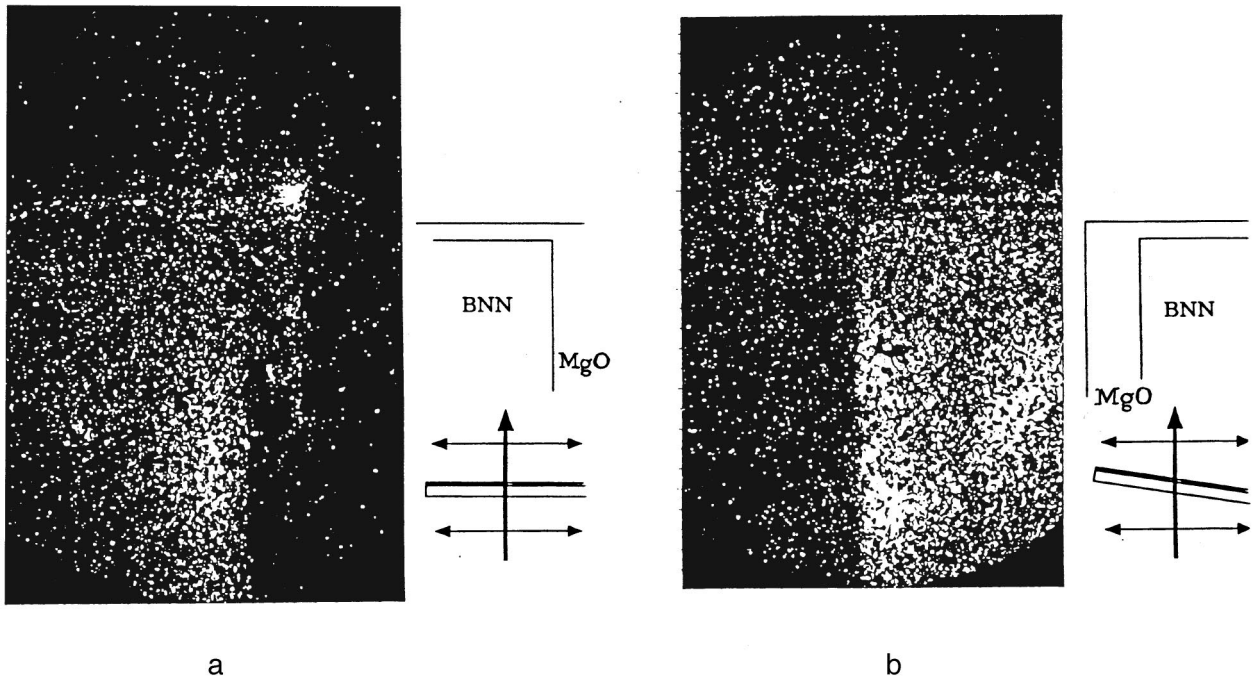

FIG. 4. SH images of ferroelectric thin film BNN/MgO. a — Shows the image with perpendicular incidence of the fundamental laser beam, b — image with small inclination of the specimen with respect to the incident direction.

is different for + and − domains and the phase difference of the SH waves produced in these domains is π. Therefore, if a standard SHG plate is placed in front of the specimen, the interference between SH waves from the plate and the specimen produce an intensity contrast as shown in Fig. 1. In order to get the maximum contrast, the amplitude and phase of SH waves from the SHG plate and one domain of the specimen should be identical. This condition can be realized by inserting a plate generating uniform SH wave and a glass plate and by rotating them to vary the amplitude and phase. Figure 2 shows two *Y*-cut plates of MgO:$LiNbO_3$ with opposite *z* axes. By rotating the glass plate, the contrast of two

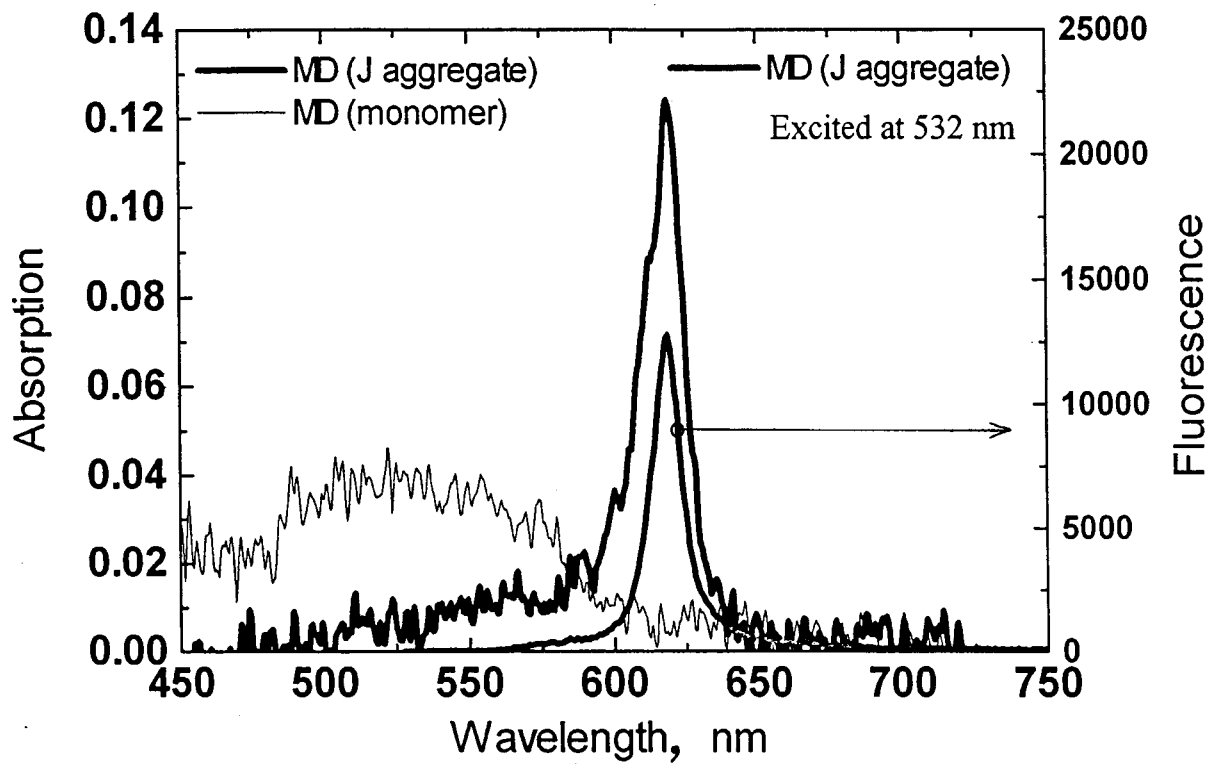

FIG. 5. Absorption and fluorescence spectra of *J* aggregate MD and monomer MD.

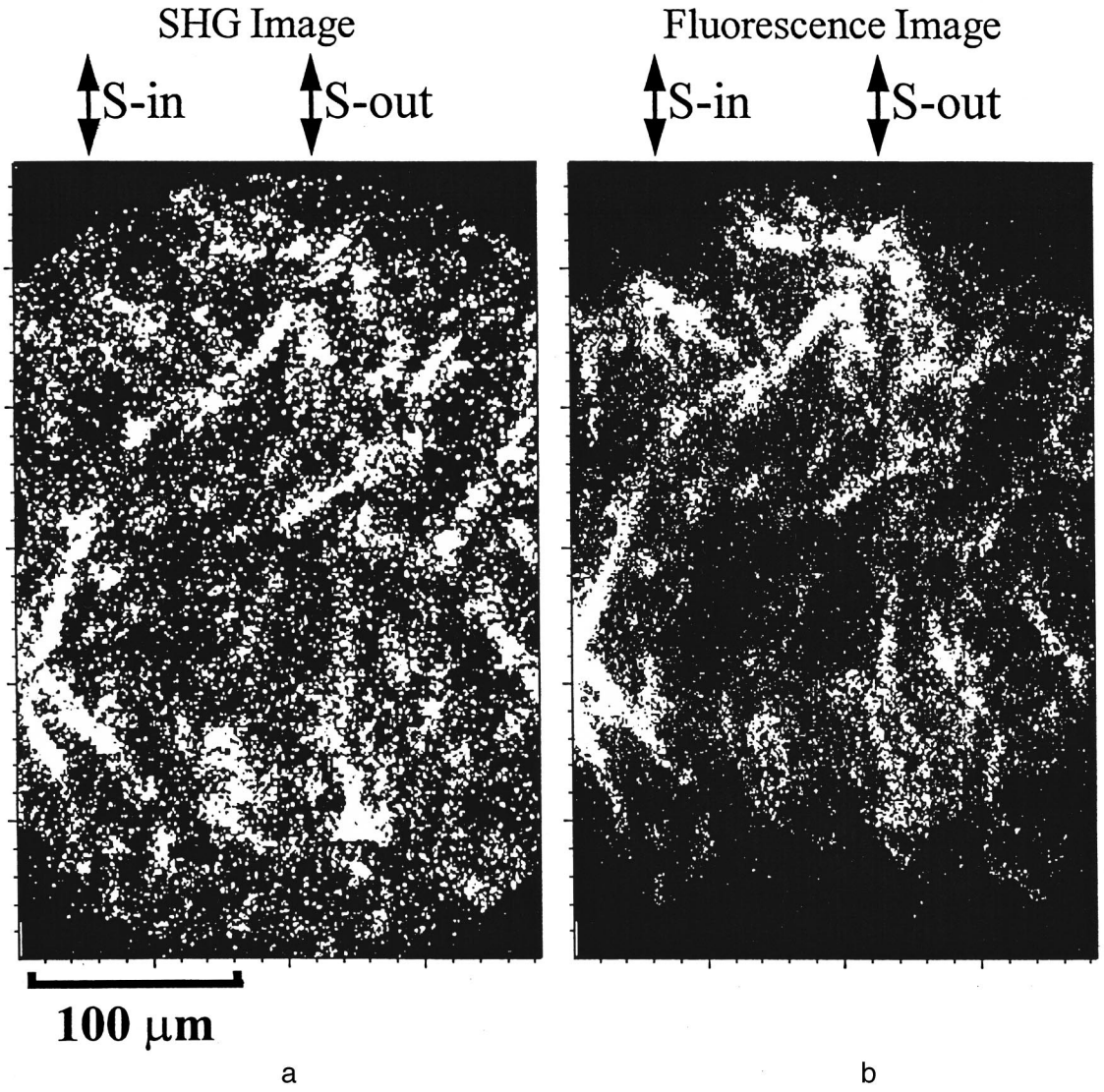

FIG. 6. SH and FL images of the same part of MD/AA mixed monolayer at air–water interface.

plates is reversed, which shows clearly the visualization of anti-parallel ferroelectric domain structure by the SHGM.

2. DETAILS OF MULTI-PURPOSE NONLINEAR OPTICAL MICROSCOPE

Schematic illustration of the SHGM is shown in Fig. 3. As a light source, Nd^{3+}:YAG laser (wavelength of 1.06 μm, repetition frequency of 10 Hz, pulse width 20 ns, maximum energy per pulse 200 mJ in front of specimen) is used. The wavelength of the incident laser beam can be varied from 1.2 to 1.3 μm using Forsterite (Cr^{4+}:Mg_2SiO_2) laser. Through a half-wave plate, a polarizer, an SHG plate and a glass plate, the incident and frequency-doubled beams enter the specimen. Then the resultant SH wave is selected by filters and its $2D$ distribution is registered by the Integrated CCD camera. When a monolayer of dye molecules is observed, a specially designed Langmuir trough is placed below an objective lens mounted with an IR filter.

Fluorescence (FL) images are obtained when the frequency-doubled beam impinges directly on a specimen. Thus SHG and FL images from the same part of specimen are compared. An optical fiber connecting an ocular and a polychromator facilitates the measurement of absorption or FL spectra.

3. OBSERVATIONS OF POLAR THIN FILMS

3.1. Ferroelectric thin films

Recent development of ferroelectric thin films for the application to non-volatile memory devices is remarkable. FeRAM will replace DRAM in some application fields in the very near future. Ferroelectric thin films are fabricated on a substrate by various techniques and their alignment should be properly evaluated. We applied the SHGM to examine the homogeneous alignment of the c-axis of $Ba_2NaNb_5O_{15}$ (BNN) thin film on MgO substrate. Figure 4 shows the result. When the c axis of BNN is perpendicular to the substrate, vertical incidence of laser beam should produce no SH wave. Figure 4a shows the existance of SHG region, and further inclination of the specimen generates more homoge-

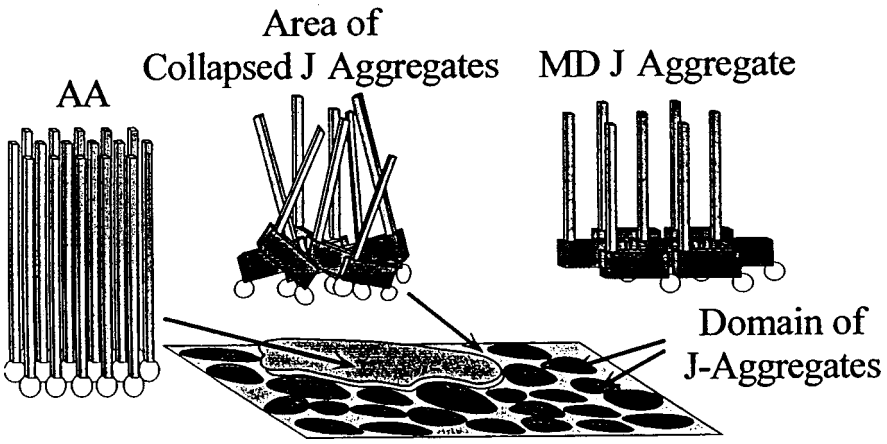

FIG. 7. Conceptual image of Md/AA mixed monolayer.

neous and more intense SH waves as shown in Fig. 4b. These facts clearly show that the c axis is inclined in this bright region in Fig. 4a.

3.2. *J* aggregate of merocyanine dye molecules

A kind of dye molecule is known to make $2D$ assemblage in a regular form. When it is exited by light illumination, the exited part consisting of several molecules forms an exiton, which propagates like a soliton on the molecular assemblage. The exited aggregate is termed the *J* aggregate.[7] The *J* aggregate lowers the interaction energy of molecules and manifests characteristic absorption and fluorescence spectra. This state of molecules is considered to be supermolecule and some applications to nonlinear optics and optoelectric transform devices are expected.[8]

Using the Langmuir trough we prepared the *J*-aggregate of merocyanine dye (MD) molecules which are used as spectral sensitizators in the photographic process. To stabilize the structure, arachidic acid (AA) molecules were mixed with MD. The *J* aggregate was formed with special kinds of ion species, NH_4^+, Mg^{2+} or Cd^{2+} in subphase. The formation was verified by absorption and fluorescence spectra as shown in Fig. 5 measured by the SHGM. Figure 6 shows the SH and FL images of the same part of MD/AA mixed monolayer at air–water interface. Mostly one to one correspondences were obtained in both images, which shows that the *J* aggregate of MD is SHG active and molecules align along the same direction. The SHG active region (bright in the figure) has a rectangular form and shows anisotropy. The long axis of the rectangle is nearly parallel to a barrier plate which compresses the molecules on water (see Fig. 6). More precise analysis of the polarization dependence shows that the long axis of MD molecules inclined to the long axis of the rectangle region.

Finally, comparing these images with AFM image,[9] we obtain a conceptual image of MD/AA mixed monolayer as shown in Fig. 7. It consists of three domains, i.e., the *J* aggregate of MD, a monomer state or a collapsed aggregation state of MD and AA regions. These three parts have different heights which AFM easily distinguishes, but AFM cannot determine polar regions. On the other hand, the SHG image discriminates the polar region where dipole moment of molecule aligns along particular direction, while FL image shows the *J* aggregate state without knowledge of polar state. Thus complementary observations of the SHGM and AFM is quite useful to study the structure of MD/AA mixed monolayer. It should be also stressed that SHGM revealed the role of ion in subphase. Among the ions used in the present experiment, NH^{4+} produces largest domain size of the *J* aggregate which is as large as 50 μm long.

The authors are grateful to H. Aida, H. Mohri, and K. Saito, Waseda University, for their participation in the experiments.

The work was supported by the Special Contraction Fund for Promoting Science and Technology, Agency of Science and Technology, Japan.

[a)]E-mail: uesu93@mn.waseda.ac.jp

[1] R. Hellwarth and P. Christensen, Opt. Commun. **12**, 318 (1974).
[2] J. N. Gannaway and C. J. R. Sheppard, Opt. Quantum Electron. **10**, 435 (1978).
[3] Y. Uesu, S. Kurimura, and Y. Yamamoto, Appl. Phys. Lett. **66**, 2165 (1995).
[4] Y. Uesu, S. Kurimura, and Y. Yamamoto, Ferroelectrics **169**, 249 (1995).
[5] Y. Yamamoto, S. Kurimura, and Y. Uesu, Appl. Opt. **36**, 602 (1997).
[6] S. Kurimua and Y. Uesu, J. Appl. Phys. **81**, 369 (1997).
[7] H. Kuhn and C. Kuhn, in *J-Aggregation*, edited by T. Kobayashi (World Scientific, 1996), p. 1.
[8] A. K. Ghosh and T. Feng, J. Appl. Phys. **49**, 5982 (1978).
[9] N. Kato, H. Aida, K. Saito, and Y. Uesu, J. Korean Phys. Soc. **32**, S1076 (1998).

Published in English in the original Russian journal. Reproduced here with stylistic changes by the Translation Editor.

Synthesis, characterization, and applications of shaped single crystals

William M. Yen

Department of Physics and Astronomy, University of Georgia, Athens, GA 30602, USA
Fiz. Tverd. Tela (St. Petersburg) **41**, 770–773 (May 1999)

In this paper we shall review techniques for the growth of single crystal, mostly of insulating material, which are shaped during the growth process. In particular, we shall focus on the growth of single-crystal fibers of optically activated materials; the emphasis will be placed on the so-called Laser Heated Pedestal Growth (LHPG) method of pulling crystalline fibers. LHPG offers a number of logistical advantages which can be exploited as a tool for materials research. Progress in the synthesis of materials using LHPG is described, as are spectroscopic techniques which are employed in characterizing the optical and physical properties of the crystal fibers obtained by this method. © *1999 American Institute of Physics.* [S1063-7834(99)00405-0]

There has been interest on crystalline materials prepared in fiber form for a sustained period of time; partially because single crystal fibers occurring naturally in the form of whiskers often possess near-ideal physical properties of crystallinity and tensile strength. Earlier work addressed itself mostly to metallic materials, for example, in 1922 von Gomperz[1] was successful in pulling single crystal metallic filaments directly from the melt. Later, in the 1950's, much of the work centered on the magnetic and mechanical properties of metallic whiskers[2]; however their size and composition could not be controlled accurately.

One method which allows the growth of crystalline fibers is the Stepanov method in which the melts are drawn through shapers and crystallization is made to occur after passage through a die.[3] Another method that enabled us to grow single crystal fibers of the desired length and diameter, with the proper crystallographic orientation and proper composition and doping is the Laser Heated Pedestal Growth (LHPG) method of fiber synthesis.[4]

LHPG and the related float zone growth technique are micro-variants of the Czochralski growth method; the feed stock used is generally in the shape of a rod and the melt is in the form of a self supporting bubble at the tip of the rod. A number of heating sources have been used to produce the melt; the most common method by far has been laser heating with focused single or multiple beams. A seed is dipped into the melt and is wetted by it; as the seed is pulled out, surface tension of the molten materials forms a pedestal around the seed, hence the name of pedestal growth. The melt is kept in place solely by surface tension, hence, this fiber growth method does not require crucibles and eliminates one source of sample contamination. This type of container-less growth also permits the synthesis of materials with extremely high melting points. The laser heated version of pedestal growth (LHPG) is illustrated in Fig. 1.[5]

In a typical LHPG fiber pulling system, a stabilized CO_2 cw laser, typically with an output of between 15–75 W, is used as a heating source. The usual focusing and turning optics for the beam are shown in Fig. 2 along with the pulling and feeding mechanisms. The fiber pulling assembly may be enclosed in a vacuum-tight chamber allowing growth in controlled atmospheres.[6]

The source rods are cut out of polycrystalline ceramics produced by mixing host and activator materials, sintering and hot pressing the mixture into flat disks. Crystal chips and fibers can be used as source materials as well. The source rods we have employed at the University of Georgia are typically $1\times1\times12\ \mathrm{mm}^3$ and our fiber diameters are in the 0.15 mm to 1.0 mm range; pulling speeds are typically 0.1–2.5 mm/min.

1. ADVANTAGES OF THE LHPG METHOD OF FIBER GROWTH

Several advantages of LHPG have become apparent, not only in the growth of fibers for applications but, more importantly, as a general way to explore material synthesis and the properties of crystal growth. Other practical advantages of the LHPG method have also become apparent, as follows.

a) The LHPG relies on surface tension to maintain the integrity of the melt and hence it is a growth method which does not require crucibles; nor does the enclosure containing the fiber growth region possesses walls heated to high temperatures as is the case in crystal growth furnaces. Both crucible and furnace surfaces are generally understood to be the primary sources of unintentional contamination in normal crystal growth, hence, it follows that the absence of these surfaces allows the growth of very pure crystal materials. The impurity levels found in LHPG fibers are solely determined by the purity of the starting materials of the source rods.

b) The source-rod length as well as the melt volume in LHPG are typically small, of the order of 10 mm and 1 mm^3, respectively. The cost of the chemical compounds required for the growth of single cristal fibers, as a consequence, is relatively small. Because of this, it is possible to grow fiber crystals of materials which would be prohibitively expensive to grow by traditional methods, specially as a basis.[7] Further, it is also generally accepted that thermal gradients within the melt container are responsible for introducing stresses and

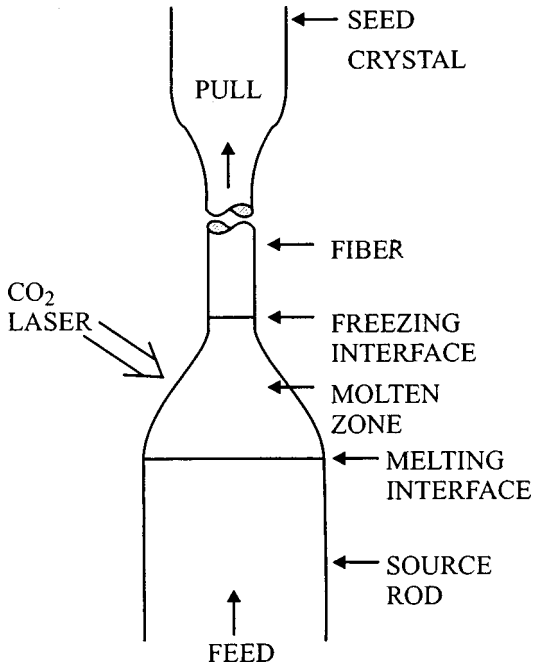

FIG. 1. Schematic representation of the LHPG method for fiber growth showing the various regions involved in the growth.

other defects in bulk crystals, because of this LHPG pulled fibers can be made practically stress free. The small volume of the growth region also facilitates the introduction of external perturbations during synthesis of the crystal. The application of an external field to the melt may influence the growing process by encouraging the inclusion of domains or the formation of other stoichiometric combinations.[8]

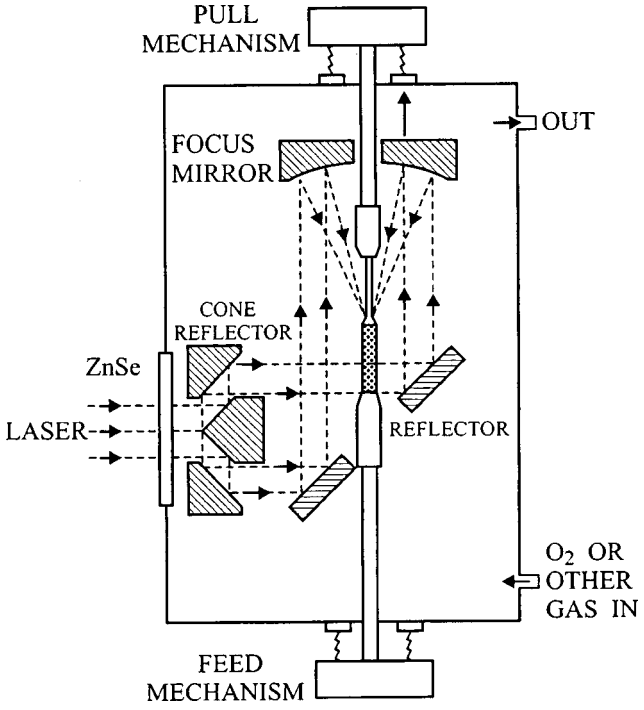

FIG. 2. Cross sectional view of the LHPG growth chamber showing details of the reflection and optical focusing system.

c) One of the most attractive features of the LHPG methods is the rapidity with which fibers can be grown. With our pulling speeds, a fiber sample of length of 1 or 2 cm, sufficient for spectroscopic characterization, can be grown and characterized in a relatively short time.[7] The information feed back made possible by this time scale allows the rapid re-adjustment of stock compositions and growth conditions for optimized materials. It is this feature that makes this method such a powerful tool in the synthesis and engineering of crystalline materials in general.

d) Finally, for those of us interested in the optical spectroscopic properties of activated materials, the fiber configuration is ideal experimentally for conducting absorption, emission and ancillary dynamical and static optical measurements.

We have been able to pull a great variety of oxide and fluoride crystal fibers doped with rare-earth and transition-metal ion activators in a wide range of concentrations; a list of the materials we have been able to grow is shown in Table I.

2. CHARACTERIZATION OF LHPG MATERIALS

The physical and mechanical properties of the fibers can be determined using the myriad of standard techniques such as x-ray diffraction, crystal birefringence, microprobe analysis and optical microscopy.[4]

We have been able to derive many characteristics of our fiber samples by investigating the static and dynamic optical properties of a fiber.[9] Static measurements obtained under steady-state conditions can be used to determine the dopant concentrations, whether or not the concentration is uniform along the length of the fiber and other species or active defect centers exist in the fiber. Dynamic measurements include the determination of radiative and non-radiative lifetimes and can yield information on the microscopic interactions between the active ions and their surroundings. Other optical determinations such as fluorescence lifetime measurements can be used to provide a quick measure of the extent of self quenching or cross relaxation present and again allows for quick adjustments of the doping levels for optimized performance. Quite generally, the macroscopic optical properties and other physical properties of materials grown in fiber form through the LHPG method have been found to be identical to those in bulk materials.[9–11]

As an example of the type of measurements which can be conducted in the fiber configuration we mention tensile stress studies. Many piezo-spectroscopic studies have been conducted in optically active insulating materials; in fact, both hydrostatic and uniaxial compressive stress studies of the behavior of the well known *R* lines of ruby have established the shift of the *R* lines as a function of applied stress as a secondary pressure standard. Complementary studies in which tensile or decompressive stresses are applied have not been carried out because of experimental difficulties encountered in stretching a bulk crystal; the fiber geometry is in fact ideal for tensile stress studies.[12] Tensile stress can be applied readily by simply attaching weight to the fiber; the behavior of the *R* line as a function of tensile stress is shown in Fig. 3.

TABLE I. Material grown by the UGA LHPG system.

Material	Dopant	Material	Dopant	Material	Dopant
Al_2O_3	Pure	$LiGa_5O_8$	Co^{2+}		Pr^{3+}
	Cr^{3+}		Ni^{2+}		Tb^{3+}
	Mg^{2+}		Co^{2+} and Mg^{2+}		Ti^{3+}
	Si^{4+}	$LiNbO_3$	Pure		Tm^{3+}
	Ti^{4+}		Er^{3+}		V^{3+}
	Fe^{2+} and Cr^{4+}		Er^{3+} and Al^{3+}		Ca^{2+} and Mn^{4+}
	Co^{2+} and Si^{4+}		Er^{3+} and Cr^{3+}		Co^{2+} and Si^{4+}
	Cr^{3+} and Ti^{3+}	$LiYF_4$	Er^{3+}		Fe^{2+} and Cr^{4+}
	Cr^{4+} and Si^{4+}	Lu_2O_2	Pure		Fe^{3+} and Nd^{3+}
	Mg^{2+} and Cr^{4+}		Ce^{3+}		Mg^{2+} and Mn^{4+}
	Mg^{2+} and Mn^{4+}	Lu_2SiO_5	Ce^{3+}		Mo^{4+} and Ca^{2+}
	Ti^{2+} and Si^{4+}	$MgAl_2O_4$	Cr^{3+}		Ti^{3+} and Nd^{3+}
	Mo^{3+}		Ti^{3+}		Ti^{2} and Si^{4+}
$BaTiO_3$	Eu^{3+}	$MgCaSiO_4$	Cr^{4+}		Tm^{3+} and Ce^{3+}
$BaYF_8$	Er^{3+}	$Mg_{1.5}Mn_{0.5}SiO_4$	Cr^{3+}		W^{4+} and Ca^{2+}
	Nd^{3+}	Mg_2SiO_0	Cr^{3+} and Cr^{4+}	$YAlO_3$	Er^{3+}
CaF_2	Pb^{2+}	Mn_2SiO_4	Pure		Er^{3+} and Eu^{3+}
	Tb^{3+}	$NaLa(WO_4)_2$	Er^{3+}	YGAG	Ca^{2+} and Cr^{4+}
$CaWO_4$	Er^{3+}		Eu^{3+}	YGG	Mg^{2+} and Cr^{4+}
	Ti^{2+}		Nd^{3+}	YIG	Pure
CsB_3O_5	Pr^{3+}		Er^{3+} and Yb^{3+}	Y_2O_3	Ce^{3+}
DyF_3	Pure	$NaY(WO_4)_2$	Eu^{3+}		Dy^{3+}
$GdEuO_3$	Nd^{3+}	NdF_3	Pure		Er^{3+}
GGG	Cr^{3+}	$PbMoO_4$	Pure		Eu^{3+}
Gd_2O_3	Pure	$RbMnF_3$	Pure		Ho^{3+}
	Eu^{3+}	Sc_2O_3	Er^{3+}		Nd^{3+}
	Nd^{3+}		Nd^{3+}		Pr^{3+}
$GdScO_3$	Nd^{3+}		Ti^{3+}		Tb^{3+}
Gd_2SiO_3	Ce^{3+}	$SrAl_2O_4$	Cr^{4+}		Tm^{3+}
$LaAlO_3$	Cr^{3+} and Eu^{3+}	$SrTiO_3$	Cr^{3+}		Dy^{3+} and Tb^{3+}
$LaAl_{0.75}Ga_{0.25}O_3$	Tm^{3+}		Eu^{3+}		Pr^{3+} and Yb^{3+}
$LaAl_{0.5}Ga_{0.5}O_3$	Tm^{3+}		Nd^{3+}		Tm^{3+} and Yb^{3+}
LaF_3	Pure	YAG	Pure	$YScO_3$	Er^{3+}
$LaGaGeO_7$	Nd^{3+}		Ca^{2+}		Eu^{3+}
$La_3Ga_5SiO_{14}$	Pure		Ce^{3+}		Nd^{3+}
La_2O_3	Pure		Cr^{3+}	Y_2SiO_5	Eu^{3+}
	Ce^{3+}		Dy^{3+}	YSAG	Ca^{2+} and Cr^{4+}
$LiAl_5O_8$	Pure		Er^{3+}	YSGG	Mg^{2+} and Cr^{4+}
	Ni^{2+}		Eu^{3+}	YVO_4	Er^{3+}
	Co^{2+}		Fe^{2+}	$ZnGa_2O_4$	Mn^{2+}
$LiCaAlF_6$	Cr^{3+}		Mo^{4+}	$ZnSiO_4$	Cr^{4+}
LiF	Pure		Nd^{3+}		

The shifts are to the blue rather than to the red, as is observed with uniaxial compressive stress, and are linear up to a tensile stress of 6 kbar, defining the yield point of the fiber. The tensile strength of the fiber was determined to be 7.7 kbar; the quality of the materials as measured by this parameter is comparable to those reported by LaBelle and Mlavsky.[13] Torsional stress can also be applied; the effects of torsional stress on the vibration Raman active modes of sapphire fiber have been reported.[14]

3. PHONON SPECTROSCOPY IN SINGLE-FIBER GEOMETRY

Crystalline fibers can be pulled so that their diameters are comparable to the mean-free-path, λ, of high-frequency, nonequilibrium (THz) phonons at low temperatures.[15] In other words, LHPG single-crystal fiber can be mesoscopic with respect to the characteristic dimensions of elementary excitations of the solid. These excitations include magnons, phonons and plasmons in insulators and conduction electrons in the case of semiconductor fibers.

The transport properties and the dynamics of narrow-band, high-frequency nonequilibrium phonons in crystalline fibers of ruby and of $YAG:Pr^{3+}$ at low temperatures have been investigated recently,[16] as have the narrow-band 29 cm^{-1} phonons in a ruby fiber.[17] These experiments have allowed us to investigate phonon-interface interaction and the energy transport across boundaries as a function of the acoustic impedance encontered at the fiber boundaries.

These initial results simply illustrate how the availability of LHPG fibers can open up whole new areas to investiga-

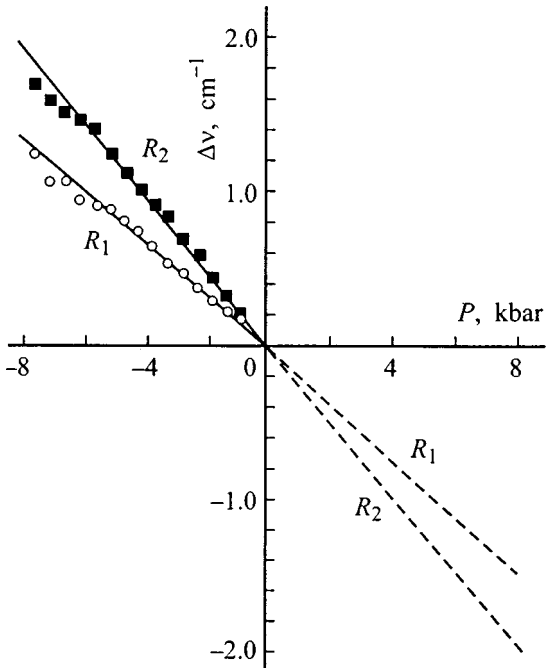

FIG. 3. Tensile stress dependence of the blue shifts of the *R* line in a ruby fiber. Shifts arising from uniaxial stress are to the red (dashed line). Tensile shifts are linear up to 6.0 kbar (yield point); the tensile strength of the fiber is 7.7 kbar.

tion simply by providing good materials configured in a useful geometry.

4. TECHNICAL APPLICATIONS OF LHPG FIBERS

In addition to using the LHPG fibers to conduct spectroscopic studies of their properties and to synthesize and optimize the physical properties of crystalline materials, fibers grown with the proper care have been found to be defect free and of very high quality. It follows that these fibers can be employed whenever materials subjected to high tensile or torsional stresses are required simply because of their excellent physical characteristics.

Much of the impetus behind the development of crystalline fibers arose because of their potential in various optoelectronic applications. The interest in these applications is motivated, in turn, by the advent of fiber-based systems which are impacting an ever increasing number of technologies. This interest is not likely to diminish in the future and we foresee additional applications of these fibers in a variety of technologies.

5. CONCLUSIONS

Though a variety of techniques is available for the growth of single-crystal fibers, the LHPG method offers a number of advantages and is a cost-efficient way for synthesizing a large number of materials for fundamental material science studies and for mechanical, electronic and optical applications.

[1] E. von Gomperz, Z. Phys. **8**, 184 (1922).
[2] C. Herring and J. K. Glat, Phys. Rev. **85**, 1060 (1952).
[3] A. V. Stepanov, Sov. Phys. JETP **29**, 339 (1959).
[4] Robert S. Feigelson, ''Growth of fiber crystals,'' in *Crystal Growth of Electronic Materials*, edited by E. Kaldis (Elsevier Science Publishers, Amsterdam, 1985), Ch. 11.
[5] For a comprehensive review of LHPG and its applications see: W. M. Yen, ''Preparation of single crystal fibers,'' in *Insulating Materials for Optoelectronics: New Developments*, edited by F. Agullo-Lopez (World Scientific, Singapore, 1995), Ch. 2.
[6] M. Fejer, J. Nightingale, G. Magel, and R. L. Byer, Rev. Sci. Instrum. **55**, 1791 (1984).
[7] S. M. Jacobsen, B. M. Tissue, and W. M. Yen, J. Phys. Chem. **96**, 1547 (1992).
[8] Kh. S. Bagdasarov and V. V. Ryabchenkov, Sov. Phys. Crystallogr. **33**, 394 (1988).
[9] W. M. Yen, Proc. SPIE **1033**, 183 (1988).
[10] W. Jia, H. Liu, K. Lim, and W. M. Yen, J. Lumin. **43**, 323 (1989).
[11] W. Jia, L. Lu, B. M. Tissue, and W. M. Yen, J. Cryst. Growth **109**, 329 (1991).
[12] H. Liu, K.-S. Lim, W. Jia, E. Strauss, W. M. Yen, A. M. Buoncristiani, and C. E. Byvik, Opt. Lett. **13**, 931 (1988).
[13] H. E. LaBelle, Jr. and A. L. Mlavsky, Nature (London) **216**, 574 (1980).
[14] W. Jia and W. M. Yen, J. Raman Spectrosc. **20**, 785 (1989).
[15] A. A. Kaplyanskii and S. A. Basun, ''Multiple resonant scattering of the 29 cm^{-1} phonons in optically excited ruby,'' in *Non-equilibrium Phonons in Nonmetallic Crystals*, edited by W. Eisenmenger and A. A. Kaplyanskii (North Holland, Amsterdam, 1986), Ch. 9.
[16] X. Wang, W. M. Dennis, and W. M. Yen, J. Lumin. **53**, 44 (1992).
[17] S. A. Basun, S. P. Feofilov, A. A. Kaplyanskii, and W. M. Yen, Phys. Rev. Lett. **67**, 3110 (1991).

Published in English in the original Russian journal. Reproduced here with stylistic changes by the Translation Editor.

Photoelectrically detected magnetic resonance spectroscopy of the excited triplet states of point defects in silicon

L. S. Vlasenko

A.F. Ioffe Physicotechnical Institute, Russian Academy of Sciences, 194021 St. Petersburg, Russia
Fiz. Tverd. Tela (St. Petersburg) **41**, 774–777 (May 1999)

Highly sensitive methods for the detection of the electron paramagnetic resonance (EPR) spectra based on the spin-dependent microwave photoconductivity were applied to investigate the structural defects in irradiated silicon. The parameters of the EPR spectra of the excited triplet states of radiation defects were determined and several models of the carbon related defects were supposed. © *1999 American Institute of Physics.* [S1063-7834(99)00505-5]

Electron paramagnetic resonance (EPR) is one of the main methods for investigating the microscopic structure of various point defects in solids, particularly in semiconductors. Among semiconductor materials the most significant results were achieved in silicon. Using the EPR technique, about three hundreds different EPR spectra of impurity atoms, their complexes, radiation and thermal defects in silicon were observed.[1] A part of them were identified and described in reviews.[2,3] Further progress in magnetic resonance spectroscopy of defects in semiconductors was related to the development of new, highly sensitive methods based on the effects of spin dependent recombination (SDR) when the recombination rate of nonequilibrium carriers depends on the spin orientation of the recombination centers.[4] These methods allow us to detect EPR spectra by measuring the intensity of the recombination luminescence or the photoconductivity of samples in magnetic field under saturation of the EPR transitions by the resonance microwave magnetic field.

The detection of microwave photoconductivity of silicon samples by the absorption of the electric component of the microwave field due to the resonance change of the concentration of photoexcited carriers increases the sensitivity of the method by four orders of magnitude.[5] It was found that the main channel of SDR is the recombination through the excited triplet states of the recombination centers. Several new SDR detected EPR spectra of the excited triplet states of different defects have been found in irradiated silicon. Some of them were identified as arising from the excited spin $S=1$ state of Substitutional carbon–Interstitial silicon–Substitutional carbon ($C_S-Si_I-C_S$) complex (spectrum Si–$PT1$),[5,6] divacancy (spectrum Si–$PT5$),[7] and complex phosphorus + vacancy (spectrum Si–$PT3$).[5,8]

In the present paper the advantages and some applications of the SDR–EPR methods for investigating the structure of the recombination centers in irradiated silicon will be described.

1. EXCITED TRIPLET STATES OF DEFECTS

The irradiation of silicon crystals by fast electrons or γ rays gives rise to various structural defects containing the dangling bonds which can form molecular orbitals. Each of the latter can be occupied by one electron or by two electrons with opposite spins. If the defects contain an even number of electrons, their ground state will be nonparamagnetic with spin $S=0$. Under band-gap illumination and in recombination process, the defects can be in the excited spin $S=1$ state when two unpaired electrons occupy different atomic or molecular orbitals.

Let us consider the Hamiltonian of two interacting electrons in magnetic field **B**

$$H=\mu_B\mathbf{B}\mathbf{g}_1\mathbf{S}_1+\mu_B\mathbf{B}\mathbf{g}_2\mathbf{S}_2+J\mathbf{S}_1\mathbf{S}_2+\mathbf{S}_1\mathbf{D}\mathbf{S}_2, \quad (1)$$

taking into account the Zeeman interaction between the ap-

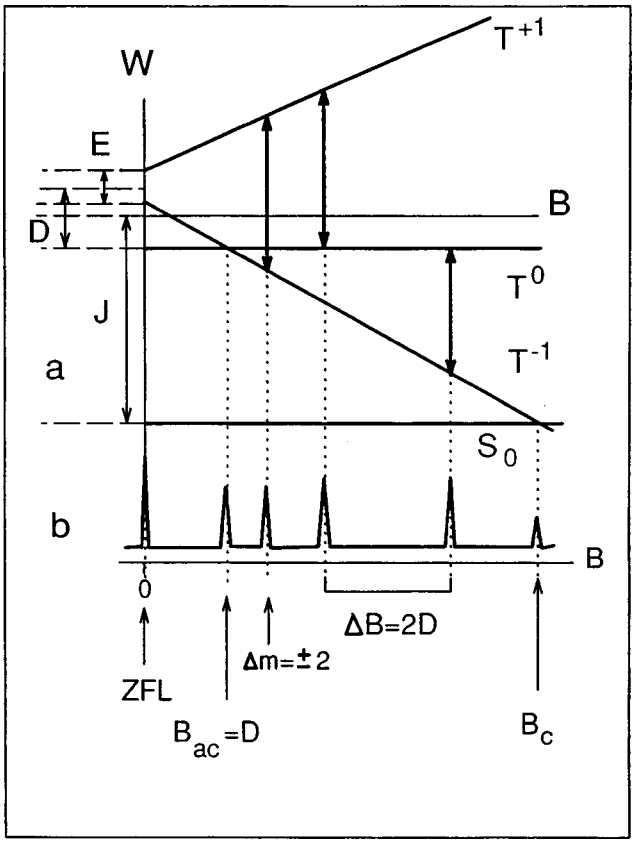

FIG. 1. Energy levels of a system of two electrons in a magnetic field B (a) and the expected positions of the SDR detected lines of the change of the microwave photoconductivity (b).

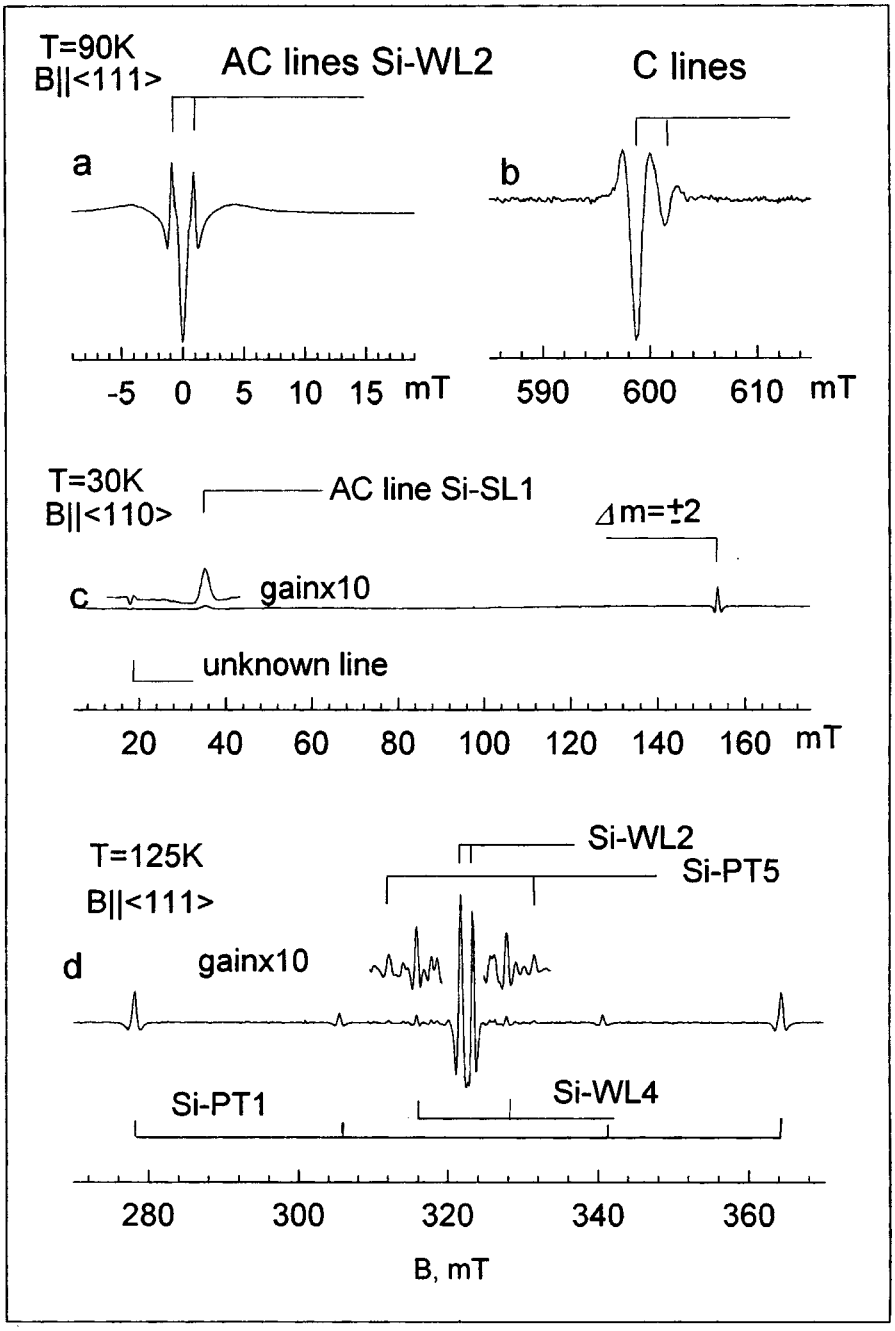

FIG. 2. SDR detected lines of microwave photoconductivity in irradiated silicon, observed in different ranges of magnetic field B for various defects. Zero field line and anticrossing (a) and crossing (b) lines correspond to the Si–$WL2$ center. Anticrossing line and line of the forbidden transition (c) are related to the excited triplet state of the oxygen + vacancy complex (Si–$SL1$ spectrum). SDR–EPR spectra of the defects with different D-constant are presented in (d).

plied magnetic field **B** and the electrons spins S_1 and S_2 (μ_B is the Bohr magneton, g_1 and g_2 are g-tensors of the first and second electrons), the isotropic exchange interaction $J\mathbf{S}_1\mathbf{S}_2$, and the anisotropic magnetic dipole-dipole interaction $\mathbf{S}_1\mathbf{D}\mathbf{S}_2$, where **D** is a symmetric traceless tensor determined by two parameters, D and E, in the principal coordinate frame corresponding to the symmetry of the defects. The energy levels obtained from the Hamiltonian (1) for the case of two identical electrons ($\mathbf{g}_1=\mathbf{g}_2$ and $S_1=S_2=1/2$) are shown in Fig. 1a.

The exchange interaction between two unpaired electrons leads to formation of a ground singlet S_0 state with spin $S=0$ and an excited metastable triplet state T ($S=1$). In zero magnetic field these states are separated by the energy $J\cong W(T)-W(S_0)$ where J is the exchange interaction constant. An additional zero-field splitting between T^{+1}, T^{-1}, and T^0 states is due to the magnetic dipole-dipole interaction $\mathbf{S}_1\mathbf{D}\mathbf{S}_2$. The expected spectrum of the change of photoconductivity of the sample containing defects in the excited triplet state is shown in Fig. 1b.

The formation of the excited triplet states of defects under illumination and the change of the recombination rate of the photoexcited carriers under saturation of the EPR transi-

tions between magnetic sublevels T^{+1}, T^0, and T^{-1} as well as the change of photoconductivity at the magnetic field $B = B_{ac}$ corresponding to the anticrossing of the sublevels T^{-1} and T^0 without magnetic resonance (see Fig. 1b) was considered in detail in Refs. 5,6. In addition, the spin dependent change of photoconductivity can be observed at zero magnetic field (ZFLine), at the magnetic field $B = B_c$ corresponding to the crossing of excited T^{-1} state and ground S_0 state, and under magnetic resonance between T^{+1} and T^{-1} sublevels (forbidden $\Delta = \pm 2$ transitions). The examples of the experimentally detected lines of the SDR related change of photoconductivity are shown in Fig. 2. The angular and temperature dependences of intensity and position of these lines allow us to get additional information about the parameters of the Hamiltonian (1).

2. PARAMETERS OF THE SPECTRA AND MODELS OF THE DEFECTS

The components of the **g** and **D** tensors determined from the experimentally observed angular dependences of the EPR spectra bear an information on the symmetry of point defects. The exchange interaction constant J and the component D of the **D** tensor depend of the distance r between interacting electrons, which is important for consideration of the models of defects.

The value of J depends exponentially on the distance r and is usually many orders of magnitude higher than the Zeeman energy. For such defects the crossing (C) lines cannot be detected at reasonable strength of the magnetic field. Defects having the value of J comparable with the Zeeman energy were found recently.[9,10] The positions and angular dependences of the anticrossing and crossing lines for such defects (see Figs. 2a and 2b) are described by the same parameters of Hamiltonian (1) as the new SDR detected Si–$WL2$[10] spectrum shown in Fig. 2d.

The value of parameter D is proportional to $1/r^3$ averaged over the electron wave function. It can be determined experimentally from the fine-structure splitting of the Zeeman lines separated by $\Delta B \cong 2D$ as well as from the position of the anticrossing line (AC) (see Fig. 1b).

The knowledge of D values allows us to estimate the average distance between two unpaired electrons forming the total spin $S = 1$ of the defects and to suggest the models of the investigated defects. The comparison of the ΔB values for Si–$WL2$ and for other SDR–EPR spectra with the theoretical dependence of ΔB on the distance r calculated in Ref. 11 is shown in Fig. 3. The models of some carbon related defects derived from the SDR–EPR spectroscopic data are shown in Fig. 4.

Carbon impurities play an important role in the formation of radiation defects in silicon. One of the main defects in the irradiated pure float-zone grown silicon is the (C_I–Si_S–C_I) complex (Fig. 4a) giving the SDR–EPR spectrum labeled Si–$PT1$. Under isochronal thermal annealing in the temperature range of 200–300°C the spectrum Si–$PT1$ decreases and new spectrum Si–$PT4$ appears simultaneously. It was found that this spectrum has a symmetry similar to the symmetry of divacancy and shows the hyperfine structure due to interaction with two equivalent carbon atoms. The model of the defects responsible for the Si–$PT4$ spectrum is shown in Fig. 4b. This defects can be considered a complex of two carbon atoms + divacancy.

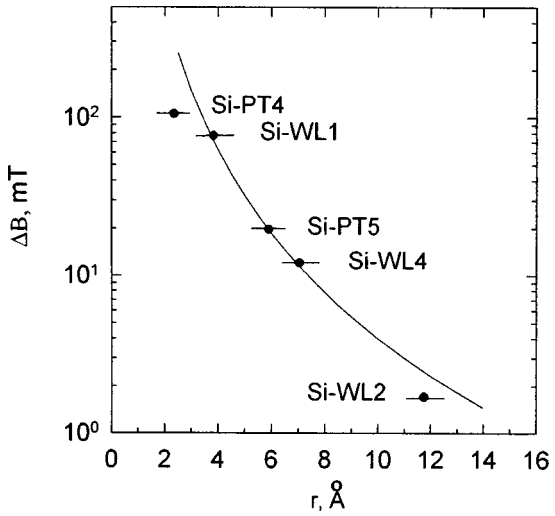

FIG. 3. Dependence of the fine structure splitting ΔB on the distance r between two interacting electrons.

Two weak spectra, Si–$WL2$ and Si–$WL4$,[10] shown in Fig. 2d are observed in the unannealed samples. The models

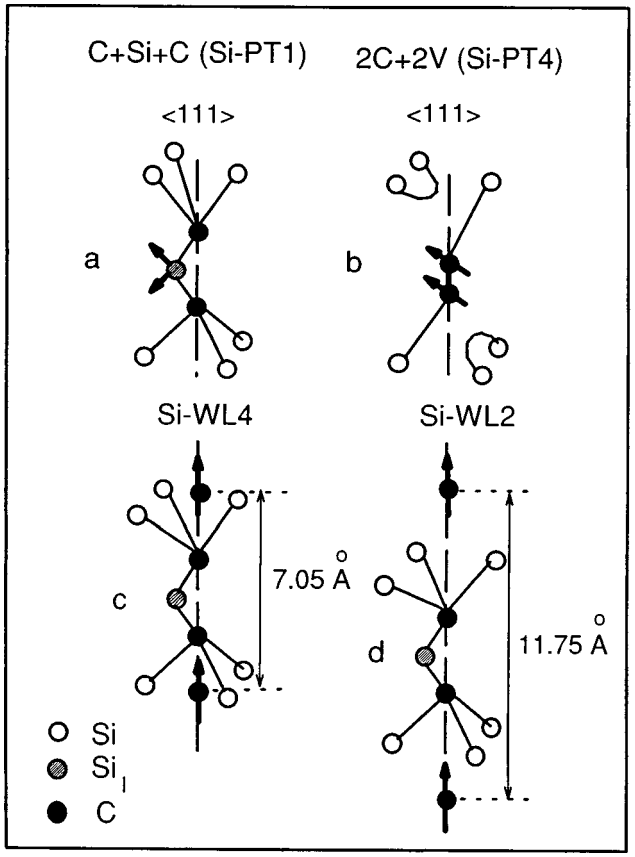

FIG. 4. The models of the carbon related defects corresponding to the SDR–EPR spectra Si–$PT1$ (a), Si–$PT4$ (b), Si–$WL1$ (c), and Si–$WL2$ (d).

of the defects giving these spectra are shown in Figs. 4c and 4d. These models were derived from the trigonal symmetry of the spectra and from the values of the fine-structure splitting $\Delta B = 2D$ determined by the distance between two electrons forming the total spin of defects $S = 1$. These electrons can be localized at the carbon atoms occupying the tetrahedral interstitial positions along $\langle 111 \rangle$ directions of the silicon lattice near the $(C_I - Si_S - C_I)$ complex.

In summary, the spin-dependent effects and detection of EPR spectra by the change of microwave photoconductivity of samples allow us to observe the spectra of the excited triplet state of defects at their low concentration, which cannot be detected by traditional EPR spectroscopy. The nonresonat crossing and anticrossing change of photoconductivity allows us to obtain additional information about the parameters of the triplet centers and to suggest their models.

The author thanks B. P. Zakharchenya for helpful discussions, R. Laiho for collaboration and helpful discussions, M. P. Vlasenko and M. M. Afanasjev for help in the experiments.

This work was supported by RFBR Grant N 97-02-18062.

[1] C. A. J. Ammerlaan, ''Paramagnetic centers in silicon,'' in *Landolt–Börnstein Numerical Data and Functional Relationship in Science and Technology*, edited by O. Madelung, Vol. 22 b, Impurity and Defects in Group IV Elements and III–V Compounds (Springer–Verlag, Berlin, 1992), p. 365.
[2] G. W. Ludwig and H. H. Woodbury, ''Electron Spin Reconance in Semiconductors,'' in *Solid State Physics*, Vol. 13, edited by F. Zeitz and D. Turnbull (Academic Press, N.Y., 1992), p. 223.
[3] G. D. Watkins, ''A Review of EPR Studies in Irradiated Silicon,'' in *Radiation Damage in Semiconductors*, edited by P. Baruch (Dunod, Paris, 1965), p. 97.
[4] D. J. Lepine, Phys. Rev. B **6**, 436 (1972).
[5] L. S. Vlasenko, M. P. Vlasenko, V. N. Lomasov, and V. A. Khramtsov, Sov. Phys. JETP **64**, 612 (1986).
[6] L. S. Vlasenko, in *Semiconductor and Insulators: Optical and Spectroscopic Research* (Nova Science Publishers, Inc., N.Y., 1992), p. 217–244.
[7] M. P. Vlasenko and L. S. Vlasenko, Sov. Phys. Solid State **33**, 1326 (1991).
[8] V. A. Khramtsov, V. N. Lomasov, Ya. Ya. Pilkevich, M. P. Vlasenko, and L. S. Vlasenko, Phys. Status Solidi A **109**, 127 (1988).
[9] L. S. Vlasenko, Y. V. Martynov, T. Gregorkiewicz, and C. A. J. Ammerlaan, Phys. Rev. B **52**, 1144 (1995).
[10] R. Laiho, M. M. Afanasjev, M. P. Vlasenko, and L. S. Vlasenko, Phys. Rev. Lett. **80**, 1489 (1998).
[11] Y. H. Lee and J. W. Corbett, Phys. Rev. B **13**, 2653 (1976).

Published in English in the original Russian journal. Reproduced here with stylistic changes by the Translation Editor.

Excitons in hybrid organic–inorganic nanostructures

F. Bassani, G. C. La Rocca,*) and D. M. Basko

Scuola Normale Superiore and INFM Piazza dei Cavalieri, I-56126 Pisa, Italy

V. M. Agranovich

Institute of Spectroscopy, Russian Academy of Sciences, 142902 Troitsk, Moscow District, Russia
Fiz. Tverd. Tela (St. Petersburg) **41**, 778–780 (May 1999)

In two-dimensional heterostructures made of semiconductor and organic layers, when resonance between the Wannier and Frenkel excitons is realized, the dipole-dipole interaction coupling them leads to novel effects. First, we discuss the pronounced nonlinear optical properties of the hybrid Frenkel–Wannier excitons appearing when the energy splitting of the excitonic spectrum is large compared to the exciton linewidths (the case of strong resonant coupling). Next, we consider the case of weak resonant coupling for which the Förster mechanism of energy transfer from an inorganic quantum well to an organic overlayer is of great interest: the electrical pumping of excitons in the semiconductor quantum well could be employed to turn on efficiently the organic material luminescence. © *1999 American Institute of Physics.* [S1063-7834(99)00605-X]

In the last few years, much attention was devoted to the study of organic crystalline layered structures, both experimental[1] and theoretical.[2] The substantial improvement in the technique of organic molecular-beam deposition has led to a variety of good quality heterostructures based on molecular solids as well as on combinations of organic and inorganic semiconductors. The possibility of growing tailor-made systems incorporating different organic crystalline materials with even more flexibility than for multiple quantum wells based on inorganic semiconductors opens up a promising field of research from the point of view of fundamental as well as applied physics.

Such technological progress prompted us to study heterostructures with resonating Frenkel excitons (FEs) in the organic material and Wannier–Mott excitons (WEs) in the inorganic one.[3] For example, the FE energy in anthracene is 3 eV, in coronene is 2.9 eV, in PTCDA 2.2 eV, in pentacene 1.5 eV. Semiconductor quantum wells with resonating WEs can be obtained from III–V and II–VI ternary solid solutions such as GaAlAs, ZnCdSe, ZnSSe, judiciously choosing the alloy composition and well thickness.

Another concern is the width of the exciton lines. In good quality inorganic semiconductor quantum wells, the WE linewidth is of the order of 1 meV (usually limited by inhomogeneous broadening). FEs in organic materials typically have a much larger linewidth (often due to strong electron-phonon coupling); for instance, about 200 meV in thin films of PTCDA.[1] However, it is possible to choose resonating organic materials with sharp FEs, such as coronene (exciton linewidth $\simeq 4$ meV [Ref. 4]) or the surface exciton of anthracene (linewidth of about 1 meV [Ref. 5]). It is important to note that the dipole-dipole interaction coupling the FEs and WEs at an organic–inorganic heterojunction can be of the order of 10 meV (Refs. 3 and 6). Therefore, the case of strong coupling (Sect. 1), in which the exciton linewidths are smaller than the anticrossing energy splitting and hybrid excitons (HEs) exhibiting pronounced optical nonlinearities are formed,[3,6] must be distinguished from the case of weak coupling (Sect. 2), in which the FEs are much broader and the dipole-dipole coupling gives rise to an irreversible energy transfer from the inorganic to the organic material.[7,8]

1. STRONG RESONANT COUPLING: HYBRID EXCITON NONLINEARITIES

In covalent semiconductor quantum wells, optical nonlinearities dominated by phase-space filling effects have already attracted much interest.[9] The density-dependent susceptibility near the excitonic resonance can be written as

$$\chi(\omega)\simeq\chi^0(\omega)\left(1-\frac{n}{n_S}\right)\simeq\frac{F^0}{\epsilon^0-\hbar\omega}\left(1-\frac{n}{n_S}\right), \tag{1}$$

where χ^0 is the linear susceptibility, ϵ^0 is the resonance energy and F^0 represents the oscillator strength of the exciton, n is the $2D$ density of excitons and n_S — the saturation density given roughly by $n_S\approx 1/a_o^2$, a_o being the exciton radius. Indicating the light intensity with I_P, we recall that $n\propto F^0 I_P$ and F^0 is, in turn, proportional to $1/a_o^2$. Thus, for a given I_P, the ratio n/n_S is approximately independent of the exciton radius. As long as the exciton radius dependence of the oscillator strength and of the saturation density cancel out, such a figure of merit of the optical nonlinear response cannot be much improved by tailoring the character of the excitonic resonance with dimensional confinement or even by changing the material class.[10]

Here, we focus on a novel way of achieving a large nonlinear optical response exploiting the HEs peculiar to organic–inorganic nanostructures for which the situation is quite different. The physical system we are referring to comprises two parallel two-dimensional layers separated by a distance of a few nanometers: the first contains tightly bound

FE (the size of which is of the order of a unit cell) and the second, loosely bound WE (with radius a_o of about 10 nanometers), having energies ϵ_F^0 and ϵ_W^0, respectively, and a center of mass momentum $\hbar\mathbf{Q}$ along the layer planes (assumed to be conserved). Near resonance ($\epsilon_F^0 \simeq \epsilon_W^0$), they mix with each other via the dipole-dipole coupling $|V_{WF}^0(\mathbf{Q})|$.[3,6] When the dipole-dipole interaction energy is larger then the exciton linewidths, the true eigenstates of the system are HEs with wavefunctions of a mixed character and modified dispersion laws,[3,6] in particular when the FE and WE are exactly in resonance the HE eigenvalues are a split doublet and the corresponding wavefunctions are superpositions of FE and WE wavefunctions with equal weights. Since the HEs possess both the large radius of Wannier excitons and the large oscillator strength of Frenkel excitons, their saturation density n_S is still comparable to that in covalent semiconductor quantum wells, but the photogenerated density n, for a given I_P, is much higher: as a consequence, the ratio n/n_S for the $2D$ HE can be two orders of magnitude larger than for the usual multiple quantum wells.[6]

The first-order nonlinear corrections can be expressed in terms of the total $2D$ HE density n[6,9]: the WE blue shift $\epsilon_W^1 \simeq 0.48 E_b \pi a_o^2 n$ (E_b being the WE binding energy), the WE Pauli blocking factor $B_W \simeq 1 - 0.14\pi a_o^2 n$ and the correction V_{WF}^1 to the hybridization due to the modification of the WE wavefunction $|V_{WF}^0 + V_{WF}^1|^2 \simeq (1 - 0.12\pi a_o^2 n)|V_{WF}^0|^2$. All these effects are typical for Wannier excitons having a small saturation density $n_S \approx 1/a_o^2$, but here they belong to the hybrid excitons which also have a large oscillator strength characteristic of Frenkel excitons. Using a standard microscopic approach,[9] we can then write the density dependent $2D$ susceptibility of hybrid excitons as[6]

$$\chi_{HE}(\omega;Q) \simeq \frac{F_F^0(\epsilon_W^0 + \epsilon_W^1 - \hbar\omega)}{(\epsilon_W^0 + \epsilon_W^1 - \hbar\omega)(\epsilon_F^0 - \hbar\omega) - B_W|V_{WF}^0 + V_{WF}^1|^2}, \tag{2}$$

where only the dominant term proportional to F_F^0 has been retained. In the linear regime, n is negligible and $\epsilon_W^1 \simeq 0$, $V_{WF}^1 \simeq 0$ and $B_W \simeq 1$; the poles of the linear susceptibility are just the HE doublet eigenvalues. With increasing excitation intensity, the FEs are not much disturbed due to their large saturation density, but the WEs start bleaching and this affects the above HE susceptibility. For realistic parameters, at $Q \simeq 10^7\ \mathrm{cm}^{-1}$ we have $|V_{WF}^0| \simeq 5$ meV (Ref. 2) and, including phenomenological linewidths of a few meV, we obtain[2,6] for the fractional nonlinear change in absorption coefficient close to resonance $|\Delta\alpha|/\alpha \approx 10^{-11}\mathrm{cm}^2\, n$, which for a given n is of the same order as for a covalent semiconductor quantum well. However, for a given pump intensity I_P, the $2D$ density of photogenerated excitons n is in our case about two orders of magnitude larger ($n \propto \chi_{HE} \propto F_F^0$), as anticipated. We wish to stress that the present effect is typical of hybrid excitons and would not be effective in the case of two coupled quantum wells of the same material.

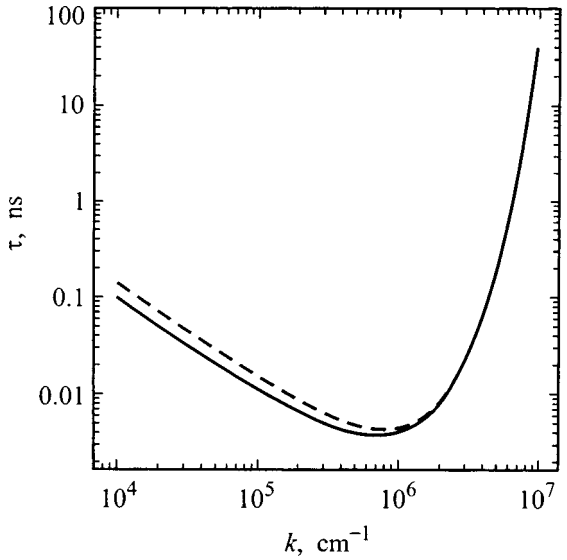

FIG. 1. Free L exciton (solid line) and Z exciton (dashed line) lifetime τ vs the center of mass in-plane wave vector k.

2. WEAK RESONANT COUPLING: FÖRSTER ENERGY TRANSFER

A large effort has recently been devoted to the study of organic light-emitting diodes and lasers. Förster-like energy transfer between different dye molecules in solid solutions has already been used to achieve light amplification in optically pumped organic thin films.[11] However, optically-active organic materials have poor transport properties compared to inorganic semiconductors and the efficient electrical pumping of such devices is a challenging problem. Prompted by the rapid advances of epitaxial growth techniques for crystalline molecular materials (even on inorganic substrates),[1] we consider here a novel hybrid configuration in which both inorganic semiconductors and organic materials are present: the basic idea is to pump the optically-active organic molecules via electronic energy transfer from the two-dimensional Wannier–Mott excitons of a semiconductor quantum well.

We consider a symmetric structure consisting of a semiconductor QW of thickness L_w between two barriers of thickness L_b each (L_b being a few nanometers), the whole semiconductor structure being surrounded by semi-infinite slabs of an isotropic organic material. We assume that, in the frequency region considered here, the semiconductor background dielectric constant ϵ_b is real (the same for the well and the barrier) and that of the organic material $\tilde{\epsilon}$ is complex (due to a broad absorption band). The irreversible Förster-like energy transfer rate due to the dipole-dipole interaction can be calculated simply from the Joule losses in the organic material.[7,8] First, we calculate the transfer rate from free excitons.[7,8] We consider two polarizations: one lying in the QW plane along $\mathbf{k}$ (L-exciton), the other perpendicular to the QW plane (Z-exciton). In Fig. 1, we plot τ_L and τ_Z as functions of exciton center of mass momentum k for parameters representative of II-VI semiconductor QWs in a realistic structural geometry. It turns out that the lifetime does not depend drastically on the polarization and the real parts of

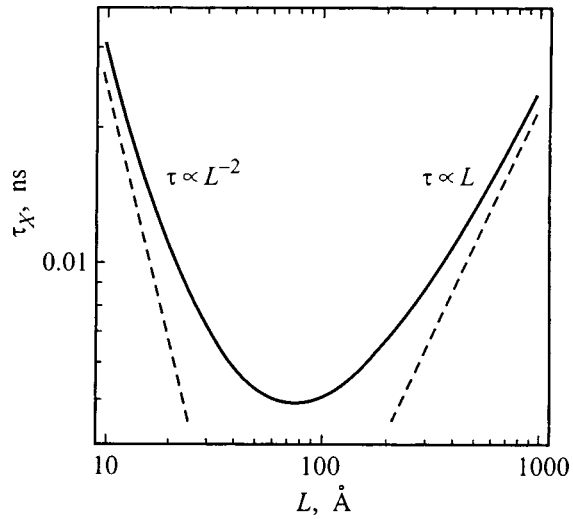

FIG. 2. Localized X-exciton lifetime τ vs the localization length L (solid line) along with the limiting cases $L \ll L_b$ and $L \gg L_b$ (dashed lines).

dielectric constants. The dependence on L_w is also weak. The barrier width L_b, when grows, gives an exponential factor e^{2kL_b}. As a function of k, τ exhibits a minimum at $k_{\min} \sim 1/L_b$. Typical values of k for a thermalized exciton distribution with temperature ~ 100 K are $\sim 3\times 10^6$ cm^{-1}. We see that the corresponding lifetimes (tens of picoseconds) are much less then the exciton recombination rate which is about $100-200$ ps in II-VI semiconductor QWs. Thus the dipole-dipole transfer mechanism proves to be efficient enough to transfer a large fraction of the semiconductor excitation energy to the organic medium.

We have also studied the situation when the QW width fluctuations or the alloy disorder localize the wave function $\Phi(\mathbf{r}_\parallel)$ of the center-of-mass exciton motion.[8] General properties of $\Phi(\mathbf{r}_\parallel)$ are: (i) it is localized within some distance $L > L_w$, (ii) it is smooth and without nodes. Assuming the disorder to be isotropic in two dimensions, we need to consider two cases of the polarization being parallel and perpendicular to the QW plane, referred to as X and Z polarizations, respectively. It is possible to get some information about the decay rate based only on general properties of the wave function, mentioned above. We have three length scales in our problem: L_w, L_b and L. First, only $L \gg L_w$ are physically meaningful. If in addition $L \gg L_b$, we obtain $\tau \propto L$, while for a thick barrier ($L \ll L_b$) we have $\tau \propto 1/L^2$. Hence, τ has a minimum at some $L \sim L_b$. For illustrative purposes, we choose a gaussian wave function of width L and show in Fig. 2 the results of the calculation (τ versus L) for realistic parameter values. We also considered the case of a quasi-thermalized plasma of free electrons and holes.[8] The dipole-dipole lifetimes obtained turn out to be as long as 300 ps (and larger) for II–VI-semiconductors.

According to our results, the kinetics of the initial free-carrier population (produced, e.g., by the electrical pumping) is not significantly changed by the presence of the organic medium, since the energy transfer from free carriers turns out to be slower than the process of exciton formation (unless excitation density and temperature are very high). On the other hand, the subsequent evolution of free or localized excitons is strongly affected by the presence of the organic medium. In an isolated QW the effective lifetime of the exciton distribution may be several hundred picoseconds. However, excitons coupled to the organic medium a few nanometers away efficiently transfer their energy to the organic molecules before they can recombine inside the QW. For quantum wells based on II–VI semiconductors and in a realistic configuration, such transfer may occur on time scales of the order of 10 ps and be effective in activating the organic material luminescence.

To summarize, the simple physical pictures presented above may lead to new concepts for optoelectronic devices based on hybrid organic-inorganic structures, especially if embedded in a suitable microcavity.[2,12] More detailed theoretical calculations would be useful, but probably the crucial factor will be the technological progress in the synthesis of such systems. We believe that this is a very promising field of research and hope that the experimental efforts to grow and investigate these novel systems will be successful.

Partial support from INFM through the project ''Photoactive Organic Materials'' (PAIS G) is acknowledged. V.M.A. is thankful to Scuola Normale Superiore (Pisa, Italy) for hospitality and support.

He also acknowledges partial support through Grant 96-0334049 of the Russian Foundation of Basic Researches, Grant from ''Physics of Nanostructures,'' the Russian Ministry of Science and Technology and INTAS Grant 93-461.

*)E-mail: larocca@ella.sns.it

[1] S. R. Forrest, Chem. Rev. **97**, 1793 (1997), and references therein.
[2] V. M. Agranovich, Mol. Cryst. Liq. Cryst. Sci. Technol., Sect. A **230**, 13 (1993); Physica Scripta **T49**, 699 (1993); V. M. Agranovich, D. M. Basko, G. C. La Rocca, and F. Bassani, J. Phys. Cond. Mat., in press.
[3] V. Agranovich, R. Atanasov, and F. Bassani, Solid State Commun. **92**, 295 (1994).
[4] M. Sakurai, M. Furukawa, K. Mizuno, and A. Matsui, J. Phys. Soc. Jpn. **61**, 445 (1992).
[5] M. Orrit, J. Bernard, J. M. Turlet, and P. Kottis, J. Chem. Phys. **78**, 2847 (1983).
[6] G. C. La Rocca, F. Bassani, and V. M. Agranovich, Nuovo Cimento D **17**, 1555 (1995); G. C. La Rocca, F. Bassani, and V. M. Agranovich, in *Notions and Perspectives of Nonlinear Optics*, edited by O. Keller (World Scientific, Singapore, 1996); G. C. La Rocca, Physica Scripta **T66**, 142 (1996).
[7] V. M. Agranovich, G. C. La Rocca, and F. Bassani, JETP Lett. **66**, 748 (1997).
[8] D. M. Basko, G. C. La Rocca, F. Bassani, and V. M. Agranovich, submitted to European Phys. Journal B.
[9] S. Schmitt-Rink, D. S. Chemla, and D. A. B. Miller, Adv. Phys. **38**, 89 (1989); H. Haug and S. W. Koch, *Quantum Theory of the Optical and Electronic Properties of Semiconductors*, 3rd ed. (World Scientific, Singapore, 1994), Ch. 16.
[10] B. I. Green, J. Orenstein, and S. Schmitt-Rink, Science **247**, 679 (1990).
[11] M. Berggren, A. Dodabalapur, R. E. Slusher, and Z. Bao, Nature (London) **389**, 466 (1997).
[12] V. Agranovich, H. Benisty, and C. Weisbuch, Solid State Commun. **102**, 631 (1997); V. Agranovich, G. C. La Rocca, and F. Bassani, Pure Appl. Opt. **7**, 119 (1998).

Published in English in the original Russian journal. Reproduced here with stylistic changes by the Translation Editor.

Phase transition to the conducting state in a system of charge-transfer excitons at a donor–acceptor interface

V. M. Agranovich* and S. A. Kiselev

Institute of Spectroscopy, Russian Academy of Sciences, 142092 Troitsk, Moscow District, Russia

Z. G. Soos and S. R. Forrest

The Princeton Materials Institute, Princeton University, Princeton, NJ 08544, USA
Fiz. Tverd. Tela (St. Petersburg) **41**, 781–784 (May 1999)

We discuss the phase transition to the conducting state in a system of $2D$ charge-transfer excitons (CTEs) at a donor–acceptor interface. The phase transition arises due to strong dipole-dipole repulsion between CTEs which stimulates the population of free carriers in higher energy states even at low temperature. We use the computer simulations with the random distribution of excitons, with finite lifetime explicitly taken into account. The critical concentration of CTEs and their energy distribution are calculated. We also discuss the possibility of observing the predicted phenomena. © *1999 American Institute of Physics.* [S1063-7834(99)00705-4]

Two models are employed to classify excitons — the small-radius Frenkel-exciton model, and the large-radius Wannier–Mott exciton model.[1] The charge-transfer exciton (CTE) occupies an intermediate place in the classification based on the exciton internal structure.[2] The lowest energy CTE usually extends over two nearest-neighbor molecules. In a CTE, the electron is localized on the acceptor and the hole, on the donor. Such localization in organic crystals is usually stable because the energy of electron-hole attraction is large compared to the corresponding widths of the conduction and valence bands and due to the strong tendency of the CTE to undergo self-trapping.[3] Due to the separation of the electron and the hole in a CTE, the static dipole moment created by positive and negative ions can assume values as large as $10-25D$. This feature determines the most characteristic properties of the CTE. For example, the CTEs contribute to the large second order nonlinear polarizability χ^2 due to their large dipole moment.[4] As it was recently shown,[5] the same feature can be responsible for a new type of photovoltaic effect in asymmetric $D-A$ superlattices,[5a] for unusual intensity dependences of nonlinear polarizabilities of $D-A$ superlattices,[5b] and also for phase transitions to conducting states in the system of CTEs.[5c] In all of these cases, it was assumed that CTEs between alternating layers of donors and acceptors at $D-A$ interfaces are the lowest-energy electronic excited states. These states are usually populated after lattice relaxation from higher-energy Frenkel-type electronic or vibronic states. In this work, we investigate the transition from a dielectric to a conducting state in a system of CTEs at a $D-A$ interface (see also Ref. 6). The realistic possibility to consider such organic crystal structures appeared recently from progress in the development of organic molecular-beam deposition and other related techniques.[7] This opens a wide range of possibilities for creating new types of ordered organic multilayer structures including ordered interfaces.

1. PHASE TRANSITION FROM DIELECTRIC TO CONDUCTING STATE

Consider the CTEs on a single $D-A$ interface. We assume that they are aligned normal to the interface plane, resulting in mutual repulsion. For example, if the static CTE dipole moment is equal to $20D$ and the distance between them is 5 Å (the lattice constant at the interface), the repulsion energy is near 1 eV. If the distance between CTEs increases to 10 Å, the repulsion energy decreases to 0.1 eV. It is important that these energies are of the order of their separation B from the lowest conduction band ($B<0.5$ eV, see Ref. 8). Thus, at high CTE concentrations, we can expect that repulsion energy populates the higher energy states with free carriers, thus producing photoconductivity even at very low temperature.[5c] In Ref. 5c the photoconductivity was considered under the assumption that the time required for a phase transition to the conducting state is smaller than the CTE lifetime. Such a phase transition was obtained by minimizing the total energy of the CTEs and dissociated excitations (free carriers). Consider, for simplicity, a $2D$ array of self-trapped CTEs at $T=0$. The energy of CTEs (concentration n_1) and the energy of dissociated e–h pairs (concentration n_2), can be calculated by assuming that the total number of excitations, determined by the optical pumping intensity, is constant: $n_1+n_2=n$. The energy of the CTE array, therefore, is $E_1=n_1\Delta+E_{int}$, where E_{int} is the total repulsion energy. This energy can be estimated using the average distance ρ between CTEs. In the case of dipoles p

$$V=\frac{Ap^2}{\rho^3}, \tag{1}$$

where A is a geometric constant depending on the CTE distribution in the interface plane. For example, for a square lattice $A\approx 10$. Since the CTE concentration, by definition, is $n_1=1/\rho^2$, the electrostatic energy of the interaction between the dipole moments is $E_{int}=Vn_1/2=Ap^2n_1^{5/2}/2$. We can ap-

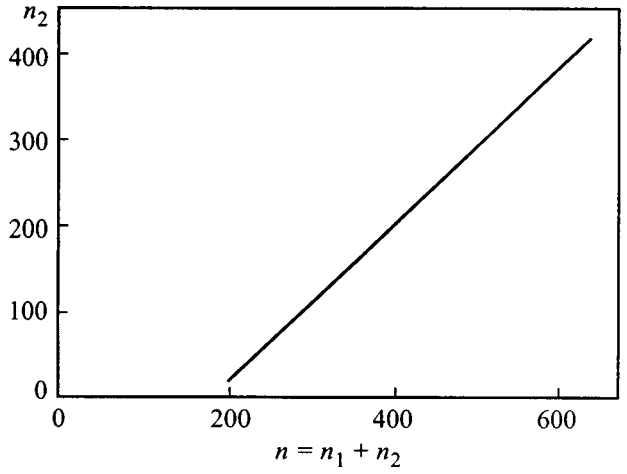

FIG. 1. The number of the charge-transfer excitons (n_1) at the donor–acceptor interface and the number of the dissociated excitons (n_2) as functions of the total number of excitations [according to the simplified analytical model, Eq. (3)].

proximate the energy of the dissociated pairs $E_2=(\Delta+B)n_2$, where the kinetic energy of the free carriers has been neglected (due to the self trapping and narrow electronic bands, see above). Near the threshold, where the consentration $n_2 \ll n_1$ and also $n_1 \ll 1$, we can neglect the interaction of the free carriers with the CTEs. The total energy of the system then can be written as

$$E=E_1(n_1)+E_2(n_2)=n\Delta+\frac{Ap^2(n-n_2)^{5/2}}{2}+Bn_2. \quad (2)$$

Minimizing the above expression with respect to n_2 gives

$$n_2=n-\left(\frac{4B}{5Ap^2}\right)^{2/3}. \quad (3)$$

It is clear from Eq. 3 that n_2 is positive at $n>n_{cr}=[4B/(5Ap^2)]^{2/3}$ (see Fig. 1). The appearance of free carriers at $n>n_{cr}$ is considered to be a phase transition from the dielectric to conducting state. This transition corresponds to photoconductivity at low temperature (i.e., to cold photoconductivity) and is due to long-range dipole-dipole interactions between CTEs. In this consideration, we neglected the randomness in the CTE distribution and did not consider the establishment of steady state in ensembles, which is dependent on the pump intensity and the CTE lifetime. These effects are explicitly taken into account in our computer simulations.[6]

2. MODEL FOR NUMERICAL SIMULATIONS AND RESULTS

The $D-A$ sites are arranged in a square lattice. The $D-A$ interface is uniformly irradiated with a time-independent source of intensity I. Only one CTE can be generated at any site. As long as the CT exciton is generated it will stay at the lattice site and it cannot move to other $D-A$ sites because of self trapping. There are two mechanisms for the CTE to disappear. First, recombination occurs because of the finite lifetime τ of the CTE. The second mechanism is dissociation. The CTE exciton dissociates when, due to the dipole-dipole interaction, the energy of the particular exciton exceeds some threshold. If there are n_1 CTEs occupying the $D-A$ interface, the electrostatic energy of the jth exciton in the electric field of the other excitons surrounding this site is

$$V_i=\sum_{j=1}^{n_1}\frac{p^2}{r_{ij}^3}, \quad (j\neq i). \quad (4)$$

The ith CT exciton dissociates when the repulsion energy, V_i, is larger than the energy B. The electrostatic potential energy of the exciton strongly increases when few CTEs occupy the nearest-neighbor lattice sites. If this occurs, one or more CTEs will dissociate. Such a mechanism should result in correlations between exciton positions, and ordering of the system of immobile CT excitons can be expected. Such spatial ordering suggests the existence of a critical pump-light intensity above which there is an onset of photoconductivity. Thus, just above this threshold, we expect an onset of cold photoconductivity. In simulations, we neglect the process of recombination of free carriers which can result in the creation of CTEs. Near the threshold, where the concentration of free carriers is small, the contribution of this process to the number of CTEs will be small and can be neglected. However, even at higher concentration, the effect of free-carrier recombination can be reduced by applying the electric field along the interface. This field will separate electrons and holes and thus will create the photocurrent which can be measured. Computer simulations were performed for a two-dimensional square lattice containing 600×600 sites. Under continuous pumping of the sample with a constant intensity, the CTEs are generated in the process described above. In order to avoid the influence of boundary conditions, we simulate the evolution of only the central part of the lattice. This square, the central sublattice, consists of 200×200 $D-A$ sites, $N=40{,}000$. Next, we replicate the central sublattice by adding 8 square sublattices surrounding the central one. That is, the exciton positions calculated for the central 200×200 sites square lattice is reflected via mirror symmetry to the surrounding 8 squares. To simulate the time evolution, we run the system through equally spaced time steps separated by interval Δt. The value of $\Delta t=\tau/50$ is chosen to be much shorter than the CTE lifetime τ. We start the simulations when there are no CTEs at the interface. Under the influence of the pumping, the excitons begin to appear. After a time $\approx\tau$, the number of CT excitons occupying the lattice reaches steady-state value. From this time on, the necessary statistical information is collected. The time evolution of the system is simulated as follows: At every time step a few CTEs (depending on the pumping intensity, I, are created at randomly chosen positions in the central sublattice. Then we go over the central sublattice sites and check every $D-A$ molecule. With some probability, the exciton at this site can recombine, as explained above. It also can dissociate if its electrostatic energy is high enough. The rules for these events to happen at one particular $D-A$ site are: 1. If the site is empty, the charge-transfer exciton can be created with a probability $P_c=I\Delta t/N$. 2. If a charge-transfer exciton already occupies this site, it can recombinate with the probability $P_r=1-\exp(-\Delta t/\tau)$.

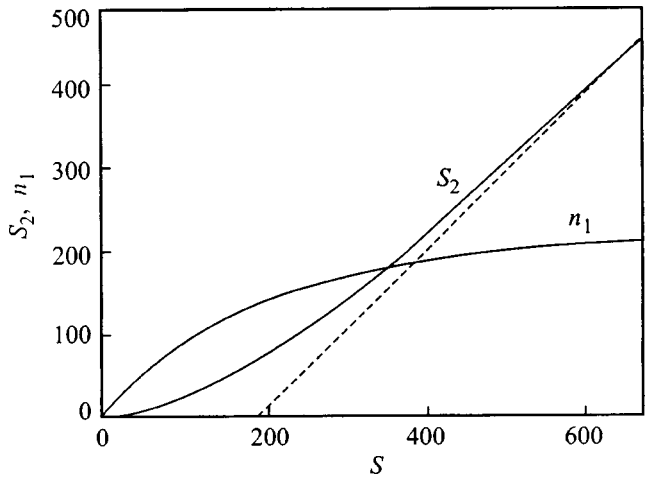

FIG. 2. The steady state number of the charge-transfer excitons (n_1) occupying the donor–acceptor interface and the number of dissociated pairs production (S_2) as functions of the pump intensity.

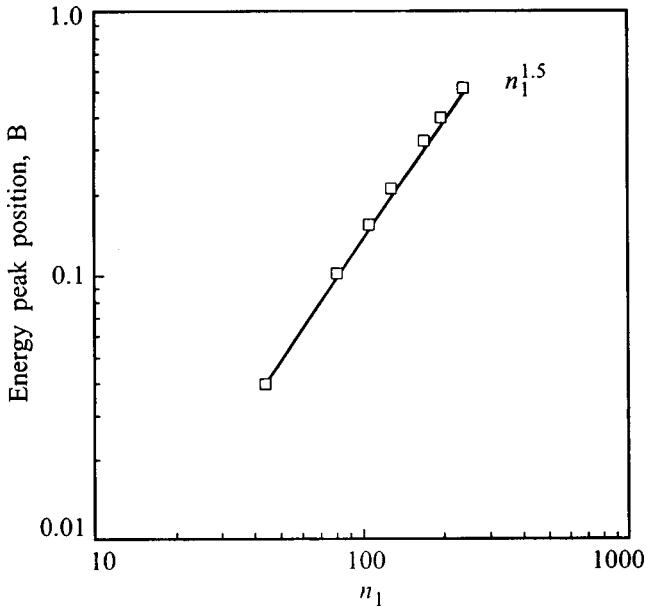

FIG. 3. Position of the energy distribution peak as a function of the number of the CT excitons, n_1.

Next, during the same time step, we calculate the energy of every CTE in the electrostatic field produced by the dipole moments of all other excitons. The energy of the ith CT exciton can be found using the Eq. (4). If this energy exceeds the dissociation threshold B, the CT exciton dissociates. Finally, we recalculate the energies of the CT excitons that remain at the $D-A$ interface.

All results reported below are collected after steady state is achieved. Fig. 2 shows the dependence of the number of CTEs (n_1) on the value S which is the product of generation intensity of the CTEs I and the CTE's lifetime τ: $S=I\tau$. The steady-state number of dissociated pairs is determined by their own lifetime, but we do not estimate here the concentration of carriers nor conductivity. Nevertheless, Fig. 2 plots the value S_2 which is equal to the number of dissociations which take place at given S in steady state during time τ. We find a qualitative agreement with the analytical theory in that the CTEs populate the $D-A$ interface only until some utmost concentration is achieved. Further increase of the pump S results mainly in the dissociation of CTEs into electron-hole pairs. When the number of CTEs reaches the saturation density, the number of dissociations S_2 increases linearly with S. It is interesting to compare the critical concentration of CTEs derived from analytical model (see Section 2) with the results of computer simulations. Following qualitatively the results of our analytical model (Fig. 1), we can take as a critical concentration of CTEs the concentration corresponding to saturation of CTEs at the interface or, what is nearly the same, the concentration of CTEs which corresponds to intersection of linear S_2 asymptote with the n_1 curve. In Fig. 2, the value of n_1 is approximately 200 and thus the corresponding critical dimensionless concentration $C_{cr}=200/40{,}000=0.5\%$. The curve in Fig. 1 corresponds to the value $M=Ba^3/p^2=0.01$. It follows from the analytical theory that for the same M the critical concentration $C_{cr}=(4Ba^3/5Ap^2)^{2/3}=(4M/5A)^{2/3}=0.85\%$. Thus, a random CTE distribution decreases the critical concentration for the transition to the conducting state. This effect could be expected, because, for random distribution, in contrast to our analytical model of ordered CTEs, the small distances between CTEs are allowed even at low CTE concentration. In both approaches, the critical concentration strongly depends on the values of B, p and a. For example, for $B=0.2$ eV, $p=20D$, and $a=5$ Å, corresponding to $M=0.1$, the analytical model yields $C_{cr}=4\%$, while the computer simulation's $C_{cr}=2.5\%$. For $M=0.05$, $C_{cr}=2.6\%$ (analytical approach) or 1.5% (computer simulations), and so on. Thus, for random CTE distribution at the $D-A$ interface, the critical concentration is almost twice as small as the analytical model predicts for ordered CTEs with infinite lifetime. The dissociation prevents the creation of clusters of the closely placed CT excitons and, especially, it prohibits CTEs from occupying adjacent sites at the $D-A$ interface. It cuts off the high-energy tail of the CTE energy-distribution function. The peak in energy distribution increases (for more details see Ref. 6) with the number of CTEs and so does the width of the distribution. It is interesting to note that the position of the peak at the repulsion energy distribution (corresponding to the energy of highest probability) varies with the steady-state number of CTEs approximately in the way in which the theoretical model of an ordered CTE lattice predicts. As it follows from Eq. (1), the CTE energy as a function of the number of CTEs should vary as $n_1^{3/2}$. Figure 3 demonstrates that such dependence take place in computer simulations for peak position, with high accuracy. At finite temperature, the repulsion also can be important because it decreases the activation energy. Such decrease in activation energy depends on the concentration of CTEs. To observe the predicted cold photoconductivity, the methods for observing photoconductivity parallel to the plane of dipoles developed in the investigations of Langmuir–Blodgett films[9] can be used. It is clear also that we need to have nearly perfectly ordered crystalline $D-A$ multilayers with a large interface area for such measurements.

Authors are thankful to Martin Pope, Jeffrey Schwartz and Vladimir Yudson for useful discussions.

*E-mail: agran@isan.troitsk.ru

[1] *Excitons*, edited by E. Rashba and M. Sturge (North-Holland, Amsterdam, 1982).
[2] M. Pope and C. E. Swenberg, *Electronic Processes in Organic Crystals* (Clarendon Press, Oxford, 1982); V. M. Agranovich and M. D. Galanin, *Electronic Excitations Energy Transfer in Condensed Matter* (North-Holland, Amsterdam, 1982).
[3] V. M. Agranovich and A. A. Zakhidov, Chem. Phys. Lett. **50**, 278 (1977).
[4] D. S. Chemla and J. Zyss, *Nonlinear Optical Properties of Organic Molecules and Crystals* (Academic Press, Orlando, 1987).
[5] (a) V. M. Agranovich, G. C. La Rocca, and F. Bassani, JETP Lett. **62**, 405 (1995); (b) V. M. Agranovich, G. C. La Rocca, and F. Bassani, Chem. Phys. Lett. **274**, 355 (1995); (c) V. M. Agranovich and K. N. Ilinski, Phys. Lett. A **191**, 309 (1994).
[6] S. A. Kiselev, E. Hartung, Z. G. Soos, S. R. Forrest, and V. M. Agranovich, Chemical Physics (1998), in press.
[7] S. Forrest, Chem. Rev. **97**, 1793 (1997).
[8] D. Haarer and M. Philpott, in *Spectroscopy and Excitation Dynamics of Condensed Molecular Systems*, edited by V. M. Agranovich and R. M. Hochstrasser (North-Holland, Amsterdam, 1983), p. 27.
[9] M. C. Petty, *Langmuir–Blodgett Films* (University Press, Cambrige, 1996), p. 134.

Published in English in the original Russian journal. Reproduced here with stylistic changes by the Translation Editor.

Hot photoluminescence spectroscopy: investigation of two-dimensional structures

D. N. Mirlin, V. I. Perel', I. I. Reshina, and V. F. Sapega

A. F. Ioffe Physicotechnical Institute, Russian Academy of Sciences, 194021 St. Petersburg, Russia
Fiz. Tverd. Tela (St. Petersburg) **41**, 785–788 (May 1999)

Studies of the secondary luminescence (Raman scattering and hot photoluminescence) in low-dimensional semiconductor structures are reviewed. [S1063-7834(99)00805-9]

During recent years (1992–1998), we have carried out a series of studies of secondary luminescence in GaAs/GaAlAs quantum-well structures (QWS) and superlattices (SL) (Raman and hot photoluminescence spectroscopy). Given below is a short review of the results of these works, which includes recent observations of a 2D–quasi-3D transition in SLs.

1. SPIN-FLIP LIGHT SCATTERING

Our investigation of spin-flip Raman scattering from bound carriers in quantum-well structures was made on both Be-doped and undoped GaAs/$Al_xGa_{1-x}As$ structures.[1]

It was shown that the Raman scattering mechanisms involved in resonant excitation of the neutral-acceptor-bound exciton (A^0X) and neutral-acceptor-localized exciton (A^0LE) complexes are different.

It was established that the process involving A^0X complexes in the Faraday backscattering geometry may be considered as a double spin-flip process, which includes, besides the mutual hole spin reversal, spin flip by the electron interacting with an acoustic phonon.

Studies of the resonant excitation of A^0LE complexes revealed a hole spin-flip mechanism caused by anisotropic exchange coupling, a process specific to quantum wells. This process becomes possible because the symmetry of the A^0LE complex is lower than that of A^0X.

The g factors of the acceptor-bound hole, electron, and localized exciton were determined directly, and the anisotropy and dependence of the g factor on quantum-well (QW) width were studied. The crystal-field splittings of the acceptor states $\Delta E(\pm 3/2 \rightarrow \mp 1/2)$ in QWs of different widths were measured.

2. LIGHT SCATTERING BY ACOUSTIC PHONONS INDUCED BY VIOLATION OF THE MOMENTUM CONSERVATION LAW

The nature of the quasi-continuous[2,3] Raman spectrum in the acoustic-phonon frequency domain was studied for the first time. This spectrum was shown to arise from violation of the superlattice-quasimomentum-conservation law in real QWSs. The reason for the violation lies in the width fluctuations of quantum wells and barriers, which inevitably appear during QWS growth. As a result of the fluctuations, a sequence of identical QWs may contain QWs of a larger or smaller width (i.e., accordingly, with a lower or higher size quantization energy). The scattering of light by a regular sequence of identical QWs takes place with conservation of the superlattice quasimomentum, whereas defective QWs scatter light with violation of the momentum conservation law. Therefore, one observes in a Raman spectrum both the known folded-phonon doublets and a continuum originating from an inhomogeneous broadening of quantum-confined levels. Our study showed also that the spectrum of acoustic phonons emitted in a resonant Raman process is determined by the actual form of the electron/hole wave function.

The clearly pronounced resonant nature of the Raman continuum of light scattered from acoustic phonons was used to study the structure of the quantum-well electronic states in quantizing magnetic and electric fields.

3. ENERGY RELAXATION OF HOT ELECTRONS IN QWSs AND SLs

Energy relaxation of hot electrons in 2D structures through electron-phonon interaction has been attracting considerable interest in recent years. Such structures are characterized not only by size quantization of the electronic spectrum, but also by modification of the phonon spectrum through the appearance of confined and interface phonons. Experimental investigation of these problems by time-resolved optical techniques met with difficulties associated with a very high excitation densities produced by laser pulses (screening, hot phonons etc.), which led to unreliable results. The method of hot-electron photoluminescence (HPL) under cw laser excitation involving measurement of the magnetic depolarization of this luminescence, which was developed by us and used earlier[4] to study bulk crystals, permitted one to overcome these difficulties in QWSs and SLs as well and to obtain reliable information on the hot-electron scattering probability and its dependence on QW width, as well as on the part played by various types of phonons in the scattering[5]. The measurements were performed on a set of GaAs/AlAs QWSs with well widths L_w in the 4–16-nm range and a fixed barrier thickness of 10 nm. Figure 1a displays an HPL spectrum for one of the QWSs. The spectrum is produced in recombination of hot photoexcited electrons with holes localized at beryllium acceptor levels (the hole concentration did not exceed 3×10^{17} cm^{-3}). The distinct oscillatory structure of the spectrum is due to the recombination of electrons both from the initial photoexcited state and in the course of energy relaxation within the first electronic subband through optic-phonon emission. The peak

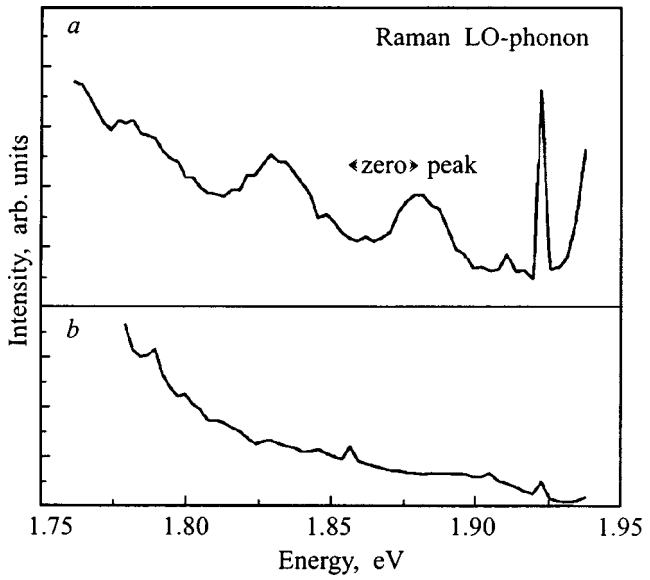

FIG. 1. HPL spectra from a 5/10-nm GaAs/AlAs QWS, $E_{exc}=1.96$ eV, $T=6$ K. N_A (cm^{-3}): (a) 3×10^{17}, (b) 4.6×10^{18}.

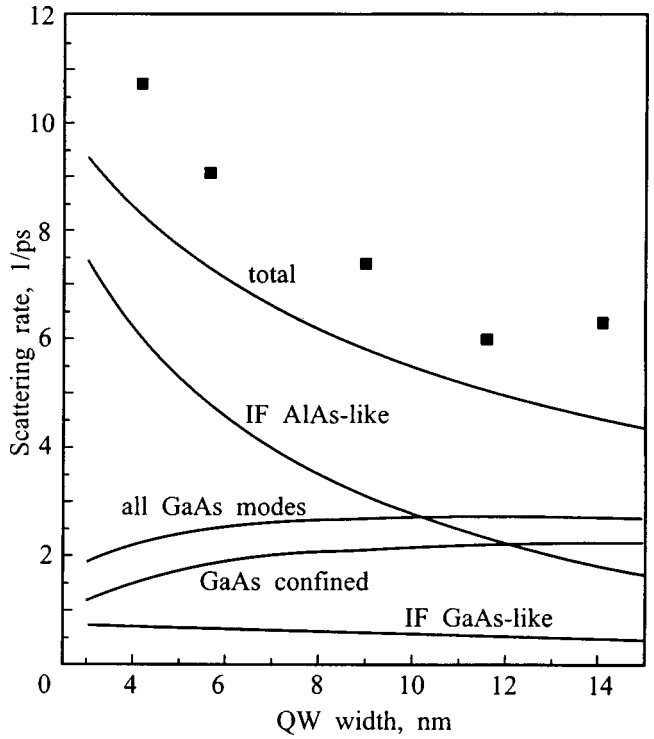

FIG. 2. Intraband scattering probability of hot (200 meV) electrons plotted vs quantum-well width in a GaAs/AlAs QWS. Solid lines — DCM calculation made for optic phonon modes of various types.

separation is equal to the energy of the phonons providing a dominant contribution to the scattering. For QWSs with $L_w > 12$ nm, this separation was 37 meV, which is the LO phonon energy. For QWSs with narrow quantum wells, the distance between the peaks was found to be 50 meV, which is close to the energy of the AlAs-type interface phonons. Measurements of the HPL magnetic depolarization at the initial hot-electron kinetic energy (the zero peak) permitted determination of the intraband scattering probability. The experimental data were compared with the scattering probabilities calculated for phonons of different types within the dielectric continuum model (DCM). The experimental and calculated results plotted against L_w in Fig. 2 are seen to agree satisfactorily both in the magnitude of the scattering probability and in the fact that AlAs-type interface phonons provide a dominant contribution to scattering in narrow quantum wells.

A study was made of the scattering and energy relaxation of hot electrons in 5/10-nm GaAs/AlAs QWSs doped by a beryllium acceptor impurity in the central part of the wells with concentrations ranging from 8×10^{17} to 5×10^{18} cm^{-3}.[6] In this case the major contribution to the scattering probability and energy relaxation comes from the hot-electron interaction with neutral acceptors entailing their excitation and ionization. A decline in the significance of phonon scattering is seen from the disappearance of phonon oscillations in the HPL spectrum in Fig. 1b. We measured the scattering probabilities from the initial photoexcited state and the times characterizing energy relaxation as a function of the acceptor concentration N_A, and found the cross sections of these processes. The scattering probabilities for electrons with an initial kinetic energy of 0.26 eV range from 10 to 25 ps^{-1}, and the cross section of this process, $\sigma_0=4\times10^{-14}$ cm^2, is nearly one half the value of σ_0 for bulk samples. The decrease of σ_0 is associated with the decrease of small-angle scattering in QWs. The energy relaxation times vary within 300 to 500 fs, and the corresponding scattering cross section is 2.4×10^{-15} cm^2. A theory was developed for scattering of hot electrons from neutral acceptors in QWs which takes into account both inelastic and elastic scattering and is not constrained by the requirements of the conventional small-angle scattering approximation. The calculations based on this theory agree with experiment. A comparison of experiment with calculations yielded 4 nm for the acceptor radius in the well plane.

4. EFFECT OF DIMENSIONALITY ON HPL POLARIZATION CHARACTERISTICS

Absorption of linearly polarized light in semiconductors with a complex valence-band structure (of the having GaAs type) gives rise to electron and hole alignment in momenta, whereas circularly polarized light creates spin-oriented particles. Recombination of momentum-aligned or spin-oriented electrons generates, accordingly, linearly or circularly polarized luminescence.[4]

Linear polarization ρ_l in a bulk semiconductor (under linearly polarized pumping) increases weakly with the energy E of the recombining electrons. On the other hand, in a two-dimensional GaAs/AlAs semiconductor QWS, $\rho_l=0$ for $E=0$ and increases to $\rho_l\sim0.5$ for $E>E_1$, where E_1 is the energy of the first quantum-confined state.

In the intermediate case of superlattices, extrapolation of $\rho_l(E)$ yields zero for electron energies E close to the width of the first electronic miniband Δ, rather than for $E=0$, as is the case with QWSs. This behavior of $\rho_l(E)$ was accounted for within the tight-binding approximation, which assumes weak coupling between adjacent quantum wells. It was shown[7] that this approximation holds for SLs with narrow electronic minibands, i.e. for GaAs/AlAs SLs with barrier

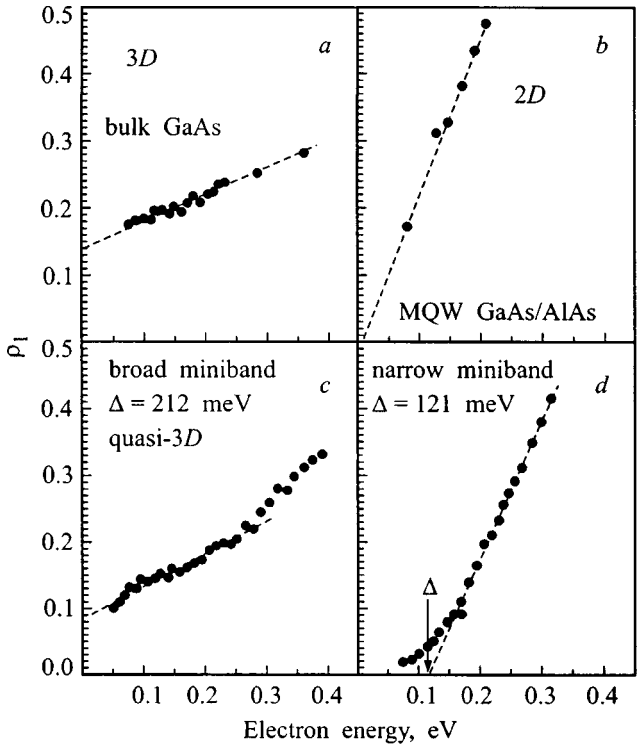

FIG. 3. HPL linear polarization ρ_l plotted vs electron energy for QWS, SLs, and bulk GaAs. With x varying from 1 to 0.3, the miniband width Δ changes from 0.121 to 0.212 eV. One clearly sees the $\rho_l(E)$ relation varies with x, i.e., with barrier height.

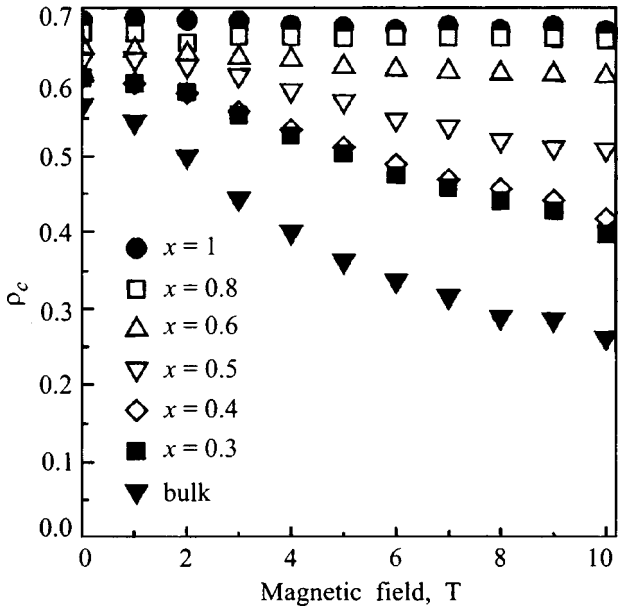

FIG. 4. HPL circular polarization ρ_c plotted vs magnetic field for SLs and bulk GaAs. In the broad-miniband SLs ($x=0.4$ and 0.3) the spin-momentum correlation is seen to be restored.

widths $L_b \geqslant 6$ Å, and for fixed quantum-well thickness $L_w = 40$ Å. One could expect that in an SL with broad minibands the energy dependence $\rho_l(E)$ would be similar to that for bulk GaAs. Figure 3 plots the energy dependence of the linear HPL polarization, ρ_l, for superlattices with different Al contents ($x=0.3$ and 1), i.e. with different barrier heights U_b (0.29 and 1.06 eV). To make the graphs more informative, the figure displays also data obtained on a QWS (Fig. 3b) and bulk GaAs (Fig. 3a). The experimental data obtained with bulk GaAs are approximated by a dotted line.

The $\rho_l(E)$ relation measured on an SL with the highest barriers ($x=1$) (see Fig. 3d) fits well to the tight-binding approximation.

As follows from this consideration, the energy dependence of ρ_l for the SL with the most narrow minibands is similar to that observed in a QWS. This is clearly seen from a comparison of the slopes of the $\rho_l(E)$ relations in these two cases (Fig. 3b and 3d). At the same time the SL $\rho_l(E)$ reaches zero for $E \sim \Delta$ (where Δ is the width of the first electronic miniband) rather than for $E \to 0$, as is the case with a QW. The same $\rho_l(E)$ relation was observed for an SL with $x=0.8$.

One observes noticeable changes in the $\rho_l(E)$ dependence already in SLs with $x \leqslant 0.6$, where a decrease in barrier height affects appreciably this relation. The largest changes are seen, however, in the $x=0.3$ SL (Fig. 3c), where $\rho_l(E)$ resembles very much the relation obtained on bulk GaAs (Fig. 3a). At the same time some details associated with quasi-two-dimensional electron motion are retained for $E > \Delta$. Indeed, the slope of $\rho_l(E)$ for $E > \Delta$ differs from that for $0 < E < \Delta$, because electrons with kinetic energies $E > \Delta$ move predominantly in the SL plane.

Another characteristic difference in HPL between bulk GaAs and a QWS is connected with circular polarization of the luminescence ρ_c (under circularly polarized pumping). In the bulk case one observes the so-called spin-momentum correlation among the photoexcited electrons. This effect increases the circular polarization of the luminescence.

Direct experimental evidence for this effect was furnished by observation of a decrease of ρ_c in a magnetic field B measured in the Faraday geometry.[8] The behavior of ρ_c with magnetic field showed that the action of a magnetic field reduces to cyclotron rotation of the momenta of photoexcited electrons and, thus, to destruction of the spin-momentum correlation. In QWs, no spin-momentum correlation exists, and the corresponding term cannot be written, because there is no electron momentum component in the direction of the angular momentum **n** (it is assumed that **n** is perpendicular to the QWS plane). Figure 4 shows the dependence of ρ_c on magnetic field measured in the Faraday geometry for electrons with a kinetic energy $E \sim 80-100$ meV. In bulk GaAs, ρ_c decreases rapidly (the filled inverted triangles) with increasing magnetic field as a result of the destruction of the spin-momentum correlation. In SLs with narrow minibands, there is no spin-momentum correlation, and ρ_c does not vary with increasing B [filled circles ($x=1$) and open squares ($x=0.8$)]. In broad-band SLs, circular polarization decreases with increasing magnetic field. This effect becomes noticeable in SLs with $x \leqslant 0.6$ and indicates that formation of a broad miniband restores the spin-momentum correlation. In SLs with $x \sim 0.3$ (filled squares in Fig. 4), the effect of destruction of the spin-momentum correlation is already comparable to that observed in bulk GaAs.

Support of the Russian Fund for Fundamental Research (Grants 96-02-16895, 96-15-96393, 96-15-96392) and the Volkswagen Stiftung (Grant I/70958) is gratefully acknowledged.

[1] V. F. Sapega, T. Ruf, E. L. Ivchenko, M. Cardona, D. N. Mirlin, and K. Ploog, Phys. Rev. B **50**, 2510 (1994).
[2] D. N. Mirlin, I. A. Merkulov, V. I. Perel', I. I. Reshina, A. A. Sirenko, and R. Planel, Solid State Commun. **82**, 305 (1992).
[3] V. F. Sapega, V. I. Belitsky, T. Ruf, H. D. Fuchs, M. Cardona, and K. Ploog, Phys. Rev. B **46**, 16005 (1992).
[4] M. A. Alekseev, I. Ya. Karlik, D. N. Mirlin, and V. F. Sapega, Fiz. Tekh. Poluprovodn. **23**, 761 (1989) [Sov. Phys. Semicond. **23**, 479 (1989)].
[5] D. N. Mirlin, B. P. Zakharchenya, I. I. Reshina, A. V. Rodina, V. F. Sapega, A. A. Sirenko, V. M. Ustinov, A. E. Zhukov, and A. Yu. Egorov, Fiz. Tekh. Poluprovodn. **30**, 699 (1996) [Semiconductors **30**, 377 (1996)].
[6] D. N. Mirlin, V. I. Perel', and I. I. Reshina, Fiz. Tekh. Poluprovodn. **32**, 866 (1998) [Semiconductors **32**, 770 (1998)].
[7] V. F. Sapega, V. I. Perel', A. Yu. Dobin, D. N. Mirlin, I. A. Akimov, T. Ruf, M. Cardona, and K. Eberl, Phys. Rev. B **56**, 6871 (1997).
[8] I. Ya. Karlik, D. N. Mirlin, L. P. Nikitin, D. G. Polyakov, and V. F. Sapega, JETP Lett. **36**, 192 (1982).

Translated by G. Skrebtsov

Radiospectroscopy of wide-gap semiconductors: SiC and GaN

P. G. Baranov*

A. F. Ioffe Physicotechnical Institute, Russian Academy of Sciences, 194021 St. Petersburg, Russia
Fiz. Tverd. Tela (St. Petersburg) **41**, 789–793 (May 1999)

The present report submitted to the Anniversary Conference of the A. F. Ioffe Physicotechnical Institute, ''Physics at the Turn of the 21st Century,'' deals with recent EPR studies of main impurities in the wide-gap semiconductors SiC and GaN, which appear to be the most promising materials for microelectronics and quantum semiconductor electronics at the start of the 21st century. © *1999 American Institute of Physics.* [S1063-7834(99)00905-3]

Silicon carbide finds an ever increasing application in microelectronics devices capable of operating under extreme environmental conditions, which will abound in the coming century unfortunately. Using nitride-based III-V semiconductor compounds may provide a solution to the problem of semiconductor lasers intended for operation in the UV and visible regions.

The report consists of three main parts and presents the results of studies carried out during the past five years primarily at the Ioffe Institute, as well as in cooperation with a number of European research institutes.

The first part discusses the investigation of the main acceptors in SiC, namely, Group III elements (B, Al, Ga), the double acceptor Be, and Sc, which occupies a somewhat special place.

The second part is devoted to transition elements in SiC and GaN, which form in the gap, as a rule, a number of deep-lying levels.

Presented briefly in the third part will be the results of our studies of rare-earth elements in SiC.

1. EPR OF ACCEPTORS IN SIC

A. Group III elements (B, Al, Ga)

(*a*) *Group-III shallow-level elements*. Group III elements B, Al, and Ga are the main acceptor impurities in SiC used to produce *p*-type materials. It was believed until recently that B has two levels, namely, a shallow one denoted by shB, and a deep one, dB. As for Al and Ga, they were assumed to create only shallow levels, which made them more promising for applications. For illustration, Fig. 1 presents a system of various acceptor levels for 6*H*-SiC. The 6*H*-SiC crystal has one hexagonal (h) and two quasicubic (k) crystallographically inequivalent sites, if one considers second coordination spheres. One immediately sees that the energy levels of shallow boron lie deeper than those of shallow aluminum, although one would expect to have the opposite pattern, as is the case, for instance, with silicon, where the level of boron is more shallow than that of aluminum. Shallow-level Group-III acceptors in SiC were studied by various radiospectroscopic methods.[1–11] An important finding made by the EPR and ODMR methods in SiC is the discovery of a strong difference in properties between shallow boron and other Group-III acceptors, such as aluminum and gallium, namely, the g factors of shallow aluminum and shallow boron have a strong axial symmetry along the hexagonal axis of the crystal (in cubic SiC no EPR spectra of shallow Al and Ga were observed) and reflect the symmetry of the valence-band maximum, i.e., they can be described in the effective-mass approximation. This approximation is inapplicable to shallow boron, because in this case the g factor is practically isotropic near $g=2.00$. The anisotropy in the EPR spectra is extremely small, and the symmetry at low temperatures is axial along the c axis only for shallow boron acceptors in the h sites. In the k sites, the shallow-boron local axis z coincides with the other Si–C bond directions not aligned with the c axis, and for cubic SiC (where, in contrast to aluminum and gallium, one did observe EPR spectra of shallow boron) the z axis coincides with the $\langle 111\rangle$ directions of the crystal. Note that in all cases $\sim 40\%$ of the spin density is localized at one of the carbon atoms closest to the boron which lies on the shallow-boron local symmetry axis z. The degree of spin localization at the boron atom is small (of the order of 1%) and comparable to those for aluminum and gallium acceptors, but in the latter two cases the spin density is apparently distributed uniformly around the impurity, primarily at carbon atoms, in accordance with the valence-band structure of SiC.

The experimental data obtained and theoretical calculations permitted a conclusion that the acceptor atom substitutes for silicon in SiC, with the difference between the size of boron, on the one hand, and of aluminum and gallium, on the other, playing a dominant role. The difference between the ionic radii of the acceptor and silicon, $\Delta R = R(A^{3+}) - R(Si^{4+})$, is -0.19, $+0.09$, and $+0.20$ Å for A=B, Al, and Ga, respectively. The selection of the ionic radii was based on a simplifying assumption that the SiC crystal consists of Si ions in the Si^{4+} valence state and of bonding electrons. In this model, the acceptor resides in the A^{3+} valence state. Thus the physical properties of shallow acceptors depend on the relative magnitude of the acceptor and silicon radii. Boron, whose radius is smaller than that of silicon, occupies typically off-center position. Boron displaces from its equilibrium position at the center of the tetrahedron to approach the center of the plane formed by the three nearest-neighbor carbon atoms. As a result, the sp^3 hybridization is disrupted, and the spin density redistributes to extend to the fourth carbon atom which is more distant from the boron

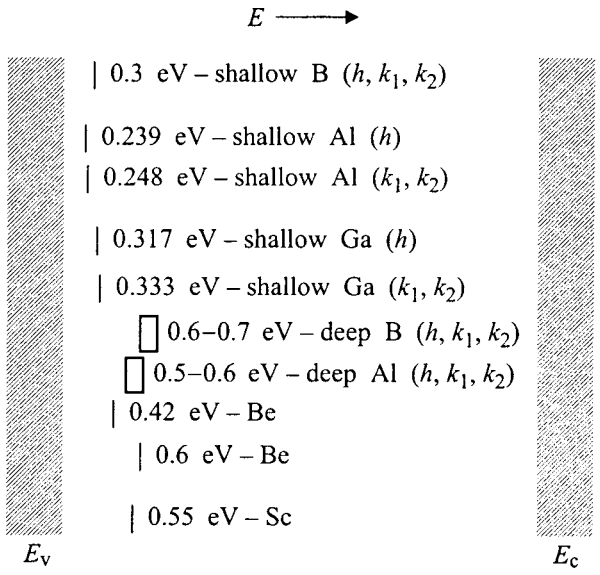

FIG. 1. Energy-level diagram of the main acceptors in 6*H*-SiC.[11]

atom. This gives rise to formation in this plane of a triangular arrangement around the central boron atom of the BC_3 type with sp^2 hybridization. Such models are valid for both the hexagonal and quasicubic boron sites. In the latter cases, boron displaces along the Si–C bonds which do not coincide in direction with the *c* axis. Al and Ga, which are larger in atomic radius than Si, occupy apparently the central position as impurities and are sp^3 hybridized, which entails mass-like acceptor properties. The acceptor (B, Al, Ga) is always neutral, and, in the case of boron, the spin density is observed to be nonuniform near the impurity because it is sitting off-center. This results also in the level of the shallow boron becoming deeper, by about 0.05 eV from our estimates, compared to the position expected for the impurity at a central site. It should be pointed out that a similar situation is known to exist in silicon, where the nitrogen donor level lies deeper than the phosphorus level because the nitrogen impurity off-center position.

(*b*) *Group-III elements with deep levels*. The next stage in the investigation of the B, Al, and Ga acceptors was the discovery and study using EPR spectra of deep B, deep Al, and deep Ga. It should be pointed out that, while the existence of deep-B levels was universally accepted and our goal was to look for EPR spectra of such centers, the aluminum and gallium impurities were believed to create only shallow acceptor levels. EPR spectra of deep boron in 6*H*-SiC were observed and studied[5,12–14] more than 30 years after the observation[1] of shallow boron EPR. The deep-boron center has a close to axial symmetry, the *g* factor anisotropy is about an order of magnitude larger than that of shallow boron, and electron localization on deep boron is as weak as it is on shallow boron.

EPR spectra similar to those observed with deep boron were revealed in gallium- and aluminum-doped crystals. The orientational dependences of EPR spectra of deep boron and of the new spectra of aluminum and gallium are qualitatively similar, but the *g* factors, $g_\parallel$, of the aluminum and gallium centers are substantially larger and close to those for the shallow Al and Ga. In all cases, however, $g_\perp \cong 2.0$ for deep B, Al, and Ga, which means that these centers cannot be treated in the effective-mass approximation. Remarkably, the aluminum and gallium deep centers were first observed by EPR and ENDOR. ODMR data[5,11] and their correlation with EPR studies suggest that the deep boron level lies at 0.6-0.7 eV, whereas deep aluminum is more shallow by ~ 0.1 eV (Fig. 1).

A model proposed for the microstructure of the deep boron, deep aluminum, and deep gallium centers, based on the totality of the radiospectroscopic studies, considers a pair of an impurity atom (B, Al, Ga) occupying the silicon site and of a closely located carbon vacancy. The impurity-vacancy direction is assumed to coincide with the *c* axis of the crystal for both the *h* and *k* sites in SiC hexagonal polytypes, and with the $\langle 111 \rangle$ direction in cubic SiC. This model considers the unpaired electron to be localized primarily at the carbon vacancy.

The existence of deep levels for all Group-III elements accounts for the onset of self-compensation in preparation of *p*-SiC materials and requires development of further improvements in the technology.

B. Beryllium and scandium acceptors

(*a*) *Beryllium*. Beryllium is a double acceptor in SiC (Fig. 1). The Be acceptors were studied by EPR and ENDOR.[15,16] The shape of beryllium EPR spectra and their orientational behavior depend on measurement temperature and undergo changes within the temperature intervals above 10 and 50 K. Below 10 K, one observed EPR spectra of three types of centers with a close-to-axial symmetry, which relate to two quasicubic and one hexagonal beryllium sites in 6*H*-SiC. Above 50 K, the symmetry of the two beryllium centers assigned by us to quasicubic beryllium sites is lower than axial, and their *z* axis is aligned with one of the Be-C bonds which does not coincide with the *c* axis. It is believed that because beryllium is smaller in radius than silicon, it occupies, similar to the shallow boron, an off-center position at the silicon site, i.e., that it is shifted from the tetrahedron center toward the center of the plane containing three carbon atoms and away from the fourth carbon with the highest spin density. Unlike the shallow boron which is neutral, beryllium must be negatively charged.

(*b*) *Scandium*. Scandium may be considered as a kind of a bridge between acceptors and transition elements; indeed, on the one hand, it is a Group-III element while, on the other, it is the first element in the transition-metal group. This is seen clearly from Table I, where Sc in neutral state (A^0) occupying the Si site (the four valence electrons bond the four C atoms) acts as acceptor, while when in the A^{2-} state it has one unpaired *d* electron. EPR spectra of at least three Sc acceptor types have been observed.[15,17] Similar to the shallow B and Be acceptors, these spectra are noticeably temperature dependent. Above ~ 30 K they exhibit axial symmetry, but it decreases at lower temperatures. Besides the spectra of the Sc acceptors, one observed EPR signals that we assign to Sc^{2+} ions, but this point will be discussed in more detail in the next Section. It may be added that

TABLE I. Transition-metal impurities in different charge states studied in SiC and GaN crystals.

SiC						
free atom	Sc ($3d^14s^2$)	Ti ($3d^24s^2$)	V ($3d^34s^2$)	Cr ($3d^54s^1$)	Mo ($4d^55s^1$)	Ta ($5d^36s^2$)
A^{2-}	$Sc^{2+}(3d^1)$ $S=1/2$			$Cr^{2+}(3d^4)$ $S=2$		
A^-	$Sc^{3+}(3d^0)$ $S=0$	$Ti^{3+}(3d^1)$ $S=1/2$	$V^{3+}(3d^2)$ $S=1$	$Cr^{3+}(3d^3)$ off-center $S=3/2$	$Mo^{3+}(4d^3)$ $S=3/2$	$Ta^{3+}(5d^2)$? $S=1$
A^0	Sc acceptor $S=1/2$	$Ti^{4+}(3d^0)$ $S=0$	$V^{4+}(3d^1)$ $S=1/2$	$Cr^{4+}(3d^2)$ $S=1$	$Mo^{4+}(4d^2)$ $S=1$	
A^+			$V^{5+}(3d^0)$ $S=0$	$Cr^{5+}(3d^1)$ $S=1/2$	$Mo^{5+}(4d^1)$ $S=1/2$	

GaN			
free atom	Mn ($3d^54s^2$)	Fe ($3d^64s^2$)	Ni ($3d^84s^2$)
A^-	$Mn^{2+}(3d^5)S=5/2$		
A^0		$Fe^{3+}(3d^5)S=5/2$	$Ni^{3+}(4d^7)S=3/2$

Note. The impurities are assumed to substitute for Si (Ga) in these crystals. The states observed by EPR are underlined.

ODMR spectra obtained by us on Sc-doped SiC crystals revealed strong anisotropic signals,[5] which, by analogy with the Ti impurity,[18] can be assigned to excitons bound to Sc acceptors.

2. TRANSITION-METAL ELEMENTS IN SiC AND GaN

Transition-metal elements can exist in SiC and GaN as residual impurities and create deep levels in the band gap. As a rule, each impurity enters the crystal in more than one charge state and affects substantially the electrical and optic characteristics of the material. Controlled incorporation of these impurities appears very promising for development of semi-insulating substrates in device fabrication. Before the initiation of our work, only titanium and vanadium in SiC (Ref. 19) and iron in GaN (Ref. 20) were detected and studied by EPR. Table I lists transition-metal elements in various charge states which have been investigated in SiC and GaN until recently. The charge states observed[21–24] by EPR are underlined. Here it should be pointed out that all available data are consistent with the assumption that impurity ions of transition elements substitute for silicon in SiC and for Ga in GaN. While in the case of GaN this assumption is not questioned, the opinions relating to SiC are rather contradictory, and they draw primarily on the fact that transition elements occupy in silicon preferably interstitial sites. For illustration, consider the Cr^{3+} ion whose EPR spectrum[21] is well accounted for by the off-center position of chromium at the silicon site (Fig. 2). The observed superhyperfine structure can be explained as due to interaction with six equivalent ^{29}Si atoms and three equivalent ^{29}Si atoms in the second coordination sphere. This arrangement appears when the chromium ion is shifted along the *c* axis.[21] No deviation from the central position was found for Cr^{2+} ions (which were observed by us only in 6*H*-SiC crystals grown on the C side) with an hfs constant of 15.8 G, which is ~1.7 times larger than that for Cr^{3+}. No deviation from the central position was observed for other transition-metal ions either. In particular, in the case of Mo^{4+} ions one can isolate only one constant of superhyperfine interaction with 12 equivalent ^{29}Si atoms in the second coordination sphere, which was found to be 8.2 G (23 MHz).

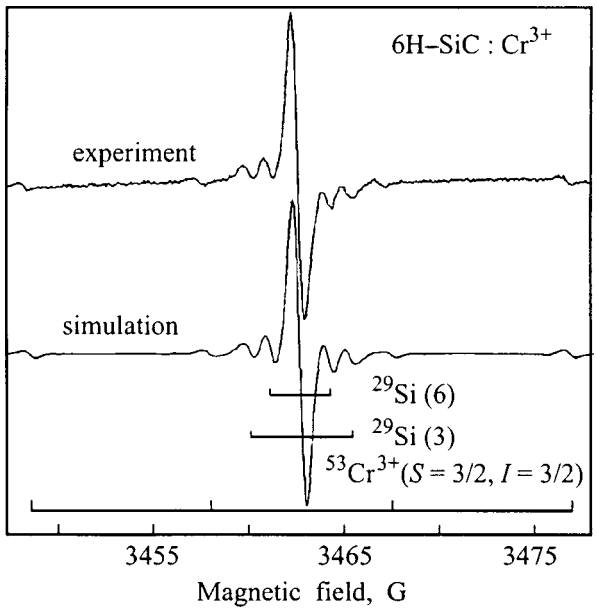

FIG. 2. EPR spectrum for one of the quasicubic sites of Cr^{3+} ions in 6*H*-SiC obtained at 9.5 GHz and 4.5 K with the magnetic field parallel to the hexagonal axis of the crystal. Shown below is a simulated spectrum calculated with the following parameters (in MHz): hfs constant for ^{53}Cr of 26.5, shfs constant for six equivalent ^{29}Si ions in the second coordination sphere of 8.4, and shfs constant for three equivalent ^{29}Si ions in the second coordination sphere of 14.56.

One may add to our previously published results that, besides chromium ions in SiC in a regular environment, one observed EPR spectra of complexes with a spin $S=3/2$, which apparently contain chromium with local axes along the Si–C bonds. One observed also EPR spectra that can be assigned to Ta^{3+} ions with an hfs constant of the order of 150 G, and they were found to correlate with five IR luminescence lines with wavelengths at 5 K of 1.074, 1.049, 1.031, 1.011, and 0.999 eV. The relevant studies are reported in more detail in our report Ref. 25.

3. RARE-EARTH ELEMENTS IN SiC

Search for semiconductor compounds doped with rare-earths for use in optical devices has recently been attracting considerable attention. Of particular interest in this connection are Er^{3+} ions with luminescence at 1.54 μm, a wavelength falling into the optical-fiber transmission region. We believe that SiC can be used to advantage for these purposes, because, on the one hand, this material has a wide band gap, which is essential for efficient Er^{3+} luminescence and, on the other, SiC:Er microelectronics can apparently be directly matched to silicon-based devices. We solved the problem of incorporating Er^{3+} ions in bulk SiC crystals in the course of growth.[26] Strong EPR signals of several types of Er^{3+} ions have been detected for the first time in these crystals. More details on studies of rare-earth elements in SiC can be found in our report Ref. 25.

Partial support of the Russian Fund for Fundamental Research (Grant 98-02-18241) is gratefully acknowledged.

*E-mail: Pavel.Baranov@pop.ioffe.rssi.ru

[1] H. H. Woodbury and G. W. Ludwig, Phys. Rev. **124**, 1083 (1961).
[2] A. G. Zubatov, I. M. Zaritskiĭ, S. N. Lukin, E. N. Mokhov, and V. G. Stepanov, Fiz. Tverd. Tela (Leningrad) **27**, 322 (1985) [Sov. Phys. Solid State **27**, 197 (1985)].
[3] N. P. Baran, V. Ya. Bratus', A. A. Bugaĭ, V. S. Vikhnin, A. A. Klimov, V. M. Maksimenko, T. L. Petrenko, and V. V. Romanenko, Fiz. Tverd. Tela (St. Petersburg) **35**, 3135 (1993) [Phys. Solid State **35**, 1544 (1993)], and references therein.
[4] K. M. Lee, Le Si Dang, G. D. Watkins, and W. K. Choyke, Phys. Rev. Lett. **45**, 390 (1980).
[5] P. G. Baranov, V. A. Vetrov, N. G. Romanov, and V. I. Sokolov, Fiz. Tverd. Tela (Leningrad) **27**, 3459 (1985) [Sov. Phys. Solid State **27**, 2085 (1985)]; P. G. Baranov and N. G. Romanov, Appl. Magn. Reson. **2**, 361 (1991); Mater. Sci. Forum **83–87**, 1207 (1992).
[6] J. Reinke, S. Greulich-Weber, and J.-M. Spaeth, Solid State Commun. **96**, 835 (1996).
[7] T. Matsumoto, O. G. Poluektov, J. Schmidt, E. N. Mokhov, and P. G. Baranov, Phys. Rev. B **55**, 2219 (1997).
[8] T. L. Petrenko, V. V. Teslenko, and E. N. Mokhov, Fiz. Tekh. Poluprovodn. **26**, 1556 (1992) [Sov. Phys. Semicond. **26**, 874 (1992)].
[9] R. Müller, M. Feege, S. Greulich-Weber, and J.-M. Spaeth, Semicond. Sci. Technol. **8**, 1377 (1993).
[10] T. L. Petrenko, A. A. Bugai, V. G. Baryakhtar, V. V. Teslenko, and V. D. Khavryutchenko, Semicond. Sci. Technol. **9**, 1849 (1994).
[11] P. G. Baranov, Defect Diffus. Forum **148–149**, 129 (1997), and references therein.
[12] P. G. Baranov and E. N. Mokhov, Semicond. Sci. Technol. **11**, 489 (1996).
[13] P. G. Baranov, I. V. Ilyin, and E. N. Mokhov, Solid State Commun. **100**, 371 (1996).
[14] A. v. Duijn-Arnold, T. Ikoma, O. G. Poluektov, P. G. Baranov, E. N. Mokhov, and J. Schmidt, Phys. Rev. B **57**, 1607 (1998).
[15] P. G. Baranov and E. N. Mokhov, Fiz. Tverd. Tela (St. Petersburg) **38**, 1446 (1996) [Phys. Solid State **38**, 798 (1996)].
[16] A. Hofstaetter, B. K. Meyer, A. Scharmann, P. G. Baranov, I. V. Ilyin, and E. N. Mokhov, Mater. Sci. Forum **264–268**, 595 (1998).
[17] P. G. Baranov, I. V. Ilyin, E. N. Mokhov, A. D. Roenkov, and V. A. Khramtsov, Fiz. Tverd. Tela (St. Petersburg) **39**, 52 (1997) [Phys. Solid State **39**, 44 (1997)].
[18] K. M. Lee, Le Si Dang, G. D. Watkins, and W. J. Choyke, Phys. Rev. B **32**, 2273 (1985).
[19] K. Maier, H. D. Müller, and J. Schneider, Mater. Sci. Forum **83–87**, 1183 (1992).
[20] K. Maier, M. Kunzer, U. Kaufmann, J. Schneider, B. Monemar, I. Akasaki, and H. Amano, Mater. Sci. Forum **143–147**, 93 (1994).
[21] P. G. Baranov, V. A. Khramtsov, and E. N. Mokhov, Semicond. Sci. Technol. **9**, 1340 (1994).
[22] K. F. Dombrowski, M. Kunzer, U. Kaufmann, J. Schneider, P. G. Baranov, and E. N. Mokhov, Phys. Rev. B **54**, 7323 (1996).
[23] J. Baur, M. Kunzer, K. F. Dombrowski, U. Kaufmann, J. Schneider, P. G. Baranov, and E. N. Mokhov, Inst. Phys. Conf. Ser. No. 155, Ch. 12, p. 933 (1997).
[24] P. G. Baranov, I. V. Ilyin, and E. N. Mokhov, Solid State Commun. **101**, 611 (1997).
[25] P. G. Baranov, I. V. Ilyin, E. N. Mokhov, A. D. Roenkov, and V. A. Khramtsov, Phys. Solid State (St. Petersburg) (this issue).
[26] P. G. Baranov, I. V. Ilyin, and E. N. Mokhov, Solid State Commun. **103**, 291 (1997).

Translated by G. Skrebtsov

Neutron transmutation doping in semiconductors: science and applications

I. S. Shlimak

Jack and Pearl Resnick Institute of Advanced Technology, Department of Physics, Bar-Ilan University, 52900 Ramat-Gan, Israel

Fiz. Tverd. Tela (St. Petersburg) **41**, 794–798 (May 1999)

Different aspects of neutron transmutation doping (NTD) of silicon and germanium are considered, with a special emphasis on the contribution by scientists of the Ioffe Physicotechnical Institute, Russian Academy of Sciences, to the solution of these problems. Fundamental studies related to determination of the cross sections of thermal-neutron capture by isotopes of semiconducting materials, annealing of radiation defects produced by fast reactor neutrons, and the use of NTD for probing the structure of the Ge impurity band are reviewed. Problems involved in industrial-scale production of NTD-Si, application of NTD-Si and NTD-Ge to fabrication of power thyristors, nuclear-particle and IR detectors, deep-cooled thermistors, and bolometers are discussed. The paper concludes with a consideration of prospects in the application of NTD-Si and NTD-Ge based on the use of materials with a controlled isotopic composition. © *1999 American Institute of Physics.* [S1063-7834(99)01005-9]

The method of neutron transmutation doping (NTD) of semiconductors is based on nuclear transformations of isotopes of semiconducting materials following their capture of slow (thermal) neutrons.[1,2] NTD is achieved by irradiating samples or whole ingots of semiconductor crystals with a neutron flux in a nuclear reactor. On capturing a neutron, a particular isotope transmutes to another isotope with a mass number larger by one:

$$\Phi \sigma_i {}_Z N^A = {}_Z N^{A+1}. \tag{1}$$

Here Φ is the integrated flux (dose) of thermal neutrons, σ_i (cm^2) is the thermal-neutron-capture cross section for a given isotope, ${}_Z N^A$ and ${}_Z N^{A+1}$ (cm^{-3}) are concentrations of the initial and final reaction products, respectively, Z is the nuclear charge, and A is the mass number of the nucleus. If the isotope thus obtained, ${}_Z N^{A+1}$, is stable, such nuclear reaction does not entail doping. Of most interest is the case where the final isotope is unstable. Then after its half-life τ_i this isotope transmutes to a nucleus of another element, with atomic number larger by one, ${}_{Z+1} N^{A+1}$, as in the case of β^- decay, or smaller by one, ${}_{Z-1} N^{A+1}$, if the decay occurred by K-capture. One may present here for illustration the reaction producing in silicon a phosphorus donor impurity:

$$_{14}\mathrm{Si}^{30} + n = {}_{14}\mathrm{Si}^{31} \xrightarrow{\beta^-(2.62\mathrm{h})} {}_{15}\mathrm{P}^{31}. \tag{2}$$

The interest in NTD stems from two of its main advantages over the conventional metallurgical methods of impurity incorporation. First, this is high-precision doping, because the concentration of impurities introduced at a constant neutron flux is proportional to irradiation time, which can be controlled with a high accuracy. The second advantage is the high homogeneity of impurity distribution, which is determined by a random isotope distribution, small neutron-capture cross sections σ_i, and the uniformity of the neutron flux. Recalling that the values of σ_i lie approximately in the region $10^{-23}-10^{-24}$ cm^{-2}, one readily finds that the phosphorus impurity concentration introduced in Si for maximum thermal-neutron fluxes in modern nuclear reactors and reasonable irradiation times does not exceed a few times 10^{15} cm^{-3}, which is, however, sufficient for a number of applications, particularly for production of high-voltage power diodes and thyristors.[3] This resulted in development in Europe and USA of NTD-Si production on an industrial scale of hundreds of tons per year in specially designed materials-science research reactors. In the former Soviet Union, an original technology of industrial production of NTD-Si was developed at the time using the already available RBMK-1000-type nuclear power reactor.[4] This permitted one to do without construction of a special-purpose reactor, which cut dramatically the cost of the technology and boosted large-scale production of NTD-Si. Scientists from the B. P. Konstantinov LNPI and A. F. Ioffe PTI made a major contribution to this project.

As for germanium, because of the large values of σ_1 and the presence of NTD-active isotopes ${}_{32}\mathrm{Ge}^{70}$, ${}_{32}\mathrm{Ge}^{74}$, and ${}_{32}\mathrm{Ge}^{76}$ it can be doped only up to the onset of metallic conduction (3×10^{17} cm^{-3}), which, on the one hand, makes possible investigation in NTD-Ge of fundamental problems of conduction in an impurity band[5,6] and of the metal-insulator transition,[7] and on the other, suggests a number of applications in the area of low-temperature resistance thermometers (thermistors) and radiation detectors[8,9]. These devices were employed widely in neutrino physics and the search for the ''hidden mass'' of the Universe.[10,11] The corresponding reactions for the active Ge isotopes are as follows

$$_{32}\mathrm{Ge}^{70} + n = {}_{32}\mathrm{Ge}^{71} \xrightarrow{K-\text{capture}\,(11.4\,\mathrm{d})} {}_{31}\mathrm{Ga}^{71}\,(\text{acceptor}), \tag{3}$$

$$_{32}\mathrm{Ge}^{74} + n = {}_{32}\mathrm{Ge}^{75} \xrightarrow{\beta^-(82\,\mathrm{min})} {}_{33}\mathrm{As}^{75}\,(\text{donor}), \tag{4}$$

$$_{32}\mathrm{Ge}^{76} + n = {}_{32}\mathrm{Ge}^{77} \xrightarrow{\beta^-(12\,\mathrm{h})} {}_{33}\mathrm{As}^{77} \xrightarrow{\beta^-(39\,\mathrm{h})} {}_{34}\mathrm{Se}^{77}\,(\text{donor}). \tag{5}$$

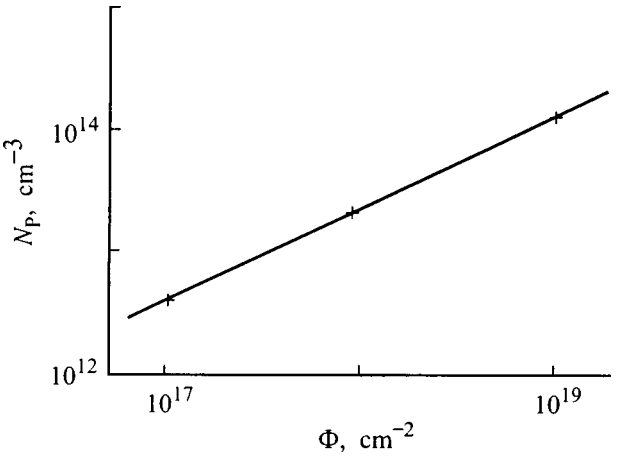

FIG. 1. Phosphorus concentration determined from Hall measurements after silicon crystal irradiation at various neutron doses and subsequent anneal at 800 °C for 1 h (after Ref. 14).

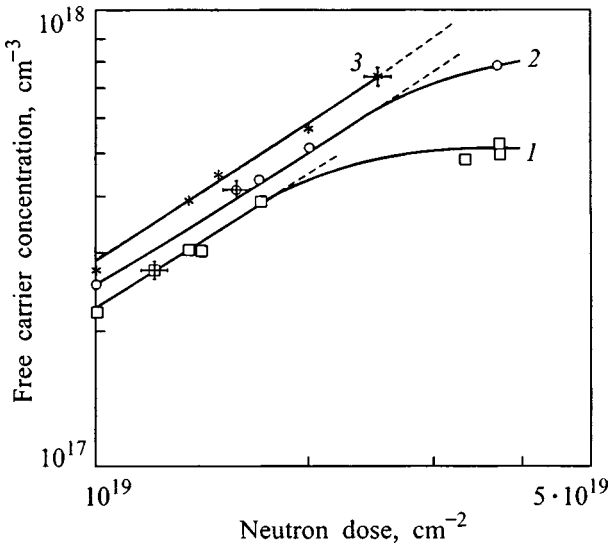

FIG. 2. Free-electron concentration in NTD-Ge^{74} vs thermal-neutron irradiation dose measured after an anneal at 460 °C for (*1*) 24 h, (*2*) 50 h, and (*3*) 100 h (after Ref. 15).

The main feature of the NTD process in Ge is that it creates in the material both acceptors (the major impurity) and donors (minor, compensating dopant). The resultant material is *p*-Ge with a compensation $K=0.32-0.40$.[5,12–14] A certain scatter in K comes from the fact that transmutation doping involves epithermal neutrons as well, so that the doping coefficient α for each impurity, which relates the impurity concentration introduced to irradiation dose $N=\alpha\Phi$, differs somewhat from the value $\alpha=\sigma_{i\,Z}N^A$ calculated using the cross section for thermal neutrons. As a result, the value of α varies slightly depending on the actual neutron energy spectrum in the reactor used for irradiation.

The NTD process does not, however, end by irradiating samples or ingots in a nuclear reactor. The presence in the reactor spectrum of fast, energetic neutrons gives rise to the creation in the sample of radiation defects or even disordered regions. Radiation-defect annealing is a complex technological problem, because radiation defects form complexes with impurities contained in the starting material, which requires development of various anneal regimes (varying in temperature, duration, and atmosphere) for different semiconductor materials, and even for the same material having different contents of some deep residual impurities (oxygen, carbon).[2]

As already mentioned, one of the merits of NTD is the precision of doping because the dopant concentration is linearly dependent on irradiation dose. Such a dependence is indeed observed typically in an experiment. For illustration, Fig. 1 presents the phosphorus impurity concentration measured from the Hall effect vs silicon irradiation dose of a neutron flux in a nuclear reactor.[15] At high doses, however, nonlinear effects become possible. Indeed, Ce^{74}-enriched material subjected to high irradiation doses exhibits deviations from the linear relation (1) toward saturation, which were partially compensated by longer anneals (Fig. 2).[16] A still more remarkable effect was observed after a repeated irradiation of the Ge^{74} samples, which were preliminarily heavily NTD-doped with As. Instead of the expected increase of the free carrier (electrons) concentration n, one detected a decrease of n, which was the larger, the more heavily was the NTD-Ge^{74} sample doped. Both these effects can be explained by the formation of complexes between radiation defects and As atoms introduced in Ge^{74} by NTD. The concentration of these As atoms does naturally increase with increasing irradiation dose, but not all of the As atoms can act as donors and supply free electrons. If a radiation defect was created near an As atom, a radiation-defect–As complex, which is hard to anneal, may form, in which As will no longer be a donor, thus decreasing n; besides, such a complex exhibits acceptor properties,[17] which results in compensation and an additional decrease of n. If the irradiation is long enough, the concentrations of radiation defects and As atoms will be high, and the probability of their forming complexes will likewise be high. For low irradiation doses this effect may be neglected, because the radiation defects and As atoms are far from one another.

Another essential merit of NTD is the high homogeneity of impurity distribution. In conventional metallurgical methods of semiconductor doping, where the impurity is introduced into the melt with subsequent growth of the crystal, obtaining a homogeneous distribution of an impurity encounters radical difficulties. They are associated with the instabilities in the frontline of crystallization of doped crystals and an unavoidable temperature gradient in the growing ingot between its center and periphery. These difficulties increase manyfold as the ingot diameter increases. By contrast, the homogeneity of doping in the NTD method is provided by the random isotope distribution in the crystal lattice, the uniformity of the neutron flux (to achieve this, the sample is rotated about its axis and pulled simultaneously through the core during the irradiation), and the small value of σ_i. The product $\sigma_i N_i$ summed over all stable isotopes of the given semiconductor determines the neutron linear absorption coefficient γ, i.e. the block effect, i.e. the shielding of the inner parts of the ingot by its outer layers. Knowing γ, one can calculate the maximum size of the crystal which can be doped by NTD with a given homogeneity. For instance, for Si $\gamma=4.5\times10^{-3}$ cm^{-1}, which permits one to achieve mac-

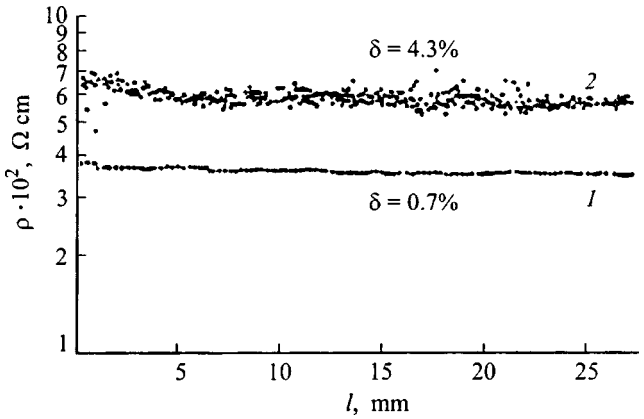

FIG. 3. Microdistribution of the resistivity of reference resistances which were prepared from germanium by (1) NTD and (2) metallurgical method (after Ref. 17).

rohomogeneity of doping to not worse than 10% even for a large ingot 200 mm in diameter. The NTD method demonstrates its superiority in microdistribution of resistivity even compared to reference resistances prepared by metallurgical techniques (Fig. 3, Ref. 18). It is the high macro- and microhomogeneities of doping that account for the widespread use of NTD-Si, including that obtained on the RBMK-1000 reactor, in production of high-voltage power converters.[19]

NTD of germanium is characterized also by the long half-life (11 d) of the Ge^{71} isotope decaying to produce the Ga acceptor impurity. On the one hand, this is inconvenient because it requires a long holdup of the irradiated material to allow all nuclear reactions to come to an end and to reduce the sample radoactivity. On the other, this offers a possibility of studying the same sample in the course of decay, at different concentrations of the continuously appearing gallium acceptor impurity as a function of time elapsed after the irradiation. Irradiation of *n*-germanium permits one to monitor the sample with progressively increasing compensation, up to its conversion to *p* type. Figure 4 shows the effect of increasing compensation on the electrical conductivity of the starting *n*-Ge sample.[20] We readily see that the activation energy of conduction grows continuously with increasing *K*, which corresponds to a shift of the Fermi level toward midgap. This phenomenon, in its turn, permitted, as it were, a spectroscopic investigation of the gap and determination of the energies and charge states of deep impurities in germanium.[21] By determining the exact point of conversion from *n*- to *p*-type made it also possible to refine the value of σ_i for Ge^{74} (Ref. 12).

Progress has recently become evident in NTD of germanium having an artificially modified isotopic composition. The main idea behind this work consists of producing NTD-Ge with different types of conduction and different compensation while maintaining a homogeneous impurity distribution. This is particularly important for the case of total compensation, which, assuming random spatial distribution of impurities, should give rise to strong fluctuations of electrostatic potential. Such a system is practically impossible to prepare by doping metallurgically; indeed, oppositely charged impurity ions remain mobile in a melt, which

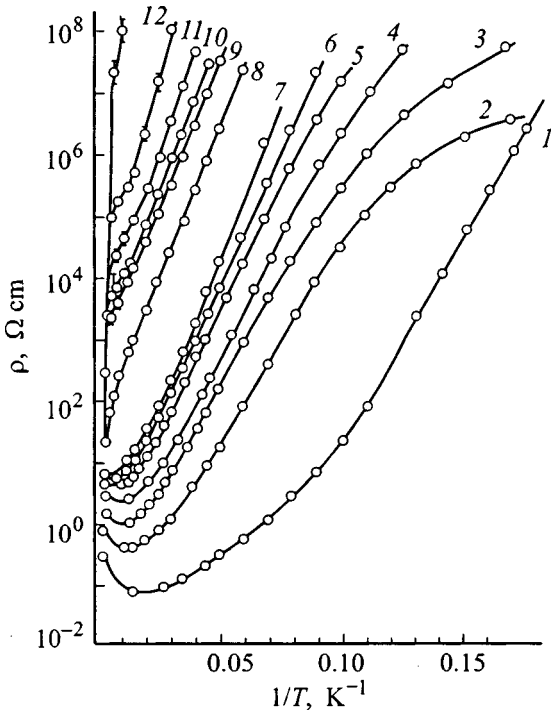

FIG. 4. Temperature dependence of the resistivity of *n*-Ge⟨*As*⟩ for different compensations (after Ref. 19): *1* — starting sample ($N_D = 1\times10^{16}$ cm^{-3}, $K=0$); *2–4* — compensation by increasing the concentration of gallium acceptor impurity produced in the sample through Ge^{70} transmutation 15, 27, and 51 days after neutron irradiation in a reactor at a dose $\Phi = 3\times10^{17}$ cm^{-2}; *5–12* — further compensation by gamma-ray irradiation. *K*: (*2*) 0.67, (*3*) 0.82, (*4*) 0.90, (*5*) 0.944, and (*6*) 0.956. For higher compensations determination of *K* from Hall measurements is impossible because the samples become inhomogeneous.

results in their correlated distribution, i.e. formation of donor-acceptor pairs. By contrast, the NTD process is run at a low (room) temperature. Even the unavoidable annealing of radiation defects is performed substantially below the melting temperature, where the impurities have a low mobility. This gives one grounds to hope to obtain closely compensated samples with a random impurity distribution.

First measurements of an NTD-doped Ge^{74}-enriched germanium were carried out at PTI in 1983.[22] One obtained by NTD a series of *n*-type samples with a small compensation, $K = 0.026-0.056$, depending on the actual enrichment by the Ge^{74} isotope and the presence of trace amounts of Ge^{70}, an isotope which transmutes to an acceptor impurity Ga^{71}. The high cost and small amounts of the isotope-enriched germanium dioxide provided by the Isotope Fund of the Kurchatov Institute required development of a technology of growing and purification of tiny Ge crystals a few grams in weight, a problem involving serious technical difficulties. By mixing the isotopically enriched Ge^{74} with natural germanium one could subsequently prepare and study *n*-type samples with compensations $K = 0.12, 0.38$, and 0.54.[23] Samples with $K > 0.8-0.9$ were also produced.

Lawrence Livermore National Laboratory in Berkeley, California, is another center where such research is being carried out. The scientists of this laboratory report of having grown miniature crystals from Ge^{70}- and Ge^{74}-enriched materials (which were obtained also from the Isotope Fund of

Kurchatov Institute) and from a mixture of these isotopes, which permitted obtaining *p*-type NTD-Ge samples with K lying within the 0–0.76 range.[24,25]

In silicon, the possibilities of isotope engineering are limited by the fact that only one Si isotope, Si^{30}, is presently used for transmutation doping. True, its natural occurrence is only 3.1%, so that enrichment of natural Si by this isotope would increase up to 30 times the limiting phosphorus concentration introduced by NTD, but the economical feasibility of this project appears doubtful. The possibility of silicon enrichment by the Si^{28} isotope is also discussed in the literature.[25] This should result in an increase of the heat conductivity of Si, which would be favorable for integrated circuit development.

In conclusion, consider the immediate prospects of research in this area, which, in our opinion, are connected with development of multilayer structures, based on alternation of the Ge^{70} and Ge^{74} isotopes in $Si/Si_{1-x}Ge_x$ heterojunctions or of three isotopes, Ge^{70}, Ge^{72}, and Ge^{74}, in a purely germanium structure,[26] with subsequent NTD. One will produce in this way *p-i-n* superlattices, with the main feature being that the processes of growth of the superlattice and of its doping are in this method separated. In a standard epitaxial approach, these processes are combined, which results in mutual detrimental effects, namely, a diffuse interface because of the impurities floating up during the layer growth, and an enhanced number of defects in the growing layer because of the influence of the impurities present in the latter. In the isotope method, the layers are grown without impurities and should have an ideal structure, because Ge isotopes are chemically identical. Subsequent transmutation doping and defect annealing would be performed at a comparatively low temperature and are not expected to degrade the interface and the layer structure.

The present report is in memory of Academician V. M. Tuchkevich, who made a large contribution to organization of NTD-Si on an industrial scale and development of the corresponding work at the PTI. I owe particular gratitude to A. N. Ionov for a long cooperation. M. L. Kozhukh, A. G. Zabrodskiĭ, M. D. Lyubalin, I. M. Lazebnik, and R. Rentzsch took active part in various stages of this work, for which I express to them sincere thanks.

*E-mail: issai@physnet.ph.biu.ac.il

[1] K. Lark-Horovitz, in *Proceedings of the Conference on Semiconducting Materials*, edited by H. K. Henish (Butterworth, London, 1951), p. 47; [Russian translation in *Semiconducting Materials*, edited by V. M. Tuchkevich (IL, Moscow, 1954), p. 62].
[2] *Neutron Transmutation Doping in Semiconductors*, edited by J. Meese (Plenum Press, New York, 1979; Mir, Moscow, 1982); *Semiconductor Doping in Nuclear Reactions* [in Russian], edited by L. S. Smirnov (Nauka, Novosibirsk, 1981).
[3] M. S. Schnoller, IEEE Trans. Electron Devices **ED-21**, 313 (1974).
[4] I. N. Voronov, A. N. Erykalov, E. I. Ignatenko, M. L. Kozhukh, M. A. Lyutov, Yu. V. Petrov, V. M. Tuchkevich, and I. S. Shlimak, USSR Inventor's Certificate 1063872 (1982).
[5] H. Fritzsche and M. Cuevas, Phys. Rev. **119**, 1238 (1960).
[6] B. I. Shklovskii and A. L. Efros, *Electronic Properties of Doped Semiconductors* (Springer, Berlin, 1984; Nauka, Moscow, 1979).
[7] N. F. Mott, *Metal-Insulator Transition* (Taylor & Francis, London, 1990).
[8] I. S. Shlimak, USSR Inventor's Certificate 437931 (1972).
[9] E. E. Haller, Infrared Phys. Technol. **35**, 127 (1994).
[10] *Low-Temperature Detectors for Neutrinos and Dark Matter IV*, edited by N. E. Both and G. L. Salmon (Oxford, 1991).
[11] T. Shutt, N. Wang, B. Ellman, Y. Giraud-Héraud, C. Stubbs, P. D. Barnes, Jr., A. Cummings, A. Da Silva, J. Emes, E. E. Haller, A. E. Lange, J. Rich, R. R. Ross, B. Sadoulet, G. Smith, W. Stockwell, S. White, B. A. Young, and D. Yvon, Phys. Rev. Lett. **69**, 3531 (1992).
[12] A. G. Zabrodskiĭ, JETP Lett. **33**, 243 (1981).
[13] E. E. Haller *et al.*, in: *Neutron Transmutation Doping of Semiconductor Materials*, edited by R. D. Larrbee (Plenum, New York, 1984), p. 21.
[14] A. N. Ionov, M. N. Matveev, and D. V. Shmikk, Zh. Tekh. Fiz. **59**, No. 6, 169 (1989) [Sov. Phys. Tech. Phys. **34**, 691 (1989)].
[15] V. A. Kharchenko and S. P. Solov'ev, Fiz. Tekh. Poluprovodn. **5**, 1641 (1971) [Sov. Phys. Semicond. **5**, 1437 (1971)].
[16] I. Shlimak, A. N. Ionov, R. Rentzsch, and J. M. Lazebnik, Semicond. Sci. Technol. **11**, 1826 (1996).
[17] J. W. Corbett and G. D. Watkins, *Radiation Effects in Semiconductors* (Plenum, New York, 1971).
[18] M. L. Kozhukh, I. S. Shlimak, V. V. Fedorov, and E. S. Yurova, Pisma Zh. Tekh. Fiz. **11**, 129 (1985) [Sov. Tech. Phys. Lett. **11**, 51 (1985)].
[19] V. M. Volle, V. B. Voronkov, I. V. Grekhov, A. N. Erykalov, M. L. Kozhukh, V. A. Kozlov, Yu. V. Petrov, N. A. Sobolev, V. M. Tuchkevich, V. E. Chelnokov, and I. S. Shlimak, Electrotehnica No. 3, 34 (1984).
[20] I. S. Shlimak and V. V. Emtsev, JETP Lett. **13**, 107 (1971).
[21] Yu. A. Osipyan, V. M. Prokopenko, and V. I. Tal'yanskiĭ, Zh. Éksp. Teor. Fiz. **87**, 269 (1984) [Sov. Phys. JETP **60**, 156 (1984)].
[22] I. S. Shlimak, L. I. Zarubin, A. N. Ionov, F. M. Vorobkalo, A. G. Zabrodskiĭ, and I. Yu. Nemish, Pisma Zh. Tekh. Fiz. **9**, 377 (1983) [Sov. Tech. Phys. Lett. **9**, 163 (1983)].
[23] R. Rentzsch, A. N. Ionov, Ch. Reich, M. Müller, B. Sandow, P. Fozooni, M. J. Lea, V. Ginodman, and I. Shlimak, Phys. Status Solidi B **205**, 269 (1998).
[24] K. V. Itoh, E. E. Haller, W. L. Hansen, J. W. Beeman, A. Rudnev, A. Tikhomirov, and V. I. Ozhogin, Appl. Phys. Lett. **64**, 2121 (1994).
[25] E. E. Haller, J. Appl. Phys. **77**, 2857 (1995).
[26] E. E. Haller, Semicond. Sci. Technol. **5**, 319 (1990).

Translated by G. Skrebtsov

Application of the theory of algebraic systems for creating a hierarchy of solid structures formed under equilibrium and nonequilibrium conditions

G. A. Domrachev*) and A. I. Lazarev

Institute of Metalloorganic Chemistry, Russian Academy of Sciences, 603600 Nizhny Novgorod, Russia
Fiz. Tverd. Tela (St. Petersburg) **41**, 799–804 (May 1999)

A unified hierarchy is proposed for molecular and solid structures formed under equilibrium (ideal crystals) or nonequilibrium conditions (real crystals, fractally ordered crystalline, quasicrystalline, and amorphous solids, as well as composite solid materials that are aperiodic on an atomic-molecular level but are periodic on a macroscopic level). The construction of this hierarchy is based on applying the theory of algebraic systems (groups, rings, and fields) to the multiplication of an initial structure in space depending on an inflation coefficient (numbers) expressed in the general form $Q=(n+m\sqrt{l})/k$. Examples are presented of molecular and polymer structures described by groups or rings, fractally ordered solids whose structures are described by fields, and solids with damped or self oscillations in their composition, whose structures are described by fields or periodic rings of fields with complex spatial multiplication factors. © *1999 American Institute of Physics.* [S1063-7834(99)01105-3]

Molecular systems and structures of crystals are described by ''groups'' as algebraic systems. Molecular systems are described by ''point group symmetries'' and crystals, by ''space groups.'' A ''ring'' algebraic system describes complicated molecular systems with partially (most often ''hidden'') ordered and almost independent subsystems (some metalloorganic compounds and complexes, oligomers and polymers, including fullerenes and nanopipes, biological molecules). A ''field'' algebraic system generates structures which have all the characteristics of fields (''sources,'' ''sinks,'' ''gradients,'' and ''vortices''). These systems describe physical systems which can be fractally ordered. These last grow in energy and concentration (mass) fields and create aperiodic structures such as quasicrystals. Their aperiodicity is caused by the absence of a translation operator in the solid, but they can have rotational symmetry and fractal ordering. A real representation of the growing spatial structures after multiplying by a complex number makes it possible to explain the different types of spatial and energy oscillations controlled by the mass and energy fluxes. The formation of macroscopic periodic systems without a periodicity on an atomic scale has been observed during MOCVD processes.

1. It is known that the metal constituent can have a large influence on the structure and properties of metalloorganic compounds (MOCs) in the molecular and condensed states, as well as of their condensed (solid or liquid) decomposition products. Both the ordering of other atoms around a given atom within an MOC molecule and the ordering of the atoms of the metal and, perhaps, of atoms of other elements present in the system of condensed decomposition products of an MOC (carbon, hydrogen, compounds of the metal with them and with other elements) depend on the position of the metal atom in the periodic table (i.e., on the energy and spatial characteristics of a metal atom).

Depending on how far the system is from a state of equilibrium, the structures of MOCs and systems of condensed decomposition products of MOCs can have a structure ranging from crystalline, where there is order on an atomic-molecular level, all the way to an x-ray amorphous state, in which there is not even short-range order on an atomic or molecular level, but periodic structures can exist on a macroscopic level.

The structures of MOC molecules, such as ferrocene–bis-cyclo pentadienyl iron or bis-chlorobenzene, can have an extremely high symmetry. At the same time, there are compounds with properties similar to them which do not have any molecular symmetries, such as cyclo- pentadienyl-chlorobenzene. The structure of MOC molecules, like other molecules, are described by the group theory of algebraic systems,[1] in particular, by ''point groups.''

The structure of the condensed state of MOCs and their decomposition products can be mono- and polycrystalline states with periodic molecular and atomic composition and order reaching a macroscopic level. The ideal structure of crystalline bodies is also described by group theory as algebraic systems, in particular, by ''space (Fedorov) groups.'' These descriptions, however, only apply to ''ideal equilibrium states'' in the condensed phase.

Under real, nonequilibrium and, essentially, irreversible conditions, when energy and mass fluxes are present, condensed states are formed by processes which take a finite time and result in the formation of a variety of different structures: gradient, fractally ordered, porous, layered with a periodicity only on a macroscopic level, etc. These structures are presently discussed in terms of synergetics or the theory of dynamic systems, as well as by using the mathematics of the theory of nonlinear oscillations.[2,3]

Because of their structure, the condensed states of MOCs and their decomposition products formed under nonequilibrium conditions have properties which are unusual for ordinary crystalline bodies. For example, nonlinear optical

properties have been observed in some industrial MOCs and polymers, liquid-crystal properties in high substitution MOCs and polymers, electrooptical effects, etc. For films of the solid decomposition products of MOCs under nonequilibrium conditions in the MOCVD process, gradient, composition-layered, and fractally-ordered structures typically develop which have high durability and corrosion resistance, anomalously low temperature coefficients of electrical resistivity (for chromium films), acoustic emission during formation, anomalous stability of pores of certain sizes, and micro- and nanocomposite compositions in the solid phase. Similar properties are possessed by the fullerenes, nanopipes in the condensed phase, in the limit, shungite, and graphite inclusion compounds, as well as numerous layered (MoS_2, TaS_2, $Fe(PS_3)_2$, double and triple oxides of P, As, and the metals Zr, Hf, U, etc.) solid compounds, and the micro and macrozeolites.

For many years, the authors have systematically studied both the structure of MOC molecules and crystals, and the structure of the condensed decomposition products of MOCs obtained by the breakup of MOCs during heterogeneous gas-solid or -liquid, liquid (or MOC solution)-solid, and solid-solid reactions, as well as during gaseous phase reactions with different methods of activation (thermal, plasma chemical, photochemical, mechanochemical).

The formation of all the above types of condensed states (from single crystal to x-ray amorphous, layered, and fractally ordered) has been observed experimentally. A theoretical (mathematical) treatment of the formation of the condensed phase for these processes was first given in Ref. 4.

For a unified treatment of the structures of MOCs and their condensed decomposition products, however, it was proposed[5,6] that the theory of algebraic systems (groups, rings, and fields)[1] and number theory be used in a qualitative classification to construct an hierarchy of the structures and the algebraic systems corresponding to them during formation of the condensed phase in the decomposition of chemical compounds, in particular, MOCs. Possibilities not encountered in the scientific literature were pointed out for treating molecules with high-symmetry fragments, oligomers, and polymers, with the aid of algebraic ''ring'' systems, along with the conditions under which they generate ''groups'' or ''fields.'' It is interesting that ''fields'' with fractional and irrational multiplication factors of the spatial structure seed generate a fractal ordering in the condensed state of the material in space. When the seed spatial multiplication factors are imaginary, the algebraic ''field'' system corresponds to processes for formation of macroperiodic structures which are not periodic on an atomic level (''manifestation'' of the imaginary nature of the multiplication factors).

Our purpose is to develop a theoretical apparatus for determining the mutual correspondence of algebraic systems and real equilibrium and nonequilibrium structures in order to predict and describe the energy and spatial characteristics of molecular and polymeric systems, and of fractally and spatially periodically ordered condensed states. There is also some interest in developing methods for estimating and predicting the nonlinear properties of substances resulting from structures described by ''rings'' and ''fields.''

The experimental tasks in this work are to verify, improve, and confirm the theoretical advances in terms of the nonlinear properties of MOCs and polymers, and of films of inorganic phases obtained through the decomposition of MOCs under equilibrium and nonequilibrium conditions.

2. We propose using general number theory to obtain an effective solution for the problem of creating models for the formation of complex molecules and solids under equilibrium and nonequilibrium (real) conditions from the vapor or liquid phase. This makes it possible to analyze the different types of molecular and solid structures as they form. Simple unit cells of a certain number of interacting atoms of one or several types can be multiplied in space using the self-similarity (or inflation-deflation) coefficient Q, which can take on any numerical value. The number Q can be written as the fraction

$$Q=(n+m\sqrt{l})/k, \tag{1}$$

where n, m, l, and k are arbitrary numbers.

When a simple unit cell is multiplied by Q, its structure is repeated over larger or smaller scale lengths and different types of spatial filling by the structure can occur, depending on n, m, l, and k.

The simplest case occurs for $m=0$ and $k=1$. Then $Q=n$. These conditions correspond to the natural series of numbers and the resulting solid structures correspond to periodic packing of solids, beginning with atomic scale lengths and on to macroscopic scale lengths. This process is known as crystallization. This case is difficult to attain under nonequilibrium conditions when energy and mass fluxes are present. Only when these fluxes are negligible does crystallization occur. Crystal structures are described by ''group'' theory[7] as an algebraic system theory. It is also applicable to molecular systems. However, molecular systems are described by point groups, and crystals, by space groups in which the point groups enter explicitly or implicitly as subgroups (in many molecular crystals or in the nearest-neighbor ions in ionic crystals). A ''group'' algebraic system is characterized by only one operation, which is additive (adding or subtracting as the opposite of adding) or multiplicative (multiplication or division as the inverse of multiplication). If the elements of the group are strongly coupled (are not localized in separate spaces), then the group is multiplicative. A given molecular system can be described by an additive or multiplicative group, depending on the force whose interaction is being considered. Additive groups are used to describe systems with a weak interaction. Here the fragments (subgroups of the additive group) are essentially independent of one another (zero overlap). Groups describe the simplest, as well as complicated, molecular systems and for the latter, with a low symmetry (e.g., C_1), this description is ineffective.

The next case occurs for integer n, m, $(l>0)$, and l/k $(k<1)$. In this case Q forms an algebraic system with two defined operations: addition and multiplication. This kind of algebraic system is referred to as a ring.[1,8] This case corresponds to complicated molecular systems containing many

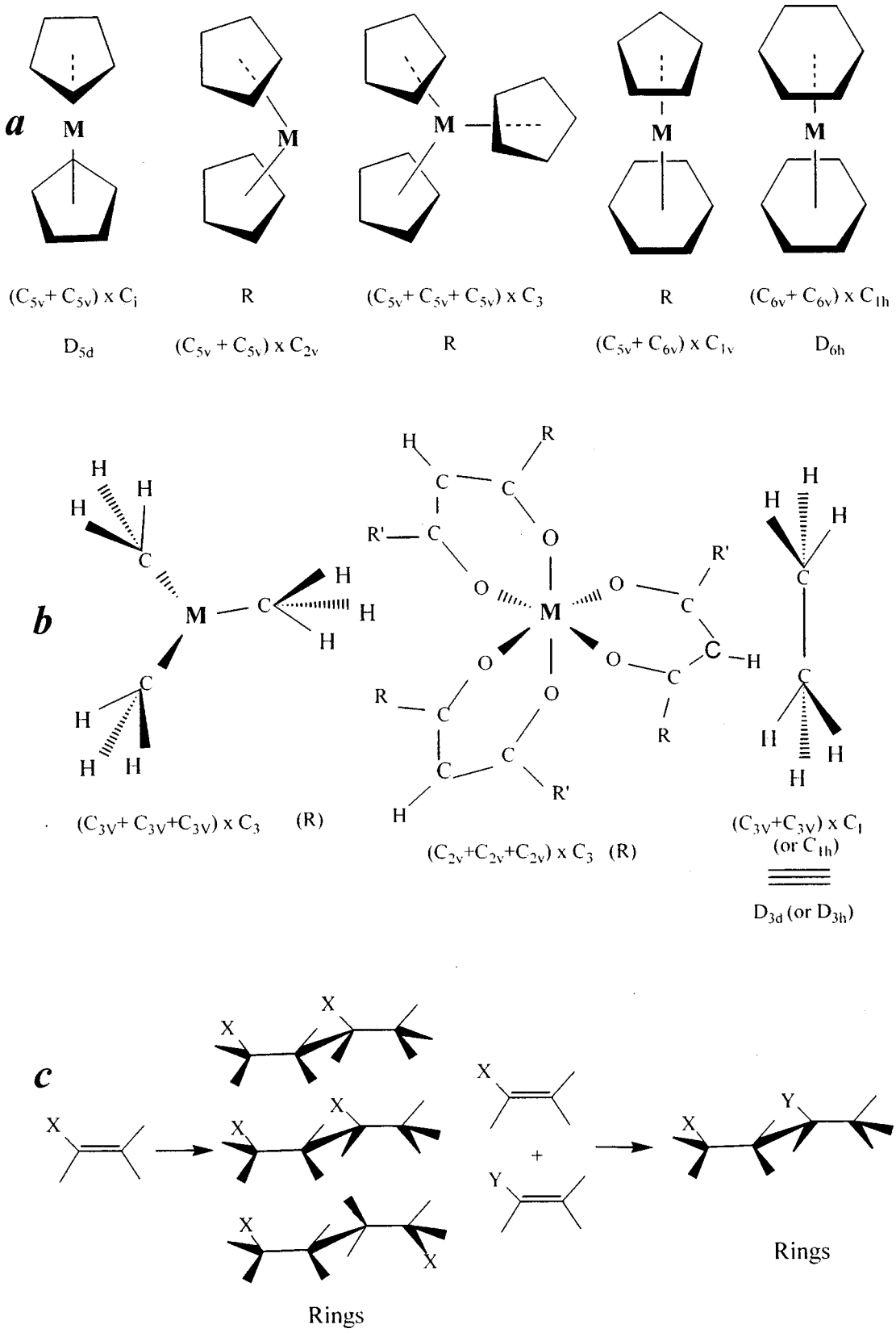

FIG. 1. Examples of organometallic compounds and polymers represented by ''groups'' and ''rings:'' (a) transition metal MOCs, (b) MOCs of transition metals, acetyl acetonates, and ethane, and (c) polymers.

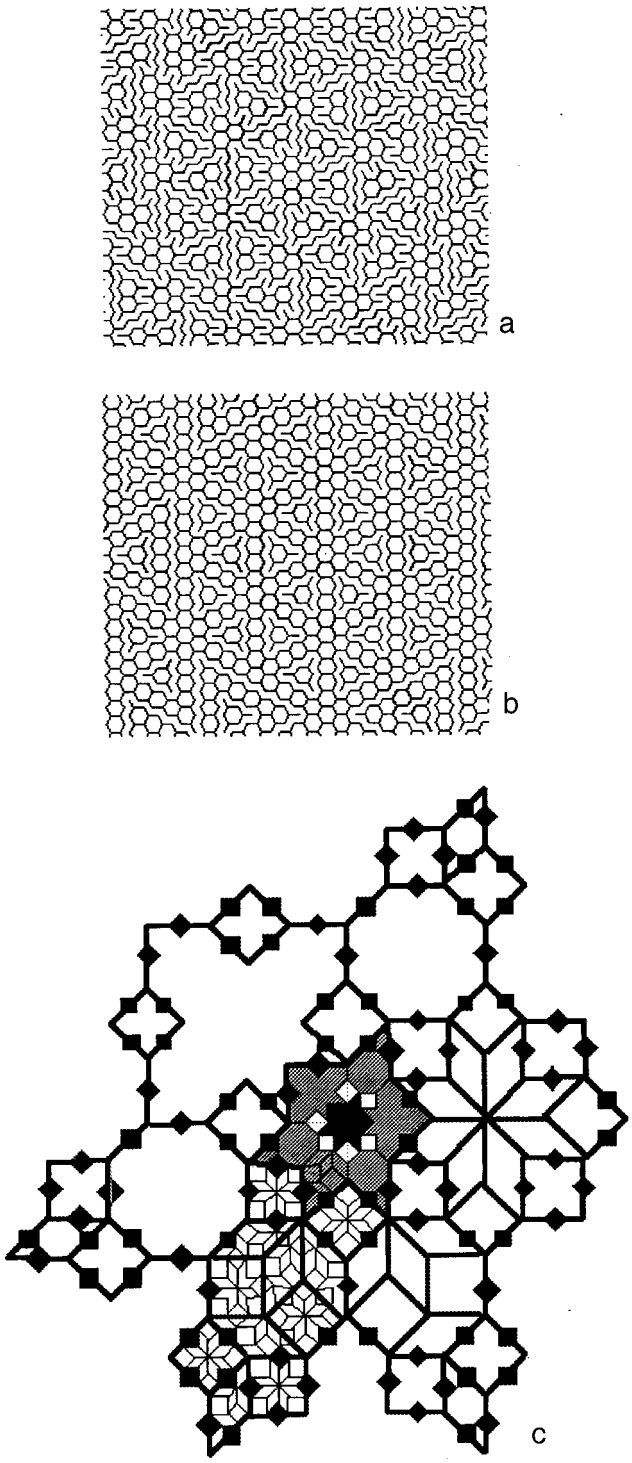

FIG. 2. Two dimensional fractally ordered quasicrystalline structures represented by a ''field:'' (a, b) modelling hexagonal carbon structures by ''fields'' that include a ''ring'' with a high degree of amorphization and filamentary elements (a) and with a high degree of aromatization with bands of polyaromatic structures as precursors of nanopipes (b); (c) the development of a two dimensional fractal structure with an inflation coefficient $Q=(2+\sqrt{2})$ and C_2 rotational symmetry and manifesting arbitrary filling of ''stable fractal structures'' by elements from preceding generations.

partially ordered and almost independent subsystems. But this type of system has not been examined in the literature, even though these conditions exist in some organometallic compounds and complexes, polymers, biological macromolecules, and, finally, pregraphite structures, fullerene derivatives, and nanopipes.

All the remaining cases, where $k\neq 0$, Q is a fraction or irrational number, and $l>0$, create ''field'' algebraic systems[1] and the structures generated in these cases have all the properties of fields (i.e., ''sources,'' ''sinks,'' ''gradients,'' and ''vortices''). These systems have spatial gradients over the elements contained in the structure and can be defined as fractally ordered spatial systems. These systems always develop under nonequilibrium conditions when energy and mass fluxes are present (in energy and concentration, or mass, fields) and create aperiodic structures, including, in particular, ''amorphous'' and quasicrystalline bodies formed under nonequilibrium conditions. The aperiodicity of these structures is related to the absence of a translation operation in the solid blocks, but they can have rotational symmetry axes of arbitrary order and retain fractal ordering. Real systems of this sort have apparently not been considered in materials science, except in a few of our recent papers[9–14] where methods were developed for constructing quasicrystalline structures over a fractal skeleton which revealed the possibility of forming structures like pores (closed, stable fractal forms), within which ''local crystallization'' is possible over many generations, i.e., the pores can be partially filled with ''primary construction material'' that has a packing structure possessed of a translation operation. The siting of these pores and, thereby, of the local crystals is fractal in nature.

For a long time architects and artists have used the ''golden mean'' for creating beautiful aperiodic structures with irrationally ordered symmetries in buildings. A much more complicated irrational ordering occurs in living nature, in an open nonequilibrium system capable of living among inorganic material on the earth, as was often pointed out by Academicians Shubnikov and Belov.

Special cases of complex system formation occur for $l<0$. A real representation of developing spatial structures obtained by multiplying by a complex number allows us to obtain an explanation for various types of spatial oscillations in the structural components under nonequilibrium and equilibrium conditions for the formation of solids (see Mel'nikov,[15] Zhuk,[15] and Almazov[16]). These oscillations, as well as stable, stationary states and self oscillations, are a consequence of nonlinear kinetics in nonequilibrium processes (often irreproducible), accompanied by mass and energy fluxes through the system that are difficult to control. This case represents the formation of macroperiodic systems with a lack, compared to crystalline systems, of periodicity (an aperiodicity) on an atomic size scale. The latter are periodic on macroscopic and atomic scale lengths. This behavior has been examined and discussed using the theory of nonlinear oscillations for deposition from the vapor phase (MOCVD processes)[15–19] in the general and some particular cases of the deposition of solids under conditions of limited mass (diffusion, laminar flows, vortices) and energy transport (heat transfer).[15] It is interesting that damped and forced oscillations produce structures that are described by ''fields,'' while self oscillating regimes in the growth of sol-

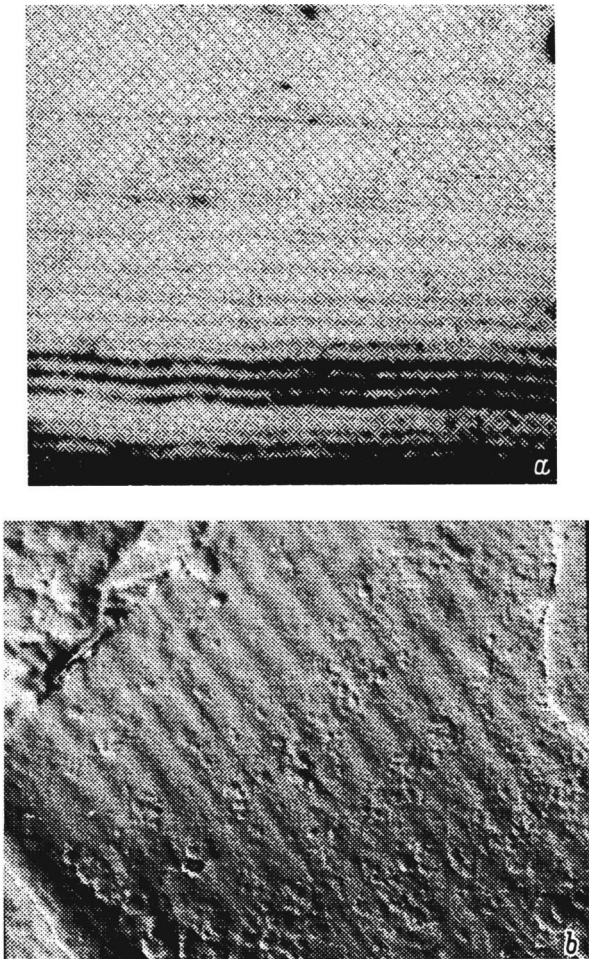

FIG. 3. Actual structures of thin slices of the transverse cross sections of chromium coatings obtained by MOCVD with damped oscillations (a) and with self oscillations (b). Case (a) corresponds to a ''field'' (gradient material) and case (b), to a periodic structure from ''rings.''

ids lead to macroperiodic structures corresponding to an additive combination of ''rings.''

3. As an illustration, we hoped to demonstrate a correspondence between groups, rings, and fields and several molecular structures in organometallic compounds, polymers, and quasicrystalline carbon compounds with inclusions, as well as some MOCVD structures corresponding to fields and rings (Figs. 1–3). It may be assumed that transcendental numbers, such as π, e, etc., also form their own sets of structures, but these numbers and the structures corresponding to them[14] have not been examined here.

This work was supported by the Russian Fund for Fundamental Research (grant No. 96-15-97455) and the Ministry of Science of the Russian Federation (grant Metall-1 in the Program on Fullerenes and Atomic Clusters).

*)E-mail: domrachev@imoc.sinn.ru

[1] A. G. Kurosh, *A Course in Higher Algebra* [in Russian] (Fizmatgiz, Moscow, 1959).
[2] A. A. Andronov, A. A. Vitt, and S. É. Khaĭkin, *Theory of Oscillations* [in Russian] (Fizmatgiz, Moscow, 1959; Nauka, Moscow, 1981).
[3] M. I. Rabinovich and A. B. Ezerskiĭ, *Dynamical Theory of Shape Formation* [in Russian] (Yanus-K, Moscow, 1998).
[4] A. I. Lazarev, A. Yu. Sukhanov, and G. A. Domrachev, Crystallogr. Rep. **41**, 798 (1994).
[5] G. A. Domrachev and A. I. Lazarev, in *Organometallic Chemistry on the Eve of the 21st Century. Workshop, INEOS'98 (1998)* (Moscow, 1998), p. 38.
[6] G. A. Domrachev and A. I. Lazarev, in *XVI-th Academician N. V. Belov Scientific Lectures. Abstracts of Talks, Nizhny Novgorod State Univ.* (Nizhny Novgorod, 1997), p. 79.
[7] M. A. Naĭmark, *Theory of Group Representations* [in Russian] (Nauka, Fizmatgiz, Moscow, 1976).
[8] M. A. Naĭmark, *Normalized Rings* [in Russian] (Nauka, Fizmatgiz, Moscow, 1968).
[9] G. A. Domrachev, E. Huipe Nava, A. I. Lazarev, A. A. Zakurazhnov, B. S. Kaverin, V. A. Kostenkov, and E. G. Domracheva, in *Memoria de XVI Simposio Nacional de Siderurgia, ''Ingenieria de Procesos''* (Secretaria de Educacion Publica, Instituto Tecnologico de Morelia, Morelia, Mich., Mexico, 1994), pp. 33-1–33-13.
[10] G. A. Domrachev, E. G. Domracheva, E. Huipe Nava, B. S. Kaverin, A. I. Lazarev, E. V. Spivak, and A. A. Zakurazhnov, in *IV International Conference on Advanced Materials (ICAM-IV), Cancun, Mexico (1995)*, pp. S14–P2.9.
[11] A. I. Lazarev and G. A. Domrachev, in *Abstracts of Papers, Workshop on Aperiodic Structures, Krakow, Poland 1996* (1996), p. 69.
[12] G. A. Domrachev, B. S. Kaverin, A. I. Lazarev, A. A. Zakurazhnov, E. G. Domracheva, E. V. Spivak, and E. Huipe-Nava, in *Abstracts of Talks at Symposium on Synergetics, Structure and Properties of Materials, and Self Organized Technologies* [in Russian], Moscow (1996), Part 1, p. 230.
[13] G. A. Domrachev, B. S. Kaverin, A. I. Lazarev, and E. G. Domracheva, in *The 3rd International Workshop in Russia. Fullerenes and Atomic Clusters, St. Petersburg, Russia (1997), Book of Abstracts*, p. 58.
[14] A. I. Lazarev, G. A. Domrachev, and A. Yu. Sukhanov, in *Abstracts of Talks, XVI-th Academician N. V. Belov Scientific Lectures. Nizhny Novgorod State Univ.* (Nizhny Novgorod, 1997), p. 85.
[15] B. G. Gribov, G. A. Domrachev, B. V. Zhuk, B. S. Kaverin, B. I. Kozyrkin, V. V. Mel'nikov, and O. N. Suvorova, *Deposition of Films and Coatings by Decomposition of Organometallic Compounds* [in Russian] (Nauka, Moscow, 1981).
[16] G. V. Almazov, Author's Abstract of Candidate's Dissertation, Inst. of Chemistry, Acad. of Sciences of the USSR, Gorky (1980).
[17] G. A. Razuvaev, B. G. Gribov, G. A. Domrachev, and B. A. Salamatin, *Organometallic Compounds in Electronics* [in Russian] Nauka, Moscow, 1972).
[18] *Applications of Organometallic Compounds in the Production of Inorganic Coatings and Materials* [in Russian] G. A. Razuvaev, (Nauka, Moscow, 1986).
[19] *Applications of Organometallic Compounds in the Production of Inorganic Coatings and Materials* [in Russian], Institute of Organometallic Chemistry, Russian Academy of Sciences, Gorky (1989).

Translated by D. H. McNeill

Disordered solids: universal behavior of structure, dynamics, and transport phenomena

V. K. Malinovskiĭ*)

Institute of Automation and Electrometry, Siberian Branch of the Russian Academy of Sciences, 630090 Novosibirsk, Russia

Fiz. Tverd. Tela (St. Petersburg) **41**, 805–808 (May 1999)

Disordered materials (glasses and amorphous substances, melts, polymers, biological media, etc.) are an important class of objects. Despite the chaos usually associated with their structure, glasses and amorphous substances of various kinds (semiconducting, dielectric, metallic) possess a universal spatial scale length ~1 nm, an order parameter, which can be as important theoretically as the unit cell for crystals. The disorder in disordered substances is not absolute; the periodicity positions of atomic inherent in crystals is maintained within a few coordination spheres and is then somehow destroyed. The way in which the order breaks down makes it possible to distinguish the glasses from amorphous materials in terms of the form of the structural correlation function. The inhomogeneities in question are not exotic, unique formations or analogs of defects in crystals, but are the fragments out of which amorphous substances and glasses are entirely constructed. The spatial inhomogeneity of disordered substances having a characteristic scale length of ~1 nm leads to some universal characteristics in their vibrational properties, changes the relaxation mechanism for electronic excitation, and determines the specific features of charge transport.
[S1063-7834(99)01205-8]

From the viewpoint of fundamental science, the structure of amorphous substances and glasses is basic to solid-state physics. How is the world constructed under the conditions of disorder with which these substances are usually associated? This question is no easier to answer than many of the fundamental problems of astrophysics and elementary particle physics.

Of all the states of matter, only the crystalline state stands out distinctly in terms of the geometric ordering and positioning of its atoms over fairly long distances. This has permitted major experimental advances in the understanding of the crystalline state and the development of satisfactory theoretical models. Noncrystalline materials (the overwhelming majority of amorphous substances, glasses, and liquids in practical use), however, do not have this order if one approaches them with ''crystalline'' measures. This creates a perception that there is no universality to their structure and the only thing one can do is to study each substance, attempt to construct a model of its structure, and find individual criteria for controlling its properties. This approach does not appear to be productive, but it is widespread.

It is well known that all amorphous materials with very different types of short-range order (covalent lattices, metallic glasses, polymers, etc.) have a number of properties in common. These include a linear temperature dependence of specific heat and a quadratic one for temperatures $T \leqslant 1$ K, an excess density of vibrational states for $T \sim 5-20$ K, the Vogel–Fulcher law for their relaxation properties at high temperatures, the 2/3 rule for the relationship between the vitrification and melting temperatures, etc. The existence of such universal behaviors suggests that it is based on common features in the structure of amorphous materials.

There are now many models for the structure of amorphous substances which explain the experimentally observed behavior to some extent. The most widely recognized of them, which describes the low-energy vibrational behavior, is the soft-potential model,[1] which arose as a generalization of a phenomenological model for two-level systems.[2,3] The microscopic nature of soft potentials is, however, still unclear and has not yet been explained.

Attempts to describe amorphous substances and glasses as ''bad'' crystals have never ceased. It is assumed that they are quasicrystalline: although the distances between neighboring atoms fluctuate irregularly, on average they differ little from the mean. In this case it is possible to introduce a coordination scale length in which the potential of a chain is approximately periodic. One of the first such approaches was used by Gubanov in the early 1960's.[4] In 1998 Alexander[5] again proposed using a Cauchy–Born expansion for describing amorphous substances. Nevertheless, he understands (a large part of the review is devoted to this point) that the main obstacle is the impossibility of defining a ''reference'' state, relative to which the expansion is carried out.

We believe that quasicrystalline concepts of the structure of amorphous substances in the sense of Refs. 4 and 5 should be avoided. The physical properties and geometry of amorphous materials are closely related. The disorder in amorphous substances is topological, and topological defects cannot be eliminated by small displacements of the atoms. This requires a global realignment of the structure.

A possible basis for new approaches to the theoretical description of amorphous substances and glasses might be a recognition of the fact that the disorder in these materials is not absolute. The periodicity in the positions of the atoms intrinsic to crystals is maintained over several coordination spheres, and then somehow destroyed. The distance over

which order is still preserved can be characterized by the correlation radius R_c of the structure. Various estimates for amorphous and glassy materials yield $R_c \sim 1$ nm.[6] Here it is appropriates to note that the way the order in the atomic positions breaks up within a few coordination spheres is different for amorphous substances and glasses. In glasses, the loss of ordering takes place comparatively smoothly (the structure correlation function $F(R)$ is exponential), while amorphous substances consist of fairly perfect small crystallites [$(F(R)$ is gaussian]. The characteristic form of the structural correlation function can be determined by Raman scattering.[7] Over scales much longer than R_c, amorphous substances are well described as continuous media to which many results of conventional crystallography apply fully. Here the situation is similar to a fractal description: fractons occur over small distances, and a continuum over long distances.

Experiments have long indicated the existence of some kind of universal structural formations on scale lengths of $\sim$1 nm. This is shown by data from x-ray structure studies (the first sharp diffraction peak), small-angle x-ray scattering, dark-field electron microscopy, neutron scattering, and Raman scattering. But, to judge from numerous articles, the overwhelming majority of experimentalists and theorists do not take this fundamental property of amorphous substances into account.

Probably the main argument against using the concept of structural inhomogeneities with a scale length of $\sim$1 nm is the question of how the boundaries between them are constructed. The microcrystallite theory of glass structure proposed by Lebedev[8] was unacknowledged precisely because the question of the structure of the boundary between crystallites was not answered. Many physicists regard the boundaries as some kind of amorphized layer with a thickness on the order of a few interatomic distances. Its structure can only be imagined.

Meanwhile, approaches have long been under development which relate the topological disorder in amorphous substances to the presence of characteristic structural elements, i.e., dislocations. One of these is associated with the names of Kleman, Sadoc, and Likhachev.[9–11] Their model proceeds from the assumption that an amorphous substance can be described as a substance with an ordered structure in a curved space. Disorder develops after the crystal is mapped from the curved space into real euclidean space. This mapping cannot be done without distortions, which lead to the loss of order. But the distortions are not arbitrary disruptions of the order; they take place in accordance with completely defined laws and, specifically, as a result of the appearance of linear, rotational defects, i.e., disclinations, which cause topological disordering of the structure of amorphous substances.

A second approach, associated with the names of Rivier, Nelson, and Sethna,[12–14] is based on introducing a nonabelian gauge field, which makes it possible to take into account the invariance of the structures of amorphous substances with respect to local rotations. Fields of this type are also associated with disclinations. Their stress tensor is proportional to the disclination density tensor.

The two approaches are interrelated. Noneuclidean geometry can be described in a language which is a special case of nonabelian gauge fields. The curvature tensor is proportional to the stress tensor of the field.

Introducing disclinations makes it possible to overcome the contradiction between the two major specifications defining the structure: minimizing the local energy and the densest possible occupation of space. The density of disclinations in an amorphous substance must be very high, while the distance between them must be on the order of a few interatomic distances. Disclinations divide an amorphous substance into regions within which the crystalline order is preserved to a substantial degree.

Thus, physicists have measured an inhomogeneity scale length which appears to be $\sim$1 nm, and the mathematicians have proposed a model of boundaries for these inhomogeneities. We showed back in 1977 that glass has a crystalline order over scale lengths $\sim$1 nm.[15,16]

The inhomogeneities of concern here are not exotic, unique formations or analogs of defects in crystals, but are the fragments out of which amorphous substances and glasses are entirely constructed. In this sense they can be regarded as analogs of the unit cells of crystals.

The spatial inhomogeneity of amorphous substances and glasses with a characteristic scale length of $\sim$1 nm leads to the appearance of universal behavior in their vibrational properties, changes the relaxation mechanism for electronic excitation, and determines the specific features of charge transport.

As noted above, glasses have an excess density (compared to the Debye density) of vibrational states at energies of 2-10 meV (3-15 K). The excess vibrational density shows up as a peak, which exceeds the Debye vibrational density for this energy by a factor of 2-6 in different materials. An excess vibrational density is observed in all glasses. It shows up in low-energy inelastic-neutron-scattering spectra, low-frequency Raman scattering (the ''boson peak''), far-IR absorption, and low-temperature specific heat and thermal conductivity. We assume that there is reason to relate the excess vibrational density in glasses at 3-15 K to their having a characteristic length, an average ordering radius, with a scale length of $\sim$1 nm. The low frequency vibrational excitations responsible for the excess vibrational density are localized in the structural nanoinhomogeneities in our model.[17] There have also been a number of experiments on models which confirm the possibility, in principle, of this mechanism for the development of an excess vibrational density.[18] Data on low-temperature heat conduction in a wide range of glasses have been analyzed[19] and it was found that, in the plateau region, the Ioffe–Regel criterion for phonon localization is satisfied: $\lambda \sim l$, where l is the mean-free path determined for strong scattering on the scale of the structural inhomogeneity and λ is the phonon wavelength. Comparing these data with measurements of the thermal conductivity in aggregates, where the localization shows up on a scale length equal to the correlation length of the structure, yielded a correlation length of 10-30 Å for the glasses. The size distribution of the nanoinhomogeneities can be described by a logarithmic

function with a universal dispersion of the logarithm of frequency $\sigma=0.48$.[17]

The low-energy features of the vibrational spectra of glasses can have a significant influence on their properties at high, as well as low T, up to the vitrification temperature. Thus, the contribution of low-energy phonons to the magnitude of the mean-square thermal vibrations of the atoms is enhanced by a factor proportional to the reciprocal of the square of their frequency. Therefore,[20] in glasses the existence of an excess low-energy vibrational density, in an integral amount of 10%, raises the amplitude of the thermal vibrations by 30-40% compared to the corresponding crystals at the same temperature. At the vitrification point, the amplitude of the thermal vibrations is extremely close to the level in the corresponding crystals at the melting point. The relationship between the vitrification and melting temperatures in materials having the same chemical composition found[20] using the Lindemann criterion is determined by the parameters of the excess low-energy vibrational density: its amplitude, the position of the maximum, and the universal dispersion of the log-normal distribution with respect to the frequency of the excess vibrational density. The ratio T_g/T_m was very close to 2/3, the well known empirical rule. In these materials, as in amorphous silicon and germanium, there is no excess vibrational density at low energies: the boson peak actually merges with the line corresponding to the *TA* mode. Thus, these materials do not vitrify and, when they are cooled below the melting point, they crystallize rapidly in accord with the fact that in them, as opposed to the glasses, the amplitude of the thermal vibrations is close to that in the crystal state.

In amorphous substances and glasses, the physics of the relaxation of electronic excitation differs fundamentally from that in crystals. In media with spatial dispersion in their properties, the excitation energy is localized over scale lengths on the order of the correlation radius of the structure. Energy transfer from the electronic subsystem to the ion core takes place in two steps: in the first, high-frequency local phonons are generated in a region bounded by the correlation radius R_c of the structure and only then, after some time delay, is energy pumped into long-wavelength vibrations. Localized phonons are ''trapped'' inside the structural correlation region and have a unique spectrum which depends on the characteristic size (only phonons with wave numbers from $k_{\max}\sim k_D$ to $\sqrt{k'}\sim 1/R_c$ are present). The excess energy associated with local vibrations is dispersed only through phonon-phonon interactions and the localization time may exceed the reciprocal of the characteristic phonon frequencies by an order of magnitude. This delay in energy removal leads to an interesting phenomenon: structural realignments in amorphous materials and glasses driven by light of arbitrarily low intensity. Each absorbed photon can change the structure of the nanoregion where it is absorbed. Structural changes of this sort have been observed most clearly in chalcogenide glasses and, to some extent, in all other glasses and amorphous substances.[6] A local heating model[21] explains the experimental data most rigorously and completely.

Nanoinhomogeneities have also been observed in experiments on current transport. Usually the temperature dependence of the conductivity is a smooth curve with an activation energy that falls as the temperature is lowered. As a rule, this is interpreted in terms of several exponential segments corresponding to the known charge-transport mechanisms: through a zone of delocalized states, through localized states near the Fermi level, and through states lying above the Fermi level of the material. However, our analysis of the numerous experimental data shows that, in a whole series of cases, the temperature dependence of the conductivity of the material can be represented in an entirely different manner, by an inverse Arrhenius law, rather than as a sum of two, three, or more exponentials having different activation energies.

Phenomenologically, an inverse Arrhenius law for the temperature dependence of the conductivity can be obtained by considering the fluctuations in the potential and the spatial fluctuations in the mobility. Then, treating the conductivity of a highly inhomogeneous medium using percolation theory, we find that the only effective participants in the conductivity are carriers lying within a narrow energy interval kT near a percolation level E_c corresponding to the development of a critical conducting cluster. The necessary calculations have been done elsewhere.[22]

Note that an inverse Arrhenius law has long been known for the temperature dependence of the photoluminescence intensity in disordered materials, in particular for amorphous silicon and chalcogenides.[23] This law is explained by a competition between radiative and nonradiative recombination channels. We have seen[24] that the transport of charged carriers and their recombination in disordered solids are closely interrelated.

Therefore, despite the chaos usually associated with the structure of disordered substances, they do have a universal spatial scale length, an order parameter that is characteristic of amorphous substances and glasses of various kinds (semiconducting, dielectric, metallic). Size effects determine the experimentally observed features of their vibrational properties, relaxation of electronic excitation, and charge transport. A continuum description of amorphous substances and glasses is applicable only on scale lengths exceeding the characteristic correlation length.

*)E-mail: malinovsky@iae.nsk.su

[1] V. G. Karpov, M. I. Klinger, and F. N. Ignat'ev, Zh. Éksp. Teor. Fiz. **84**, 760 (1983) [Sov. Phys. JETP **57**, 439 (1983)].
[2] P. W. Anderson, B. I. Halperin, and C. M. Varma, Philos. Mag. **2**, 1 (1972).
[3] W. A. Phillips, J. Temp. Phys. **7**, 351 (1972).
[4] A. I. Gubanov, *Quantum-Electronic Theory of Amorphous Semiconductors* [in Russian] (Izd-vo. AN SSSR, Moscow–Leningrad, 1963).
[5] S. Alexander, Phys. Rep. **296**, 65 (1998).
[6] V. K. Malinovskiĭ, Avtometriya No. 1, 25 (1985).
[7] V. K. Malinovskiĭ, V. N. Novikov, and A. P. Sokolov, Fiz. Khim. Stekla **15**(3), 31 (1989).
[8] A. A. Lebedev, in *The Glassy State. Proceedings of the III-rd All-Union Conference* (AN SSSR, Leningrad, 1960), p. 7.
[9] M. Kleman and J. F. Sadoc, J. Physique Lett. **40**, L569 (1979).
[10] M. Kleman, J. Physique **43**, 1389 (1982).
[11] V. A. Likhachev, A. E. Volkov, and V. E. Shudegov, *Continuum Theory of Defects* [in Russian] (LGU, Leningrad, 1986).
[12] N. Rivier and D. M. Duffy, J. Physique **43**, 293 (1982).
[13] J. P. Sethna, Phys. Rev. Lett. **51**, 2198 (1983).

[14] D. R. Nelson, Phys. Rev. B **28**, 5515 (1983).
[15] V. G. Zhdanov and V. K. Malinovskiĭ, Pis'ma Zh. Tekh. Fiz. **3**, 943 (1977) [Sov. Tech. Phys. Lett. **3**, 387 (1977)].
[16] V. G. Zhdanov, B. T. Kolomietz, V. M. Lyubin, and V. K. Malinovsky, Phys. Status Solidi A **52**, 621 (1979).
[17] V. K. Malinovskiĭ, V. N. Novikov, and A. P. Sokolov, Usp. Fiz. Nauk **163** (5), 119 (1993) [Phys. Usp. **36**, 440 (1993)].
[18] V. K. Malinovsky, V. N. Novikov, A. P. Sokolov, and V. G. Dodonov, Solid State Commun. **67**, 725 (1988).
[19] C. Yu. Clar and J. J. Freeman, Phys. Rev. B **36**, 7620 (1987).
[20] V. K. Malinovsky and V. N. Novikov, J. Phys.: Condens. Matter **4**, L139 (1992).
[21] V. K. Malinovsky and V. G. Zhdanov, J. Non-Cryst. Solids **51**, 31 (1982).
[22] O. A. Gudaev, V. K. Malinovsky, and E. E. Paul, Solid State Commun. **74**, 55 (1990).
[23] *Amorphous Semiconductors*, edited by M. H. Brodsky (Springer Verlag, Berlin–Heidelberg–N.Y., 1979).
[24] O. A. Gudaev and V. K. Malinovskĭ, Fiz. Tverd. Tela **37**, 81 (1995) [Phys. Solid State **37**, 41 (1995)].

Translated by D. H. McNeill

Energy characteristics of carbon clusters with passivated bonds

V. V. Rotkin*) and R. A. Suris

A. F. Ioffe Physicotechnical Institute, Russian Academy of Sciences, 194021 St. Petersburg, Russia
Fiz. Tverd. Tela (St. Petersburg) **41**, 809–812 (May 1999)

A modified phenomenological model is proposed for calculating the formation energy of carbon nanoclusters which makes it possible to analyze the regions of existence of clusters of various forms. A new parameter of the model, which corresponds to passivation of broken carbon bonds, affects the shape of the equilibrium optimum clusters, i.e., those having a minimum energy for a fixed number of atoms. Analytic dependences of equilibrium-configuration states determining the existence of spheroidal closed clusters, nanopipes, and fragments of a graphite plane, on the broken-bond energy parameter obtained in this model are presented.
 [S1063-7834(99)01305-2]

Theoretical studies of the synthesis of carbon nanoclusters in electric arcs or by laser ablation of graphite, in molecular and atomic beams, by igniting hydrocarbons, or by other methods are difficult since the conditions for synthesis (Cluster production techniques have been reviewed by Smolley *et al.*[1]) are utterly different and the set of synthesized clusters is usually diverse and hard to classify. At present it has been established firmly that a large number of small carbon clusters are present in the synthesis products: presumably linear chains (carbene type or with free bonds) or fragments of a monolayer of a graphite plane (graphene fragments). More compact nanoclusters have also been found: with cylindrical and spherical shapes or unclosed fragments of these with characteristic radii of a few nm. Conditions have been found[2] for synthesizing rather long (several μm) cylindrical clusters, i.e., nanopipes, with various diameters. Fragments of conical surfaces, multilayer clusters, etc., have been observed among the clusters. The theoretical description of the synthesis of carbon nanoclusters is also complicated because, up to now, no final conclusion has been reached as to how much this process is determined by the reaction kinetics, or by an energy or entropy factor. Little is known about the reaction kinetics for formation of the various clusters, while the formation energies of a large number of isomers C_N have been calculated by various methods, ranging from phenomenological to first-principles calculations. We have proposed[3] a unified approach to the energy characteristics of the formation of carbon nanoclusters with a curved surface like graphite. It allows us to compare the formation energy of fullerenes with different shapes, so that it is possible to determine the most energetically favorable clusters (i.e., the clusters having the minimum formation energy for a fixed number of atoms) in a continuum approximation. These calculations allow us to judge the probability of forming clusters of a given shape for an equilibrium synthesis process (while including the entropy factor does not significantly change the free energy), as well as whether a given isomer is in equilibrium. Note that an (energetically) nonequilibrium state of the cluster C_N is not necessarily unstable. Examining the stability of a state requires a detailed study of the kinetics of a specific transition by the cluster from one state of configuration space to another.

Our method has been formulated in earlier papers[4] and is based on expanding the total formation energy of a cluster into independent (in our approximation) terms corresponding to: (1) the ''seed'' formation energy of graphene (this constant term determines the reference level and will not be included in the following calculations); (2) the energy of curvature of the cluster surface, which is analogous to the elastic deformation energy of a plane; (3) the energy associated with pentagonal defects that are not characteristic of graphene; and, (4) the energy of broken bonds. This paper is devoted to accounting for the passivation of broken bonds, which in terms of the model corresponds to varying the broken-bond energy parameter. Here we show that this modification of the model leads to a change in the results on the energy equilibrium in the configuration space of clusters having different shapes. Specifically, it has been shown[5] that ''softening'' the bonds changes the energy diagram for the phases relationship between flat fragments of graphene and spheres (and nanopipes) in favor of the uncoiled fragments.

In the first part of the paper, we formulate a model and study the effect of the magnitude of the broken bond energy on the shape of an optimum cluster with nanopipes as an example. The energy diagram for the coexistence of nanopipes and flat graphene fragments is constructed in the second part. We also illustrate the change in the diagram when the bonds are ''softened.'' The third part is devoted to calculating the critical value of the bond ''softness,'' which is defined as the value at which the equilibrium positions of the different states in configuration space undergo a change.

1. EFFECT OF THE ''SOFTNESS'' OF BROKEN BONDS ON THE OPTIMUM CLUSTER SHAPE

We shall specify the formation energy of a cluster through its geometric dimensions and shape. The greater the curvature of the cluster surface, the higher the energy associated with bond deformation. The first parameter of the model is a phenomenological parameter that specifies the characteristic deformation energy of a single bond for unit curvature and has been chosen equal to $E_c \simeq 0.9$ eV.[6] The

second model parameter takes the nonequivalence of the bonds into partial account: it is the appearance energy for 12 pentagons in a hexagonal graphene lattice forming a closed cluster[3] and it was $E_5 \simeq 17.7$ eV. (Each closed polyhedral cluster consisting of vertices with three edges should, according to the Gauss–Bonnet theorem, have 12 pentagonal facets. Each pentagon in the cluster lattice is associated with a topological surface curvature of $4\pi/12$. It is easy to understand that a pentagonal disclination corresponds to the removal of 1/6 of a hexagonal lattice.) The broken bond energy, the last model parameter, was considered to be invariant and equal to the dissociation energy of a carbon bond in graphite, $E_b = 2.355$ eV.

It is energetically favorable to reduce the radius of a cluster, so as to reduce the number of broken bonds on the open perimeter. This process leads to an increase in the curvature and in the energy associated with it. Thus, the energy of formation can be optimized with respect to the geometric shape of the cluster. We shall refer to a cluster having minimum formation energy for a constant number N of atoms as ''optimum.'' The optimum is attained by varying the cluster dimensions while leaving the topological surface type unchanged. For example, for a cylindrical surface the total energy of an optimum nanopipe increases as $N^{1/3}$ (Ref. 6), where $N = 8\pi RH/3\sqrt{3}$ is the number of atoms in the nanopipe, and H and R are its length and radius. (Note that all the distances here and in the following are given in units of carbon bonds, which we assume to be fixed and equal to $b \simeq 1.4$ Å.) We can calculate H and R of an optimum nanopipe for arbitrary fixed N:

$$R_0 = R_*\left(\frac{N}{N_*}\right)^{1/3}, \quad H_0 = 2R_*\left(\frac{N}{N_*}\right)^{2/3}; \tag{1}$$

and thereby completely determine the shape of an optimum cluster. Here we use the constant $R_* = 3E_c/E_b$ and the $N_* = 16\pi R_*^2/3\sqrt{3} \simeq 13$ atoms determined by it. Obviously, ''softening'' of the bonds shows up formally in the transformation $E_b \to \xi E_b$, where the new model parameter ξ varies from unity to zero as the broken bonds are passivated. By bond passivation we mean both any possible real physical-chemical processes and a partial accounting for the fact that the initial and final reaction products can contain other elements besides carbon, for example, during burning of hydrocarbons to yield purely carbon clusters.

Formal substitution of ξ in Eq. (1) for R and H shows that the length of the optimum nanopipe decreases, while the radius increases as $H \sim \xi^{1/3}$ and $R \sim \xi^{-1/3}$ when ξ is reduced. For the same number of atoms the optimum cluster shape becomes flatter, corresponding to dominance of the energy of curvature and the growth of the perimeter resulting from the reduction in the curvature of the surface.

We also write down an expression for the total energy of the optimum cluster (Recall that this is the minimum energy that a nanopipe can have for a fixed number of atoms.)

$$E_0 = 6\pi\sqrt{3}E_c\left(\frac{N}{N_*}\right)^{1/3}. \tag{2}$$

This dependence for the energy is important in studying the region of equilibrium between nanopipes and flat clusters.

2. EQUILIBRIUM BETWEEN NANOPIPES AND FLAT FRAGMENTS OF GRAPHENE

In our model the specific energy of a carbon atom in graphene is exactly zero (by definition), so that an infinite flat sheet of graphite would be the most energetically favorable (equilibrium) configuration. But for a finite, flat cluster we necessarily obtain a number of broken bonds. The total energy of the broken bonds is not small and often sets the direction of cluster conformation processes toward the formation of maximally closed clusters. In any case, reducing the open perimeter of an unclosed cluster is energetically favorable. Therefore, of the flat fragments, the clusters with a circular shape have the minimum energy.[a)] The formation energy of this type of cluster, which is proportional to its perimeter, depends on the number of atoms as $\sqrt{N}$.

Let us now find the domain of existence of nanopipes with energies lower than that of a flat graphene fragment, including the possible passivation of the broken bonds. Among arbitrary nanopipes, the optimum clusters have a minimum energy, so we shall calculate first the energy difference between an optimum nanopipe and a flat, circular cluster. Obviously, this difference should change sign, since the energy of a nanopipe increases more slowly with the number of atoms and, for a small cluster size this shape should be energetically unfavorable.[5] In fact, this occurs for

$$N \leqslant N_t = 729N_*/64 \simeq 148 \text{ atoms}. \tag{3}$$

Beginning with this number of atoms, the formation of a nanopipe is more energetically favorable than that of a flat cluster. Figure 1 is a configurational-equilibrium energy diagram for nanopipes and flat clusters. When $N = N_t$, nanopipes of a fixed shape defined by Eqs. (1) can develop.

We have obtained an analytic (in the limit $R \gg R_*$) relation for the cluster dimensions which determine the boundaries of the nanopipe region,

$$N_1 \simeq N_*\left(\frac{R}{R_*}\right)^2 - O\left(\frac{R}{R_*}\right) \tag{4}$$

for the right-hand boundary, at which the clusters have the same length and diameter. A flattened shape of this sort corresponds to a negligible energy of curvature, while the energies of the broken bonds in the two types of clusters almost compensate one another. Obviously, the position of this boundary should not be sensitive to ''softening'' of the binding energy. In fact, neither N_1, nor R_1 or H_1 contain the parameter ξE_b. On the other hand, the left boundary,

$$N_2 \simeq 4N_*\left(\frac{R}{R_*}\right)^4 - 4N_*\left(\frac{R}{R_*}\right)^3 + O\left(\frac{R^2}{R_*^2}\right) \tag{5}$$

is shifted significantly: $N_2 \sim \xi^2$ for constant R. This is understandable since, in this case, a nanopipe is extremely elongated, while the energy of its broken bonds is extremely low compared to the energy of curvature, which also compensates the energy of a flat graphene fragment. The latter de-

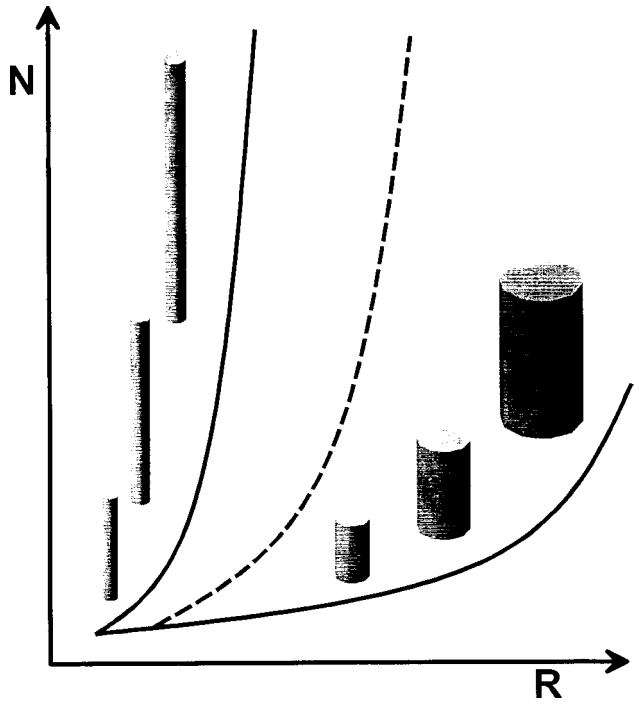

FIG. 1. The domain of existence of nanopipes including the possible passivation of broken bonds in the R, N plane (the radius and the number of atoms in relative units). The smooth curves represent the boundaries of the region of nanopipes whose formation energy is less than for a circular fragment of graphene with the same number of atoms. The dashed curve shows the change in the boundary of the region where nanopipes exist with passivation of the broken carbon bonds. The shape of the clusters differs at the boundaries of the region; this is determined by the ratio of the energies of curvature and of the broken bonds at the perimeter of the nanopipe.

creases when the broken bonds are ''softened'' and the nanopipe that was energetically favorable before, now has a higher energy than a flat cluster. The domain of existence of the nanopipes, therefore, becomes narrower when the bonds are ''softened.''

The minimum size of a nanopipe, which is energetically favorable compared to a flat fragment and is specified by Eq. (3), also increases, with

$$N_t(\xi)=N_*\left(1+\frac{1}{2\xi}\right)^6. \tag{6}$$

When ξ is reduced by a factor of two, the minimum size increases by a factor of 5.6.

3. ENERGY CHARACTERISTICS OF CLUSTERS WITH PASSIVATED BONDS

In terms of our model, it was found that a spherical cluster with minimum surface curvature and no broken bonds has (for a fixed number of atoms) the lowest energy of formation. Thus, a cluster with a different shape is out of equilibrium compared to a spheroidal shape for any number of atoms. (This is not true for spherical clusters with a small number of atoms, since their formation energy is underestimated by this model because of the very large curvature and because pentagonal defects inevitably adjoin one another for cluster sizes $N<60$. The energy of a cluster of this type cannot be described in a continuum approximation. Although $N_{\rm lim}$ gives a formal limit to the domain of applicability of Eq. (7), it is clear physically that, as soon as the number of atoms in the cluster becomes equal to or less than $5\times$ the number of defects, the assumption that their interactions are small ceases to be correct, as does the entire interpolation formula (7), which is based on the assumption that most of the atoms belong to a graphite-type hexagonal lattice.) For large clusters the formation energy can be written in the form[5]

$$E_{\rm sph}=N_sE_c\left(\frac{1}{N_{\rm lim}}-\frac{1}{N}\right), \tag{7}$$

where we have used the constants $N_s=2\times60\times16\pi/3\sqrt{3}\simeq1161$ and $N_{\rm lim}=N_s/(E_5/E_c+16\pi/\sqrt{3})\simeq24$, which is defined in terms of $E_5\simeq17.7$ eV (the second parameter of our model), the energy of the 12 noninteracting pentagonal defects in a closed spheroidal cluster.

In Ref. 5 we showed that the equilibrium among spherical and flat clusters, as well as among spheres and nanopipes, shifts when the bonds are softened. Let us consider the difference in the formation energies of several clusters and spheres. This quantity is positive for any number of cluster atoms, since the energy of a sphere is minimal. Let us assume that the energy of a given cluster is a universal power law function $E=W(N/N_*)^dE_c$ of the number of atoms in the cluster relative to N_* (as was found for an optimum nanopipe or for a flat circular fragment of graphene with exponents $d=1/3$ and $1/2$, respectively). Then, for some critical softening ξ_c the difference in the formation energies first goes to zero for a certain number N_c of atoms. This cluster is in equilibrium with a sphere. Its size and critical softening are given by

$$N_c=N_{\rm lim}\left(1+\frac{1}{d}\right),$$

$$\xi_c=\sqrt{\frac{1}{\sqrt[d]{Wd}}\left(\frac{d}{1+d}\right)^{(1+d)/d}\frac{N_*}{N_{\rm lim}}\left(\frac{N_*}{N_{\rm lim}}\right)^{1/d}}, \tag{8}$$

where W is a dimensionless coefficient for a universal function of energy of these clusters, which equals $4\pi\sqrt{3}$ for a flat circular cluster and $6\pi\sqrt{3}$ for an optimum nanopipe. The values of the critical softening for these cases are 0.63 and 0.44.

In this paper, we have shown, therefore, that a phenomenological continuum model proposed for calculating the formation energies of carbon nanoclusters with curved surfaces can be modified to account for the passivation of broken carbon bonds at the cluster boundary (or to account for the participation of pure carbon, as well as of clusters, in the reactions of carbon compounds). The broken-bond energy is used as a new parameter in the model. With an optimum nanopipe as an example, it is shown that, in the general case, this parameter affects the shape of an optimum cluster and, therefore, can change the region where clusters of different shapes coexist. The above analysis indicates that the domain where energetically favorable (compared to a flat graphene fragment) cylindrical clusters exist becomes narrower with bond ''softening.'' Analytical dependences of the numbers of atoms for equilibrium configurations of states on the

broken-bond energy parameter have been obtained in the region where spheroidal closed clusters, nanopipes, and fragments of a graphene plane coexist. Since an infinite graphite crystal (without broken bonds) is the most energetically favorable configuration for carbon atoms, while the equilibrium energy characteristics of relatively small clusters are determined mainly by the size of the open perimeter of a cluster, even weak bond passivation causes a significant shift in the equilibrium toward flat fragments. One might expect energetically favorable (equilibrium) unclosed (nonspherical) clusters containing about a hundred atoms to appear when the broken bond energy is ''softened'' by a minimum of a factor of two.

This work was partially supported by Grants No. 98602 of the Program on Fullerenes and Atomic Clusters, No. 1-001 of the Russian Program on the Physics of Solid Nanostructures, and No. 96-15-96348 of the Russian Fund for Fundamental Research

*)E-mail: Rotkin@theory.ioffe.rssi.ru

a)Although an ideal circular fragment cannot be separated from the hexagonal lattice of graphene, we can achieve a minimum in the perimetral energy of the broken bonds for a fixed area by choosing a path that is close to a circle along the directrices of the hexagonal lattice. The density of broken bonds per unit length of the perimeter will be minimal when the directrices are chosen to have the same direction as in the case of a ''zigzag'' nanopipe. (See V. V. Rotkin, Candidates Dissertation in Phys.-Math. Sciences, St. Petersburg (1997).)

[1] R. E. Smolley, R. F. Kerl, and G. Kroto, Usp. Fiz. Nauk **168**, 323 (1998).
[2] S. Iijima, Nature (London) **354**, 56 (1991); D. S. Bethune *et al.*, Nature (London) **363**, 605 (1993); A. Thess *et al.*, Science **273**, 483 (1996).
[3] V. V. Rotkin and R. A. Suris, in *Proceedings of the 2nd International Workshop on Fullerenes and Atomic Clusters, St. Petersburg, Russia (1995)*, p. 25.
[4] V. V. Rotkin and R. A. Suris, Mol. Mater. **8**, 111 (1996); V. V. Rotkin and R. A. Suris, MRS Symposium Proc. **529**, 169 (1998); S. V. Rotkin, in *Recent Advances in Chemistry and Physics of Fullerenes and Related Materials*, Vol. VI, edited by K. M. Kadish and R. S. Ruoff, ECS, Pennington, NJ (1998), PV 98–8, p. 68.
[5] S. V. Rotkin and R. A. Suris, in *International Symposium ''Nanostructures: Physics and Technology,'' St. Petersburg, Russia (1997)*, p. 335.
[6] V. V. Rotkin and R. A. Suris, in *Recent Advances in the Chemistry and Physics of Fullerenes and Related Materials*, Vol. II, edited by R. S. Ruoff and K. M. Kadish, ECS, Pennington, NJ (1995), p. 1263.

Translated by D. H. McNeill

Physics of the *f*-electron intermetallics

Wojciech Suski

W. Trzebiatowski Institute of Low Temperature and Structure Research, Polish Academy of Sciences, P.O. Box 1410, PL–50–950 Wroclaw 2, Poland;
International Laboratory of High Magnetic Fields and Low Temperatures, PL–53–421 Wroclaw, Poland
Fiz. Tverd. Tela (St. Petersburg) **41**, 813–817 (May 1999)

Properties of lanthanide and actinide intermetallics are extremely interesting both for applications and fundamental research. The impetus to start fundamental research on *f*-electron materials doubtlessly was the determination of the ferromagnetic properties of UH_3 and UD_3 by the research group of the Institute of Low Temperature and Structure Research in Wroclaw and detection of the mixed valence state in samarium monochalcogenides at A. F. Ioffe Physicotechnical Institute in Leningrad (at that time). Since then, the phenomena of the mixed valence, heavy-fermion, state as well as complicated magnetic structures have been under intensive investigation in numerous laboratories all over the world. As examples, the exotic magnetic structures of CeSb and UNi_4B are described. Then the problems of the heavy-fermion state existing in UBe_{13} and $UCu_{4+x}Al_{8-x}$ are presented. Next, the non-Fermi-liquid behavior appearing due to magnetic instability is discussed. Finally, some perspective for further research is proposed.
 [S1063-7834(99)01405-7]

Solid-state physics is strongly attached to materials. The examples of materials which have recently been broadly investigated in many solid-state laboratories are those containing lanthanide and, to a lesser extent, actinide elements. Lanthanides and actinides are representatives of two families that involve the *f*-electron shell (however, heavier actinides are only artifically obtained) and are radioactive. The physical properties of these two groups of elements and their compounds deserve much interest because of their intriguing fundamental properties resulting from the electronic structure and broad application. This last reason concerns, obviously, only lanthanides.

The properties of actinides became known after the results of the Manhattan Project were released, but the broad interest started as soon as pecularities of the actinide electronic structure became apparent.

Investigation of the physical properties of lanthanide intermetallics started about four decades ago when separated lanthanide elements became available and reasonably good samples were succesfully prepared (at first polycrystals and latter single crystals).

Magnetic studies soon found that a plentitude of magnetic behavior exists in these intermetallics, which in many instances is observed nowhere else. Therefore it is no wonder that one of the most important applications of the $4f$-electron materials is their use as hard magnetic materials. Another promising direction is the vast field of high-temperature superconductivity.

1. ELECTRONIC STRUCTURE

As mentioned above, both lanthanides and actinides are families of the elements which involve the *f*-electron shell.

However, there are striking differences between the individual representatives of these families depending on the degree of localization of the *f*-electrons resulting from their location in relation to the Fermi level, to the band states, and to the spatial extension of the *f*-shell. In the majority of lanthanides and heavier actinides the *f*-electrons are localized, located below the Fermi level and protected from the influence of surrounding and external factors. They exhibit localized magnetic moments whose value is close to that of the free ion. These elements exhibit also magnetic order. However, light actinides and some lanthanides which have electronic configurations close to the particularly stable ones, f^0, f^7, and f^{14}, exhibit different behavior. The *f* level is located fairly close in energy to the valence and bonding electrons, and to the Fermi level. As a result, the *f* electrons contribute to the conduction process along with the *d* and *s* electrons and hybridize with them strongly. The spatially extended *f* shell is extremely sensitive to any influence of external factors such as pressure and magnetic and crystal fields. Therefore, different interactions, existing in the *f*-electron ion in a delicate balance, are the reason for the unusual properties. Examples of some of them will be described below, e.g., the strong hybridization, huge magnetocrystalline anisotropy, complex magnetic ordering, spin-fluctuation, heavy-fermion, Kondo lattice, mixed valence, etc., when *f*-electron elements form compounds.

2. ANOMALOUS LANTHANIDES AND ACTINIDES

The celebration of the Ioffe Institute Anniversary is a good occasion to remind us that the initiation of the fundamental research on *f*-electron materials came from the Jubilee Institute as well as from the team in which the present speaker has spent all his scientific life. It is odd that the first experiments concerned the actinides. In the late 1940s, W. Trzebiatowski and his coworkers, examining the magnetic properties of uranium hydride and deuteride to determine the uranium electronic structure in these compounds, discovered ferromagnetism in both compounds below

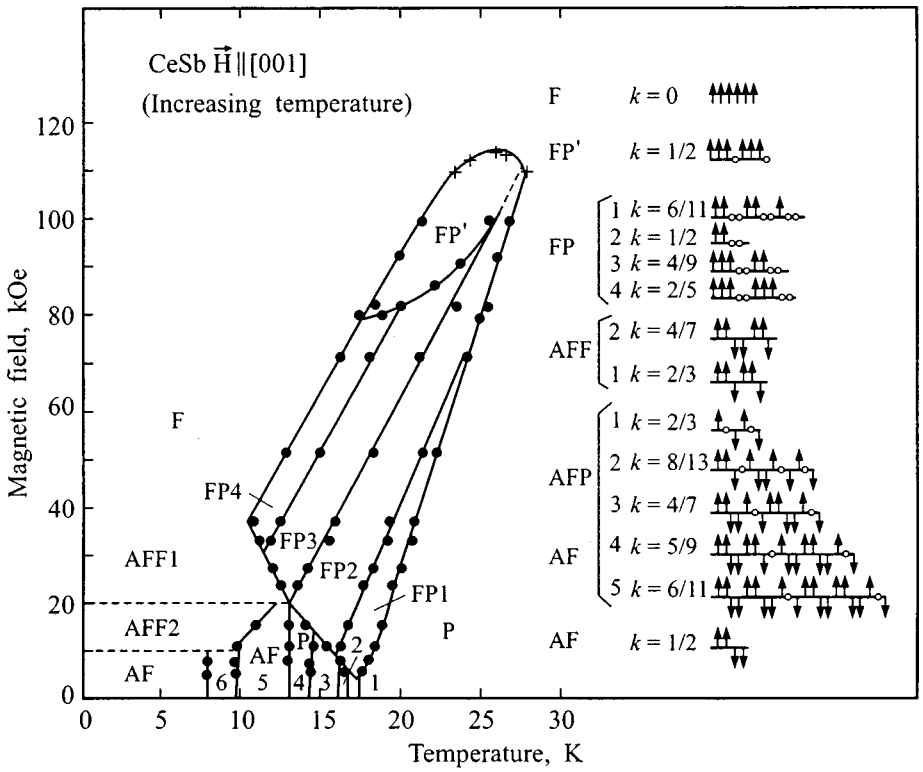

FIG. 1. Magnetic (H,T) phase diagram for CeSb.[8]

$\sim$180 K (for detailed references see Ref. 1). The authors hesitated for a long time to publish unexpected results up to 1952 when this fact was confirmed by other laboratories (see Ref. 1). The electronic structure of the uranium in semi- or intermetallic compounds is still a puzzle but magnetic ordering has been discovered in numerous compounds of uranium and other actinides.[2–4] Now all types of magnetic ordering and coherent states have been found in these compounds. Available space does not permit us to discuss this problem in detail but some examples will be presented below.

The other phenomenon — mixed valence state — was discovered in the Ioffe Institute in the 1960s when the change in color of magnetic semiconductors — monochalcogenides of samarium — was observed after applying a small stress. It was also found that the electrical resistivity of these compounds, having semiconductor character, suddenly decreases under pressure, indicating the transformation to a metallic state. Then such behavior was found in other compounds of Ce, Sm, Eu, Tm and Yb, developing under the influence of other factors, not only pressure. The early period of this research is summarized in Ref. 5; terminology, the models explaining this phenomenon, as well as more recent experimental results are collected in Ref. 6; and the most recent experimental results are presented in Ref. 7.

Both these groups of phenomena are an indication that the unusual electronic structure of lanthanides and actinides is the reason for the uncommon properties of these materials.

Below, we are going to discuss some examples of this behavior, starting with unusual magnetic structures. Figure 1 shows the (H,T) phase diagram observed for CeSb (see Ref. 8, for additional sources see Ref. 9). This phase diagram contains the largest number of collinear magnetic phases ever known. It can be noted that there are 15 distinct phases, 7 of which are successively stabilized in zero field when the temperature is decreased, corresponding to long-period commensurate structures, as shown in Fig. 1.[8] The magnetic field creates the ferromagnetic layers and, at low temperatures, finally forms a simple ferromagnetic (F) structure. At higher temperatures, the field destroys antiferromagnetic (AF) layers and rearranges a sequence of paramagnetic layers from single to double ones. Only the ferro-paramagnetic (FP) phase persisting in the highest field contains again simple paramagnetic layers. The most unusual feature of CeSb, however, comes from the coexistence in the so-called antiferro-paramagnetic (AFP) and FP phases in which several regions of magnetic and non- (or para-)magnetic Ce atoms are observed. Inelastic scattering of polarized neutrons giving magnetic spectra have determined the crystal-electric-field (CEF) ground state of magnetic Ce atoms as a Γ_8 quartet with large magnetic moment $(2.1\,\mu_B)$, whereas that of paramagnetic Ce atoms as a Γ_7 doublet with smaller moment $(0.7\,\mu_B)$.[10] This unusual phase diagram is not yet fully understood but its origin seems to be found in the large anisotropic hybridization between p holes of Sb and the Γ_8 states of Ce^{3+}. Other concepts, such as sole CEF effects, devil's staircase and ANNNI (anisotropic next-nearest-neighbor Ising) models have been considered but no appreciable results have been obtained (for references see Ref. 9). Different approachs for explaining this complex phase diagram have been applied by introducing an incommensurate mean-field model.[11] In this model, paramagnetism on one part of Ce atoms arises because there is no exchange field at their sites. This phase diagram undergoes also a dramatic change under pressure (for references see Ref. 9). The existence of the paramagnetic (P) phases is actually suppressed above 1 GPa. It is clear that more theoretical investigations are still

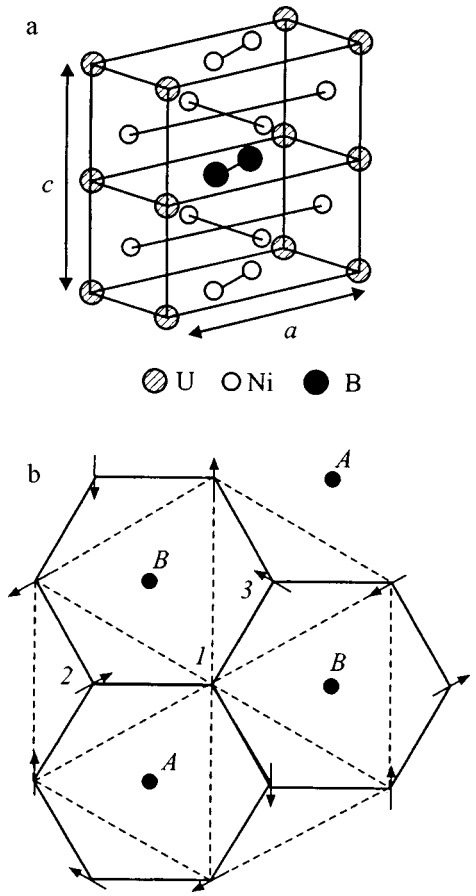

FIG. 2. Crystal and magnetic structure of UNi_4B. a — Crystal structure of the $CeCo_4B$-type subcell UNi_4B; b — zero-field magnetic structure of UNi_4B (projection on the basal plane). The arrows show the magnetic moments, while the solid circles represent the Kondo screened U sites (according to Ref. 16). Lattice distortions differentiate *A* and *B* nonmagnetic sites, reducing (increasing) the distance between *1* and *2* (*1* and *3*) magnetic U atoms.

needed to account for this exceptional behavior.

One of the most unusual magnetic structures has been detected in UNi_4B.[12–16] In this crystal structure (hexagonal, $CeCo_4B$-type, $P6/nmm$ space group), presented in Fig. 2a, only U atoms have a magnetic moment and they have a hexagonal arrangement in the basal plane. The separation of the nearest-neighbor (nn) U atoms in the basal plane is larger than that in the perpendicular direction ($a/0.5c=1.4$), creating a triangular lattice of F chains. This arrangement is certainly related to the geometrical frustration of this triangular lattice by AF interaction. Below 20 K, the neutron diffraction (ND) experiments[12,13] show that only 2/3 of the U moments order in a complex structure AF in which the magnetic unit cell contains nine U atoms as it is shown in Fig. 2b.[14] Six ordered magnetic U moments are arranged perpendicularly to the *c* axis forming a 120° angle between the next-nearest neighbors (nnn). Application of magnetic field along the *c* axis or parallel to the basal plane reveals strong anisotropy in the system. This magnetic structure has been described[12] as two independent spin systems, of which one orders while the other remains paramagnetic down to low temperatures. It was proposed that 1/3 of the U atoms form chains within the ordered spin matrix that stabilize their one-dimensional character because the local field vanishes at those sites. The expected ordering of these ''paramagnetic'' sites when a small field is applied is not, however, experimentally confirmed, suggesting another explanation for the 1/3 U atom behavior. Lacroix *et al.*[16] suggest that these 1/3 U atoms are nonmagnetic due to the Kondo effect. They present a model in which the coexistence of magnetic and nonmagnetic U atoms is the consequence of competition between frustration of the crystallographic structure and the instability of $5f$ moments.

The heavy-fermion (HF) state is one of the most exciting topics contemporary solid-state physics. At low temperatures, some of the *f*-electron systems exhibit properties that seem to have switched upon cooling from those of a system of local moments to those of a narrow energy band of mobile electrons. These materials sometimes order magnetically, but the ordered magnetic moments are a fraction of the large high-temperature *f*-electron moment. Interest in this problem heightened when it was discovered that one of these compounds, $CeCu_2Si_2$, is a superconductor.[6,17,18] The large specific heat discontinuity at the superconducting transition shows that the itinerant electrons act as though they have a mass some 100 times larger than that of an electron in a typical metal. The superconducting state often displays unusual properties and complicated phase diagrams involving several superconducting phases. A large number of HF systems are now known. Most of these materials are intermetallic compounds containing Ce or U, whose atoms have incomplete *f* shells. A few contain the lanthanide Yb or the actinide Np or Pu as the essential ingredient. It is now well established that the *f* electrons on the lanthanide or actinide atoms are responsible for all of the unusual properties, but there is no agreement among the investigators regarding the mechanism or mechanisms by which *f*-shell electrons can produce the observed effects.

The cubic actinide compound UBe_{13} has been identified as the second HF conductor by Ott *et al.*[19] but its magnetic properties have been determined by a team from the author's Institute.[20] Preliminary observation of superconductivity in a UBe_{13} sample[21] has been interpreted as resulting from precipitations of spurious phases in form of fine filaments. The results concerning UBe_{13} and its solid solutions are collected in Refs. 4, 6, and 22. UBe_{13} does not exhibit three-dimensional magnetic ordering. Its electrical resistivity, upon cooling, first increases and passes through a maximum at about 30 K. In pure UBe_{13} this maximum is hardly resolvable, as $\rho(T)$ increases again sharply to a second maximum at about 2.5 K.[22] At even lower temperatures, $\rho(T)$ decreases steeply. In the low-temperature range of this decrease, an extraordinarily strong negative magnetoresistivity is observed. At these temperatures, HF behavior occurs with $\gamma=0.72-0.86\,\mathrm{J/K^2mol}$ (see Ref. 22). UBe_{13} becomes superconducting at about 0.9 K. The properties of UBe_{13} can be influenced dramatically by deliberate doping with an extremely strong influence of substitution in the Be sites.

The HF state has been also detected in Wroclaw in the $UCu_{4+x}Al_{8-x}$ system which exists for $0\leqslant x\leqslant 2$ (for review see Ref. 23). The simple AF ordering was determined in the U sublattice by neutron diffraction (ND) for x not far from $x=0$ ($T_N(x=0)\approx 40$ K). The electronic specific-heat coeffi-

cient amounts to about $0.12\,\mathrm{J/K^2mol}$, however, for $x=1.5$, the magnetism disappears and γ increases to $0.8\,\mathrm{J/K^2mol}$, suggesting HF-like behavior. The reason for such a high γ value is a mystery since the material does not transform to the superconducting state at low temperature.[23] Structural disorder has been excluded as the reason for both high γ and the absence of magnetic ordering and superconducting state for higher x by a recent ND experiment.[23] It might be that the increase of Cu concentration causes a volume compression, which is not large enough to decrease the U–U separation below the Hill limit necessary for the superconducting state by uranium compounds, but which might result in an enhanced $5f$-ligand hybridization. Then in the spirit of the Doniach[24] phase diagram, the $5f$-conduction-electron-exchange coupling is shifted from below to above the critical value at which the AF order vanishes. Further on, the L-absorption-edge-shift experiment[25] shows that the uranium valence depends strongly on stoichiometry (x) and for all x, uranium exhibits nonintegral occupance of the $5f$ shell. This phenomenon results probably from simultaneous existence of the uranium $5f$ electrons in two states, itinerant and localized, with the decrease of the occupance of the $5f$ shell corresponding to the increase of x, the $5f$ shell thus getting closer to the Fermi level. At the same time, the density of states at the Fermi level increases substantially, which is related to the observed increase of γ.

Recently, the transition from heavy Landau Fermi liquid (HLFL) to non-Fermi liquid (NFL) behavior has been observed in numerous U- and Ce-containing systems. HLFL and NFL states can be distinguished by different temperature dependences of magnetic susceptibility, χ, electrical resistivity, ρ, and specific heat, C or C/T. In HLFL, the susceptivility follows the Curie–Weiss law at high temperature and at low temperature exhibits almost temperature independent paramagnetism (Pauli type), $\rho\sim AT^2$ and $C\sim\gamma T$, respectively. In NFL, $\chi\sim\ln T$ or $\chi\sim(1-T^{1/2})$, $\rho\sim T$ and $C\sim -T\ln T$, respectively. Both regimes are separated by the quantum critical point (QCP) but they can also coexist. This state can be induced by a change in composition and also by pressure. The HLFL state can coexist with anti- and ferromagnetic ordering, spin fluctuation (SF) and spin-glass state, whereas the NFL state appears in a very narrow compositon range (pressure) in which magnetic instability disappears. Nishioka *et al.*[26] have presented the phase diagram of $UCu_{4+x}Al_{8-x}$ system for x dependence of C/T at 0.5 K and Néel temperature, derived from the specific heat and magnetic measurements, shown in Fig. 3. It is to be seen that three states can exist in this sytem: AF, HLFL, and NFL, depending on x. Moreover, Krimmel *et al.*[27] claim that, for $x=0.75$, an indication of SF is seen. It is clear that the NFL state arises due to very tiny composition change and exists over a considerable concentration range. A two-channel Kondo model was proposed to explain the NFL behavior in uranium compounds. Unfortunatelly, this model turns out to be inadequate to describe NFL behavior in Ce alloys.[28] It was also suggested that the NFL state for many materials, in which this state is artificially induced by alloying or pressure, has a lattice distortion as the reason for formation. The persistence of NFL behavior over an extended range of concentration and coexistence of Fermi-liquid and non-Fermi-liquid characteristics indicates a complex nature of the low-temperature state.

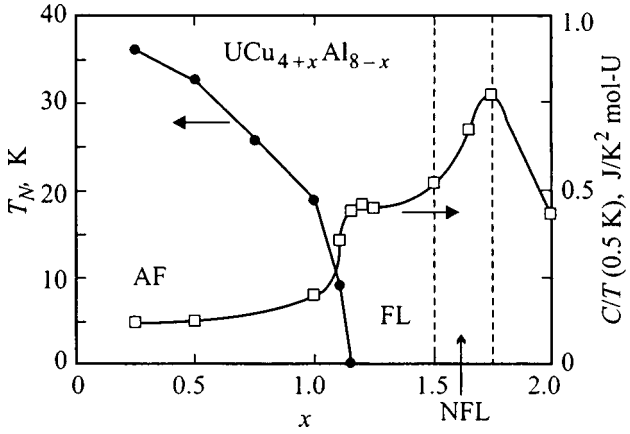

FIG. 3. Phase diagram of $UCu_{4+x}Al_{8-x}$ (Ref. 26); C/T at 0.5 K (right scale — squares).

In summary, most probably, the coming XXI century will see further progress in the solid-state physics of *f*-electron materials. But serious development will be possible only if three particular problems find sufficient support.

1. Development of technology, especially for single-crystal samples, including transuranium elements. The basis for this is an improvement of the Czocharalski multi-arc method. Also MBE and laser ablation methods should produce new magnetic and superconducting materials.

2. Further progress in experimental methods, particularly those which extend nuclear-physics methods to solid-state physics. Some of them allow determining local properties. The present author believes that, for example, the magnetic resonance and x-ray scattering will supply new information concerning electronic structure including the ratio of orbital and spin parts of magnetic moments for light actinides and anormal lanthanides (see Ref. 29).

3. Development of multibody-interaction theory and further progress in computational techniques which enable complicated band-structure calculation.

However, all presently-observed phenomena can be extended if society will understand that the progress in solid-state physics means progress in technology and in industry so that enough money should be available. Solid state physics is not an extremely expensive research, after all.

[1] R. Troć and W. Suski, J. Alloys Compd. **219**, 1 (1995).
[2] J.-M. Fournier and R. Troć, in *Handbook on the Physics and Chemistry of the Actinides*, Vol. II, edited by J. A. Freeman and G. H. Lander, (Elsevier, N.-Y., 1985), p. 29.
[3] V. Sechovsky and L. Havela, in *Handbook of Magnetic Materials*, Vol. 4, edited by E. P. Wohlfarth and K. H. J. Buschow (Elsevier, Amsterdam, 1988), p. 310.
[4] W. Suski and R. Troć, in *Landolt–Börnstein Numerical Data and Functional Relationships in Science and Technology, New Series*, edited by W. Martienssen, Group III: Solid State Physics, vol. 19, subvol. f2: Actinide Elements and Their Compounds with Other Elements. Part 2 edited by H. P. J. Wijn (Springer, Berlin, 1993), p. 1.
[5] I. A. Smirnov and V. S. Oskotskiĭ, Usp. Fiz. Nauk **124**, 241 (1978) [Sov. Phys. Usp. **21**, 117 (1978)].

[6] P. Wachter, in *Handbook on the Physics and Chemistry of Rare Earths*, Vol. 19, edited by K. A. Gschneidner, Jr., L. Eyring, G. H. Lander, and G. R. Choppin, (North–Holland, Amsterdam 1993), p. 1.
[7] T. Palewski and W. Suski, in *Landolt–Börnstein Numerical Data and Functional Relationships in Science and Technology, New Series*, edited by
W. Martienssen. Group III: Condensed Matter, vol. 27: Magnetic Properties of Non-Metallic Inorganic Compounds Based on Transition Elements, subvol. C1: *Binary Lanthanide Oxides*, edited by H.P.J. Wijn, Springer, Berlin (1997), p. 1; *ibid*., *Binary Lanthanide Chalcogenides*, edited by H. P. J. Wijn, (Springer, Berlin 1998), in press.
[8] J. Rossat-Mignod, P. Burlet, L. P. Regnault, C. Vettier, J. Magn. Magn. Mater. **90/91**, 5 (1990).
[9] T. Palewski and W. Suski, in *Landolt–Börnstein Numerical Data and Functional Relationships in Science and Technology, New Series*, edited by W. Martienssen, Group III: Condensed Matter, vol. 27: Magnetic Properties of Non-Metallic Inorganic Compounds Based on Transition Elements, subvol. B1: Binary Lanthanide Pnictides, edited by H. P. J. Wijn (Springer, Berlin, 1998), p. 1.
[10] L. P. Regnault, J. L. Jacoud, C. Vettier, T. Chattopadhyay, J. Rossat-Mignod, T. Suzuki, T. Kasuya, and O. Vogt, Physica B **156/157**, 798 (1989).
[11] M. Date, J. Phys. Soc. Jpn. **57**, 3682 (1988).
[12] S. A. M. Mentink, A. Drost, G. J. Nieuwenhuys, E. Frikkee, A. A. Menovsky, and J. A. Mydosh, Phys. Rev. Lett. **73**, 1031 (1994).
[13] S. A. M. Mentink, G. J. Nieuwenhuys, H. Nakotte, A. A. Menovsky, A. Drost, E. Frikkee, and J. A. Mydosh, Phys. Rev. B **51**, 11 567 (1995).
[14] S. A. M. Mentink, G. J. Nieuwenhuys, A. A. Menovsky, J. A. Mydosh, A. Drost, and E. Frikkee, Physica B **206/207**, 473 (1995).
[15] S. A. M. Mentink, H. Nakotte, A. de Visser, A. A. Menovsky, G. J. Nieuwenhuys, and J. A. Nydosh, Physica B **186/188**, 270 (1993).
[16] C. Lacroix, B. Canals, and M. D. Núñez-Regueiro, Phys. Rev. Lett. **77**, 5126 (1996).
[17] G. R. Stewart, Rev. Mod. Phys. **56**, 755 (1984).
[18] N. Grewe and F. Steglich, in *Handbook on the Physics and Chemistry of Rare Earths*, Vol. 14, edited by K. A. Gschneidner, Jr. and L. Eyring (Elsevier, Amsterdam, 1991), p. 343.
[19] H. R. Ott, H. Rudiger, Z. Fisk, and J. L. Smith, Phys. Rev. Lett. **50**, 1595 (1983).
[20] R. Troć, W. Trzebiatowski, and K. Piprek, Bull. Acad. Polon. Sci., Sér. Sci. Chim. **19**, 427 (1971).
[21] E. Bucher, J. P. Maita, G. W. Hull, R. C. Fulton, and A. S. Cooper, Phys. Rev. B **11**, 440 (1975).
[22] U. Rauchschwalbe, Physica B **147**, 21 (1987).
[23] W. Suski, Lith. Phys. J. **37**, 21 (1997).
[24] S. Doniach, Physica B **91**, 231 (1977).
[25] A. V. Tiunis, V. A. Shaburov, Yu. P. Smirnov, A. E. Sovestnov, W. Suski, and L. Folcik, Fiz. Tverd. Tela **38**, 1653 (1996) [Phys. Solid State **38**, 913 (1996)].
[26] T. Nishioka, Y. Kurakahashi, R. Fukuda, and M. Kotani, Czech. J. Phys. **46**, 2065 (1996).
[27] A. Krimmel, A. Severing, S. Spitzfaden, A. Grauel, B. Buschinger, C. Geibel, and A. Loidl, Z. Phys. B **102**, 9 (1997).
[28] K. Umeo, H. Kadomatsu, T. Takabatake, J. Phys.: Condens. Matter **8**, 9743 (1996).
[29] G. H. Lander, W. G. Stirling, S. Longridge, and D. Gibbs, J. Magn. Magn. Mater. **140–144**, 1349 (1995).

Published in English in the original Russian journal. Reproduced here with stylistic changes by the Translation Editor.

From Röntgen to Ioffe, from Giessen to Saint Petersburg — relations between Russian and German physics

A. Scharmann*)

Physics Institute, Justus–Liebig–University Giessen, D 35392 Giessen, Germany
Fiz. Tverd. Tela (St. Petersburg) **41**, 818–821 (May 1999)

Two former professors of physics at Giessen university contributed significantly to the development of the Ioffe Institute: Wilhelm Conrad Röntgen as a teacher of Abram Ioffe, and Wilhelm Hanle, whose effect found various applications, e.g., in the spectroscopy of hot electrons in low-dimensional structures. A few examples will illustrate how topics of their scientific work found a continuation in the research activities at Giessen, but also in the collaboration between Giessen and Saint Petersburg. They range from sodium chloride, the old Röntgen/Ioffe material where we could prove the existence of an unusual isotope effect in nickel-doped crystals, over level-crossing experiments in gases, to GaAs/AlAs superlattices, where level-anticrossing spectroscopy of excitons reveals detailed information about recombination processes and interface quality. A short summary of the efforts to keep the traditionally close and good relations between Russian and German physics vital completes the report. [S1063-7834(99)01505-1]

A talk given by a physicist from Giessen, Germany, at a conference with the title ''Physics at the turn of the 21 century'' naturally starts with the beginning of the 20 century and Wilhelm Conrad Röntgen, winner of the first Nobel prize in 1901. He became well known in the scientific community already before detecting the x-rays by an experiment which he did during his time in Giessen where he held the physics chair from 1879 to 1888. Rowland proved in 1876 that a moved electrostatic charge, called a convection current, had the same magnetic effect as a normal conduction current. In 1885 Röntgen repeated these experiments first in a much improved form and then extended them to the first experimental proof of Maxwell's dielectric displacement current.[1] For this purpose he used an apparatus in which a disk made from a dielectric material was rotating between two ring electrodes. The upper one was grounded, the lower one consisted of two halves with opposite electric potentials. This caused a change of sign of the polarization inside the dielectric two times per turn, and Röntgen succeeded in an unambiguous proof of the magnetic field connected to this displacement current. In this field we find our first example of relations between Russian and German physics, since the Russian physicist A. Eichenwald later continued these experiments at the engineering school in Moscow and was the first to demonstrate the quantitative agreement of this magnetic field with that of a normal conduction current.[2]

More important for the anniversary we celebrate this week was, of course, the long-lasting connection between Röntgen and Ioffe. At the end of a century in which the existence of quarks and Z bosons has been demonstrated, it is very informative to read about the years from 1902 to 1905 which the founder of our Physical-Technical Institute spent as Röntgen's student and assistant at Munich University. In his book *Meeting with Physicists*[3] he gives a very detailed description of Röntgen as an excellent experimentator, but of very conservative physicist, who did not allow use of the word ''electron'' in his institute. Without this restriction, perhaps, Röntgen and Ioffe instead of Pohl, Gudden and Gyulai would have been the discoverers of the F center since during their extensive experiments on the effect of x-rays and light on the electrical conduction in crystals[4] they certainly encountered such defects.

One year after Röntgen's death in 1923, another physicist who became important for Giessen University, namely Wilhelm Hanle, holder of the physics chair at Giessen from 1941 to 1969, reported[5] an effect which later was named after him. This Hanle effect, depolarization of (resonance) fluorescence by an external magnetic field due to destruction of the coherence existing at zero-field level-crossing, is still one of the most accurate methods for measuring atomic lifetimes. Its main advantage is the low densities at which the experiments can be done in order to avoid disturbing effects like collision broadening, etc.

For that reason it has been widely used in the Ioffe Institute[6] as well as in Giessen. Two examples shall be given here: The group of Boris Zakharchenya studied the photoluminescence of ''hot'' electrons created in a GaAs/AlGaAs multiple-quantum-well structure by excitation with a krypton laser.[7] In the emission, a pronounced peak shows up at the high-energy edge of the spectrum arising from the recombination of electrons from the point of photocreation, that is, prior to any energy relaxation. The degree of polarization in this peak decreases with increasing magnetic field in the form of a typical Hanle curve $P(B)/P(0)=(1+4\omega_c^2\tau_0^2)^{-1}$ and allows determining the ''lifetime'' τ_0 of the hot electrons which, in that case, corresponds to the emission time of an LO phonon. It is obvious that such results can be obtained only in experiments which avoid complicating factors like, for instance, phonon heating leading to a large spread in the times observed.

The second example is a result from my institute.[8] In this case, the level-crossing technique is used in a rather different way. Light emitted from the helium 4^1D level excited by atomic collisions with He^+ or Ne^+ projectiles, having a polarization parallel to the ion beam, has been measured as having a function of external electric and magnetic fields. For zero electric field, only the Hanle effect influences the intensity $I(B)$ of this (polarized) light which, therefore, has a Lorentzian line shape with a half-width depending on the lifetime of the excited state. At non-zero but constant electric field, the quadratic Stark effect causes several additional level crossings, but only those with $\Delta m = \pm 2$ can be observed with the experimental geometry used. A splitting of the Hanle curve into three Lorentzians results, therefore, whose intensity directly reflects the sublevel populations.

From these examples you may see the common interests that existed in our institutes for a long time, and not only in this field. But all of you are aware of the problems hampering the relations between Russian and (West) German physics. Already Röntgen and Ioffe shared a fate which many of us experienced for a long time, too, namely to live in countries being for some time very unfriendly to each other. This becomes obvious from Röntgen's statement ''Of course I could not publish during the war against Russia a scientific article together with a Russian physicist'' (in Ref. 3), explaining the long delay (from 1913 to 1921) between the two parts of their joint paper[4] about ''Electrical conductivity in some crystals and the influence of irradiation on it.'' I still remember my first visit in this beautiful city on the occasion of the International Conference on Luminescence in 1972 and the strong barriers between East and West which existed at that time. Fortunately the situation became better and better beginning in the 1980s. Especially in my field, interaction of radiation with matter, the scientific community in Russia and Germany is very indebted to Albrecht Winnacker, who participates in this conference, and Kurt Schwarz, at that time in Riga, for organizing a series of Soviet- (now Russian-) German seminars on ''Point defects in insulators and deep-level centers in semiconductors,'' and to the Russian Academy of Sciences and Deutsche Forschungsgemeinschaft for funding.

From these seminars, starting with the first meeting at Heidelberg in 1983, emanated a vivid scientific exchange between Giessen and Leningrad/Saint Petersburg. During one of these research stays we returned to ''Steinsalz'' (NaC1), the original material of Röntgen and Ioffe.[4] Now, however, in a special form, namely, doped with divalent nickel. This incorporation reqiures a charge compensation by sodium vacancies. Andrey Badalyan detected by EPR two different center configurations, one with the vacancy along a $\langle 100 \rangle$, the other along a $\langle 110 \rangle$ direction.[9] We concentrated one the first species. We have three of them, besides the one shown with a nickel-vacancy axis along [001], two others along [100] and [010] respectively. What do we expect from this $3d^8$ system? Its level scheme in a cubic environment with tetragonal distortion can be found in many textbooks. For our EPR experiment only the orbital singlet ground state with triplet spin configuration (the two d electrons couple to $S=1$) is relevant. The axial crystal field causes a fine-structure splitting between the three m_S states competing with the Zeeman effect which makes the situation a little bit more complicated when the external magnetic field is not directed along the center axis. Exact diagonalization of the appropriate spin Hamiltonian, however, with help of the program ''V-epr''[10] it is possible to understand and fit completely the angular dependence observed in [001] rotation. What was interesting and puzzling in these results is the structure observed at resonance. A deconvolution of the integrated spectrum yields 5 Gaussians with an intensity ratio 1:6:13:6:1.

The inability to explain by a superhyperfine interaction with surrounding chlorine nuclei arose already in the case of silver chloride doped with Ni^{2+}, where a similar structure was observed.[11] The authors explained this by a different distribution of the two chlorine isotopes among the four neighboring lattice sites in the plane perpendicular to the center axis. Taking into account the natural abundance of ^{35}Cl, which is three times larger than that of ^{37}Cl, one readily calculates probabilities of 1:6:13:6:1 for the different configurations. This is based on a distortion of the square by different vibrational amplitudes as a result of the different isotope masses. This distortion leads to an orthorombic component in the crystal field and, from that, to a deviation of the resonance position proportional to x^2-y^2. So the model can explain the existence of 5 lines with the observed intensity ratio, but until now no direct determination of the real distribution of the isotopes was done. Therefore we performed an electron-nuclear double resonance (ENDOR) experiment in this system. The result is a large number of ENDOR lines, which again using the ''V-epr'' program can be analyzed completely. Analyzing the ENDOR intensities respectively for the ^{35}Cl and ^{37}Cl nuclei at 100 position among the five lines, one finds a decrease for chlorine 37, an increase for chlorine 35, and, surprisingly, a ratio 1:5 on the central line instead of the natural isotope ratio (1:3). Thus our ENDOR experiments completely proved the model.

After the dramatic changes in 1989, further programs were started to support the cooperation between Russian and German physicists. Here I want to mention especially the Volkswagen Foundation which financed between 1990 and 1998 eighteen projects with scientific groups in Saint Petersburg, among them eleven at the Ioffe institute. Altogether 17 million DM were given to Russia (10 percent of them to Saint Petersburg), a sum which amounts to nearly one half of the total funding for Central and Eastern Europe. An important role was played here by Gottfried Landwehr from Würzburg University as a head of the selection committee.

I am very glad that one of the eleven projects mentioned above was carried out by Boris Zakharchenya's and Pavel Baranov's groups at the Ioffe institute and my group at Giessen. Its topic was photoluminescence of hot electrons and magnetic resonance in quantum-well structures and superlattices. GaAs/AlAs superlattices are grown by molecular beam epitaxy and consist of a sequence of alternating GaAs and AlAs layers. This periodic arrangement shows up nicely in high-resolution transmission electron microscopy. In addition, Röntgen's discovery also plays an important role for the characterization of such nanostructures, x-ray diffraction

supplying complementary information about layer dimensions. Since these are of the order of a few monolayers, extreme quantum confinement effects appear. We studied a series of samples with nominally 5.5 monolayers (1.73 nm) GaAs and 8.5 monolayers (2.65 nm) A1As. For quantum wells with such dimensions the energy of the lowest electron state in A1As is lower than that in GaAs, so excitons are formed from X_z electrons in the A1As layer and from Γ holes in the GaAs layer. This characterizes a type-II superlattice and leads to a localization of the excitons at the interfaces. Due to the very low temperatures of our experiments (1.5 K) only the lowest energy excitons (more exactly: the heavy-hole excitons) play a role. The radius of such an exciton, which amounts to more than 10 nm, in the bulk material, is strongly reduced in the growth direction. This fact together with the low local symmetry of the interface result in an exchange (or zero-field) splitting of all four exciton sublevels. The heavy holes states $m_J = \pm 3/2$ couple with the $m_s = \pm 1/2$ states of the electron to produce $m = 2$, 1, -1, and -2 exciton states. In magnetic field, circularly polarized optical transitions are allowed only from the $m = \pm 1$ states. If we connect them by microwave transitions to one of the nonradiative, higher populated $m = \pm 2$ states, we increase either the intensity of the σ^+ or the σ^- radiation. This shows up in the circular polarization of emission and can be used to detect magnetic resonance and to examine the energy level system of the excitons. Very important in this context is the fact that coupling of levels not only occurs due to microwave transitions, but also when the external magnetic field brings energy levels close to each other. Zero-field level crossing is the origin of the Hanle effect, which we discussed before. Here a level anticrossing occurs, which also effects level populations showing up in the intensity of circular or linear polarization of emission. Level anticrossing is a very helpful method of spectroscopy[12] since it does not have the limitations of optically detected magnetic resonance (ODMR), which usually fails for radiative lifetimes shorter than 0.1 μs. A systematic investigation of a large number of superlattices[12,13] reveals an approximately exponential dependence of the exchange splitting on the superlattice period. The isotropic exchange splitting of excitons can be used to determine the period of a SL. Together with the dependence of the hole g factor on the thickness of the GaAs layer, a complete geometrical characterization with very high resolution becomes possible.

The main topic of our collaboration in recent times was the investigation of ODMR together with the linear polarization of level anticrossing signals. The reason for that is the following: The sequence of layers in the growth direction changes the respective orientation of the gallium and aluminum bonds to arsenic atoms in the interface. Whereas in the so-called normal (AlAs on GaAs) interface, the AlAs bonds lie in a (110) plane, oriented along a $[1\bar{1}0]$ direction, and the GaAs bonds in a $(1\bar{1}0)$ plane, oriented along [110], for the inverted interface (GaAs on AlAs) the situation is just opposite. This results in an inversion of the radiative levels. The first level anticrossing (with increasing magnetic field) for the normal interface leads to a population increase of the level, from which light linearly polarized along [110] is emitted. The second anticrossing accordingly increases the intensity of the $[1\bar{1}0]$ light. For the inverted interface the sequence is reversed. In that way one can even distinguish at which interface the recombining exciton is localized.[14] Since the whole luminescence is a dynamic process and all levels are coupled by rate equations a population increase of one radiative level may cause a decrease in the other. Another consequence is the different dependence of ODMR of different excitons on the microwave chopping frequency we use to modulate the effect.[15] This provides an additional possibility to study exciton dynamics and to unravel different contributions.

Very detailed information obtained experimentally was used to study the influence of growth parameters on the interface quality of superlattices in collaboration with Franz Ahlers and Klaus Pierz from the Physikalisch-Technische Bundesanstalt in Braunschweig. In a sample grown at 600 °C, with growth interruptions of 50 s after deposition of each GaAs layer, two luminescence lines were observed. In the ODMR experiment it could be clearly seen that the low-energy line arises from the recombination of an exciton with a smaller exchange splitting than that of the excitons contributing to the high-energy line. From the sign and shape of the level anticrossings in linear polarization we showed that only excitons localized at the inverted interface were observed in the low-energy line, in the high-energy line, two excitons localized at both the inverted and normal interface were clearly separated.[16] In this way, one can now determine the dependence of the growth parameters on the ratio of excitons localized at different interfaces, check the physical background for this, control the quality of superlattices, etc. It should be mentioned that the energy levels deduced from ODMR and from the level anticrossing resonance fields are absolutely consistent. The two different exchange splittings observed for the two luminescence lines prove the existence of regions larger than the radius of the exciton which differ in the local period and the GaAs layer thickness by one monolayer. Obviously, the increased possibility for relaxation of the GaAs surface by the pause during growth enables the appearance of monolayer-high interface islands.

These few examples hopefully illustrated that relations between Russian and German physics are in a good shape and that Giessen and Saint Petersburg keep the old traditions vital.

*)E-mail: Arthur.Scharmann@exp1.physik.uni-giessen.de

[1] W. C. Röntgen, Wiedemanns Annalen **40**, 1, 97 (1890).
[2] A. Eichenwald, Annalen der Physik **13**, 919 (1904).
[3] A. Ioffe, *Meetings with Physicists* [in Russian] (Govt. Publisher of Physics-Mathematics Literature, Moscow, 1962; [German translation] B. G. Teubner, Leipzig, 1967).
[4] W. C. Röntgen, Annalen der Physik **64**(1), 1 (1921).
[5] W. Hanle, Z. Phys. **30**(1), 93 (1924).
[6] *Optical Orientation*, edited by F. Meier and B. P. Zakharchenya, Modern Problems of Condensed Matter Physics, Vol. 8, (North Holland, 1984).
[7] B. P. Zakharchenya, P. S. Kop'ev, D. N. Mirlin, D. G. Polakov, I. I. Reshina, V. F. Sapega, and A. A. Sirenko, Solid State Commun. **69**, 203 (1989).

[8] M. Anton, K.-H. Schartner, D. Hasselkamp, and A. Scharmann, Z. Phys. D **18**, 53 (1991).
[9] A. G. Badalyan and J. Rosa, in *Proceedings of the XIIth International Conference on Defects in Insulating Materials. Nordkirchen (1992)*, edited by J.-M. Spaeth and O. Kanert (World Scientific, Singapore, 1993), p. 608.
[10] V. G. Grachev, JETP **92**, 1834 (1987).
[11] M. Höhne, M. Stasiw, and A. Watterich, Phys. Status Solidi **34**, 319 (1969).
[12] P. G. Baranov and N. G. Romanov, in *Proceedings of the 22nd International Conference on the Physics of Semiconductors, Vancouver, (1994)*, edited by D. J. Lockwood (World Scientific, 1994), p. 1400.
[13] P. G. Baranov, I. V. Mashkov, N. G. Romanov, P. Lavallard, and R. Planel, Solid State Commun. **87**, 649 (1993).
[14] P. G. Baranov, I. V. Mashkov, N. G. Romanov, C. Gourdon, P. Lavallard, and R. Planel, JETP Lett. **60**, 445 (1994).
[15] P. G. Baranov, N. G. Romanov, A. Hofstaetter, C. Schnorr, W. von Foerster, and B. K. Meyer, in *Proceedings of the 6th International Symposium on Nanostructures: Physics and Technology*, edited by Zh. Alferov and L. Esaki (St. Petersburg, 1998), p. 366.
[16] P. G. Baranov, N. G. Romanov, A. Hofstaetter, A. Scharmann, C. Schnorr, F. A. Ahlers, and K. Pierz, in *Proceedings of the International Symposium on Compound Semiconductors, St. Petersburg (1996)*, Inst. Phys. Conf. Series N 155 (IOP Publ. Ltd., 1996), p. 893.

Published in English in the original Russian journal. Reproduced here with stylistic changes by the Translation Editor.

Progress in the growth and research of crystals for wide-gap semiconducting materials

Yu. A. Vodakov and E. N. Mokhov*)

A. F. Ioffe Physicotechnical Institute, Russian Academy of Sciences, 194021 St. Petersburg, Russia
Fiz. Tverd. Tela (St. Petersburg) **41**, 822–825 (May 1999)

The feasibility of a sublimation sandwich method for controlled growth of single crystals and epitaxial layers of different SiC and GaN polytypes is demonstrated. The controlled production of pure ($n_i < 10^{16}$ cm^{-3}) and heavily-doped crystals and epitaxial layers of these materials has made it possible to study their semiconducting parameters in detail and to identify the nature of a number of the most important impurity centers. It is shown for the example of SiC that the typically high chemical-binding energy of atoms in these compounds is the reason for the formation of stable metastable compounds, among them associations and clusters that include intrinsic defects which have a significant effect on the properties of the material. Clusters formed on the surface can serve as seeds for different polytypes during crystal growth.
 [S1063-7834(99)01605-6]

Wide-gap semiconducting materials are those with a wide band gap close to or exceeding 2.3 eV. Materials in this group can be used for creating various electrooptical devices, including light-emitting diodes and lasers for operation in the short-wavelength visible and UV spectrum.[1] The outstanding representatives of this group are SiC and GaN, which are also characterized by high binding energies (5–6 eV). These materials are extremely promising for the production of high-power, high-temperature devices. For example, the maximum operating temperature for various devices based on SiC lie within 730–1300 °C, which is 400 °C or more higher than for Si and GaAs. The breakdown voltages for SiC and GaN structures are an order of magnitude higher than for classical semiconductor structures.

We have been actively studying wide-gap semiconducting materials (primarily SiC and GaN) since the 1960's. The major emphasis was on developing the technological basis for manufacturing these materials, including growing crystals and epitaxial layers, with controlled doping by impurities for creating device structures. Complex studies have been made of the properties of the materials, and of the behavior of impurities and intrinsic defects in them, in connection with the conditions for fabricating them and the subsequent relaxation annealing. Special attention has been devoted to the polytypism of SiC. The major parameters of the polytypes of SiC that we determined in the 1960's and 1970's are still quite reliable and have only been modified slightly in the ensuing years. In particular, the promise of a polytype such as 4*H* was demonstrated.[2]

In this paper we present some original data from a study of the growth and doping of SiC and GaN. Most of the information on an analysis of the doping behavior concerns SiC. This is explained by the fact that SiC, as opposed to GaN, is relatively stable thermally and does not decompose at high temperatures.

1. GROWTH AND DOPING OF SiC AND GaN

1.1. *The sublimation sandwich method.* We have proposed a method for growing epitaxial layers and single crystals, initially of SiC[3] and later of GaN,[4] which is now known as the sublimation sandwich method. The concept of the method has been described previously.[5]

The main advantages of this method are:

(1) Inside a sandwich growth cell, it is possible to create and maintain conditions close to equilibrium over a wide range of temperatures, supersaturations, external pressures, and compositions of the vapor phase. As a result, it is possible to obtain extremely perfect single-crystal layers, even of such decomposing compounds as GaN, with sublimation mass transport of material from the source to the substrate at extremely high rates (up to 1–2 mm/h) without a chemical transporter. Here the efficiency of material transport is close to 100%.

(2) The composition of the vapor phase is easily controlled, so it is possible to ensure the required doping level of the growing crystal, and vary its stoichiometric composition and polytype.

(3) With this method it is possible to obtain additional information on the mechanisms of growth and doping (including the elementary stages), so that it is easier to model the mass transfer process theoretically and to verify the model.

1.2. *Gallium nitride.* Epitaxial layers of GaN were first obtained by sublimation on SiC and sapphire substrates in a horizontal reactor with rf heating.[4,6] GaN powder or metallic Ga were used as a sublimation source. Growth proceeded at a temperature of 1100–1300 °C in a nitrogen flow. Here it was possible to attain very high growth rates, up to 1 mm/h. It was found possible to grow thick epitaxial layers, as well as bulk crystals with thicknesses of up to 0.8 mm and linear dimensions of up to 15–20 mm.

The undoped *n*-type samples had electron concentrations of 2×10^{17} cm^{-3} or more. Samples of GaN doped with Fe, Mn, Ni, and V impurities were also obtained. The nature of most of these impurity centers was first identified using electron paramagnetic resonance (EPR). A typical luminescence spectrum for these samples is shown in Fig. 1. A single, sharp exciton peak and a broad band in the yellow portion of

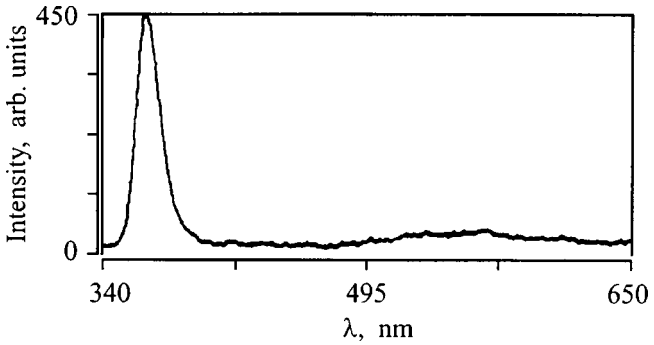

FIG. 1. Luminescence spectrum of GaN grown on a SiC substrate.

the spectrum can be seen. It should be noted that the intensity of the yellow band depends strongly on the structural perfection of the grown sample. A high intensity of this band was observed near structural and morphological defects of the crystal. An enhancement in the intensity of the yellow luminescence was observed in the epitaxial layer adjoining the substrate, evidently owing to stresses generated by the mismatch between the lattices of the substrate and the GaN. These data, along with x-ray data, demonstrate the possibility of obtaining extremely perfect layers of GaN by sublimation.

1.3. *Silicon carbide.* Epitaxial layers of SiC were grown at temperatures of 1700–2600 °C in an inert atmosphere or in vacuum. Bulk crystals of SiC of polytypes 4 and 6*H* were also grown, with diameters up to 40 mm and thicknesses up to 15 mm. The purest undoped SiC layers had electron concentrations of 10^{15} cm^{-3}. The possibility of growing heavily-doped SiC crystals of either *n*- or *p*-type with extremely high doping levels close to 10^{21} cm^{-3} was demonstrated. Data on the maximum concentrations in SiC layers for more than 20 impurities are given in Ref. 7.

The degree of doping in the growing level depends strongly on many factors, including the substrate orientation, the growth temperature and rate, and the stoichiometric composition of the vapor phase.[5] These effects can be explained by a lack of equilibrium in the vapor–crystal system under the growth conditions achievable in practice. The condition for such an equilibrium is known to be $V_g < D_i/h$ (where V_g is the growth rate, D_i is the impurity diffusion coefficient, and h is the thickness of the growing layer). Using experimental values of D_i, it is easy to show that this condition is not met for most impurities. Thus, the doping anisotropy is a consequence of a difference in the adsorption properties of the polar {0001} facets. For example, the concentration of the acceptor impurities Al and Ga in layers grown on polar {0001} facets can vary by factors of 5–10. However, the orientational doping anisotropy can be greatly reduced by raising the growth temperature or changing the composition of the vapor phase by, for example, introducing silicon vapor into the growth zone.

As a rule, the concentration of most impurities is higher on a (0001)Si face than on a (0001)C face because of the higher surface energy of the former. An exception is group V and VI donor impurities, which are better adsorbed on a carbon face.

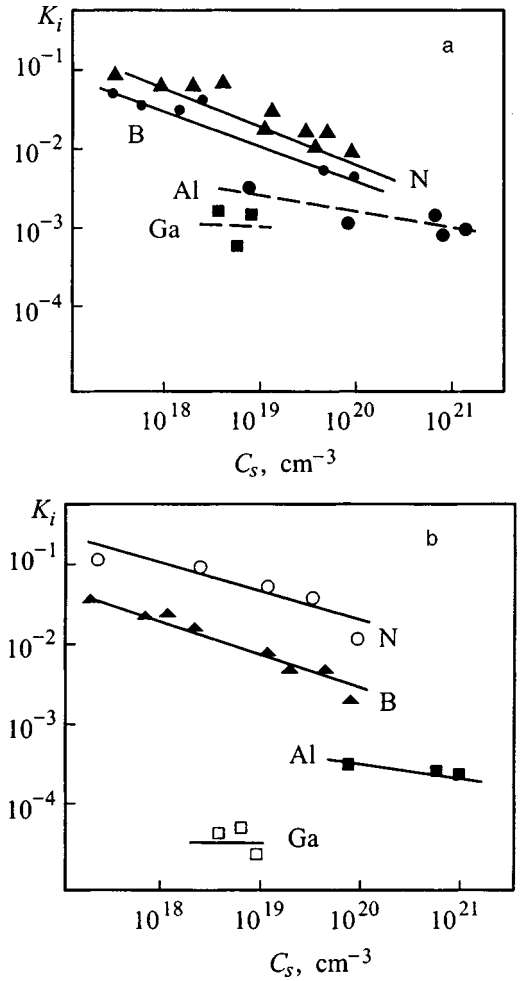

FIG. 2. Elementary capture coefficient of N, B, Al, and Ga as functions of source impurity concentration. Direction of growth: [0001]C (a), [0001]Si (b). $T_G = 1850$ °C.

By using a sandwich system it was possible to calculate the elementary capture coefficients for the most important impurities (K_i) as functions of the growth conditions and substrate orientation (Fig. 2). It turned out that the elementary capture coefficients for the impurities are much lower than for the matrix atoms. As the growth temperature is raised, the capture efficiency of most of the impurities increases, while, on the other hand, that of the donor impurity elements from group V decreases.

Increasing the impurity concentration, as well as additional implantation of surface-active impurities (e.g., silicon) in the growth zone, cause a reduction in K_i.

For group V impurities (nitrogen, phosphorus) these effects can be attributed to desorption of impurities from the surface layer. Another reason for the low values of K_i is the formation, on the growing surface, of inclusions of a second phase, which have been enriched by an introduced impurity. Similar processes with precipitate formation near structural and morphological defects have been found to be most typical for boron impurities.[8]

2. INTRINSIC DEFECTS IN GROWN SiC CRYSTALS

We have examined various ways of introducing nonstoichiometric intrinsic defects into a growing crystal. All these

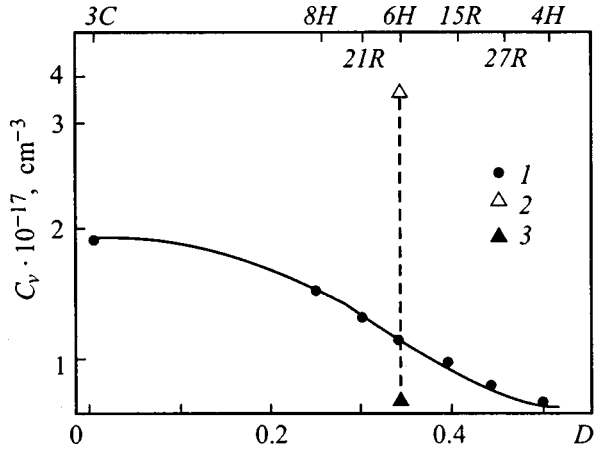

FIG. 3. Concentration of carbon vacancies as a function of the polytype hexagonality fraction in samples grown under different conditions: Lely method, $T=2600\,^{\circ}$C (*1*); sublimation sandwich method with excess Si, $T=1900\,^{\circ}$C (*2*); sublimation sandwich method with excess C (SiC–Sn system), $T=2200\,^{\circ}$C (*3*).

methods are based on the low relaxation rate at the phase boundary and in the bulk of the crystal. For example, lowering the sublimation growth temperature or increasing the rate of condensation leads to enrichment of the growing crystal with excess silicon. The same effect was achieved by introducing Si into the system, as well as impurity Ta, Zr, Hf, P, and Ba.[9] For relative enrichment of a crystal with carbon, the most promising impurities are elements of the 1V-b group, especially tin.[10]

In a study of the crystal properties as a function of the growth conditions, it was found that intrinsic defects show up first in SiC crystals grown at relatively low temperatures and containing excess silicon.[11]

Various methods, among them EPR, positron diagnostics, nonstationary deep level spectroscopy, and luminescence analysis, revealed the existence of associates in them, including intrinsic defects, as well as impurity atoms. For example, positron diagnostic data demonstrate directly the presence of an elevated concentration of vacancy defects in these crystals at a level of 3×10^{17} cm^{-3} (Fig. 3). EPR was used to reveal and identify associates, with an acceptor impurity and carbon vacancy in them. Note that the latter are responsible for deep centers with an ionization energy $E_V+0.5-0.6$ eV. The crystals enriched in silicon have a characteristic defect luminescence with a D_I spectrum that has been observed previously only in crystals containing radiation defects. The center for this luminescence is obviously a vacancy associate.

Intrinsic defects in SiC crystals enriched with silicon often are in the form of clusters.[11,12] The enhanced thermal stability of nonequilibrium defect centers is evidently explained precisely by the presence of clusters. For example, the annealing temperature in them for D_I and D defect-luminescence centers introduced through irradiation by high-energy particles at 600–800 °C is higher than in SiC samples with similar impurity composition grown by the Lely method under standard conditions ($T_g=2600\,^{\circ}$C).

The enhanced susceptibility to dislocation and crack formation in samples containing excess Si can be related to the presence of clusters as stress concentrators. Clusters are also obviously responsible for the microplasma breakdown of epitaxial $p-n$-junctions typical of this group of crystals. As opposed to the ordinary microplasmas caused by extended defects, these microplasmas are annealed at temperatures $T_a>2550\,^{\circ}$C. Note that complete relaxation annealing, with loss of the behavior specific to a nonstoichiometric crystal, takes place only at temperatures $T_a>2550\,^{\circ}$C. This is also explained by the presence of clusters which are stable up to high temperatures.

Clusters have little effect on the semiconducting properties of a material, since they are electrically inactive, but their breakup at high temperatures owing to Oswald ripening does favor a greater thermal stability on the part of the simpler centers, such as D_I centers, which are luminescence activators. Here impurities (such as nitrogen and boron) which facilitate clusterization have been found to play a significant role. The existence of latent nonstoichiometry in SiC[10] can also be explained by the presence of clusters. Given that an enhanced intrinsic defect content is observed in samples grown with an excess of silicon, we should expect that the clusters include interstitial silicon atoms or carbon vacancies. Direct proof of the presence of clusters of both the interstitial and vacancy types, which are stable to temperatures in excess of 2000 °C has been obtained in studies of SiC samples irradiated with high-energy particles by means of electron microscopy, x-ray diffractometry, and positron diagnostics.

The very possibility of developing different kinds of clusters with intrinsic defects and impurities, which are stable at high crystal-growth temperatures, is a factor which favors polytypism. We believe that clusters can be nucleation centers for various kinds of polytype.[8] The probability of forming a surface cluster depends little on the amount of supersaturation. Thus, this growth mechanism shows up most distinctly at low supersaturations during growth on a singular surface without any structural or morphological defects that might favor maintenance of the substrate polytype.[13] When there are no external factors favoring the appearance of a certain polytype, seeds for different polytypes develop on this surface and this leads to a polytype instability effect.[13] At the same time, the structure of a developing polytype seed depends on the Si:C ratio in the vapor phase.[10] For example, when there is excess Si, the probability of forming a seed for a cubic polytype (3*C*) is high and when there is a relative excess of carbon (or in the vapor of isovalent impurities of the 1Vb group), seeds for the hexagonal polytype 4*H* develop.[14]

Therefore, the most important specific feature of wide-gap materials with a high binding energy is that relaxation processes involving intrinsic defects and impurity atoms take place very slowly in them, so that it is difficult to achieve equilibrium in the solid phase, even at the high (industrial) temperatures at which growth, diffusion, or ion implantation take place. As a result, the grown crystals can contain nonequilibrium metastable states which include intrinsic defects and impurities, so that the crystal properties depend on the temperature and other fabrication conditions. These specific features of the material are extremely stable. Eliminating

them completely requires extremely high annealing temperatures.

We have pointed out, therefore, the prospects for the sublimation sandwich method as a means for growing SiC and GaN doped with various impurities. It has been found that the doping of these materials is essentially a nonequilibrium process. In SiC crystals grown with excess Si, an enhanced concentration of intrinsic defects has been observed in the form of metastable associates and clusters which include intrinsic defects and impurities and have a substantial effect on the properties of the material. The possibility of changing the stoichiometric composition and polytype in a controlled fashion during the growth of SiC has been demonstrated.

This work was partially supported by the Russian Fund for Fundamental Research (Grant No. 98-02-18241).

*)E-mail: mokhov@sic.ioffe.rssi.ru

[1] H. Morkoc, S. Strite, G. B. Gao, M. E. Lin, B. Sverdlov, and M. Burns, J. Appl. Phys. **76**, 13639 (1994).
[2] Yu. A. Vodakov, G. A. Lomakina, E. N. Mokhov, V. G. Oding, V. V. Semenov, and V. I. Sokolov, in *Problems in the Physics and Technology of Wide-Gap Semiconductors* [in Russian] (Leningrad, 1979), p. 164.
[3] Yu. A. Vodakov and E. N. Mokhov, ''A method for obtaining semiconducting silicon carbide,'' Inventor's Certificate No 403275 (1970); Patents UK: No. 1458445 (1977); Germany: No. 2409005 (1977); USA No. 414572 (1979).
[4] Yu. A. Vodakov, M. I. Karklina, E. N. Mokhov, and A. D. Roenkov, Izv. Akad. Nauk SSSR, Neorg. Mater. **16**, 537 (1980).
[5] Yu. A. Vodakov, A. D. Roenkov, M. G. Ramm, E. N. Mokhov, and Yu. N. Makarov, Phys. Status Solidi **202** 177, (1997).
[6] Yu. A. Vodakov, E. N. Mokhov, A. D. Roenkov, M. E. Boiko, and P. G. Baranov, J. Cryst. Growth **183**, 10 (1998).
[7] Yu. A. Vodakov, E. N. Mokhov, M. G. Ramm, and A. D. Roenkov, Springer Proc. Phys. **56**, 329 (1992).
[8] E. N. Mokhov, Author's Abstract of Doctoral Dissertation, St. Petersburg (1998).
[9] Yu. A. Vodakov, E. N. Mokhov, A. D. Roenkov, and M. M. Anikin, Pis'ma Zh. Tekh. Fiz. **5**, 367 (1979) [Sov. Tech. Phys. Lett. **5**, 147 (1979)].
[10] Yu. A. Vodakov, G. A. Lomakina, and E. N. Mokhov, Fiz. Tverd. Tela **24**, 1377 (1982) [Sov. Phys. Solid State **24**, 780 (1982)].
[11] Yu. A. Vodakov and E. N. Mokhov, ''Point Defects in Silicon Carbide,'' Inst. Phys. Conf. Ser. No. 137, Ch. 3, 197 (1994).
[12] E. N. Mokhov and Yu. A. Vodakov, Inst. Phys. Conf. Ser. No. 155, Ch. 3, 177 (1997).
[13] G. V. Saparin, S. K. Obyden, P. V. Ivannikov, E. N. Mokhov, and A. D. Roenkov, Scanning **19**, 269 (1997).
[14] E. N. Mokhov, A. D. Roenkov, G. V. Saparin, and S. K. Obyden, Scanning **18**, 67 (1996).

Translated by D. H. McNeill

EPR of defects in semiconductors: Past, present, future

G. D. Watkins*)

Department of Physics, Lehigh University, Bethlehem, PA 18015, USA
Fiz. Tverd. Tela (St. Petersburg) **41**, 826–830 (May 1999)

Important physical concepts learned from early EPR studies of defects in silicon are reviewed. Highlighted are the studies of shallow effective-mass-like donors and acceptors by Feher, of deep transition-element impurities by Ludwig and Woodbury, and of vacancies and interstitials by Watkins *et al.* It is shown that the concepts learned in silicon translate remarkably well to corresponding defects in the other elemental and compound semiconductors. The introduction of sensitive optical and electrical detection methods during the intervening years, and the recent progress in single-defect detection insure the continued vital role of EPR in the future.
 [S1063-7834(99)01705-0]

For over forty years, electron paramagnetic resonance (EPR) has played a key role in the study of point defects in semiconductors. Because of the detailed structural information available from the spectrum of a defect — symmetry from its angular dependence, and the atomic and lattice structure from its hyperfine interactions — it has proven to be uniquely able to identify a defect, to map out its wavefunction in the lattice, and determine its microscopic structure.

In this short presentation, I can present only a very few of the highlights, with apologies to the many, many EPR scientists who have made, and are continuing to make, vital contributions to our understanding of defects in semiconductors.

I. PAST

1. Shallow effective-mass impurities

Over forty years ago, Feher[1] introduced the important technique of electron-nuclear double resonance (ENDOR), where the nuclear resonance of nearby lattice atoms could be detected as a change in the EPR signal of a defect. With this, he was able to map out for the first time the wavefunction of the $S=1/2$ bound electron of the shallow donor in silicon over the surrounding silicon lattice sites.[2] This served to establish in beautiful detail the correctness of the theory of Kohn and Luttinger,[3] which described the wavefunction as a large-orbit hydrogenic envelope function (effective-mass electron, dielectric shielded from the positive core) multiplying a sum of the free-electron states at the conduction-band valley minima.

The shallow acceptor in silicon was more difficult because, for it, the top of the valence band is at the Γ point ($k=0$), with orbital angular momentum $L=1$, giving $J=3/2$ for the bound hole. The hole is strongly sensitive, therefore, to random strains in the crystal and the acceptor resonance was too broad to detect. Feher solved the problem by applying a uniaxial stress to the crystal, which lifted the degeneracy of the bound $J=3/2$ hole and made the resonance observable,[4] again confirming the general features of the Kohn–Luttinger theory. Twenty years later, with higher quality, lower internal strain crystals, Neubrand was able to detect for the first time the acceptor resonance in the absence of external strain, and confirm the complete $J=3/2$ spectrum for the bound hole.[5]

This pioneering EPR work in silicon has served to set the pattern of understanding for all of the elemental and compound semiconductors. Similar shallow $S=1/2$ effective-mass donor resonances have been observed subsequently in many of the semiconductors, but the shallow $J=3/2$ acceptors have resisted detection, the valence band maximum being at $k=0$ for all. The acceptors have been observed in a very few cases, but again only either when stress was externally applied to the cubic semiconductor, or when internally available for a few non-cubic semiconductors.

2. Deep transition element impurities

At about the same time, Ludwig and Woodbury initiated a systematic study of the $3d$ transition-element impurities in silicon, which continued through the 1960's.[6] Using EPR and ENDOR, several charge states of most of the $3d$ transition-element impurities were observed and a simple physical picture of their properties emerged.

This is summarized in Fig. 1. The sign of the crystal fields experienced by the d electrons is reversed for the interstitial and substitutional sites. For the interstitial site, the crystal field can be considered to arise primarily from the positive cores of the four nearest silicon atoms, which are exposed because their charge compensating valence electrons are involved in bonds pointing away from the interstitial site. Therefore, as shown in Fig. 1, the triply degenerate $d(t_2)$ orbitals are lower in energy because they interact more strongly with the neighbors than the doubly degenerate $d(e)$ orbitals, which better avoid them. In the substitutional site, the negative charge of the electrons in the bonds to the impurity dominate, and the level order is reversed.

Starting from the free ion $3d^{\alpha}4s^{\beta}$ configuration for a particular charge state, all $\alpha+\beta$ electrons go into these orbitals for the non-bonding interstitial case, as expected. For the substitutional impurities, which require four electrons to

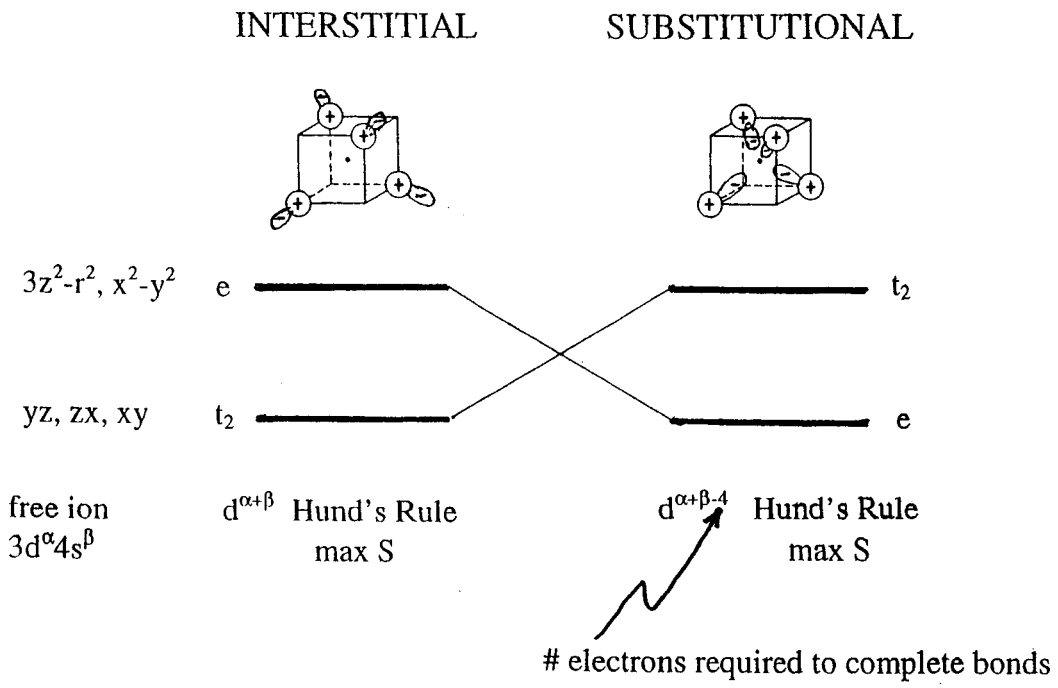

FIG. 1. Simple crystal field model deduced for $3d$ transition-element impurities in silicon.[6]

complete their bonds to the four silicon neighbors, $\alpha+\beta-4$ remain to go into the d orbitals. In both cases, the levels are filled according to Hund's Rule, electrons paired (maximum S), first filling the lower level, spin-up, then the upper, spin-up, before filling, spin-down, in the lower, etc. The repulsive electron–electron interactions between the localized $3d$ orbitals, which force maximum spin, therefore dominate over the crystal-field energy.

This general pattern, established very early for silicon, has been remarkably successful in interpreting the many subsequent EPR and optical results for transition elements in all of the semiconductors — elemental, III–V, and II–VI alike. In the compound semiconductors, the impurities tend to enter substitutionally the metal sublattice. For them, the substitutional rules are the same as above, except that $\alpha+\beta-3$ electrons go into the d levels in the III–V's, the three electrons replacing now the three valence electrons associated with the neutral group–III atom that the impurity ion replaces. Similarly, for the II–VI's, the d-level occupancy number is $\alpha+\beta-2$.

Of course, the excitement, and new physics, arises when departures are found, although there have been few so far. One interesting one is that of the shallow manganese acceptor in GaAs. In that case it has been found that Mn^0 is not d^4, as expected by the simple rules above, but the Hund's rule d^5, with a shallow bound hole[7]. Another departure has been found for substitutional Ni^- in silicon[8] and also for the corresponding d^7 substitutional ions of the $4d$ (Pd^-) and $5d$ (Pt^-, Au^0) series. For them, a Jahn–Teller distortion sets in, which overcomes the electron–electron coupling, giving $S=1/2$ for their $e^4t_2^3$ paramagnetic charge states. This anomaly has been explained as a result of strong charge transfer of the paramagnetic d orbitals onto the four neighbors in the particular case of the transition elements at the end of each series.[9]

3. Vacancies and self-interstitials

Also, begun at about the same time and continuing through the 1980's, my students and I have systematically probed the properties of the intrinsic defects — vacancies and self-interstitials — in silicon.[10–12] The approach taken was to produce the defects by 1–3 MeV electron irradiation *in situ* at cryogenic temperatures and to study by EPR the frozen-in isolated vacancies and interstitials, and then to warm up and study their migrational properties.

Figure 2 summarizes the experiment and the overall pattern of results. Immediately after irradiation, EPR of the isolated vacancy in two different charge states, V^+ and V^-, is observed. Long-range migration of the vacancy with subsequent trapping by impurities occurs at $\sim$70 K in n-type material, $\sim$200 K in high-resistivity material, and $\sim$150 K in p-type material. As shown, a whole host of trapped vacancies have been identified by EPR, confirming unambiguously that the annealing is indeed the result of long-range diffusion of the vacancy. Kinetic studies of the annealing have revealed the activation energies for vacancy diffusion as shown in Fig. 2, along with the corresponding defect charge states. This was the first surprise. The high mobility well below room temperature, and its large dependence on the vacancy charge state, were not anticipated.

A second surprise was the experimantal observation that vacancy annealing can be stimulated even at 4.2 K by shining near bandgap light on the sample or by injecting electrons and holes electrically, This phenomenon, called recombination-enhanced migration, was also established to

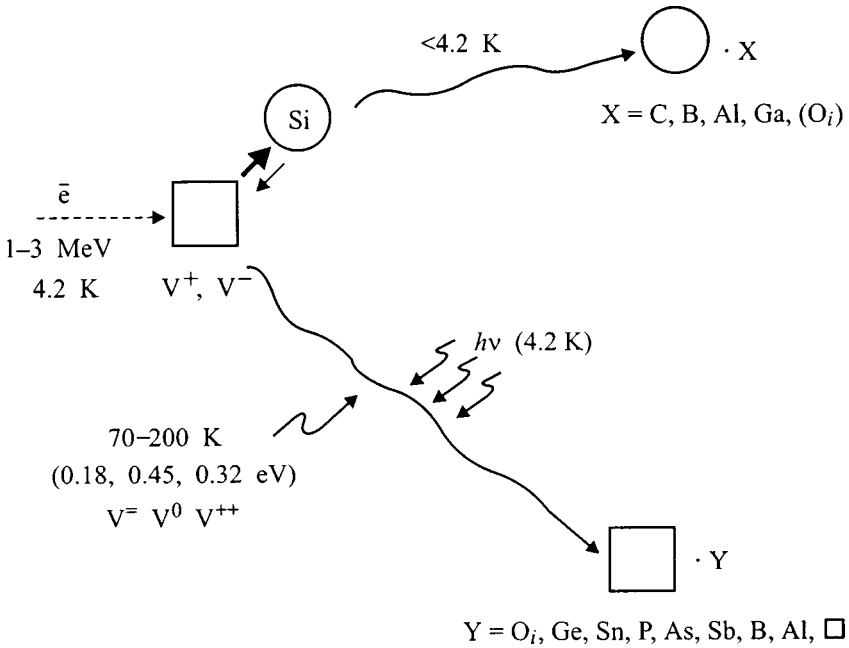

FIG. 2. Evolution of events after a vacancy-interstitial pair is produced by an electron irradiation event in silicon.[11,12]

be occurring to a limited extent during the electron irradiation itself, which also generates substantial electron-hole pair ionization.

A third even greater surprise was the observation, in the *p*-type material studied, that the interstitial had already migrated long distances during the initial electron irradiation at 4.2 K. Immediately after the irradiation, only interstitials trapped by impurities were observed, as illustrated in Fig. 2, and in ~1:1 concentration to the isolated vacancies. Apparently, the interstitial is even more efficient in converting the capture of electrons and holes into the energy required for its migration.

Figure 3 provides a simple interpretation of the electronic and lattice structure of the vacancy that has evolved from the EPR studies. Using the concept of simple molecular orbitals made up from the dangling bonds of the four vacancy neighbors, the various charge states can be understood by their successive population with the appropriate number of electrons, two for V^{++}, three for V^+, etc. Here, the electron–electron interactions are weaker than in the transition-element ion case, being spread mostly over the four nearest-atom neighbors, but also onto their neighbors as well, and each level is filled before proceeding to the next. The interesting feature here is that Jahn–Teller energy-lowering distortions occurs as soon as partial occupancy of the degenerate t_2 orbital occurs. A tetragonal distortion occurs for V^+, as observed in its EPR, because of its single occupancy in the t_2 orbital. A much larger tetragonal distortion occurs for V^0 being driven by the energy gain of two electrons in the orbital. For V^-, an additional dihedral distortion occurs.

These distortions turn out to have important consequences. For example, the increased two-electron Jahn–Teller energy lowering for V^0 over the one-electron energy lowering for V^+, actually serves to overcome the Coulomb repulsion between the two electrons and lower the vacancy first donor level $(0/+)$ to a position, below the second donor level $(+/++)$. This rare phenomenon, called negative-*U*, implies a net attraction between electrons at the vacancy. To account for this, the Jahn–Teller energy lowering for the vacancy single-donor level $(0/+)$ can be estimated to be at least ~0.5 eV in Ref. 13. With relaxation energies this large (~1/2 the bandgap!), it is easy to understand how capture of electrons and holes at the vacancy can supply the necessary vibrational energy to overcome the small diffusion barriers indicated in Fig. 2, and explain its athermal 4.2 K migration under electronic excitation.

Inspection of the wide variety of observed configurations for the trapped interstitials, combined with predictions of recent *ab initio* calculations for interstitial boron[14] and silicon,[15,16] has served to suggest a similar simple physical picture for predicting the properties of such interstitials. Consider the *s* and *p* valence orbitals for the interstitial atom when placed in the high-symmetry T_d interstitial position of the lattice. Populate them in the normal atomic order with electrons appropriate for the charge state of the interstitial. For $B_i^+(2s^2)$, $Al_i^{++}(3s^1)$ and $Si_i^{++}(3s^2)$, there is no orbital degeneracy, therefore no Jahn–Teller distortion, and the interstitial should stay on-center, as indeed observed for Al_i^{++}, and predicted by theory for the other two. For $B_i^0(2s^2 2p)$, $C_i^+(2s^2 2p)$, $Si_i^+(3s^2 3p^1)$, and their further degenerate *p*-level occupancy charge states, off-center Jahn–Teller distortions should occur into symmetry lowering bonding configurations, as indeed observed for B_i^0 and $C_i^{+,0,-}$, and predicted for all three atoms. Considering the large energies involved in *p* bonding, it is again easy to understand efficient recombination-enhanced migration for the interstitial as it cycles back and forth between its various configurations during electron and hole capture.

Remarkably, therefore, the electronic and lattice structures for vacancies and interstitials in silicon can be understood in almost identical fashion, as summarized in Fig. 4. In each case, there is a non-degenerate (a_1, s) level lowest and

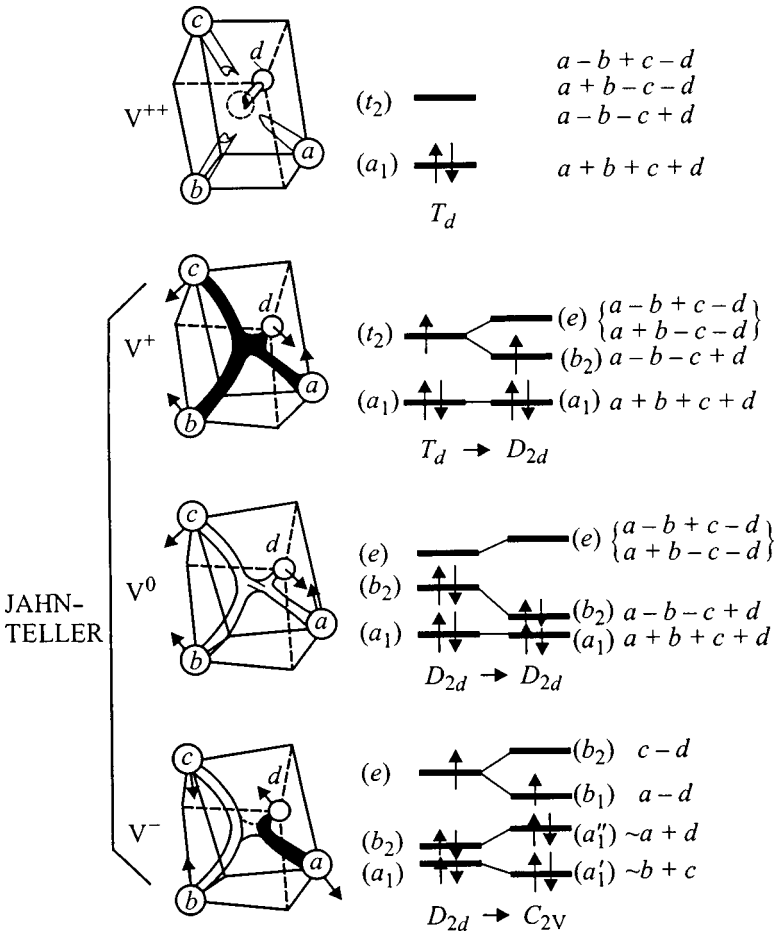

FIG. 3. Simple one-electron model for the various charge states of the vacancy in silicon.

a threefold degenerate (t_2,p) level higher, which are filled by the electrons appropriate for the charge state of the defect. Each level is filled before going to the next, and when orbital degeneracy results, symmetry-lowering Jahn–Teller distortions occur as bond reconstructions, rebonding configurations, etc.

The one-electron orbital pictures for vacancies and interstitials in Fig. 4 must, of course, be generally applicable to all semiconductors — a vacancy always produces four dangling bonds, an interstitial in the undistorted tetrahedral site is always an ion surrounded by four non-bonding neighbors. In the II–VI semiconductors, for example, it provides a natural explanation for the on-center character observed by EPR for the chalcogen vacancies, $V_{\mathrm{VI}}^{+}(a_1^1)$, and the trigonally distorted metal vacancies, $V_{\mathrm{II}}^{-}(a_1^2t_2^5)$.[11] In ZnSe, the interstitial $\mathrm{Zn}_i^{+}(s^1)$, has also been observed, and is on-center, as predicted.[11] For the many other semiconductors about which no clear experimental defect identifications exist, these models may provide useful predictive properties, which, incidentally, provide a remarkable consistent simple physical explanation for the large lattice configurational changes currently often being predicted in modern state-of-the-art *ab initio* theoretical calculations. However, a word of caution is in order. It can also be considered to work for the only other identified intrinsic defects, V_{Ga}^{0} in GaP[17], V_{C}^{-} in diamond[18] and V_{Si}^{-} in 3C–SiC.[19] However, there is an important difference. For their $a_1^2t_2^3$ configuration, Hund's rule occupancy dominates, giving a nondegenerate $S=3/2$ half-filled t_2 shell with no degeneracy and full undistorted T_d summetry. Apparently, in these wider bandgap materials, with more localized vacancy orbitals, the electron–electron interactions are beginning to dominate. We may expect interesting surprises, therefore, as we begin to probe the intrinsic defects in these materials. Theorists, who do not have the ability so far to properly include these multiplet effects, must also beware.

II. PRESENT AND FUTURE

Intensive EPR studies continue today and will in the future, particularly in probing defects in the wide bandgap

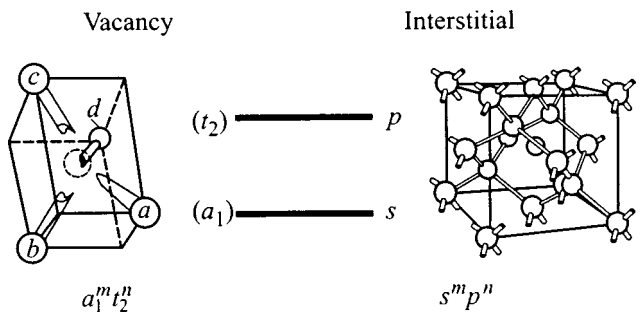

FIG. 4. An identical simple one-electron orbital model appears to work for both vacancy and interstitial in silicon, the levels being filled, first the lower non-degenerate one, then the higher threefold degenerate one. When partial occupancy of the degenerate (t_2,p) orbitals results, $0<n<5$, large Jahn–Teller relaxations occur. Such a model should apply for all semiconductors.

semiconductors of high current interest today for visible/UV light-emitting and high-temperature electronic applications. To the arsenal of conventional EPR and ENDOR techniques discussed above have been added the powerful and greatly increased sensitivity optical and electrical detection methods. For example, the only EPR detection of an isolated interstitial in any semiconductor has been that of the zinc interstitial in ZnSe, performed by optical detection methods.[20,21] Here at the Ioffe Institute, important studies using the optical methods have been carried out in the groups of Romanov and Baranov, and much of the pioneering studies of electrical detection have been made by Vlasenko. In addition, a great deal of excitement is currently centered on the possibility of combining some of the various microscopic scanning techniques (optical, STM, AFM, magnetic cantilever) with the increased sensitivity EPR techniques spatially to resolve single defects. Promising recent success in this regard has been reported by Gruber *et al.*[22] Using optical confocal microscopy, they have resolved and optically detected single isolated nitrogen-vacancy-pair defects in diamond.

EPR will remain a uniquely powerful tool for defect identification and electronic and lattice structure determination. As new semiconducting materials and device structures emerge in the future, it will continue therefore to play a vital role, particularly as promising new and more sensitive techniques for its detection evolve.

Support for the preparation of this review was provided by the National Science Foundation under Grant N DMR-92-094114, and the U.S. Navy Office of Naval Research (Electronic and Solid State Sciences Program) under Grant N N00014-94-1-0117.

*)E-mail: gdw0@lehigh.edu

[1] G. Feher, Phys. Rev. **103**, 834 (1956).
[2] G. Feher, Phys. Rev. **114**, 1219 (1959).
[3] W. Kohn and J. M. Luttinger, Phys. Rev. **97**, 1721 (1955); *ibid.* **98**, 915 (1955).
[4] G. Feher, J. C. Hensel, and E. A. Gere, Phys. Rev. Lett. **5**, 309 (1960).
[5] H. Neubrand, Phys. Status Solidi B **86**, 269 (1978).
[6] G. W. Ludwig and H. H. Woodbury, in *Solid State Physics*, Vol. 13, edited by F. Seitz and D. Turnbull (Academic Press, N.Y., 1962), p. 223.
[7] J. Schneider, U. Kaufmann, W. Wilkening, M. Baeumler, and F. Köhl, Phys. Rev. Lett. **59**, 240 (1987).
[8] L. S. Vlasenko, N. T. Son, A. B. van Oosten, C. A. J. Ammerlaan, A. A. Lebedev, E. S. Taptygov, and V. A. Khramtsov, Solid State Commun. **73**, 393 (1990).
[9] G. D. Watkins and P. M. Williams, Phys. Rev. B **52**, 16 575 (1995).
[10] G. D. Watkins, in *Deep Centers in Semiconductors*, edited by S. Pantelides (Gordon and Breach, N.Y., 1986), Ch. 3. (This provides a detailed description of the properties of the vacancy in silicon.)
[11] G. D. Watkins, in *Electronic Structure and Properties of Semiconductors*, edited by W. Schröter, Materials Science and Technology (VCH, Weinheim, 1991), Vol. 4, Ch. 4. (This includes a review of vacancies and interstitials in all semiconductors.)
[12] G. D. Watkins, in *Defects and Diffusion in Silicon Processing*, edited by T. D. de la Rubia, S. Coffa, P. A. Stolk, and C. S. Rafferty, MRS Symp. Proc. Vol. 469 (Pittsburgh, 1997), p. 139. (This is a concise review of vacancies and interstitials in silicon.)
[13] G. A. Baraff, E. O. Kane, and M. Schlüter, Phys. Rev. B **21**, 3563 (1980).
[14] E. Tarnow, Europhys. Lett. **16**, 449 (1991).
[15] R. Car, P. J. Kelly, A. Oshiyama, and S. T. Pantelides, in *13th Conference on Defects in Semiconductors*, edited by L. C. Kimeling and J. M. Parsey, Jr. (Metallurgical Soc. of AIME, Warrendale, 1985), p. 269.
[16] Y. Bar-Yam and J. D. Joannopoulos, in *13th Conference on Defects in Semiconductors*, edited by L. C. Kimeling and J. M. Parsey, Jr. (Metallurgical Soc. of AIME, Warrendale, 1985), p. 261.
[17] T. A. Kennedy, N. D. Wilsey, J. J. Krebs, and G. H. Strauss, Phys. Rev. Lett. **50**, 1281 (1983).
[18] J. Isoya, H. Kanda, Y. Uchida, S. C. Lawson, S. Yamasaki, H. Itoh, and Y. Morita, Phys. Rev. B **45**, 1436 (1992).
[19] H. Itoh, M. Yoshikawa, I. Nashiyama, and E. Sakuma, IEEE Trans. Nucl. Sci. **NS37**, 1732 (1990).
[20] F. Rong and G. D. Watkins, Phys. Rev. Lett. **58**, 1486 (1987).
[21] K. H. Chow and G. D. Watkins, Phys. Rev. Lett. **81**, 2084 (1998).
[22] A. Gruber, A. Dräbenstedt, C. Tietz, L. Fleury, J. Wrachtrup, and C. von Borczyskowski, Science **276**, 2012 (1997).

Published in English in the original Russian journal. Reproduced here with stylistic changes by the Translation Editor.

Exciton-electron interaction in quantum wells with a two dimensional electron gas of low density

W. Ossau, D. R. Yakovlev, and C. Y. Hu

Physikalisches Institut der Universität Würzburg, Am Hubland, 97074 Würzburg, Germany

V. P. Kochereshko, G. V. Astakhov, and R. A. Suris

A.F. Ioffe Physicotechnical Institute, Russian Academy of Sciences, 194021 St. Petersburg, Russia

P. C. M. Christianen and J. C. Maan

Research Institute for Materials, High Field Magnet Laboratory, University of Nijmegen, 6525 ED Nijmegen, The Netherlands

Fiz. Tverd. Tela (St. Petersburg) **41**, 831–836 (May 1999)

II–VI quantum-well structures containing a 2DEG of low density have been investigated by means of polarized photoluminescence, photoluminescence excitation and reflectivity in external magnetic fields up to 20 T. The spin splittings of the exciton X and the negatively charged exciton X^- are measured as a function of the magnetic field strength. The behavior of the magnetic-field-induced polarization degree of the luminescence line related to X^- demonstrates the formation process of negatively charged excitons from excitons and free carriers polarized by the external magnetic field. We have determined the binding energies of the trion formed either with the heavy-hole or the light-hole exciton. The optically detected magnetic resonance (ODMR) technique was applied for the first time to study the optical transition processes in a nanosecond timescale. The electron ODMR was observed with the detection on either the direct exciton or the negatively charged exciton X. Further evidence for the interaction of excitons with the electrons of the two-dimensional gas are demonstrated by a combined exciton-cyclotron resonance line observed in reflectivity and luminescence excitation, shake-up processes observed in photoluminescence, as well as inelastic and spin-dependent scattering processes. [S1063-7834(99)01805-5]

Effects resulting from the exciton-electron interaction in the presence of a two-dimensional electron gas (2DEG) of low density at $n_e a_B \ll 1$, where n_e is the electron concentration and a_B is the exciton Bohr radius, became a subject of intensive investigations very recently. This interest has been stimulated by the observation of a negatively charged exciton X^- in CdTe/(Cd,Zn)Te modulation-doped quantum-well (QW) structures.[1]

In this paper we review several new effects observed in structures where the exciton interacts with a 2DEG of low carrier density. In detail we discuss: the spin splitting and polarization dependence of X and X^- in high magnetic field;[2] the combined exciton-cyclotron resonance;[3] the optically detected magnetic resonance (ODMR) on X^-;[4] the shake-up process[5,6] and the spin-dependent broadening of excitonic states.[7]

1. SAMPLE STRUCTURES AND EXPERIMENTAL DETAILS

In this study we performed measurements on two different types of structures. We used modulation-doped CdTe/(Cd,Mg)Te or ZnSe/(Zn,Mg)(S,Se) QWs with a 2DEG of low density of about $1.5\times10^{10}\,\mathrm{cm}^{-2}$. The structures were grown by molecular-beam epitaxy on (100) oriented GaAs substrates and selectively doped with iodine or chlorine separated by a spacer layer from the QW. Furthermore, we investigated specially designed structures, where we varied the carrier concentration by external optical illumination.[3] To achieve this, the heterostructures are sandwiched between short-period superlattices, where the QWs are separated from the superlattice (SL) by 20 nm thick barriers, which leads to a much higher probability for the electrons to tunnel from the SL to the QW, as compared to holes, due to the difference in the effective masses. Consequently, the electron concentration in the QW can be varied accurately by the intensity of illumination with a radiation energy exceeding the SL band gap. For the experiments with additional microwave illumination we used a back-wave oscillator, whose frequency can be tuned from 55 GHz to 80 GHz by the application of different dc voltages. For these ODMR experiments the microwaves were chopped at 45 Hz and the synchronous changes of the PL intensities were recorded by a two-channel photon-counter.

2. MAGNETO-OPTICAL STUDY OF THE TRION

2.1. Zeeman splitting and polarization degree

In the first part of this paper we concentrate on the properties of negatively charged exciton states in the magnetic field range extending up to 20 T. PL was excited with a Ti-sapphire laser at energies below the band gap of the bar-

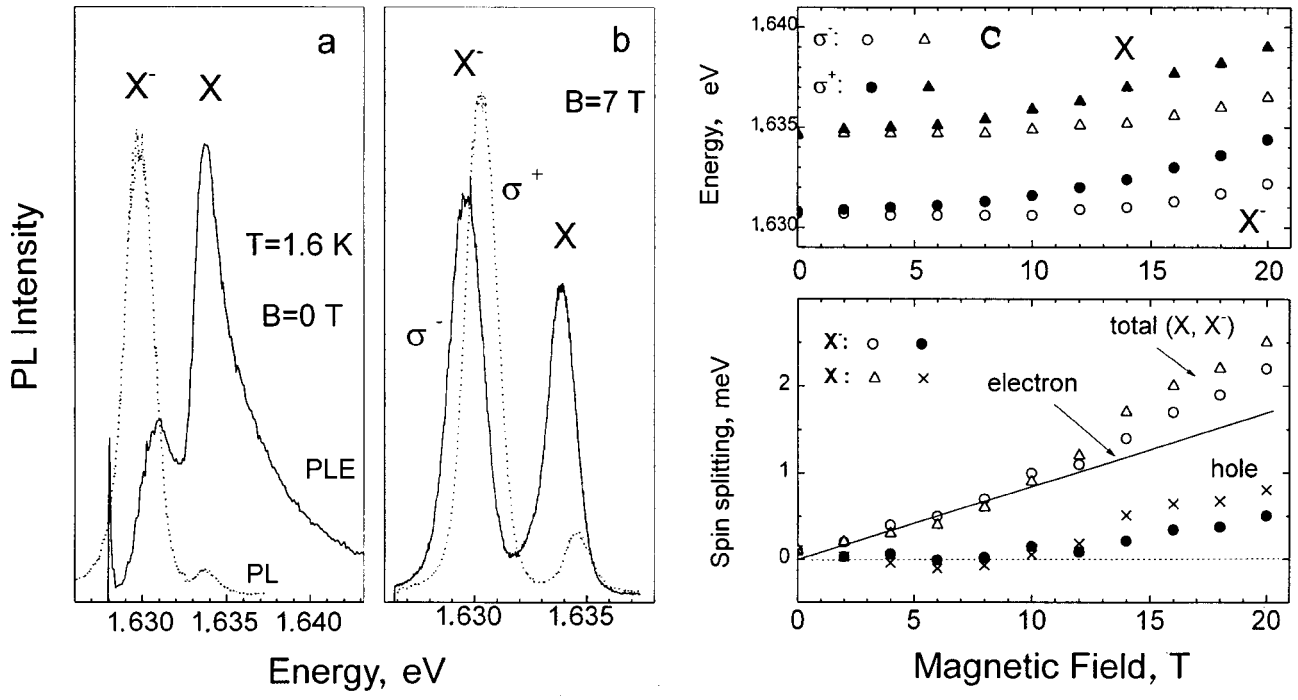

FIG. 1. a — Photoluminescence and PLE spectra of an 8 nm-thick CdTe/$Cd_{0.7}Mg_{0.3}$Te modulation-doped SQW structure. X and X^- label the heavy-hole exciton and the negatively charged exciton lines; b — PL spectra taken in the magnetic field of 7 T are shown for two circular polarizations σ^+ (dotted) and σ^- (solid) lines, respectively; c — magnetic field dependence of the PL line positions (upper panel) and the Zeeman splitting (lower panel). The electron-spin splitting calculated for $g_e=-1.46$ is plotted by a solid line. The heavy-hole splitting is calculated from the electron and the X and X^- splitting respectively. For details see text.

riers while the external magnetic fields were applied perpendicular to the QW layers (Faraday geometry).

In Fig. 1a the PL and PLE spectra detected for a 8 nm-thick CdTe/$Cd_{0.7}Mg_{0.3}$Te QW at a temperature of 1.6 K and at zero magnetic field are shown. The exciton line X dominates in the PLE spectrum but is much weaker than the negatively charged exciton line X^- in the PL spectrum, which reflects the strong probability for excitons to be bound in the X^- complex. This situation is changed under applied magnetic fields when the 2DEG is polarized (Fig. 1b). At 7 T the σ^- polarized PL component of the exciton line increases strongly in intensity and becomes comparable with the X^- line intensity. We also stress here that at 7 T the X and the X^- PL lines are polarized with opposite signs and for the X^- line the high energy component is stronger in intensity than the lower one. Detailed dependencies of X and X^- PL intensities on the magnetic field strength are plotted in the upper panel of Fig. 3 and will be discussed below.

For a detailed analysis of the observed PL polarization a precise knowledge about the spin splitting of the exciton and the free carrier states is essential first. The experimentally determined spin splittings for excitons and X^- are very close to each other (Fig. 1c, upper panel). The excitonic g factor has a positive sign (lower part of Fig. 1). The electron g factor at the bottom of the conduction band in an 8 nm-thick CdTe/$Cd_{0.7}Mg_{0.3}$Te QW ($g_e=-1.46$) is known with high accuracy.[4,8] The heavy-hole spin splitting was deduced by subtracting the electron splitting from the excitonic one. The hole splitting is zero at magnetic fields below 12 T and increases at higher fields giving rise to a positive g factor value. There is no significant difference observable whether the hole g factor is determined by the splitting of X or X^-. Schematically the spin splitting for 2DEG elecrons, excitons and X^- are presented in Fig. 2. Note that the X^- state is split due to the heavy-hole contribution only, but the spin splitting of the X^- optical transitions is also determined by the splitting of the conduction-band states (g_e), as the 2D electron is the final state after X^- recombination (for details see referance).[9]

The magnetic-field-induced polarization degree for X and X^- PL lines in QWs with and without 2DEG is displayed in the lower part of Fig. 3. In undoped QWs the X^-

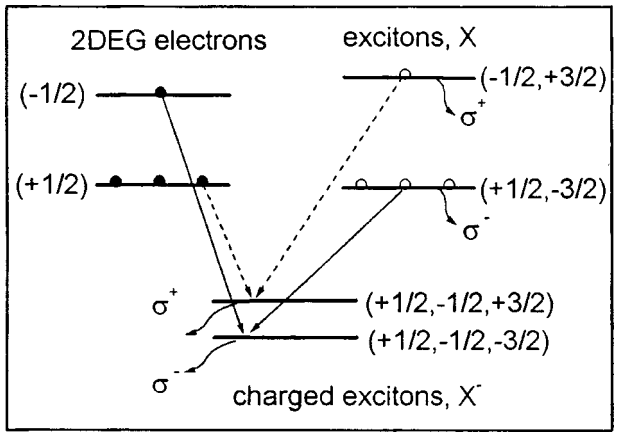

FIG. 2. Schematical presentation of an X^- formation process in external magnetic fields from excitons and 2DEG electrons.

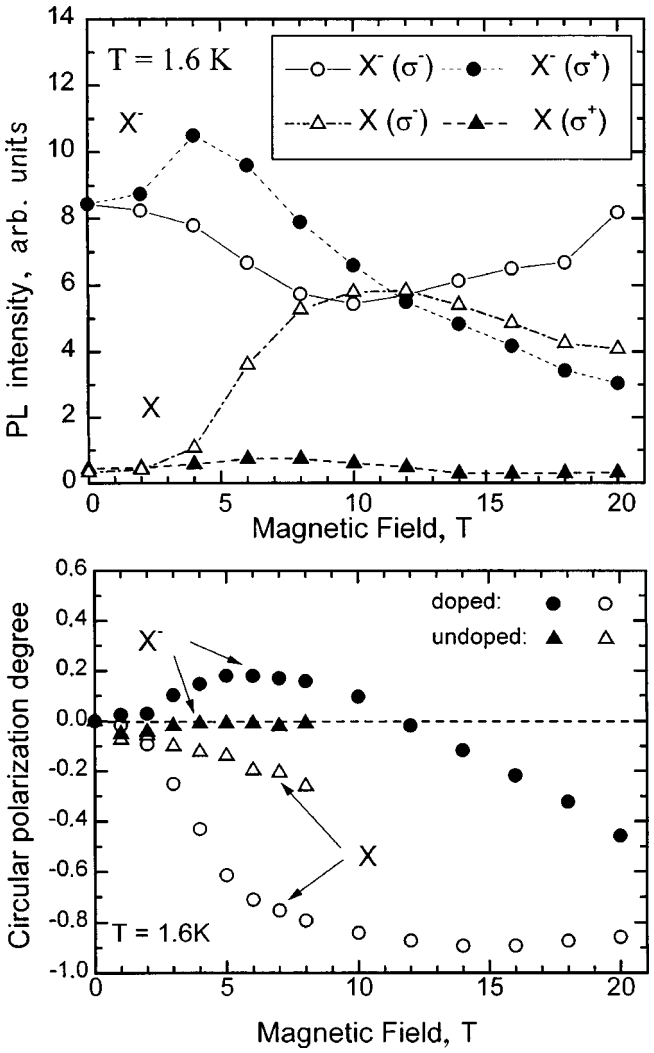

FIG. 3. Magnetic field variation of the PL line intensities detected for different circular polarizations for an 8 nm-thick $CdTe/Cd_{0.7}Mg_{0.3}Te$ modulation-doped QW (upper panel). Magnetic-field-induced circular polarization degree of the exciton and negatively charged exciton PL lines with (circles) and without (triangles) modulation doping (lower pannel).

line is unpolarized and the X line polarization increases linearly with a slope of $0.04T^{-1}$ only, which is considerably smaller than the thermal equilibrium value of $0.3T^{-1}$. In modulation-doped QWs the polarization degree of the X^- line is nonmonotonic and alters its sign at 12 T and the exciton line polarization is strongly enhanced. It is obvious that the presence of a strongly polarized 2DEG induces such strong modification. One can see in Fig. 2 that in magnetic fields the X^- formation process is limited to the creation of a $(+1/2, -1/2, +3/2)$ state constructed from a $(+1/2)$ electron and a $(-1/2, +3/2)$ exciton. The $(+1/2, -1/2, -3/2)$ X^- state is populated by relaxation from the $(+1/2, -1/2, +3/2)$ state. In magnetic fields below 12 T these states are not split and the state which contribute to the σ^+ polarized transition is preferably populated. At higher fields, when the state contributing to the σ^- polarized transition becomes the lowest one, its thermal occupation leads to the rise of the negative polarization. The exciton polarization under these conditions is determined by the X^- formation process: $(-1/2, +3/2)$ excitons are washed out for X^-, but $(+1/2, -3/2)$ excitons are preserved as the $(-1/2)$ electron states are empty. As a result the exciton PL increases strongly for the σ^- polarized component (see Fig. 3, upper panel).

2.2. The effect of microwave radiation on the trion

The formation process of the trion is also reflected in the PL spectra which are taken with and without additional microwave illumination. These experiments have been performed on an 8 nm-thick QW structures with optical tuning of the 2DEG density.[3,4] At $B=0$ T the microwaves decrease the X^- emission and increase the X emission, whereas at magnetic fields above 3 T the microwave radiation increase the X^- emission and decrease the X emission in σ^- polarization and have no obvious influence on X^- and X emission in σ^+ polarization. The ODMR (70 GHz) spectrum detected on X and X^- emission are shown in Fig. 4a for σ^- polarization and Fig. 4b for σ^+ polarization. The changes are normalized by their respective total intensities of X and X^- emission, and the positive and negative signs represent the increase and decrease of PL intensity, respectively. The maximal change is about 8% of the total intensities of X and X^- emission. With the increase of the magnetic field strength, the σ^- ODMR signals decline fast to zero and then change their signs, whereas the σ^+ ODMR signals decline slowly to zero. In σ^- polarization a sharp positive and negative ODMR line (at $B\approx 3.42$ T) appears respectively on the broad ODMR background signals detected on X^- and X emission. However, no sharp ODMR lines was observed in σ^+ polarization.

The details of the sharp ODMR lines are shown in the inset of Fig. 4a. For 70 GHz microwaves the resonant lines lie at $B_{res}=3.424$ T with the linewidth $\Delta B=39$ mT. From the resonant magnetic field strength for different microwave frequencies $g^*=-1.461\pm 0.002$ was obtained very precisely. We identify the sharp lines as the ODMR of the electrons of the 2D gas, whereas the broad background and the polarization dependence is determined by the formation process of X^-.

The scheme of the formation of X^- under magnetic field is shown in Fig. 2 where the g factor of the electron is negative and that of a heavy hole is very small for low fields and positive for higher field strength. The formation and the recombination of X^- from the optically active exciton can be written

$$e_{(-1/2)}+X_{(-1)}\rightarrow X^-_{(-3/2)}\rightarrow \text{photon}\,(\sigma^-)+e_{(-1/2)} \qquad (1)$$

$$e_{(+1/2)}+X_{(+1)}\rightarrow X^-_{(+3/2)}\rightarrow \text{photon}\,(\sigma^+)+e_{(+1/2)}\,. \qquad (2)$$

Under the applied excitation conditions in this structure, the electron density is estimated to be less than $4\times 10^{10}\,\text{cm}^{-2}$. Therefore, at the resonant magnetic field $B_{res}=3.424$ T and $T=1.6$ K all electrons lie in the $N=0$ Landau level and most of them populate the lower spin state $(+1/2)$ by thermalization because of the long lifetime ($\tau=2.7\,\mu$s) of the excess electrons.[3] In addition, the measured large exciton polarization (see Fig. 3b) shows that most excitons are populating the (-1) state.

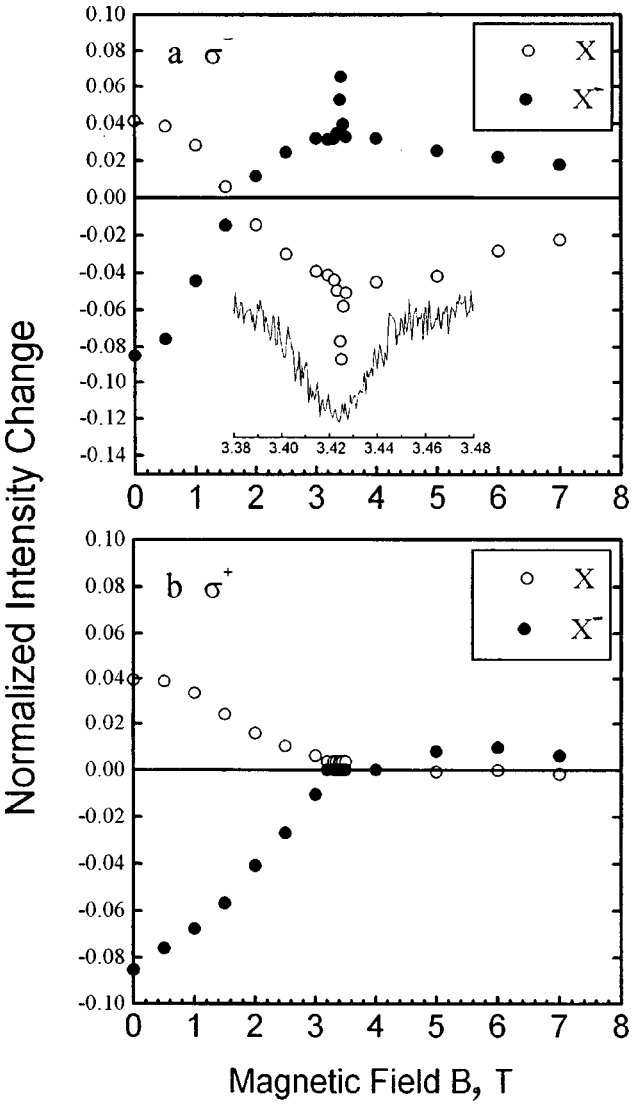

FIG. 4. ODMR (70 GHz) signals detected from an 8 nm thick $CdTe/Cd_{0.7}Mg_{0.3}Te$ QW with optical tuning of 2DEG density on X emission and X^- emission for (a) σ^- and (b) σ^+ polarization. The changes are normalized by the respective total intensities of X and X^- emissions. In σ^- polarization sharp ODMR lines were observed on the broad ODMR background signals. In the inset the sharp electron ODMR (70 GHz) line detected on X emission in σ^- polarization is shown. The resonance position lies at $B_{res}=3.424$ T with a linewidth $\Delta B=39$ mT.

For the σ^- polarized luminescence of the trion, there is a small electron population in the $(-1/2)$ state and a strong exciton population in the (-1) state. Microwave resonant absorption increases the electron population in the $(-1/2)$ state and enhances the formation probability of the $(-3/2)$ X^-. Therefore, we observed a positive electron ODMR signal detected on the X^- emission and simultaneously a negative electron ODMR signal detected on the X emission since the enhanced formation of X^- is in expense of X.

In σ^+ polarization, there exists a strong electron population in the $(+1/2)$ state and a small exciton population in the $(+1)$ state. The formation probability of the $(+3/2)$ X^- therefore in not sensitive to changes of the $(+1/2)$ electron population. Thus, the sharp electron ODMR line can not be observed for the $(-3/2)$ X^- in σ^+ polarization although the microwave resonant absorption induces a decrease of the $(+1/2)$ electron population.

The microwave radiation pumps electrons from the low spin state $(+1/2)$ to the upper spin state $(-1/2)$ continuously until the electrons reach a new steady population. The change of the electron population by the magnetic resonant absorption results in the change of the formation probability of X^-. This is the reason why the magnetic resonance of electrons can be detected in the X^- or the X emission.

From the descussion above, it is obvious that electron spin-dependent and the electron spin-conserving formation and recombination processes of X^- makes the electron ODMR detectable. This formation mechanism of X^- can be further supported by the broad ODMR background (at $B>3$ T) shown in Fig. 4a and 4b. Besides the microwave resonant absorption, the heating of electrons in the microwave field[10,11] also induced an increase in the $(-1/2)$ electron population and a decrease in the $(+1/2)$ electron population due to raising of the excess electron temperature.[12] This enhances the formation probability of the $(-3/2)$ X^- just as the resonance case discussed above. The broad background signals (at $B>3$ T) decrease with the magnetic field strength due to the suppression of the microwave heating by magnetic field.[13]

We could say that the above microwave heating effect is polarized since the background (at $B>3$ T) occur only in σ^- polarization. At low magnetic fields ($B<1$ T), where the two electron spin states have nearly the same population, another microwave heating effect occurs and we call it non-polarized because the background occurs in both circular polarizations. The increase of the electron kinetic energy by microwave heating decreases the probability for an exciton trapping an electron. This is in accord with the temperature experiments on X^-.[14] So we observed a decrease of X^- emission and an increase of X emission in both circular polarization at $B<1$ T shown in Figs. 4a and 4b.

In σ^- polarization, the polarized effect of the microwave heating plays the main role at high magnetic fields ($B>3$ T) and the non-polarized effect at low magnetic fields ($B<1$ T). For $1<B<3$ T, the two effects compete with each other, so the ODMR background signals decline fast to zero and change their signs with increasing magnetic field strength. In σ^+ polarization, only the non-polarized effect plays a role and the ODMR background signals decline slowly to zero due to the suppression of the microwave heating. Since the polarized ODMR background (at $B>3$ T) is due to the microwave heating of excess electrons while electrons which are bound to impurities can not be heated by microwaves, the ODMR measurements prove clearly the attribution of the PL line to X^- and not to an impurity bound exciton.

2.3. Trions formed with the light hole exciton

A fingerprint of X^- is the strong polarization of its resonance in external magnetic fields. When the excess electrons are strongly polarized by the external magnetic field, excitation of the X^- singlet state is allowed for one defined polarization only. In contrast to the CdTe/(Cd,Mg)Te structures

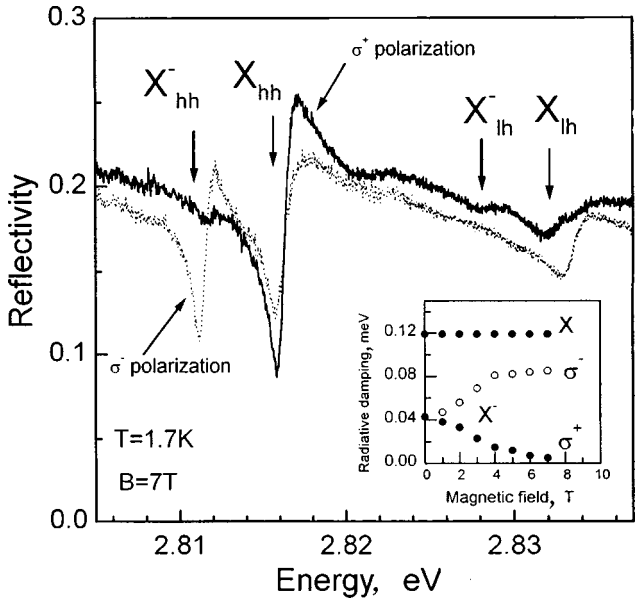

FIG. 5. Reflectivity spectra of a 10 nm $ZnSe/Zn_{0.89}Mg_{0.11}S_{0.18}Se_{0.82}$ quantum well at 1.6 K and 7 T for σ^+ (solid) and σ^- (dotted) lines. The insert shows the radiative damping (oscillator strength) for the exciton and the trion.

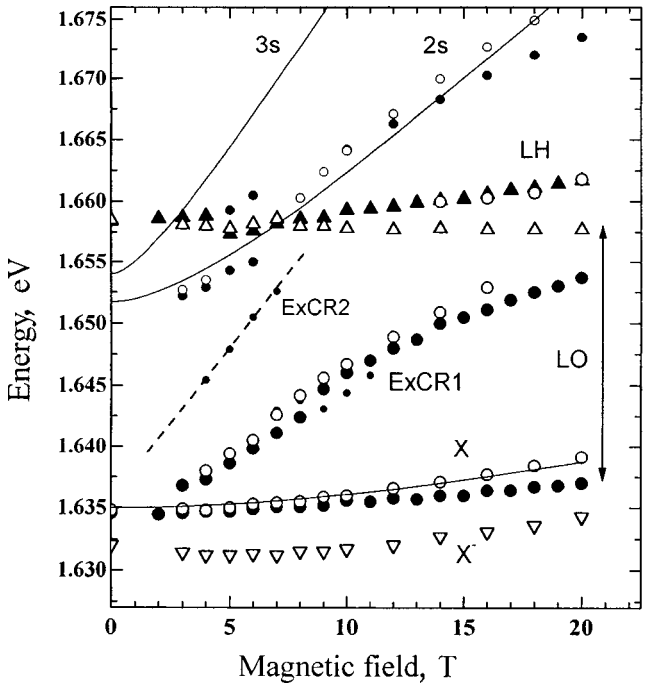

FIG. 6. Fan chart of an 8 nm $CdTe/Cd_{0.7}Mg_{0.3}Te$ quantum well. Open symbols represent σ^+ and closed symbols σ^- polarization respectively. The lines represent calculation for the exciton 1s, 2s, and 3s states applying the model described in Ref. 18.

discussed so far the g factor of the electron in ZnSe/(Zn,Mg)(S,Se) QWs is positive ($g_e = 1.1$). Therefore, the allowed transition for X^- formed with the heavy-hole exciton in these structures is the σ^- polarization, whereas σ^+ is the allowed polarization for the trion formed with the light-hole exciton. Such a behavior is demonstrated for a 10 nm $ZnSe/Zn_{0.89}Mg_{0.11}S_{0.18}Se_{0.82}$ QW with $n_e \approx 4\times 10^{10}\,\mathrm{cm}^{-2}$ in Fig. 5. The resonance indeed appears in opposite circular polarization of the reflected light. Furthermore, the binding energy of the trion can be determined from Fig. 5. At $B = 7$ T, the binding energy of X^- formed with the heavy-hole exciton is 4.6 meV, and 3.8 meV for X^- formed with the light-hole exciton.

We have fitted all experimentally observed resonances within a model of a nonlocal dielectric response.[15] In the insert of Fig. 5 we have plotted the dependencies of the exciton and trion radiative damping as a function of the magnetic field. It is obvious that the exciton radiative damping constant Γ_0 (i.e. the exciton oscillator strength) shows no dependence on the magnetic field strength for both circular polarizations. The trion oscillator strength, in contrast to the excitonic one, decrease with the magnetic field for the σ^+ polarization and increases for the σ^- polarization. This different behavior of Γ_0 for σ^+ and σ^- polarizations is due to the singlet structure of the trion ground state, where the two electrons involved have opposite spins. In the presence of a magnetic field the background electrons are polarized and the trions could be created by photons of one polarization only.

3. COMBINED EXCITON-CYCLOTRON RESONANCE

In external magnetic fields, besides the trion line, another new line appears in the PLE and reflectivity spectra, which can not be attributed to the normal magneto-exciton peaks. This line is attributed to a combined exciton-cyclotron resonance (ExCR) and is a supplementary example for new features observable in semiconductor quantum wells containing an electron gas of low density.[3] An incident photon creates an exciton in the ground state and simultaneously excites one of the resident electrons from the lowest to first (ExCR1) or to the second (ExCR2) Landau level. As can be seen from Fig. 6, the energy positions of these ExCR lines are in the range of the Coulomb-bound states, but they behave very differently. For instance, the intensity of the ExCR line increase strongly for larger n_e, whereas the magnetoexciton lines are insensitive to this parameter. Furthermore, Fig. 6 shows that the ExCR lines shift linearly in magnetic fields with a slope of 1.2 meV/T (ExCR1) or 2.9 meV/T (ExCR2), respectively, which is comparable to the electron cyclotron energies in CdTe/(Cd,Mg)Te QWs. An extrapolation of these shifts to zero field meets approximately the energy of the 1s state of the heavy-hole exciton ($1s-hh$). This linear shift of the ExCR lines, as opposed to the quadratic one of the heavy-hole excitons ($1s$, $2s$, and $3s$ states also displayed in Fig. 6), shows that the free electrons contribute to the observed process. Theoretically the shift of the ExCR lines in an external magnetic field behave like $N\cdot\hbar\omega_{c,e}(1+m_e/M)$, where m_e is the electron and $M = m_e + m_h$ is the exciton mass, $\hbar\omega_{c,e}$ is the cyclotron energy and N an integer (details of the theoretical consideration are in Ref. 3). Applying the experimentally obtained mass values $m_e = 0.11m_0$ and $m_{hh} = 0.48m_0$ gives 1.24 meV/T very close to the experimental value.

The ExCR line is strongly σ^- polarized, when the spin of the free electron gas is parallel to the free electron gas polarization in the external field direction. As a σ^- photon

creates an electron with the same spin orientation as the background electron. In this case the exciton angular momentum in the final state is (-1), and the recombination of such a photon is dipole allowed. On the other hand, a σ^+ polarized photon leads to a final state exciton with a magnetic moment of 2, whose recombination is dipole forbidden. Such excitons can recombine only after a spin flip of either the electron or the hole caused by scattering processes, and therefore their contribution to the PL intensity is much weaker.

In addition, it can be seen in Fig. 6 that for magnetic field above 11 T the ExCR1 line exhibits a strong bowing and splitting into two components. In this field range, the LO-phonon energy equals the cyclotron energy resulting in a resonant polaron coupling,[16] which can be established from the typical anticrossing behavior caused by the mixing of electron and phonon states. The observation of a resonant polaron coupling via the ExCR line also evidences the participation of $2D$ electrons in the ExCR process.

4. ADDITIONAL FEATURES CORRELATED WITH THE 2DEG

Besides the linear blue shift of the ExCR line observed in PLE and reflectivity, the PL spectra of QWs with an electron gas of low density exhibit lines that are correlated with shake-up processes.[17] We observed a series of low-energy satellites related to the excitation of the 2DEG.[5] In emission, the transition energy of the photon is lowered by energy conservation. The shake-up process excites, similarly to the ExCR mechanism, inter-Landau-level transitions giving rise to red-shifted PL lines with an energy separation from the trion energy of about $-N\hbar\omega_{c,e}$.

Besides all of the above-discussed elastic-scattering processes we would like to mention inelastic and spin-dependent scattering processes, where the photo-generated excitons lose their energy by scattering to an ortho-exciton state and the simultaneous excitation to an upper Zeeman sublevel. Details of these scattering processes are published elsewhere.[7]

The authors would like to thank T. Wojtowicz, G. Karczewski, and J. Nürnberger for providing the excellent structures. Without them these studies would not have been possible.

This work has been supported in part by the European Commission TMR program Access to Large Scale Facilities, contract ERB FMGE CT950079, the Volkswagen Foundation and the mutual grant of the Russian Fund for Fundamental Research and the Deutsche Forschungsgemeinschaft N 98-02-04089 and Os98/5.

[1] K. Kheng, R. T. Cox, Y. Merle d'Aubigne, F. Bassani, K. Saminadayar, and S. Tatarenko, Phys. Rev. Lett. **71**, 1752 (1993).
[2] D. R. Yakovlev, V. P. Kochereshko, W. Ossau, G. Landwehr, P. C. M. Christianen, J. C. Maan, T. Wojtowicz, G. Karczewski, and J. Kossut, *Proceedings of the 24th International Conference on the Physics of Semiconductors, Jerusalem (1998)*, in press.
[3] D. R. Yakovlev, V. P. Kochereshko, R. A. Suris, H. Schenk, W. Ossau, A. Waag, G. Landwehr, P. C. M. Christianen, and J. C. Maan, Phys. Rev. Lett. **79**, 3974 (1997).
[4] C. Y. Hu, W. Ossau, D. R. Yakovlev, G. Landwehr, T. Wojtowicz, G. Karczewski, and J. Kossut, Phys. Rev. B **58**, R1766 (1998).
[5] V. P. Kochereshko, D. R. Yakovlev, W. Ossau, G. Landwehr, T. Wojtowicz, G. Karczewski, and J. Kossut, J. Cryst. Growth **184/185**, 826 (1998).
[6] W. Ossau, V. P. Kochereshko, D. R. Yakovlev, R. A. Suris, D. Turchinovich, G. Landwehr, T. Wojtowicz, G. Karczewski, and J. Kossut, Phys. Low-Dimens. Semicond. Struct. **1/2**, 205 (1998).
[7] V. P. Kochereshko, D. R. Yakovlev, A. V. Platonov, W. Ossau, A. Waag, G. Landwehr, and R. T. Cox, *Proceedings of the 23rd International Conference on the Physics of Semiconductors, Berlin, Germany (1996)*, edited by M. Scheffler and R. Zimmermann, (World Scientific, Singapore, 1996) p.1943.
[8] A. A. Sirenko, T. Ruf, M. Cardona, D. R. Yakovlev, W. Ossau, A. Waag, and G. Landwehr, Phys. Rev. B **56**, 2114 (1997).
[9] K. Kheng, R. T. Cox, V. P. Kochereshko, K. Saminadayar, S. Tatarenko, F. Bassani, and A. Franciosi, Superlattices Microstruct. **15**, 253 (1994).
[10] R. Romestain and C. Weisbuch, Phys. Rev. Lett. **45**, 2067 (1980).
[11] B. C. Cavenett and E. J. Pakulis, Phys. Rev. B **32**, 8449 (1985).
[12] The electron Zeeman splitting energy, $\Delta E = 0.25$ meV at $B = 3$ T, is in the same range as the thermal energy $kT \approx 0.14$ meV at $T = 1.6$ K. This means that the electron population between two spin states is very sensitive to the electron temperature.
[13] K. Seeger, *Semiconductor Physics* (Springer-Verlag, Wien, 1973), Ch. 11.
[14] B. Kowalski, P. Omling, B. K. Meyer, D. M. Hofmann, C. Wetzel, V. Härle, F. Scholz, and P. Sobkowicz, Phys. Rev. B **49**, R14786 (1994).
[15] E. L. Ivchenko, A. V. Kavokin, V. P. Kochereshko, G. R. Pozina, I. N. Uraltsev, D. R. Yakovlev, R. N. Bichnell-Tassius, A. Waag, and G. Landwehr, Phys. Rev. B **46**, 7713 (1992).
[16] R. J. Nicholas, S. Sasaki, N. Miura, F. M. Peeters, J. M. Shi, G. Q. Hai, J. T. Devreese, M. J. Lawless, D. E. Ashenford, and B. Lunn, Phys. Rev. B **50**, 7596 (1994).
[17] K. J. Nash, M. S. Skolnick, M. K. Saker, S. J. Bass, Phys. Rev. Lett. **70**, 3115 (1993).
[18] N. A. Gippius, A. L. Yablonskii, A. B. Dzyubenko, S. G. Tikhodeev, L. V. Kulik, V. D. Kulakovskii, and A. Forchel, J. Appl. Phys. **83**, 5410 (1998).

Published in English in the original Russian journal. Reproduced here with stylistic changes by the Translation Editor.

Influence of disorder in compensation-doped germanium on the critical indices of the metal-insulator transition

Rolf Rentzsch*) and Ch. Reich

Freie Universität Berlin, FB Physik, WE I, Institut für Ex-physik, 14195 Berlin, Germany

A. N. Ionov

A. F. Ioffe Physicotechnical Institute, Russian Academy of Sciences, 194021 St. Petersburg, Russia

V. Ginodman and I. Shlimak

The Resnick and Pearl Inst. Bar-Ilan University, Dept. of Physics, Ramat-Gan, Israel

P. Fozooni and M. J. Lea

Department of Physics, Royal Holloway University of London, Egham, Surrey, UK
Fiz. Tverd. Tela (St. Petersburg) **41**, 837–840 (May 1999)

We present a critical review of the present state of the critical exponent puzzle of the metal-insulator transition of doped semiconductors with emphasis on the role of meso- and macroscopic inhomogeneity caused by the disorder of intended or unintended acceptors and donors in crystals. By using both isotopic engineering and neutron transmutation doping (NTD) of germanium we found for low compensations (at $K=1.4$ and 12%) that the critical exponents of the localization length and the dielectric constant are nearly $\nu=1/2$ and $\zeta=1$, which double for medium compensations (at $K=38$ and 54%) to $\nu=1$ and $\zeta=2$, respectively.
 [S1063-7834(99)01905-X]

Until now there has been an intensive debate in the literature whether the metal-insulator transition (MIT) is a phase transition of first or second order and what the experimental conditions are to obtain it at finite temperatures and in real (disordered) systems.[1,2] If the MIT is a second-order phase transition, a further challenge is the puzzle of the critical index μ for the scaling behavior of the metallic conductivity near the MIT, i.e. just above the critical impurity concentration N_c and as small compensation K.[2–14] In particular, in several uncompensated materials (Si:P [Refs. 2–4], Si:As [Refs. 5,6], Ge:As [Refs. 7,8]) some experimental groups obtained $\mu\approx 1/2$, others obtained $\mu\geqslant 1$ (Si:P, [Ref. 13] Ge:As and Ge:Ga),[14] which also has been found in different compensated material.[9–12] On the other, hand the value of $\mu\approx 1/2$ is significantly smaller than $\mu=1$ to 1.3 predicted theoretically for an Anderson transition driven only by disorder[15–20] and also less than Chayes *et al.*[21] inequality $\mu>2/3$ for a MIT caused by both disorder and electron–electron interactions.

The main uncertainty in all previous experimental work is whether the impurities, for instance, the donors at *n*-type conductors, are distributed macroscopically homogeneously during doping or not and whether, during any chemical doping, an unintended disorder via compensation by (background) acceptors or defects is present or not. The disorder in doped semiconductors arises mainly from the intended or unintended compensation K which is, for *n*-type material, $K=N_a/N_d$, as well as from correlated incorporation of donors and acceptors from melt-grown crystals and macroscopic inhomogeneity in the impurity distribution. To avoid these uncertainties, we have prepared four sets of germanium samples which were both isotopically engineered and neutron-transmutation doped. The crystals have in this case a well controlled disorder from the compensation by the isotopic enrichment of ^{74}Ge ($K=0.014$, 0.12, 0.38 and 0.54 for *n*-type conductivity) and of a mesoscopically as well as macroscopically homogeneous distribution of the impurities with N near N_c. In the case of low compensations, we got samples on both sides of the MIT.

1. SAMPLE PREPARATION

Isotopically engineered, bulk Ge crystals were grown from pure ^{74}Ge, enriched up to 94%, or by a mixture of ^{74}Ge with Ge of natural isotopic content. The isotopes ^{74}Ge and ^{70}Ge transmute after irradiation by thermal neutrons to ^{75}As donors and ^{71}Ge acceptors. The four series of *n*-type Ge with different isotopic abundance (in %) and different K after NTD are listed in Table I. The values of K are proportional to the product of the isotopic abundance and the thermal neutron cross-sections of all isotopes producing impurities, $K\cong N_{\mathrm{Ga}}/N_{\mathrm{As}}$, whereas the impurity concentration is proportional to the irradiation dose.

2. RESULTS AND DISCUSSION

All samples with $N<N_c$ at $T<1$ K exhibited a temperature dependence of resistivity according to

$$\rho(T)=\rho_0\exp(T_0/T)^{1/2}. \tag{1}$$

Equation (1) corresponds to variable-range hopping conductivity with a Coulomb gap at the Fermi level[22] and with

TABLE I. Isotopic abundance in the four series of NTD Ge after mass-spectroscopic analysis, compensation degree, conduction type and critical impurity concentration (see text).

Isotope	^{70}Ge	^{72}Ge	^{73}Ge	^{74}Ge	^{75}Ge	K (%)	Type	N_c (cm^{-3})
Series 1	0.2	0.7	3.2	93.8	2.1	1.4	n	3.5×10^{17}
Series 2	1.7	2.4	1.0	93.9	1.0	12	n	4.0×10^{17}
Series 3	5.0	6.5	2.4	82.8	3.3	38	n	7.1×10^{17}
Series 4	8.1	11.2	ca.4	72.3	ca.4	54	n	1.5×10^{18}

$$T_0 = 2.8e^2/a\kappa, \tag{2}$$

where a is the localization length and κ is the dielectric constant. Figures 1 and 2 show typical dependencies of the resistivity on temperature for low ($K=1.4$ and 12%) and medium ($K=38\%$) disorder. One can see that Eq. (1) is fulfilled at low temperatures for all impurity concentrations where variable-rangle hopping is obtained. According to scaling theory of the MIT, both a and κ diverge at the MIT with power laws[2,15]

$$a = C_1 a_B |(N/N_c) - 1|^{-\nu}, \tag{3a}$$

$$\kappa = C_2 \kappa_0 |(N/N_c) - 1|^{-\zeta}, \tag{3b}$$

with $\zeta/\nu = 2$, in Eq. (3a,b) $a_B \cong 4$ nm is the Bohr radius of the Arsenic donor, $\kappa_0 \cong 15.2$ is the static dielectric constant and C_1 and C_2 are constants. As the result, the slope of the curves in Figs. 1 and 2, i.e., T_0 must decrease with a power $p = \zeta + \nu$ approaching $T_0 = 0$ at $N \cong N_c$. Figure 3 shows T_0 as function of $N_d = n/(1-K)$ for different K, where n is the free-carrier concentration. The linear extrapolation of the curves in Fig. 3. gives us the value of N_c which rapidly increases with K. The scaling relation of T_0 versus $|(N/N_c) - 1|$ at different K are shown in Fig. 4. At low disorder ($K = 1.4$ and 12%) the power p is close to the value of 3/2 and doubles at medium disorder ($K = 38$ and 54%) to a value of about 3. Taking into account $\zeta/\nu = 2$, one obtains $\nu \cong 1/2$ and 1, and $\zeta \cong 1$ and 2, at low and medium K respectively. The values of $a(K)$ can be independently determined from measurements of the positive magnetoresistance. In all samples at $T < 0.5$ and at $B = 0.5 - 2$ T the positive magnetoresistance was found[23] to fulfill the theory in Ref. 22:

$$\ln(\rho(B)/\rho(0)) = +(e^2/\alpha h^2)\, a^4 (B^2/T^{3/2}) = +B^2/B_0(a,T)^2, \tag{4}$$

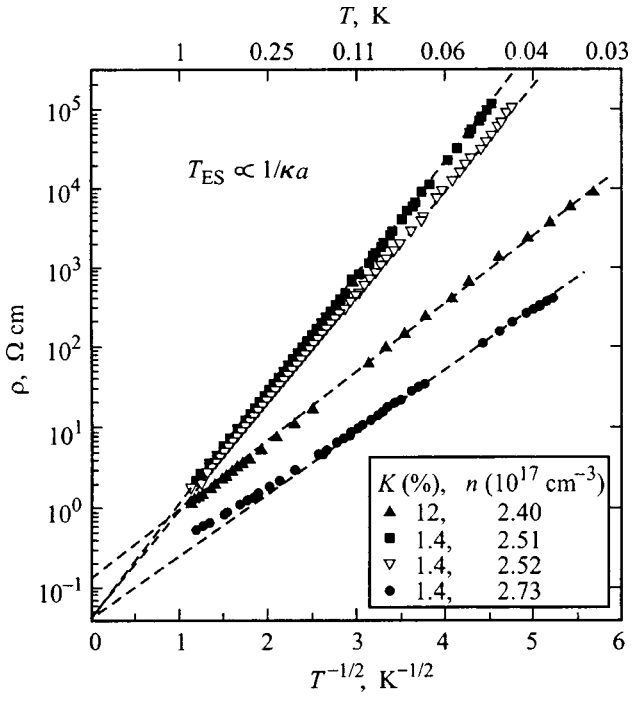

FIG. 1. Temperature dependence of resistivity at low compensation, $K = 0.014$, 0.12.

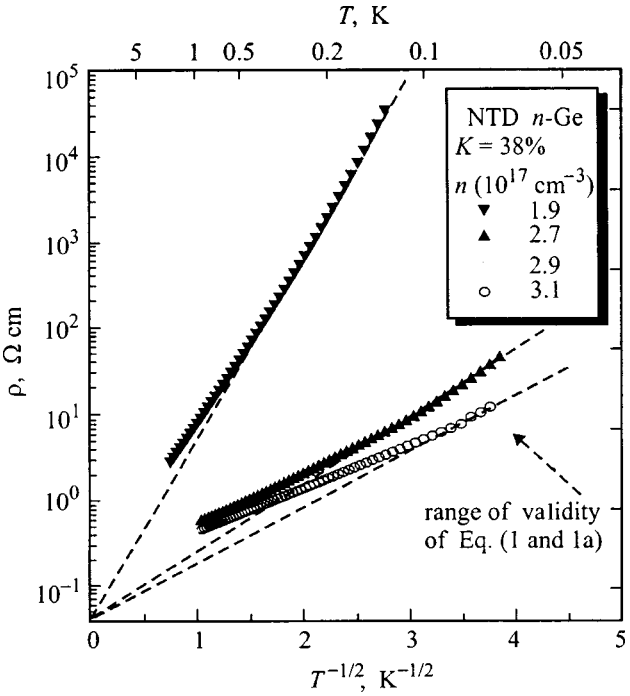

FIG. 2. Temperature dependence of resistivity at medium compensation, $K = 0.38$.

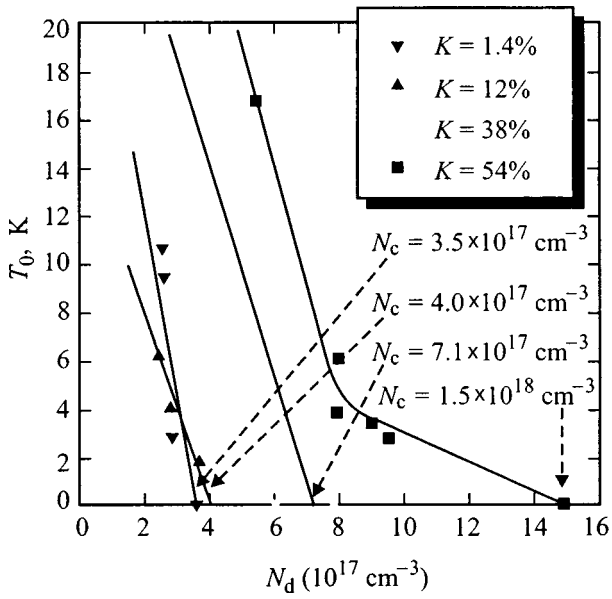

FIG. 3. Determination of N_c at $T_0 \to 0$.

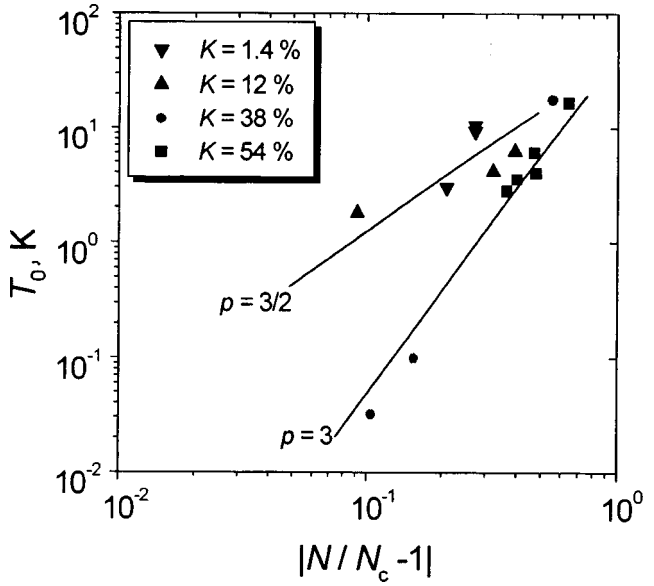

FIG. 4. T_0 vs $|(N/N_c)-1|$ at different K.

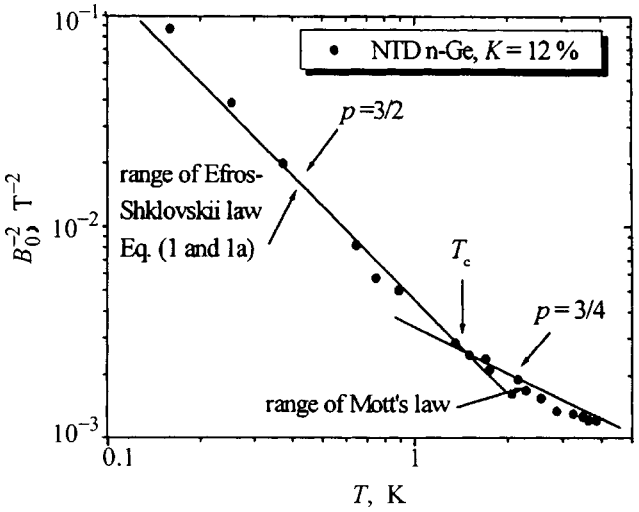

FIG. 6. Temperature dependence of the positive hopping magnetoresistance. The upper straight line shows the range of validity of Eq. (4).

where $\alpha\cong 660$ is a numerical coefficient. Figure 5 shows the typical dependence of the hopping magnetoresistance, which confirms the appearance of quadratic dependence on a low magnetic field in all samples. The analysis of the temperature dependence according to Eq. (4) is shown in Fig. 6 indicating the range of validity at about $T=0.2-1.5$ K for this sample. From Eq. (4) we calculated $a(K)$ of all samples. By a combination of $T_0 \propto (a\kappa)^{-1}$ of the temperature dependence of resistivity without magnetic field by using Eqs. (1 and 2) we also estimated $\kappa(K)$. Both dependencies as functions of $|(N/N_c)-1|$ are shown in Figs. 7 and 8, confirming the above estimates for the slopes $\nu\cong 1/2$ and 1, and $\zeta\cong 1$ and 2 for the scaling behavior of a and κ, at low and medium K respectively.

From the experimental point of view the puzzle of the critical indices has been solved by well-controlled disorder via the compensation degree and homogeneous doping by a combination of artificially changed isotopic content (isotopic engineering) and NTD which give rise to mesoscopic and macroscopic homogeneity. The determination of N_c from the extrapolation of $T_0(N)\rightarrow 0$ at Efros–Shklovskii variable-range hopping agrees well with N_c from the metallic side.

For low disorder (at $K=1.4$ and 12%), the critical exponents of the localization length and the dielectric constant are nearly $\nu=1/2$ and $\zeta=1$, respectively. The value of $\nu=\mu$ at low disorder agree well with early Si : P (Ref. 2) and Ge : As (Ref. 6) as well as with recent results on uncompensated NTD Ge : Ga (Ref. 8) results. At medium desorder (at $K=38$ and 54%), the critical indices double to $\nu=1$ and $\zeta=2$, respectively. These results accord with results on different chemically doped material Si : P (Ref. 13) and Ge : As/Ga (Ref. 14) where the crystal homogeneity could be less. Additionally, some disorder by unintended compensation or correlated impurity distribution is possible.[11] However, the disparity of the critical indices between theory and experiment remains unresolved because, to our knowledge, until

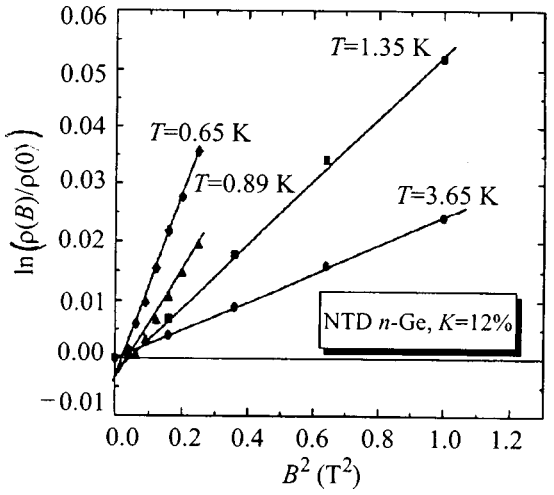

FIG. 5. Typical dependence of the hopping magnetoresistance on B^2.

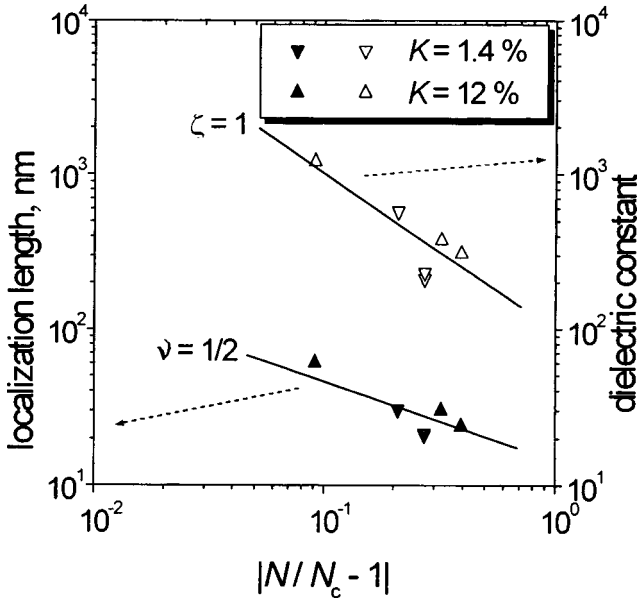

FIG. 7. a and κ vs $|(N/N_c)-1|$ at low K.

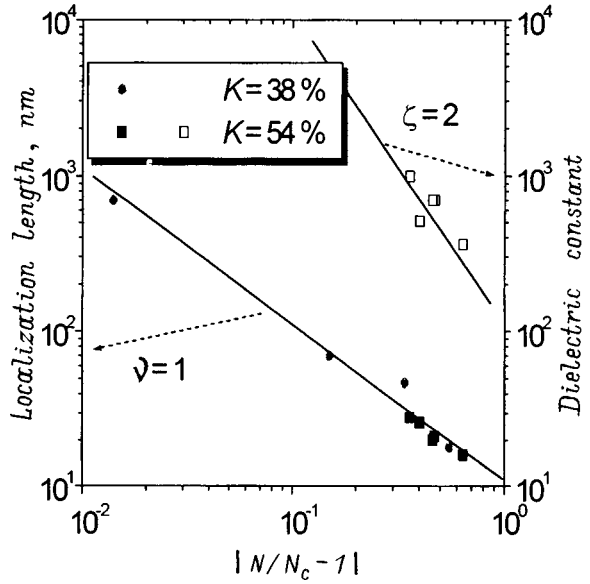

FIG. 8. a and κ vs $|(N/N_c)-1|$ at medium K.

now there is no unique theory taking into accounts both disorder and strong electron–electron interaction.

We thank Dr. M. Lyubalin for the crystal growth of isotopic engineered undoped material, Drs. I. M. Lazebnik, W. Gatschke, and D. Gawlik for the neutron irradiation of the samples, Dr. V. Karataev for the mass-spectroscopic analysis of the isotopic abundance, M. Mueller, R. Ullrich and V. Zarygina for the crystal preparation.

This work was only possible by financial support of the RFFI (Grant N 97-02-18280), INTAS Grant (93-1555/Ext.), German–Israeli Foundation (Grant N I-0319-199.07) and the British–German Foundation (Grant N 313/ARC 93-97).

*)E-mail: rentzsch@physik.fu-berlin.de

[1] See for a review A. Moebius *et al.*, Phys. Rev. B (1998), to be published.

[2] R. F. Milligan, T. F. Rosenbaum, R. N. Bhatt, and G. A. Thomas, in *Electron–Electron Interactions in Disordered Systems*, edited by A. L. Efros and M. Pollak, Modern Problems in Condensed Matter Sciences, Volume 10, (Elsevier Science, North Holland, 1985), p. 231.
[3] T. F. Rosenbaum, K. Andres, G. A. Thomas, and R. N. Bhatt, Phys. Rev. Lett. **45**, 1723 (1982); M. A. Paalanen, T. F. Rosenbaum, G. A. Thomas, and R. N. Bhatt, Phys. Rev. Lett. **48**, 1284 (1982).
[4] P. F. Newman and D. F. Holcomb, Phys. Rev. B **28**, 638 (1983).
[5] W. N. Shafarman, D. W. Koon, and T. G. Castner, Phys. Rev. B **40**, 1216 (1989).
[6] A. N. Ionov, M. J. Lea, and R. Rentzsch, Pis'ma Zh. Éksp. Teor. Fiz. **54**, 470 (1989) [JETP Lett. **54**, 473 (1991)].
[7] P. Dai, Y. Zhang and M. P. Sarachik, Phys. Rev. Lett. **66**, 1914 (1991).
[8] K. M. Itoh, E. E. Haller, J. W. Hansen, J. Emes, L. A. Reichertz, E. Kreysa, T. Shutt, A. Cummings, W. Stockwell, B. Sadoulet, J. Muto, J. W. Farmer, and V. I. Ozhogin, Phys. Rev. Lett. **77**, 4058 (1996).
[9] G. Hertel, D. J. Bishop, E. G. Spencer, J. M. Rowell, and R. C. Dynes, Phys. Rev. Lett. **50**, 743 (1983).
[10] M. Yamaguchi, N. Nishida, T. Furubayashi, K. Morigaki, H. Ishimoto, and K. Ono, Physica B **118**, 694 (1983).
[11] R. Rentzsch, K. J. Friedland, A. N. Ionov, M. N. Matveev, I. S. Shlimak, C. Gladun, and H. Vinzelberg, Phys. Status Solidi B **137**, 691 (1986); R. Rentzsch, K. J. Friedland, and A. N. Ionov, Phys. Status Solidi B **146**, 199 (1988).
[12] M. Rohde and H. Micklitz, Phys. Rev. B **36**, 7572 (1987).
[13] H. Strupp, M. Hornung, M. Lackner, O. Madel, and H. V. Loehneysen, Phys. Rev. Lett. **71**, 2634 (1993).
[14] I. Shlimak, M. Kaveh, R. Ussyshkin, V. Ginodman, and L. Resnick, Phys. Rev. Lett. **77**, 1103 (1996).
[15] E. Abrahams, P. W. Anderson, D. C. Licciardello, and T. V. Ramakrishnan, Phys. Rev. Lett. **42**, 673 (1979).
[16] A. MacKinnon and B. Kramer, Phys. Rev. Lett. **47**, 1546 (1981).
[17] T. Ohtsuki, B. Kramer, and Y. Ono, Solid State Commun. **81**, 477 (1992).
[18] M. Henneke, B. Kramer, and T. Ohtsuki, Europhys. Lett. **27**, 389 (1994).
[19] E. Hofstetter and M. Schreiber, Phys. Rev. Lett. **73**, 3137 (1994).
[20] T. Kawabayashi, T. Ohtsuki, K. Slevin, and Y. Ono, Phys. Rev. Lett. **77**, 3593 (1996).
[21] J. Chayes, L. Chayes, D. S. Fisher, and T. Spencer, Phys. Rev. Lett. **54**, 2375 (1986).
[22] A. L. Efros and B. I. Shklovskii, in *Electronic Properties of Doped Semiconductors*. (Springer–Verlag, Berlin, 1984), pp. 240, 211.
[23] R. Rentzsch, A. N. Ionov, Ch. Reich, M. Müller, B. Sandow, P. Fozooni, M. J. Lea, V. Ginodman, and I. Shlimak, Phys. Status Solidi B **205**, 269 (1998); R. Rentzsch, Ch. Reich, A. N. Ionov, P. Fozooni, and M. J. Lea, *Proceedings of the 24th International Conference on the Physics of Semiconductors ICPS–24. Jerusalem (1998).*

Published in English in the original Russian journal. Reproduced here with stylistic changes by the Translation Editor.

Emission processes accompanying deformation and fracture of metals

K. B. Abramova,*) I. P. Shcherbakov, A. I. Rusakov, and A. A. Semenov

A. F. Ioffe Physicotechnical Institute, Russian Academy of Sciences, 194021 St. Petersburg, Russia
Fiz. Tverd. Tela (St. Petersburg) **41**, 841–843 (May 1999)

Present-day physical methods of investigation reveal that the fracture and plastic deformation of metals is accompanied by emission processes, in particular, by luminescence and emission of electrons. All the metals studied thus far exhibit a capability of luminescence. The intensity, duration, and spectrum of mechanoluminescence are different for different metals. The intensity is determined by the mechanical and thermal characteristics. For a given metal, the intensity depends on dislocation density in the structure and the sample loading rate. The spectrum of noble metals is governed by the electronic structure of surface states. The dynamics of mechanoluminescence and electron emission (exoemission) depends on the rate of stress variation in the sample under study. This permits one to consider the mechanoluminescence and exoemission not only as physical characteristics but also as a potential tool for probing surface states in metals and the kinetics of emergence of mobile dislocations on the surface with a high time resolution. [S1063-7834(99)02005-5]

Deformation and fracture of all solids, including insulators, semiconductors, and metals, excites in them a number of nonequilibrium processes, such as electron and ion emission, emission of light (mechanoluminescence), generation of sound, electromagnetic radiation in the rf range, and even x-rays.[1–7] In metals, these processes have been studied least of all, but experimental observations have been accumulated, and their interpretation suggested. The mechanism proposed to account for the mechanoluminescence in metals is as follows.[8,9] In the course of fracture, plastic zones with a high dislocation density form at the crack tip. Unloading the sample results in a dislocation-assisted relief of the strained layer associated with annihilation of pairs of dislocations of opposite sign and emergence of mobile dislocation on the surface. Real dislocations in a metal have a complex structure, which makes their total annihilation hardly probable. In each dislocation reaction, only separate parallel sections can annihilate. The annihilation of such sections is accompanied by liberation of a considerable energy, which may be as high as a few eV per interatomic distance along the axis. Annihilation of dislocations in noble metals may give rise to term crossing of the inner *d* electrons localized in the dislocation core region with free *s-p* band states. The nonadiabatic transitions originating in such a crossing produce holes in quasilocal *d* states near the dislocations, which form in dislocation reactions. It thus follows that the luminescence intensity should be connected with the dislocation concentration in the near-surface strained layer, and its dynamics, with that of dislocation motion or stresses.

To verify the existence of such relations experimentally, we used samples with initially different microstructure, i.e. different dislocation densities, and two different methods of sample deformation, namely (i) illumination with a laser pulse of a preset and high enough pulse energy and (ii) passing an electric current pulse, likewise with a preset and sufficiently high energy.

When irradiating a sample with laser pulses, one usually studies the attendant processes initiated directly in the illuminated spot and around it. At the same time the parts of the target which were not acted upon directly by the radiation are also subject to the stresses propagating outward from the spot. Using a laser pulse for investigating the emission phenomena induced on the back side of the target appears both experimentally appropriate and informative. The interaction of a laser pulse with the surface of a metallic target within a broad energy range, including pulse energies below the spallation threshold, was studied, in particular, in Refs. 10 and 11. One can calculate with a good enough accuracy and in absolute units the temporal and spatial distribution of temperature and stresses in the irradiated target and compare them with the onset of luminescence and exoemission pulses induced on its back side, find the minimum stresses generating the luminescence and exoemission, and verify or establish the correlation between the stresses and emission.[12]

Correlation of the stresses and temperatures, as well as of their temporal and spatial distributions with the evolution in time of the emission of photons (mechanoluminescence) and electrons (exoemission) in the samples where they were detected from their back side permits one to draw the following conclusions: (i) the dynamics of the emission processes are connected with that of the stresses, namely, the higher the stress variation rate, the higher is the intensity of the mechanoluminescence and exoemission, and (ii) mechanoluminescence and exoemission are initiated in the stage where the stresses in a sample are close to the material yield point.

The experimentally found[13] dependence of the intensity of mechanoluminescence on the original sample microstructure provides support for its dislocation mechanism. At the same time one measured and compared only the time-integrated radiation. No spectral measurements were attempted because of the low intensity of the radiation. To support the main points underlying the dislocation model, it would be important to check whether the mechanolumines-

cence spectrum does indeed depend on the original microstructure of a sample.

The process of deformation and fracture of a conductor through which a large current is passed is accompanied by a bright light flash.[14] The emission spectrum contains a number of lines and bands, i.e. it carries a large amount of information on the system and dynamics of electronic levels of a metallic sample, both of the metal itself and of its constituent atoms. A study was made of the emission spectrum excited in the fracture of copper conductors.[15,16] The observed emission bands were identified. It was established, in particular, that the excitation produced by energetic electrons which are generated in the fracture induced by a heavy current is accompanied by a luminescence associated with the fracture process itself.

In the experiments described in the present paper, copper conductors with originally differing microstructure were fractured by passing through them an electric current with a density of $(0.7–1.0)\times 10^7$ A/cm^2. The conductors were dia. 0.5 mm, 70-cm long sections of technical-grade M0 copper wire. The energy was provided by a 400-μF capacitor bank charged to 1.5 kV. The loading rate was $V=1\times 10^3$ m/s, and the pulse duration $t=20\,\mu$s. The radiation under study was focused onto the entrance slit of a diffraction-grating spectrometer; in its focal plane was mounted an FPP31L ccd-based scanner, whose output was fed through an ADC into a computer. This arrangement permitted measurement of the spectral characteristics of radiation flashes produced in the fracture of a sample within the 5400–8100-Å interval with a resolution of 6 Å.

The continuous emission spectrum accompanying MHD fracture of copper had been measured previously within a broader range (4500–9000 Å). The measurements were performed, however, only at 20 points in this spectral range, and to obtain an average intensity, ten samples had to be fractured at each point.

The present measurements have been carried out in more detail and on a radically improved level. First, the complete emission spectrum was measured in one experiment. Second, the measurements were performed at 500 points in the 5400–8100-Å range. Third, one measured not only the continuous but the line spectrum as well. This permitted one to improve the precision and reliability of the results obtained.

It is known that dislocations lying in the same slip plane but having oppositely directed Burgers vectors annihilate on contact. If such dislocations lie in different slip planes, their annihilation requires previous creep. Annealing favors creep of the dislocations and in this way reduces their concentration. Microphotographs of samples before and after annealing were obtained and presented in Ref. 13.

A comparison of the spectra of annealed and unannealed copper samples showed that the cathodoluminescence and photoluminescence bands of copper are actually replicas of one another.[16] This is apparently due to the fact that they are produced by excitation of bulk states, which undergo only small changes in the course of annealing. In other intervals the spectra differ in intensity, which implies changes in the relative intensity of luminescence bands of different nature. The spectral interval discussed in the present work relates to the mechanoluminescence band. As expected, the mechanoluminescence band intensity generated in the fracture of an annealed sample was found to be weaker than that of the unannealed one. These observations provide supportive evidence for the dislocation mechanism of mechanoluminescence; indeed, annealing produced a decrease of dislocation concentration and a weaker intensity of the band associated with excitation of hole states in the nonadiabatic transitions which are initiated at the annihilation of dislocations and at their emergence on the surface.

An analysis of the spectra of the emission generated in the fracture of conductors by a large-density current permits the following conclusions: (1) The annealing-induced change of the microstructure reduces the excitation probability of the surface electronic states responsible for the mechanoluminescence band, and (2) The annealing-induced change of the microstructure does not affect the bulk electronic states responsible for the cathodoluminescence and photoluminescence bands.

Thus the results obtained in all the above experiments support the dislocation mechanism of mechanoluminescence and give one grounds to assume a similar nature of the electron exoemission observed to occur in plastic deformation of metals.

Support of the Russian Fund for Fundamental Research (Grant 97-02-18097) and of the Integration Project (Grant K0854) is gratefully acknowledged.

*)E-mail: abramova.mhd@pop.ioffe.rssi.ru

[1] N. A. Krotova and V. V. Karasev, Dokl. Akad. Nauk SSSR **92**, 607 (1953).
[2] N. R. Valuev, V. I. Eremenko, N. N. Nikonenkov, and A. A. Tupik, Pis'ma Zh. Tekh. Fiz. **11**, 401 (1985) [Tech. Phys. Lett. **11**, 165 (1985)].
[3] O. V. Gusev, *Acoustic Emission Generated in Deformation of Refractory Metals* [in Russian] (Nauka, Moscow, 1982).
[4] K. B. Abramova and I. P. Shcherbakov, Zh. Tekh. Fiz. **64**, No. 9, 76 (1994) [Tech. Phys. **39**, 901 (1994)].
[5] A. J. Walton, Adv. Phys. **26**, 887 (1977).
[6] V. A. Klyuev, A. G. Lipson, Yu. P. Toporov, A. D. Aliev, and A. E. Chalykh, Pis'ma Zh. Tekh. Fiz. **10**, 1135 (1984) [Tech. Phys. Lett. **10**, 480 (1984)].
[7] T. Ya. Gorazdovskiĭ, JETP Lett. **5**, 64 (1967).
[8] M. I. Molotskiĭ, Fiz. Tverd. Tela (Leningrad) **20**, 1651 (1978) [Sov. Phys. Solid State **20**, 956 (1978)].
[9] M. I. Molotskii, Chem. Rev. **13**, Pt. 3, 1 (1989).
[10] S. I. Anisimov, Ya. O. Imas, P. S. Solonov, and Yu. V. Khodyko, *Effect of High-Power Radiation on Metals* [in Russian] (Nauka, Moscow, 1970).
[11] J. F. Ready, *Effets of High-Power Laser Radiation* (Academic Press, Orlando, 1971; Mir, Moscow, 1974).
[12] K. B. Abramova, A. I. Rusakov, A. A. Semenov, and I. P. Shcherbakov, Fiz. Tverd. Tela (St. Petersburg) **40**, 957 (1998) [Phys. Solid State **40**, 877 (1998)].
[13] K. B. Abramova, I. P. Shcherbakov, I. Ya. Pukhonto, and A. M. Kondyrev, Zh. Tekh. Fiz. **66**, No. 5, 190 (1996) [Tech. Phys. **41**, 511 (1996)].
[14] K. B. Abramova and B. P. Peregud, Zh. Tekh. Fiz. **41**, 2216 (1971) [Sov. Phys. Tech. Phys. **16**, 1758 (1971)].
[15] K. B. Abramova, B. P. Peregud, Yu. N. Perunov, V. A. Reĭngol'd, and I. P. Shcherbakov, Opt. Spektrosk. **58**, 809 (1985) [Opt. Spectrosc. **58**, 496 (1985)].
[16] M. I. Molotskiĭ and B. P. Peregud, Zh. Tekh. Fiz. **51**, 618 (1981) [Sov. Phys. Tech. Phys. **26**, 369 (1981)].

Translated by G. Skrebtsov

Quasielastic light scattering in the near IR from photoexcited electron-hole plasma created in a GaAs layer with embedded InAs quantum dots

B. Kh. Baĭramov, V. A. Voĭtenko, B. P. Zakharchenya, V. V. Toporov

A. F. Ioffe Physicotechnical Institute, Russian Academy of Sciences, 194021 St. Petersburg, Russia

M. Henini and A. J. Kent

Department of Physics, University of Nottingham, Nottingham, NG7 2RD, UK
Fiz. Tverd. Tela (St. Petersburg) **41**, 844–847 (May 1999)

The paper reports the development of a high-sensitivity technique for measurement of inelastic electronic light-scattering spectra in the near-IR region, which are excited by a stable single-mode cw YAG:Nd laser operating at 1064.4-nm. This technique has permitted detection for the first time of quasielastic scattering of light by a photoexcited electron-hole plasma generated in a GaAs layer with an embedded self-organized ensemble of InAs quantum dots. A considerable resonant enhancement of the quasielastic electronic scattering intensity exceeding the level characteristic of the bulk material by two orders of magnitude has been revealed. The main scattering mechanism, involving joint diffusion of electrons and holes, has been elucidated. © *1999 American Institute of Physics.* [S1063-7834(99)02105-X]

Size quantization in all three directions attained in semiconductor structures containing quantum dots (QD) embedded in a wide-gap matrix results in a substantial modification of the density of electronic states and a considerably stronger carrier localization, which is expected to improve appreciably the principal characteristics of some nanoelectronics devices. We are reporting here on a further development of a high-sensitivity technique[1] for measuring of inelastic electronic light-scattering spectra in the near-IR region and on using it to study light-scattering spectra from QD structures. We have succeeded in detecting quasielastic electronic light scattering from free carriers in an InAs QD system embedded in a GaAs matrix. It is shown that this scattering is caused by the electron-hole plasma generated in the bulk of GaAs with embedded InAs QDs by incident light. The ensemble of self-assembled QDs is produced through spontaneous breakup of a strongly strained InAs layer grown on GaAs surface into coherent islands. It was established that the observed considerable enhancement of the quasielastic electronic light-scattering intensity is caused by the resonant nature of this scattering. It permitted us to measure for the first time spectra of quasielastic electronic light scattering from QD structures at an intensity level considerably in excess of the values established for the bulk material.

The study was made of undoped structures MBE grown on *n*-type, semi-insulating *si*-GaAs substrates with a faceted (311)B surface. The islands grew by the Stranski-Krastanov mechanism. The active region of the sample consisted of ten rows of quantum dots formed by deposition of alternating InAs layers with an effective thickness of 1.8 ML and 5.1-nm thick GaAs layers. The effective size of such InAs QDs was $\sim 12\times 6$ nm.

The spectra were excited by a high-stability cw YAG:Nd laser operating at a wavelength of 1064.4 nm. The spectra obtained were backscattered from the (311)B plane for parallel (yy) incident- and scattered-light polarizations, with the y axis along the $[\bar{2}33]$ crystallographic direction. The scattered light was analyzed with a large collecting power ($f=1:3$) double-grating monochromator and detected with a cooled PM tube in a two-channel photon-counting arrangement. The spectral resolution was 2 cm^{-1}. The measurements were performed at pump densities within the interval $P=(0.2-1.0)$ kW/cm^2, which do not produce local heating of the samples.

Figure 1a and 1b presents fragments of inelastic light-scattering spectra obtained directly from the InAs QD layer in the GaAs matrix at $T=194$ and 77 K, respectively. These spectra, which lie in a hard-to-reach low-frequency region directly adjoining the exciting laser line, demonstrate convincingly the Lorentz wing of quasielastic electronic light scattering. A similar spectrum for the *si*-GaAs substrate obtained at $T=300$ K in identical experimental conditions is shown in Fig. 2. The fairly strong lines seen in these spectra at 271.3 and 294.3 cm^{-1}, 269.7 and 292.8 cm^{-1}, 268.0 and 291.3 cm^{-1} originate from lattice scattering of light from the *si*-GaAs substrate by TO(Γ) and LO(Γ) phonons at 77, 194, and 300 K, respectively. The strongest line seen at 159.7 cm^{-1} against the background of comparatively weak lines corresponding to overtone scattering in a portion of the *si*-GaAs substrate spectrum amplified here 20 times is due to overtone scattering involving two acoustic 2TA(X,K) GaAs phonons. Remarkably, the intensity of the observed quasielastic electronic light scattering in this spectrum is comparable to that of the 2TA(X,K) phonons. This observation, as well as the pattern and shape of the scattering line, imply that the *si*-GaAs substrate has *n*-type conduction with a free carrier concentration $n=1.0\times 10^{15}$ cm^{-3} (Ref. 2). This quasielastic electronic light scattering drops sharply in absolute intensity with decreasing temperature, to disappear alto-

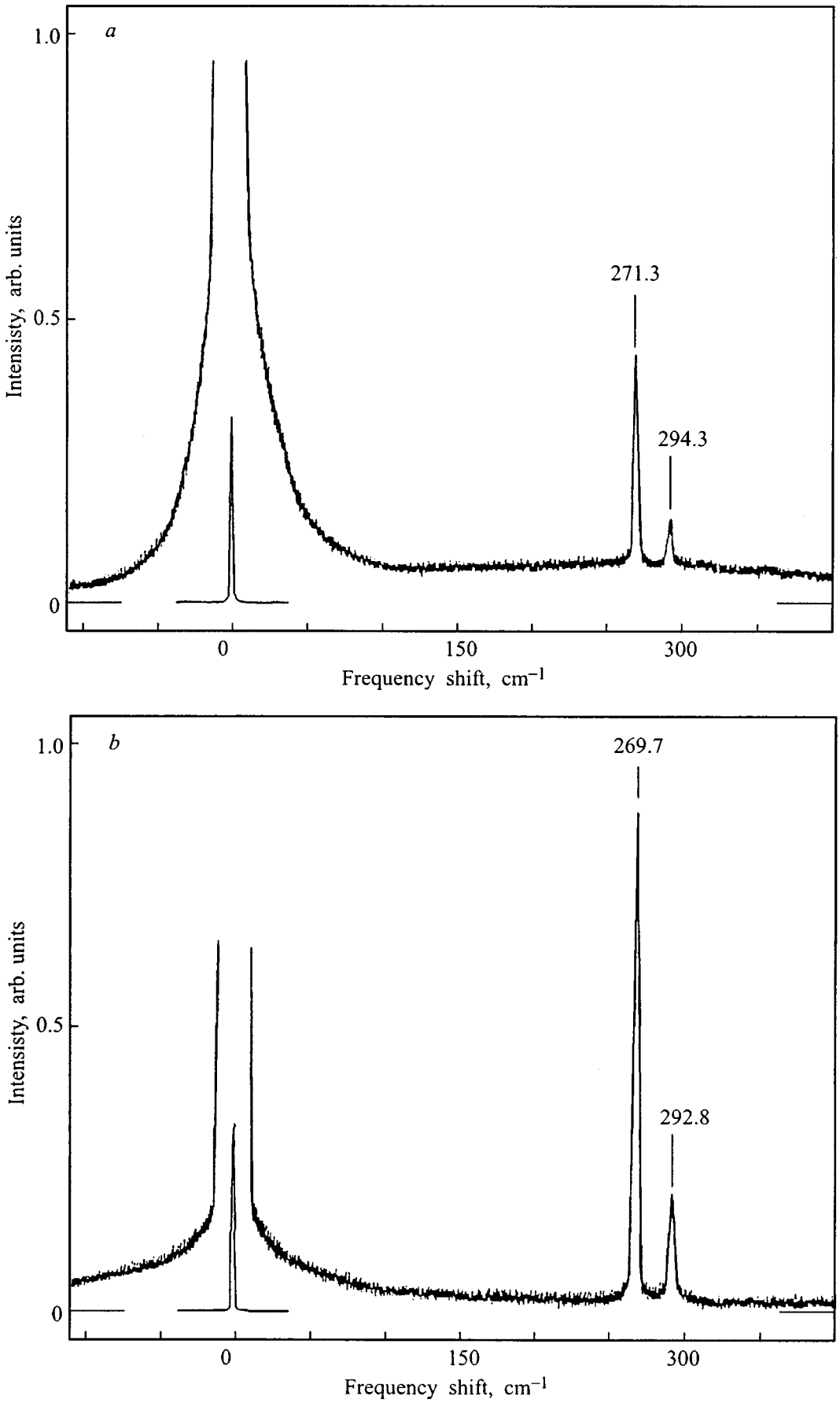

FIG. 1. Fragments of spectra obtained from an InAs QD layer embedded in a deliberately undoped GaAs matrix grown on a semi-insulating *si*-GaAs substrate. The spectra were measured at (a) $T=194$ K and (b) $T=77$ K.

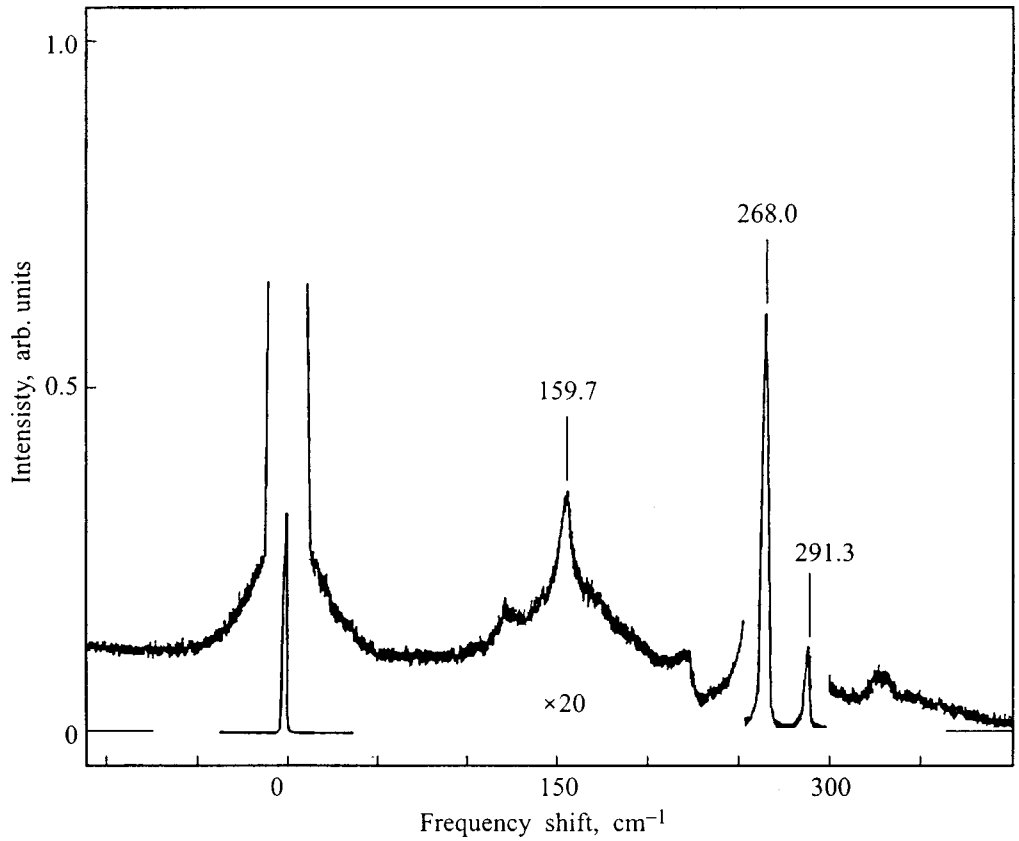

FIG. 2. A fragment of the spectrum from a semi-insulating *si*-GaAs substrate on which deliberately undoped structures were grown consisting of InAs QDs embedded in a GaAs matrix. The spectrum was obtained at $T=300$ K.

gether in the spectrum obtained at $T=77$ K, in full agreement with Ref. 3.

The spectra of structures with InAs QDs embedded in a GaAs matrix exhibit a distinctly different pattern. This scattering also differs strongly from the process of inelastic light scattering by free holes in *p*-GaAs.[4] As evident from the spectra in Fig. 1, at $T=77$ K the contribution of lattice scattering is not dominant. Moreover, these spectra reveal an anomalous increase in the absolute intensity of quasielastic light scattering with decreasing temperature. We have also observed an increase in the absolute intensity of quasielastic electronic light scattering in structures with InAs QDs embedded in the GaAs matrix. This increase in intensity exceeds the corresponding bulk levels by about two orders of magnitude. Besides, an anti-Stokes component of such scattering appears at low temperatures. At still lower temperatures a fairly broad one-phonon luminescence band appears, and a narrow shoulder corresponding to the acoustic plasmon becomes visible at 20 cm^{-1} (these features are not shown in Fig. 1).

We believe that the observed intensity increase may originate from the resonant nature of the scattering, which is due to a selectively photoexcited electron-hole plasma induced in the GaAs layer in the presence of a self-organized ensemble of InAs QDs. Because the characteristic dimensions of a quantum dot are small compared to the light wavelength ($d \ll \lambda$), its electromagnetic-field eigenmodes can be found essentially in the electrostatic approximation. The electric field in QDs embedded in an effective dielectric medium will be determined by the difference between the dielectric constants of InAs and GaAs at the pump frequency. The luminescence line peaking at 1031.4 nm indicates electron quantization in quantum dots. Because the characteristic dimensions of the QDs arranged in periodic rows are comparable to the periods of the structure in both directions, in the growth direction and perpendicular to it, the electronic states of the discrete spectrum in such structures become multiply coupled. The extent of this coupling, i.e. the number of the dots involved, depends on the dot size dispersion and, in particular, decreases strongly with the onset of coalescence, i.e. of the stage where large dots form at the expense of the other dots decreasing in size.[5] Viewed on the energy scale, this coupling of quantum states manifests itself in breaking up of the electronic bands and in the appearance in the gap between $E_{g1}=0.424$ eV (InAs) and $E_{g2}=1.519$ eV (GaAs) of allowed minibands and minigaps. For an incident photon energy $\hbar\omega=1.165$ eV, most of the volume of the system under study with an effective band gap E_g can satisfy the resonance condition $\hbar\omega=E_g$.

In accordance with the above-mentioned resonant nature of the scattering, its excitation produces photoionization of electron-hole pairs, which build up near the InAs QDs. Considered from the classical viewpoint, the photoinduced exciton liquid is injected from its localization region near the dots into the GaAs volume transparent to the incident light, where it generates a two-component plasma. As fluctuations

of the dielectric permittivity in such a system, one should take the sum of the contributions due to electrons and holes[3] with a resonance factor[6] determined by the gap width E_g and equal to $R_{eh}=E_g^2/[E_g^2-(\hbar\omega_i)^2]$. Our estimates show that it is this factor that provides a dominant contribution to the observed enhancement in the quasielastic light-scattering intensity, while the contribution associated with the decreasing amplitudes of the incident and scattered wave fields is only a factor of two to three. This yields $R=3R_{eh}^2$ for the maximum net-intensity increase.

To consider the Lorentzian wing of the quasielastic electronic light scattering, recall that the photoinduced nonequilibrium carriers have zero macroscopic spreadout velocity and a low mobility. On writing out all possible spectral correlation functions of electrons and holes, one comes to the following expression for the quasielastic scattering cross section[7]

$$\frac{\partial^2\Sigma}{\partial\omega\partial\Omega}=8\pi VR(e_ie_s)^2\frac{q^2F(\omega)}{\varepsilon^2}\left(\frac{e^2}{mc^2}\right)^2 \times(\mu_e+\mu_h)^2\tau_M^2\frac{D_e\left(\frac{\partial n_e}{\partial\zeta_e}\right)_T\sigma_h^2+D_h\left(\frac{\partial n_h}{\partial\zeta_h}\right)_T\sigma_e^2}{\omega^2+(q^2D_\alpha-\omega^2\tau_M)^2}. \quad (1)$$

Here $\tau_M=\varepsilon/[4\pi(\sigma_e+\sigma_h)]$ is the Maxwellian relaxation time,

$$D_\alpha=\frac{\sigma_eD_h+\sigma_hD_e}{\sigma_e+\sigma_h}$$

is the ambipolar diffusion coefficient, $F(\omega)=h\omega/[1-\exp(-h\omega/T)]$, n_α is the steady-state nonequilibrium density of particles of species α, ζ_α are their Fermi quasilevels, α labels the particles (electrons and holes), and μ_e and $\mu_h=\gamma_l$ are their inverse reduced masses, with the latter equal to the corresponding Luttinger Hamiltonian parameter γ_l.

According to Eq. (1), the relaxation seen in the quasielastic light scattering spectra with the Lorentzian profile width $\Gamma=q^2D_\alpha$ is due to the joint diffusion of electrons and holes. Note that the mobility of electrons $b_e=e\tau_e/m_e^*$ exceeds that of heavy holes: $b_h/b_e=m_e^*\tau_h/m_h^*\tau_e\ll1$. Therefore Γ in Fig. 1b is determined by the smallest of the possible diffusion coefficients, which is that of holes. That the experimental values of Γ are a few times smaller than those for bulk *n*-InP and *n*-GaAs crystals with comparable impurity concentrations is also a new observation.[2–4,7–9]

Remarkably, at lower temperatures one observes carrier motion between quantum dots to follow a drift pattern, which may result in an increase of the average dot population compared to the case of ambipolar diffusion.

We note in conclusion that practical realization of the possibility of obtaining near-IR spectra of resonant quasielastic electronic light scattering from structures with QDs offers a new potential for studying the interaction of electromagnetic waves and carrier diffusion in semiconductor nanostructures.

Partial support of the Russian Fundamental Research Foundation (Grant 98-02-18384) is gratefully acknowledged.

*E-mail: bairamov@bahish.ioffe.rssi.ru

[1] B. Kh. Baĭramov, B. P. Zakharchenya, and V. V. Toporov, JETP Lett. **67**, 352 (1998).
[2] B. Kh. Baĭramov, V. A. Voĭtenko, and I. P. Ipatova, Usp. Fiz. Nauk **163**, 67 (1993) [Phys. Usp. **36**, 392 (1993)].
[3] B. H. Bairamov, V. A. Voitenko, and I. P. Ipatova, Phys. Rep. **229**, 223 (1993).
[4] B. Kh. Baĭramov, V. A. Voĭtenko, I. P. Ipatova, V. K. Negoduĭko, and V. V. Toporov, Fiz. Tekh. Poluprovodn. **28**, 913 (1994) [Semiconductors **28**, 531 (1994)].
[5] W. Ostwald, Z. Phys. Chem. **32-35**, 495 (1900).
[6] M. V. Klein, *Light Scattering in Solids*, edited by M. Cardona (Springer, Berlin, 1975; Mir, Moscow, 1979, p. 174).
[7] B. H. Bairamov, V. A. Voitenko, B. P. Zakharchenya, V. V. Toporov, M. Henini, and A. J. Kent, JETP Lett. **67**, 428 (1998).
[8] B. H. Bairamov, V. A. Voitenko, I. P. Ipatova, V. K. Negoduyko, and V. V. Toporov, Phys. Rev. B **50**, 14923 (1994).
[9] B. H. Bairamov, G. Irmer, J. Monecke, V. A. Voitenko, V. V. Toporov, and B. P. Zakharchenya, Phys. Status Solidi B **204**, 456 (1997).

Translated by G. Skrebtsov

Rate spectra of small deformations in solids

N. N. Peschanskaya, P. N. Yakushev,*) V. V. Shpeĭzman, A. B. Sinani, and V. A. Bershteĭn

A. F. Ioffe Physicotechnical Institute, Russian Academy of Sciences, 194021 St. Petersburg, Russia
Fiz. Tverd. Tela (St. Petersburg) **41**, 848–850 (May 1999)

The method of constructing the temperature dependence for the rate of small creep deformation (strain-rate spectra) is applied to determine relaxation transitions in solids. This method is based on precision measurements of the rate using a laser interferometer and is distinguished by its high resolution. The possibility of using the spectra for predicting critical temperatures in the fracture kinetics of polymers and metals, as well as changes in the electrical properties (for example, the superconducting transition in Y–Ba–Cu–O ceramics) is pointed out. © *1999 American Institute of Physics.* [S1063-7834(99)02205-4]

Research on deformation kinetics in connection with molecular dynamics and the structure of materials[1–3] is one of the fundamental concerns in the physics of durability and plasticity. The deformability of materials shows up most distinctly in creep. Creep develops with constant external parameters (stress and temperature) and is an example of structural self organization. The principal characteristic of any process, including creep, is its rate, and the accuracy with which it is measured determines the reliability of the results. Creep kinetics is traditionally studied in terms of average rates in its steady state, which limits the range of possible studies. A fundamentally new detection scheme based on a laser interferometer has been devised[4] for more accurate measurement of the rate for small strain increments at any ''point'' of the process. This precision technique has opened up new approaches to the study of creep kinetics and made it possible to discover previously unknown behavior, in particular the spectral temperature dependences of the rates of small inelastic deformations.[5–13] Major studies have been devoted to polymers,[5–8,12] but similar behavior has been found in metals and ceramics,[9–11,13] as well. We shall examine the prospects of the creep-rate spectrum technique for predicting critical temperatures for various material properties.

1. EXPERIMENTAL METHOD

Rate spectra can be obtained for different forms of loading. Here we have used unilateral loading. The loading device and detector portions of the apparatus, including a Michelson interferometer using a low-power laser with a wavelength $\lambda = 0.63$ μm, have been described elsewhere.[6,7,12] The strain rate $\dot{\varepsilon}$ is determined by the beat frequency ν of interfering beams (one at the initial frequency and one that has changed frequency owing to the Doppler shift): $\dot{\varepsilon} = \lambda \nu / 2 l_0$, where l_0 is the sample length. The smallest deformation on the basis of which $\dot{\varepsilon}$ can be determined with an error of $\sim 1\%$ is 0.15 μm (half a beat in the interferometer). The method for constructing a spectrum is as follows: the sample is cooled to the lowest temperature within the range being studied, loaded to low stresses equal to 0.1–0.3 times the yield point at the highest temperature, and, after a deformation $\varepsilon = (1-3) \times 10^{-4}$, the sample is unloaded, heated by 3–10 K, loaded with the same load, etc. The rate measurement at all temperatures is made with the same creep duration relative to the half beat arriving at the time of the measurement. The resulting dependences of $\dot{\varepsilon}$ on T have the form of spectra with peaks which indicate a change in the mobility of the structure. The correlation frequency of the experiment for the creep duration of 10–30 s is roughly 10^{-2} Hz.

2. RESULTS AND DISCUSSION

The anomalies in the temperature dependences of the mechanical characteristics found in the past have been explained by relaxation transitions which change the deformability, i.e., the degree of brittleness (plasticity), of the material.[2,3,7] Rate spectra provide more complete information on critical temperatures for the development of various physical and mechanical properties than do other standard methods such as internal friction. The creep-rate spectrum has been used to study polymers of various types, metals and alloys, ceramics (including superconducting ones), etc.

2.1. *Polymers.* Figure 1 shows plots of the microcreep rate and rupture point as functions of temperature, together with internal friction spectra, for polystyrene. Four peaks corresponding to relaxation transitions can be seen clearly in the rate spectra. The two low-temperature relaxation regions correspond more precisely to breaks in the temperature dependence of the toughness than do the indistinct relaxations in the internal-friction spectra. Near 320 K the toughness of polystyrene is very low and was not measured in the region where the material becomes soft. Similar correlations have been observed for other polymers.[5–8]

2.2. *Metals.* Data for zinc are shown in Fig. 2 as an example. The creep rate spectrum has three peaks corresponding to breaks in the temperature dependence of the toughness for different forms of the stressed state. The breaks in these curves correspond to regions of ductile-brittle transitions.[9] Therefore, the embrittlement temperature does not vary arbitrarily, but is drawn toward the lowest peak in the creep-rate spectrum. Similar data have been obtained for

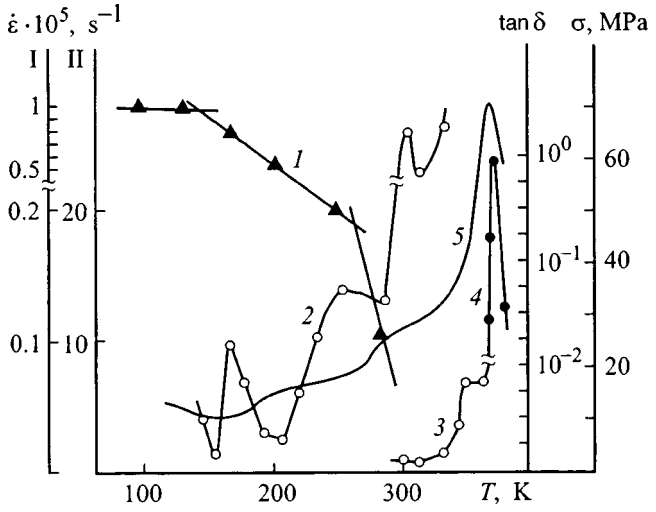

FIG. 1. Polystyrene. Temperature dependences of the breaking point σ (*1*), creep rate $\dot{\varepsilon}$ [$\sigma=10$ MPa (*2*—scale I) and (*3*—scale II); $\sigma=0.5$ MPa (*4*—scale III)], and internal-friction spectrum,[14] $\tan\delta$, 1 Hz (*5*).

polymers.[7] The creep-rate spectra can be used, therefore, to predict the embrittlement temperature as the loading conditions are varied; this is an important practical result. Breaks in plots of toughness against temperature have been discussed before and a physical model for brittle fracture was proposed that takes the role of local strains into account.[2] The rapidly damped, small inelastic deformations mentioned there are caused by local shear distributed within the elastic matrix. The nonmonotonicity is a general feature of the temperature dependences of the rates of local strains in materials of various classes, and the high resolution of this method

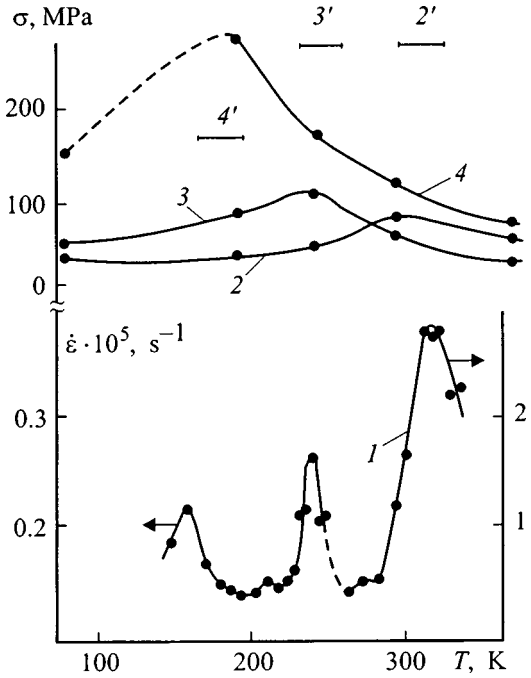

FIG. 2. Zinc. Temperature variations of the strain rate for $\sigma=50$ MPa (*1*), breaking points under tension (*2*), torsion (*3*), compression for $T<200$ K (4), and under compression for $T>200$ K (4). The ductile–brittle transition regions under tension (*2′*), torsion (*3′*), and compression (*4′*).

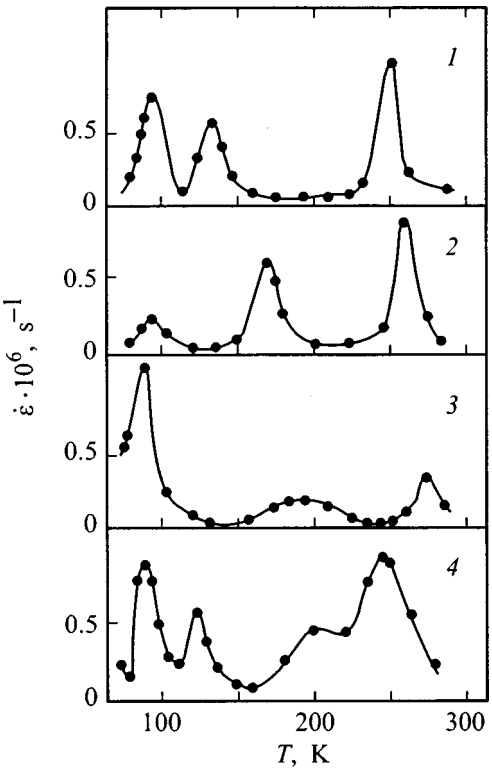

FIG. 3. Inelastic strain rate spectra for compression of Y–Ba–Cu–O ceramics, $\sigma=10$ MPa. Grain size (μm): 1–3 (*1*), 10–30 (*2*).

makes it possible to study even extremely brittle materials, where macroscopic plasticity never develops.[10–14]

2.3. *Superconducting ceramics.* Y–Ba–Cu–O ceramics were studied using samples with different grain sizes and different oxygen contents.[10,11] Over the range from 77 to 300 K, three peaks are usually observed in the creep rate spectrum, one of which corresponds to the superconducting transition temperature $T_c\approx90$ K. In Fig. 3, spectrum *1* was obtained from a fine-grained ceramic, spectra *2* and *3*, from single-phase large-grained ceramics with different densities, and spectrum *4* from a multiphase large-grained ceramic. The peak near T_c is the most stable peak in all the ceramics, while the positions of the others depend on the structure. These data suggest that an electronic state affects the rate of small inelastic strains, and this has also been confirmed by the destruction of the superconducting state in a magnetic field or by an electric current, as opposed to temperature changes.[15] It was shown with ceramics containing different amounts of oxygen that the rate peak can be maintained even when the superconducting transition vanishes as the oxygen content is reduced.[11] This effect is explained by a nonuniform distribution of oxygen, i.e., the rate spectrum reveals microstructural inhomogeneities capable of a superconducting transition, even when the sample as a whole no longer manifests superconducting properties.

Spectra of the rate of small inelastic strains, therefore, do reflect temperature variations in the mobility of the molecular (or crystal) structure and can be used as an independent spectroscopic technique for determining the temperature regions for low-frequency relaxation in solids of various kinds.

Rate spectra are a convenient, high-resolution method for determining the critical temperatures of the most rapid changes in the physical and mechanical characteristics of polymers, metals, and ceramics.

*)E-mail: yak@pav.ioffe.rssi.ru

[1] R. F. Boyer, Polym. Eng. Sci. **8** (3), 161 (1968).
[2] V. A. Stepanov, N. N. Peschanskaya, and V. V. Speĭzman, *Durability and Relaxation Phenomena in Solids* [in Russian] (Nauka, Leningrad, 1984).
[3] A. B. Sinani and V. A. Stepanov, Mekh. Kompozit. Mater. No. 1, 109 (1981).
[4] N. N. Peschanskaya, G. S. Pugachev, and P. N. Yakushev, Mekh. Polim., No. 2, 357 (1977).
[5] N. N. Peschanskaya, P. N. Yakushev, and V. A. Stepanov, Fiz. Tverd. Tela **26** 1202 (1984) [Sov. Phys. Solid State **26**, 729 (1984)].
[6] N. N. Peschanskaya, P. N. Yakushev, Yu. Khristova, and A. Topliĭska, Vysokomol. Soedin., Ser. A Ser. B **35**, 1493 (1993).
[7] N. N. Peschanskaya, P. N. Yakushev, A. B. Sinani, and V. A. Bershtein, Thermochim. Acta **238**, 429 (1994).
[8] N. N. Peschanskaya, P. N. Yakushev, and V. Yu. Suvorova, Fiz. Tverd. Tela **37**, 2602 (1995) [Phys. Solid State **37**, 1429 (1995)].
[9] V. V. Shpeĭzman and N. N. Peschanskaya, in *Physical Aspects of Predicting Fracture and Deformation in Heterogeneous Materials* [in Russian], (Leningrad, 1989), p. 166.
[10] N. N. Peschanskaya, B. I. Smirnov, Yu. P. Stepanov, V. V. Speĭzman, and P. N. Yakushev, Fiz. Tverd. Tela **31** (4), 271 (1989) [Sov. Phys. Solid State **31**, 703 (1989)].
[11] V. V. Speĭzman, N. N. Peschanskaya, B. I. Smirnov, and Yu. P. Stepanov, Fiz. Tverd. Tela **31** (12), 105 (1989) [Sov. Phys. Solid State **31**, 2084 (1989)].
[12] N. N. Peschanskaya, P. N. Yakushev, A. B. Sinani, and V. A. Bershtein, Macromol. Symp. **119**, 79 (1997).
[13] N. A. Zlatin, N. N. Peschanskaya, and P. N. Yakushev, Zh. Tekh. Fiz. **57**, 2346 (1987) [Sov. Phys. Tech. Phys. **32**, 1419 (1987)].
[14] J. Heijboer, in *Physics of Non-Crystalline Solids, Proceedings of the International Conference, Delft, 1964*, (Amsterdam, North-Holland Publ., 1965), p. 231.
[15] V. V. Speĭzman, B. I. Smirnov, N. N. Peschanskaya, and L. K. Markov, Fiz. Tverd. Tela **33**, 2198 (1991) [Sov. Phys. Solid State **33**, 1238 (1991)].

Translated by D. H. McNeill

Mechanisms of excitation and thermal quenching of erbium-ion luminescence in crystalline and amorphous silicon

M. S. Bresler,*) O. B. Gusev, N. A. Sobolev, E. I. Terukov, I. N. Yassievich, and B. P. Zakharchenya

A. F. Ioffe Physicotechnical Institute, Russian Academy of Sciences, 194021 St. Petersburg, Russia

T. Gregorkevich

Amsterdam University, Amsterdam, the Netherlands

Fiz. Tverd. Tela (St. Petersburg) **41**, 851–855 (May 1999)

A short review is presented of the erbium-ion excitation mechanisms in crystalline and amorphous silicon and of the processes governing thermal quenching of erbium luminescence in these materials, which draws both from the studies carried out by the present authors and from available literature data. © *1999 American Institute of Physics.* [S1063-7834(99)02305-9]

The recent interest in studies of the luminescence of erbium-doped crystalline silicon[1,2] stems from the fact that the 1.54 μm wavelength of erbium-ion emission created in transitions from the first excited state $^4I_{13/2}$ to the ground state $^4I_{15/2}$ coincides with the wavelength of minimum transmission losses in quartz optical-fiber communication lines. Therefore erbium-doped silicon is a promising material for developing of a new type of optoelectronic devices.

The efficiency of optoelectronic devices based on an erbium-doped semiconductor matrix should be determined primarily by that of energy transfer from the matrix carriers to the inner $4f$ shell of the erbium ion. This energy transfer in a semiconductor originates from Coulomb interaction between free carriers (electrons and holes) and the strongly localized $4f$ electrons whose ground state lies below the valence-band minimum by about 10 eV. One can conceive of two mechanisms of erbium-ion electronic excitation,[3] namely, Auger recombination of an electron-hole pair, in which the energy is transferred to a $4f$ electron of the erbium ion, and impact excitation of ions by hot carriers having an energy in excess of the first erbium-ion excited state ($\approx$0.8 eV).

1. EXCITATION AND DEEXCITATION OF ERBIUM IN CRYSTALLINE SILICON

It was experimentally established that erbium luminescence in silicon is enhanced considerably if oxygen is implanted in silicon simultaneously with erbium in concentrations exceeding that of erbium by an order of magnitude. These conditions favor formation of a complex of erbium surrounded by oxygen, with a corresponding donor level having a binding energy $E_D = 150 - 200$ meV.

Absorption of light in silicon doped comparatively weakly with erbium ($\sim 10^{17}$ cm^{-3}) and oxygen creates free excitons, whose lifetimes in crystalline silicon are of the order of 10 μs. A free exciton has a high probability to be captured by a neutral donor center formed by an erbium complex. Recombination of a bound exciton gives rise to Auger excitation of the Er^{3+} $4f$ shell, with the energy excess being transferred to the electron present at the neutral donor center, which subsequently becomes ejected into the conduction band (Fig. 1a). This mechanism was proposed by the present authors,[4,5] who observed a notable enhancement of exciton luminescence with increasing pumping level only after the erbium luminescence had reached saturation (Fig. 2). The temperature dependence of the erbium luminescence intensity has two portions with different slopes; the low-temperature slope describes the weakening of the erbium luminescence resulting from detachment of the bound exciton from the erbium complex (the binding energy is 15 meV), and the high-temperature one is due to thermal ionization of the neutral donor center with an ionization energy $\sim 150 - 200$ meV (Fig. 3).

Excitation of erbium in silicon more heavily doped with erbium ($>10^{18}$ cm^{-3}) and oxygen occurs in Auger recombination of the electron captured by the donor level of the erbium complex with a hole in the valence band. The excess energy liberated in this Auger process is transferred to local phonons of the erbium center or to a third body (an electron or a hole) if it happens to be close to the erbium center (Fig. 1b). The characteristic energy of thermal quenching of the erbium luminescence in this mechanism is the same as that in the exciton mechanism, $\sim$150 meV, because the donor level is thermally ionized. Because of the interaction with phonons, the probability of this process may be expected to be lower than that involving exciton transitions, and there is experimental evidence to support this conclusion.

Impact excitation of erbium ions by hot electrons in an inversely biased *p-n* junction was successfully demonstrated in Refs. 6 and 7. Such a *p-n* junction in crystalline silicon can be obtained by doping it with erbium and oxygen (*n* region) and boron (*p* region). The conclusion that erbium is impact excited is based on the observation by the present authors[7] of hot electroluminescence simultaneously with that due to erbium. The erbium electroluminescence obtained under impact excitation within the 77–300-K temperature interval is practically temperature independent (Fig. 4).

If the *p-n* junction in a structure prepared on a (111) silicon substrate is inversely biased, Auger excitation arises

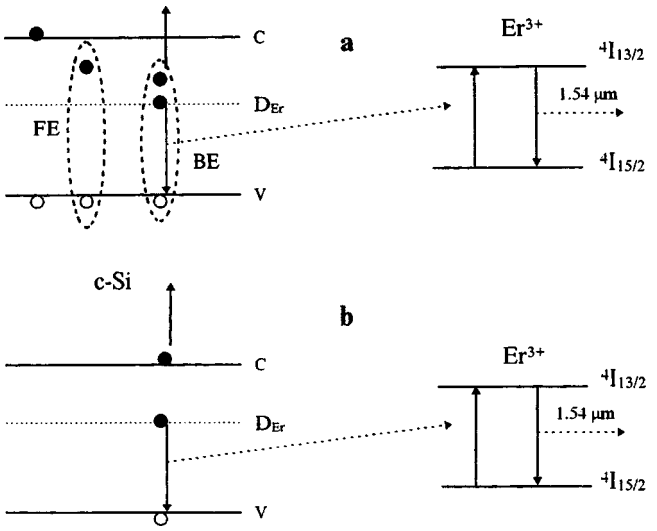

FIG. 1. (a) Schematic presentation of erbium-ion excitation by the excitonic mechanism. FE — free exciton, BE — bound exciton, D_{Er} — donor level of the erbium complex. (b) Scheme of the Auger excitation of an erbium ion through recombination of an electron at the erbium-complex donor level with a valence-band hole. The excess energy is transferred to either a third body (in the diagram, a conduction-band electron), or local phonons of the erbium complex.

involving hot electrons from the upper subband of the conduction band whose bottom lies higher than the bottom of the main subband by about 100 meV (Fig. 5). The possibility of such a process and its high efficiency was first pointed out in Ref. 3. Our experiments suggest that the probability of such an Auger excitation in silicon in the 150–300-K region increases strongly due to resonant excitation of the erbium ion to the second excited state $^4I_{11/2}$.[8] Under resonant conditions the excitation efficiency approaches unity.

The main obstacle to developing high-efficiency light-emitting diodes operating at 1.54 μm and based on erbium-doped silicon is thermal quenching of the luminescence. It may be caused both by a weakening of the excitation efficiency by the above mechanisms and by nonradiative deexcitation of erbium ions. The difference between these processes can be revealed by studies of the temperature

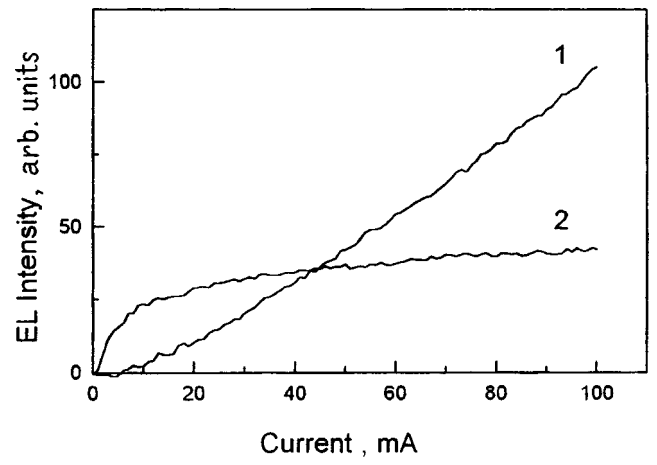

FIG. 2. Intensity of excitonic ($\lambda = 1.12\ \mu$m) and erbium ($\lambda = 1.54\ \mu$m) electroluminescence in c-Si:Er vs pump power. $T = 80$ K.

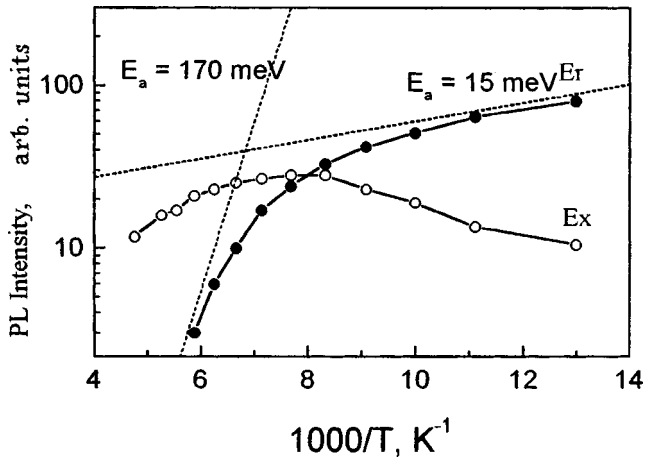

FIG. 3. Temperature dependences of the excitonic ($\lambda = 1.12\ \mu$m) and erbium ($\lambda = 1.54\ \mu$m) photoluminescence.

dependence of the erbium-ion lifetime in excited state; in the first case the lifetime should not depend on temperature and, in the second, it should decrease with increasing temperature.

It was shown[9,10] that the erbium ion is deexcited predominantly through energy transfer from a $4f$ electron at an excited level to a free carrier (Fig. 6a). This process is the reverse of impact ionization of an erbium ion by a hot carrier, it does not follow an activation behavior, and should result in temperature-independent deexcitation. Significantly, deexcitation via free carriers permits considerable reduction of the erbium-ion lifetime in the excited state (from ~ 1 ms

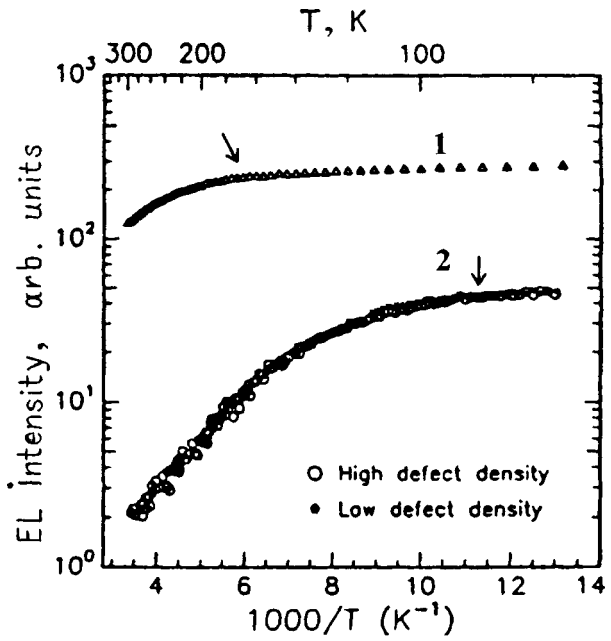

FIG. 4. Temperature dependence of erbium ($\lambda = 1.54\ \mu$m) electroluminescence for a structure made of erbium-doped crystalline silicon, with a (1) forward and (2) inversely biased *p-n* junction.

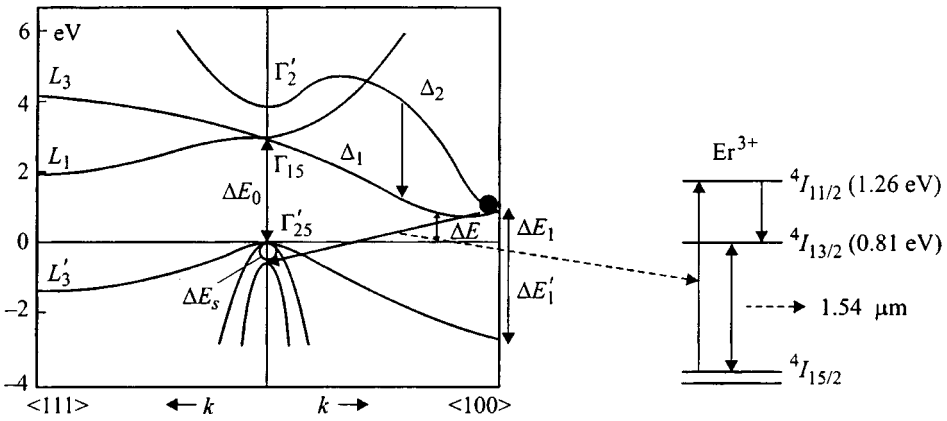

FIG. 5. Schematic presentation of erbium-ion Auger excitation through recombination of an electron from the upper conduction subband with a valence-band hole (resonant excitation to the second excited state of the erbium ion $^4I_{11/2}$).

to $<1\,\mu$s) and, thus, a substantial increase of the operating frequency of inversely biased Si:Er light-emitting diodes.[7] The reason for this lies in that the active region of the *p-n* junction expands when the voltage is removed, and the excited erbium ions fall into a region with a high free-carrier concentration.

The erbium ion can become deexcited through creation of an electron-hole pair (the electron can be created both at a donor level of the erbium complex and in the conduction band (Fig. 6b).[11] This process is the reverse of the Auger excitation of erbium when an electron bound at an erbium donor level recombines with a valence-band hole. While the excess energy released in the excitation of erbium is transferred to local phonons, in the inverse transition (deexcitation) the missing energy is compensated by lattice vibrations. The activation energy of this process is $\sim$150 meV if the electron is created at the donor level, and $\sim$300 meV, if it appears in the conduction band.[12]

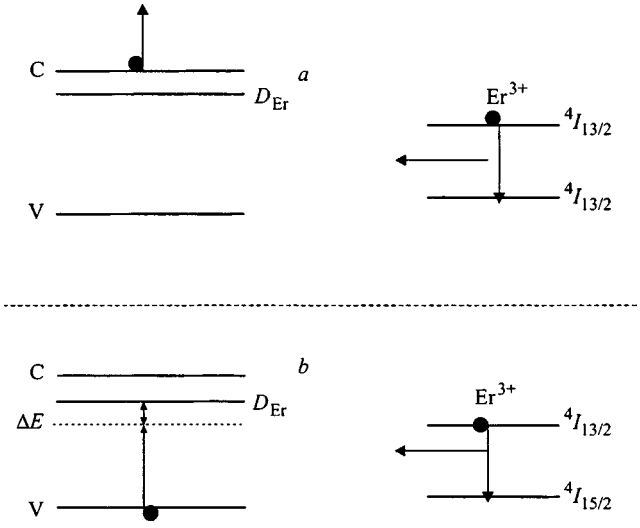

FIG. 6. (a) Scheme of erbium-ion deexcitation in interaction with a free carrier (conduction-band electron). (b) Scheme of erbium-ion deexcitation through trapping of a valence-band electron to a donor level of the erbium complex. ΔE — energy taken from the lattice and determining the activation energy of the deexcitation process.

2. ERBIUM EXCITATION AND DEEXCITATION IN AMORPHOUS SILICON

Erbium ions in amorphous hydrogenated silicon are excited through the Auger process, which reflects the specific features of this material. Doping amorphous silicon with erbium produces erbium-oxygen complexes similar to those observed in crystalline silicon. Besides, the doping of amorphous silicon initiates formation of high concentrations of defects (dangling bonds), which can reside in two charge states, neutral (the so-called D^0 centers) and singly-charged D^- centers. The erbium ions are excited via capture of conduction-band electrons by D^0 centers which become D^- centers (Fig. 7). The excess energy is transferred to local phonons, but the energy released in the capture is close to that for excitation of the $^4I_{13/2}$ level, and, therefore, the Auger process is nearly resonant [estimates show its activation energy to be only $\sim$6 meV, and the probability of this defect-related Auger excitation (DRAE) is practically temperature independent]. Calculations of the DRAE probability and of the competing processes, namely, of the radiative electron transfer to a D^0 center and of the nonradiative multiphonon capture show the DRAE process to have the highest efficiency within a broad temperature region, including room temperature.[14]

At the same time it is because the probability of nonradiative multiphonon trapping increases with temperature that this channel begins to dominate over the erbium ion excitation, a process leading to thermal quenching of luminescence

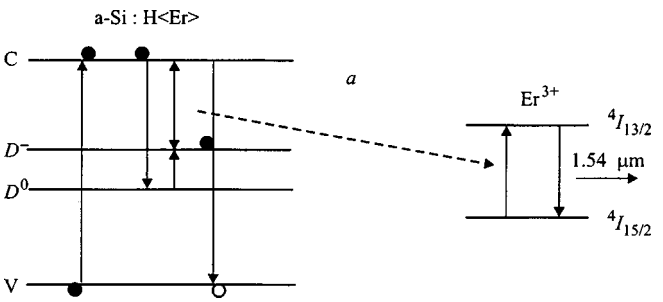

FIG. 7. Scheme of erbium-ion Auger excitation in amorphous silicon through trapping of a conduction-band electron by a D^0 center (DRAE process).

observed at temperatures above ~ 300 K.[13,14]

Thus our critical consideration of the phenomena associated with excitation and deexcitation of erbium shows that the most promising for development of high-efficiency light-emitting devices are diodes of erbium-doped crystalline silicon with an inversely biased *p-n* junction, where erbium is excited by hot electrons or through Auger recombination of electrons from the upper conduction subband with valence-band holes, as well as structures made of erbium-doped amorphous silicon.

Support of the Russian Fund for Fundamental Research (Grants 96-02-16931a and 97-02-18079), of the Ministry of Science of the RF (Project 97-1036), International R & D Center (Grant 168-95), Copernicus Program (Grant 977-048SIER), INTAS-RFBR (Grant 95-0531), and NATO Linkage (Grant HTECH.LG 972032) is gratefully acknowledged.

*)E-mail: mikhail.bresler@pop.ioffe.rssi.ru

[1] *Rare-Earth Doped Semiconductors-I*, edited by G. S. Pomrenke, P. B. Klein, and D. W. Langer (Mater. Res. Soc. Proc. 301, Pittsburg, 1993).
[2] *Rare-Earth Doped Semiconductors-II*, edited by S. Coffa, A. Polman, and R. N. Schwartz (Mater. Res. Soc. Proc. 422, Pittsburg, 1996).
[3] I. N. Yassievich and L. C. Kimmerling, Semicond. Sci. Technol. **8**, 718 (1993).
[4] M. S. Bresler, O. B. Gusev, B. P. Zakharchenya, P. E. Pak, N. A. Sobolev, E. I. Shek, I. N. Yassievich, M. I. Makoviĭchuk, and E. O. Parshin, Fiz. Tekh. Poluprovodn. **30**, 898 (1996) [Semiconductors **30**, 479 (1996)].
[5] M. S. Bresler, O. B. Gusev, B. P. Zakharchenya, and I. N. Yassievich, Fiz. Tverd. Tela (St. Petersburg) **38**, 1474 (1996) [Phys. Solid State **38**, 813 (1996)].
[6] S. Coffa, G. Franzo, and F. Priolo, Appl. Phys. Lett. **69**, 2077 (1996).
[7] G. Franzo, S. Coffa, F. Priolo, and C. Spinella, J. Appl. Phys. **81**, 2784 (1997).
[8] M. S. Bresler, O. B. Gusev, P. E. Pak, N. A. Sobolev, and I. N. Yassievich, *Proc. EMRS* (Strasbourg, 1998) (to be published in J. Lumin.).
[9] J. Palm, F. Gan, B. Zheng, J. Michel, and L. C. Kimerling, Phys. Rev. B **54**, 17603 (1996).
[10] F. Priolo, G. Franzo, S. Coffa, and A. Carnera, Phys. Rev. B **57**, 4443 (1998).
[11] S. Coffa, G. Franzo, F. Priolo, A. Polman, and R. Serna, Phys. Rev. B **49**, 16313 (1994).
[12] J. Michel, B. Zheng, J. Palm, E. Quelletti, F. Gan, and L. C. Kimerling, in *Rare-Earth Doped Semiconductors-II*, edited by S. Coffa, A. Polman, and R. N. Schwartz (Mater. Res. Soc. Proc. 422, Pittsburg, 1996), p. 317.
[13] W. Fuhs, I. Ulber, G. Weiser, M. S. Bresler, O. B. Gusev, A. N. Kuznetsov, V. Kh. Kudoyarova, E. I. Terukov, and I. N. Yassievich, Phys. Rev. B **56**, 9545 (1997).
[14] I. N. Yassievich, M. S. Bresler, and O. B. Gusev, J. Non-Cryst. Solids **226**, 192 (1998).

Translated by G. Skrebtsov

Magnetic moment of quantum cylinders

I. I. Chuchaev, V. A. Margulis,*) A. V. Shorokhov, and S. E. Kholodova

Mordovian State University, 430000 Saransk, Russia
Fiz. Tverd. Tela (St. Petersburg) **41**, 856–858 (May 1999)

The magnetic response of a two-dimensional layer rolled into a cylinder and located in a longitudinal magnetic field is examined. The magnetic moment of the degenerate electron gas is studied as a function of the magnetic flux. The shape of the fluctuation maxima is analyzed in detail. It is shown that at zero temperature there are breaks in each period of the change in the magnetic moment. Over this period, a plot of the magnetic moment depends strongly on the ratio of the Fermi energy to the size-confinement energy. In particular, there are no breaks for integral or semi-integral values of the square root of this ratio. © *1999 American Institute of Physics.* [S1063-7834(99)02405-3]

Studies of the magnetic response in various low-dimensional systems provide valuable information on the electronic energy spectrum and lateral confinement potential in these structures.[1–11] Applying a magnetic field to a nanostructure creates additional possibilities for studying these structures. This is because a magnetic field can create additional, or enhance existing, lateral confinement in a nanostructure.

The equilibrium properties of the electron gas in nanostructures are mainly determined by the electronic energy spectrum, which, in turn, depends on the geometry of the system.

The magnetic response of nanostructures with cylindrical symmetry at a temperature $T=0$ have been studied[3] for the case of a weak magnetic field, which was regarded as a perturbation. Note that the magnetic response is studied both using the canonical Gibbs distribution (constant number of electrons) and the grand canonical distribution (constant chemical potential of the gas, $\mu(B)=\text{const}$). In most situations the results obtained with these distributions differ very little. This is because the oscillatory portion of $\mu(B)$ is very small for a constant number of electrons.[12] For a degenerate electron gas, however, it is more convenient to use the grand canonical distribution in the calculations. Thus, in the following we shall use this approach, i.e., assume that $\mu=\text{const}$. In addition, we shall consider exclusively a noninteracting electron gas.

The purpose of this paper is to study theoretically the magnetic response of a two-dimensional degenerate electron gas rolled up into a cylinder (a quantum cylinder) in a constant and uniform magnetic field **B** parallel to the axis of a cylinder of radius ρ.

In the effective-mass approximation, the Hamiltonian H of the one-electron spinless states for a vector potential **A** chosen to have the form $\mathbf{A}=(By/2-Bx/2,0)$ is given in cylindrical coordinates by

$$H=-\varepsilon\frac{d^2}{d\varphi^2}-\frac{i\hbar\omega_c}{2}\frac{d}{d\varphi}+\frac{m^*\omega_c^2}{2}\rho^2+\frac{p^2}{2m^*}, \tag{1}$$

where $\omega_c=|eB|/m^*c$ is the cyclotron frequency, φ is the polar angle, m^* is the effective mass, p is the momentum along the axis of the cylinder, and $\varepsilon=\hbar^2/2m^*\rho^2$ is the size confinement energy.

The spectrum of this Hamiltonian has the form

$$\varepsilon_{mp}=\varepsilon\left(m+\frac{\Phi}{\Phi_0}\right)^2+\frac{p^2}{2m^*}. \tag{2}$$

Here $m=0,\pm1,\pm2,\ldots$, the flux of the magnetic field **B** through the cross section of the cylinder is $\Phi=\pi\rho^2B$, and $\Phi_0=hc/|e|$ is the flux quantum. Using the standard expression for the thermodynamic potential Ω,[13] we find the magnetic moment from

$$\frac{M}{\mu_B}=\frac{Lm_0}{\pi\hbar m^*}\sum_{m=-\infty}^{\infty}\int_0^{\infty}\frac{(m+\Phi/\Phi_0)dp}{1+\exp[(\varepsilon_{mp}-\mu)/T]}, \tag{3}$$

where m_0 is the free-electron mass and μ_B is the Bohr magneton.

For further analysis it is convenient to expand the magnetic moment of the cylinder in a Fourier series using the Poisson summation formula. After some simple, but fairly protracted transformations, we obtain

$$-\frac{M}{\mu_B}=\sum_{n=1}^{\infty}C_n(T)\sin\left(2\pi n\frac{\Phi}{\Phi_0}\right), \tag{4}$$

where the Fourier coefficients $C_n(T)$ are given by

$$C_n(T)=\frac{Lm_0}{\pi^3\hbar m^*}\int_0^{\infty}dz z\,\sin(nz)\int_0^{\infty}dp\{1+\exp[(\varepsilon z^2/4\pi^2+p^2/2m^*-\mu)/T]\}^{-1}. \tag{5}$$

We introduce the new variables $x=z\sqrt{\varepsilon}/2\pi$ and $y=p/\sqrt{2m^*}$ and transform to polar coordinates (r,ψ) in the xy plane in Eq.(4). Then for the $C_n(T)$ we obtain the expression

$$C_n(T)=\frac{2L\sqrt{2m^*\varepsilon}m_0}{\hbar m^*}\int_0^{\infty}\frac{x^2J_1(2\pi nx)dx}{1+\exp[(\varepsilon x^2-\mu)/T]}. \tag{6}$$

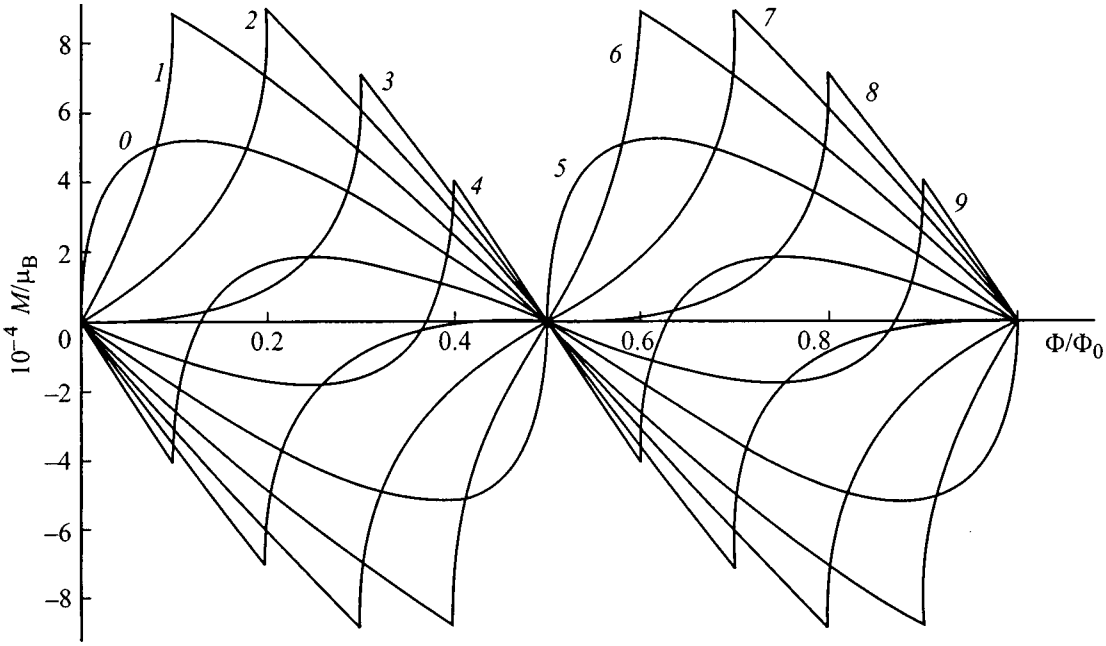

FIG. 1. Magnetic response of a quantum cylinder as a function of magnetic flux. The number N of a curve corresponds to the value of $\eta = N \times 10^{-1}$, where $N = 0,1,\ldots,9$.

As Eqs. (6) and (4) imply, the magnetic moment of the quantum cylinder is an oscillating function of the flux with a period equal to the quantum of flux.

For a qualitative study of the character of these oscillations, we shall examine the case of $T=0$. Then, we obtain

$$C_n(0)\frac{L\mu\sqrt{2m^*}m_0}{\pi\hbar m^*\sqrt{\varepsilon}}\ \frac{J_2(2\pi n\sqrt{\mu/\varepsilon})}{n}. \tag{7}$$

For real situations, $\mu \gg \varepsilon$. Using the asymptotic form of the Bessel function $J_2(x)$ for large arguments, we obtain the estimate

$$\frac{M(T=0)}{\mu_B}\ \frac{\sqrt{2}Lm_0}{\pi^2\hbar\sqrt{m^*}}\left(\frac{\mu^3}{\varepsilon}\right)^{1/4}\sum_{n=1}^{\infty}\frac{1}{n^{3/2}}\sin(2\pi n\xi) \times\cos\left(2\pi n\eta-\frac{\pi}{4}\right), \tag{8}$$

where ξ and η denote the fractional parts of Φ/Φ_0 and $\sqrt{\mu/\varepsilon}$, respectively.

Equation (8) implies that it is sufficient to carry out our investigation of the oscillations of the magnetic moment in the region where $0 \leqslant \xi < 1$ and $0 \leqslant \eta < 1$.

Equation (8) implies that $M(\xi,\eta) = -M(1-\xi,\eta)$ and $M(\xi+1/2,\eta-1/2) = M(\xi,\eta)$. For this symmetry we consider only the region $\xi,\eta \leqslant 1/2$. We can see at once that, for integral values of $\sqrt{\mu/\varepsilon}$, there is only one extremum within this half period (a maximum or minimum depending on whether $\eta < 1/2$ or $\eta > 1/2$). For $\eta < 1/2$, Eq. (8) gives

$$\frac{M(\xi,\eta)}{4\pi A\mu_B}\zeta(-1/2,\xi+\eta)-\zeta(-1/2,1-\xi+\eta);\quad \xi \geqslant \eta,$$

$$\frac{M(\xi,\eta)}{4\pi A\mu_B}\zeta(-1/2,\xi+\eta)-\zeta(-1/2,\eta-\xi);\quad \eta > \xi, \tag{9}$$

where $\zeta(x,s)$ is the Hurwitz ζ function and $(Lm_0)/(2\pi^2\hbar\sqrt{m^*})(\mu^3/\varepsilon)^{1/4} \equiv A$. As Eq. (9) implies, the critical point on the graph of $M(\xi)$ on the interval $0 < \xi < 1/2$ is the point where $\xi = \eta$. Let us examine the behavior of the graph in the neighborhood of this point. We shall use the shift formula for the Hurwitz ζ function in this analysis. Then the second of Eqs. (9) can be written as

$$\frac{M(\xi,\eta)}{4\pi A\mu_B} = \zeta(-1/2,\xi+\eta)-\zeta(-1/2,1-\xi+\eta) - \sqrt{\eta-\xi};\quad \eta > \xi, \tag{10}$$

A comparison of Eqs. (9) and (10) shows, however, that at the point $\eta = \xi$ there is a break in the $M(\xi,\eta)$ curve owing to the third term in Eq. (10). In addition, this term can add another zero to the function $M(\xi,\eta)$ within the interval $0 < \xi < 1/2$. In this case there are two extrema (a maximum and a minimum) within a half period of the function.

Some plots constructed from Eq. (8) are shown in Fig. 1. The form of the curves is consistent with the above analytic results for the properties of the magnetic moment.

Note that, for $T \neq 0$, the breaks in the curves are smoothed out but, on the whole, the pattern of the oscillations remains the same.

As the results obtained here show, in a quantum cylinder the amplitudes of the oscillatory peaks in the $M(B)$ curve depend on the magnitude of the chemical potential, but their locations are determined by the relationship between ξ and η. Here the period of the oscillations is independent of μ and equal to the quantum of flux (Aaron–Bohm oscillations). This originates in the purely geometric circumstance that, for any of the possible electron energies, the projection of its quasiclassical trajectory in a plane perpendicular to the mag-

netic field is fixed, and coincident with the generatrix of the cylinder.

It is interesting to note that adding the Aaron–Bohm flux Φ_{AB} (the flux of the magnetic field created by a thin, and, ideally, infinitely long solenoid lying along the symmetry axis of the nanostructure) preserves the oscillatory pattern for all the cases considered here. This flux leads only to an overall shift in the magnetic response curve $M(\Phi)$ by Φ_{AB}.

This work was supported by Grants from the Russian Fund for Fundamental Research, Ministry of Public and Professional Education of the Russian Federation, and the program ''The Universities of Russia–Basic Research.''

*)E-mail: margulis@mrsu.ru

[1] M. F. Lin, and K. W.-K. Shung, Phys. Rev. B **52**, 8423 (1995).
[2] H.-F. Cheung, Y. Gefen, E. K. Riedel, and W.-H. Shin, Phys. Rev. B **37**, 6050 (1988).
[3] Yu. N. Ovchinnicov, W. Legle, and A. Schmid, Ann. Phys. **6**, 489 (1997).
[4] Y. Meyr, O. Entin-Wohlman, and Y. Gefen, Phys. Rev. B **42**, 8531 (1990).
[5] R. Merlin, Solid State Commun. **64**, 99 (1987).
[6] V. A. Geĭler, V. A. Margulis, and I. V. Chudaev, Zh. Éksp. Teor. Fiz. **109**, 762 (1996) [JETP **82**, 409 (1996)].
[7] V. A. Geĭler, V. A. Margulis, and O. B. Tomilin, Pis'ma Zh. Éksp. Teor. Fiz. **63**, 549 (1996) [JETP Lett. **63**, 578 (1996)].
[8] V. A. Geyler and V. A. Margulis, Phys. Rev. B **55**, 2543 (1997).
[9] M. Büttiker, Y. Imry, and R. Landauer, Phys. Lett. **96**, 365 (1983).
[10] M. Büttiker, Phys. Rev. B **32**, 1846 (1985).
[11] H. Ajiki and T. Ando, J. Phys. Soc. Jpn. **62**, 1255 (1993).
[12] D. Shenberg, *Magnetic Oscillations in Metals* [Russian translation] (Mir, Moscow, 1986).
[13] E. M. Lifshitz and L. P. Pitaevskii, *Statistical Physics*, Part 1 [in Russian] (Nauka, Moscow, 1976).

Translated by D. H. McNeill

Molecular mobility and strengthening of oriented liquid-crystal polymers

E. A. Egorov, A. V. Savitskiĭ, V. V. Zhizhenkov, and I. A. Gorshkova

A. F. Ioffe Physicotechnical Institute, Russian Academy of Sciences, 194021 St. Petersburg, Russia
Fiz. Tverd. Tela (St. Petersburg) **41**, 859-861 (May 1999)

Broad-line proton magnetic resonance has been used to study cooperative mesophase molecular motion in the example of a fully-aromatic oriented liquid-crystal polymer Vectra A950. The molecular mobility is found to decrease as a result of heat treatment, which is considered to be the reason for a higher tensile (rupture) strength owing to an increase in the activation energy for the fracture process. © *1999 American Institute of Physics.* [S1063-7834(99)02505-8]

A substantial increase in the strength of rigid-chain polymers results from an increase in the fracture activation energy[1] U_0 which occurs during chemical or thermal processing of oriented fibers.[2] Table I lists some examples of thermo- and lyotropic liquid-crystal polymers for which the strength σ and U_0 increase during thermal processing. Proton magnetic resonance (PMR) has been used[3] to study the molecular mobility in the fully aromatic liquid-crystal polymer Vectra. Above the transition temperature to the mesophase (T_m), a fine structure is observed in the PMR spectra. An analysis of these spectra revealed the features of the molecular motion in the mesophase and made it possible to relate them to strengthening during thermal processing.

In this paper our task is to study the molecular motion over a wide range of temperatures in more detail for different sample orientations in a magnetic field and to clarify the molecular mechanisms for polymer strengthening during thermal processing. The main objects of study were highly-oriented fibers made of the copolymer Vectra A950 (a copolymer of 4-hydroxybenzoic and 2-hydroxy-6-naphthoic acids in a 7:3 ratio) manufactured by the Celanese Research Co. PMR spectra were recorded on a broad-line NMR spectrometer.[4] The samples were heated in a nitrogen atmosphere.

Figure 1 shows PMR spectra for fibers oriented parallel and perpendicular to the magnetic field of the spectrometer at temperatures ranging from 20 to 300 °C. The spectra were recorded in the form of the first derivative with a low modulation of the magnetic field. According to differential thermal analysis data, the temperature T_m of the transition to the mesophase was 285 °C. At temperatures up to 150 °C, the spectra are triplets, as reported previously.[5] However, at temperatures close to T_m, a fine structure appeared in the spectra that is more distinct in freshly prepared (not subjected to thermal processing) fiber. Thermal processing causes the fine structure to smooth out. The structure of these spectra indicates that the high-molecular nature of the material does not prevent cooperative motion in the liquid-crystal phase. In order to obtain more detailed information on the molecular motion in the mesophase we have analyzed the fine structure of the spectrum of fibers oriented along a magnetic field. Data on the proton-proton distances and angular parameters for the rings were taken from the literature.[6,7] The structure of the spectrum is caused by dipole-dipole magnetic interactions among nearest protons in the rings. Isolated pairs of phenylene rings and triads of protons in the naphthalene rings yield two and seven lines, respectively.[8,9] It was assumed that each of these lines is Gaussian broadened with dispersions β_p^2 and β_n^2 for the phenylene and naphthalene-rings. These parameters are the contributions to the second moment from protons which are external with respect to the groups.

In the first approximation the spectrum was calculated for the simplest case of ideal orientation of the chains by choosing values of β. This spectrum shape agreed fairly well with the experimental one (300 °C, initial sample) but the distance between the components was somewhat larger than in the experiment.[10] This difference cannot be caused by static (constant in time) misorientation of the segments in the fiber. Obviously, a new type of motion must be considered, specifically a cooperative type such that, as the liquid-crystal state is entered, the angular distribution of the directors of the fragments of the chains must be regarded as dynamic, rather than static. Suppose the cooperative molecular motion produces a continuous variation in the orientation of all the

TABLE I. Characteristics of the materials.

	Before annealing		After annealing		
Polymer	σ, GPa	U_0, kcal/mole	σ, GPa	U_0, kcal/mole	LC type
Vectra A950	1.3	31	2.8	42	Thermo-
Poly-n-phenylphenylene-terephthalate	1.0	29	3.0	53	tropic
Polyamido-benzimideazole	1.7	31	3.6	58	Lyo-
Poly-n-benzamide	1.4	45	1.8	56	tropic

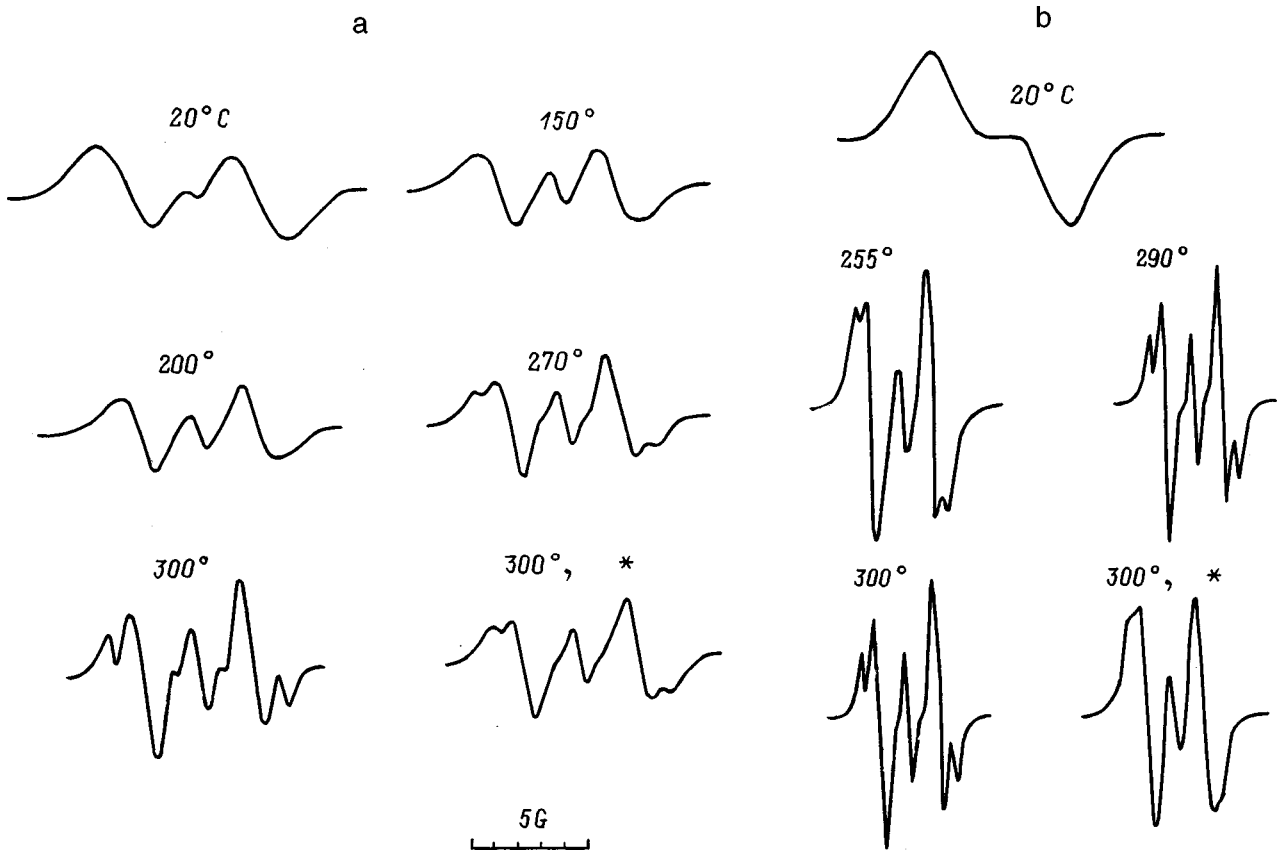

FIG. 1. PMR spectra of Vectra fibers: fiber parallel (a) and perpendicular (b) to the magnetic field. The last spectra in the series were obtained after thermal processing (indicated by an asterisk), the rest are spectra of the original fibers.

directors within the limits of a constant angular amplitude φ. These vibrations should be rather rapid: for averaging the local magnetic fields, according to PMR theory the period of the oscillations should not exceed 10^{-4} s. As a result of this sort of motion, all the segments appear to be in an identical state and φ can be used as a measure of the cooperative motion in the mesophase. But even this assumption could not bring all the components of the theoretical spectrum into agreement with experiment.

We believe the main reason for this difference is that, in real fibers, the phenylene rings (their axis of rotation) deviate in the mesophase from the orientation axis of the fiber by some angle Ψ_0, which must also be regarded as a time average, since the cooperative motions of the macromolecules cause additional oscillations of the rings. The best agreement between the theoretical and experimental (at 300 °C) spectra was obtained for the following values of the parameters: $\varphi = 23°$, $\Psi_0 = 17°$, $\beta_p^2 = 0.26G^2$, and $\beta_n^2 = 0.14G^2$ (see Fig. 2a). Obviously, the agreement between theory and experiment is better, especially if we note that the spectra are shown in first-derivative form. This result means that we can regard these parameters as the actual characteristics of the motion of the chains in the mesophase.

Additional information on the molecular motion in the liquid-crystal phase can be obtained from spectra for fibers oriented perpendicular to the spectrometer magnetic field. The good resolution of the spectrum in this case means that the segments of the macromolecules rotate or vibrate addi-

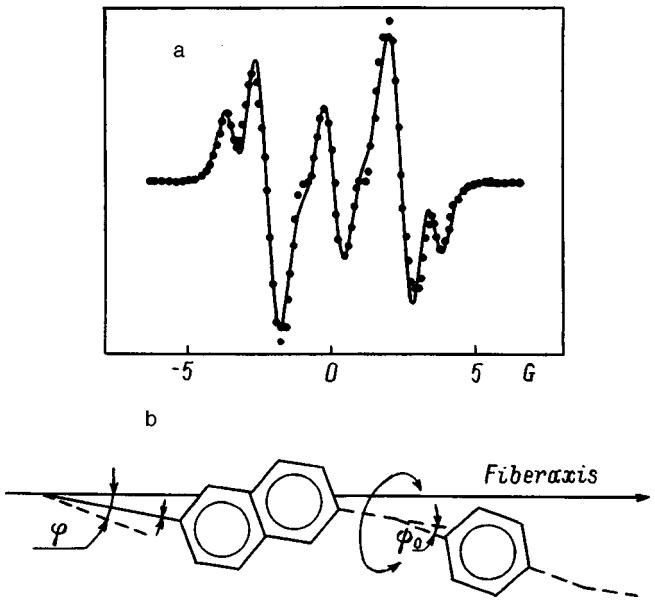

FIG. 2. Spectra: theoretically calculated (smooth curve) and experimental (points) for 300 °C and orientation of the fibers parallel to the magnetic field (a). The model for the motion of a fragment of a macromolecule in the mesophase: the director of the fragment oscillates within a range φ and the fragments undergo rotational vibrations around the axis (b).

tionally at a large amplitude about axes parallel to the fiber axis, since, otherwise, the interproton vectors would have an angular (azimuthal) distribution that was constant in time in the same plane as the spectrometer magnetic field vector, and this would cause smoothing of the spectral structure.

In the mesophase, therefore, large scale conformational motions, which can be regarded as ''quasisegmental'' motions are intrinsic to the macromolecules of the fully aromatic liquid-crystal copolymer. A model for the motion of a fragment of the chain in the mesophase is suggested in Fig. 2b. The spectra of thermally processed samples indicate that thermal processing slows down the quasi-segmental motion above T_m. Annealed samples are dynamically inhomogeneous: they contain both residual liquid-crystal regions and newly formed ''rigid'' microsegments. We denote the fraction of the former by α and assume that the shape of their spectrum is similar to that of freshly produced fiber at 300 °C. In the ''rigid'' regions only local rotation of the rings can occur. Conformational motions do not occur there, i.e., the situation is the same as at 150 °C. Then the dynamic inhomogeneity can be estimated in the same way as for flexible chain polymers.[4] Let us assume that the high-temperature spectrum of an annealed sample is the sum of the spectra at 300 and 150 °C. The best agreement between the observed spectrum and the one obtained by summing occurs for $\alpha = 0.4$. Therefore, as a result of thermal processing, about 60% of the volume of the sample goes into a phase that is solid above T_m. (Obviously, these regions include more than three-dimensional crystals.[11]) Strengthening, like the magnitude of α, depends on the thermal processing conditions, so that α can be used as a characteristic of the process. It is precisely an increase in the rigidity of the material on a microscopic level that can explain the rise in U_0 owing to thermal processing: in a thermally processed sample an external load is distributed among rigid regions, in which the ''weak bonds''[12] appear to be blocked by neighboring chains, rather than among individual macromolecules. This effect should lead to a higher activation energy for the fracture process.

We thank the Russian Fund for Fundamental Research for support of this work (Grant No. 97-03-32624).

[1] S. N. Zhurkov, Int. J. Fract. Mech. **1**, 311 (1965).
[2] A. V. Savitskiĭ, B. Ya. Levin, L. E. Utevskiĭ, and L. P. Zosin, Vysokomol. Soedin., Ser. B **16**, 810 (1974).
[3] E. A. Egorov, A. V. Savitskiĭ, V. V. Zhizhenkov, and I. A. Gorshkova, Fiz. Tverd. Tela **40**, 1173 (1998) [Phys. Solid State **40**, 1071 (1998)].
[4] E. A. Egorov and V. V. Zhizhenkov, J. Polym. Sci., Polym. Phys. Ed. **20**, 1089 (1982).
[5] R. A. Allen and I. M. Ward, Polymer **32**, 202 (1991).
[6] M. Bailey and C. J. Brown, Acta Crystallogr. **22**, 387 (1967).
[7] A. Biswas and J. Blackwell, Macromolecules **21**, 3146 (1988).
[8] G. E. Pake, J. Chem. Phys. **16**, 327 (1948).
[9] E. R. Andrew and R. Bersohn, J. Chem. Phys. **18**, 159 (1950).
[10] E. A. Egorov, V. V. Zhizhenkov, I. A. Gorshkova, and A. V. Savitsky, Polymer Communications (1999), in press.
[11] E. M. Antipov, S. D. Artamonova, I. A. Volegova, and Yu. K. Godovskiĭ, Vysokomol. Soedin., Ser. A **37**, 800 (1995).
[12] V. R. Regel', A. I. Slutsker, and É. E. Tomashevskiĭ, *The Kinetic Nature of the Strength of Solids* [in Russian], Nauka, Moscow (1974).

Translated by D. H. McNeill

Relaxation into tunnel induced nonequilibrium states in metal-oxide semiconductor structures

A. Vercik*) and A. Faigón

Devices Physics-Microelectronics Laboratory, Faculty of Engineering, University of Buenos Aires, Paseo Colón 850, (1063) Buenos Aires, Argentina

Fiz. Tverd. Tela (St. Petersburg) **41**, 862–864 (May 1999)

The relaxation of a metal-oxide semiconductor structure from deep depletion towards a tunnel-induced non-equilibrium steady state is addressed in this work. A simple model was constructed, taking into account thermal generation, tunneling of both types of carriers and impact ionization. Experimental results obtained on *p*- and *n*-type Si substrates and oxides thinner than 6.5 nm are shown to be well fitted by the proposed model. A map describing the possible behavior patterns for a structure with given oxide thickness and effective generation velocity is presented. © *1999 American Institute of Physics.* [S1063-7834(99)02605-2]

The transients in a metal-oxide sdemiconductor (MOS) structure relaxing from deep depletion towards equilibrium were previously investigated in connection with the characterization of the minority-carrier-generation mechanisms. It is assumed, for the methods to be applicable, that the transient ends in the thermal equilibrium state. The presence of tunneling currents alters this behavior, affecting the transient to yield a steady state different from thermal equilibrium.[1–5]

Very thin oxide samples exhibit similar transients for both *p*- and *n*-type substrates. This symmetry breaks down for oxide thicknesses above 3.5 nm. Three qualitatively different behavior patterns, depending of the oxide thickness, can be identified through current transient curves for the *n*-type substrate samples. From analysis of the associated currents, the three patterns correspond to i) *p*-type substrate samples and very thin oxide *n* samples for which minority carriers seem to dominate the tunneling current, ii) intermediate oxide thickness (3–6 nm) on *n* substrates, for which the tunneling current is dominated by majority carriers but the whole current is limited by the generation of minority carriers, and iii) thicker oxides on *n* substrates, for which the impact ionization mechanism removes the limit imposed to the current by supplying minority carriers.

The problem of modeling the relaxation of a MOS structure from deep depletion to tunnel-induced non-equilibrium states is addressed in this work.

An exact formulation of this problem requires the coupling Poisson equation, continuity equations for holes and electrons, and complete expressions for the pair-generation process, tunneling, and impact ionization. An integral treatment for the continuity equations, as used in this work, leads to a unique differential equation describing the evolution towards equilibrium.

The model was tested by reproducing experimental results in the three regimes, and was used to analyze the dependence of each type of behavior on the thickness and generation parameters.

A map for the relationship between oxide thickness and thermal treatment to obtain a given behavior pattern is given.

1. THEORY

The measured current in the external circuit after applying a reverse voltage step to an *n*-MOS diode is given by[5]

$$J_m = J_{\text{disp}} + J_{tp} + J_{tn} = J_g + \frac{dQ_{\text{dep}}}{dt} + J_{tn}, \tag{1}$$

where J_{disp} is the displacements current due to changes in the charge distribution within the semiconductor, and J_{tp} and J_{tn} are the conduction currents which in this case correspond to tunneling currents for holes and electrons, respectively. J_g is the minority carrier generation current into the inversion layer, and Q_{dep} is the space charge in the depleted region.

Charge conservation in integral form, applied to the inversion layer, is expressed as follows:

$$\frac{dQ_{\text{inv}}}{dt} = J_g - J_{tp}, \tag{2}$$

where Q_{inv} is the inversion layer charge. Using the conservation of the electric displacement vector, the inversion layer charge takes the form

$$Q_{\text{inv}} = |V_g - V_s| \frac{\varepsilon_{\text{ox}}}{d} - qNW, \tag{3}$$

where V_g is the applied voltage, V_s is the semiconductor potential, d is the oxide thickness, ε_{ox} is the oxide dielectric permittivity, q is the electron charge, N is the dopant concentration, and W is the depletion region width. Using the known dependence of W on V_s, the variation of Q_{inv} with time in terms of variations of V_s results in

$$\frac{dQ_{\text{inv}}}{dt} = \left[\frac{\varepsilon_{\text{ox}}}{d} + \frac{\varepsilon_s}{W(V_s)}\right]\frac{dV_s}{dt}, \tag{4}$$

where ε_s is the semiconductor dielectric permittivity. Replacing in Eq. (2) we obtain the differential equation for V_s

$$\frac{dV_s}{dt} = \frac{J_g - J_{tp}}{\left[C_{\text{ox}} + \dfrac{\varepsilon_s}{W}\right]}. \tag{5}$$

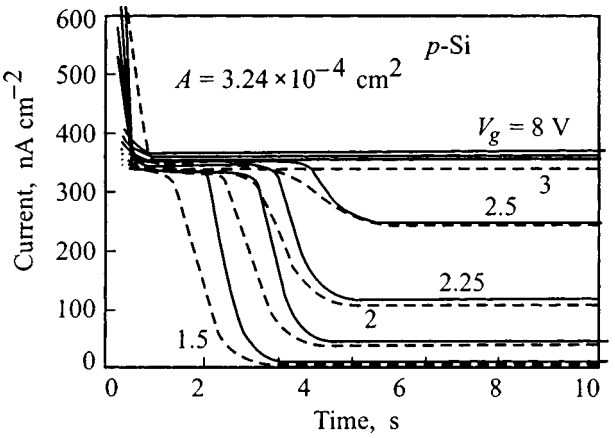

FIG. 1. Experimental (solid) and calculated (dashed) curves, for a *p*-type sample, 4.5 nm oxide thickness, with different voltage pulses. *A* is the gate area.

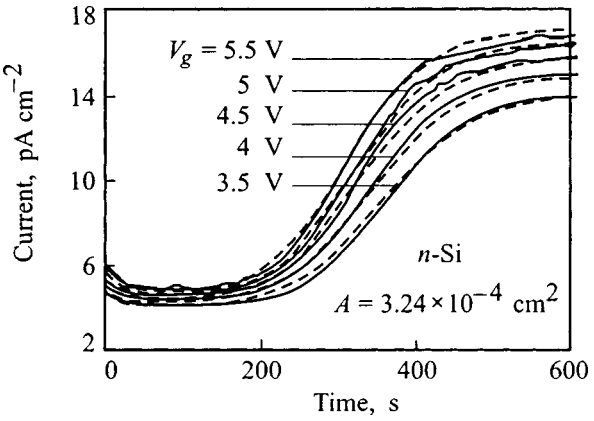

FIG. 2. Experimental (solid) and calculated (dashed) curves, for an *n*-type sample, 3.7 nm oxide thickness.

The total generation current is written as

$$J_g = qn_i\left(\frac{W}{2\tau_g}+S_i\right)\left[1-\exp\left(\frac{V_g-\theta}{2kT}\right)\right]+qS_d(p_s^{eq}-p_s), \quad (6)$$

where n_i is the intrinsic concentration, k is the Boltzmann constant, τ_g is the bulk generation lifetime, S_i is the value of the surface generation when the surface is inverted, and S_d is the generation velocity for the depleted surface, given by Ref. 6:

$$S_d = S_0\frac{N}{(p_s+2n_i)},$$

where S_0 is a constant parameter, θ is the difference between the metal Fermi level and the minority carrier quasi Fermi level, p_s is the surface minority carrier concentration, which in terms of V_s is

$$p_s = \frac{(V_g-V_s)^2}{2kT\varepsilon_s}\left(\frac{\varepsilon_{ox}}{d}\right)^2-\frac{qN}{kT}\left(|V_s|-\frac{kT}{q}\right), \quad (7)$$

where p_s^{eq} is the equilibrium minority-carrier concentration at the surface calculated from Eq. (7) with $V_s = V_s^{eq}$, the equilibrium semiconductor voltage drop calculated in Refs. 4 and 7. The number of pairs generated by impact in the space charge region for $V_{ox} > 1.7$ V, approximately,[8] ($V_{ox} = V_g - V_s$) is

$$J_{gi} = \alpha W J_{tn}, \quad (8)$$

where α is the number of ionized pairs per unit distance and J_{tn} is the majority-carrier tunneling current.[9]

The extraction of minority carriers by tunneling was modeled by the following expression:

$$J_{tp} = \left(C_h\frac{p_s}{\alpha_h^2 N_v}+J_g\right)\exp(-2k_0 d)\exp(-\alpha_h q V_{ox}), \quad (9)$$

where C_h, and α_h are numerical constants for hole tunneling. Equation (9) keeps the exponential dependence of the current on the oxide voltage drop reported for the direct tunneling regime.[9] The prefactor in this expression represents the total supply of carriers with velocity normal to the barrier. It is composed by carriers in the inversion layer with the first term proportional to p_s (Ref. 10), and the carriers generated and driven to the surface, J_g.

2. EXPERIMENTAL RESULT FITTING

The transient currents of a pulsed MOS diode to depletion can be classified, as was shown in a recent work,[5] in three different behavior patterns, as follows.

a) Dominance of the current by minority-carrier tunneling.

b) Tunneling of both type of carriers, with the current llimited by the generation of minority carriers.

c) Tunneling of both type of carriers without limitation by the minority-carrier generation which is enhanced by impact ionization.

Case a) is observed in the *p*-type substrate capacitors or in *n*-type with very thin insulators (up to about 3 nm). In *n* samples with oxides between 3 and 6 nm, the impact ionization may occur but is insufficient for removing the generation limitation (case b). Case c) occurs for *n*-substrate samples with oxides thicker than about 6 nm.

Figures 1 to 3 show a family of experimental curves

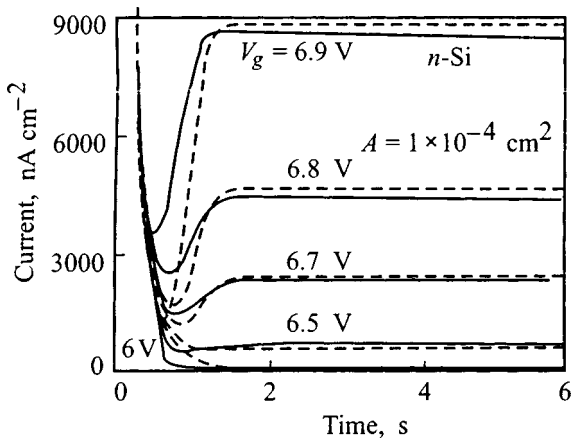

FIG. 3. Experimental (solid) and calculated (dashed) curves, for an *n*-type sample, 6.3 nm oxide thickness.

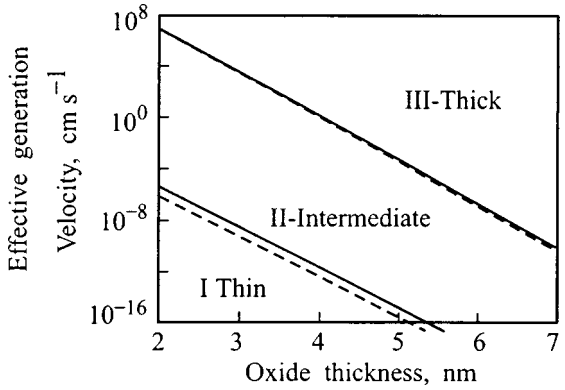

FIG. 4. Behavior pattern map for MOS tunnel diodes with *n*-type substrate. The boundaries between regions were calculated for 3 V (solid line) and 50 V (dashed line) applied to the gate.

pertaining to each one of the described cases fitted with the model proposed above. Details of the experimental work are given in Ref. 5.

3. DISCUSSION

In contrast to *p* samples in which a unique kind of transient curve is measured, the behavior during the relaxation into tunnel-induced non-equilibrium states in metal-oxide semiconductor structures with *n*-Si is determined by the oxide thickness and minority-carrier generation parameters. The carrier generation can be characterized by an effective velocity, S_{eff}, as the total generation current density J_g divided by qn_i. In the steady state, the generation current should equal the hole tunnel current, J_{tp}. Thus, for the steady state, the effective generation velocity is

$$S_{\text{eff}}=\frac{J_{tp}(V_{ox},d)}{qn_i}. \tag{10}$$

A map for the different behaviors can be constructed plotting this velocity versus the oxide thickness (Fig. 4). This plot is divided into three regions. Structures laying in region I will exhibit curves like those shown in Fig. 1 for 3 and 8 V. No transient other than the decay of the surface generation velocity from its depleted value, S_0, to a steady-state value, greater or equal to S_i, can be measured in these diodes. Structures with parameters in region III, are those for which impact ionization spontaneously begins, enhancing generation of minority carriers (Fig. 3). Diodes between these two regions will show an increasing current transient (Fig. 2) due to the presence of a majority tunneling current without impact ionization — region II.

The boundaries between these regions, can be determined as follows. The condition to be fulfilled by a diode to be in region III is that the steady-state oxide voltage drop must exceed the threshold for impact ionization, to ensure that impact ionization will begin during the transition to equilibrium. Thus, from Eq. (10) with $V_{\text{ox}}=1.7$ V, the boundary between regions II and III is obtained. Diodes with higher S_{eff} or thicker oxide will exhibit the typical thick-structure-like behavior pattern.

Structures will be in region I if the surface is not inverted in the steady state, so the surface-generation velocity will take on a value between S_0 and S_i. Any tunneling current growth will be screened by the decreasing generation current. The minimum level of generation current before the inversion (or the maximum generation current when the surface is inverted) is obtained by replacing, in the bulk generation expression, the depletion width value immediately after the pulse, W_0, given by

$$W_0=\frac{A\varepsilon_s}{C_{\text{ox}}}\left(\sqrt{1-\frac{2V_gC_{\text{ox}}^2}{qN\varepsilon_sA^2}}-1\right), \tag{11}$$

and then, the generation in this case will be

$$J_g=qn_i\frac{W_0}{2\tau_g}+qn_iS_i. \tag{12}$$

The initial oxide voltage in this situation is

$$V_{\text{ox}}^0=V_g-\frac{qNW_0^2}{2\varepsilon_s}. \tag{13}$$

The prefactor in expression (9) for J_{tp}, i.e., the incident current, will be governed by J_g provided that the minority-carrier concentration at the surface is too small. Replacing (9), (12) and (13) in Eq. (10), the resulting S_{eff} vs d curve represents the lowest boundary between regions I and II, i.e., diodes with smaller S_{eff} or d will exhibit a thin-structure-like behavior pattern.

*)E-mail: avercik@fi.uba.ar

[1] M. A. Green and J. Schewchun, Solid-State Electron. **17**, 349 (1974).
[2] W. E. Dahlke and J. A. Shimer, Solid-State Electron. **26**, 465 (1983).
[3] S. J. Wang, B. C. Fang, F. C. Tzeng, C. T. Chen, and C. Y. Chang, J. Appl. Phys. **60**, 1080 (1986).
[4] B. Majkusiak and A. Strojwas, J. Appl. Phys. **74**, 5638 (1993).
[5] A. Vercik and A. Faigon, J. Appl. Phys. **84**, 329 (1998).
[6] A. S. Grove, *Physics and Technology of Semiconductor Devices*, (John Wiley & Sons, 1967).
[7] R. Seiwatz and M. Green, J. Appl. Phys. **29**, 1034 (1958).
[8] C. Chang, C. Hu, and R. W. Brodersen, J. Appl. Phys. **57**, 302 (1985).
[9] A. Faigon and F. Campabadal, Solid-State Electron. **39**, 251 (1996).
[10] H. C. Card and E. H. Rhoederick, J. Phys. D **4**, 1602 (1971).

Published in English in the original Russian journal. Reproduced here with stylistic changes by the Translation Editor.

Transition and rare-earth elements in the SiC and GaN wide-gap semiconductors: recent EPR studies

P. G. Baranov, I. V. Il'in,*) E. N. Mokhov, and V. A. Khramtsov

A. F. Ioffe Physicotechnical Institute, Russian Academy of Sciences, 194021 St. Petersburg, Russia
Fiz. Tverd. Tela (St. Petersburg) **41**, 865–867 (May 1999)

EPR studies of transition-element ions in SiC and GaN and of erbium in 6*H*-SiC are reported. Data are presented on Sc^{2+} ions and scandium acceptors, and chromium and molybdenum ions in various charge states in SiC. A study was made of nickel and manganese in nominally pure GaN grown by the sandwich sublimation method. The first EPR investigation of Er in 6*H*-SiC is reported. Erbium was identified from the hfs of the EPR spectra. Various possible models of erbium centers in silicon carbides are discussed. Strong room-temperature erbium-ion luminescence was observed. © *1999 American Institute of Physics.* [S1063-7834(99)02705-7]

The wide-gap semiconductors SiC and GaN having a high binding energy are among the most promising materials for use in opto- and microelectronics, as well as in high-frequency and power electronics. GaN-based materials are expected to produce revolutionary changes in information recording. Doping SiC and GaN with transition elements creating deep levels in the semiconductor, and fabrication of semi-insulating layers of these materials are presently an important problem. EPR is the main and most informative tool for studying defect structure at the atomic level.

This work discusses the use of EPR to investigate a number of impurity centers of transition and rare-earth elements in SiC.

1. IONS OF TRANSITION ELEMENTS IN SiC

A. Scandium

The two types of Sc EPR spectra observed in 6*H*-crystals were assigned by us to scandium acceptors and Sc^{2+} ions.[1] At temperatures close to 40 K, one observed Sc acceptor signals Sc_a(HT) (HT stands here for high temperature) and signals due to Sc^{2+} ions ($3d^1$, $S=1/2$). Both centers have axial symmetry relative to the *c* axis and can be described by a spin Hamiltonian

$$H=\mu_B \mathbf{BgS}+\mathbf{SAI}, \tag{1}$$

where *S* and *I* are the electron and nuclear spins, μ_B is the Bohr magneton, and **A** is the hyperfine (hf) structure tensor. The *z* axis is parallel to the *c* axis of the crystal. The Sc impurity was identified from the hf structure of the spectra caused by interaction with the ^{45}Sc isotope ($I=7/2$). The Sc_a(HT) acceptor has the following parameters: $g_\parallel=2.0016$, $g_\perp=2.0011$, $A_\parallel=10.1\times10^{-4}$ cm^{-1}, and $A_\perp=22.6\times10^{-4}$ cm^{-1}; for Sc^{2+} they are: $g_\parallel=2.0047$, $g_\perp=2.0002$, $A_\parallel=44.6\times10^{-4}$ cm^{-1}, and $A_\perp=8.4\times10^{-4}$ cm^{-1}. As the temperature is lowered to 4 K, these spectra disappear to be replaced by at least two different signals due to lower-symmetry Sc acceptors, denoted by Sc_a(LT) and Sc_{a1}(LT) (with LT standing for low temperature). The parameters of Sc_{a1}(LT) are: $g_x=2.001$, $g_y=2.016$, $g_z=2.008$, $A_x=15.0\times10^{-4}$ cm^{-1}, $A_y=3.0\times10^{-4}$ cm^{-1}, and $A_z=5.0\times10^{-4}$ cm^{-1}. The Sc_a(LT) signals were not studied thoroughly, but qualitatively the local axes of the corresponding centers can be identified as directed along the Si-C bonds which do not coincide with the *c* axis. The low symmetry of the low-temperature Sc signals may be due to spin-density redistribution and, possibly, to off-center position of the scandium atom. An alternative possibility is a more complex defect structure (a complex including a carbon vacancy, etc.).

B. Chromium

Studies of 6*H*-SiC:Cr crystals revealed EPR signals due to chromium ions in the charge states Cr^{3+} ($3d^3$, $S=3/2$), Ref. 2, and Cr^{2+} ($3d^4$, $S=2$). The chromium was identified from the hf structure of the ^{53}Cr nuclei ($I=3/2$). The 6*H*-SiC lattice has three inequivalent sites, namely, a hexagonal (h) and two quasicubic ones ($k1$ and $k2$). The Cr^{3+} signals observed originated from two inequivalent lattice sites (apparently $k1$ and $k2$). The hf structure was reliably identified only in the $\mathbf{B}\|c$ orientation and was found to be: for the $k1$ sites $A_\parallel=8.67\times10^{-4}$ cm^{-1}, and for $k2$ $A_\parallel=9.11\times10^{-4}$ cm^{-1}. The Cr^{3+} signals can be described by the spin Hamiltonian

$$H=g_\parallel\mu_B B_z S_z+g_\perp\mu_B(B_xS_x+B_yS_y)+D[S_z^2-1/3S(S+1)]+\mathbf{SAI}, \tag{2}$$

where *D* relates to the fine structure. Because in zero-field splitting $D\gg g\mu_B B$, one observes only the $M_s=\pm1/2$ transition within the Kramers doublet, which is described by an effective spin $S'=1/2$ and Hamiltonian (1) with effective g' factors. The *g* factors have the following effective values: $g'_\parallel=4.0$ and 4.02, $g'_\perp=1.97$ and 1.96 for the $k1$ and $k2$ sites, respectively. It can be shown that the experimental values g' are related to the true values of the *g* factor in the following way: $g'_\parallel=g_\parallel$, $g'_\perp=2g_\perp[1-3/16(h\nu/2D)^2]$. Our estimates give $D>40$ GHz.

TABLE I. Parameters of Mn and Ni ions in GaN (Ref. 4).

Ion	$g_{\parallel}$	$g_{\perp}$	$\lvert D\rvert$, 10^{-4} cm^{-1}	A, 10^{-4} cm^{-1}	Note
$Mn^{2+}(3d^5)$	1.999	1.999	240	70	$S=5/2$
$Ni^{3+}(3d^7)$	2.10	$\cong$4.2			$S'=1/2$
	2.10	$\cong$2.1	$\geqslant 1.5\times10^4$		$S=3/2$

We observed hyperfine interaction not only with the ^{53}Cr nucleus, but with nuclei of the Cr^{3+} nearest-neighbor ions in the lattice as well.[2] These interactions can be accounted for by assuming the chromium atom to be shifted along the c axis from the silicon site.

The signal of the divalent chromium Cr^{2+} ($3d^4$, $S=2$), which was observed only in crystals grown on the C side of SiC, can be described by spin Hamiltonian (2). Its parameters are: $g_{\parallel}=1.987$, $g_{\perp}=1.942$, $A\cong 15\times10^{-4}$ cm^{-1}, and $|D|=1.285$ cm^{-1}.

C. Molybdenum

We observed signals in 6H crystals from molybdenum ions in two charge states, Mo^{4+} and Mo^{3+}. The hf structure of the spectra produced in interaction with the nuclear spins of the ^{95}Mo ($I=5/2$) and ^{97}Mo ($I=5/2$) isotopes permitted unambiguous identification of the impurity.[3] Weakly n-type crystals exhibit signals due to Mo^{4+} ($3d^2$, $S=1$) occupying the $k1$ and $k2$ sites, and in strongly n-type ones, only $k2$-site signals, which shows that the Mo^{4+} impurity sitting at different sites produces levels with strongly differing energies in the gap. The line positions can be described by spin Hamiltonian (2). Its parameters are $g_{\parallel}=1.977$, 1.975; $g_{\perp}=1.976, 1.977$; and $|D|=1018\times10^{-4}$ and 1108×10^{-4} cm^{-1} for the $k1$ and $k2$ sites, respectively. Mo^{3+} ions ($4d^3$, $S=3/2$) were observed to create signals in n-type crystals. The corresponding parameters are: $g_{\parallel}=1.945$, $g_{\perp}=1.969$, and $|D|>2$ cm^{-1}. Signals from Mo^{5+} ($4d^1$) were also detected; they can be described by the spin Hamiltonian (1) for $S=1/2$ with the parameters $g_{\parallel}=1.9679$ and $g_{\perp}=1.9747$.[3] In p-type crystals Mo signals are not observed, which suggests that the nonparamagnetic Mo^{6+} state ($4d^0$) is here in equilibrium.

2. Mn AND Ni IN GaN

EPR signals of manganese and nickel were observed in nominally pure GaN crystals grown by the sandwich sublimation method.[4] The manganese impurity was identified from the characteristic hf structure of the spectra due to interaction with the nuclear spin of the ^{55}Mn isotope ($I=5/2$, 100%).The charge state of the manganese is Mn^{2+} ($3d^5$, $S=5/2$). We observed Ni signals with an angular dependence characteristic of a system with an electronic spin $S=3/2$ in a strong axial crystalline field. The charge state of the nickel here is Ni^{3+} ($3d^7$, $S=3/2$). The Ni spectra can be described by spin Hamiltonian (2) (the true spin $S=3/2$) or, because the crystalline field is strong, $D\gg g\mu_B B$, by spin Hamiltonian (1) (with an effective spin $S'=1/2$). The parameters for the two ions are listed in Table I. Both ions occupy gallium sites in the GaN lattice.

TABLE II. Parameters of erbium centers in 6H-SiC:Er.

Spectrum	g_x	g_y	g_z	A_x, 10^{-4} cm^{-1}	A_y, 10^{-4} cm^{-1}	A_z, 10^{-4} cm^{-1}
LS_1	12.2	3.35	1.5	450	124	55
LS_2	10.6	6.16	1.26	390	227	46
LS_3	9.25	7.2	1.45	353	276	53
Ax_2	8.28	8.28	1.07	290	290	38
Ax_3	8.07	8.07	1.16	285	285	41

3. ERBIUM IN 6*H*-SiC

The 6H-SiC:Er crystals were grown by sandwich sublimation and doped during growth. They exhibited EPR signals of two types, low (orthorhombic) symmetry (LS) and axial (Ax).[5] The LS signals were found to have an hf structure due to interaction with the ^{167}Er nuclei ($I=7/2$, 22.8%) and are assigned to the Er^{3+} impurity occupying three crystallographically inequivalent sites in the 6H-SiC lattice. The LS signals can be described by spin Hamiltonian (1) with parameters given in Table II. The structure of the low-symmetry erbium centers is shown in Fig. 1a for the h and $k1$ sites. As follows from the nature of the angular dependences, the axis of the center does not coincide with the c axis of the crystal and is deflected from it by 70° (110°), while the center itself (the z axis) is oriented along one of the Si-C bonds. This orientation shows that the low-symmetry erbium centers represent actually an Er^{3+} ion at the silicon site bound in a complex with another defect (a carbon or oxygen vacancy) occupying the nearest carbon site; it should be added that, for any inequivalent site, the defect (see Fig. 1a) can occupy carbon sites 1, 2, or 3, but not site 4.

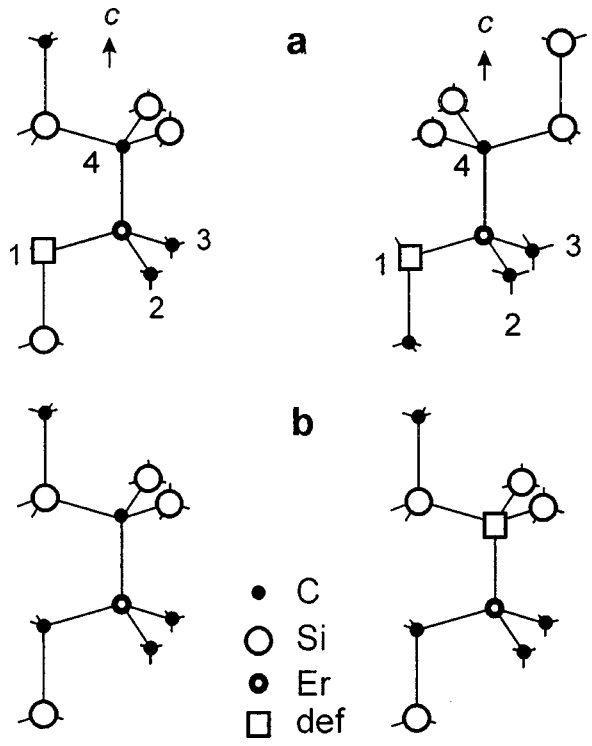

FIG. 1. Models of Er^{3+} centers in 6H-SiC. (a) Orthorhombic centers in h and k sites. (b) Two models of axial centers (h sites).

We detected in 6*H*-SiC:Er crystals six signals with an axial symmetry with respect to the hexagonal axis (Ax_1-Ax_6). Only for two lines (Ax_2 and Ax_3) could one detect reliably an hf structure. Similarly to the case of low-symmetry centers, it consists of eight weak lines and originates from interaction with ^{167}Er nuclei. The axial angular dependences of the erbium centers can be described by spin Hamiltonian (1) (see Table II for the corresponding parameters) and accounted for by two models of the center presented in Fig. 1b for the *h* site. In the first model, erbium occupies silicon sites in a regular lattice. In the second model, besides an Er^{3+} ion at the silicon site, there is also a defect in the adjacent carbon site along the *c* axis. It should be stressed that the defect axis in axial centers is parallel to the *c* axis of the crystal for all inequivalent sites. The crystals in which EPR of erbium was observed exhibited strong luminescence at the wavelength of 1.54 μm associated with erbium ions.[6]

In this way we have studied in the recent few years EPR spectra of several transition-element impurities substituting for silicon in 6*H*-SiC, namely, scandium, molybdenum, and chromium, as well as scandium acceptors. Preliminary EPR data on transition-metal impurities, manganese and nickel, in gallium nitride have been obtained. EPR spectra of Er in SiC have been investigated for the first time.

Partial support of the Russian Fund for Fundamental Research (Grant 98-02-18241) is gratefully acknowledged.

*)E-mail: Ivan.Ilyin@pop.ioffe.rssi.ru

[1] P. G. Baranov, I. V. Il'in, E. N. Mokhov, A. D. Roenkov, and V. A. Khramtsov, Fiz. Tverd. Tela (St. Petersburg) **39**, 52 (1997) [Phys. Solid State **39**, 44 (1997)].
[2] P. G. Baranov, V. A. Khramtsov, and E. N. Mokhov, Semicond. Sci. Technol. **9**, 1340 (1994).
[3] J. Baur, M. Kunzer, K. F. Dombrowski, U. Kaufmann, J. Schneider, P. G. Baranov, and E. N. Mokhov, Inst. Phys. Conf. Ser. **155**, No. 12, 933 (1997).
[4] P. G. Baranov, I. V. Ilyin, and E. N. Mokhov, Solid State Commun. **101**, 611 (1997).
[5] P. G. Baranov, I. V. Ilyin, and E. N. Mokhov, Solid State Commun. **103**, 291 (1997).
[6] P. G. Baranov, I. V. Il'in, E. N. Mokhov, A. B. Pevtsov, and V. A. Khramtsov, Fiz. Tverd. Tela (St. Petersburg) **41**, No. 38 (1999) [Phys. Solid State **41**, 32 (1999)].

Translated by G. Skrebtsov

Charge displacement induced by intercalation of graphite-like nanoclusters in amorphous carbon with copper

V. I. Ivanov-Omskiĭ* and É. A. Smorgonskaya

A. F. Ioffe Physicotechnical Institute, Russian Academy of Sciences, 194021 St. Petersburg, Russia
Fiz. Tverd. Tela (St. Petersburg) **41**, 868–870 (May 1999)

Interaction of an impurity Cu atom with carbon in copper-intercalated graphite-like nanoclusters in a-C:H has been considered in a simple tight-binding approximation. Clusters with simple configurations were used to show that partial ionization of Cu gives rise to metallization of a semiconductor cluster and to a substantial charge redistribution in the latter. The presence of copper initiates in the cluster internal polarization with components directed both normal to the graphene-fragment plane and parallel to it. The lowering of the cluster symmetry induced by copper intercalation activates the Raman band *G* in the IR spectrum of a-C:H. © *1999 American Institute of Physics.* [S1063-7834(99)02805-1]

It is known that metallic copper does not interact chemically with carbon and does not form with it oriented valence bonds characteristic of metal carbides. Copper is difficult to insert into crystalline graphite as an intercalant. At the same time copper as an impurity enters amorphous carbon (a-C:H) easily and modifies strongly its electrical and optical properties.[1] Unlike graphite, a-C:H is a semiconductor transparent in the visible. The structure of a-C:H represents a system of graphite-like nanoclusters 5–20 Å in size embedded in a wide-gap diamond-like matrix. It is the size quantization of the electronic spectrum in such nanoclusters that creates an optical gap in a-C:H.[2] Doping the a-C:H opens up new possibilities for probing the interaction of copper with carbon by both electrical and optical methods. To cite one example, an investigation of IR absorption and Raman spectra of a-C:H⟨Cu⟩ showed[3] that Cu atoms preferentially enter graphite-like nanoclusters in a-C:H without forming of Cu-C bonds, i.e., by the intercalation mechanism.

This work presents calculated electronic spectra of simple graphite-like carbon nanoclusters containing a small fragment of the graphene plane and one Cu atom near the plane. An analysis is made of the effects accompanying the event of cluster intercalation with copper, namely, charge redistribution in the cluster and the Cu-induced static dipole moment, as well as changes in the vibrational spectrum.

1. MODEL AND MAIN APPROXIMATIONS

The electronic spectrum of a graphene nanocluster with a Cu impurity atom was calculated in the well-known tight-binding formalism, or the LCAO method, in the nearest-neighbor approximation. The main relations obtained in the frame of LCAO for such clusters were given in Ref. 4. The numerical calculations were performed for clusters of various sizes.

It was found that the main features in the variation of cluster properties induced by copper intercalation can be readily exemplified by two clusters of two or four regular six-membered carbon rings containing, respectively, $N=10$ or 16 carbon atoms (Fig. 1a and 1b). It was assumed that the Cu atom does not enter the carbon ring and interacts only with its π electrons, and that the perturbation of the strong C-C covalent σ bonds within the ring may be neglected. It was also assumed that the principal contribution to the interaction is due to one outer *s* electron of the Cu atom. The corresponding *s* orbital and N p_z valence orbitals of the C atoms made up a system of $(N+1)$ basis functions χ_i of Hamiltonian $\hat{H}$ (the *z* axis is orthogonal to the *xy* graphene plane, and index $i=1,2,\ldots,N+1$ labels the atoms). The wave function of the jth state in the cluster was written in the LCAO form with coefficients u_{ji}:

$$|\psi_j\rangle=\sum_i^{N+1} u_{ji}|\chi_i\rangle\,.$$

The matrix elements of the Hamiltonian, $\chi_{ij}=\langle\chi_j^*|\hat{H}|\chi_i\rangle$, were determined in the Harrison approximation[5]. The diagonal matrix elements χ_{ii} are essentially the energies of $2p$ and $4s$ states of isolated C and Cu atoms relative to the vacuum level: $\varepsilon_p=\langle p_z^*|\hat{H}|p_z\rangle=-8.97$ eV and $\varepsilon_s=\langle s^*|\hat{H}|s\rangle=-6.92$ eV. The off-diagonal matrix elements $(i\neq j)$ describing interatomic interaction were calculated as $\chi_{ji}=n_{ji}\hbar^2/\mu d_{ji}$, where μ is the electronic mass, d_{ji} is the distance between atoms i and j, and n_{ji} are tabulated[6] universal coefficients depending on the type of the wave functions of the interacting atoms. In our case the χ_{ji} quantities reduce to two parameters, $V_{pp\pi}$ and $V_{sp\sigma}$, which correspond to the π coupling among the p_z electrons of the neighboring C atoms and to σ coupling between the Cu *s* electron and the p_z electrons of the nearest C atoms. The distance between the neighboring carbon atoms was assumed equal to the C-C covalent bond length in graphite, $d_{\mathrm{CC}}=1.42$ Å.

While the exact position of the Cu atom in the cluster is not known, the most likely should be the one providing the strongest coupling with the carbon fragment. This condition was shown[5] to be met if the Cu atom lies on the hexagonal axis *z* of the carbon ring (Fig. 1) at a distance $z_0=d_{\mathrm{CC}}/\sqrt{2}\cong 1$ Å from the ring plane.

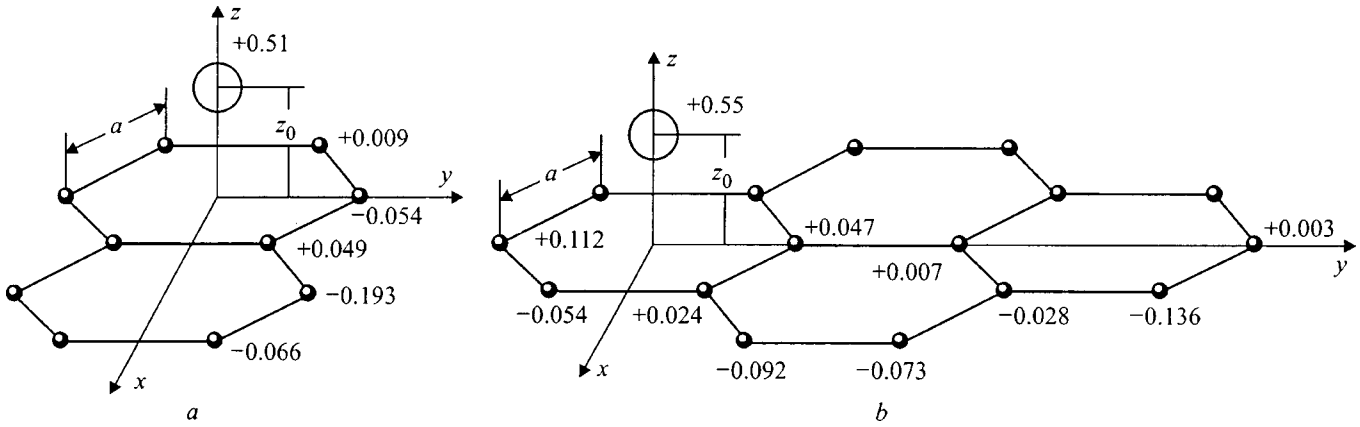

FIG. 1. Schematic presentation of graphite-like nanoclusters containing (a) 10 and (b) 16 C atoms (filled circles) and one Cu atom (open circle). The figure adjoining a circle specifies the effective charge of the given ion, e_i^*/e.

2. NANOCLUSTER METALLIZATION BY COPPER

Figures 2 and 3 present energy-level splittings of the C and Cu $2p_z$ and $4s$ states of (a) isolated atoms, (b) in a graphene layer, and (c) after its subsequent intercalation by a Cu atom, calculated for clusters with $N=10$ and 16 atoms whose configuration is shown in Fig. 1a and 1b. The discrete spectrum of both clusters is seen to have ''bands'' of π bonding and π^* antibonding states separated by a gap. The gap width is determined only by the cluster size and decreases with increasing N, which coincides with the calculations[2] made for purely carbon clusters. The value $E_g=2.6$ eV for $N=16$ is in a satisfactory agreement with the experimentally determined[1] optical gap.

For $T=0$, all levels of the π bonding states are filled by electrons, and the extra electron of the Cu atom falls to the bottom of the band of π^* antibonding states, which in the absence of Cu were totally empty. Thus an intercalated cluster resembles a degenerate semiconductor whose Fermi level lies in the conduction band. In this case the dc conduction of a-C:H⟨Cu⟩ will be dominated by electron tunneling and/or hopping between ''metallized'' copper-carbon clusters. This mechanism can apparently be analyzed by methods of percolation theory. Copper metallization of graphite-like clusters should result in a fast rise of the conductivity of a-C:H, exactly what is observed[1] in experiment, and the corresponding activation energy should be substantially smaller than the optical gap. The conductivity may be expected to grow with increasing Cu content in a-C:H⟨Cu⟩ as long as the concentration of copper-carbon graphite-like clusters continues to increase.

3. COPPER-INDUCED POLARIZATION OF NANOCLUSTERS

The Cu atom in the semiconductor nanoclusters considered here behaves as a donor with the level lying within the region of unoccupied π^* states of the C atoms, which makes the donor partially ionized. Intercalation gives rise to a displacement and redistribution of charge of the valence electrons among the cluster atoms. The effective charge e_i^* of

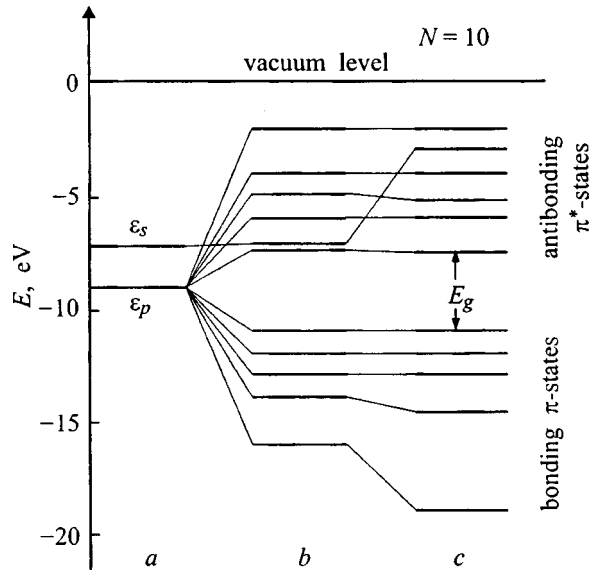

FIG. 2. Splitting and shift of the C and Cu $2p_z$ and $4s$ levels of (a) isolated atoms, (b) π bound in the graphene layer, and (c) π bound in the graphene layer and σ bound in the bulk of the nanocluster, for a cluster containing 10 C atoms.

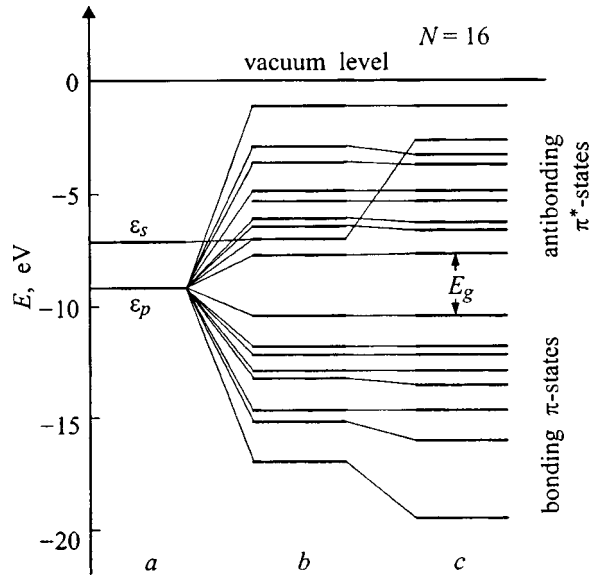

FIG. 3. Same as in Fig. 2 for a nanocluster containing 16 C atoms.

the ith atom can be readily estimated within the LCAO approximation through the squared moduli of coefficients u_{ji}:

$$e_i^*/e=(N+1)^{-1}\sum_j (2|u_{\pi i}|^2+2|u_{\pi^* i}|^2),$$

where the summation is performed over all occupied states j (e is the electronic charge).

The results of the estimates of e_i^*/e are shown in Fig. 1a and 1b by figures adjoining the corresponding atoms. The positive charge of the Cu ion was found to be slightly larger than $+0.5\,e$ in both clusters, and the charge of the fragment of the graphene layer has the same magnitude but the opposite sign. Thus a nonzero component P_z of the static dipole moment **P** is induced in the cluster along the normal z to the layer. For clusters with $N=10$ and 16, we obtained $P_z/ed_{\mathrm{CC}}=0.36$ and 0.38, respectively. In a general case, with the Cu atom located not on the cluster symmetry axis normal to the layer, a static dipole moment appears in the xy layer plane as well. For clusters symmetric with respect to the xz or yz plane, which are under consideration here, this dipole moment is parallel either to the x axis ($N=10$) or to the y axis ($N=16$). Estimates made for the corresponding components yield $P_x/ed_{\mathrm{CC}}=-0.95$ and $P_y/ed_{\mathrm{CC}}=-1.53$. In the absence of correlation among clusters, i.e. for random cluster geometry and mutual arrangement, the net polarization in a-C:H is zero.

4. VIBRATIONAL PROPERTIES OF COPPER-INTERCALATED NANOCLUSTERS

The internal polarization of a Cu-intercalated graphite-like nanocluster should produce dipole activity in atomic vibrations. This should give rise to the appearance of new bands in IR spectra of a-C:H⟨Cu⟩ which were absent in those of pure a-C:H. One can now explain, in particular, the experimentally observed[3] strong increase in the intensity of the so-called band G (1580 cm^{-1}) in the IR absorption spectrum of copper-doped a-C:H. This band, associated with symmetric vibrations of the C-C bonds in the carbon ring plane of graphite-like nanoclusters, is known to be active in the Raman spectrum of a-C:H while being practically not seen in absorption. Note that in a single infinite graphene layer the corresponding E_{2g} mode is forbidden in absorption altogether.[6] The presence of a Cu atom lowers the cluster symmetry; indeed, the carbon ring atoms become essentially inequivalent (Fig. 1), their vibrations change the in-plane dipole-moment component and, hence, should become allowed in absorption. The G bands observed in a-C:H⟨Cu⟩ in absorption and Raman scattering coincide in position with a good accuracy. There are therefore grounds to believe that intercalation with copper does not affect strongly the carbon ring geometry and, hence, the C-C σ bonds, as assumed in our model. G band activation was observed in absorption in nitrogen-doped a-C:H, but N atoms, unlike copper, become incorporated in carbon rings to form C-N bonds.[7]

To conclude, intercalation of graphite-like nanoclusters in a-C:H with copper affects the electronic and vibrational properties of the clusters themselves and of the system as a whole. Our simplified model is applicable to low Cu concentrations, because it disregards the possibility of two or more Cu atoms entering the same cluster. In the opposite case one should take into consideration the interaction among the intercalant atoms, which will affect noticeably the copper binding energy in a cluster. For one Cu atom this energy was estimated as 0.4–0.7 eV, depending on the size of the graphene fragment.[5] For high Cu contents, a cluster may not be able to hold the intercalant in its state, so that the inserted copper will condense to form pure copper clusters. This will be accompanied by an abrupt drop in the conductivity of a-C:H ⟨Cu⟩, if the concentration of such clusters in the a-C:H matrix is below the percolation threshold. This effect was observed experimentally at a Cu content of $\sim$15 at.%.[1]

*E-mail: ivanov.ivom@pop.ioffe.rssi.ru

[1] V. I. Ivanov-Omskiĭ, in *Diamond-Based Composites and Related Materials*, edited by M. Prelas, A. Benedictus, L.-T. S. Lin, G. Popovici, and P. Gielisse, NATO ASI Series-3, Vol. 38, High Technology (Kluwer Academic Publishers, Dordrecht, 1997), p. 171.
[2] J. Robertson and E. P. O'Reilly, Phys. Rev. B **35**, 2946 (1987).
[3] V. I. Ivanov-Omskiĭ and G. S. Frolova, Zh. Tekh. Fiz. **65**(9), 186 (1995) [Tech. Phys. **40**, 966 (1995)].
[4] V. I. Ivanov-Omskiĭ and É. A. Smorgonskaya, Fiz. Tekh. Poluprovodn. **32**, 931 (1998) [Semiconductors **32**, 831 (1998)].
[5] W. A. Harrison, *Electronic Structure and the Properties of Solids* (W. H. Freeman and Co., San Francisco, 1980).
[6] R. J. Nemanich, G. Lucovsky, and S. A. Solin, Solid State Commun. **23**, 117 (1977).
[7] J. H. Kaufman, S. Metin, and D. D. Saperstein, Phys. Rev. B **39**, 13053 (1989).

Translated by G. Skrebtsov

Electron spin beats in InGaAs/GaAs quantum dots

V. K. Kalevich*) and M. N. Tkachuk

A. F. Ioffe Physicotechnical Institute, Russian Academy of Sciences, 194021 St. Petersburg, Russia

P. Le Jeune, X. Marie, and T. Amand

Laboratoire de Physique de la Matière Condensée CNRS-UMR 5830 INSA, Complexe scientifique de Rangueil, 31077 Toulouse cedex, France

Fiz. Tverd. Tela (St. Petersburg) **41**, 871–874 (May 1999)

Time-resolved picosecond spectroscopy is used for the first time to study optical orientation and spin dynamics of carriers in self-organized In(Ga)As/GaAs quantum-dot (QD) arrays. Optical orientation of carriers created by 1.2 ps light pulses, both in the GaAs matrix and wetting layer, and captured by QDs is found to last a few hundreds of picosecond. The saturation of electron ground state at high-excitation-light intensity leads to electron polarization in excited states close to 100% and to its vanishing in ground state. Electron-spin quantum beats in a transverse magnetic field are observed for the first time in semiconductor QDs. We thus determine the quasi-zero-dimensional electron g factor in $In_{0.5}Ga_{0.5}As/GaAs$ QDs to be: $|g_\perp| = 0.27 \pm 0.03$. [S1063-7834(99)02905-6]

Semiconductor structures with quantum dots are currently the subject both of fundamental studies and of practical applications. In the last few years much attention was given to the study of the energy relaxation of carriers in these structures.[1–7] Taking into account the spin of carriers makes it possible to obtain additional information on the energy relaxation processes and the structure of the electron energy levels. In the present work, time-resolved spectroscopy with picosecond resolution has been used for the first time to investigate spin dynamics in semiconductor quantum dots embedded in a semiconductor matrix. Spin polarization of carriers was created as a result of their optical orientation[8] by short (~1 ps) pulses of circularly polarized light. It has been found that the spin polarization of electrons generated in the matrix or in the wetting layer, can survive their capture by the QDs and last a few hundreds of picoseconds. This allowed us to observe quantum beats of electron spin in a transverse magnetic field and thus to determine the magnitude of the transverse g factor of quasi-zero-dimensional electrons in $In_{0.5}Ga_{0.5}As/GaAs$ quantum dots.

The structures studied were grown by solid-source molecular beam epitaxy in Riber-32P machine on semi-insulating GaAs (100) substrates. Active region was inserted into the middle of a 0.2 μm thick undoped GaAs layer confined by AlAs(2 nm)/GaAs(2 nm) superlattices to prevent escape of nonequilibrium carriers to the sample surface and substrate. In the first structure, denoted as 1, the active region consists of 6 planes of QDs separated by 50 Å-thick GaAs spacers. Each QD plane was formed by deposition of 4 monolayers (MLs) of $In_{0.5}Ga_{0.5}As$. In structure 2 the active layer consists of 10 planes of 1.7 ML InAs QDs separated by 200 Å-thick GaAs spacers. Sample 3 contains one plane of 2.7 ML InAs QDs. The growth temperature was set to be 485 °C for In-containing layers and 600 °C for the other parts of the structures.[9]

A tunable Ti-sapphire laser producing 1.2 ps-long light pulses with a repetition frequency of 82 MHz was used to excite the investigated structures. The time resolution of the experiment based on parametric up-conversion, was limited by the laser pulse duration. The exciting circularly-polarized light was obtained by passing linearly-polarized laser beam through a quarter-wave plate. The luminescence was registered along the growth axis (Oz) in back-scattering geometry.

The results of polarization measurements in the different structures under study are qualitatively the same. Presented below are the results of experiments on sample 1. Figure 1 shows normalized luminescence spectra obtained under excitation of carriers in GaAs matrix. Spectrum 1 is a recorded under continuous-wave (cw) excitation with a pump density of 1 W/cm^2. An increase of the cw-excitation intensity by two orders of magnitude did not change the shape position of the spectrum. This indicates that spectrum 1 results from the emission of ground-state electrons and holes. We associate the presence of two strongly overlapping lines in this spectrum with radiative recombination of two groups of dots having different mean sizes. Spectra 2 and 3 are registered under pulse excitation with pump densities of 0.1 and 1.6 MW/cm^2, respectively. As seen from comparison with spectrum 1, an increase in the pulse-excitation intensity results in a significant (up to 50 meV) blue shift of the luminescence line. Such transformation of the luminescence spectra of quantum dots at high excitation levels has been observed before[4,6,7] and was due to the filling of the ground states of electrons and holes and to the appearance of an intense light emission from the excited states. Indeed, as an estimate shows, at the maximum pump density of 1.6 MW/cm^2 that we used, the number of photoexcited electron-hole pairs exceeds by several times the number of quantum dots in the illuminated region; this leads to population of the excited states, since they can no longer relax to the filled ground states. The excited states, in turn, give rise to an intense

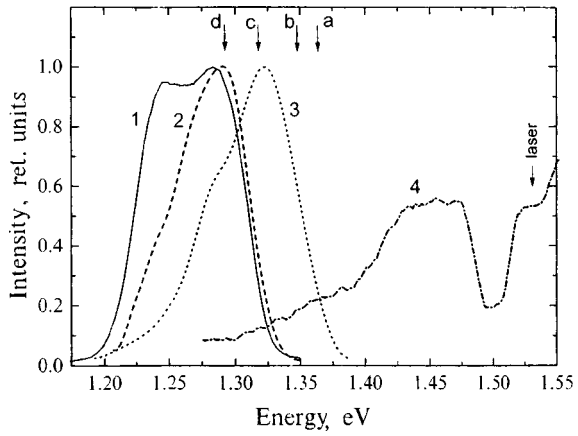

FIG. 1. Photoluminescence spectra of $In_{0.5}Ga_{0.5}As/GaAs$ QDs (sample 1). $T=10$ K. *1* — cw. excitation with $E_{exc}=1.610$ eV and power density 1 W/cm^2; *2* and *3* — short pulse pumping with power densities 0.1 and 1.6 MW/cm^2, $E_{exc}=1.531$ eV, time delay after excitation pulse equals 200 ps; *4* — cw photoluminescence excitation spectra at $E_{det}=1.248$ eV.

luminescence spectral component. Curve *4* in Fig. 1 represents the cw-photoluminescence excitation spectrum recorded at a registration energy $E_{det}=1.245$ eV (the position of the low-energy maximum in spectrum 1). We, as well as the authors of Refs 4 and 7 assign the relatively broad band (1.42–1.48 eV) near the edge of the fundamental absorption of GaAs to the absorption of the wetting layer.

In our experiments the spin orientation of electrons and holes was created by cicularly polarized light. The recombination radiation involving spin-oriented carriers also turns out to be circularly polarized. Therefore the luminescence circular-polarization degree $\rho=(I^+-I^-)/(I^++I^-)$ can be used to measure the carrier spin polarization and their spin dynamics. Here I^+ and I^- denote the respective intensities of the left-hand and right-hand circularly polarized luminescence components.

Figure 2 shows the time dependences $\rho(t)$ measured at four different energies of recombination radiation quanta E_{det} (marked by arrows in Fig. 1) under excitation into the GaAs barrier ($E_{exc}=1.531$ eV) with pulse density of 1.6 MW/cm^2. It can be seen from Figs. 2a and 2b that at the high-energy edge of the luminescence line the initial value of ρ is large (it reaches 80% at $E_{det}=1.363$ eV) and slowly decreases with a characteristic time of about 300–400 ps. When going down to the low-energy part of the luminescence spectrum, the maximum value of ρ significantly decreases and the polarization decay time is drastically reduced (Figs. 2c and 2d). Thus, at $E_{det}=1.292$ eV, ρ decreases from an initial value of $\rho(0)\approx 22\%$ down to 5% within 15 ps (Fig. 2d).

Let us first remark on the nature of the slow decay of ρ at large E_{det}. The rate of the change of ρ is determined by the slowest of the spin-relaxation processes in electrons and holes. Due to the strong spin-orbit interaction in the valence

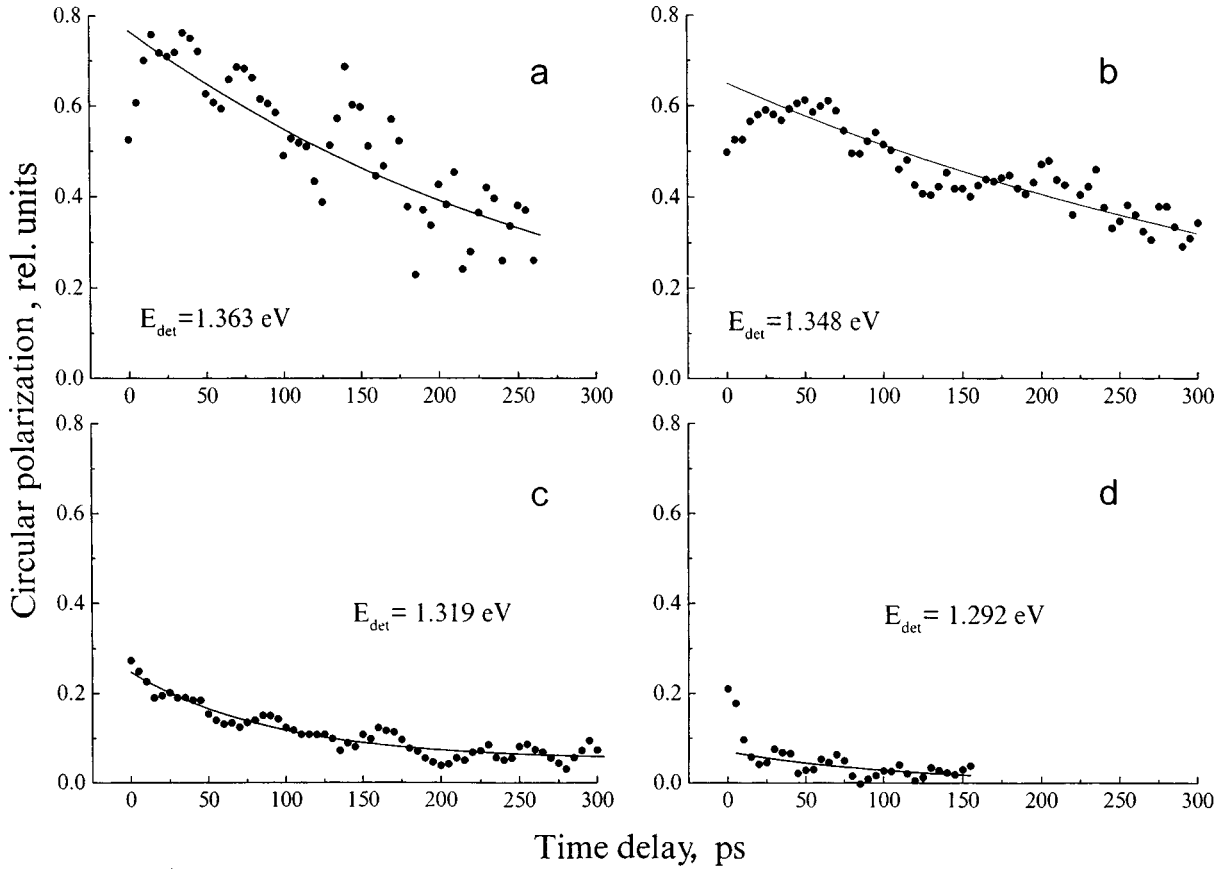

FIG. 2. Luminescence circular polarization dependence on time delay at different detection energies E_{det}. $E_{exc}=1.531$ eV, $T=10$ K. Solid lines show the exponential decay of the polarization degree with time constant τ_S. τ_S (ps): a — 290, b — 400, c — 211, d — 92.

band, the spin-relaxation time of holes is significantly shorter than that of electrons[8] and does not exceed a few picoseconds in bulk intrinsic semiconductors of the GaAs type.[10] For this reason, we think that the luminescence polarization is only determined by the spin polarization of electrons, while the slow change of ρ is due to the large value of their spin relaxation time.

Quite surprising was the fact that, at large E_{det} during some tens of picoseconds, the values of ρ substantially exceed 50%, reaching 80% at $E_{det}=1.363$ eV (Fig. 2a). Since the holes participating in the radiative recombination in investigated dots are heavy holes,[11] the value of ρ is numerically equal to the spin polarization of electrons P_e: $\rho=P_e$ (Ref. 8). At the same time, in accord with the optical selection rules,[8] spin polarization of the electrons generated in bulk GaAs cannot exceed 50%.

A qualitative explanation of the appearance of ρ values larger than 50% on the high-energy side of the QD spectra may be obtained in the following simple model. Suppose that the electrons generated in the GaAs barrier, with a spin polarization equal to 50%, are trapped by QDs with such polarization, while the holes lose entirely their polarization during their energy relaxation process. In dots analogous to ours, besides the ground level there are excited levels of both holes and electrons.[6,11–16] By virtue of Pauli's principle each level can accomodate no more than two electrons with opposite spins. As at $P_e=0.5$, there are three times as many electrons with spin $-1/2$ than electrons with spin $+1/2$, so, with the increase of the concentration of photoexcited carriers leading to the saturation of the ground state, the highest electron levels will be populated predominantly by electrons with spin $-1/2$, which leads, at the limit, to the 100% polarization of the associated recombination radiation. The scatter of the QD sizes, resulting in the inhomogeneous broadening of the luminescence line, diminishes this effect; at the high-energy edge of the line, however, the value of ρ may exceed 50%, which is just what we observe in our experiments. On the contrary, the radiation from the ground state must be unpolarized, since two electrons occupying this state have opposite spins. This is also observed experimentally (see Fig. 2d).

The long-lived and large polarization of electrons enables the observation of their spin beats in transverse magnetic fields and determination of the g-factor magnitude. Electron-spin quantum beats set in under coherent excitation of the two electron-spin levels by a short pulse of circularly polarized light and may be considered to result from Larmor precession of electron spins about the magnetic field **B** with a frequency $\mathbf{\Omega}=g\mu_B\mathbf{B}/\hbar$, where g is the electron g factor and μ_B is the Bohr magneton.[17] The pump pulse is substantially shorter than the electron-lifetime and spin-relaxation time, denoted τ and τ_S, respectively. Therefore the motion of the average spin **S** of electrons excited during the pump pulse obeys the equation

$$\frac{d\mathbf{S}}{dt}=(\mathbf{\Omega}\times\mathbf{S})-\frac{\mathbf{S}}{\tau_S}, \tag{1}$$

where the first term on the right-hand side describes the Larmor precession, and the second, spin relaxation. Since in our experiments, a long-living luminescence polarization is created by the electron polarization $\rho=-2S_z$, and, in a magnetic field directed perpendicular to the exciting beam, ρ varies with time as

$$\frac{\rho(t)}{\rho(0)}=e^{-t/\tau_S}\cos\Omega t. \tag{2}$$

It is easy to determine the magnitude of the electron g factor by measuring the beat frequency as a function of the magnetic field.

The dependence $\rho(t)$ measured in a magnetic field $B=3.5$ T at $E_{det}=1.355$ eV is shown in Fig. 3. It can be seen that ρ oscillates with time in agreement with Eq. (2). The dependence of the spin-beat frequency on the magnetic field is presented on Fig. 4. It is quite linear. Thus the modulus of the electron transverse g factor of $In_{0.5}Ga_{0.5}As/GaAs$ QDs can be accurately deduced. We find: $|g_\perp|=0.27\pm0.03$. Note that it is the g factor for electrons in the excited state.

To conclude, electron-spin orientation and its subsequent dynamics in self-organized In(Ga)As/GaAs QDs have been studied for the first time using picosecond time-resolved luminescence spectroscopy. It has been found that optical ori-

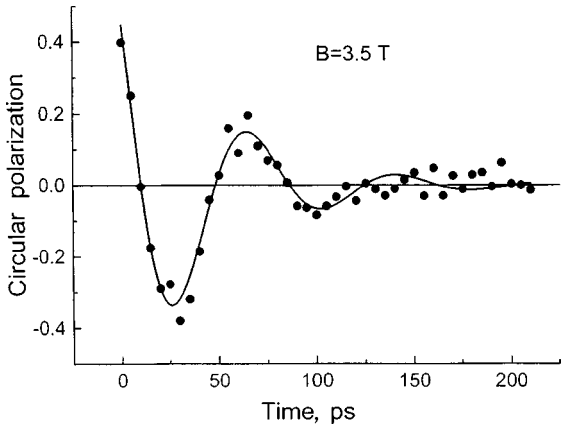

FIG. 3. Luminescence polarization oscillations in a transverse magnetic field $B=3.5T$. $T=1.7$ K. The solid line is drawn on formula (2) with Larmor precession period equal to 76 ps.

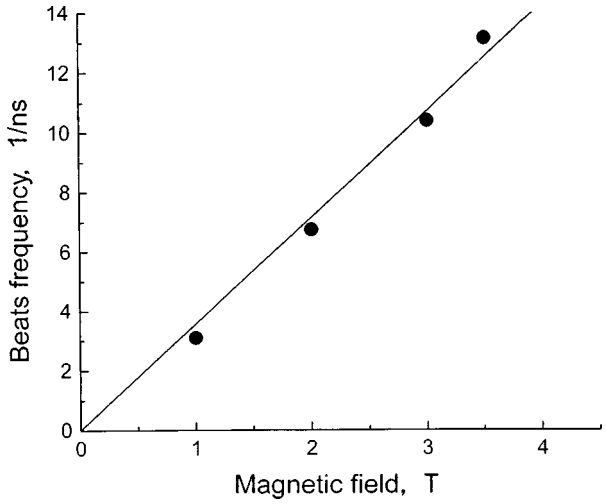

FIG. 4. Spin beat frequency versus magnetic field.

entation of electrons, excited in the matrix or in the wetting layer, can last after their capture by the QDs during some hundred picoseconds. The saturation of electron ground states at high excitation intensity leads to electron spin polarization in the excited states close to 100%, and to vanishing values in the ground state. Electron-spin quantum beats in transverse magnetic field are observed for the first time in semiconductor QDs, leading to determination of the magnitude of the transverse electron g factor in $In_{0.5}Ga_{0.5}As/GaAs$ QDs.

The authors are grateful to N. N. Ledentzov, V. M. Ustinov, A. E. Zhukov, and A. F. Tsatsul'nikov for supplying the samples and useful discussions, I. A. Merkulov and K. V. Kavokin for fruitful discussions.

Partial support of the Russian Fundamental Research Foundation (Grants 96-02-16941 and 98-02-18213) is acknowledged.

*)E-mail: kalevich@solid.ioffe.rssi.ru

[1] G. Wang, S. Fafard, D. Leonard, J. E. Bowers, J. L. Merz, and P. M. Petroff, Appl. Phys. Lett. **64**, 2815 (1994).
[2] A. Takeuchi, Y. Nakata, S. Muto, Y. Sugiyama, T. Usuki, Y. Nishikawa, N. Yokoyama, and O. Wada, Jpn. J. Appl. Phys., Part 2 Part 2 **34**, L1439 (1995).
[3] N. Vollmer, E. J. Mayer, W. W. Ruhle, A. Kurtenbach, and K. Eberl, Phys. Rev. B **54**, R17292 (1996).
[4] R. Heitz, M. Veit, N. N. Ledentsov, A. Hoffman, D. Bimberg, V. M. Ustinov, P. S. Kop'ev, and Zh. I. Alferov, Phys. Rev. B **56**, 10435 (1997).
[5] M. Grundman and D. Bimberg, Phys. Rev. B **55**, 9740 (1997).
[6] S. Grosse, J. H. H. Sandmann, G. von Plessen, J. Feldmann, H. Lipsanen, M. Sopanen, J. Tulkki, and J. Aporelto, Phys. Rev. B **55**, 4473 (1997).
[7] R. Heitz, A. Kalburge, Q. Xie, M. Grundmann, P. Chen, A. Hoffman, A. Madhukar, and D. Bimberg, Phys. Rev. B **57**, 9050 (1998).
[8] ''Optical Orientation,'' edited by F. Meier and B. Zakharchenya, in *Modern Problems in Condensed Matter Sciences*, Vol. 8 (North-Holland, Amsterdam, 1984; Nauka, Leningrad, 1989).
[9] A. Yu. Egorov, A. E. Zhukov, P. S. Kop'ev, N. N. Ledentsov, M. V. Maximov, and V. M. Ustinov, Semiconductors **28**, 809 (1994); N. N. Ledentsov, M. Grundmann, N. Kirstaedter, O. Schmidt, R. Heitz, J. Bohrer, D. Bimberg, V. M. Ustinov, V. A. Shchukin, A. Yu. Egorov, A. E. Zhukov, S. V. Zaitsev, P. S. Kop'ev, Zh. I. Alferov, S. S. Ruvimov, P. Werner, U. Gosele, and I. Heidenreich, Solid-State Electron. **40**, 785 (1996).
[10] P. Le Jeune, X. Marie, T. Amand, J. Barrau, and R. Planel, *Proceedings of the 24th International Conference on the Physics of Semiconductors, Jerusalem, Israel (1998)*, to be published.
[11] M. Grundman, O. Stier, and D. Bimberg, Phys. Rev. B **52**, 11969 (1995).
[12] C. Guasch, C. M. Sotomayor Torres, N. N. Ledentsov, D. Bimberg, V. M. Ustinov, and P. S. Kop'ev, Superlattices Microstruct. **21**, 509 (1997).
[13] R. J. Warburton, C. S. Durr, K. Karrai, J. P. Kottaus, G. Medeiros-Ribeiro, and P. M. Petroff, Phys. Rev. Lett. **79**, 5282 (1997).
[14] E. Itskevich, I. A. Trojan, S. G. Lyapin, D. Mowbray, M. S. Skolnick, M. Hopkinson, L. Eaves, P. C. Main, and M. Henini, *Proceedings of the 24th International Conference on the Physics of Semiconductors, Jerusalem, Israel (1998)* to be published.
[15] Craig Pryor, Phys. Rev. Lett. **80**, 3579 (1998); Craig Pryor, Phys. Rev. B **57**, 7190 (1998).
[16] O. Stier, M. Grundmann, and D. Bimberg, *Proceedings of the 24th International Conference on the Physics of Semiconductors, Jerusalem, Israel (1998)*, to be published; O. Stier, M. Grundmann, and D. Bimberg, Phys. Rev. B, to be published.
[17] A. P. Heberle, W. W. Ruhle, and K. Ploog, Phys. Rev. Lett. **72**, 3887 (1994); R. M. Hannak, M. Oestreich, A. P. Heberle, W. W. Ruhle, and K. Kohler, Solid State Commun. **93**, 313 (1995).

Published in English in the original Russian journal. Reproduced here with stylistic changes by the Translation Editor.

Chemical effects during formation of the electronic surface structure of III-V semiconductors in a sulfide solution.

V. N. Bessolov, E. V. Konenkova, and M. V. Lebedev

A. F. Ioffe Physicotechnical Institute, Russian Academy of Sciences, 194021 St. Petersburg, Russia

D. R. T. Zahn

Institut für Physik, TU-Chemnitz, D-09107 Chemnitz, Germany
Fiz. Tverd. Tela (St. Petersburg) **41**, 875–878 (May 1999)

The electronic properties of the (100) surface of *n*-GaAs, *p*-GaAs, and *n*-InP semiconductors treated with various sulfide solutions have been studied. Sulfide treatment was shown to increase the photoluminescence intensity, decrease the depth of the near-surface depleted region in the semiconductor, and shift the surface Fermi level toward the conduction band. These effects are the stronger, the higher the sulfur chemical activity in the solution. © *1999 American Institute of Physics.* [S1063-7834(99)03005-1]

The properties of a real surface of most III–V semiconductors are determined by the high density of surface states and, as a consequence, by a high rate of surface nonradiative recombination. The improvement in the performance of a GaAs/AlGaAs bipolar transistor following its treatment in a water solution of sodium sulfide[1] initiated studies of the interaction of sulfur in solution and the gas phase with the surface of GaAs and other III–V semiconductors.

Investigation of the electronic properties of the sulfur-modified GaAs(100) surface showed that sulfide treatment results, first, in a decrease of the surface density of states at midgap[2] and, second, in a change of the near-surface band warping and a shift of the surface Fermi level, which depends on the actual treatment used. For instance, treating *n*-GaAs(100) with a water solution of ammonium sulfide does not practically affect the surface Fermi level,[3] whereas molecular sulfur shifts the Fermi level by 0.2 eV toward the conduction band. Treating *n*-GaAs(100) with an alcohol solution of ammonium sulfide brings about a still larger (by ~ 0.5 eV) shift of the Fermi level.[4] In other words, the chemical state of sulfur atoms before adsorption has a pronounced effect on the electronic structure of the sulfide-treated surface.

This work studies the electronic properties of GaAs(100) and InP(100) surfaces passivated by various sulfide solutions.

The samples were GaAs:Te(100) ($n=1\times10^{18}$ cm^{-3}) and GaAs:Zn(100) ($p=1\times10^{18}$ cm^{-3}) plates, which prior to the sulfide passivation were treated with HCl for 100 s, as well as *n*-InP(100) plates ($n=1\times10^{18}$ cm^{-3}), which were pretreated with HF for 1 min.

The sulfide treatment lasted 1 min in an ammonium sulfide solution $(NH_4)_2S$ (20%) and saturated solutions of sodium sulfide ($Na_2S{:}xH_2O$) in water, isopropanol (i-C_3H_7OH) and tret-butanol (t-C_4H_9OH), as well as in solutions of sulfur monochloride S_2Cl_2 in carbon tetrachloride CCl_4.

X-ray photoelectron spectra of the surface were obtained with a Perkin-Elmer PHI 5400 spectrometer using Mg $K\alpha$ radiation ($h\nu=1253.6$ eV), 300-W power. The valence-band spectra were measured at room temperature with a He lamp ($h\nu=21.2$ eV).

The Raman spectra were taken in the range of 200 to 400 cm^{-1} with a Dilor XY spectrometer.[4] The spectra were excited by an Ar^+ laser line at $\lambda=457.9$ nm [radiation penetration depth in GaAs is 50.3 nm (Ref. 5)], and the laser power was 2.5 mW. One studied the intensity ratio of the LO peak associated with the depleted layer on the semiconductor surface to the L^- peak due to scattering from a coupled phonon-plasmon mode in the bulk, which permitted measurement of the thickness of the near-surface semiconductor depleted layer.[4]

The photoluminescence was excited with the $\lambda=530.9$-nm line of a 100-mW Kr^+ laser at room temperature. The spectra were recorded with an IFS-66 spectrometer.

The electron work function for a semiconductor surface was determined by the Kelvin method by measuring the contact potential difference between the semiconductor and a gold film deposited on a SiO_2 substrate with a dynamic capacitor.[6]

The sulfide treatment results in a substantial thinning and, in some cases, in a complete removal of the native oxide layer from the semiconductor surface, followed by formation of a thin sulfide layer on the surface. The thickness of this layer, as derived from XPS data, was 0.5–1.2 ML for GaAs, and 1.5–4.0 ML for InP. The rate constant for the sulfide layer formation, which is a measure of the chemical activity of sulfur ions in solution, i.e. the rate of the sulfide layer formation referred to the sulfur concentration in the liquid phase, grows exponentially with increasing inverse dielectric constant of the solvent used,[7] which argues for a predominantly electrostatic interaction of the ions with the semiconductor surface.[8]

UV photoelectron spectroscopic studies of the *n*-GaAs(100) and *p*-GaAs(100) surfaces passivated in a $(NH_4)_2S+i$-C_3H_7OH solution showed that the surface

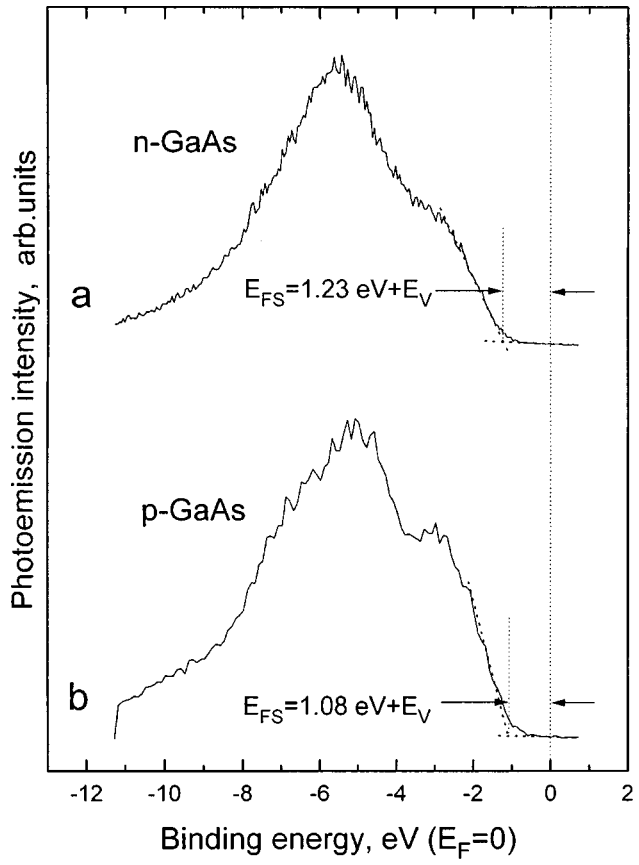

FIG. 1. Room-temperature valence-band photoemission spectra of (a) *n*-GaAs with $n=1\times10^{18}$ cm^{-3} and (b) *p*-GaAs with $p=1\times10^{18}$ cm^{-3} obtained after a sulfide treatment in a $(NH_4)_2S(20\%)+i$-C_3H_7OH (1:10) solution obtained with a He lamp ($h\nu=21.2$ eV).

Fermi level lies at 1.23 and 1.08 eV above the semiconductor valence-band edge in *n*-GaAs and *p*-GaAs, respectively (Fig. 1), while using for this purpose a water solution of $(NH_4)_2S$ leaves the Fermi level at 0.8 eV (Ref. 3) and 0.5 eV (Ref. 9) for *n*-GaAs and *p*-GaAs, respectively, the positions characteristic of the unpassivated semiconductor. Annealing the *p*-GaAs(100) surface treated in a $(NH_4)_2S+i$-C_3H_7OH solution changes the position of the Fermi level relative to the semiconductor band edges, while annealing to 400°C the *n*-GaAs(100) surface treated in the same solution practically does not affect the Fermi level at all (Fig. 2).

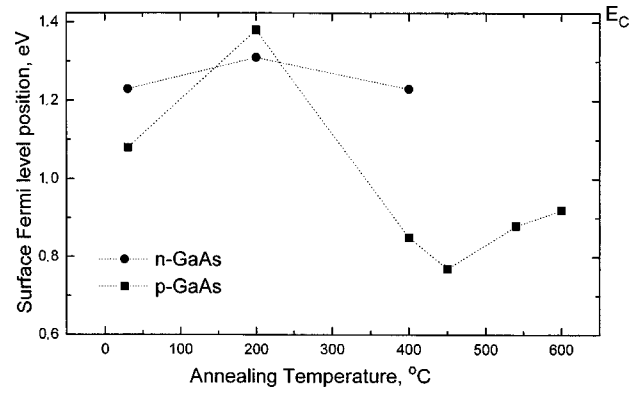

FIG. 2. Position of the surface Fermi level (E_{FS}) relative to the valence-band (E_V) and conduction-band (E_C) edges in *n*-GaAs with $n=1\times10^{18}$ cm^{-3} and *p*-GaAs with $p=1\times10^{18}$ cm^{-3} sulfide-treated with a $(NH_4)_2S(20\%)+i$-C_3H_7OH (1:10) solution as a function of annealing temperature.

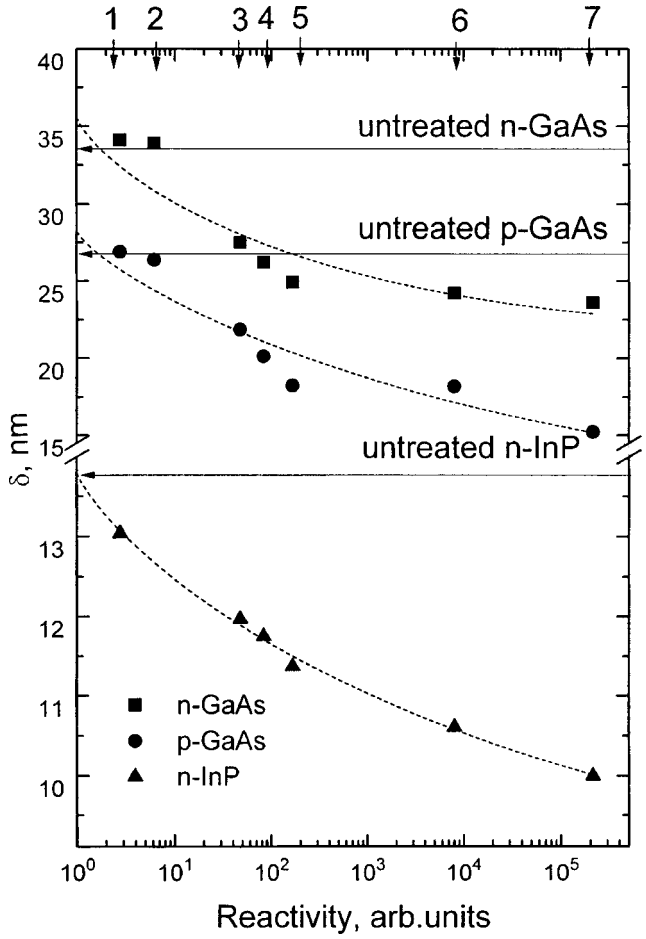

FIG. 3. Depth of the near-surface depleted region δ in *n*-GaAs with $n=1\times10^{18}$ cm^{-3}, *p*-GaAs with $p=1\times10^{18}$ cm^{-3}, and *n*-InP with $n=1\times10^{18}$ cm^{-3} passivated in various solutions, as a function of the sulfur chemical activity in solution. The chemical activity was estimated in Ref. 10. The arrows refer to: *1* — $(NH_4)_2S$, *2* — Na_2S+H_2O, *3* — $S_2Cl_2+CCl_4$, *4* — $(NH_4)_2S+i$-C_3H_7OH, *5* — $(NH_4)_2S+t$-C_4H_9OH, *6* — Na_2S+i-C_3H_7OH, *7* — Na_2S+t-C_4H_9OH.

A Raman spectroscopic study of *n*-GaAs(100), *p*-GaAs(100), and *n*-InP(100) showed passivation to reduce the depth of the near-surface depleted region in the semiconductor, this reduction being the larger, the higher the sulfur chemical activity in the solution (Fig. 3). The decrease in the depth of the depleted region evidences a decrease in the density of surface states in the semiconductor band gap. That the surface barrier in *p*-GaAs(100) is shown by UPS to increase noticeably under passivation in an alcohol sulfide solution indicates that this barrier is due to the formation of a dipole layer on the surface resulting from the capture by the electronegative sulfur atoms of electrons from the semiconductor. Indeed, sulfide treatment increases the work function of the semiconductor, as well as increases its ionization energy, which argues for the formation of a dipole layer on the surface (Fig. 4). The ionization energy increases to a greater degree in a solution with a higher chemical activity of sulfur.

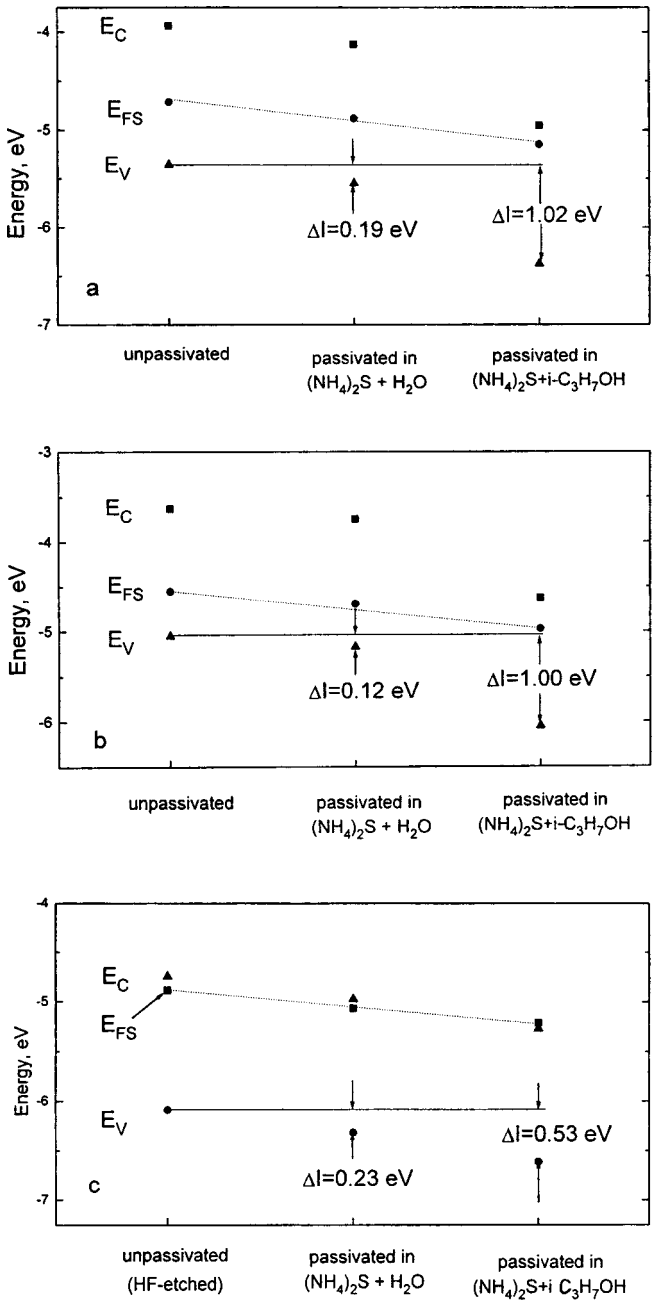

FIG. 4. Position of the surface Fermi level (E_{FS}) and of the valence-band (E_V) and conduction-band (E_C) edges relative to vacuum level in (a) *n*-GaAs with $n=1\times10^{18}$ cm^{-3}, (b) *p*-GaAs with $p=1\times10^{18}$ cm^{-3}, and (c) *n*-InP with $n=1\times10^{18}$ cm^{-3} before and after sulfide treatment in water and isopropanol solutions of ammonium sulfide.

Sulfide treatment of the *n*-GaAs(100) and *p*-GaAs(100) surface results in a notable increase in the semiconductor photoluminescence intensity, this increase being the larger, the higher the chemical activity of the sulfur atom before adsorption (Fig. 5). We readily see that the improvement in the photoluminescence properties of GaAs correlates well with the decrease in the depth of the depleted region and, hence, with the decrease of the surface density of states in the semiconductor band gap.

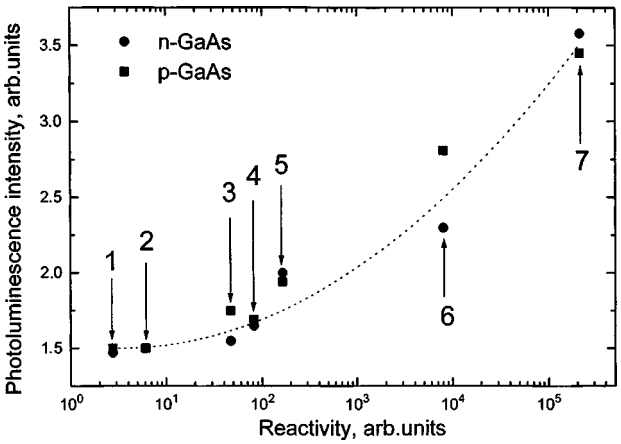

FIG. 5. The increase in photoluminescence intensity of *n*-GaAs with $n=1\times10^{18}$ cm^{-3} and *p*-GaAs with $p=1\times10^{18}$ cm^{-3} passivated in various solutions as a function of the sulfur chemical activity in solution. The photoluminescence intensity was reduced to that of an untreated semiconductor. The arrows refer to various sulfide solutions (see caption to Fig. 3).

Thus the chemical activity of an atom before adsorption plays a dominant part in modification of the electronic structure of a semiconductor surface. An increase in the chemical activity of sulfur atoms is accompanied by an increase in the efficiency of electronic passivation of the GaAs(100) surface, which is evidenced by an increase in photoluminescence intensity and a decrease of the near-surface depleted region in depth. The growth in the chemical activity of sulfur atoms in solution increases the work function and ionization energy of GaAs and InP.

[1] C. J. Sandroff, R. N. Nottenburg, J.-C. Bischoff, and R. Bhat, Appl. Phys. Lett. **51**, 33 (1987).
[2] J.-F. Fan, Y. Kurata, and Y. Nannichi, Jpn. J. Appl. Phys., Part 2 **28**, L2255 (1989).
[3] H. Sugahara, M. Oshima, R. Klauser, H. Oigawa, and Y. Nannichi, Surf. Sci. **242**, 335 (1991).
[4] V. N. Bessolov, M. V. Lebedev, and D. R. T. Zahn, J. Appl. Phys. **82**, 2640 (1997).
[5] D. E. Aspnes and A. A. Studna, Phys. Rev. B **27**, 985 (1983).
[6] R. Maeckel, H. Baumgärtner, and J. Ren, Rev. Sci. Instrum. **64**, 694 (1993).
[7] V. N. Bessolov, E. V. Konenkova, and M. V. Lebedev, Mater. Sci. Eng., B **44**, 376 (1997).
[8] E. A. Moelwyn-Hughes, *The Chemical Statics and Kinetics of Solutions* (Academic, New York, 1971; Khimiya, Moscow, 1975).
[9] D. Paget, A. O. Gusev, and V. L. Berkovits, Phys. Rev. B **53**, 4615 (1996).
[10] V. N. Bessolov, M. V. Lebedev, N. M. Binh, M. Friedrich, and D. R. T. Zahn, Semicond. Sci. Technol. **13**, 611 (1998).

Translated by G. Skrebtsov

Weak localization with a specific role of *t* symmetry (2D and 3D holes in tellurium)

N. S. Averkiev, V. A. Berezovets, N. I. Sablina, and I. I. Farbshteĭn*)

A. F. Ioffe Physicotechnical Institute, Russian Academy of Sciences, 194021 St. Petersburg, Russia
Fiz. Tverd. Tela (St. Petersburg) **41**, 879–881 (May 1999)

The anomalous magnetoresistance in crystalline tellurium is analyzed for different *p*-type carrier dimensions: a bulk sample, size-quantized accumulation layers on different tellurium crystallographic surfaces, and tellurium clusters (tellurium embedded in a dielectric opal matrix). It is shown that the effect can be interpreted in all cases in terms of the theory of weak localization of noninteracting particles with inclusion of the specific features of the tellurium band spectrum, namely, fully lifted spin degeneracy, trigonal spectrum distortion, and a specific role played by the *t* symmetry in inter-valley scattering. The differences observed among the various manifestations of the weak localization effect are determined by the hole wave function phase-relaxation channel which is dominant in a particular case. A case is discussed where the time characterizing the inter-valley transition probability becomes comparable to the momentum relaxation time. © *1999 American Institute of Physics.* [S1063-7834(99)03105-6]

Negative magnetoresistance (NMR) was discovered[1] in bulk tellurium samples in 1948 and confirmed later[2,3] in special experiments. Positive anomalous magnetoresistance (AMR) in a close-to-zero magnetic field was observed in a study of two-dimensional holes in quantum-confined accumulation layers (AL) on the (0001) and $(10\bar{1}0)$ tellurium crystallographic surfaces.[4–6] Later, AMR was observed to occur also in tellurium clusters (tellurium embedded in a dielectric opal matrix).[7] We are going to show that the observed variety of AMR manifestations in tellurium can be interpreted by a theory of weak localization with inclusion of the specific symmetry characteristics of a tellurium crystal.

1. EXPERIMENTAL STUDIES OF AMR IN TELLURIUM

A. 3D case (bulk crystal)

The behavior of NMR in a bulk crystal is presented graphically in Fig. 1.[8] Shubnikov–de Haas-type oscillations in strong magnetic fields confirm a strong carrier degeneracy.

B. 2D layer on (0001)

Three quantum-confined subbands with $E_F \approx 30$ meV form in an AL of natural origin on the (0001) surface in the initial state.[9] The AMR is seen in weak magnetic fields ~ 1 Oe and is positive (Fig. 2).[4] Lowering the temperature enhances the effect. When the 2D-hole concentration decreases, and a positive bias is applied in a MIS capacitor geometry, a NMR portion appears within the $150 < H < 400$ Oe region.

C. 2D layer on $(10\bar{1}0)$

In this case, the AL has two subbands,[9] and E_F becomes as high as 44 meV. In this geometry one observes only positive AMR (Fig. 3), which transforms in strong magnetic fields to a classical relation of the type H^2 (Refs. 5 and 6).

D. Tellurium cluster crystal

The low-temperature magnetoresistance in the tellurium cluster crystals studied is similar in behavior to that observed in a 2D layer on (0001) of Te under maximum bias (curve *5* in Fig. 2), but the pattern is displaced toward strong magnetic fields.[8]

2. DISCUSSION

A. Weak localization effect

The extrema of the valence and conduction bands in tellurium are located at the *M* and *P* corners of the Brillouin zone and are related only through the time inversion operation. The wave functions at the *M* and *P* points are superpositions of states with the angular-momentum projection $M_z = \pm 3/2$ and transform into one another under time inversion operation. The quantum correction to the conductivity of noninteracting particles is determined by the sum of the cooperons made up of wavefunctions of the same valley, $C_{MM} = C_{PP}$, and of those which are off-diagonal with respect to the valleys, $C_{MP} = C_{PM}$. Expressions were obtained[10–12] relating the weak localization effect in a magnetic field to the hole-wave function phase-relaxation processes in 3D and 2D systems, respectively:

$$\Delta\sigma(H) = \sigma_0 \sqrt{\frac{eH}{\hbar c}} \left\{ f_3\left(\frac{H}{H_\phi + H_\nu + H_\gamma}\right) + \frac{1}{2} f_3\left(\frac{H}{H_\phi + 2H_\nu}\right) - \frac{1}{2} f_3\left(\frac{H}{H_\phi}\right) \right\}, \quad (1)$$

$$\Delta\sigma(H) = \sigma_0 \left\{ f_2\left(\frac{H}{H_\phi + H_\nu + H_\gamma}\right) + \frac{1}{2} f_2\left(\frac{H}{H_\phi + 2H_\nu}\right) - \frac{1}{2} f_2\left(\frac{H}{H_\phi}\right) \right\}, \quad (2)$$

where $\sigma_0 = e^2/(2\pi^2\hbar)$, f_3 and f_2 are known functions, and $H_{\phi,\nu,\gamma} = c\hbar/(4eD\tau_{\phi,\nu,\gamma})$. The magnetic field H_ϕ is related

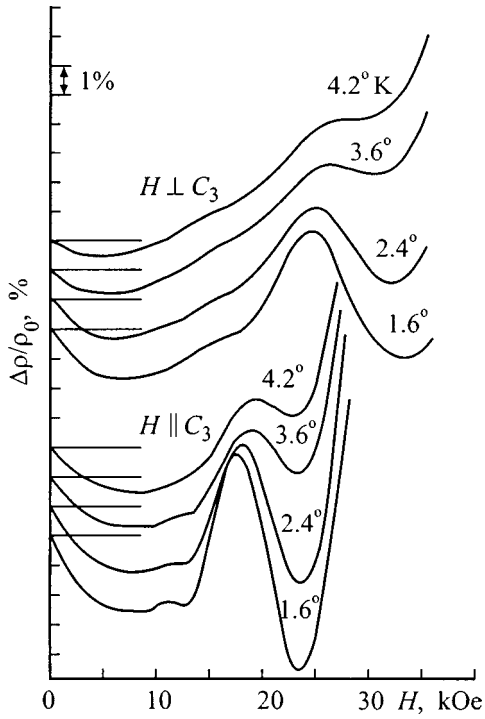

FIG. 1. Transverse magnetoresistance of single-crystal tellurium with a hole concentration $p(77)=6.3\times10^{16}$ cm^{-3} (Ref. 8).

to the wavefunction phase-relaxation time τ_ϕ, and the fields H_ν and H_γ, to the elastic scattering times in inter- and intra-valley transitions τ_ν and τ_γ, respectively. The trigonal distortion of the Fermi surface[10] brings about phase relaxation of the hole wave function in intra-valley scattering, because $E(\mathbf{k})\neq E(-\mathbf{k})$. The field H_γ is proportional to k_F^6. Because of the M and P valleys being spin inequivalent, elastic inter-valley scattering results in phase relaxation, similar to the SO scattering in semiconductors[10–12].

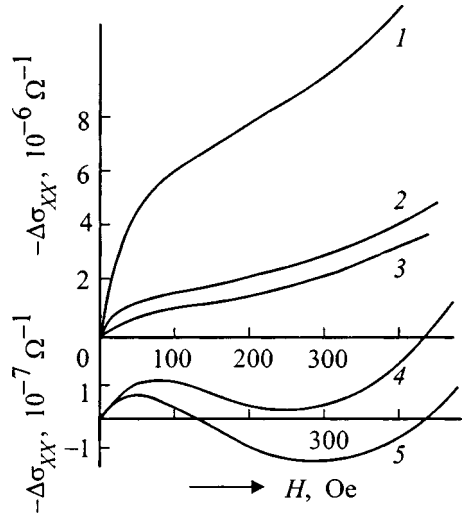

FIG. 2. AMR of a Te sample with a 2D layer on the (0001) surface. $T=0.44$ K. *1* — $P_{AL}=2\times10^{12}$ cm^{-2}, *2–5* — $U_g(2)<U_g(3)<U_g(4)<U_g(5)$.

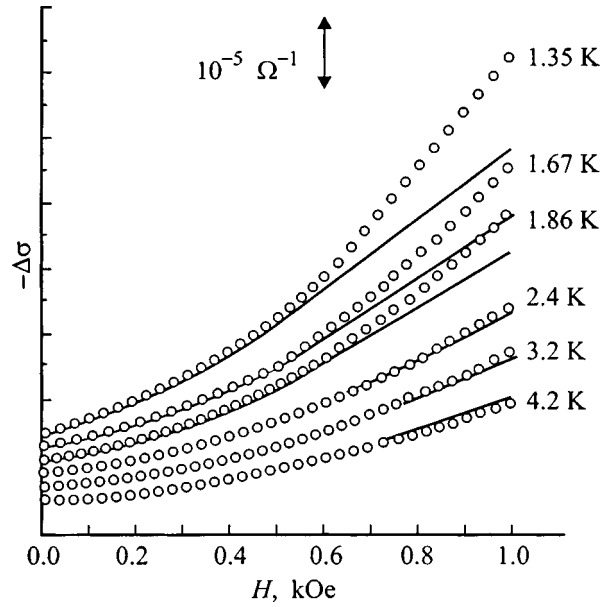

FIG. 3. AMR of a Te sample with a 2D layer on the $(10\bar{1}0)$ surface. Solid line — experiment, circles — calculation.

B. Comparison with experiment

A comparison[4–6] of relation (2) with experimental data permitted determination of the quantities H_i.

(i) 2D layer on the (0001) surface. Here $H_\phi(T)=(5T+5)$ Oe, $H_\nu=7$ Oe, and $H_\gamma=100$ Oe.[4] The formation of a NMR region is due to the decrease of H_γ with decreasing 2D-hole concentration.

(ii) A layer on the $(10\bar{1}0)$ surface. $H_\phi(T)=(9.7T+2T^2)$ Oe, $H_\nu\approx300$ Oe, $H_\gamma\geqslant100$ Oe, and the AMR is always positive (Fig. 3).[6] Calculations showed that $H_\nu\approx H_{tr}>H_\phi, H_\gamma$. Such a strong difference between the values of H_ν in the two above cases suggests that inter-valley transitions are initiated by holes scattering from surface roughness, which is substantially different for these two orientations, namely, the cleavage plane $(10\bar{1}0)$ and the break plane (0001).

Equations (1) and (2) are applicable in cases where the magnetic length $l(H)$ exceeds the mean free path l. The wave function phase of holes undergoes relaxation in their multiple collisions with impurities. When $l(H)$ becomes of the order of l with increasing magnetic field, phase relaxation will occur already in a small number of collisions with impurities. It can be shown that a deviation from the diffusion regime under isotropic scattering reduces the conductivity in magnetic field.[13,14] Then in fields such that $l(H)\sim l$, calculations made in the diffusion approximation should yield an overestimate for the magnitude of the effect. This is borne out by the graphs in Fig. 3.

(iii) The 3D case. In the 3D case, the contributions due to different channels change considerably. While the phase relaxation probability in inelastic scattering retains roughly its magnitude, the phase relaxation associated with the trigonal distortion of the Fermi surface is here practically absent because of a comparatively small Fermi energy in the samples studied. Assuming inter-valley transitions in a bulk

crystal to also occur in scattering from surface states, we come to a conclusion that the significance of the latter in the phase relaxation processes should be negligible. Under these conditions, the quantity in braces in Eq. (2) will be positive, and AMR will always have a negative sign.

Seen from this viewpoint, the cluster crystal occupies an intermediate position. The trigonal distortion of the Fermi surface does not play a significant part in the weak localization effect, but the probability of scattering by the cluster surface is sufficiently high. As a result, the behavior of AMR in this case is similar to that shown by curve *5* in Fig. 2.

We note in conclusion that G. E. Pikus initiated this work and participated in its early stages.

Support of the Russian Fund for Fundamental Research (Grants 96-02-16959 and 98-02-18424), FTNS Program (Grants 97-1035 and 97-1042), and Integration Project (Grant 326.37) is gratefully acknowledged.

*)E-mail: Iosif.Farbstein@shuvpop.ioffe.rssi.ru

[1] R. A. Chentsov, Zh. Éksp. Teor. Fiz. **18**, 374 (1948).
[2] A. M. Pogarskiĭ, M. S. Bresler, I. I. Farbshteĭn, and S. S. Shalyt, Fiz. Tekh. Poluprovodn. **2**, 139 (1968) [Sov. Phys. Semicond. **2**, 782 (1968)].
[3] K. Takita, T. Hagiwara, and S. Tanaka, J. Phys. Soc. Jpn. **34**, 1548 (1973).
[4] V. A. Berezovets, I. I. Farbshteĭn, and A. L. Shelankov, JETP Lett. **39**, 74 (1984).
[5] V. A. Berezovets, Yu. B. Lyanda-Geller, A. O. Smirnov, and I. I. Farbshteĭn, JETP Lett. **58**, 770 (1993); V. A. Berezovets, I. I. Farbstein, and A. O. Smirnov, Phys. Low-Dimens. Semicond. Struct. **12**, 301 (1995).
[6] N. S. Averkiev, V. A. Berezovets, G. E. Pikus, N. N. Sablina, and I. I. Farbshteĭn, Fiz. Tverd. Tela (St. Petersburg) **40**, 1554 (1998) [Phys. Solid State **40**, 1409 (1998)].
[7] V. A. Berezovets, V. N. Bogomolov, A. I. Zadorozhnyĭ, T. M. Pavlova, A. O. Smirnov, I. I. Farbshteĭn, and A. L. Shelankov, *Abstracts of the XXV All-Union Conference on Low-Temperature Physics* (Leningrad, 1988), Pt. III, p. 31.
[8] L. S. Dubinskaya, G. E. Pikus, I. I. Farbshteĭn, and S. S. Shalyt, Zh. Éksp. Teor. Fiz. **54**, 754 (1968) [Sov. Phys. JETP **27**, 402 (1968)].
[9] V. A. Berezovets and I. I. Farbshteĭn, Fiz. Tekh. Poluprovodn. **29**, 965 (1995) [Semiconductors **29**, 500 (1995)].
[10] A. L. Shelankov, Solid State Commun. **53**, 465 (1985).
[11] N. S. Averkiev and G. E. Pikus, Fiz. Tverd. Tela (St. Petersburg) **38**, 1748 (1996) [Phys. Solid State **38**, 964 (1996)].
[12] N. S. Averkiev and G. E. Pikus, Fiz. Tverd. Tela (St. Petersburg) **39**, 1659 (1997) [Phys. Solid State **39**, 1481 (1997)].
[13] A. Kawabata, J. Phys. Soc. Jpn. **53**, 3540 (1984).
[14] M. I. Dyakonov, Solid State Commun. **92**, 711 (1994).

Translated by G. Skrebtsov

Ceramic materials for use in microwave electronics

E. A. Nenasheva and O. N. Trubitsyna

GIRIKOND Research Institute, 194223 St. Petersburg, Russia

N. F. Kartenko and O. A. Usov

A. F. Ioffe Physicotechnical Institute, Russian Academy of Sciences, 194021 St. Petersburg, Russia
Fiz. Tverd. Tela (St. Petersburg) **41**, 882–884 (May 1999)

A study is reported of the structure and electrical properties of $BaLn_2Ti_4O_{12}$ compositions (BLT), where Ln=La, Nd, or Sm, with calcium, strontium, or lead substituted for barium, and bismuth for the lanthanide. The BLT compound is shown to be characterized by a broad isomorphicity region, at the edge of which form solid solutions with the highest dielectric permittivity reached thus far, up to about 170. A number of thermally stable ceramic materials with a high dielectric permittivity of 80 to 120, which permit construction of microwave dielectric resonators with Q factors of up to 600 for $\varepsilon=120$ and up to 3000 for $\varepsilon=80$ at $f=4$ GHz, have been developed based on BLT solid solutions. © *1999 American Institute of Physics.* [S1063-7834(99)03205-0]

The recently increasing interest in microwave communications has stimulated progress in research and developments in the area of microwave ceramics employed universally in microwave electronics devices.

The main requirements imposed on the ceramic materials to be used in microwave-range devices are a high dielectric permittivity ε for a vanishingly small temperature coefficient TC_ε and low dielectric losses within a broad temperature and frequency range. An increase in dielectric permittivity of a ceramic material results in a smaller size of microwave devices, while reducing dielectric losses increases their Q factor ($Q\sim 1/\tan\delta$).

Ceramic materials based on barium, titanium, and rare-earth (RE) oxides[1–3] exhibit a unique combination of a high dielectric permittivity at a near-zero TC_ε and low dielectric losses within a broad temperature and frequency range.

The main component of such materials is the compound $BaO\cdot Ln_2O_3\cdot 4TiO_2$ ($BaLn_2Ti_4O_{12}$, or BLT) with Ln=La, Nd, Sm,[4] whose structural formula, according to Ref. 5, is given in the form[6] $Ba_{3.5}[Ba_{1.0}Ln_{9.0}][Ti_9O_{27}]_2$. The rhombically distorted perovskite-like BLT structure[5] contains elements characteristic of the lattice of tetragonal tungsten bronzes and has voids (structural vacancies in the barium sublattice).

The explanation[7] of the high ε typical of BLT compounds combined with a near-zero TC_ε assumes a dominant contribution of low-frequency vibrational modes to ε'. The observed splitting of these modes and a possible thermal compensation of the dielectric contributions due to the components of this splitting may account for the enhanced thermal stability of the ε of BLT-based materials.

Studies[7,8] of dielectric spectra of BLT compounds revealed an absence of ε' dispersion over a broad frequency range, including submillimeter waves. These features make BLT compounds promising for development of microwave ceramics.

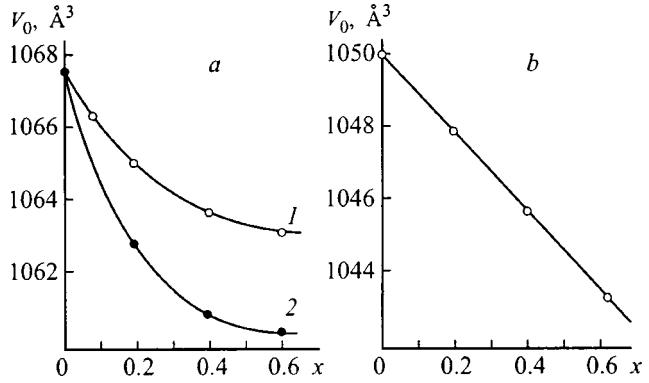

FIG. 1. Dependence of unit-cell volume V_0 of BLT solid-solution samples on composition in the $(A_xBa_{1-x})La_2Ti_4O_{12}$ system, where (a) A = Sr (*1*) and Ca (*2*), and (b) $(Sr_xBa_{1-x})Nd_2Ti_4O_{12}$.

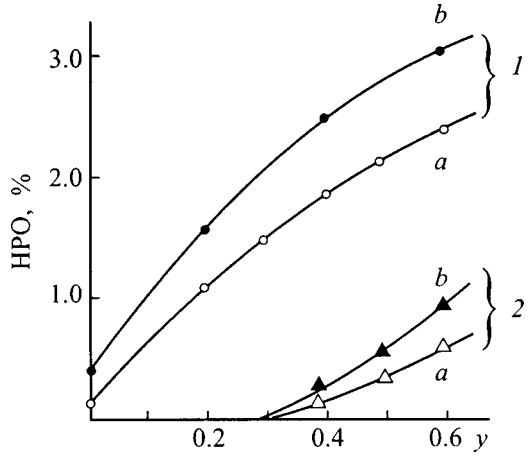

FIG. 2. Content of insoluble residue in samples of $(Pb_xBa_{1-x})(Bi_yNd_{2-y})Ti_4O_{12}$ for (a) $x=0.10$ and (b) $x=0.15$, obtained by (*1*) solid-state synthesis and (*2*) chemical coprecipitation.

TABLE I. X-ray diffraction data for some $(Pb_xBa_{1-x})(Nd_yBi_{2-y})Ti_4O_{12}$-based BLT solid-solution compositions.

Composition		Cell parameters			Cell volume	
x	y	a, Å	b, Å	c, Å	V_0, Å^3	Impurity
0.1	1.4	22.346(6)	12.211(2)	3.8634(5)	1061.5	$(Ba,Pb)Bi_4Ti_4O_{15}$ barium polytitanates.
0.15	1.6	22.340(6)	12.218(2)	3.8470(5)	1050.0	$(Ba,Pb)Bi_4Ti_4O_{15}$, $Nd_2Ti_2O_7$ barium polytitanates.
0.15	1.4	22.358(6)	12.210(2)	3.8612(5)	1061.3	$(Ba,Pb)Bi_4Ti_4O_{15}$, $Nd_2Ti_2O_7$, $BaTi_4O_9$
0.25	1.8	22.364(6)	12.200(2)	3.8424(5)	1048.4	$(Ba,Pb)Bi_4Ti_4O_{15}$, $Nd_2Ti_2O_7$, TiO_2

1. TECHNOLOGY OF PREPARATION

New materials based on barium, titanium, and RE oxides with various compositions were obtained both by solid-state synthesis from oxides and carbonates and by chemical coprecipitation from salt solutions followed by thermal treatment of the precipitates.[9] The ceramic powders thus synthesized were hydraulically pressed into discs of the size required for measurements of the electrical properties within the ranges of (10^5-10^6) GHz and $4-5$ Hz, as well as for x-ray diffraction studies. Prior to measurements, these discs were sintered until zero water absorption.

2. DISCUSSION OF RESULTS

A study has been made of the structure and electrical properties of BLT samples with calcium, strontium, and lead substituted for barium, and of bismuth, for the RE element. Single-phase BLT solid solutions form in the $(A_xBa_{1-x})Ln_2Ti_4O_{12}$ system, where A=Ca, Sr, with x increasing to 0.1 for Ca and to 0.2 for Sr. A second, $ALn_2Ti_4O_{12}$-type, perovskite phase with a doubled unit cell was found to appear starting with $x=0.2$ for Ca and with $x=0.4$ for Sr.[10] Substituting Sr^{2+} or Ca^{2+} cations for Ba^{2+} was observed to decrease the unit-cell volume of BLT solid solutions (Fig. 1). For $x>0.4$, the unit-cell parameters of the BLT-type phase practically do not change, which in the given case implies the constancy of its chemical composition. At the same time the second phase with a $SrLa_2Ti_4O_{12}$-type superstructure discovered in samples with $x=0.4$ for Sr has a cell parameter $a=7.772$ Å which exceeds slightly that of the same $SrLa_2Ti_4O_{12}$ phase with stoichiometric composition, $x=1.0$ ($a=7.769$ Å). This is probably associated with a partial incorporation of barium into the strontium sublattice. Thus two phases, representing solid solutions with BLT-type and $SrLa_2Ti_4O_{12}$ structures were detected in the $(Sr_xBa_{1-x})La_2Ti_4O_{12}$ system within the concentration interval of $x=0.4$ to 0.8. For $0.8<x\leqslant 1$, there exist only solid solutions with the $SrLa_2Ti_4O_{12}$ structure. When neodymium is substituted for lanthanum, the region of $Sr^{2+}\rightarrow Ba^{2+}$ isomorphism extends to $x=0.6$.

In $(Sr_xBa_{1-x})Sm_2Ti_4O_{12}$-based materials, a pyrochlore phase is seen to exist already starting with $x=0.2$, and for $x=0.6$ a third, perovskite-structure phase $SrSm_2Ti_4O_{12}$ ($a=7.722$ Å) appears. Similar results were obtained with lead substituted for barium, and bismuth for RE elements in BLT. X-ray diffraction data obtained for some compositions in the $(Pb,Ba)(Nd,Bi)_2Ti_4O_{12}$ system are listed in Table I.

As seen from these data, the unit cell volume in BLT solid solutions increases when Bi^{3+} ions are incorporated and decreases with increasing lead concentration. When both elements are introduced, isomorphous solid solutions with close cell parameters form within a broad compositional range.

Chemical coprecipitation of BLT solid solutions from salt solutions, followed by thermal treatment of the precipitates, described in Ref. 9, increases the yield of the reaction of solid-solution formation and permits one to decrease the synthesis temperature by about 100 K compared to solid-phase preparation.

Figure 2 displays data on the content of insoluble impurity-phase residues in the $(Pb,Ba)(Nd,Bi)_2Ti_4O_{12}$ compositions obtained by solid-state (*1*) and chemical coprecipitation (*2*) methods vs composition. The amount of the insoluble residues was determined to within ± 0.02 wt.%.

The electrical parameters of BLT solid solutions vary within a broad range with composition. The highest ε, up to 170, are obtained in the system where bismuth was partially substituted for lanthanum at the boundary of the isomorphicity region (Fig. 3). The TC_ε parameter may vary from $-800\times10^{-6}\,K^{-1}$ to $+100\times10^{-6}\,K^{-1}$. For a thermally stable ceramic with $TC_\varepsilon=(0\pm30)\times10^{-6}\,K^{-1}$, ε of the

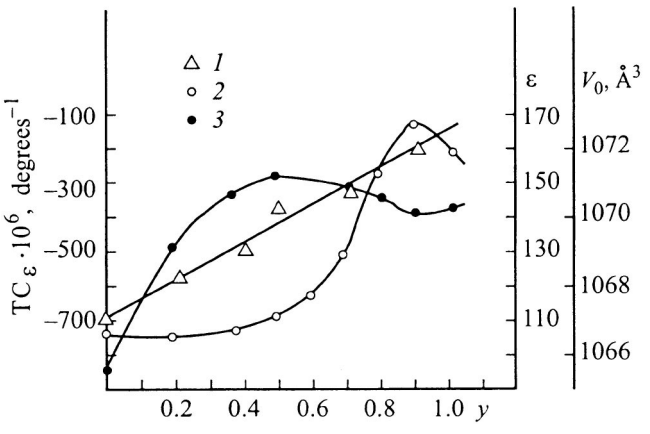

FIG. 3. Dependence of unit cell volume V_0, dielectric permittivity ε, and of its temperature coefficient TC_ε on bismuth content in a BLT solid solution $(Ba_{0.9}Ca_{0.1})(Bi_yLa_{2-y})Ti_4O_{12}$ system.

TABLE II. Main electrical characteristics of thermally stable BLT solid-solution-based materials in the microwave range.

Material	ε	$Q(f=4\ \text{GHz})$	$Q \cdot f$, GHz
B80	80	3000	12000
B90	90	1900	7500
B92	92	1600	6400
B100	100	1300	5200
B120	120	600	2400

substitutional solid solutions lies from 70 to 120, depending on the composition.

The main characteristics of a number of BLT-based thermally stable materials which can be used in microwave electronics are listed in Table II.

Thus an analysis of the structure and electrical properties of materials of varying composition made in the region of isomorphicity of $(A_xBa_{1-x})(Ln_{2-y}Bi_y)Ti_4O_{12}$ systems, where A=Ca, Sr, Pb, and Ln=La, Nd, and Sm, shows that isovalent solid solutions prepared at the edge of the isomorphicity region exhibit a high dielectric permittivity and low dielectric losses within a broad frequency range.

These isovalent solid solutions were used to develop a number of high-Q thermally stable materials for microwave technology applications.

The new materials permit one to vary the main electrical parameters of microwave devices within a broad range and to choose purposefully an optimum ceramic composition best suitable for a given problem.

[1] D. Kolar, S. Gaberščček, Z. Stadler, and D. Suvorov, Ferroelectrics **27**, 269 (1980).
[2] B. A. Rotenberg, L. P. Mudrolyubova, and E. A. Nenasheva, Élektr. Tekhn., Ser. Radiodet. Radiokomp. No. 2, 3 (1987).
[3] Ye. A. Nenasheva, Mater. Res. Soc. Symp. Proc. **269**, 607 (1992).
[4] L. P. Mudrolyubova, B. A. Rotenberg, N. F. Kartenko, A. N. Borshch, V. G. Prokhvatilov, Yu. P. Kostikov, and M. P. Ivanova, Izv. Akad. Nauk SSSR, Neorg. Mater. **17**, 683 (1981).
[5] R. G. Matveeva, M. B. Varfolomeev, and L. S. Il'yushchenko, Zh. Neorg, Khim. **29**, 31 (1984).
[6] Ye. A. Nenasheva, N. F. Kartenko, I. B. Kamushkina, and V. P. Pyshkov, in *Proceedings of the International Conference on Electrical Ceramics, Production and Properties, Riga (1990)*, Pt. II, p. 79.
[7] V. I. Butko, A. G. Belous, E. A. Nenasheva, Yu. M. Poplavko, and E. F. Ushatkin, Fiz. Tverd. Tela (Leningrad) **26**, 2951 (1984) [Sov. Phys. Solid State **26**, 1783 (1984)].
[8] Ye. A. Nenasheva, L. P. Mudrolyubova, N. F. Kartenko, G. V. Kozlov, and B. P. Gorshunov, in *Proceedings of the International Conference on Electrical Ceramics, Production and Properties, Riga (1990)*, Pt. II, p. 82.
[9] T. F. Limar', A. N. Borshch, I. G. Slatinskaya, L. P. Mudrolyubova, and E. A. Nenasheva, *Obshcheotr. Vopr.* (NIITEKhIM, Moscow, 1988), No. 10.
[10] E. A. Nenasheva, B. A. Rotenberg, and N. F. Kartenko, in *Abstracts of the All-Union Conference on the Physics of Dielectrics, Baku (1982)*, p. 42.

Translated by G. Skrebtsov

Electronic and optical properties of fullerene nanostructures

Yu. I. Prilutski*) and S. S. Durov

Kiev Shevchenko University, 252033 Kiev, Ukraine
Fiz. Tverd. Tela (St. Petersburg) **41**, 885–887 (May 1999)

Two new types of molecular/electronic fullerene nanostructures are considered: 1) highly stable hydrated clusters (I_h symmetry group) and microcrystals (T_h symmetry group) of fullerene C_{60} in water solution and 2) the single-walled carbon nanotube from C_{60} fullerenes. The vibrational spectra of these fullerene nanostructures are calculated using molecular dynamics. The electronic properties of a single-walled fullerene nanotube are investigated using the tight-binding method. The theoretical results obtained were compared with available experimental data.
 [S1063-7834(99)03305-5]

Fullerenes are widely investigated currently and have potential for various technical applications.[1] In particular, for biomedical testing, water-soluble forms of fullerenes are undoubtedly of great interest. Poor solubility in water of fullerenes and their derivatives limits biological and medical studies, even though there were reports of successfully prepared micro- and macro-colloidal particle solutions in organic solvents or in water.[2–7] In particular, G. V. Andrievsky and collaborators[5–7] recently proposed a method for obtaining molecular-colloidal dispersions of fullerenes in water without any stabilizers and this resulted in the generation of solutions with fullerene aggregate sizes from several nanometers to 200 nm. These aggregates consisted of smaller spherical particles with diameter approximately $2-3$ nm containing $4-13$ molecules of C_{60}.[6] The fullerene water solutions (FWS), being molecular-colloidal systems, were found to be stable for more than 12 months at ambient conditions. At present, the highest concentration of C_{60} achieved in the FWS is ~ 1.4 g/l.[5–7] It should be noted that the formation of similar fullerene C_{60} structures in different organic solvents was not observed[2–4] showing the important influence of water on their formation and existence.[5–7]

The discovery of single-walled carbon nanotubes[8,9] has provided the opportunity to study their mechanical, optical and electronic properties.[10,11] Specifically, their electronic characteristics are predicted to vary depending upon the nanotube symmetry and diameter, thus giving either metallic or semiconducting behavior.[1] It is very important for the creation of novel materials for nanoengineering.

The geometric structure of possible fullerene aggregates in water was studied in detail in Ref. 12. The present paper is devoted to the calculation of the vibrational spectrum of fullerene aggregates in water solution and the structure of a single-walled fullerene nanotube (SWFN), as well as its electronic and optical properties. The theoretical results obtained were compared with available experimental data.[13–15]

1. STUDY OF VIBRATIONAL SPECTRUM OF FULLERENE C_{60} AGGREGATES IN WATER

Using the atom–atom potential method, the closest-packing, and symmetry principles, we have calculated the structure of fullerene aggregates C_{60} in water solution.[12] The main results were as follows: a) the spherical clusters (I_h symmetry group) with a diameter of 3.56 nm containing 33 molecules of C_{60} (see Fig. 1) were shown to be the most stable ones among possible hydrated aggregates; b) possible existence of stable hydrated microcrystals C_{60} (the space group is T_h, the lattice parameters are $a=1.002$ nm and $c=1.636$ nm [Ref. 16]) having a linear size of $(2.51-5.84)$ nm in water solution of fullerenes was stated; c) the water effect on a geometry of the fullerene aggregates was discussed; d) the obtained theoretical results were experimentally confirmed.

The calculated vibrational frequencies of the most stable hydrated fullerene cluster consisted of 33 C_{60} molecules ($\omega=(14-152)\ \mathrm{cm}^{-1}$) which lie significantly lower than the fundamental intramolecular modes for the individual C_{60}

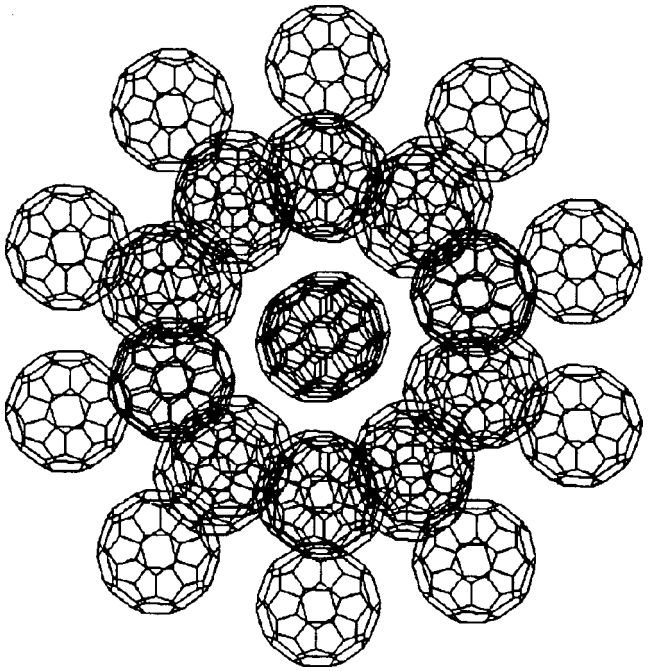

FIG. 1. The calculated structure of a fullerene cluster consisting of 33 C_{60} molecules.

TABLE I. Calculated Raman frequencies (cm^{-1}) of hydrated fullerene cluster consisting of 33 C_{60} molecules.

Symmetry	Theory (cluster C_{60})	Theory[17] (molecule C_{60})
H_g	14	296
H_g	28	437
A_g	33	476
H_g	58	721
H_g	63	780
H_g	82	1142
H_g	85	1288
H_g	94	1406
A_g	101	1485
H_g	103	1550

fullerene ($\omega=(296-1590)\ cm^{-1}$).[17] The Raman spectrum of this cluster is presented in Table I.

The limiting intermolecular spectrum of hydrated microcrystal C_{60} is presented in Table II. As we can see the calculated vibrational frequencies lie below the fundamental modes for solid C_{60}.[18]

It should be noted that low vibrational frequencies of fullerene cluster C_{60} ($2H_g$ and A_g modes, see Table I) can coincide with some intermolecular frequencies of microcrystal C_{60} (E_g, E_u and F_u modes, see Table II).

The numerical calculations were carried out in the approximation of a Lennard–Jones (12–6) atom–atom potential only (the entropy factor did not arise because an assumption was made that the formation of orientationally ordered structures in water takes place [Ref. 12] using the proposed molecular-dynamics model for a fullerene crystal C_{60}.[18]

2. STUDY OF ELECTRONIC AND VIBRATIONAL PROPERTIES OF THE SWFN

The simulated structure of the SWFN is presented in Fig. 2. The radius and the length of the ideal part of a nanotube are equal to 0.35 nm (Ref. 19) and 0.43 nm, respectively.

As is known,[1,11] the dependence of the gap on the radius R of a single-walled carbon nanotube may be approximately described by

$$\varepsilon_g=\varepsilon_{\pi\pi}\frac{d_0}{R}.$$

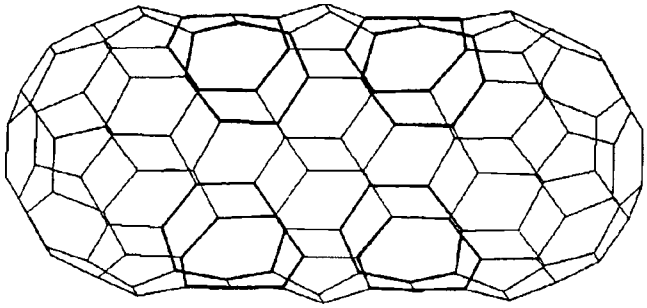

FIG. 2. The calculated structure of a single-walled fullerene nanotube.

In our case, $\varepsilon_{\pi\pi}$ is the average interaction energy between two π electrons located on the single and double bonds in the C_{60} molecule; d_0 is the average distance between the neighboring carbon atoms in C_{60} molecule. The numerical calculations carried out by using the tight-binding method[20] have shown that $\varepsilon_{\pi\pi}=2.35$ eV and $d_0=0.14$ nm. The presence of a heptagon–heptagon pair as a defect in the structure of the SWFN leads to a change of its radius from 0.35 to 0.38 nm (the average distance between the neighboring carbon atoms in the heptagon is equal to d_0 also). As a result, the decrease of the gap from 0.94 to 0.87 eV takes place. Thus, the semiconductor–semiconductor heterojunction having different values of the gap is formed. It should be noted that a similar heterojunction was really observed in the experiment[13,14] for the single-walled carbon nanotube with a pentagon–heptagon defect.

The calculated vibrational frequencies of the SWFN (in the framework of the proposed molecular-dynamics model[17]) lie in the range of $\omega=(49-1744)\ cm^{-1}$. The Raman spectrum of this nanotube is presented in Table III. As we can see, they are in satisfactory agreement with the available experimental results[15] for the single-walled carbon nanotube of ''armchair'' configuration.

3. CONCLUSION

The main results obtained are as follows.

1) The vibrational spectra of possible fullerene C_{60} aggregates in water (clusters of I_h symmetry and microcrystals of (T_h symmetry group) are calculated using the molecular-dynamics approach.[18] The theoretical results obtained can be useful in further optical experiments;

TABLE II. The calculated limiting ($\mathbf{k}=0$) intermolecular frequencies (cm^{-1}) of hydrated microcrystal C_{60}.

Symmetry	Theory (microcrystal C_{60})	Theory[18] (solid C_{60})
A_u	21	35
E_u	27	48
F_u	23	43
F_u	30	53
A_g	13	19
E_g	14	20
F_g	9	17
F_g	11	18
F_g	18	23

TABLE III. The calculated and experimental Raman-active vibrational frequencies (cm^{-1}) for a single-walled nanotube.

Symmetry	Theory	Experiment[15]
H_g	119	116
H_g	190	186
A_g	396	377
H_g	770	755
H_g	885	855
H_g	1356	1347
H_g	1525	1526
H_g	1549	1550
A_g	1583	1567
H_g	1606	1593

2) As a model for the calculation of electronic and optical properties of a single-walled carbon nanotube, the nanotube formed of C_{60} molecules was proposed. The presence of a heptagon–heptagon pair as a defect in the structure of this nanotube leads to the formation of a semiconductor–semiconductor heterojunction with a different gap value. The electronic characteristics and vibrational spectrum of a single-walled fullerene nanotube are investigated using the molecular-dynamics model[17] and the tight-binding method.[20] The theoretical results obtained are in good agreement with the available experimental data.[13–15]

*)E-mail: prilut@office.ups.kiev.ua

[1] M. S. Dresselhaus, G. Dresselhaus, and P. C. Eklund, *Science of Fullerenes and Carbon Nanotubes* (Academic Press, N.Y., 1996).
[2] T. Anderson, K. Nilsson, M. Sundahl, G. Westman, and O. Wennerstrom, J. Chem. Soc. Chem. Commun. **8**, 604 (1992).
[3] R. S. Ruoff, D. S. Tse, M. Malhotra, and D. C. Lorents, J. Phys. Chem. **97**, 3379 (1993).
[4] W. A. Scrivens, J. M. Tour, K. F. Creek, and L. Pirisi, J. Am. Chem. Soc. **116**, 4517 (1994).
[5] G. V. Andrievsky, M. V. Kosevich, O. M. Vovk, V. S. Shelkovsky, and L. A. Vashchenko, J. Chem. Soc. Chem. Commun. **12**, 1281 (1995).
[6] G. V. Andrievsky, V. K. Klochkov, A. D. Roslyakov, and A. Yu. Platov, *International Workshop ''Fullerenes and Atomic Clusters.'' Abstracts of invited lectures and contributed papers. St. Petersburg, Russia (1977)*, p. 262.
[7] N. O. Mchedlov-Petrossyan, V. K. Klochkov, and G. V. Andrievsky, J. Chem. Soc., Faraday Trans. **93**, 4343 (1997).
[8] S. Iijima and T. Ichihashi, Nature (London) **363**, 603 (1993).
[9] D. S. Bethune, C. H. Kiang, M. S. de Vries, G. Gorman, R. Savoy, J. Vazquez, and R. Beyers, Nature (London) **363**, 605 (1993).
[10] N. Hamada, S. I. Sawada, and A. Oshiyama, Phys. Rev. Lett. **68**, 1579 (1992).
[11] C. T. White, D. H. Robertson, and J. W. Mintemire, Phys. Rev. B **47**, 5485 (1993).
[12] Yu. I. Prilutski, Ukr. Fiz. Zh. **43**, 1245 (1998).
[13] R. Saito, G. Dresselhaus, and M. S. Dresselhaus, Phys. Rev. B **53**, 2044 (1996).
[14] P. Lauginie and J. Conard, J. Phys. Chem. Solids **58**, 1949 (1997).
[15] A. M. Rao, E. Richter, S. Bandow, B. Chase, P. C. Eklund, K. A. Williams, S. Fang, K. R. Subbaswamy, M. Menon, A. Thess, R. E. Smalley, G. Dresselhaus, and M. S. Dresselhaus, Science **275**, 187 (1997).
[16] W. Kraetschmer, L. D. Lamb, K. Fostiropoulos, and D. R. Huffman, Nature (London) **347**, 354 (1990).
[17] Yu. I. Prilutski, V. O. Gubanov, and S. S. Durov, Ukr. Fiz. Zh. **42**, 1143 (1997).
[18] Yu. I. Prilutski and G. G. Shapovalov, Phys. Status Solidi B **201**, 361 (1997).
[19] H. W. Kroto, J. R. Health, S. C. O'Breine, R. F. Curl, and R. E. Smalley Nature (London) **318**, 162 (1985).
[20] J. Q. You, F. Nori, and Y. L. Lin, Solid State Commun. **91**, 117 (1994).

Published in English in the original Russian journal. Reproduced here with stylistic changes by the Translation Editor.

Optical detection of magnetic resonance and of exciton-level anticrossing in quantum wells and superlattices

P. G. Baranov and N. G. Romanov

A. F. Ioffe Physicotechnical Institute, Russian Academy of Sciences, 194021 St. Petersburg, Russia
Fiz. Tverd. Tela (St. Petersburg) **41**, 888–890 (May 1999)

Recent studies of excitonic and electron-hole recombination in GaAs/AlAs quantum wells and superlattices are reported using microwave-optical spectroscopy of low-dimensional structures developed by the authors. © *1999 American Institute of Physics.*
[S1063-7834(99)03405-X]

The studies dealing with optical detection of magnetic resonances were initiated at the A. F. Ioffe Physicotechnical Institute in 1977 by the discovery of the effect of free-carrier cyclotron resonance on luminescence in semiconductors.[1] The electron and hole cyclotron resonance was found to suppress dramatically the luminescence intensity of excitons and electron-hole drops. Besides the enhanced sensitivity and spatial selectivity, optically-detected cyclotron resonance, ODCR, possesses such important merits as the possibility of studying undoped samples with simultaneous observation of the electron and hole cyclotron resonance, investigation of the dynamics of carriers and the nature of their trapping and recombination, and probing the band structure and effects of carrier localization in thin epitaxial layers and nanostructures. ODCR has become a powerful tool in semiconductor research,[2,3] which is employed particularly effective in studies of low-dimensional systems.[4–7]

The Physicotechnical Institute carried out a series of pioneering studies of tunneling and photostimulated recombination processes in irradiated ionic crystals by optically detected magnetic resonance (ODMR).[8–10] The effect of impurity-spin polarization on recombination-luminescence intensity was discovered, and energy transport processes were investigated in ionic and semiconductor crystals with magnetic impurities.[10,11] Optical pumping and cross relaxation were employed to develop novel techniques for optical detection of electronic and nuclear magnetic resonance without application of microwaves.[10,12] Numerous studies of excitonic and donor-acceptor recombination in the GaP, GaSe, II–VI, and SiC semiconductors were carried out, and, in particular, the first ODMR investigations of acceptors in silicon carbide doped by gallium, boron, and scandium were made.[10,13,14] The multi-photon ODMR spectroscopy was used for the first time to probe semiconductors and silver halides.[15]

The present paper reports on the recent studies of GaAs/AlAs and GaAs/AlGaAs quantum wells and superlattices (SL) by ODMR and on the exciton level anticrossing (LAC) spectroscopy developed on this basis.

The GaAs/AlAs systems allow development of both direct (type I) and indirect (type II) superlattices. In type-II SLs, the electrons ($S=1/2$) and heavy holes ($J_z=\pm 3/2$) making up the heavy-hole excitons are localized in adjacent AlAs and GaAs layers, respectively, and recombination between them can be used to probe the microscopic structure of the interfaces. Because of the low local symmetry of the interface (C_{2v}), all the four exciton levels are exchange split, and the excitons located on opposite interfaces have inverted radiative-level systems.

Nanostructures are presently studied primarily by photoluminescence techniques. The traditional methods of radiospectroscopy are inapplicable here because of the not high enough sensitivity, but this difficulty can be overcome by employing ODMR. Already the very first ODMR experiments made on GaAs/AlAs SLs permitted one to obtain accurate and unambiguous information on the energy level system of localized excitons and their fine-structure parameters, as well as on the magnetic g factors of unbound electrons and holes.[16–19] It was demonstrated that the isotropic exchange splitting Δ in type-II SLs depends primarily on the SL period and varies with the latter as shown in Fig. 1.[19,20] The splitting of the radiative levels $\delta_1 \cong \Delta/2$, and that of the nonradiative ones is small. The hole g factor is determined by the thickness of the GaAs layers.

In type-II SLs one observed also broad ODMR lines of exchange-coupled electron-hole pairs. Multi-photon ODMR studies revealed that the linewidth and line shape of ''localized'' electrons in such pairs is dominated not by scatter in the g factor but rather by the exchange-splitting distribution resulting from the statistical distribution of the pair-partner distances.

The results of the ODMR studies were used by the present authors to develop level anticrossing spectroscopy.[20] Anticrossing of a more populated nonradiative level with a radiative one gives rise to a resonant enhancement in the luminescence intensity of the corresponding polarization. The position of LAC signals depends on the exchange splittings and g factors, as well as on the magnetic-field orientation with respect to the SL plane. It can be calculated by exciton spin-Hamiltonian diagonalization as this is done with ODMR signals. It should be noted that, in contrast to ODMR, observation of anticrossing does not require saturation of EPR transitions and has no limitations associated with the radiative lifetime. ODMR can be observed only for states with lifetimes in excess of 0.1 μs, i.e., only in type-II SLs. Anticrossing observations based on the linear polarization of

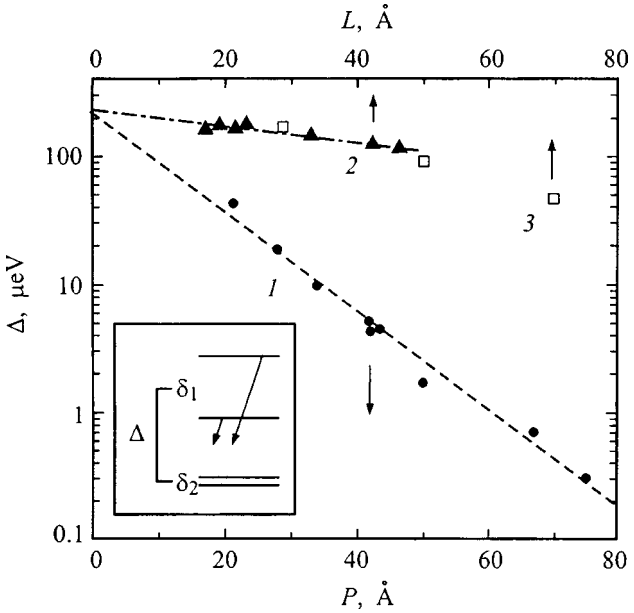

FIG. 1. Experimental dependences of the exciton isotropic-exchange splitting Δ in (*1*) type-II GaAs/AlAs superlattices on SL period *P*, and in (*2*) type-I GaAs/AlAs superlattices and (*3*) type-I GaAs/AlGaAs quantum wells on GaAs layer thickness *L*. The inset shows exciton energy levels in zero magnetic field.

luminescence permit determination of the polarization of the lowest exciton radiative level, which turns out to be essential for interface identification in type-II structures and for revealing anisotropy of the localizing potential in type-I structures.

The investigation of the transition region and the first observation of LAC in type-I structures were made on a specially prepared sample with an in-plane composition gradient and a smooth transition from type-II to type-I SL.[21,22] Application of LAC spectroscopy to quantum wells and type-I SLs provided the first reliable measurements of the exciton exchange splitting[21] and of its dependence on well thickness. The results obtained for GaAs/AlAs SLs and GaAs/AlGaAs quantum wells are presented in Fig. 1. One immediately sees that as the type-II SL period and the well thickness in a type-I SL decrease, the splittings Δ tend to the same value of $\cong 235\,\mu$eV. Additional information on excitons can be gained from studies of the orientational dependences of LAC and measurements of cross-relaxation resonances.[23]

An essential merit of the ODMR and LAC spectroscopies is the possibility of selective investigation of excitons localized at opposite interfaces in type-II GaAs/AlAs SLs. Specially prepared ''asymmetric'' superlattices, in which excitons are localized at an existing interface, were employed to establish a one-to-one correspondence between the interface type and the sequence of the exciton radiative levels.[24] It was shown convincingly that the lowest radiative level is polarized along [110] for excitons at the normal (AlAs on GaAs) interface and along $[1\bar{1}0]$ for excitons on the inverted (GaAs on AlAs) one. ODMR and LAC studies showed that such excitons in ''conventional'' type-II SLs differ in the exchange splitting, which can be accounted for by the asymmetry in the compositional profiles of the opposite interfaces because of different surface segregation of gallium and aluminum.[25,26] Exciton localization at opposite interfaces was investigated as a function of superlattice growth conditions, in particular, of growth interruptions after deposition of GaAs or AlAs layers.[27] Measurements of the luminescence response to application of a resonant microwave field permitted one to start ODMR studies of the dynamic characteristics of excitons.[28]

Detection of LAC signals by the linear polarization of luminescence in type-I systems showed that the exciton radiative levels are split in these structures too, with the radiation emitted from the lowest level being polarized along $[1\bar{1}0]$. This argues for the interface islands being preferentially $[1\bar{1}0]$ oriented, which agrees with data obtained by electron and tunneling microscopy.

Thus studies of type-II GaAs/AlAs superlattices, as well as of quantum wells and type-I GaAs/AlGaAs and GaAs/AlAs superlattices by optically detected level anticrossing and magnetic resonance provided information on the relation of exchange splittings, *g* factors, and the sequence of exciton radiative levels with superlattice parameters and the interface structure. This information can be used for nanostructure diagnostics.[27,29]

Development of methods of optically detected cyclotron and magnetic resonance, level anticrossing spectroscopy, cross-relaxation spectroscopy, and multi-photon magnetic resonance has provided a solid basis for initiating a new direction in research, namely, radiospectroscopy of carriers and excitations in low-dimensional structures.

Partial support of the Russian Fundamental Research Foundation (Grant 96-02-16927) is gratefully acknowledged.

[1] P. G. Baranov, Yu. P. Veshchunov, R. A. Zhitnikov, N. G. Romanov, and Yu. G. Shreter, JETP Lett. **26**, 249 (1977).
[2] T. Tomaru, T. Ohyama, and E. Otsuka, Appl. Magn. Reson. **2**, 379 (1991).
[3] M. Godlewski, W. M. Chen, and B. Monemar, Crit. Rev. Solid State Mater. Sci. **19**, 241 (1994).
[4] B. C. Cavenett, Phys. Rev. B **32**, 8449 (1985).
[5] R. T. Warburton, J. G. Michels, R. J. Nicholas, J. J. Harris, and C. T. Foxon, Phys. Rev. B **46**, 13394 (1992).
[6] D. M. Hofmann, M. Drechsler, C. Wetzel, B. K. Meyer, F. Hirler, R. Strenz, G. Abstreiter, G. Böhm, and G. Weimann, Phys. Rev. B **52**, 11313 (1995).
[7] Y. F. Chen, Y. T. Dai, J. C. Fan, T. L. Lee, and H. H. Lin, Appl. Phys. Lett. **67**, 1256 (1995).
[8] P. G. Baranov, Yu. P. Veshchunov, and N. G. Romanov, Fiz. Tverd. Tela (Leningrad) **22**, 3732 (1980) [Sov. Phys. Solid State **22**, 2186 (1980)].
[9] N. G. Romanov, V. A. Vetrov, and P. G. Baranov, JETP Lett. **37**, 386 (1983).
[10] P. G. Baranov and N. G. Romanov, Appl. Magn. Reson. **2**, 361 (1991).
[11] P. G. Baranov, M. F. Bulanyĭ, V. A. Vetrov, and N. G. Romanov, JETP Lett. **38**, 623 (1983).
[12] N. G. Romanov, V. V. D'yakonov, V. A. Vetrov, and P. G. Baranov, Fiz. Tverd. Tela (Leningrad) **31**, 106 (1989) [Sov. Phys. Solid State **31**, 58 (1989)].
[13] P. G. Baranov, V. A. Vetrov, N. G. Romanov, and V. I. Sokolov, Fiz. Tverd. Tela (Leningrad) **27**, 3459 (1985) [Sov. Phys. Solid State **27**, 2085 (1985)].
[14] P. G. Baranov, V. A. Vetrov, N. G. Romanov, and V. G. Oding, Pisma Zh. Tekh. Fiz. **11**, 1168 (1985) [Sov. Tech. Phys. Lett. **11**, 483 (1985)].
[15] N. G. Romanov and P. G. Baranov, Semicond. Sci. Technol. **9**, 1080 (1994).
[16] H. W. van Kesteren, E. C. Cosman, W. A. J. A. van der Pool, and C. T. Foxon, Phys. Rev. B **41**, 5283 (1990).

[17] J. M. Trombetta, T. A. Kennedy, D. Gammon, B. V. Shanabrook, and S. M. Prokes, Mater. Sci. Forum **83-87**, 1361 (1991).
[18] P. G. Baranov, P. Lavallard, R. Planel, and N. G. Romanov, Superlattices Microstruct. **12**, 327 (1992).
[19] P. G. Baranov, I. V. Mashkov, N. G. Romanov, P. Lavallard, and R. Planel, Solid State Commun. **87**, 649 (1993).
[20] P. G. Baranov and N. G. Romanov, in *Proceedings of the 22nd International Conference on the Physics of Semicondconductors*, edited by D. J. Lockwood (World Scientific, Singapore, 1994), p. 1400.
[21] N. G. Romanov, I. V. Mashkov, P. G. Baranov, P. Lavallard, and R. Planel, JETP Lett. **57**, 802 (1993).
[22] N. G. Romanov, I. V. Mashkov, P. G. Baranov, P. Lavallard, and R. Planel, Solid-State Electron. **37**, 911 (1994).
[23] P. G. Baranov, V. A. Vetrov, B. R. Namozov, and N. G. Romanov, JETP Lett. **61**, 792 (1995).
[24] P. G. Baranov, I. V. Mashkov, N. G. Romanov, C. Gordon, P. Lavallard, and R. Planel, JETP Lett. **60**, 445 (1994).
[25] P. G. Baranov, N. G. Romanov, A. Hofstaetter, A. Scharmann, C. Schnorr, F. A. Ahlers, and K. Pierz, JETP Lett. **64**, 754 (1996).
[26] P. G. Baranov, N. G. Romanov, A. Hofstaetter, A. Scharmann, C. Schnorr, F. A. Ahlers, and K. Pierz, Inst. Phys. Conf. Ser. No. 155 (IOP Publ. Ltd, 1996), p. 893.
[27] P. G. Baranov, N. G. Romanov, A. Hofstaetter, C. Schnorr, W. von Förster, B. K. Meyer, A. Scharmann, F. A. Ahlers, and K. Pierz, in *Proceedings of the 5th International Symposium on Nanostructures: Physics and Technology*, edited by Zh. Alferov and L. Esaki (St. Petersburg, 1997), p. 47.
[28] P. G. Baranov, N. G. Romanov, A. Hofstaetter, C. Schnorr, W. von Förster, and B. K. Meyer, in *Proceedings of the 6th International Symposium on Nanostructures: Physics and Technology*, edited by Zh. Alferov and L. Esaki (St. Petersburg, 1998), p. 366.
[29] P. G. Baranov, N. G. Romanov, I. V. Mashkov, G. B. Khitrova, H. M. Gibbs, and O. Lungres, Fiz. Tverd. Tela (St. Petersburg) **37**, 2991 (1995) [Phys. Solid State **37**, 1648 (1995)].

Translated by G. Skrebtsov

Structural studies of nanoporous carbon produced from silicon carbide

R. N. Kyutt, É. A. Smorgonskaya, and A. M. Danishevskiĭ

A. F. Ioffe Physicotechnical Institute, Russian Academy of Sciences, 194021 St. Petersburg, Russia

S. K. Gordeev and A. V. Grechinskaya

Central Institute of Materials Research, St. Petersburg, Russia
Fiz. Tverd. Tela (St. Petersburg) **41**, 891–893 (May 1999)

X-ray diffraction and small-angle scattering study of nanoporous carbon samples prepared from polycrystalline α SiC and single-crystal 6*H* SiC is reported. The distribution function of carbon nanoclusters in size was found. In α SiC samples, the small size (10–12 Å) of nanoclusters is combined with their high size uniformity. Graphite-like nanoclusters 30–60 Å in size were found in samples of both types. In 6*H* SiC samples, such clusters make up a notable fraction of the volume. The experimentally observed structural anisotropy of the samples is discussed.
 [S1063-7834(99)03505-4]

Solid carbon exists in a variety of forms differing in structural organization on the short-, medium- (nanometers), and long-range scales. The actual form a sample acquires depends on the method of preparation. It is known, in particular, that by chemical removal of non-carbon atoms from carbide compounds one can obtain compact, highly porous carbon materials with a very uniform nanopore distribution in size (~ 1 nm).[1–3] These materials have been attracting recently considerable attention in connection with their application potential. Besides, nanoporous carbon (npor-C) is of interest by belonging to a group of novel nanostructures displaying manifestations of various carbon phases or morphology, including some not observed before. The very first x-ray small-angle scattering data on compact npor-C samples prepared of polycrystalline α SiC, TiC, and Mo_2C (Ref. 4) revealed the nanocluster nature of the structure of the npor-C framework including clusters 10–25 Å in size, which depends on the type of the initial carbide used. The correlation between the npor-C structure and carbide type requires a comprehensive study. This work reports a comparative investigation of the structure of npor-C prepared from single-crystal 6*H*-SiC and polycrystalline α SiC, which was carried out by x-ray diffraction and small-angle x-ray scattering. The results obtained shed light on the extent to which the parameters of nanoclusters in npor-C and their internal organization depend on the initial structural anisotropy for a given carbide-forming element (Si) and hexagonal symmetry of the SiC lattice.

1. SAMPLE PREPARATION AND MEASUREMENTS

The npor-C samples were prepared by treating carbide materials with chlorine at temperatures of 700–1000 °C (see Refs. 2–4). The starting materials were compact composites produced from polycrystalline α SiC powder and single-crystal 6*H*-SiC plates cut along the (0001) planes. The reaction rate in the case of 6*H*-SiC was slower by more than two orders of magnitude than that with composites.

X-ray measurements were performed on a two-crystal diffractometer with a perfect Ge crystal serving as monochromator [(111) reflection], which provided an angular divergence of the incident beam of 20″. The dependence of scattered intensity on scattering angle, $I(2\theta)$, was measured in reflection from the sample surface ($\theta/2\theta$ scanning) and in transmission (2θ scans). In the first case one measured the intensity distribution in the scattering plane in the direction of the scattering vector $\mathbf{s}=\mathbf{k}_1-\mathbf{k}_0$, which was normal to the sample surface ($\mathbf{k}_0$ and $\mathbf{k}_1$ are the incident and scattered wave vectors, respectively). In the second case one obtained the distribution of scattered intensity in a plane perpendicular to vector $\mathbf{k}_1$. In small-angle x-ray scattering ($2\theta < 10°$, $\mathbf{k}_1 \perp \mathbf{s}$), this distribution corresponds to a direction **s** parallel to the sample surface. The resolution in the scattering angle 2θ was 0.16°.

Due to the low extinction coefficients of npor-C for Cu $K\alpha$ radiation (1.6–2.2 cm^{-1}), the effective scattering volume in small-angle scattering was assumed to be practically constant throughout the 2θ interval covered, except the domain of very small angles ($2\theta < 0.7°$) in the reflection mode, where the incident beam impinged partially onto the end face of the sample. Measurements performed in the above two modes yielded information on the structural anisotropy of the samples.

2. RESULTS AND DISCUSSION

Figure 1 shows typical diffraction patterns for npor-C ⟨poly-SiC⟩ and npor-C⟨6*H*-SiC⟩ samples (shown in the angular brackets is the type of the starting SiC). The broad diffraction peaks observed with both samples near $2\theta = 26$ and 44° are close in position to the known (0002) and (011) graphite reflections or the (111) reflection of diamond. Hence the structure of npor-C obtained of both poly-SiC and 6*H*-SiC contains fairly large graphite-like fragments (clusters). The cluster thickness in the direction normal to the (0002) planes estimated from the peak halfwidth at 26° in both experiment geometries is 30–60 Å. This means that this

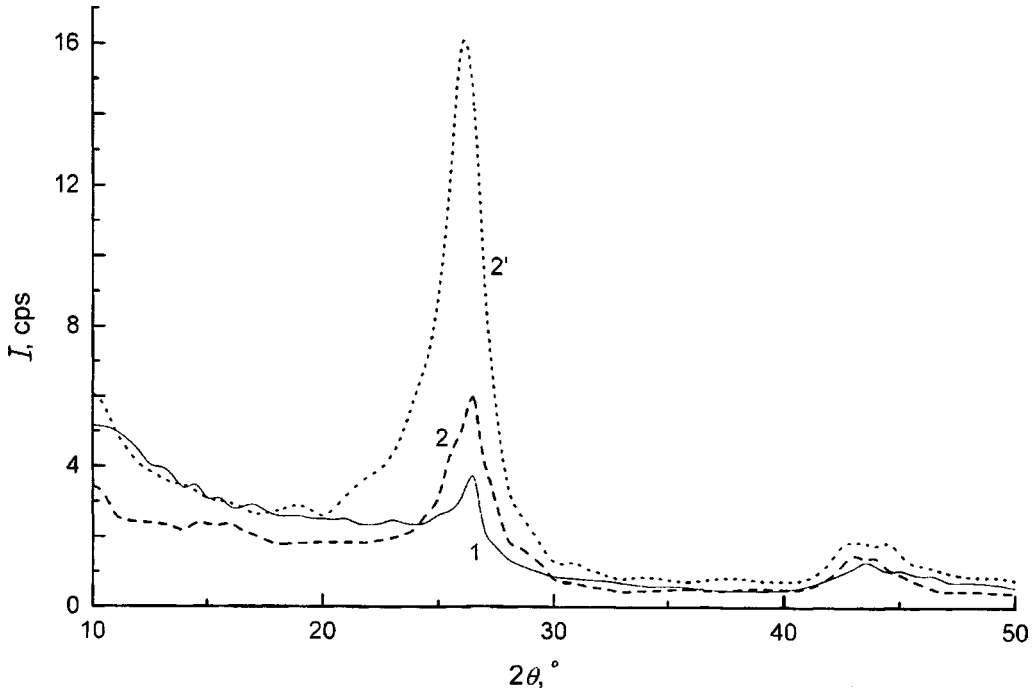

FIG. 1. X-ray diffraction patterns of (*1*) npor-C⟨poly-SiC⟩ and (*2*,*2′*) npor-C⟨6H-SiC⟩ samples obtained in (*1*,*2*) transmission and (*2′*) reflection geometry.

dimension does not depend on the orientation of the graphite-like nanoclusters in the bulk of the sample.

The peak at 26° observed on npor-C⟨6*H*-SiC⟩ samples in reflection is substantially stronger than the one seen in transmission. This means that the (0002) diffracting planes in npor-C⟨6*H*-SiC⟩ are predominantly parallel to the sample surface, i.e. they coincide in direction with the (0001) basal planes of the starting 6*H*-SiC single crystal. Thus the (0002) planes originate actually from the (0001) planes of 6*H*-SiC and mostly retain their orientation when the Si–C bonds are ruptured and layers of Si atoms are removed. Because 6*H*-SiC crystallites in poly-SiC are randomly oriented, the graphite-like nanoclusters in npor-C⟨poly-SiC⟩ samples retain their orientation, and the intensity of the 26° peak does not depend on the experiment geometry.

Figure 2 presents small-angle scattering curves $I(s)$, $s=4\pi\sin(\theta/\lambda)$ for npor-SiC samples of both types measured in transmission and reflection. Within the s interval studied, there is no region where the scattering curves would obey the Porod law $I(s)\propto s^{-4}$ for the asymptotic behavior of $I(s)$ for $s\gg d^{-1}$, where d is the size of identical smooth-surface scatterers[5]. Therefore the $I(s)$ curves were assigned to scattering from an ensemble of particles of the same dimensions. Because the shape of the particles was not known, their size was characterized by the gyration radius (Guinier radius) R_g. For small s ($sR_g\ll 1$)

$$I(s)=I(0)\exp[-(sR_g)^2/3]\,.$$

Considering the small-angle scattering curves $I(s)$ as a sum of a finite number of partial contributions $I_k(sR_{gk})$ of particles with different R_{gk}, one can readily expand these curves in components corresponding to given R_{gk} (see Ref. 6). In this way one can determine the discrete values of R_{gk} and the corresponding mass (volume) fractions of particles m_k. The curves drawn through the $m_k(R_{gk})$ points are approximate distribution functions of the scatterers in size $m(R_g)$.

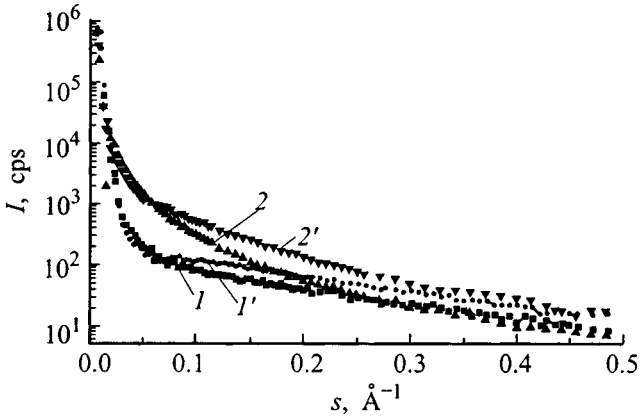

FIG. 2. Small-angle x-ray scattering curves obtained on (*1*,*1′*) npor-C ⟨poly-SiC⟩ and (*2*,*2′*) npor-C⟨6*H*-SiC⟩ samples in (*1*,*2*) transmission and (*1′*,*2′*) reflection.

Figure 3 shows the points $m_k(R_{gk})$ and functions $m(R_g)$ derived by us from small-angle scattering data for npor-C ⟨poly-SiC⟩ and npor-C⟨6*H*-SiC⟩ samples. The $m(R_g)$ functions fall off more or less rapidly with increasing R_g, so that the smallest clusters that can still be observed by small-angle scattering make up the largest mass fraction. For these clusters, $R_{g\min}\equiv 5$ Å, and the linear dimension $d\sim 2R_g\equiv 10$ Å. The fraction of larger clusters and, hence, the average nanocluster gyration radius $R_g^{\rm av}$ and dispersion ΔR_g in npor-C ⟨6*H*-SiC⟩ samples were found to be markedly larger than those for npor-C⟨poly-SiC⟩. The estimates of $R_{g\min}$, $R_g^{\rm av}$, and ΔR_g for both samples made, as in Ref. 4, from the $m(R_g)$ distribution functions, are listed in Table I. It is seen

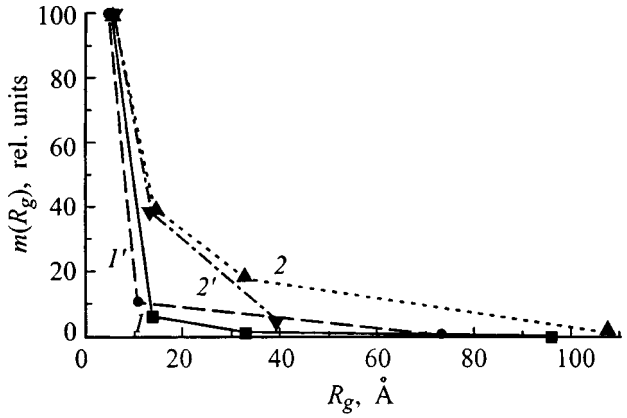

FIG. 3. Nanocluster distribution functions in size in (*1*,*1′*) npor-C⟨poly-SiC⟩ and (*2*,*2′*) npor-C⟨6*H*-SiC⟩ derived from small-angle scattering data in (*1*,*2*) transmission and (*1′*,*2′*) reflection.

that the nanoclusters forming in npor-C⟨6*H*-SiC⟩ are, on the average, approximately twice larger than those in npor-C ⟨poly-SiC⟩, where small clusters are substantially more uniform in size.

The cluster parameters estimated from small-angle scattering data obtained in transmission and reflection differ somewhat. This transverse-longitudinal structural anisotropy is associated most likely with a nonspherical shape and not fully random spatial orientation of the clusters. The relative magnitude of the parameters suggests that oblate nanoclusters in our samples are predominantly oriented parallel to the surface.

The anisotropy in npor-C⟨6*H*-SiC⟩ is much more strongly pronounced than that in npor-C⟨poly-SiC⟩ or other samples prepared of polycrystals.[4] This effect is associated with the strong intrinsic anisotropy of 6*H*-SiC. Small-angle scattering data indicate the presence in npor-C⟨6*H*-SiC⟩ of a noticeable fraction of large clusters, whose dimension in the direction parallel to the surface is 30–120 Å. At the same time x-ray diffraction data show that it is in this direction that the (0002) planes in large graphite-like npor-C⟨6*H*-SiC⟩ clusters formed of the (0001)6*H*-SiC planes are predominantly oriented.

The weak anisotropy of npor-C⟨poly-SiC⟩, which is not seen in x-ray diffraction but manifests itself in small-angle scattering, originates most probably from an oriented motion of the ''averaged-out'' frontline of the carbide chlorination reaction along the normal to the sample surface. It may be conjectured that the conditions of growth of carbon nanoclusters along the reaction frontline and perpendicular to it are different. In this case the nonspherical clusters formed of randomly oriented starting crystallites of macroscopically isotropic poly-SiC will not acquire any orientation in space with equal probability.

To conclude, the high size uniformity of nanoclusters is inherent primarily in npor-C⟨poly-SiC⟩ samples. In this case the chlorine and reaction products penetrate during the preparation of npor-C between crystallites, which favors development of a locally nonflat reaction front and a growth of its rate. In these conditions, it is primarily small nanoclusters, 10–12 Å in size, that form preferably. This result correlates well with the high uniformity of nanopore size[2,3] in npor-C⟨poly-SiC⟩. The longer time it takes to produce npor-C⟨6*H*-SiC⟩ favors formation of graphite-like nanoclusters 30–120 Å in size or larger. The structural anisotropy observed in npor-C is associated primarily with that of the starting material.

TABLE I. Parameters of nanoclusters in npor-C prepared of silicon carbide.

Starting material	Polycrystalline SiC		6H–SiC single crystal	
Experiment geometry	Transmission	Reflection	Transmission	Reflection
$R_{g\,\min}$, Å	4.8	4.3	5.0	5.2
ΔR_g, Å	3.4	3.5	7.6	5.2
R_g^{av}, Å	5.8	5.2	11.5	8.7

Support of the Ministry of Science Project ''Fullerenes and Atomic Clusters'' (Grant 98-059) is gratefully acknowledged.

[1] N. F. Fedorov, G. K. Ivakhnyuk, and D. N. Gavrilov, Zh. Prikl. Khim. **55**, 46 (1981); *Ibid.* **55**, 272 (1981).
[2] S. K. Gordeev and A. V. Vartanova, Zh. Prikl. Khim. **63**, 1178 (1991); *Ibid*. **66**, 1080 (1994); *Ibid*. **66**, 1375 (1994).
[3] S. K. Gordeev, A. V. Vartanova, S. G. Zhukov, I. N. Gran', V. V. Sokolov, T. I. Mazaeva, and R. G. Avarbé, RF Patent No. 2026735.
[4] R. N. Kyutt, É. A. Smorgonskaya, S. K. Gordeev, A. V. Grechinskaya, and A. M. Danishevskiĭ, Fiz. Tverd. Tela (St. Petersburg), in press.
[5] D. I. Svergun and L. A. Feĭgin, *X-Ray and Neutron Small-Angle Scattering* [in Russian] (Nauka, Moscow, 1986).
[6] A. I. Kitaĭgorodskiĭ, *X-Ray Diffractometry of Dispersed Crystalline and Amorphous Solids* [in Russian] (GITTL, Moscow, 1952).

Translated by G. Skrebtsov

Titanium *K*-edge absorption structure in $Ti_{1-x}Nb_xO_2$

O. A. Usov, K. Yu. Pogrebitskiĭ, B. T. Melekh, and Yu. N. Yur'ev

A. F. Ioffe Physicotechnical Institute, Russian Academy of Sciences, 194021 St. Petersburg, Russia

Se Ahn Song

Analytical Engineering Laboratory, Samsung Advanced Institute of Technology, 440-600 Suwon, Republic of Korea

Fiz. Tverd. Tela (St. Petersburg) **41**, 894–896 (May 1999)

The fine structure in the titanium x-ray *K*-edge absorption has been measured in $Ti_{1-x}Nb_xO_2$ mixed dioxides ($x=0-0.1$) with rutile structure in a laboratory-type spectrometer by total electron quantum-yield measurement. The position of the XANES lines is shown to be in good agreement with classical x-ray absorption spectra obtained in transmission. The structure and main features of the XANES spectra, including the effects of impurities and many-electron excitations, are discussed. It is suggested that the intensity of the *B* peak characteristic of the titanium *K* edge depends on the Nb concentration and correlates with the charge state of titanium ions. © *1999 American Institute of Physics.* [S1063-7834(99)03605-9]

X-ray absorption spectroscopy (XAS) is a unique method to probe the composition, local atomic structure, and electronic properties of substances in solid and liquid states.[1] The absorption cross section of a compound excited by x rays reaching a deep atomic level is a jump in ionization, on which a number of resonant peaks characteristic of the region near the absorption edge (XANES) and a series of extended fine-structure (FS) oscillations (EXAFS) are superimposed. The latter are produced from interference between the photoelectron wave excited at the absorbing atom and the wave reflected partially from neighboring atoms. XAS studies of the local atomic structure and of the electronic properties of transition-metal oxides are presently attracting considerable interest, both fundamental and applied, because of a wide range of unusual electrical, magnetic, and optical properties characteristic of these compounds, as well of the considerable progress in synthesis of materials of various compositions and structures. Titanium oxides and related materials are employed efficiently in various areas of industry, including production of pigments, microelectronics and microwave technology, optoelectronics, catalysis, electrochemistry, biochemistry, etc. The titanium dioxide TiO_2 is known to exist in three modifications, namely, rutile, anatase, and brookite,[2] and at high pressures, as columbite, baddeleyite, and, possibly, fluorite.[3] The local atomic structure of oxides in the transition-metal region is made up usually of oxygen octahedra, both regular, as in perovskites, or distorted, as in rutile, which form numerous crystal structures, depending on the composition and octahedron arrangement. This rich variety of structures, which is typical of oxides, is accounted for by a fine balance between the forces associated with ligand charge transfer and narrow $3d$-band and many-electron d–d correlation effects. It is therefore believed that x-ray absorption spectroscopy may turn out to be an informative tool for probing the local atomic structure and electronic properties of these compounds.

1. EXPERIMENT

Crystals of pure and mixed $Ti_{1-x}Nb_xO_2$ titanium oxides ($x=0.0$, 0.03, 0.07) were grown from a melt ($T\sim 2100$ K) of the corresponding OSCh-grade (99.99%) oxides by cold-crucible rf induction melting (5.28 MHz, 60 kV). The ingots obtained by directed crystallization, which was controlled by lowering the crucible from the inductor at a rate less than 15 mm/h, were black, had a diameter of about 80 mm, and weighed about 1.5 kG. After annealing, the ingots were ground to powder, which was subsequently used to prepare samples as usual for x-ray absorption measurements.[4–6]

The fine structure in the x-ray absorption *K* edge was recorded with a laboratory spectrometer of an original design[6] providing measurement of the total electron quantum yield (TEY). The spectrometer consists of two main parts, a monochromator unit and a vacuum chamber, which housed a sample and an electron detector (channel electron multiplier). The x radiation was generated by a sharp-focus (6°) tube with a silver anode. The x-ray tube was rotated together with the entrance slit (0.03 mm) coaxially with the Ge(111) crystal monochromator, which permitted one to scan the total radiation spectrum while leaving the monochromatized beam fixed. With the entrance slit 0.02 mm wide, the resolution at the titanium *K* edge was about 3 eV. A step motor providing θ–2θ rotation permitted scanning with a step of 2.5 eV. The sample maintained in the vacuum chamber at a pressure not over 10^{-6} Torr was irradiated by a monochromatized x-ray beam at an angle of 3° to the surface. The total electron quantum yield was measured by a detector along the normal to the surface with an extraction potential of 100 V.

2. DISCUSSION OF RESULTS

The dependence of the total electron quantum yield on photon energy at the Ti *K* edge in mixed titanium dioxides with rutile structure, $Ti_{1-x}Nb_xO_2$ ($x=0-0.1$), is displayed graphically in Fig. 1, and the assignment and energies of the main peaks, as well as the most essential of the available

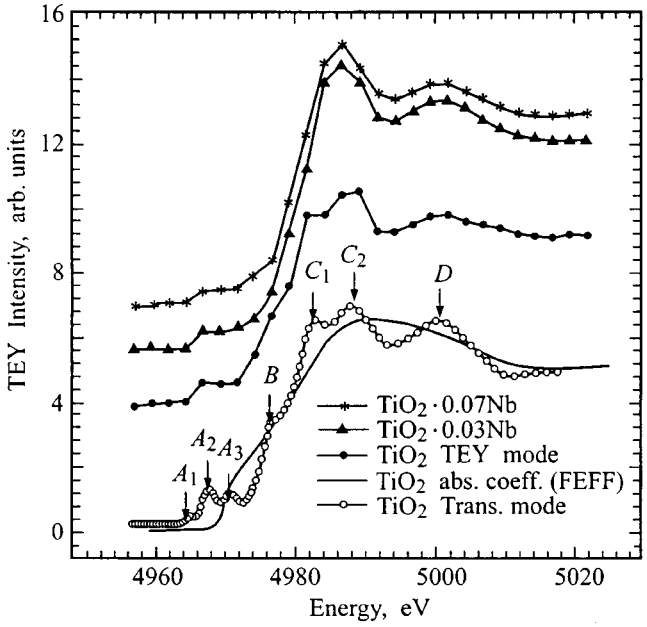

FIG. 1. Titanium K edge structure in $Ti_{1-x}Nb_xO_2$ mixed oxides.

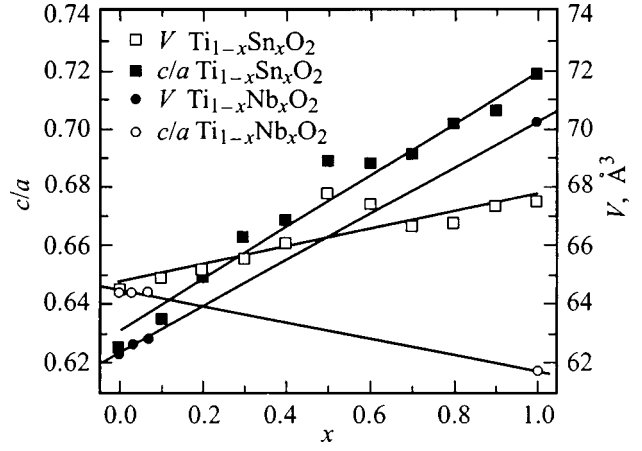

FIG. 2. Dependence of the unit cell volume V_0 and c/a ratio on composition x in $Ti_{1-x}M_xO_2$ mixed oxides (M = Nb, Sn).

published data, are listed in Table I. Shown for comparison are absorption edge data obtained[7] at the PLS synchrotron in Pohang. Figure 1 presents also the results of a preliminary fine-structure simulation made with inclusion of multiple scattering of photoelectrons near titanium atoms (using FEFF-type[8] programs). One observes here only a qualitative agreement with experiment, which can be accounted for by the insufficiently large size of the cluster used in the calculation and the inadequacy of the model concepts chosen. Figure 2 shows the dependence of the unit cell parameter ratio c/a and cell volume $V=a^2c$ on impurity concentration x for the $Ti_{1-x}M_xO_2$ mixed oxides, where M=Nb, Sn.[5] As follows from an analysis of known compounds, in rutile crystals the values of c/a and of parameter u characterizing the oxygen atom positions are confined to a narrow interval: $c/a \sim 0.5-0.7$ and $u \sim 0.30-0.31$. The Ti–O bond lengths between the nearest neighbors (d_1, d_2) and the Ti–O–Ti angle (θ) are determined only by the parameters a, c, and u. Therefore in a tetragonal crystal the oxygen octahedron can theoretically be ideal ($d_1=d_2, 2\theta=\pi/2$) for $c/a=2u=2-\sqrt{2}\sim 0.586$. As seen from Fig. 2, the dependences of c/a on concentration x behave differently for the Nb and Sn impurities, which is associated with different local-distortion patterns of the octahedra in the vicinity of titanium atoms, namely, unlike $Ti_{1-x}Sn_xO_2$, the oxygen tetrahedron in $Ti_{1-x}Nb_xO_2$ mixed oxides approaches the ideal arrangement. The relations presented in Fig. 3 are characteristic of rutile-type structures, where the oxygen position is determined by the independent parameter u. This permits one to use both local XAFS (d_2/d_1) and diffraction ($c/a, u$) experimental data for a refinement of structural parameters, particularly in the cases where one cannot prepare high-quality single crystals required for diffraction measurements.

TABLE I. Position of levels at the titanium K edge for $Ti_{1-x}Nb_xO_2$ rutile-structure mixed oxides.

Substance	Ref.	Level assignment and energy, eV					
		$3d$		$4s/4p$	$4p$	$5p$	(1)
		t_{2g}	e_g		$4t_{1u}$	$5t_{1u}$	(2)
				$3a_{1g}/4t_{1u}$ Ti^{3+}			(3)
	[9]	A_1	A_2	A_3	B	C_1/C_2	D
	[12]	A_1	A_3	B	C_1/C_2	D_1	
TiO_2	(4)	–	0.0		−9.0	15.0/22.5	35.0
	[8]		0.0	3.0	8.8	13.3/15.5	
	[2]	−2.7	0.0	3.2	9.0	15.0/20.6	32.3
	[9]	−3.1	0.0	3.0	8.6	15.6	
	[13]		0.0	2.1	8.4	15.8	
0.07Nb	(4)	–	0.0	–	9.0	20.0	35.0
0.04Nb	[10]	−3.0	0.0	3.0	9.0	18.0/24.0	36.0

Note. The energy of the near-edge peak A_2 (Ref. 9) was measured as 4971.0 eV, whereas Ref. 2 sets it at 4968 eV.

(1)Atomic orbital type;

(2)Coinciding level notation in Refs. 2,8–13;

(3)Discrepancy in notation: a_{1g} in Refs. 9,13 and t_{1u} in Ref. 8;

(4)Spectrum obtained in this work by the total quantum yield (TEY) method.

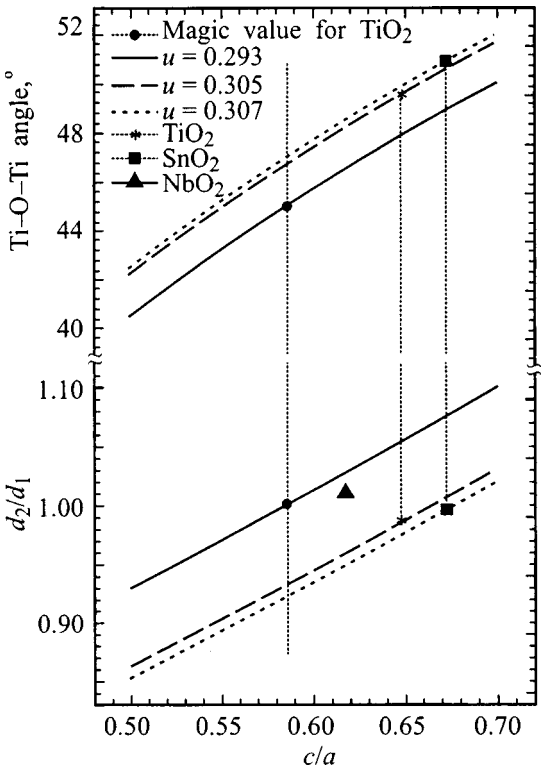

FIG. 3. Dependence of the ratio of local Ti–O interatomic distances and Ti–O–Ti angles on c/a for various values of parameter u characteristic of the rutile structure.

The interpretation of the near-edge FS (XANES) given in Table I includes the formal assignment[9–14] and a description based on the electronic-level symmetry of TiO_6 clusters. The level energies are reckoned from the energy of the near-edge level A_2, whose most reliable value is 4971.0 eV. As seen from Table I, the largest controversy is observed in the assignment of peak *B*, which is characteristic of the titanium *K* edge and is seen in many compounds. We have found that the *B* peak intensity depends on the Nb dopant concentration, and this gives one grounds to assume that the peak is due to the charge state of titanium ions, which is determined by nonstoichiometry or defects introduced during the doping.

Thus we have measured the fine structure in the titanium x-ray absorption *K* edge in $Ti_{1-x}Nb_xO_2$ mixed dioxides. The local atomic structure in the vicinity of titanium atoms derived from an FS analysis is in satisfactory agreement with x-ray diffraction (XRD) data. The correlations between the structural parameters determined from XRD and EXAFS measurements and possibilities of their combined use are discussed. The *B* peak intensity near the titanium *K* edge in mixed oxides is shown to depend on the concentration of impurity atoms.

Support of Samsung Electronic Co. Ltd (Suwon, Korea) (Contract No. SEC/PTI-95-01) is gratefully acknowledged.

[1] *X-Ray Absorption: Principles, Applications, Techniques of EXAFS, SEXAFS, and XANES*, edited by D. C. Kroningsberger and R. Prins (Wiley, New York, 1988).
[2] B. Poumellec, J. F. Marucco, and B. Touzelin, Phys. Rev. B **35**, 2284 (1987).
[3] J. K. Dewhurst and J. E. Lowther, Phys. Rev. B **54**, R3673 (1996).
[4] A. Fahmi, C. Minot, B. Silvi, and M. Causá, Phys. Rev. B **47**, 11717 (1993).
[5] T. Hirata, K. Ishioka, M. Kitajima, and H. Doi, Phys. Rev. B **53**, 8442 (1996).
[6] S. G. Konnikov and K. Ju. Pogrebitskii, Surf. Sci. **228**, 532 (1990).
[7] W. B. Kim, S. H. Lee, and J. S. Lee, in *Proceedings of the 10th Synchrotron Radiation User Workshop* (Pohang Accelerator Laboratory, Korea, 1998), p. 33.
[8] S. I. Zabinsky, J. T. Rehr, A. Ankudinov, R. C. Albers, and M. J. Eller, Phys. Rev. B **52**, 2995 (1995).
[9] K. Tsutsumi, O. Aita, and K. Ichikawa, Phys. Rev. B **15**, 4638 (1977).
[10] L. A. Grunes, Phys. Rev. B **27**, 2111 (1983).
[11] B. Poumellec, F. Lagnel, J. F. Marucco, and B. Touzelin, Phys. Status Solidi B **133**, 371 (1986).
[12] S. A. Chambers, Y. Gao, Y. J. Kim, M. A. Henderson, S. Thevuthasan, S. Wen, and K. L. Merkle, Surf. Sci. **365**, 625 (1996).
[13] R. Brydson, H. Sauer, W. Engel, J. M. Thomson, E. Zeitler, N. Kosugi, and H. Kuroda, J. Phys.: Condens. Matter **1**, 797 (1989).
[14] D. W. Fisher, Phys. Rev. B **5**, 4219 (1972).

Translated by G. Skrebtsov

Electronic and electron-phonon phenomena in low-dimensional BEDT–TTF-based organic conductors and superconductors

R. M. Vlasova, O. O. Drozdova, and V. N. Semkin

A. F. Ioffe Physicotechnical Institute, Russian Academy of Sciences, 194021 St. Petersburg, Russia

N. D. Kushch, E. I. Zhilyaeva, R. N. Lyubovskaya, and É. B. Yagubskiĭ

Institute of Chemical Physics, Russian Academy of Sciences, 142232 Chernogolovka, Moscow District, Russia

Fiz. Tverd. Tela (St. Petersburg) **41**, 897–899 (May 1999)

Two related groups of *k*-phase ion-radical salts (BEDT–TTF) with different electrical properties, namely, superconductors with different transition temperatures and conductors, which transfer to insulating state with decreasing temperature, have been studied by micro-optic spectroscopy. Polarized reflectance spectra of microcrystals have been measured for the three principal crystallographic directions within the 700–40000 cm^{-1} region, and the corresponding spectra of the optical functions obtained. The anisotropy of the electronic system in the crystals has been established as two-dimensional. The spectra obtained were quantitatively analyzed, the key parameters of the electronic structure and the vibronic coupling constants determined. It is concluded that the conductors have smaller vibronic coupling constants, more narrow allowed electronic bands, and stronger electron-electron interaction compared to those of the superconductors, and that vibronic coupling is the necessary condition for the onset of superconductivity in the superconductors studied. © *1999 American Institute of Physics.* [S1063-7834(99)03705-3]

A purposeful search for high-conductivity organic materials for use in molecular electronics and for organic superconductors has recently led to synthesis of two related groups of new ion-radical salts based on bis(ethylenedithio)-tetrathiafulvalene (BEDT–TTF).[1,2] While the compounds of both groups have a similar crystal structure consisting of layers of $(BEDT–TTF)_2^+$ orthogonal dimers (*k* phase) separated by layers of the corresponding polymer anions, they differ marked by in electrical properties.

Salts of the first group are superconductors differing in their transition temperature to the superconducting state, T_c, including a few with record-high ones for organic compounds, namely, $k(BEDT–TTF)_2Cu[N(CN)_2]X$, with X= Cl ($T_c=12.3$ K), Br ($T_c=11.6$ K), and $Cl_{0.5}Br_{0.5}$ ($T_c=11.3$ K). Salts belonging to the second group are conductors which become insulators with decreasing temperature: $k(BEDT–TTF)_2[Hg(SCN)_{3-n}X_n]$ (X=Cl, Br; $n=1,2$).

This paper briefly reviews our recent microscopic studies[3–10] of the optical properties of single-crystal compounds belonging to the two above-mentioned groups. The main objective of this work was to investigate the electronic energy structure of the crystals and the electron-phonon and electron-electron interactions and their significance in formation of the ground state in the crystals, and to establish the main differences in the key electronic-system parameters and vibronic coupling constants between superconductors with different transition temperatures, as well as between conducting and superconducting crystals.

1. EXPERIMENT

Crystals of both groups belong to the rhombic or monoclinic symmetries and are thin black rhombic platelets with metallic luster measuring $0.5\times0.5\times0.05$ mm. The conducting layers of BEDT–TTF molecules in the crystals are arranged parallel to the largest faces, (010) and (100), for the first and second group, respectively. We measured room-temperature polarized reflectance spectra $R(\omega)$ within the 700–40000 cm^{-1} region under normal incidence of light on different crystal faces and in polarizations where the light-wave electric vector **E** is parallel and perpendicular to the BEDT–TTF layers. The corresponding optical functions of the crystal were obtained. The experimental technique used and some specific features in the treatment of spectra are described elsewhere.[6,8]

2. EXPERIMENTAL RESULTS

Figure 1 presents reflectance spectra $R(\omega)$ of the superconductor $k(BEDT–TTF)_2Cu[N(CN)_2]X$ ($X=Cl_{0.5}Br_{0.5}$) obtained from the largest, (010), and the narrow, (101), side crystal faces in the polarizations for which **E** vector is parallel ($\mathbf{E}\|a$, $\mathbf{E}\|c$) and perpendicular ($\mathbf{E}\|b$) to the BEDT–TTF conducting layers. Similar spectra were also obtained by us for the crystals with X = Br and Cl,[8] as well as presented earlier[11,12] for the $\mathbf{E}\|a$ and $\mathbf{E}\|c$ cases. As seen from Fig. 1, the crystals exhibit in the $\mathbf{E}\|a$ and $\mathbf{E}\|c$ polarizations intense electronic reflectance with a strong vibrational structure in the 700–1500 cm^{-1} region, a clearly pronounced plasma edge near 4500 cm^{-1}, and the associated deep minimum at 5500 cm^{-1}; one sees also that the anisotropy in the BEDT–

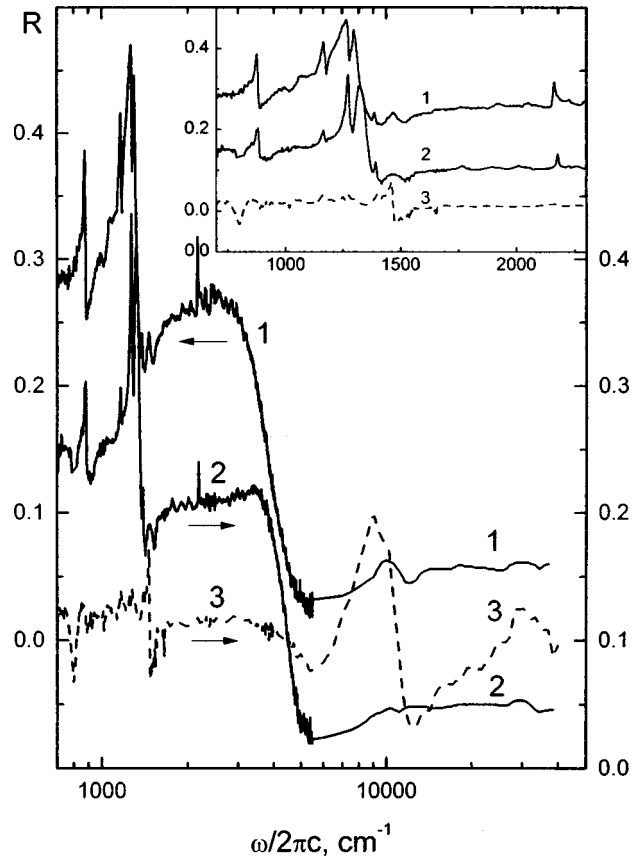

FIG. 1. Reflectance spectra of the k(BEDT–TTF)$_2$ Cu[N(CN)$_2$]Cl$_{0.5}$Br$_{0.5}$ superconductor for (*1*) $\mathbf{E}\|a$, (*2*) $\mathbf{E}\|c$, and (*3*) $\mathbf{E}\|b$.

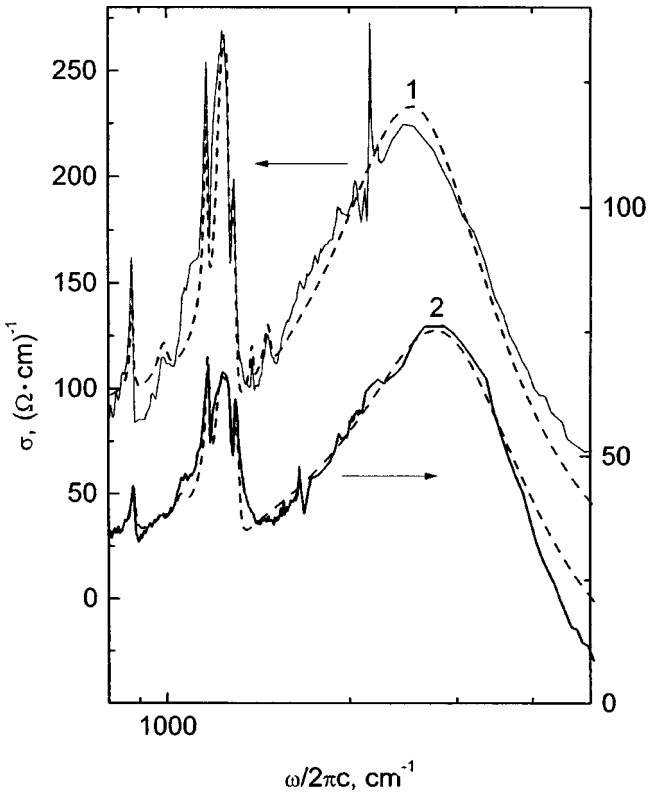

FIG. 2. Optical conductivity spectra of (*1*) the k(BEDT–TTF)$_2$ Cu[N(CN)$_2$]Cl$_{0.5}$Br$_{0.5}$ superconductor and (*2*) k(BEDT–TTF)$_2$ [Hg(SCN)Cl$_2$] conductor.

TTF conducting-layer plane is not large. By contrast, in the $\mathbf{E}\|b$ polarization, where $\mathbf{E}$ is perpendicular to the BEDT–TTF layers, the IR reflectance (700–5500 cm^{-1}) is as low as it would be in an insulator, and is practically frequency independent. The observed optical anisotropy indicates a quasi-two-dimensional nature of the conducting electronic system in the crystals.

In the 9000–40000 cm^{-1} region, one observes broad bands, which are most clearly seen for $\mathbf{E}\|b$ and relate to electronic intramolecular transitions in the (BEDT–TTF)$_2^+$ cations polarized along the long axis of the BEDT–TTF molecule.

Measurements showed the spectra of the conductors to be qualitatively similar to those of the superconductors.[7,9,10] The difference is that the reflectance spectrum of the quasi-two-dimensional electronic system, including the vibrational structure, is weaker than that of the superconductors, and the plasma minimum lies at a lower frequency.

The optical conductivity spectra $\sigma(\omega)$ of the k(BEDT–TTF)$_2$Cu[N(CN)$_2$]Cl$_{0.5}$Br$_{0.5}$ superconductor ($\mathbf{E}\|a$) and of the k(BEDT–TTF)$_2$ [Hg(SCN)Cl$_2$] conductor ($\mathbf{E}\|b$) are displayed in Fig. 2 for the 700–5500 cm^{-1} region. These spectra are qualitatively typical of other compounds of both groups as well. As expected, the spectra deviate substantially from the simple Drude relation $\sigma(\omega)$ characteristic of metals, namely, one observes in them a broad maximum near 2300 and 2600 cm^{-1}, respectively, with a strong vibrational structure lying at its low-frequency edge. As evident from Fig. 2, the optical conductivity of the superconductor, viz. the amplitude of the maximum and the intensity of the vibrational structure, is noticeably higher than that of the conductor. A similar broad maximum in the $\sigma(\omega)$ spectra observed for $\mathbf{E}\|c$ lies in both crystals at a higher frequency (3000 cm^{-1}).

3. DISCUSSION OF RESULTS

The nature of the broad maximum in the $\sigma(\omega)$ spectra of the superconductors apparently originates from interband electronic transitions superposed on intraband carrier transitions.[11,12] We believe that the broad maximum in the spectra of the conductors is due to electronic transitions between neighboring molecules in two adjacent (BEDT–TTF)$_2^+$ orthogonal dimers.[9] The strong vibrational structure at the low-frequency edge of the maxima derives from the interaction of the above electronic transitions with the fully symmetric a_g intramolecular vibrations in BEDT–TTF. The assignment of this vibronic structure to the a_g intramolecular mode is discussed by us in more detail in Refs. 4 and 6–8.

Our quantitative analysis of the above spectra was based on the theory[13] of optical properties of low-dimensional organic conductors. Fitting the theoretical to experimental $\sigma(\omega)$ spectra (Fig. 2) permitted determination of the key parameters characterizing the quasi-two-dimensional system (ω_p, Δ, V/Δ, Γ_e)[1)] and the vibronic coupling constants (individual, λ_α, and net, $\lambda=\Sigma\lambda_\alpha$). The values of the parameters thus obtained are given in Refs. 4 and 6–8.

TABLE I. T_c and λ of the organic superconductors studied.

Compound	T_c, K	λ	T_c (K)/4.3 K (exp.)	T_c (K)/4.3 K (calc.)
$(ET)_4Hg_{2.89}Br_8$	4.3	0.20	1	1
$k(ET)_2Cu(NCS)_2$	10.4	0.25	2.5	2.7
$k(ET)_2Cu[N(CN)_2]Cl_{0.5}Br_{0.5}$	11.3	0.26	2.7	3.2
$k(ET)_2Cu[N(CN)_2]Br$	11.6	0.26	2.7	3.2
$k(ET)_2Cu[N(CN)_2]Cl$	12.8	0.26	2.7	3.2

Table I presents the values of λ for the studied organic superconductors; in the order in which they are arranged, T_c increases in the ratio 1:2.5:2.7. We readily see that superconductors with a higher T_c exhibit a larger vibronic coupling constant λ. It was found that the T_c ratio calculated by us from the well-known BCS relation $k_BT_c \approx 1.13h\omega_D \exp(-1/\lambda)$ using the values of λ from Table I is close to the above experimental ratio. In our opinion, this indicates that vibronic coupling plays a substantial role in the onset of superconductivity in the compounds studied.

As already mentioned, the conductors exhibit a considerably lower optical conductivity originating from electronic transitions in the quasi-two-dimensional electronic system and the related vibronic structure, than is the case with the superconductors. To assess quantitatively this difference, we determined the plasma frequency $\omega_p^2 = 8\int\sigma(\omega)d\omega$ characterizing the oscillator strength of this transition (with the integration performed from zero to 6000 cm^{-1}). It was found that for the k(BEDT–TTF)$_2$ [$Hg(SCN)Cl_2$] and k(BEDT–TTF)$_2$ [$Hg(SCN)_2Br$] conductors, $\omega_p = 3270$ and 4240 cm^{-1} ($\mathbf{E}\|b$), respectively. For the superconductors the minimum value $\omega_p = 5600$ cm^{-1} [for $k(BEDT–TTF)_2Cu[N(CN)_2]Cl_{0.5}Br_{0.5}$], and the maximum value $\omega_p = 6800$ cm^{-1} [for $k(BEDT–TTF)_2Cu[N(CN)_2]Br$]. Evaluation of the effective electronic mass m^* using the relation $\omega_p^2 = 4\pi Ne^2/m^*$ (where N is the carrier concentration equal to the dimer concentration, $N_d = 1.1\times10^{21}$ cm^{-3}) yielded $(m^*/m) = 8.4$ for k(BEDT–TTF)$_2$ [$Hg(SCN)Cl_2$] and $(m^*/m) = 2.6$ for $k(BEDT–TTF)_2Cu[N(CN)_2]Br$. The large effective mass obtained for the conductors is apparently not related to formation of molecular polarons, because the vibronic coupling constant found by us for the conductors, $\lambda = 0.18$,[7] is smaller than that for the superconductors [$\lambda = 0.26$ (Refs. 6 and 8)]. This gives us grounds to suggest that the large m^* implies a substantial part played by electron-electron interactions in the conductors studied by us.

Support of the Russian Fundamental Research Foundation (Grants 98-02-18303, 97-03-33686a, and 97-03-33581) is gratefully acknowledged.

[1)] ω_p is the plasma frequency, Δ and V are the band gaps with and without inclusion of vibronic coupling, and Γ_e is the electronic damping parameter.

[1] J. M. Williams, J. R. Ferraro, R. J. Thorn, K. D. Carlson, U. Geiser, H. H. Wang, A. M. Kini, and M.-H. Whangbo, *Organic Superconductors (Including Fullerenes): Synthesis, Structure, Properties, and Theory* (Prentice Hall, Englewood Cliffs, 1992).
[2] M. Z. Aldoshina, R. N. Lyubovskaya, S. V. Konovalikhin, O. A. Dyachenko, G. V. Shilov, M. K. Makova, and R. B. Lyubovskii, Synth. Met. **55–57**, 1905 (1993).
[3] R. M. Vlasova, R. N. Lyubovskaya, E. I. Zhilyaeva, S. Ya. Priev, and V. N. Semkin, Fiz. Tverd. Tela (Leningrad) **32**, 3024 (1990) [Sov. Phys. Solid State **32**, 1755 (1990)].
[4] R. M. Vlasova, S. Ya. Priev, V. N. Semkin, R. N. Lyubovskaya, E. I. Zhilyaeva, E. B. Yagubskii, and V. M. Yartsev, Synth. Met. **48**, 129 (1992).
[5] R. M. Vlasova, O. O. Drozdova, V. N. Semkin, N. D. Kushch, and É. B. Yagubskiĭ, Fiz. Tverd. Tela (St. Petersburg) **35**, 795 (1993) [Phys. Solid State **35**, 408 (1993)].
[6] O. O. Drozdova, V. N. Semkin, R. M. Vlasova, N. D. Kushch, and E. B. Yagubskii, Synth. Met. **64**, 17 (1994).
[7] R. M. Vlasova, O. O. Drozdova, R. N. Lyubovskaya, and V. N. Semkin, Fiz. Tverd. Tela (St. Petersburg) **37**, 703 (1995) [Phys. Solid State **37**, 382 (1995)].
[8] R. M. Vlasova, O. O. Drozdova, V. N. Semkin, N. D. Kushch, and É. B. Yagubskiĭ, Fiz. Tverd. Tela (St. Petersburg) **38**, 869 (1996) [Phys. Solid State **38**, 481 (1996)].
[9] V. M. Yartsev, O. O. Drozdova, V. N. Semkin, and R. M. Vlasova, J. Phys. I France **6**, 1673 (1996).
[10] R. M. Vlasova, N. V. Drichko, O. O. Drozdova, and R. N. Lyubovskaya, Fiz. Tverd. Tela (St. Petersburg) **39**, 1313 (1997) [Phys. Solid State **39**, 1165 (1997)].
[11] J. E. Eldridge, K. Kornelsen, H. H. Wang, J. M. Williams, A. V. Strieby Crouch, and D. M. Watkins, Solid State Commun. **79**, 583 (1991).
[12] K. Kornelsen, J. E. Eldridge, H. H. Wang, H. A. Charlier, and J. M. Williams, Solid State Commun. **81**, 343 (1992).
[13] M. J. Rice, Phys. Rev. Lett. **37**, 36 (1976).

Translated by G. Skrebtsov

Electronic excitations owing to plastic deformation of ionic crystals

V. A. Zakrevskiĭ*) and A. V. Shul'diner

A. F. Ioffe Physicotechnical Institute, Russian Academy of Sciences, 194021 St. Petersburg, Russia
Fiz. Tverd. Tela (St. Petersburg) **41**, 900–902 (May 1999)

Electron emission and luminescence accompanying plastic deformation of alkali halide crystals are studied. It is shown that the intersection of dislocations can cause electronic excitation. Deformation electron emission and luminescence are produced by relaxation of these excitations.
 [S1063-7834(99)03805-8]

In studies of the effect of mechanical stresses on solids, primary attention is focussed on the reaction of the lattice to loading, i.e., to the change in the mutual position of the atoms, structural defect formation, and disruptions of continuity (crack formation). Less attention has been paid to evaluating the response of the electronic subsystem, so that, until recently, it was unclear whether electronic transitions can be induced by mechanical loads. In the meantime, it is obvious that lattice distortions can create conditions for the realization of electronic transitions that are unrealizable in unstressed materials. Since the properties of solids are determined by both subsystems, the reaction of the electronic subsystem to loading must be taken into account in studies of deformation and fracture processes. In fact, energy can be stored in the electronic subsystem in the form of electronic excitations, as well as in the elastically deformed lattice. Deformation and fracture processes can be accelerated by the release of electronic excitation energy.

Electronic relaxation is accompanied by the emission of photons and electrons. Before the present experiments, it was known that when large cracks develop, light and electron emission are observed.[1–3] However, these observations were made in air or in a relatively low vacuum and some of the data indicated a connection between the detected radiation and electrical discharges initiated by polarization of crystals under loading.[4] The contribution of plastic deformation, which always accompanies fracture, was also undetermined. Thus, we faced the problem of conducting experiments under conditions which exclude discharge formation and make it possible to evaluate the role of plastic deformation. These conditions correspond to plastic deformation of crystals at a constant rate in ultrahigh vacuum. The choice of alkali halide crystals for this investigation allowed us to evaluate the interrelation of deformation processes and emission phenomena in a well-founded manner, since the evolution of dislocation structures in these crystals is well known.

We examined nominally pure single crystals of LiF and NaF. The samples were heated in vacuum at 550 K for 6 h and then compressed at a constant rate along the [001] direction. The deformation rate $\dot{\varepsilon}$ could be varied from 10^{-5} to $10^{-1}\,s^{-1}$, and the sample temperature from 200 to 700 K. The residual gas pressure was 10^{-8} Pa. The electron emission and luminescence were detected by a secondary electron multiplier (VÉU-6) and a photomultiplier (FÉU-106), respectively. Photon counting detection was used. Two photomulitpliers were used to measure the luminescence spectrum, one to detect the integrated emission and the other, located at the output slit of a DMR-4 monochromator, to detect emission at a definite wavelength.

Figure 1 shows typical measurements of the deformation electron emission (DEE) and deformation luminescence (DL) obtained from an LiF sample deformed at a rate of $\dot{\varepsilon} = 2\times10^{-3}\,s^{-1}$ at room temperature. The figure shows plots of the deformation electron emission (I_{DEE}) and deformation luminosity (I_{DL}) intensities, and of the load F on the sample, as functions of the degree of deformation, ε. As a rule, the DEE and DL appear simultaneously after completion of the easy slip stage, when the deformation has reached 1–2%. Usually the intensities of DEE and DL remain roughly constant after a short rise time. Similar results were obtained for NaF crystal samples.

Plastic deformation of alkali halide crystals is, therefore, accompanied by electron emission and luminescence. It should be noted that we have used here crystals that were not subjected to any exciting interactions prior to deformation.

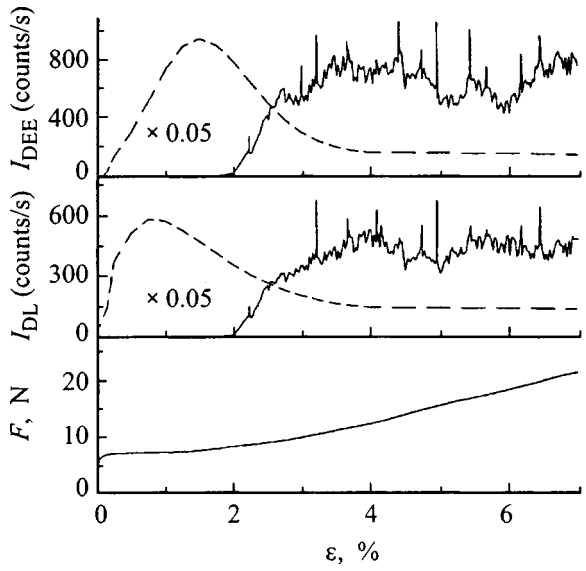

FIG. 1. The intensity of deformation electron emission, I_{DEE}, the intensity of deformation luminosity, I_{DL}, and the load at the sample, F, as functions of the relative strain ε for a LiF crystal. The dashed curves show I_{DEE} and I_{DL} for samples with a dislocation forest.

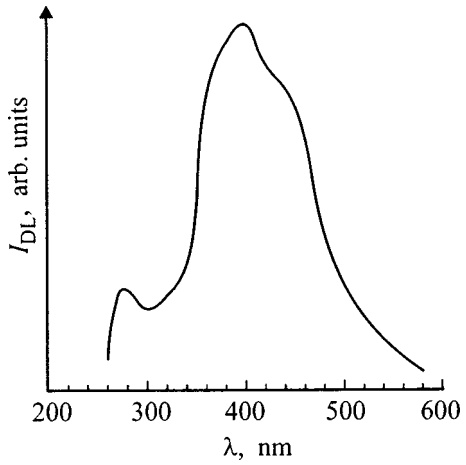

FIG. 2. Deformation luminescence spectrum of an LiF crystal.

This suggests a radical difference between the observed phenomena (DEE and DL) and the luminescence of the deformed, colored (irradiated beforehand) crystals studied by a number of others.[5] The luminescence of irradiated crystals is caused by the breakup of radiation-induced color centers stimulated by deformation[6] and for this reason, it is best to refer to it as deformation-stimulated luminescence, rather than DL.

The data shown in Fig. 1 suggest that DEE and DL are associated with the intersection of dislocations. In fact, in LiF the intersection of dislocations begins before completion of the easy slip stage,[7] causing deformation hardening of the crystal, and DEE and DL appear at this time. A close interrelation among intersection of dislocations and DEE and DL was confirmed in experiments with LiF crystals that have a dislocation forest and an isolated system of slip planes prepared by a method proposed by Smirnov.[7] Deformation of crystals with a single slip system, in which dislocations do not intersect, was not accompanied by emission phenomena. Deformation of crystals with an oblique deformation forest, on the other hand, leads to intense DEE and DL (dashed curves in Fig. 1). They showed up right after the yield point was passed, i.e., when the moving dislocations began to intersect the forest dislocations.

It has been shown that the intensities of DEE and DL in LiF crystals vary with temperature and strain rate. An analysis of the temperature dependences of the emission intensities showed that DEE and DL are thermally stimulated processes with activation energies of about 0.3 eV.[4]

Observation of electron emission and luminescence indicates that electronic excitation (electron and hole color centers) occurs in deformed crystals. Data on the nature of these centers were obtained by studying the DL spectrum, as well as photostimulated electron emission and thermally stimulated electron emission from deformed crystals.

A DL spectrum was obtained for LiF at room temperature. It is shown in Fig. 2 without correction for the spectral sensitivity of the photomultiplier. The spectrum is similar in structure to the x-ray luminescence spectrum of LiF[8] and contains two bands with $\lambda_{max1} \approx 280$ nm and $\lambda_{max2} \approx 400$ nm. According to Ref. 8, the short wavelength band is caused by recombination of F centers with V_K- (or V_F-) centers (α centers) that are mobile at room temperature. The long wavelength band is associated with the presence of impurities in the crystal and, most likely, arises during recombination of electronic centers containing an Mg ion with V_K- centers.[4]

A selective photoeffect was observed in deformed NaF crystals owing to the development of F centers during loading of the samples. In addition, thermally stimulated electron emission was observed in LiF and NaF as a result of the thermal destruction of electronic color centers produced by plastic deformation.[9]

These experimental data show that, during plastic deformation of alkali halide crystals, color centers develop which are similar to those formed by bombardment with ionizing radiation. On the other hand, these data show that DEE and DL cannot develop because of microcracks which, according to some authors,[10] are formed in these crystals even with small deformations. In fact, DEE and DL set in at the end of the easy slip stage in LiF, when crack formation is improbable. As deformation and load increase during compression, the rate of crack formation should rise, but the intensity of DEE and DL remain essentially unchanged. Lowering the temperature and increasing the deformation rate also cause the probability of crack formation to rise, but here the number of photons emitted over a time corresponding to an increase in the strain by 1% is less.[4] The absence of a relationship between crack formation and the emission phenomena is also confirmed by an analysis of the pulse height distribution at the photomultiplier output during detection of DEE.[4]

In order to establish the mechanism for this phenomenon it was important to establish precisely what kind of intersections lead to the production of color centers. It is known that crystals with an NaCl-type lattice have six equivalent systems of slip planes which intersect at angles of 90° (orthogonal) or 60° (oblique). It has been shown[4] that DEE and DL result only from the intersection of oblique dislocations.

It is clear from general considerations that electronic transitions leading to the appearance of color centers can occur as the result of the strong local distortions of the lattice accompanying the intersection of dislocations. The electronic excitation energy in alkali halide crystals is[11] $\Delta = (\alpha e^2/c) + E_A - E_I$, where α is the Madelung coefficient, e is the electronic charge, $2c$ is the lattice constant, E_A is the electron affinity of the haloid atom, and E_I is the ionization energy of the metal atom. For sufficiently strong distortions of the lattice, α can decrease for an isolated anion-cation pair to a value that satisfies the condition for overlap of the ground and excited states of the quasimolecule ($\Delta \approx 0$). As a result, nonadiabatic electronic transitions between these levels, accompanied by the creation of electron-hole pairs, become possible.[12]

Of all the types of intersections of dislocations, the ones that cause the strongest distortion of NaCl-type lattices are thermally activated intersections of oblique dislocations.[12] It might be thought that DEE and DL are associated with intersections of this type. It is important, however, to note that intersection of oblique dislocations in LiF occurs mainly through the athermal Orowan mechanism.[7] The fraction of thermally activated intersections is small and increases expo-

nentially with temperature, like the intensity of DEE and DL. The activation energy for intersection of oblique dislocations in LiF has been estimated to be 0.3 eV,[4] the same as the activation energy for DEE and DL. These data support our hypothesis about an interrelation of DEE and DL precisely with thermally activated intersections of oblique dislocations. The dependence of the emission intensity on the strain rate can be explained in this case by the fact that, when $\dot{\varepsilon}$ is increased, the interaction time of the intersecting dislocations decreases and, therefore, so does the fraction of thermally activated intersections. There is a corresponding drop in the number of emitted photons and electrons.

The data obtained here yield the following conclusions. For intersections of dislocations of the type noted above, which are accompanied by a strong reorganization of the atomic structure, conditions are created such that nonadiabatic electronic transitions can take place (with a probability of [12] $\sim 10^{-2}$). Excited electrons are captured by anion vacancies which develop during deformation to form electron color centers. The resulting hole V_K- and V_F- centers migrate over the crystal and recombine with immobile electron centers. This results in DEE and DL, with DEE being a consequence of an intercenter three-body Auger process. Finally, it should be noted that radiationless recombination is accompanied by local heating of the lattice. This may cause the deformation and fracture processes to be accelerated significantly, since an energy of several eV has been released in a volume corresponding to a single unit cell.

*)E-mail: V.Zakrevsky@pop.ioffe.rssi.ru

[1] N. A. Krotova and V. V. Karasev, Dokl. Akad. Nauk SSSR **92**, 607 (1953).
[2] L. M. Belyaev and Yu. N. Martyshev, Phys. Status Solidi **34**, 57 (1969).
[3] J. Wollbrandt, E. Linke, and K. Meyer, Phys. Stat. Sol. **27**, K53 (1975).
[4] V. A. Zakrevskii and A. V. Shuldiner, Philos. Mag. B **71**, 127 (1995).
[5] Molotskii and S. Z. Shmurak, Phys. Lett. A **166**, 286 (1992).
[6] A. V. Shuldiner and V. A. Zakrevskii, Radiat. Protection Dosimetry **65**, 113 (1996).
[7] V. I. Smirnov, *Dislocation Structure and Hardening of Crystals* [in Russian] (Nauka, Leningrad, 1981).
[8] A. Tomita, N. Hirai, and K. Trutsumi, Jpn. J. Appl. Phys. **15**, 1899 (1976).
[9] V. A. Zakrevskiĭ and A. V. Shul'diner, Fiz. Tverd. Tela **27**, 3042 (1985) [Sov. Phys. Solid State **27**, 1826 (1985)].
[10] R. Albrecht, V. Schmidt, and V. I. Betekhtin, Phys. Status Solidi **39**, 621 (1977).
[11] R. Knox, *Theory of Excitons* [Russian translation] (Nauka, Moscow, 1966).
[12] A. A. Kusov, M. I. Klinger, and V. A. Zakrevskiĭ, Fiz. Tverd. Tela **32**, 1694 (1990) [Sov. Phys. Solid State **32**, 987 (1990)].

Translated by D. H. McNeill

Orthorhombic symmetry of valence-band states in CdTe/$Cd_{1-x}Mn_xTe$ quantum wells

I. G. Aksyanov, A. V. Kudinov, Yu. G. Kusraev, and B. P. Zakharchenya

A. F. Ioffe Physicotechnical Institute, Russian Academy of Sciences, 194021 St. Petersburg, Russia

T. Wojtowicz, G. Karczewski, and J. Kossut

Institute of Physics, Polish Academy of Sciences, 02-668 Warsaw, Poland
Fiz. Tverd. Tela (St. Petersburg) **41**, 903–906 (May 1999)

A study is reported of the anisotropy in magnetic-field-induced linear polarization in (001) CdTe/$Cd_{1-x}Mn_xTe$ quantum wells. The observed limiting anisotropy is shown to be due to the low C_{2v} symmetry of the quantum well. The relations obtained for the C_{2v} point group are in a good agreement with experiment. Considered on the microscopic scale, the effect is associated with the heavy-hole *g*-factor anisotropy in the well plane. © *1999 American Institute of Physics.* [S1063-7834(99)03905-2]

The point symmetry of quantum wells and superlattices grown from zinc-blende compounds along the [001] direction is lowered from T_d to D_{2d}. In these conditions, the strong spin-orbit coupling in the valence band characteristic of these compounds results in a strong anisotropy in the hole-subband spin structure. This anisotropy manifests itself in an experiment primarily in the appreciable difference between the Zeeman splittings of excitonic (hole) states in a magnetic field directed parallel and perpendicular to the heterostructure growth axis.[1,2] The heavy-hole *g*-factor anisotropy caused by the symmetry lowering of the (001)GaAs/AlGaAs structure from T_d to D_{2d} was studied also by spin-flip scattering spectroscopy,[3] where the transverse component of the *g* factor was estimated as $g_\perp < 10^{-2}$. In semimagnetic semiconductors, the strong anisotropy of the hole spin structure ($g_\perp \ll g_{zz}$) produces interesting dynamic effects,[4–7] which originate from magnetic-ion spin precession in the anisotropic exchange field of the holes[8]. At the same time it is the smallness of the transverse component of the hole *g* factor that makes it extremely sensitive to various violations of the D_{2d} symmetry of an ideal quantum well (QW).

This communication reports on an experimental and theoretical investigation of the lateral anisotropy in the properties of excitons in CdTe/$Cd_{1-x}Mn_xTe$ quantum wells, which becomes evident in the angular dependences of the magnetic-field-induced linear polarization of exciton emission. Experimental data on the angular dependences of the linear polarization suggest that the symmetry of the QWs under study is lowered from D_{2d} to C_{2v}, which makes the (110) and $(1\bar{1}0)$ axes inequivalent. It turns out that the transverse *g* factor, which has a sizable magnitude, is itself essentially anisotropic in the well plane, i.e., $g_{xx} \neq g_{yy}$.

We used CdTe/$Cd_{1-x}Mn_xTe$ structures grown by MBE on (001)–GaAs substrates in our measurements. Structure I contained four CdTe QWs with thicknesses $L = 20$, 40, 60, and 100 Å, separated by $Cd_{1-x}Mn_xTe$ barriers with a manganese concentration $x = 0.3$ and width $L = 500$ Å. Structure II had three QWs with thicknesses $L = 40$, 60, and 100 Å, and the manganese concentration in the barrier was $x = 0.1$. The structures were placed in a helium cryostat with a superconducting coil and, by pumping out the helium vapor, the temperature could be lowered to 2 K. The luminescence was excited with a He-Ne or Ar laser with a power about 1 W/cm^2, and the radiation propagating along (001) (*z* axis) was measured. The degree of linear polarization was measured by counting photons polarized in two orthogonal directions in two channels. The polarization of the pump light in our experiments did not produce any effect on that of the luminescence. The magnetic field $\mathbf{B} = (B_x, B_y, 0)$ was parallel to the well plane. To study the dependence of radiation polarization on magnetic-field direction in the well plane, the sample immersed in helium was rotated about the *z* axis.

Two parameters were measured to characterize the linear polarization in our experiments

$$\rho_0 = (I_\alpha - I_\beta)/(I_\alpha + I_\beta), \quad \text{and}$$

$$\rho_{45} = (I_{\alpha'} - I_{\beta'})/(I_{\alpha'} + I_{\beta'}). \tag{1}$$

Here I_k are the intensities polarized along the α, β directions (i.e., perpendicular and parallel to the magnetic field) and α', β' (rotated by 45° around the *z* axis with respect to α and β). This choice of parameters is not only convenient from a practical viewpoint (only the sample is rotated, while the magnetic field and the measurement system remain fixed) but physically reasonable as well. If the quantum wells had axial symmetry (C_∞), the ρ_0 and ρ_{45} parameters, as can be shown, would not depend on the angle φ between the magnetic field and the [110] axis with $\rho_0 = \text{const}$, $\rho_{45} = 0$, which corresponds to purely isotropic polarization. In the other limiting case, where the polarization plane is fixed relative to the crystallographic axes (the so-called built-in polarization, with a linear dipole rotating together with the sample), $\rho_0 \sim \cos 2\varphi$, $\rho_{45} \sim \sin 2\varphi$. In the case of a four-fold symmetry axis (D_{2d} symmetry), the ρ_0 and ρ_{45} parameters should contain $\cos 4\varphi$ and $\sin 4\varphi$.

Figure 1a and 1b displays spectra of the luminescence and linear polarization (ρ_0 parameter) obtained from QWs

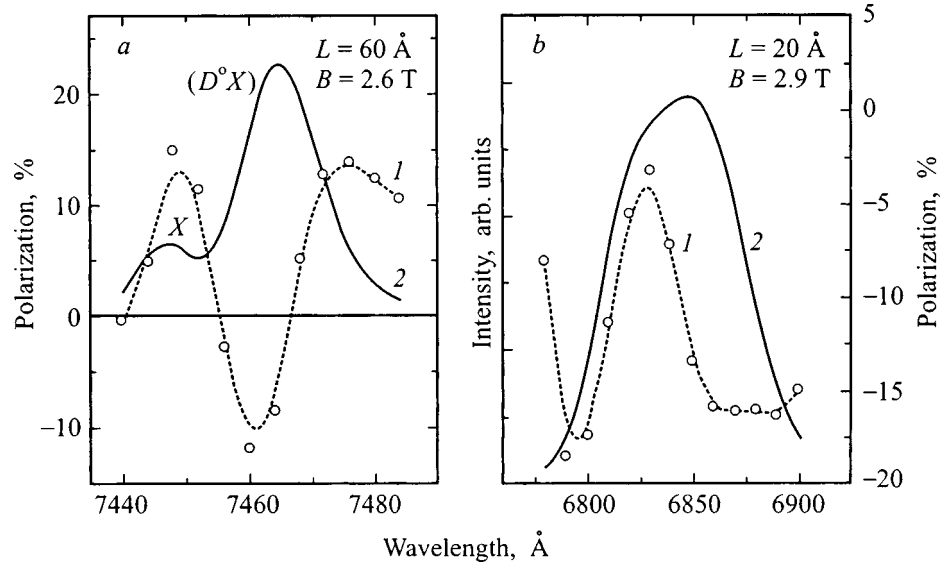

FIG. 1. Spectra of intensity (solid lines) and degree of linear polarization (dotted lines) of the emission from a quantum well with thickness (a) 60 Å and (b) 20 Å in structure I. Excitation with a He–Ne laser (1.96 eV), temperature 2 K, in-plane magnetic field $B=2.6$ T.

60 and 20 Å thick (structure I). In zero field, one detects only a small linear polarization of the luminescence, which does not exceed 2% while, in a magnetic field of about 1 T, the polarization increases by an order of magnitude. By rotating the crystal in a fixed field, one could make angular scans of ρ_0 and ρ_{45} for different QWs. Figure 2a and 2b shows the dependences of ρ_0 and ρ_{45} on φ for a 60-Å thick QW measured at $B=0$ and 2.6 T, respectively. The dependences in Fig. 2a are conventional crystal-rotation scans and are presented only to illustrate the measurement error. By contrast, the result demonstrated in Fig. 2b is totally unexpected and suggests a conclusion which might seem at first glance paradoxical, namely, that a magnetic field induces a linear polarization of the luminescence, but neither the magnitude of this polarization nor its orientation in the crystal depend on the field direction. This situation was observed to occur in QWs with thicknesses $L=40$ and 60 Å in structure I.

Studies of QWs with other parameters revealed a rich variety of $\rho_0(\varphi)$ and $\rho_{45}(\varphi)$ relations. Figure 3a and 3b shows angular dependences of the linear polarization parameters for QWs with thicknesses $L=60$ Å in structure II (Fig. 3a) and $L=20$ Å in structure I (Fig. 3b). Besides the actual appearance of such a strong angular dependence implying a substantial anisotropy in in-plane properties, there is one more remarkable point. In all cases, application of a field along [110] ($\varphi=0°$, 180°) and $[1\bar{1}0]$ ($\varphi=90°$, 270°) produces different results, whereas for an ideal structure with symmetry D_{2d} these axes are equivalent. It should be noted that the inequivalence of the [110] and $[1\bar{1}0]$ directions in

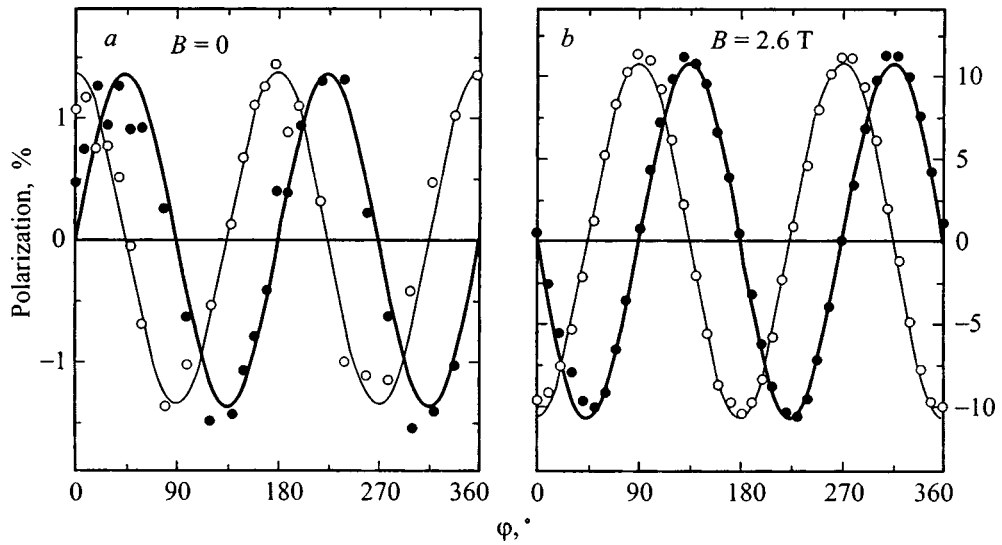

FIG. 2. Dependence of the luminescence polarization from a quantum well (structure I) with thickness (a) $L=20$ Å in zero magnetic field and (b) $L=60$ Å in $B=2.6$ T on in-plane field orientation. Fitting parameters (in units of T^{-2}) (b): $aD=0.016$, $b=c=0$. $\varphi=0$ corresponds to $\mathbf{B}\|[110]$.

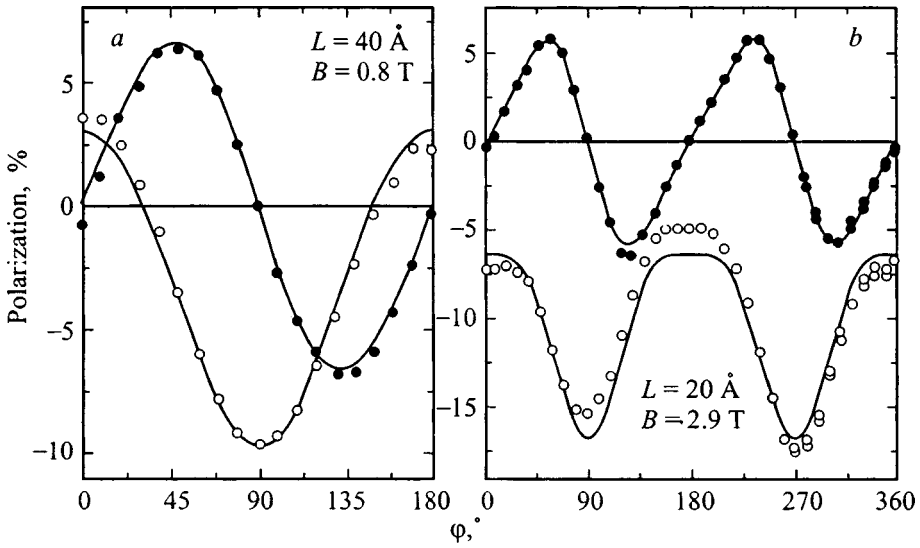

FIG. 3. Same as in Fig. 2b for quantum wells with thickness of 60 Å (structure II) and 20 Å (structure I): (a) $aD=0.10, bD=cD=-0.05$; (b) $aD=0.008, bD=-0.008, cD=-0.006$.

GaAs/AlAs superlattices, which is observed in the fine structure of the excitonic spectrum, has recently been revealed in ODMR (Ref. 9) and exciton optical orientation[10] experiments. In our case, however, manifestation of the exciton fine structure is hardly possible, because the corresponding splittings are usually on the order of a few tens of μeV, while the energy of localized-carrier interaction with magnetic fluctuations in semimagnetic semiconductors is estimated[11] to be a few meV.

The linear polarization of radiation is described by the symmetric part of the polarization tensor $\langle E_\alpha E_\beta \rangle$. Restricting ourselves to the weak magnetic-field domain,

$$\langle E_\alpha E_\beta \rangle^{\text{symm}} = A^0_{\alpha\beta} + A_{\alpha\beta\gamma\delta} B_\gamma B_\delta , \tag{2}$$

we readily see that the angular dependence of ρ_0 for an ideal QW (D_{2d} symmetry) can contain only the zeroth and fourth harmonics (and that of ρ_{45}, only the fourth harmonic). None of the quantum wells studied exhibits, however, dependences of this kind. At the same time, if we assume that the symmetry of the system dropped for some reasons from D_{2d} to C_{2v}, the minimum step required to make the [110] and $[1\bar{1}0]$ axes inequivalent, the results will be completely different. For the sake of conveniency we write it first in a system of parameters based on the crystallographic axes

$$\rho_0' = DB^2(a + b\cos 2\varphi) , \tag{3}$$

$$\rho_{45}' = DB^2 c \sin 2\varphi . \tag{4}$$

Here the angle φ is reckoned from the [110] direction, $a=A_{11}-A_{21}-A_{22}+A_{12}$, $b=A_{11}-A_{21}+A_{22}-A_{12}$, and $c=4A_{66}$. To make possible comparison of the calculations with experiment, we have to recast the above relations, in accordance with the actual measurement conditions, to a laboratory frame tied to the magnetic field

$$\rho_0 = DB^2\left(\frac{b+c}{2} + a\cos 2\varphi + \frac{b-c}{2}\cos 4\varphi\right) , \tag{5}$$

$$\rho_{45} = DB^2\left(a\sin 2\varphi + \frac{b-c}{2}\sin 4\varphi\right) . \tag{6}$$

In a general case, the $(b-c)$ coefficient is nonzero, and the angular dependence of linear polarization may contain the fourth harmonic. Note that, in a cubic crystal or a system with D_{2d} symmetry, $a=0$ (because $A_{11}=A_{22}$, and $A_{21}=A_{12}$), and it is only the fourth harmonic that can exist. The solid lines in Figs. 2 and 3 are plots of the degree of linear polarization as functions of angle constructed using Eqs. (5) and (6). For QWs with thicknesses $L=40$ and 60 Å in structure I, the $(b-c)$ and $(b+c)$ coefficients were found to be practically zero, i.e., $b=0, c=0$. This means that $\rho_0' = aDB^2 = \text{const}$ and $\rho_{45}'=0$ do not depend on φ [see Eqs. (3) and (4)], in other words, the plane of polarization of the emitted light is fixed with respect to the crystal axes.

For the thinner well, $L=20$ Å (Fig. 3b), the contribution of the fourth harmonic, as well as of the constant component of polarization, becomes substantial. At the same time for structure II with $L=40$ and 60 Å (Fig. 3a), $(b-c)=0$, and the isotropic part of polarization provides a contribution comparable to that of the anisotropic one. Thus relations (3) and (4) describe properly the totality of the experimental data obtained on different structures and quantum wells of different thickness.

A rigorous quantum-mechanical calculation shows that the anisotropy in the magnetic-field-induced linear polarization can be explained in terms of a model considering the effective spin $j=1/2$ of a heavy hole with an anisotropic g factor $J_\beta = g_{\alpha\beta} j_\alpha$ ($g_{xx} \neq g_{yy}$). We shall present here only the final expressions for the parameters ρ_0' and ρ_{45}':

$$\rho_0' = kB^2((g_{xx}-g_{yy}) + (g_{xx}+g_{yy})\cos 2\varphi) , \tag{7}$$

$$\rho_{45}' = kB^2(g_{xx}+g_{yy})\sin 2\varphi , \tag{8}$$

where coefficient k accounts for the specific features of spin polarization in a semimagnetic semiconductor. As seen from

a comparison with symmetry relations, the model of the anisotropic hole g factor corresponds to the case of $b=c=g_{xx}+g_{yy}$ and, hence, the ρ_0 and ρ_{45} relations will not contain the fourth harmonic [see Eqs. (3) and (4)]. The surprising result in Fig. 2b reflects the limiting g factor anisotropy, $g_{xx}=-g_{yy}$ (this relation indicates that the heavy-hole g factor acquires notable magnitude only due to a low-symmetry perturbation[12]), and the result in Fig. 3a is for the case of moderate anisotropy $|g_{xx}|>|g_{yy}|$. The appearance of the fourth harmonic in the angular dependences obtained for thin QWs (Fig. 3b) also can be explained within the effective-spin model if one takes into account the spin correlation of the electron and the hole in the magnetic polaron.

Thus our experimental data can be explained by assuming the existence of a low-symmetry perturbation. Such a perturbation in symmetry could be here a uniaxial strain parallel to the well plane[10], heterointerface anisotropy,[13] or the hole localization potential.

The authors owe sincere thanks to K. V. Kavokin and E. L. Ivchenko for fruitful discussions.

Partial support of the Russian Fundamental Research Foundation (Grants 96-02-16887 and 98-02-18213) and of the Polish State Committee on Research (Grant PBZ 28.11) is gratefully acknowledged.

[1] B. Kuhn-Heinrich, W. Ossau, E. Bangert, A. Waag, and G. Landwehr, Solid State Commun. **91**, 413 (1994).
[2] P. Peyla, A. Wasiela, Y. Merle d'Aubigné, D. E. Ashenford, and B. Lunn, Phys. Rev. B **47**, 3783 (1993).
[3] V. F. Sapega, M. Cardona, K. Ploog, E. L. Ivchenko, and D. N. Mirlin, Phys. Rev. B **45**, 4320 (1992).
[4] J. Stühler, G. Schaack, M. Dahl, A. Waag, G. Landwehr, K. Kavokin, and I. A. Merkulov, Phys. Rev. Lett. **74**, 2567 (1995).
[5] S. A. Crooker, J. J. Baumberg, F. Flack, N. Samarth, and D. D. Awschalom, Phys. Rev. Lett. **77**, 2814 (1996).
[6] Yu. G. Kusraev, A. V. Koudinov, K. V. Kavokin, B. P. Zakharchenya, D. E. Ashenford, and B. Lunn, in *Proceedings of the XXIII International Conference on the Physics of Semiconductors (Berlin, 1996)*, edited by M. Sheffer and R. Zimmermann (World Scientific, Singapore, 1996), p. 2459.
[7] D. R. Yakovlev, K. V. Kavokin, I. A. Merkulov, G. Mackh, W. Ossau, R. Hellmann, E. O. Göbel, A. Waag, and G. Landwehr, Phys. Rev. B **56**, 9782 (1997).
[8] I. A. Merkulov and K. V. Kavokin, Phys. Rev. B **52**, 1751 (1995).
[9] H. W. van Kesteren, E. C. Cosman, W. A. J. A. van der Poel, and C. T. Foxon, Phys. Rev. B **41**, 5283 (1990).
[10] C. Gourdon and P. Lavallard, Phys. Rev. B **46**, 4644 (1992).
[11] J. Warnock, R. N. Kershaw, D. Ridgely, K. Dwight, A. Wold, and R. R. Galazka, J. Lumin. **34**, 25 (1985).
[12] G. E. Pikus and F. G. Pikus, Solid State Commun. **89**, 319 (1994).
[13] I. L. Aleiner and E. L. Ivchenko, JETP Lett. **55**, 692 (1992).

Translated by G. Skrebtsov

Model of spinodal decomposition of phases under hyperbolic diffusion

N. M. Antonov and I. Yu. Popov

St. Petersburg Institute of Precision Mechanics and Optics, St. Petersburg, Russia

V. V. Gusarov

I. V. Grebenshchikov Institute of Silicate Chemistry, Russian Academy of Sciences, 199155 St. Petersburg, Russia

Fiz. Tverd. Tela (St. Petersburg) **41**, 907–909 (May 1999)

A model is proposed for the kinetics of spinodal decomposition at high diffusion rates described by a hyperbolic equation. The formation of new phases is described using a zero-radius nonlinear potential model. It is shown that a regular distribution in space of the phases during spinodal decomposition is initiated by suitable initial conditions for the concentration gradient with constant initial concentrations of the components. © *1999 American Institute of Physics.* [S1063-7834(99)04005-8]

As a process which makes it possible to form materials with spatial phase regions of extremely small size, spinodal decomposition of phases is of considerable interest in the synthesis of high-temperature superconductors, dispersion-hardened materials, porous glasses, etc.[1] The major features of the phase-transformation process during spinodal decomposition of phases can be formulated as follows: the new phases are formed in a state far from equilibrium, and the spinodal deformation rate greatly exceeds the phase-transition rate in the region where the phases exist in a metastable state. Spinodal liquefaction processes are characterized by an especially rapid rate.[2] The classical theory of spinodal decomposition, which is based on the Cahn-Hilliard model,[3–6]

$$\frac{\partial C_i}{\partial t} = -\Delta(K_i \Delta C_i) + D_i \Delta C_i$$

(where C_i is the concentration of the ith component in the decomposing phase, t is the time, K_i is a positive coefficient, D_i is the diffusion coefficient of the ith component, and Δ is the Laplacian operator), provides a rather good description of the spinodal decomposition process for relatively low mass-transport rates of the components.[a)] In addition, the customary description of the transport of the components in terms of a parabolic model is not always correct, since it neglects the diffusion relaxation time, which may be comparable to the structural relaxation time for the phase formation process. In these cases, a wave equation for the transport process must be used.[7–9] Given the above comments and assuming to a first approximation that the coefficients K_i are constant, the spinodal decomposition of the phases can be described by the system of equations

$$\tau_{\mathrm{di}} \frac{\partial^2 C_i}{\partial t^2} + \frac{\partial C_i}{\partial t} = -K_i \Delta^2 C_i + D_i \Delta C_i,$$

where τ_{di} is the diffusion relaxation time of the ith component. Note that, for the hyperbolic equations used here, the initial conditions must be supplemented by conditions for

$$\left.\frac{\partial C_i}{\partial t}\right|_{t=0}.$$

Without loss of generality, for simplicity we shall consider the spinodal decomposition of a two-component phase with variable-composition. Since the concentration of the second component is given by $C_2 = 1 - C_1$, the system of hyperbolic equations in this case will consist of a single equation for the variable $C \equiv C_1$. It is natural to assume that at the initial time the concentration C is constant (the condition of chemical homogeneity of the phase). In addition, the spatial distribution of $\partial C_i / \partial t|_{t=0}$ is, in general, nonuniform, which corresponds to the presence of several active centers in the decomposing phase (the seed formation centers for the new phases). These centers can, for example, be dislocations, stacking faults in crystals, boundaries, and triple junctions of grains in polycrystals, or associates in melts.

For describing the formation of new phases by spinodal decomposition we propose using a zero-radius nonlinear potential model for the hyperbolic diffusion equation. It is known that specifying a zero-radius linear potential reduces to constructing a self-conjugated expansion of some symmetric operator.[10–13] Briefly speaking, the procedure for this construction, usually referred to as a ''contraction-expansion'' procedure, is as follows. We start with a self-conjugated operator $K\Delta^2 - D\Delta$ in a space of quadratically summable functions. We contract it onto a manifold of smooth functions which go to zero at some point. The closure of this operator will be a symmetric operator with deficiency indices (6,6). The deficiency element corresponding to the point λ_0 is obtained from the fundamental solution ψ of the equation

$$\frac{K}{D}\Delta^2 \psi - \Delta \psi - \chi_0 \psi = \delta(\mathbf{r}),$$

which is found in the explicit form

$$\psi(\mathbf{r})=\frac{1}{8ik_0}(H_0^{(1)}(k_0^{1/2}r)+H_0^{(2)}(k_0^{1/2}r))$$
$$-r^{-1}\left[\mathbf{J}\left(4k^{5/2}\left(\frac{K}{D}k^4-\lambda_0\right)^{-1}\right.\right.$$
$$\left.\left.\times\left(\frac{K}{D}k^4+k^2-\lambda_0\right)^{-1}\right)\right](r),$$

where $r=|\mathbf{r}|$, $[\mathbf{J}(f(k))](r)$ is the Bessel transform of the function $f(k)$ at the point r,[14] $\lambda_0=k_0^2$, and $H_0^{(1)}$ and $H_0^{(2)}$ are Hankel functions of the first and second kinds, respectively. The set of deficiency elements is

$$\psi,\psi_{x1},\psi_{x2},\psi_{x1x2},\psi_{x1x1},\psi_{x2x2}.$$

It has self-conjugated expansions which also gives our model. The domain determining the expansion includes functions from the region of conjugation (to the initial) operator which satisfy some additional conditions. Specifically, elements from the domain defining the conjugation operator have the form

$$u(r)=\sum_{i,j=1}^{2}b_{ij}\psi_{x_ix_j}(\mathbf{r})+\sum_{i=1}^{2}b_i\psi_{x_i}(\mathbf{r})+b_0\psi(\mathbf{r})+\xi(\mathbf{r})$$
$$\times\left(a_0-\sum_{i=1}^{2}a_ix_i+\sum_{i,j=1}^{2}a_{ij}g_{ij}x_ix_j\right)+u^{(0)}(\mathbf{r}),$$

where

$$u^{(0)}(0)=u_{x_i}^{(0)}(0)=u_{x_ix_j}^{(0)}(0)=0,$$

$$g_{ij}=1,\quad i=j,\quad g_{ii}=1/2;\quad i,j=1,2,$$

$\xi(\mathbf{r})$ is a smooth cutoff function, with $\xi(\mathbf{r})=1$ for $r<1$ and $\xi(\mathbf{r})=0$ for $r>2$.

Note that, in the neighborhood of the selected point, these elements have the asymptote

$$C=b_0r^2\ln r+b_1r\ln r\cos\varphi+b_2r\ln r\sin\varphi+b_{11}(2\ln r+1$$
$$+2\cos^2\varphi)+b_{12}\sin 2\varphi+b_{22}(2\ln r+1+2\sin^2\varphi)+a_0$$
$$+a_1r\cos\varphi+a_2r\sin\varphi+a_{11}r^2\cos^2\varphi+a_{12}r^2\sin 2\varphi$$
$$+a_{22}r^2\sin^2\varphi+o(r^2),\quad r\to 0.$$

Carrying out the expansion actually reduces to specifying the relationship among the coefficients b_i,b_{ij} and da_i,a_{ij}.[11–13] Note that the self-conjugated expansions naturally include an initial operator corresponding to the case when there is no potential at all. In this problem we propose introducing a zero-radius nonlinear potential, i.e., a nonlinear expansion of the diminished operator. We choose it in the following way. If $C<C_*$ (i.e., the concentration at the given point is less than some fixed value), then the expanded operator is the initial self-conjugated operator. If, on the other hand, C exceeds this threshold, then we choose an operator for the expansion corresponding to a ''source'' (more precisely, ''sink'') of strength proportional to the excess above the threshold. The physical significance of this model is that, on reaching a certain value of the concentration of a component, the nucleation center transforms into a nucleus for the new phase. Here we are describing the initial stage of spinodal decomposition, when the sizes of the growing nuclei are negligible compared to their separation. When singularities (nuclei) appear, the situation changes. New centers are not formed, since further growth in the concentration wave above the given level does not take place at other points, because the excess is absorbed by centers that have already been formed.

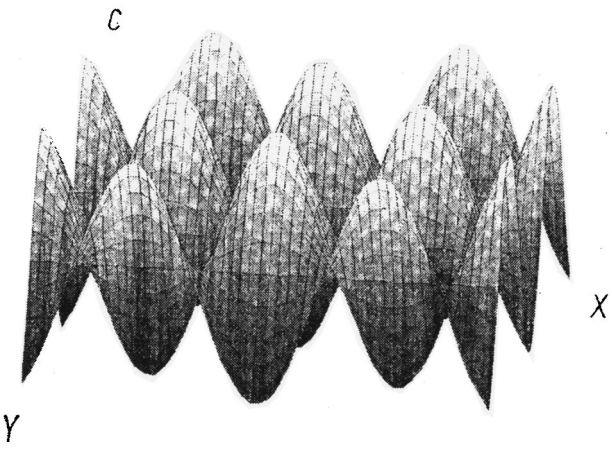

FIG. 1. Distribution of the concentration C of a component over the space coordinates X and Y during spinodal decomposition of a phase under hyperbolic diffusion conditions.

For simplicity let us consider the case where the nucleation centers of the two phases alternate spatially and form a square two-dimensional lattice with sides of length L. From a formal mathematical point of view, this corresponds to the following initial conditions. The initial value of the concentration is constant, while the initial rate of change of the concentration is a function u which is close to

$$u_{nm}=\cos(n\pi x/L)\cos(m\pi y/L),$$

where n and m are integers. At the boundary of the square $(0\leqslant x\leqslant L,\ 0\leqslant y\leqslant L)$ we assume that the Neumann boundary conditions $\partial C/\partial\nu=0$ are satisfied. In this situation, a single mode (standing concentration wave) will dominate in the solution,

$$\exp(-\alpha_{nm}t)\sin(\beta_{nm}t)\cos(\pi nx/L),$$
$$\cos(m\pi y/L).$$

The amplitude increases in the initial time period. If at some moment it reaches the threshold, then nuclei of the new phases appear, simultaneously, at the antinodes of the standing waves. Figure 1 shows the spatial distribution of the concentration at a time when the threshold has not yet been reached. In the calculations it was assumed that $u-u_{nm}$ is a piecewise linear function and

$$\int|u-u_{nm}|^2dv<0.1.$$

Therefore, the periodic siting of the phases during spinodal decompositon is initiated by a ''periodic'' initial condition, which is related to the corresponding arrangement of the nucleation centers determined by the structure of the initial phase.

Note that, from a physical standpoint, cases of regular, but nonperiodic siting of the nucleation centers is possible, as typical in liquefaction of melts and glasses. This may, for example, reflect initial conditions corresponding to the sum of two standing waves. We emphasize that using a hyperbolic mass-transport equation makes it possible to obtain a periodic arrangement of material regions formed during spinodal decomposition of phases with a constant initial concentration of the components.

This work was supported by the Russian Fund for Fundamental Research and the Ministry of Public and Professional Education (Project No. 97-18-1.2-29).

[a)]We neglect the problem of divergence in the coefficients K_i at long times.[6]

[1] V. V. Gusarov, A. A. Malkov, Zh. N. Ishutina, and A. A. Malygin, Pis'ma Zh. Tekh. Fiz. **24**, 3 (1998) [Tech. Phys. Lett. **24**, 1 (1998)].
[2] S. V. Kazakov and N. I. Chernova, Zh. Fiz. Khim. **63** (1), 223 (1989).
[3] J. W. Cahn and J. E. Hilliard, J. Chem. Phys. **28**, 258 (1958).
[4] J. W. Cahn and J. E. Hilliard, J. Chem. Phys. **29**, 131 (1959).
[5] J. S. Langer, Ann. Phys. (Leipzig) **78**, 421 (1973).
[6] I. K. Kudryavtsev, *Chemical Instabilities* [in Russian] (Izd-vo. MGU, Moscow, 1987).
[7] W. E. Alley and B. J. Alder, Phys. Rev. Lett. **43**, 653 (1979).
[8] A. V. Lykov, Inzh.-Fiz. Zh. **9**, 287 (1965).
[9] I. N. Taganov, *Modelling Mass- and Energy-Transport Processes* [in Russian] (Khimiya, Leningrad, 1979).
[10] B. S. Pavlov, Usp. Mat. Nauk **42**, 99 (1987).
[11] I. Yu. Popov, Applicable Analysis **69** (1-2), 15 (1998).
[12] I. Yu Popov, Revistra Mat. Univ. Compl. Madrid **9**, 235 (1996).
[13] I. Yu. Popov, in *Proc. Zel'dovich Memorial*, edited by S. M. Frolov, Moscow (1994), p. 305.
[14] V. A. Ditkin and A. P. Prudnikov, *Integral Transforms and Operational Calculus* [in Russian] (Fizmatgiz, Moscow, 1961).

Translated by D. H. McNeill

Localization in a system of bound Aaronov–Bohm rings

I. Yu. Popov

Institute of Precision Mechanics and Optics, 197101 St. Petersburg, Russia

V. A. Geĭler and A. V. Popov

Mordovian State University, 430000 Saransk, Russia

Fiz. Tverd. Tela (St. Petersburg) **41**, 910–912 (May 1999)

[S1063-7834(99)04105-2]

In the past decade, quantum transport in mesoscopic systems has been studied actively from both theoretical and experimental standpoints.[1–3] For systems of mesoscopic rings in magnetic fields, there is special interest in the study of the relationship between the transmission coefficient and the magnitude of the field, more precisely the magnetic flux Φ.[1,4–6] In particular, Ref. 5 is devoted to a study of resonance transport phenomena in a system of serially connected rings. It has been found that all states near $\Phi_0/2$ (Φ_0 is the quantum of magnetic flux) are antiresonant.

In our article we propose three explicitly soluble models based on operator expansion theory.[7–9] The first model treats a system of Aaronov–Bohm rings connected into an infinite chain. It is shown that for $\Phi=\Phi_0(1/2+k)$, where k is an integer, the spectrum consists only of localized states. In the second model a system of rings is coupled to an infinite quantum wire. The localization condition includes a relation between the radius of the rings and the length of the segment of wire between two neighboring points of the combination. In addition, there are also delocalized states in the spectrum. The third model describes a square lattice of rings joined at their points of tangency. Here it is shown that there are localized states and properties of the spectrum are noted which are analogous to the corresponding properties for a quantum billiard.

An Aaronov–Bohm ring of radius R with magnetic flux Φ is described by the Hamiltonian

$$H_0^{AB}=\frac{\hbar^2}{2m^*R^2}\left(-\frac{\partial^2}{\partial\phi^2}+2i\frac{\Phi}{\Phi_0}\frac{\partial}{\partial\phi}+\left(\frac{\Phi}{\Phi_0}\right)^2\right),$$

where m^* is the effective charge carrier mass and ϕ is the polar angle. It is known that the spectrum of H_0^{AB} consists of the eigenvalues

$$E_m=\frac{\hbar^2}{2m^*R^2}\left(m-\frac{\Phi}{\Phi_0}\right)^2,\quad m\in Z,$$

which corresponds to the normalized eigenfunctions $\psi_m(\phi)=\exp(im\phi)/\sqrt{2\pi R}$.

The space of states for the ring is $\mathcal{H}_0^{AB}=L_2(S_R)$, where S_R is a circle of radius R. The space of states $\mathcal{H}_0^{AB}$ for an infinite system of isolated rings is an orthogonal sum of spaces $\mathcal{H}_0^{AB}$. The expansion-theory method is used in order to ''join'' a ring.[7,9–11] Let us consider a set $\mathcal{D}_1^{AB}$ of functions from the domain defining the operator $\mathcal{H}_0^{AB}$, which go to zero at the points $\phi=0$ and $\phi=\pi$. We denote the orthogonal sum to $\mathcal{D}_1^{AB}$ by $\mathcal{D}^{(1)}$ and the collapse of H^{AB} onto this set by $S^{(1)}$. We seek the Hamiltonian for the model among the self-conjugated expansions $S^{(1)}$. For describing the expansions it is convenient to use the Crane formula for the resolvent

$$G^{(1)}(\zeta)=G^{AB}(\zeta)-\Gamma^{(1)}(\zeta)[Q^{(1)}(\zeta)+A]^{-1}\Gamma^{(1)*}(\overline{\zeta}),\tag{1}$$

where A is a self-conjugated operator in $l_2(Z)\otimes C^2$, $Q^{(1)}$ and $\Gamma^{(1)}$ are the so-called Crane $\mathcal{Q}$ and Γ functions of the operator $S^{(1)}$. In our case, the $\mathcal{Q}$ function $Q^{(1)}(\zeta)$ is an analytic operator-function which acts in the Hilbert space $l_2(Z)\otimes C^2$, while the Γ function $\Gamma^{(1)}(\zeta)$ acts from $l_2(Z)\otimes C^2$ to $\mathcal{H}^{AB}$, and they are found explicitly. The operator A is represented using the block matrix $||A_{m,n}||$, each element $A_{m,n}$ of which is a 2×2 matrix. Given that the rings are joined serially, we choose the matrices as follows: $A_{m,n}=0$, for $m\neq n\pm1$ and

$$A_{m,m-1}\begin{pmatrix}0&\tau\\0&0\end{pmatrix},\quad A_{m,m+1}\begin{pmatrix}0&0\\\tau&0\end{pmatrix},$$

where $\tau\neq0$ is a real parameter depending on the properties of the contact between rings. As a result, we obtain the following dispersion relation

$$\frac{m^*}{\hbar^2E}\sin^2(\pi R\sqrt{2m^*E}/\hbar)\frac{4\tau}{\hbar}\sqrt{\frac{m^*}{2E}}\left(\sin(\pi R\sqrt{2m^*E}/\hbar)\times\cos\left(\pi\frac{\Phi}{\Phi_0}\right)\cos(2\pi p)\right)+\tau^2\left(\cos(2\pi R\sqrt{2m^*E}/\hbar)-\cos\left(2\pi\frac{\Phi}{\Phi_0}\right)\right),\tag{2}$$

where $0\leqslant p<1$ is the quasimomentum. Equation (2) shows that for $\Phi=(1/2+n)\Phi_0$, where n is an integer, the spectrum of $H^{(1)}$ consists only of eigenvalues E_m which are independent of the quasimomentum p. These values are the roots of the equation

$$\tan^2(\pi R\sqrt{2m^*E}/\hbar)=\frac{2\hbar^2\tau^2E}{m^*}.$$

Let us consider a system of rings joined to an infinite wire. Specifically, we connect the nth ring to the wire at the point $x_n=a_n$, where $a>0$ and $n=0,\pm1,\pm2,\ldots$. The space of the system of states is $\mathcal{H}=L_2(R)\otimes\mathcal{H}^{AB}$. We construct the model by analogy to the previous case. Here we only add a one-dimensional Hamiltonian for the axis,

$$H_{\text{free}}=-\frac{\hbar^2}{2m^*}\frac{d^2}{dx^2}.$$

Without describing the construction, which is analogous to the previous case again, we simply note the result. The dispersion relation has the form

$$\frac{1}{\hbar}\sqrt{\frac{m^*}{2\zeta}}\frac{\sin(a\sqrt{2m^*\zeta}/\hbar)}{\cos(a\sqrt{2m^*\zeta}/\hbar)-\cos(2\pi p)}=\tau^2\hbar\sqrt{\frac{2E}{m^*}}\frac{\cos(2\pi R\sqrt{2m^*E}/\hbar)-\cos\left(2\pi\frac{\Phi}{\Phi_0}\right)}{\sin(2\pi R\sqrt{2m^*E}/\hbar)}. \tag{3}$$

Note that the left-hand side of Eq. (3) is the same as the well-known expression in the Kronig–Penney model.[8] The dispersion relation shows that the spectrum of $H^{(2)}$ has a band structure; $E=E_s(p)$, where $p\in T$ and $s=1,2,\ldots$. We now find the condition for the appearance of localized states in the spectrum of $H^{(2)}$. Let $E_k=\pi^2\hbar^2k^2/(2m^*a^*)$, where $k=1,2,\ldots$ be the eigenvalues for an interval of length a with Dirichlet conditions at the ends. Equation (3) shows that the E_k will be localized states in the spectrum of $H^{(2)}$, if the flux Φ satisfies the condition

$$\Phi\left(\pm\frac{\pi R}{a}k+n\right)\Phi_0 \tag{4}$$

for integral n. Note that, if $a=l\pi R$ for some integral l, then condition (4) is satisfied for all k. But even in the case of $a=\pi R$, the spectrum of $H^{(2)}$ contains delocalized states besides E_k. In this case the continuous bands of the spectrum are specified by the dispersion relation

$$\cos(2\pi p)=\frac{m^*}{2\tau^2\hbar^2E}\cos(\pi R\sqrt{2m^*E}/\hbar)+\cos(\pi R\sqrt{m^*E}/\hbar).$$

We now consider a square lattice of tangential Aaronov–Bohm rings. Here we shall assume additionally that the field $\mathbf{B}$ is the sum $\mathbf{B}=\mathbf{B}_0+\mathbf{B}_{AB}$. The first term is the uniform magnetic field B_0. The additional term $\mathbf{B}_{AB}$ describes the magnetic field created by a periodic system of infinitely thin solenoids (Aaronov–Bohm solenoids) located at the center of each ring. We shall assume that the magnetic flux in each of the solenoids is the same and equal to Φ_{AB}. In this situation, the Hamiltonian H_{AB} of an electron in a ring is a self-adjoint operator in the space $\mathcal{H}_\lambda=L^2(\mathcal{S}_\lambda)$ ($\mathcal{S}_\lambda$ is a circle of radius R) of the form

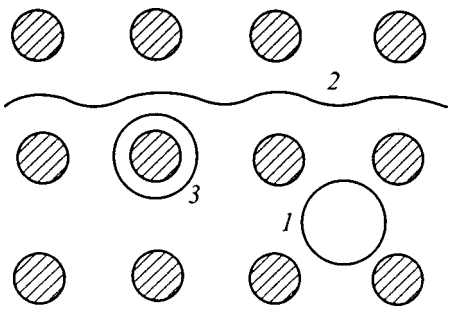

FIG. 1. Different types of quasiclassical trajectories in a massif of quantum antipoints: (1) closed trajectories which do not encompass quantum antipoints, (2) open trajectories describing the propagation of an electron, and (3) closed trajectories surrounding one or several antipoints.

$$H_{AB}=-\frac{\hbar^2}{2m^*}\frac{1}{R^2}\frac{\partial^2}{\partial\phi^2}+\frac{i\hbar e}{2m^*c}\left(B_0+\frac{\Phi_{AB}}{\pi R^2}\right)\frac{\partial}{\partial\phi}+\frac{e^2}{8m^*c^2}\left(B_0^2R^2+\frac{2B_0\Phi_{AB}}{\pi}+\frac{\Phi_{AB}^2}{\pi^2R^2}\right), \tag{5}$$

where m^* and e are the mass and charge, respectively, of the particle. Let Φ be the total magnetic flux through the ring, $\Phi=(\pi R^2B_0+\Phi_{AB})/\Phi_0$, where $\Phi_0=hc/e$ is the quantum of magnetic flux. Let $\eta=4R^2B_0/\Phi_0$ be the flux of the uniform field component through a unit cell of the lattice.

We specify the coupling among the rings using a scheme from operator expansion theory, proceeding in the spirit of Ref. 12. Here we note that the model Hamiltonian must be invariant with respect to the magnetic translation group. We end up with the following result.

Let η be a rational number, $\eta=N/M$. Then the spectrum of the model self-adjoint operator H_A consists of two parts, σ_1 and σ_2. The first, σ_1, consists of (infinitely degenerate) eigenvalues of H_A, which are simultaneously eigenvalues ε_n of the operator H_{AB}. The second part, σ_2, is the band structure of H_A. This spectrum consists of bands Z_0, Z_1, Z_2, ..., Z_l, ... lying within the intervals ($[-\infty,\varepsilon_3]$, $[\varepsilon_0,\varepsilon_4]$, $[\varepsilon_1,\varepsilon_5]$, ..., $[\varepsilon_n,\varepsilon_{n+4}]$ ... (the band Z_0 can be empty)); each band Z_n, $n\geqslant1$, is divided into M ''magnetic'' subbands. For a fixed value of the quasimomentum, each point σ_2 is degenerate with multiplicity M.

Next, if the total flux Φ is not an even integer, then the part σ_1 for an arbitrary choice of model parameters is empty, in general. If Φ is an even integer, then σ_1 contains all the eigenvalues of H_{AB}.

There is yet another possibility for bound states to appear in the spectrum of $\sigma(H_A)$; it can show up as a ''degenerate subband.'' Specifically, if η is integral, $\eta=N$, then for a certain choice of model parameters, the dispersion relation has a solution independent of the quasimomentum.

Therefore, if the flux of the uniform component of the magnetic field η is an integer and the total flux Φ through the ring is an even integer, then the spectrum of the model Hamiltonian H_A for a square lattice of coupled Aaronov–Bohm rings consists of three parts: (1) levels of an isolated ring, (2) a band spectrum (bands split into ''magnetic subbands''), and (3) coupled states which satisfy the dispersion

relation and do not coincide with the levels for an isolated ring. Note that this sort of structure for the spectrum also exists in the quantum billiard model, viz., a periodic massif of quantum antipoints.[12] Here the different parts of the spectrum correspond to different quasiclassical electron trajectories: (1) closed trajectories, which do not surround quantum antipoints, (2) open trajectories describing the propagation of an electron through the lattice, and (3) closed trajectories enclosing one or several antipoints (see Fig. 1). Thus, from the standpoint of the spectrum, the model constructed here can be regarded, in some sense, as the simplest model for a quantum billiard.

This work was partially supported by a Grant from the Russian Fund for Fundamental Research.

[1] Y. Gefen, Y. Imry, M. Ya. Azbel, Phys. Rev. Lett. **52**, 129 (1984).
[2] R. Landauer, Phys. Rev. B **33**, 6497 (1986).
[3] M. Büttiker, Y. Imry, and R. Landauer, Phys. Lett. A **96**, 365 (1983).
[4] A. Aldea, P. Gartner, and I. Corcotoi, Phys. Rev. B **45**, 14122 (1992).
[5] J. Li, Z.-Q. Zhang, and Y. Liu, Phys. Rev. B **55**, 5337 (1997).
[6] I.-R. Shi and B.-Y. Gu, Phys. Rev. B **55**, 4703 (1997).
[7] B. S. Pavlov, Lect. Notes Phys. **324**, 3 (1989).
[8] S. Albeverio, F. Gesztesy, R. Hoegh-Krohn, and H. Holden, *Solvable Models in Quantum Mechanics* (Springer, Berlin, 1988).
[9] I. Yu. Popov and S.L. Popova, Europhys. Lett. **24**, 373 (1993).
[10] V. A. Geyler and I. Yu. Popov, Z. Phys. B **93**, 437 (1994).
[11] V. A. Geyler and I. Yu. Popov, Z. Phys. B **98**, 473 (1995).
[12] V. A. Geyler, B. S. Pavlov, and I. Yu. Popov, J. Math. Phys. **37**, 5171 (1996).

Translated by D. H. McNeill

Optic-fiber communications: Nonlinear-transformation group

S. Lekić*)

''Kosmos,'' Cetinjska 1, 78000 Banja Luka, Republic of Srpska, Bosnia and Herzegovina

S. Galamić and Z. Rajilić

Physics Department, Faculty of Science, M. Stojanovića 2, 78000 Banja Luka, Republic of Srpska, Bosnia and Herzegovina

Fiz. Tverd. Tela (St. Petersburg) **41**, 913–917 (May 1999)

A new method for finding solutions of the nonlinear Schrödinger equation is proposed. A comutative multiplicative group of nonlinear transformations, which operate on stationary localized solutions, enables a consideration of fractal subspaces in the solution space, stability, and deterministic chaos. An increase of the transmission rate in the optic-fiber communications can be based on new forms of localized stationary solutions, without significant change of input power. The estimated transmission rate is 50 Gbit/s, for certain available soliton transmission systems. © *1999 American Institute of Physics.* [S1063-7834(99)04205-7]

The propagation of pulsed light in an optical fiber can be described by the nonlinear Schrödinger equation,

$$i\frac{\partial q(\xi,\tau)}{\partial \xi}+\frac{1}{2}\frac{\partial^2 q(\xi,\tau)}{\partial \tau^2}+|q(\xi,\tau)|^2 q(\xi,\tau)=0, \tag{1}$$

where $q(\xi,\tau)$ is a complex envelope function of the effective electric field amplitude and

$$\xi \propto x, \quad \tau \propto \left(t-x\frac{\partial k}{\partial \omega}\right). \tag{2}$$

The higher-order dispersion and the effect of fiber loss are neglected here.[1] We take

$$q=q_0 e^{i\frac{q_0^2}{2}\xi} y(\tau), \tag{3}$$

where $y(\tau)$ is a real function, and get

$$y-\frac{1}{q_0^2}\frac{d^2y}{d\tau^2}-2y^3=0. \tag{4}$$

The solution of this equation[2]

$$y_0(\tau)=\frac{1}{\cosh q_0\tau} \tag{5}$$

describes an optical soliton. Its unchangeable shape is a property that makes it attrative for applying to ultra-high-speed optic communications.[3,4] Equation (1) is completely integrable. The inverse scattering transformation method[5] yields general solutions of such nonlinear partial-differential equations. Our aim is to propose here an alternative approach to the nonlinear Schrödinger equation and discuss applicability of the results obtained to optic-fiber communications.

Equation (4) describes a stationary pulse in an optic fiber. We take a localized solution $y(\tau)$ of this equation and define the nonlinear operator H_{c_1}

$$H_{c_1}y=\sum_{j=1}^{\infty} c_j y^j, \tag{6}$$

where c_j are real coefficients. Does $H_{c_1}y$ satisfy Eq. (4)? When the case $y=y_0$ is considered, the answer is positive.[6] Substituting $H_{c_1}y$ in Eq. (4), we find that $H_{c_1}y$ is actualy a solution of this equation if

$$c_{2j}=0, \tag{7}$$

while c_{2j+1} satisfy the recursion relation

$$c_{2j+1}=\frac{1}{2j(j+1)}\left\{j(2j-1)c_{2j-1}-\sum_{n=2}^{2j} c_{2j+1-n}\sum_{k=1}^{n-1} c_{n-k}c_k\right\}, \tag{8}$$

where c_1 is an arbitrary coefficient. Using the relations (6)–(8), with $c_1=1$, we get

$$H_1 y=y. \tag{9}$$

In the following, H_{c_1} will mean both the series (6) and the recursion (8) with (7). For a localized $y(\tau)$ and a finite c_1, convergence of the series (6) can be tested numerically. Our calculations show that $H_{c_1}y$ is localized also. Therefore, using different values of c_1, we are able to get uncountably many new localized solutions of Eq. (4) from only one known localized solution (Fig. 1). In the following ''the solution'' will mean ''the localized solution of Eq. (4).'' The solution's preciseness will be limited only by the number of calculated coefficients. A solution in a form different from (6) does not exist. Each solution pair $z(\tau)$ and $y(\tau)$ must obey relation $z=H_{c_1}y$, for a specific value of c_1:

$$c_1=\lim_{\tau\to\pm\infty}\frac{z(\tau)}{y(\tau)}. \tag{10}$$

Starting with a solution $y(\tau)$ we can construct the complete solution space. There is an analogy to the superposition principle from linear theory. According to relation (10), a solution is determined by its asymptotics.

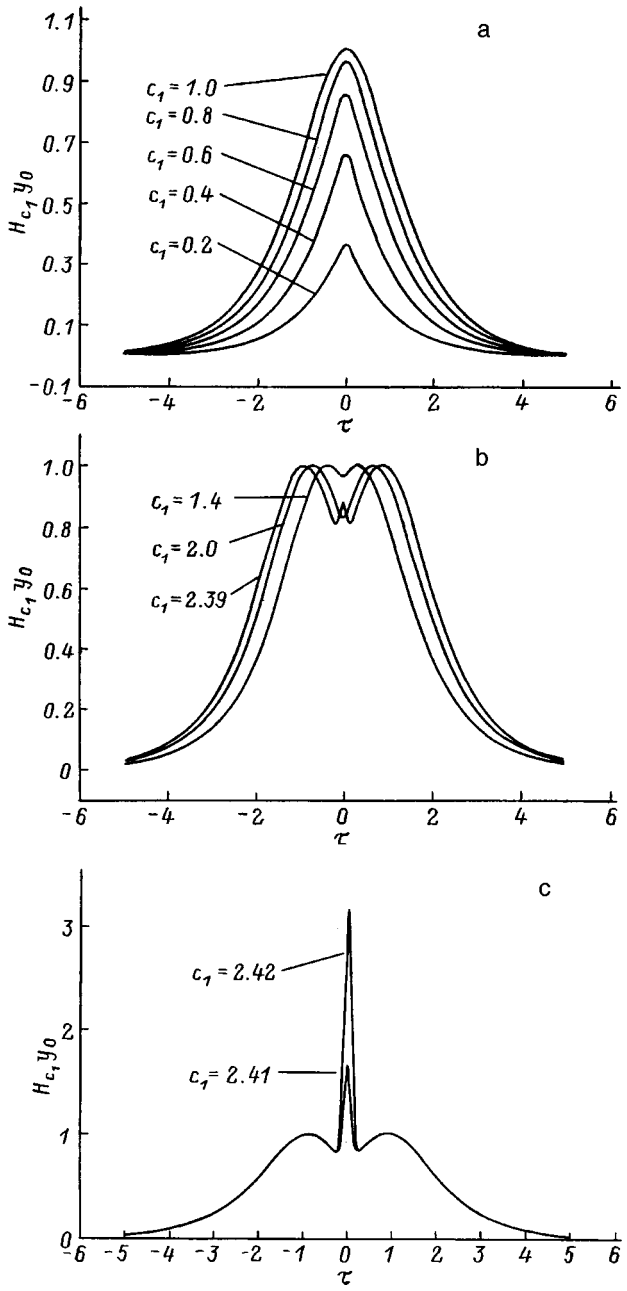

FIG. 1. Solutions $H_{c_1} y_0$. a — Stable solutions with $c_1 = 0.2$, 0.4, 0.6, 0.8, 1.0; b — stable solutions with $c_1 = 1.4$, 2.0, 2.39; c — unstable solutions with $c_1 = 2.41$, 2.42.

The nonlinear Schrödinger equation has an infinite number of symmetries corresponding to the conserved quantities: total energy, momentum, Hamiltonian etc.[1] We find that there are actually infinite conserved quantities. Let us consider the total energy only (for $H_{c_1} y$):

$$q_0^2 \int_{-\infty}^{\infty} (c_1 y + c_3 y^3 + c_5 y^5 + \ldots) d\tau. \tag{11}$$

We can choose infinitely different values of c_1 and use relations (7) and (8).

Relations (6)–(8) yield

$$H_{a_1} H_{b_1} = H_{a_1 b_1}. \tag{12}$$

Hence

$$\{H_{c_1};\, c_1 \neq 0\} \tag{13}$$

is the comutative multiplicative group of the nonlinear transformations (GNT). Group properties of the GNT originate from group properties of real numbers $c_1 \neq 0$. For example,

$$H_{c_1} H_{1/c_1} = H_1. \tag{14}$$

For definite coefficient c_1 and solution $y(\tau)$, we can construct a fractal subspace in the solution space. The fractal subspace covers solutions of form

$$H_{c_1} H_{c_1} \ldots H_{c_1} y. \tag{15}$$

In the phase plane, a fractal subspace is represented by a geometrical fractal (Fig. 2).

For optic-fiber communications it is important to know whether small disturbances will destroy the information carrying pulses. Solution parameters, amplitude (pulse width) and velocity (frequency), are affected by various perturbations: outside produced noise, incoherence of the light source, fiber inhomogenities, absorption, amplifier noise, soliton interactions, etc. It is an experimental fact that optical solitons (Eq. (5)) are unlikely to be destroyed by perturbations — they are very robust. We expect that at least a part of new solutions we have expressed here is actually stable. We are going to consider this problem theoretically, although it will remain open until experimental verification. The GNT method enables the following statement: the stability of a solution $y(\tau)$ is equivalent to the relation

$$\lim_{\varepsilon \to 0} H_{1+\varepsilon} y = y. \tag{16}$$

Relations (6)–(8) and (16) yield

$$|y(\tau)| \leqslant 1. \tag{17}$$

A localized solution of Eq. (4) is stable if and only if relation (17) holds (Figs. 1a and 1b). As well as for the *KdV* soliton,[7] the classical argument about the counterbalance between nonlinearity and dispersion is not sufficient to explain the stability. Consideration of the Lyapunov exponent,

$$\lambda(c_1) = \lim_{j \to \infty} \frac{1}{j} \ln \left| \frac{dc_{2j+1}}{dc_1} \right|, \tag{18}$$

indicates that deterministic chaos will appear at close packing of solitons, when c_1 is sufficiently large (Fig. 3a). We can expect deterministic chaos for $c_1 > 2.4$. Near $c_1 = 1$, stability is unusual (Fig. 3b).

New forms of localized stationary solutions of the nonlinear Schrödinger equation enable an increase in the transmission rate of optic-fiber communications, without significant change of input power. Information may be contained in the special form of soliton (Figs. 1a and 3b). The known optical soliton, described by (5), is one of many possible stationary pulses. Let us consider an available soliton transmission system. If the fiber core cross-sectional area is *S*

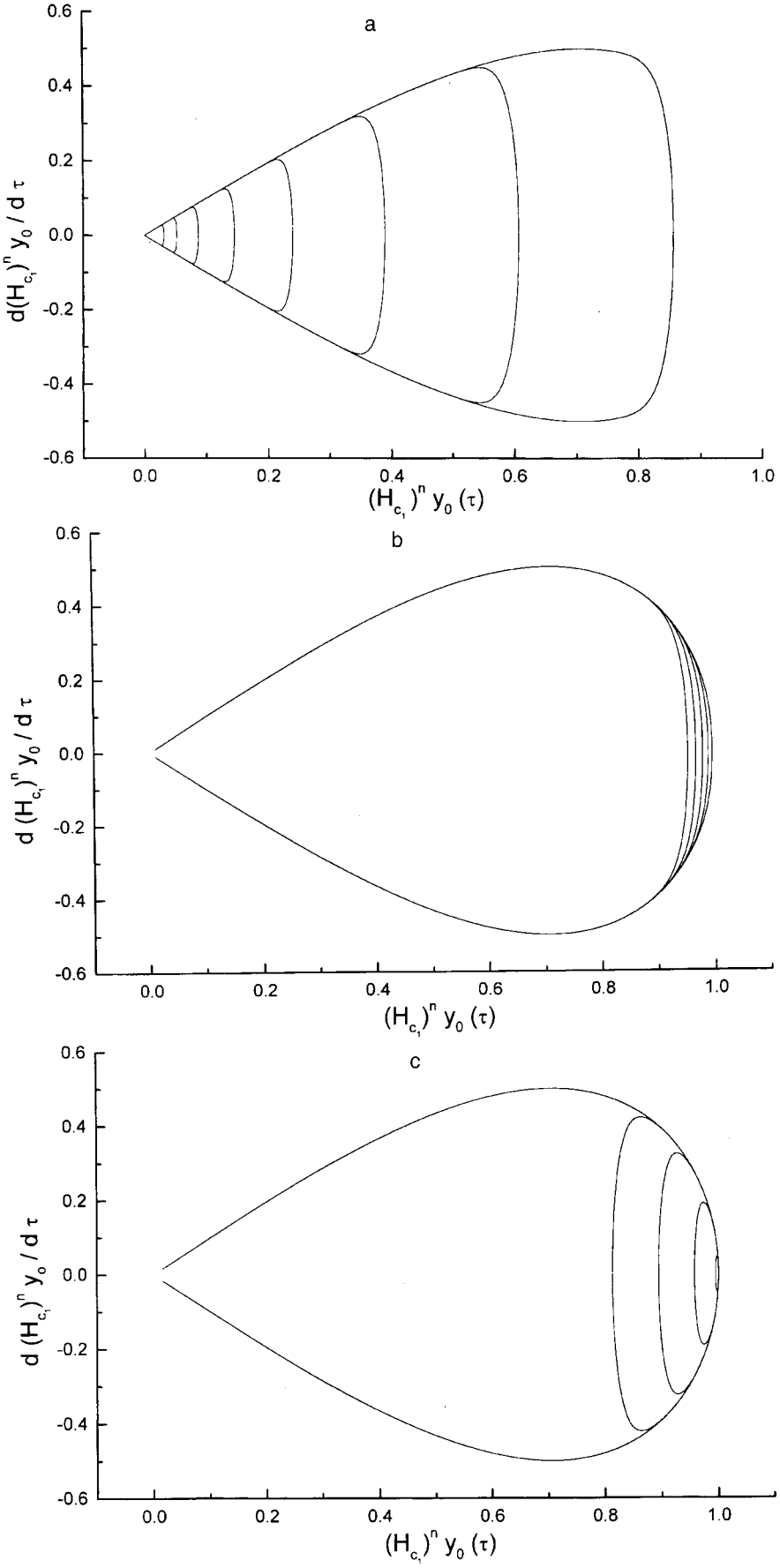

FIG. 2. Phase diagrams of the solutions $(H_{c_1})^n y_0$. a — $c_1=0.6$, $n=1$ to 8; b — $c_1=0.95$, $n=1$ to 5; c — $c_1=1.2$, $n=1$ to 5.

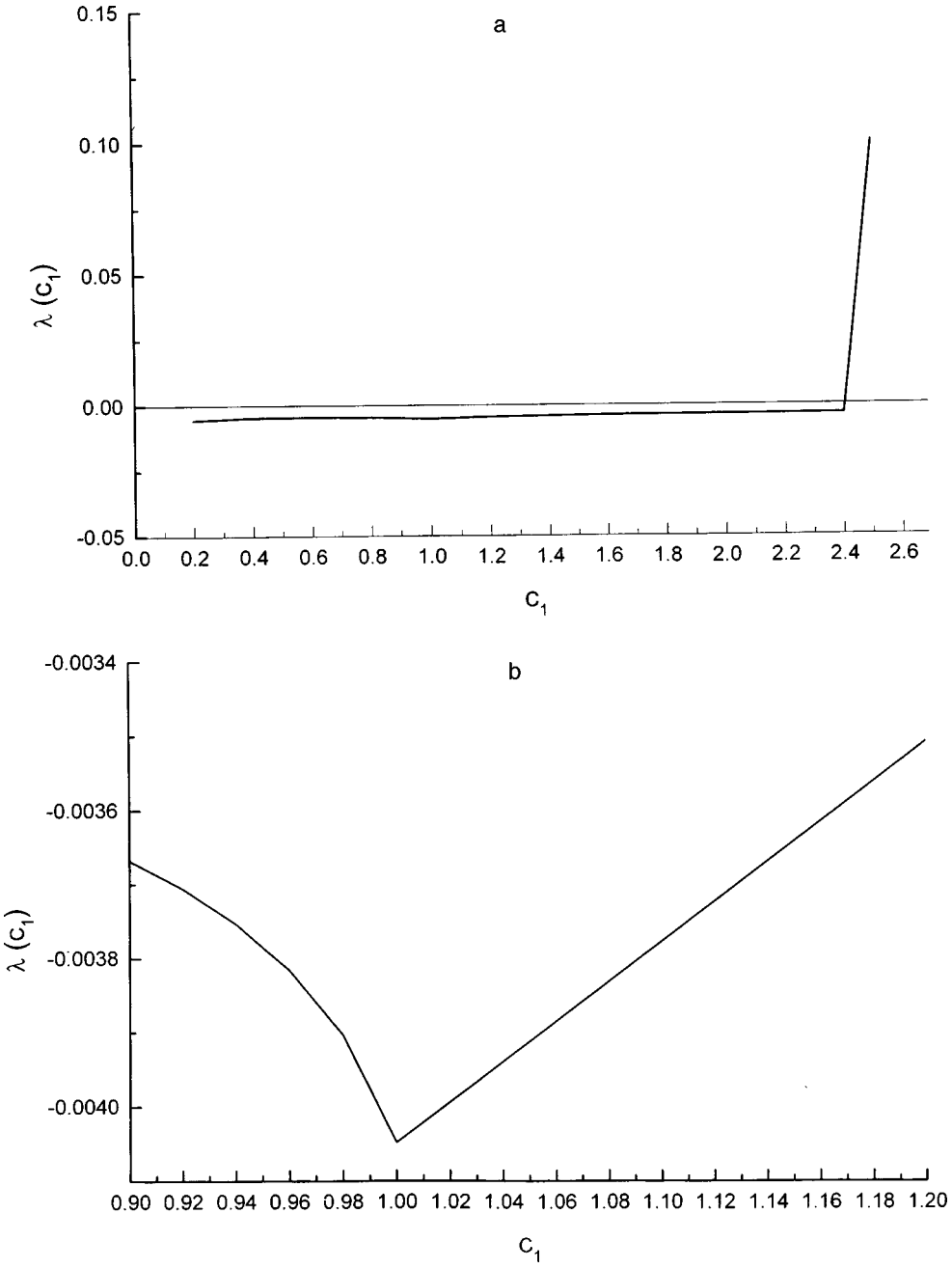

FIG. 3. a — Lyapunov exponent; b — exceptional stability near $c_1=1$.

$=60\ \mu m^2$, the carrier wavelength is $\lambda=1.55\ \mu m$, the soliton pulse (Eq. (5)) width is $\tau_s=25$ ps, the peak power is $P_m=2.1$ mW, and the separation between two adjacent solitons is $3\tau_s$, then the transmission rate is 10 Gbit/s.[8] In the same transmission system, using stable pulses of form H_{c_1} with different c_1 (Fig. 1a), the transmission rate will be faster. It becomes equal to 50 Gbit/s, at 40-photons energy resolution. The new forms of stable solutions (Fig. 1b) make possible increasing the transmission rate in the same system.

In conclusion, we have proposed the GNT method for solving of the nonlinear Schrödinger equation. New forms of the stationary localized solutions, usable for improving optic-fiber communications, are obtained.

The authors would like to thank H. J. S. Dorren for useful discussion of the GNT method.

This work was supported by the Soros Fund Open Society (Bosnia and Herzegovina) and the World University Service (Austria).

*)E-mail: slekic@urc.bl.ac.yu

[1]F. H. Abdullaev, S. A. Darmanyan, and P. K. Habibullaev, *Optical Solitons* [in Russian] (Fan, Tashkent, 1987).
[2]V. E. Zakharov and A. B. Shabat, Zh. Éksp. Teor. Fiz. **61**, 118 (1971) [Sov. Phys. JETP **34**, 62 (1971)].

[3] A. Hasegawa and F. Tappert, Appl. Phys. Lett. **23**, 142 (1973).
[4] A. Haus and W. S. Wong, Rev. Mod. Phys. **68**, 423 (1996).
[5] M. J. Ablowitz and H. Segur, *Solitons and the Inverse Scattering Transform* (SIAM Publication, Philadelphia, 1981).
[6] S. Lekić, Lj. Mitranić, and Z. Rajilić, Solid State Phenom. **61/62**, 331 (1998).
[7] H. J. S. Dorren and R. K. Snieder, ''A Stability Analysis for the Korteweg–de Vries Equation,'' submitted to Physica D (1997).
[8] A. Hasegawa and Y. Kodama, *Solitons in Optical Communications* (Clarendon Press, Oxford, 1995), p. 39.

Published in English in the original Russian journal. Reproduced here with stylistic changes by the Translation Editor.

The design and fabrication of one-dimensional random surfaces with specified scattering properties

T. A. Leskova

Institute of Spectroscopy, Russian Academy of Sciences, 142092 Troitsk, Moscow District, Russia

A. A. Maradudin*)

Department of Physics and Astronomy and Institute for Surface and Interface Science, University of California, Irvine, CA 92697 USA

E. R. Méndez

División de Física Aplicada Centro de Investigación Científica y de Educación Superior de Ensenada, Apartado Postal 2732, Ensenada, Baja California, 22800 México

A. V. Shchegrov

Rochester Theory Center for Optical Science and Engineering, Department of Physics and Astronomy, University of Rochester, Rochester, NY 14627 USA

Fiz. Tverd. Tela (St. Petersburg) **41**, 918–924 (May 1999)

We describe methods for designing and fabricating one-dimensional random surfaces that scatter light uniformly within a specified range of scattering angles, and produce no scattering outside this range. These methods are tested by means of computer simulations. Preliminary experimental results are presented. © *1999 American Institute of Physics.* [S1063-7834(99)04305-1]

The first theoretical study of the scattering of light from a randomly rough surface was published by Mandel'shtam in 1913, in the context of the scattering of light from a liquid surface.[1] In the succeeding years, the overwhelming majority of the theoretical work in this field has continued to be devoted to the solution of such direct problems, namely, given the statistical properties of a random surface, to calculate the angular and polarization dependence of the intensity of the scattered light. In contrast, in this paper we study theoretically and experimentally an inverse problem in rough surface scattering, namely, the design and fabrication of a random surface that scatters light in a prescribed way.

For many practical applications, it is desirable to have optical elements whose light-scattering properties can be controlled. In particular, a non-absorbing diffuser that scatters light uniformly within a specified range of scattering angles, and produces no scattering outside this range, would have applications, for example, to projection systems, where it is important to produce even illumination without wasting light. We will call such an element a band-limited uniform diffuser.

The design of uniform diffusers has been considered by several authors. The case of binary diffusers has been studied by Kurtz,[2] and work on special cases of one-dimensional diffusers has been reported by Kurtz *et al.*[3] and by Nakayama and Kato.[4] Some work on the more general two-dimensional case has been carried out by Kowalczyk.[5] In addition, diffractive optical elements that scatter light uniformly throughout specified angular regions have recently become commercially available. These elements, however, are not truly random, and possess the desired characteristics over only a relatively narrow range of wavelengths.

Despite the interest in the problem, there are no clear procedures at present for designing and fabricating random, band-limited, uniform diffusers, and it is unclear what kind of statistics are required for the production of such an optic element. In this paper, extending earlier work by the authors,[6,7] we address these questions for the case of one-dimensional diffusers. We illustrate the ideas involved by considering the scattering of *s*-polarized light from a one-dimensional, randomly rough, perfectly conducting surface. By working within the Kirchhoff approximation, and justify this approach by taking the geometrical optics limit of this approximation, we describe methods for designing and fabricating achromatic, random, uniform diffusers of light, and test these methods by computer simulations and experimentally.

1. LIGHT SCATTERING IN THE GEOMETRICAL OPTICS LIMIT OF THE KIRCHHOFF APPROXIMATION

To justify the calculations that follow, we begin by considering the scattering of *s*-polarized light from a one-dimensional, randomly rough, perfectly conducting surface defined by $x_3=\zeta(x_1)$. The region $x_3>\zeta(x_1)$ is vacuum, the region $x_3<\zeta(x_1)$ is the perfect conductor. The plane of incidence is the x_1x_3-plane. The surface-profile function $\zeta(x_1)$ is assumed to be a differentiable, single-valued function of x_1, and to constitute a random process, but not necessarily a stationary one.

The surface is illuminated from the vacuum region. The single nonzero component of the total electric field in this

region is the sum of an incident wave and of the scattered field

$$E_2(x_1,x_3|\omega)=\exp[ikx_1-i\alpha_0(k)x_3]+\int_{-\infty}^{\infty}\frac{dq}{2\pi}R(q|k)\exp[iqx_1+i\alpha_0(q)x_3], \tag{1.1}$$

where $\alpha_0(q)=[(\omega/c)^2-q^2]^{1/2}$, $\mathrm{Re}\,\alpha_0(q)>0$, $\mathrm{Im}\,\alpha_0(q)>0$, and ω is the frequency of the incident light. A time dependence of the form of $\exp(-i\omega t)$ is assumed, but explicit reference to it is suppressed.

In the Kirchhoff approximation, which we adopt here for simplicity, the scattering amplitude $R(q|k)$ is given by

$$R(q|k)=\frac{-i}{2\alpha_0(q)}\int_{-\infty}^{\infty}dx_1F(x_1|\omega)\times\exp[-iqx_1-i\alpha_0(q)\zeta(x_1)], \tag{1.2}$$

where the source function $F(x_1|\omega)$ is

$$F(x_1|\omega)=2\left(-\zeta'(x_1)\frac{\partial}{\partial x_1}+\frac{\partial}{\partial x_3}\right)\times E_2(x_1,x_3|\omega)_{inc}|_{x_3=\zeta(x_1)}. \tag{1.3}$$

Substitution of Eq. (1.3) into Eq. (1.2), followed by an integration by parts, yields the result that

$$R(q|k)=\frac{\omega^2/c^2+\alpha_0(q)\alpha_0(k)-qk}{\alpha_0(q)[\alpha_0(q)+\alpha_0(k)]}\times\int_{-\infty}^{\infty}dx_1\exp[-i(q-k)x_1-ia\zeta(x_1)], \tag{1.4}$$

where, to simplify the notation, we have defined $a=\alpha(q)+\alpha_0(k)$.

The mean differential reflection coefficient $\langle\partial R_s/\partial\theta_s\rangle$, which is defined such that $\langle\partial R_s/\partial\theta_s\rangle d\theta_s$ gives the fraction of the total, time-averaged, flux incident on the surface that is scattered into the angular interval $(\theta_s,\theta_s+d\theta_s)$, is given in terms of $R(q|k)$ by

$$\left\langle\frac{\partial R_s}{\partial\theta_s}\right\rangle=\frac{1}{L_1}\frac{\omega}{2\pi c}\frac{\cos^2\theta_s}{\cos\theta_0}\langle|R(q|k)|^2\rangle, \tag{1.5}$$

where the angle brackets denote an average over the ensemble of realizations of the surface profile function $\zeta(x_1)$, θ_0 and θ_s are the angles of incidence and scattering respectively, which are related to the wave numbers k and q by $k=(\omega/c)\sin\theta_0$ and $q=(\omega/c)\sin\theta_s$, and L_1 is the length of the x_1-axis covered by the random surface.

With the use of Eq. (1.4) the average $\langle|R(q|k)|^2\rangle$ entering Eq. (1.5) can be written as

$$\langle|R(q|k)|^2\rangle=\left[\frac{1+\cos(\theta_0+\theta_s)}{\cos\theta_s(\cos\theta_0+\cos\theta_s)}\right]^2\times\int_{-\infty}^{\infty}dx_1\int_{-\infty}^{\infty}dx_1'\exp[-i(q-k)(x_1-x_1')]\langle\exp[-ia(\zeta(x_1)-\zeta(x_1'))]\rangle. \tag{1.6}$$

We focus on the integral in Eq. (1.6). With the change of variable $x_1'=x_1+u$ it becomes

$$I(q|k)=\int_{-\infty}^{\infty}dx_1\int_{-\infty}^{\infty}du\exp[i(q-k)u]\times\langle\exp[-ia(\zeta(x_1)-\zeta(x_1+u))]\rangle. \tag{1.7}$$

The geometrical optics limit of the Kirchhoff approximation is obtained by expanding the difference $\zeta(x_1)-\zeta(x_1+u)$ in Eq. (1.7) in power of u and retaining only the leading nonzero term:

$$I(q|k)\cong\int_{-\infty}^{\infty}dx_1\int_{-\infty}^{\infty}du\exp[i(q-k)u]\times\langle\exp[iau\zeta'(x_1)]\rangle. \tag{1.8}$$

Because we have not assumed $\zeta(x_1)$ to be a stationary random process, we cannot assume that $\zeta'(x_1)$ is a stationary random process. The average $\langle\exp[iau\zeta'(x_1)]\rangle$, therefore, has to be assumed to be a function of x_1, and we cannot out the integral over x_1 to yield a factor of L_1, as we could if $\zeta(x_1)$ were a stationary random process.

2. DESIGN OF A BAND-LIMITED UNIFORM DIFFUSER

To evaluate the average in Eq. (1.8) we begin by writing the surface-profile function $\zeta(x_1)$ in the form

$$\zeta(x_1)=\sum_{l=-\infty}^{\infty}c_l s(x_1-2lb), \tag{2.1}$$

where the $\{c_l\}$ are independent, positive, random deviates. These properties of the $\{c_l\}$ are dictated by the fabrication process, described in Section 4. The function $s(x_1)$ is defined by

$$\begin{aligned}
s(x_1)\quad &=0, && x_1<-(m+1)b,\\
&=-(m+1)bh-hx_1, && -(m+1)b<x_1<-mb,\\
&=-bh, && -mb<x_1<mb,\\
&=-(m+1)bh+hx_1, && mb<x_1<(m+1)b,\\
&=0, && (m+1)\,b<x_1,
\end{aligned} \tag{2.2}$$

where m is a positive integer and b is a characteristic length.

The derivative of the surface-profile function, $\zeta'(x_1)$, is then given by

$$\zeta'(x_1)=\sum_{l=-\infty}^{\infty}c_l d(x_1-2lb), \tag{2.3}$$

where

$$\begin{aligned}
d(x_1)\quad &=0, && x_1<-(m+1)b,\\
&=-h, && -(m+1)b<x_1<-mb,\\
&=0, && -mb<x_1<mb,\\
&=h, && mb<x_1<(m+1)b,\\
&=0, && (m+1)b<x_1.
\end{aligned} \tag{2.4}$$

The function $s(x_1)$ and $d(x_1)$ are shown in Fig. 1.

In what follows the surface will be sampled at the set of equally spaced points $\{x_p\}$ defined by

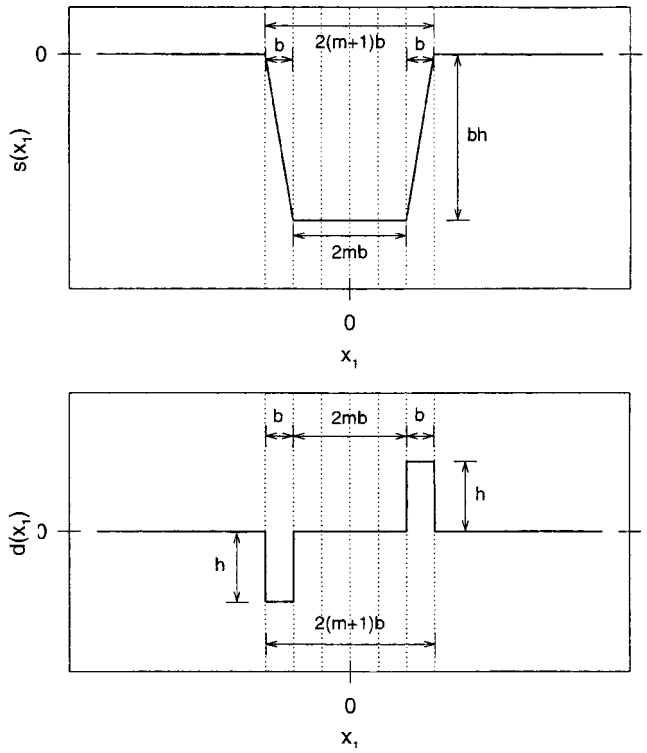

FIG. 1. The functions $s(x_1)$ and $d(x_1)$.

$$x_p=\left(p+\frac{1}{2}\right)b/Np=0,\pm1,\pm2,\ldots, \tag{2.5}$$

where N is a large positive integer. None of these values of x_p equals an integer multiple of b, at which $d(x_1)$ is discontinuous.

When the probability-density function (pdf) of c_l,

$$f(\gamma)=\langle\delta(\gamma-c_l)\rangle, \tag{2.6}$$

is known, a long sequence of the $\{c_l\}$ can be generated, e. g. by the rejection method,[7] from which the surface profile function $\zeta(x_1)$ can be obtained by the use of Eqs. (2.1) and (2.2). We note that, since the $\{c_l\}$ are positive random deviates, $f(\gamma)$ will be nonzero only for positive values of γ.

The average $\langle\exp iau\zeta'(x_1)\rangle$ can now be written as

$$\begin{aligned}\langle\exp iau\,\zeta'(x_1)\rangle&=\left\langle\exp\left\{iau\sum_{l=-\infty}^{\infty}c_l d(x_1-2lb)\right\}\right\rangle\\&=\left\langle\prod_{l=-\infty}^{\infty}\exp\{iau\,c_l d(x_1-2lb)\}\right\rangle\\&=\prod_{l=-\infty}^{\infty}\langle\exp\{iau\,c_l d(x_1-2lb)\}\rangle,\end{aligned} \tag{2.7}$$

where the independence of the $\{c_l\}$ has been used in the last step. With the form of $d(x_1)$ given by Eq. (2.4), for any value of x_1 chosen from the set of sampling points $\{x_p\}$ given by Eq. (2.5) only one factor in the infinite product on the right hand side of Eq. (2.7) is different from unity. Indeed, we find for $m=2$ that when $2nb<x_1<(2n+1)b$ $(n=0,\pm1,\pm2,\ldots)$

$$\begin{aligned}\langle\exp iau\,\zeta'(x_1)\rangle&=\langle\exp\{iauhc_{n-1}\}\rangle\\&=\int_{-\infty}^{\infty}d\gamma\,f(\gamma)\exp(iauh\gamma),\end{aligned} \tag{2.8a}$$

while when $(2n-1)b<x_1<2nb$ $(n=0,\pm1,\pm2,\ldots)$

$$\begin{aligned}\langle\exp iau\,\zeta'(x_1)\rangle&=\langle\exp\{-iauhc_{n+1}\}\rangle\\&=\int_{-\infty}^{\infty}d\gamma\,f(\gamma)\exp(-iauh\gamma).\end{aligned} \tag{2.8b}$$

When the results given by Eqs. (2.8) are substituted into Eq. (1.8), the latter becomes

$$\begin{aligned}I(q|k)&=\sum_n\int_{2nb}^{(2n+1)b}dx_1\int_{-\infty}^{\infty}du\,\exp[i(q-k)u]\\&\quad\times\int_{-\infty}^{\infty}d\gamma f(\gamma)\exp(ia\gamma hu)\\&\quad+\sum_n\int_{(2n-1)b}^{2nb}dx_1\int_{-\infty}^{\infty}du\,\exp[i(q-k)u]\\&\quad\times\int_{-\infty}^{\infty}d\gamma\,f(\gamma)\exp(-ia\gamma hu)\\&=\frac{L_1}{2}\int_{-\infty}^{\infty}du\,\exp[i(q-k)u]\int_{-\infty}^{\infty}d\gamma\,f(\gamma)\\&\quad\times[\exp(ia\gamma hu)+\exp(-ia\gamma hu)]\\&=\pi L_1\int_{-\infty}^{\infty}d\gamma f(\gamma)[\delta(q-k+ah\gamma)\\&\quad+\delta(q-k-ah\gamma)]\\&=\frac{\pi L_1}{ah}\left[f\left(\frac{k-q}{ah}\right)+f\left(\frac{q-k}{ah}\right)\right].\end{aligned} \tag{2.9}$$

We note that although Eqs. (2.8) were obtained for the case that $m=2$, the result given by Eq. (2.9) is valid for any m.

When the results given by Eqs. (1.7), (1.8) and (2.9) are substituted into Eq. (2.6), we find that the mean differential reflection coefficient is given by

$$\begin{aligned}\left\langle\frac{\partial R_s}{\partial\theta_s}\right\rangle&=\frac{1}{2h}\frac{[1+\cos(\theta_0+\theta_s)]^2}{\cos\theta_0(\cos\theta_0+\cos\theta_s)^3}\\&\quad\times\left[f\left(\frac{\sin\theta_0-\sin\theta_s}{h(\cos\theta_0+\cos\theta_s)}\right)\right.\\&\quad\left.+f\left(\frac{\sin\theta_s-\sin\theta_0}{h(\cos\theta_0+\cos\theta_s)}\right)\right].\end{aligned} \tag{2.10}$$

Thus, we find that, in the geometrical optics limit of the Kirchhoff approximation, the mean differential reflection coefficient is determined by the pdf $f(\gamma)$ of the coefficient c_l entering the expansions (2.1) and (2.3). We also note that it is independent of the wavelength of the incident light.

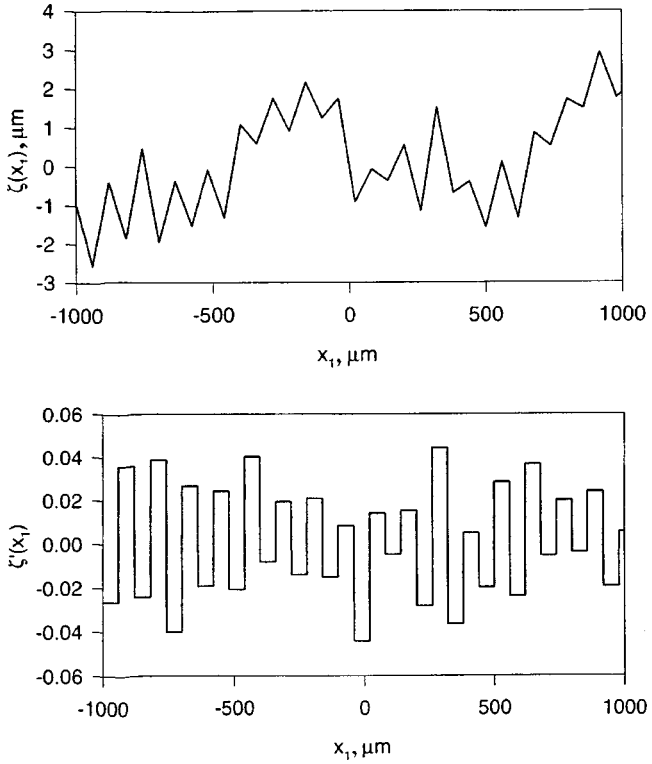

FIG. 2. Numerical generation of a surface profile and its derivative. The parameters employed are $b=60\ \mu$m, $m=1$, $\gamma_m=1$ and $\theta_m=5°$.

The result given by Eq. (2.10) simplifies significantly in the case of normal incidence, $\theta_0=0°$:

$$\left\langle \frac{\partial R_s}{\partial \theta_s} \right\rangle = \left(1+\tan^2 \frac{\theta_s}{2} \right) \frac{f\left(-\frac{1}{h}\tan\frac{\theta_s}{2} \right) + f\left(\frac{1}{h}\tan\frac{\theta_s}{2} \right)}{4h}. \tag{2.11}$$

The mean differential reflection coefficient given by this result is normalized to unity,

$$\int_{-\pi/2}^{\pi/2} d\theta_s \left\langle \frac{\partial R_s}{\partial \theta_s} \right\rangle = 1. \tag{2.12}$$

From the result given by Eq. (2.11) we find that if we wish a constant value for $\langle \partial R/\partial \theta_s \rangle$ for $-\theta_m < \theta_s < \theta_m$, we must choose

$$f(\gamma) = \frac{h}{\tan^{-1}\gamma_m h} \frac{\theta(\gamma)\,\theta(\gamma_m-\gamma)}{1+\gamma^2 h^2}, \tag{2.13}$$

where $\gamma_m=[\tan(\theta_m/2)]/h$, because in this case

$$\left\langle \frac{\partial R_s}{\partial \theta_s} \right\rangle = \frac{\theta(\theta_m-|\theta_s|)}{2\theta_m}. \tag{2.14}$$

It is worth noting that, if the maximum scattering angle $\theta_m = 2\tan^{-1}(h\gamma_m)$ is small enough, e.g., $\theta_m=20°$, so that $\gamma_m h=0.1763$, with little error we can neglect $\gamma^2 h^2$ compared to unity in the denominator on the right-hand side of Eq. (2.13) ($\gamma^2 h^2 < \gamma_m^2 h^2 = 0.0311$), and can replace $\tan^{-1}\gamma_m h$ by $\gamma_m h$ as well ($\tan^{-1}\gamma_m h = 0.1745$), to obtain for $f(\gamma)$ the simple form

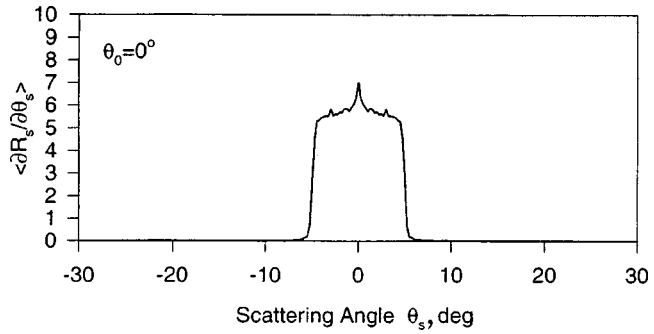

FIG. 3. The mean differential-reflection coefficient for normal incidence calculated from $N_p=3000$ realizations of the surface profile function. The parameters employed are $\lambda=0.6328\ \mu$m, $b=60\ \mu$m, $m=1$, $\gamma_m=1$, and $\theta_m=5°$. The sampling interval on the surface was $\Delta x=b/N=0.2\ \mu$m ($N=300$), and the length of the surface was $L_1=2000\ \mu$m.

$$f(\gamma) \cong \theta(\gamma)\,\theta(\gamma_m-\gamma)/\gamma_m. \tag{2.15}$$

If the required maximum scattering angle is not small, one has to use the result given by Eq. (2.13) for $f(\gamma)$.

3. COMPUTER SIMULATIONS

The approach to the design of band-limited uniform diffusers presented in the preceding sections was tested by means of computer simulation calculations. One-dimensional random surfaces were generated numerically on the basis of Eqs. (2.1) and (2.2) with the coefficients $\{c_l\}$ determined by the rejection method with the use of the pdf (2.15). As an example, we show in Fig. 2 a realization of a sample profile and its derivative, generated in this way.

For a given surface profile the scattering amplitude $R(q|k)$ can be calculated in the Kirchhoff approximation, but without passing to the geometrical optics limit, from Eq. (1.4). The mean differential-reflection coefficient can then be calculated from Eq. (1.5) by generating a large number N_p of surface profiles and averaging over the resulting scattering distributions. In Fig. 3 we show an example of a calculated mean differential-reflection coefficient determined by averaging results obtained for 3000 realizations of the surface profile function. It is seen that the scattering distribution is close to the desired result. There is almost no light outside the range $-\theta_m < \theta_s < \theta_m$ and, apart from a small peak in the specular direction, the distribution is fairly uniform. This peak is part of the diffuse component of the scattered light, as the spercular component is negligible in this case. It is due to the fact that our analysis is based on the geometrical optics approximation, and it is worth discussing this point in more detail.

We see from Eqs. (2.11) and (2.15) that, in the geometrical optics limit of the Kirchhoff approximation, the scattering distribution consists of two tectangular distributions, and it is clear that diffraction effects will smooth these two contributions. The peak observed in the specular direction in the scattering distribution plotted in Fig. 3 is due to the overlap of the tails of the two distributions predicted on the basis of the geometrical optics approximation. To illustrate this point

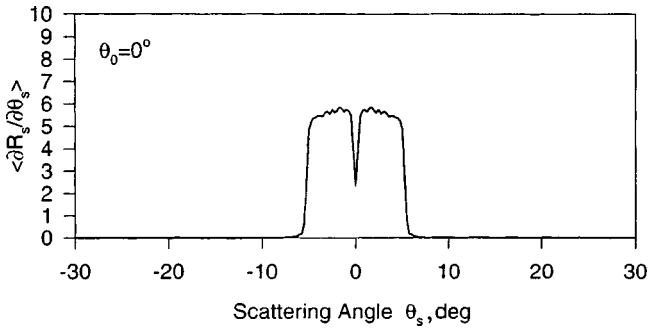

FIG. 4. The same as Fig. 3, but with random deviates $\{c_l\}$ drawn from the distribution given by Eq. (3.1) with $\varepsilon = 0.05$.

we present, in Fig. 4, a mean differential-reflection coefficient for the case in which the random numbers are generated from a drc of the form

$$f(\gamma) = \theta(\gamma - \varepsilon)\,\theta(\gamma_m + \varepsilon - \gamma)/\gamma_m, \tag{3.1}$$

where $\varepsilon = 0.05$. In our approximation, the scattering distribution is then given by

$$\left\langle \frac{\partial R_s}{\partial \theta_s} \right\rangle \cong \frac{1}{4\gamma_m h}\left[\theta\left(-\frac{\theta_s}{2h} - \varepsilon \right) \theta\left(\gamma_m + \varepsilon + \frac{\theta_s}{2h} \right) + \theta\left(\frac{\theta_s}{2h} - \varepsilon \right) \theta\left(\gamma_m + \varepsilon - \frac{\theta_s}{2h} \right) \right], \tag{3.2}$$

where the smallness of θ_m has been used to obtain this result. It can be seen that this distribution agrees well with the result shown in Fig. 4, the main difference being that, in the numerical results, the two sections of the scattering distribution are not completely separated due to the overlap of their tails, which give rise to a dip in $\langle \partial R_s/\partial \theta_s \rangle$. Thus, a value of ε intermediate between 0 and 0.5 should yield an approximately flat scattering curve. That this is the case is shown in Fig. 5, where $\langle \partial R_s/\partial \theta_s \rangle$ is plotted for a surface the basis of the pdf (3.1) with $\varepsilon = 0.01$, and for the same values of θ_0, b, m, γ_m, and θ_m used in obtaining Figs. 3 and 4. Results are presented for three wavelengths of the incident light: *a* — $\lambda = 0.6328\,\mu$m (He–Ne laser); *b* — $\lambda = 0.532\,\mu$m (the second harmonic of the YAG laser); *c* — $\lambda = 0.442\,\mu$m (He–Cd laser). These wavelengths cover the entire visible region of the optical spectrum. For each wavelengh the result for $\langle \partial R_s/\partial \theta_s \rangle$ is seen to consist of a nearly constant scattered intensity for θ_s between $-5°$ and $+5°$, and a zero scattered intensity outside this interval. Moreover, these results confirm the expected independence of the scattering pattern from the wavelength of the incident light over a significant range of wavelengths.

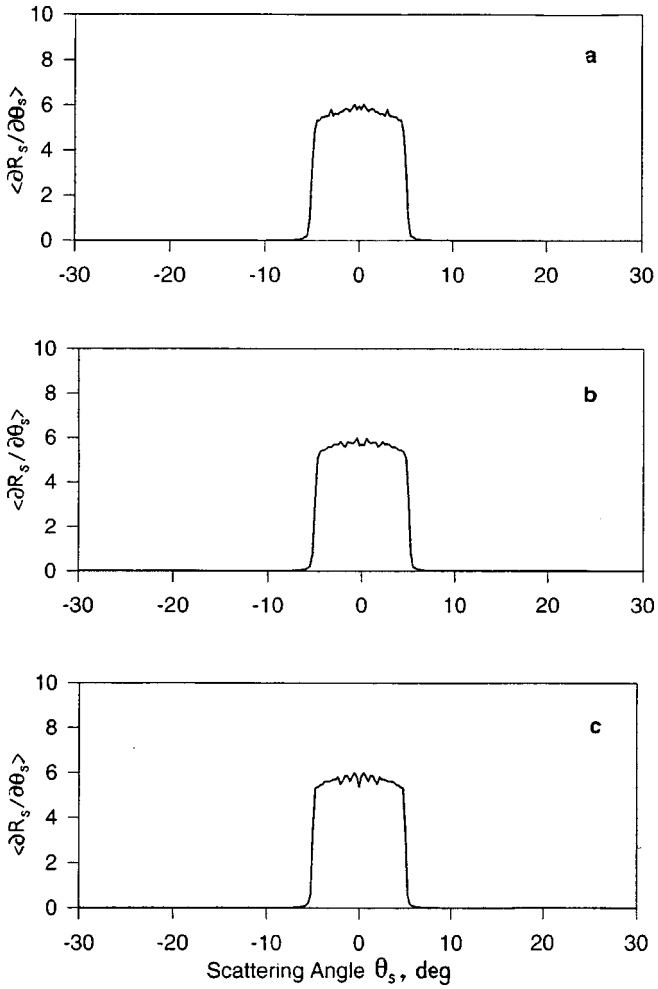

FIG. 5. The same as Fig. 4, but with $\varepsilon = 0.01$. a — $\lambda = 0.6328\,\mu$m; b — $\lambda = 0.532\,\mu$m; c — $\lambda = 0.442\,\mu$m.

4. EXPERIMENTAL RESULTS

A schematic diagram of the optical system used in our efforts to fabricate the kind of surface studied in this paper is shown in Fig. 6. The illumination is provided by a He–Cd laser (wavelength $\lambda = 442$ nm). An optical system concentrates the light transmitted through a rotating ground glass on

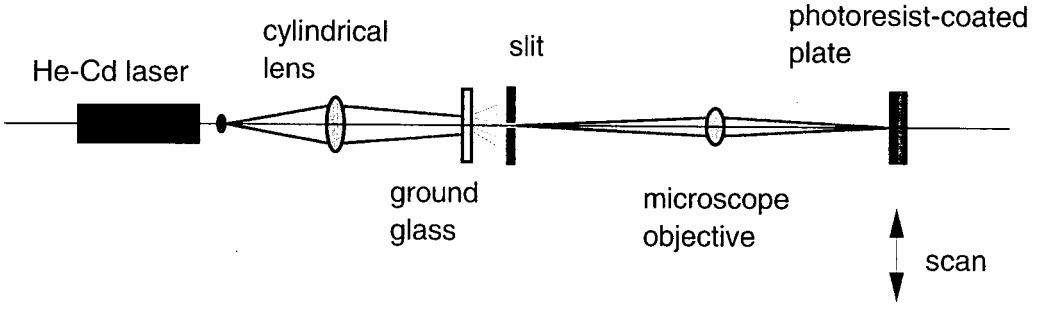

FIG. 6. Schematic diagram of the experimental arrangement employed for the fabrication of the diffusers.

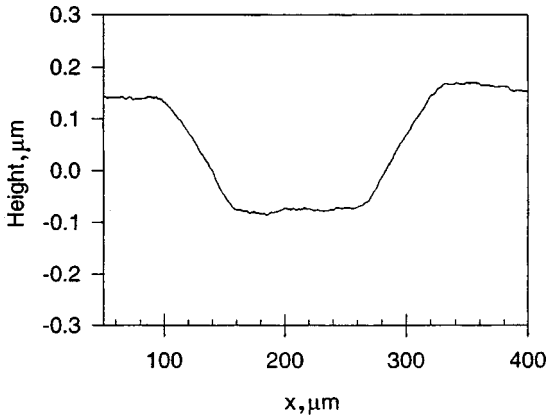

FIG. 7. Measured profile that illustrates the experimental realization of the function $s(x_1)$. The profile was measured by means of a Dektak$^{(st)}$ mechanical profilometer.

a slit, providing illumination that is effectively incoherent. An incoherent image of the slit is formed by an $\times 1$ (numerical aperture 0.05) microscope objective on a photoresist-coated glass plate.

The width of the slit is approximately $l=180\,\mu$m, and its incoherent image has a nearly restangular shape (smoothed by diffraction). In order to fabricate grooves with the desired trapezoidal shape on the photoresist, the plate is exposed while executing a scan of length $b=l/(2m+1)$. This procedure generates, basically, a function $s(x_1)$ with the shape defined by Eq. (2.2). The depth of the groove is determined by the time of exposure. An example of such a fabricated groove is shown in Fig. 7, which presents the measured surface profile of a section of a photoresist plate that was exposed in this fashion. Althought the corners are not as sparp as the ones in Fig. 1a, the result approximates the desired shape quite well.

The photoresist plate is exposed to grooves generated in this fashion, with random depths and displaced sequentially in steps of $2b$. Several hundred uncorrelated random numbers $\{c_l\}$ are generated in the computer with the specified $f(\gamma)$. At each position $x_1=2bl$, The exposure time of the groove is proportional to the random number c_l generated in the computer.[8]

In Fig. 8 we present a profileometer trace of one of the samples fabricated according to Eq. (2.1). The faceted nature

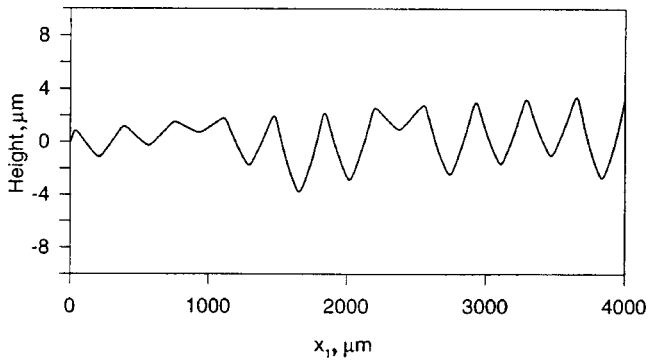

FIG. 8. Measured segment of a surface profile for a fabricated sample. The parameters are $b=60\,\mu$m, $m=0$.

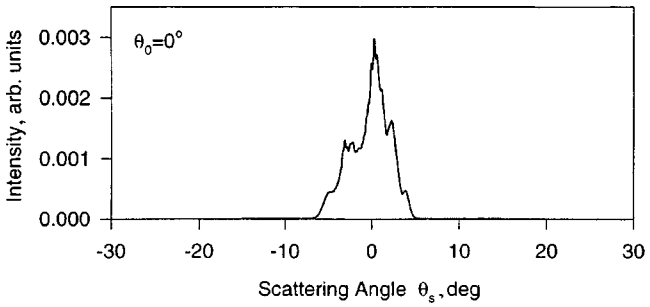

FIG. 9. Experimental result for the anglular dependence of the intensity of *s*-polarized light of wavelength $\lambda=0.6328\,\mu$m transmitted through a photoresist film. The angle of incidence is $\theta_0=0°$. The illuminated surface of the film is a one-dimensional random surface through which light is transmitted within the angle $-5°<\theta_s<5°$, and is not transmitted outside this range.

of the surface is clearly visible in Fig. 8. In the example displayed, we chose $m=0$, which produces a function $s(x_1)$ of triangular rather than trapezoidal form. The resulting symmetric triangular indentations are clearly visible in the figure. Thus, these preliminary results indicate that the proposed fabrication method is able to produce random uniform diffusers.

In order to study experimentally the scattering properties of these photoresist diffusers in reflection they would have had to be coated with a thin metallic layer. Instead, we studied these properties in the simpler case of the transmission of *s*-polarized light through them. Although the theoretical work motivating the method for fabricating the uniform diffusers described in the preceding sections was based on reflection, an analysis carried out within the framework of the geometrical optics limit of the thin-phase screen model[9] shows that surfaces that act as band-limited uniform diffusers in reflection also act as uniform band-limited diffusers in transmission, althought the maximum scattering angle θ_m in transmission is different than it is in reflection.[10] However, the transmission patterns obtained with the diffusers fabricated up to now, although band-limited, are not uniform (Fig. 9). Large intensity fluctuations are present in the angular region in which a constant intensity would be expected. The origin of these fluctuations is the small number of randomly oriented facets that are etched in our surfaces. They represent, simply, statistical noise. For the lengths of the surfaces that we have fabricated only about two hundred random numbers c_l are employed. Efforts are currently under way to fabricate surfaces with a larger number of randomly oriented facets.

5. SUMMARY AND CONCLUSIONS

In this paper we have described approaches to designing and fabricating one-dimensional, random, band-limited, uniform diffusers. These approaches are well suited for the generation of such surfaces on photoresist. The results of computer simulations, and some preliminary experimental results, indicate that uniform band-limited diffusers can be fabricated by the method proposed.

The design of band-limited uniform diffusers is but one interesting inverse problem involving the design of random

surfaces with specified scattering properties. The design of a Lamberitian diffuser, namely a random surface that produces a scattered intensity proportional to the cosine of the polar scattering angle, is another.[11] Finally, the design and fabrication of two-dimensional random surfaces with specified light scattering properties pose interesting theoretical and experimental challenges. Some first steps in this direction have been taken recently,[12] but more remains to be done.

This paper is dedicated to the A. F. Ioffe Physicotechnical Institute on the occasion of its 80th anniversary, with best wishes for many more years of significant contributions to science. The work reported here was supported in part by Army Research Office Grants DAAH 04–96–1–0187 and DAAG 55–98–C–0034.

*)E-mail: aamaradu@usi.edu

[1] L. I. Mandel'shtam, Ann. Phys. (Leipzig) **41**, 609 (1913).
[2] C. N. Kurtz, J. Opt. Soc. Am. **62**, 929 (1972).
[3] C. N. Kurtz, H. O. Hoadley, and J. J. DePalma, J. Opt. Soc. Am. **63**, 1080 (1973).
[4] Y. Nakayama and M. Kato, Appl. Opt. **21**, 1410 (1982).
[5] M. Kowalczyk, J. Opt. Soc. Am. A **1**, 192 (1984).
[6] E. R. Méndez, G. Martínez-Niconoff, A. A. Maradudin, and T. A. Leskova, SPIE **3426** (1998), in print.
[7] W. H. Press, S. A. Teukolsky, W. T. Vetterling, and B. P. Flannery, *Numerical Recipes, in Fortran, 2nd Edition* (Cambridge University Press, N.Y., 1992), p. 281.
[8] E. R. Méndez, M. A. Ponce, V. Ruiz-Cortés, and Zu-Han Gu, Appl. Opt. **30**, 4103 (1991).
[9] W. T. Welford, Opt. Quantum Electron. **9**, 269 (1977).
[10] T. A. Leskova, A. A. Maradudin, I. V. Novikov, A. V. Schchegrov, and E. R. Méndez, *Technical Report N98-2* (University of California, Irvine, Department of Physics and Astronomy, 1998).
[11] H. P. Balthes, in *Inverse Scattering Problems in Optics*, edited by H. P. Balthes, (Springer-Verlag, N.Y. 1998), p. 1.
[12] E. R. Méndez, G. Marínez-Niconoff, A. A. Maradudin, and T. A. Leskova, *Proc. Reunion Iberoamericana de Optica, Cartagena, Columbia (1998)*, in press.

Published in English in the original Russian journal. Reproduced here with stylistic changes by the Translation Editor.